

POLISH SOCIETY OF THEORETICAL AND APPLIED MECHANICS

**JOURNAL OF THEORETICAL
AND APPLIED MECHANICS**

No. 1 • Vol 54

Quarterly

WARSAW, JANUARY 2016

JOURNAL OF THEORETICAL AND APPLIED MECHANICS

(until 1997 Mechanika Teoretyczna i Stosowana, ISSN 0079-3701)

Beginning with Vol 45, No. 1, 2007, *Journal of Theoretical and Applied Mechanics* (JTAM) has been selected for coverage in Thomson Reuters products and custom information services. Now it is indexed and abstracted in the following:

- **Science Citation Index Expanded** (also known as SciSearch®)
- **Journal Citation Reports/Science Edition**

Advisory Board

MICHAŁ KLEIBER (Poland) – Chairman

JORGE A.C. AMBROSIÓ (Portugal) * ANGEL BALTOV (Bulgaria) * ROMESH C. BATRA (USA) *
ALAIN COMBESCURE (France) * JÜRI ENGELBRECHT (Estonia) * WITOLD GUTKOWSKI (Poland) *
JÓZEF KUBIK (Poland) * GERARD A. MAUGIN (France) * ZENON MRÓZ (Poland) *
RYSZARD PARKITNY (Poland) * EUGENIUSZ ŚWITOŃSKI (Poland) * HISAAKI TOBUSHI (Japan) *
DIETER WEICHERT (Germany) * JOSE E. WESFREID (France) * JÓZEF WOJNAROWSKI (Poland) *
CZESŁAW WOŹNIAK (Poland) * JOSEPH ZARKA (France) * VLADIMIR ZEMAN (Czech Republic)

Editorial Board

WŁODZIMIERZ KURNIK – Editor-in-Chief,

KRZYSZTOF DEMS, KURT FRISCHMUTH (Germany), PIOTR KOWALCZYK, ZBIGNIEW KOWALEWSKI,
TOMASZ KRZYŻYŃSKI, TOMASZ ŁODYGOWSKI, EWA MAJCHRZAK, WIESŁAW NAGÓRKO,
JANUSZ NARKIEWICZ, ANDRZEJ STYCZEK, ANDRZEJ TYLIKOWSKI, UTZ VON WAGNER (Germany),
JERZY WARMIŃSKI, ELŻBIETA WILANOWSKA – Secretary

Language Editor – PIOTR PRZYBYŁOWICZ



Articles in JTAM are published under Creative Commons Attribution – Non-commercial 3.0. Unported License <http://creativecommons.org/licenses/by-nc/3.0/legalcode>. By submitting an article for publication, the authors consent to the grant of the said license.

* * * * *

Editorial Office

Building of Civil Engineering Warsaw University of Technology
Al. Armii Ludowej 16, room 650
00-637 Warszawa, Poland
phone (+48 22) 825 7180, (+48) 664 099 345, e-mail: biuro@ptmts.org.pl

www.ptmts.org.pl/jtam.html

* * * * *

Publication supported by Ministry of Science and Higher Education of Poland

CONTINUOUS AND DISCRETE SLIDING MODE CONTROL OF AN ACTIVE CAR SUSPENSION SYSTEM

JAN ŁUCZKO, URSZULA FERDEK

Cracow University of Technology, Faculty of Mechanical Engineering, Kraków, Poland
e-mail: jluczko@mech.pk.edu.pl; uferdek@mech.pk.edu.pl

In this paper, sliding mode control (SMC) algorithms are tested for their use in an active car suspension system. Using the quarter model of the car as an example, the comparison of the efficiency of the algorithms is made. A continuous and two discrete versions of the sliding mode control are taken into consideration. The study is limited to finding the relation between the control parameters and the comfort factor. This is done by analyzing the response of the model to the harmonic and impulse excitation.

Keywords: sliding mode control, active damping, car suspension

1. Introduction

The most common types of suspension systems used in automobiles are passives ones. Their construction is based on several spring and damping elements with constant, linear or nonlinear characteristics. When designing a passive car suspension, it is necessary to choose the optimal damping coefficient that would allow both the comfort and safety to be on a high enough level (Łuczko and Ferdek, 2012). An alternative option is to use suspension which can modify its properties during ride of the vehicle – namely an active or a semi-active system. In the case of active suspension, the spring and damping elements are replaced with servomotors. This way the force generated in the suspension can be used to influence both the comfort and safety of the ride. Although active suspension systems are more complex and require more energy, they are more and more often considered and included in designs of modern vehicles.

One of the possible options for the active suspension control is to use a sliding mode control (SMC) algorithm (Yoshimura *et al.*, 2001; Sam *et al.*, 2004; Lin *et al.*, 2009). The idea of the algorithm is to guide the model in the state-space, to a specific plane called “the sliding plane” and to keep it as close to this plane as possible. Therefore, two separate phases of this control can be listed: the “approach” phase, which lasts until the point describing the dynamics of the system reaches the switching hyperplane, and the “sliding” phase. In the second phase, the system is forced to “slide” along a sliding plane up to the desired point by using a discontinuous control signal. Most often, it is assumed that the sliding plane equation is linear and related to the regulation error.

The application of the sliding mode control to a physical system is accompanied by the so-called “chattering” effect (Lee and Utkin, 2007) – high-frequency oscillations which might cause wear or damage to the actuator. It is therefore essential to eliminate this effect from the regulation process.

As most of modern control systems are implemented as digital, below a procedure for designing a discrete sliding mode controller (DSMC) for control of a car suspension is presented. The most important advantages of the digital control are reduction of device cost, possibility to implement complicated control rules and higher control precision.

In this study, a quarter model of the car is used for the purpose of testing the efficiency of damping the vibration by application of different control strategies. The performance factor includes parameters related to comfort of the ride.

2. Model of the system

The analysis has been performed on a quarter model of the car (Huang and Chen, 2006; Rajeswari and Lakshmi, 2008; Snamina *et al.*, 2011) consisting of a non-spring-supported mass m_w (mass of the wheel, axle and some elements of the drive transmission) and a spring-supported mass m_b (1/4 of the other mass, mostly the car body). It has been assumed that the road influence on the wheel can be described using a harmonic or impulse kinematic excitation $w(t)$. The analysis included the influence of the control and disturbance on the behavior of the system. Both the control and disturbance forces have been assumed to act at the point connecting the car body and the suspension.

The oscillation of the system around the static equilibrium point can be given by a set of the two second-order differential equations

$$\begin{aligned} m_w \ddot{y}_w &= -c_w(\dot{y}_w - \dot{w}) - k_w(y_w - w) + c_b(\dot{y}_b - \dot{y}_w) + k_b(y_b - y_w) - u - z \\ m_b \ddot{y}_b &= -c_b(\dot{y}_b - \dot{y}_w) - k_b(y_b - y_w) + u + z \end{aligned} \quad (2.1)$$

where y_w and y_b are the displacement of the non-spring-supported and spring-supported mass, respectively. The parameters k_w and c_w define the stiffness and damping of the wheel, while k_b and c_b are the same for the passive vibro-isolation system.

By configuring the velocities and displacements of both masses to be included in the state vector $\mathbf{x} = [y_w, y_b, \dot{y}_w, \dot{y}_b]^T$, Eqs. (2.1) can be written in the form of a first-order matrix differential equation

$$\dot{\mathbf{x}} = \mathbf{A}\mathbf{x} + \mathbf{B}(u + z) + \mathbf{F}w \quad (2.2)$$

where

$$\begin{aligned} \mathbf{A} &= \begin{bmatrix} 0 & 0 & 1 & 0 \\ 0 & 0 & 0 & 1 \\ -(k_w + k_b)/m_w & k_b/m_w & -(c_w + c_b)/m_w & c_b/m_w \\ k_b/m_b & -k_b/m_b & c_b/m_b & -c_b/m_b \end{bmatrix} \\ \mathbf{B} &= \begin{bmatrix} 0 \\ 0 \\ -1/m_w \\ 1/m_b \end{bmatrix} & \mathbf{F} &= \begin{bmatrix} 0 \\ 0 \\ k_w/m_w \\ 0 \end{bmatrix} \end{aligned} \quad (2.3)$$

3. SMC continuous regulation algorithm

Figure 1 shows a block diagram of the system with the sliding mode control (Sam and Osman, 2005; Chen and Huang, 2005; Sam *et al.*, 2008).

In order to increase the ride comfort, the parameters of the regulator are adjusted using the minimization condition for the variables that describe the movement of the spring-supported mass. The reduction of the car body vibration can be accomplished by introducing the following sliding plane

$$S = \mathbf{D}\mathbf{x} \quad (3.1)$$

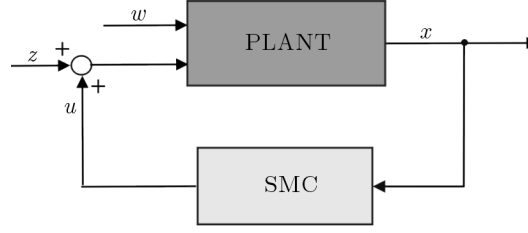


Fig. 1. Block diagram of a continuous SMC

where the transposed vector \mathbf{D} is defined as follows

$$\mathbf{D} = [0, \kappa, 0, 1] \quad (3.2)$$

This definition of the vector \mathbf{D} should provide the minimal displacement $x_2 = y_b$ and velocity $x_4 = \dot{y}_b$ of the spring-supported mass. From the dynamical condition of the ideal sliding motion

$$\dot{\mathbf{S}} = \mathbf{D}\dot{\mathbf{x}} = \mathbf{D}[\mathbf{A}\mathbf{x} + \mathbf{B}(u + z) + \mathbf{F}w] = \mathbf{0} \quad (3.3)$$

the equivalent (compensation) control $u^{eq}(t)$ is obtained, which after the omission of the excitation and disturbance influence can be written using the formula

$$u^{eq}(t) = -(\mathbf{DB})^{-1}\mathbf{DA}\mathbf{x} \quad (3.4)$$

An additional switching control $u^{sw}(t)$ is also included in order to guarantee the stability of the system. The control u^{sw} is discontinuous with the sliding plane set as the switching line. This control can be calculated from the equation

$$u^{sw}(t) = -K^{sw}(\mathbf{DB})^{-1} \text{sgn}(\mathbf{D}\mathbf{x}) \quad (3.5)$$

The sliding mode control is the sum of both of these components

$$u(t) = u^{eq}(t) + u^{sw}(t) \quad (3.6)$$

The sliding control realized in accordance to the algorithm presented above operates by dynamical compensation of the suspension stiffness and the introduction of additional damping. The switching component of control keeps the system close to the sliding plane. If the constant K^{sw} is large enough, then the system becomes resistant to inaccuracies of the model. In practice, in order to limit the excessive switching ("chattering" effect) the signum function present in Eq. (3.5) is substituted by its approximation, e.g. "saturation" function. For the purpose of numerical calculations performed in this study, an arctangent approximation function has been used.

4. SMC discrete regulation algorithm

Due to the fact that the modern control systems are more often realized using digital devices, the sliding algorithm presented above needs to be modified. In order to choose the parameters for the discrete sliding mode controller, the following discrete equations are used (Yu *et al.*, 2004; Yan and Fan, 2012)

$$\mathbf{x}_{k+1} = \mathbf{A}_d\mathbf{x}_k + \mathbf{B}_d(u_k + z_k) + \mathbf{F}_dw_k \quad (4.1)$$

where

$$\mathbf{A}_d = \Phi(T_s) \quad \mathbf{B}_d = \Psi\mathbf{B} \quad \mathbf{F}_d = \Psi\mathbf{F} \quad (4.2)$$

with T_s being the sampling time. The matrix functions Φ and Ψ are defined as

$$\Phi(\tau) = \exp(\mathbf{A}\tau) \quad \Psi = [\Phi(T_s) - \mathbf{I}]\mathbf{A}^{-1} \quad (4.3)$$

The sliding plane can be chosen in the similar form as before (3.1)

$$\mathbf{S}_k = \mathbf{D}\mathbf{x}_k \quad (4.4)$$

By introducing

$$f_k = \mathbf{B}_d z_k + \mathbf{F}_d w_k \quad (4.5)$$

from the condition

$$\mathbf{S}_{k+1} = \mathbf{D}\mathbf{x}_{k+1} = \mathbf{D}(\mathbf{A}_d \mathbf{x}_k + \mathbf{B}_d u_k + f_k) = 0 \quad (4.6)$$

the equivalent control can be found

$$u_k^{eq} = -(\mathbf{D}\mathbf{B}_d)^{-1} \mathbf{D}(\mathbf{A}_d \mathbf{x}_k + f_k) \quad (4.7)$$

Usually, f_k component, whose value changes depending on the unknown excitation and disturbance, can be omitted, and the equivalent control component can be calculated from the equation

$$u_k^{eq} = -(\mathbf{D}\mathbf{B}_d)^{-1} \mathbf{D}\mathbf{A}_d \mathbf{x}_k \quad (4.8)$$

In order to eliminate the component f_k from Eq. (4.7), an assumption is made that its value varies only slightly from the value in the previous step, giving $f_k \approx f_{k-1}$. By using additionally discrete state equation (4.1), it can be shown that

$$f_k \approx f_{k-1} = \mathbf{x}_k - \mathbf{A}_d \mathbf{x}_{k-1} - \mathbf{B}_d u_{k-1} \quad (4.9)$$

After transformation, the final form of the equation describing the equivalent control can be written

$$u_k^{eq} = u_{k-1} - (\mathbf{D}\mathbf{B}_d)^{-1} [(\mathbf{D}\mathbf{A}_d + \mathbf{D})\mathbf{x}_k - \mathbf{D}\mathbf{A}_d \mathbf{x}_{k-1}] \quad (4.10)$$

The switching component u_k^{sw} is defined by a similar equation as Eq. (3.5)

$$u_k^{sw} = -K^{sw} (\mathbf{D}\mathbf{B}_d)^{-1} \text{sgn}(\mathbf{D}_d \mathbf{x}_k) \quad (4.11)$$

where the final control is the sum of both components.

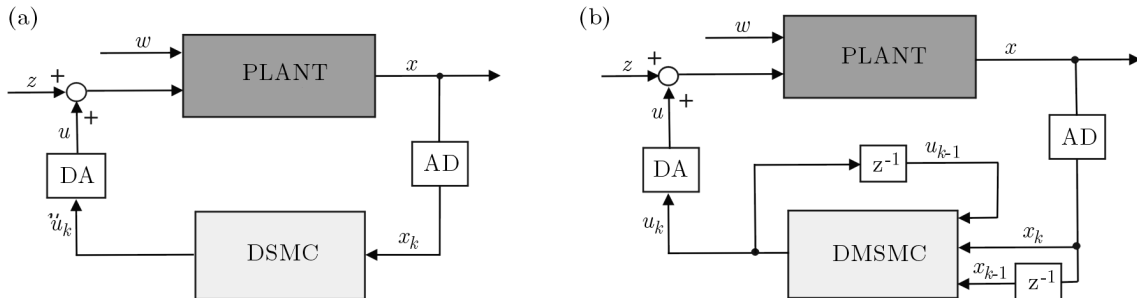


Fig. 2. Block diagrams of the discrete system (AD – analog/digital converter, DA – digital/analog converter): (a) DSMC, (b) DMSMC

Using numerical calculations, the efficiency of the DSMC regulator (Fig. 2a) with the equivalent control obtained using formula (4.8) is compared with the efficiency of the modified DMSMC regulator (Fig. 2b) related to equation (4.10).

5. Results of numerical calculations

The emphasis of the numerical simulation is placed on finding the influence of the disturbance on the behavior and efficiency of the continuous SMC, discrete DSMC and DMSMC controllers. The following parameter values are chosen for matrices (2.3): $m_w = 28$ kg, $m_b = 510$ kg, $k_w = 180000$ N/m, $k_b = 20000$ N/m, $c_b = 1000$ Ns/m. The analysis is limited to the response of the system under the harmonic excitation of amplitude $a_0 = 0.005$ m and angular frequency $\omega = 8.396$ rad/s (first vibration mode of the passive system without control) and to the impulse excitation described in detail later on.

Several dimensionless parameters are introduced: β_x , β_v , γ , τ_s and defined using equations: $\beta_x = \kappa_x K_x$, $\beta_v = \kappa_v K_v$, $\gamma = K^{sw}/\omega_0$ and $\tau_s = T_s/T_0$, where: $K_x = a_0$, $K_v = \omega_0 a_0$, $T_0 = 2\pi/\omega_0$, and $\omega_0 = \sqrt{k_b/m_b}$ correspond to the first vibration mode of the system. The function $\text{sgn}(S)$ present in Eqs. (3.5) and (4.11) is substituted by continuous $2/\pi \arctan(\eta S)$ with $\eta = 100$ used for the calculations.

It is assumed that the disturbance is in the form of a Gaussian white noise of zero average value and variance of value 25 N^2 (standard deviation $s_0 = 5$ N). An exemplary realization of this disturbance for the sampling time $T_s = 0.05T_0$ is shown in Fig. 3.

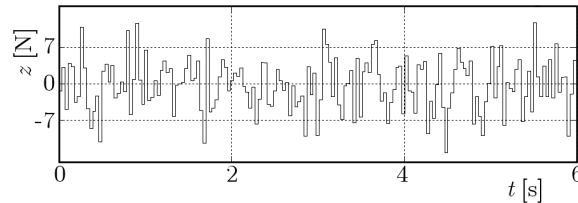


Fig. 3. An example of the disturbance signal

Figure 4 shows the displacement of the spring-supported mass for the continuous SMC, discrete DSMC, Eq. (4.8), and modified discrete DMSMC regulator, Eq. (4.10). For the discrete control, the sampling time was $T_s = 0.02T_0$ ($\tau_s = 0.02$). By comparing the results, one can notice that in the case of discrete control, the response looks periodic in contrast to the aperiodic continuous control SMC. On the assumed control parameters, the efficiency of SMC and DMSMC regulator is comparable.

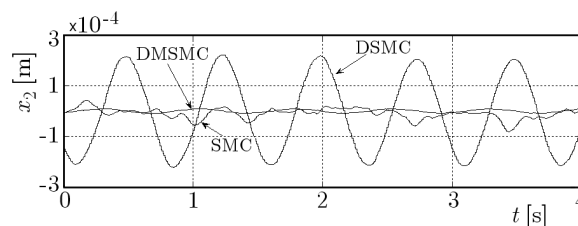


Fig. 4. Displacement plot: SMC ($\beta_x = \beta_v = 1$, $\gamma = 0.1$), DSMC ($\beta_x = \beta_v = 1$, $\gamma = 0.001$), DMSMC ($\beta_x = \beta_v = 1$, $\gamma = 0.001$)

The irregularity seen in the response to the SMC regulator is caused by the high sensitivity of the system to the external disturbance. This fact is supported by Fig. 5 in which the response to three disturbance signals of different standard deviations $s = 5, 10$ and 15 N is shown (for $s = ns_0$, $n = 1, 2, 3$, $s_0 = 5$ N). The change in the response to these disturbances is nearly linear (with linear rise of the disturbance). Although the amplitude of vibration can be attenuated by increasing the value of parameters β_x and γ , setting them too high is undesirable due to the effect of “chattering”, and also due to the time delay present between the regulator and the actuator.

In the case of the modified DMSMC digital controller, the response to the disturbance is definitely lower. When using the same values of n that define the disturbance as before,

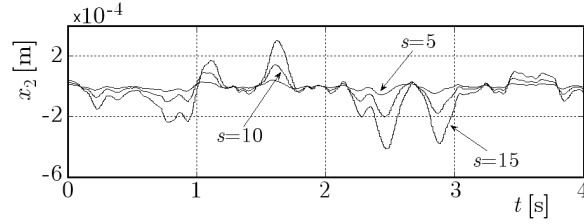


Fig. 5. Influence of the disturbance on the displacements – SMC ($\beta_x = \beta_v = 1$, $\gamma = 0.1$)

the difference between the responses is practically undetectable. Therefore, Fig. 6 shows the displacement for $n = 1$ and $n = 20$ (with $\tau_s = 0.02$). Even with twenty times higher value of s ($s = 5$ N and 100 N), the differences are still minor, which means that the DMSMC system is resistant to the disturbance.

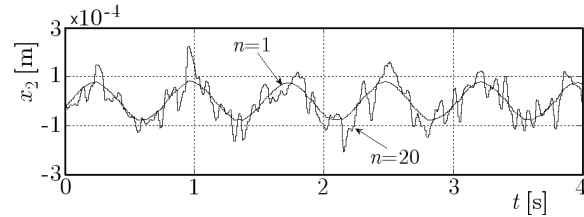


Fig. 6. Influence of the disturbance on the displacements – DMSMC ($\beta_x = \beta_v = 1$, $\gamma = 0.001$)

The efficiency of the discrete regulator is decreased when the sampling time increases (Fig. 7). The presented displacements are obtained for the DMSMC with different sampling times $\tau_s = 0.01, 0.02, 0.03$ and $\beta_x = \beta_v = 1$, $\gamma = 0.001$ and $s = 5$ N. The relation of the amplitude of vibration with the sampling time is nonlinear, e.g. a change in τ_s from 0.01 to 0.02 leads to the amplitude rise by ten times. When rise of τ_s is continued, the amplitude of vibration is changed by a smaller factor. On the other hand, too small sampling time is undesirable due to computation time taken for the realization of digital control.

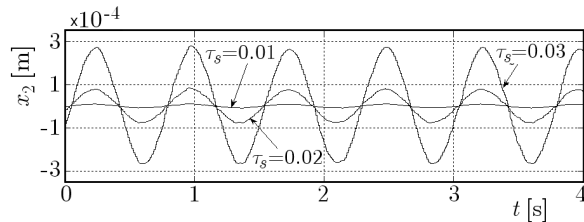


Fig. 7. Relation between the sampling time and displacements – DMSMC ($\beta_x = \beta_v = 1$, $\gamma = 0.001$)

Figure 8 shows the displacements (Fig. 8a – for $\beta_x = 0.1, 1, 2$) and velocities (Fig. 8b – for $\beta_x = 1$ only) of the spring-supported mass in the DMSMC system ($\beta_v = 1$, $\gamma = 0.001$, $\tau_s = 0.02$).

With the rise of value β_x , the maximal displacements are decreased but the maximal velocities and accelerations are increased. In addition to that, the character of vibration is changed, with more influence of high-frequency component present in the system. For high enough values of β_x , the chattering effect starts to occur.

In order to test the behavior of the vibroisolation system, when crossing an obstacle, analysis of the response to the impulse excitation has been performed.

To describe the excitation in simulations, the bump “rounded pulse” function has been used. It is defined as follows (Shekhar *et al.*, 1999)

$$w(t) = \frac{1}{4}h[e\eta(t - t_0)]^2 \exp[-\eta(t - t_0)]H(t - t_0) \quad (5.1)$$

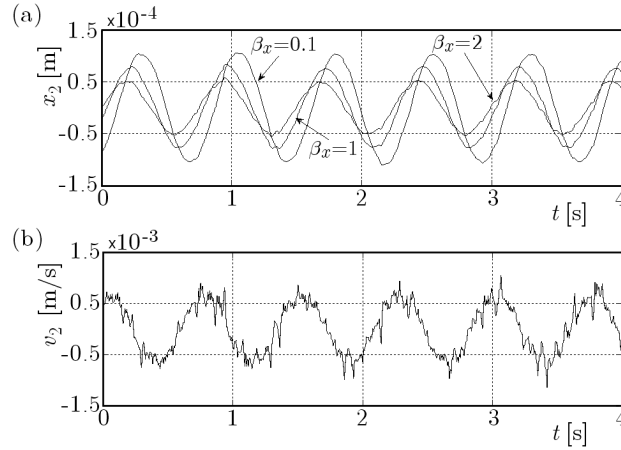


Fig. 8. Effect of the parameter β_x – DMSMC system ($\beta_v = 1$, $\gamma = 0.001$, $\tau_s = 0.02$): (a) displacements, (b) velocities ($\beta_x = 1$)

where $H(t-t_0)$ is the Heaviside function. Equation (5.1) has continuous first and second derivatives and the maximal value equal to h (Fig. 9). The parameter η defines the sharpness of the impulse. At $\eta = \omega_{n1} = 8.396$ rad/s, the impulse duration is equal to the half of the first vibration mode period. In numerical calculations, the value h has been chosen to be equal to 0.05 m.

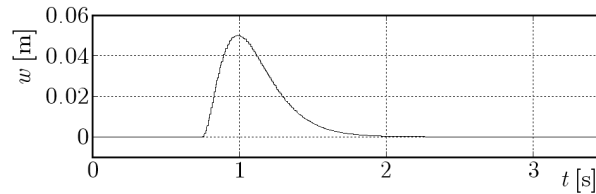


Fig. 9. Impulse excitation ($\gamma = 8.396$ rad/s, $h = 0.05$ m)

Figure 10 shows the response of the SMC ($\beta_x = \beta_v = 1$, $\gamma = 0.1$) and DMSMC ($\beta_x = \beta_v = 1$, $\gamma = 0.001$) system to impulse excitation (5.1). In both cases, the rate of displacement reduction is similar. In the case of the SMC, the damping of the disturbance (Fig. 10a) is slower when considered in relation to DMSMC, but it is also less steep, see the velocity plot in Fig. 10b.

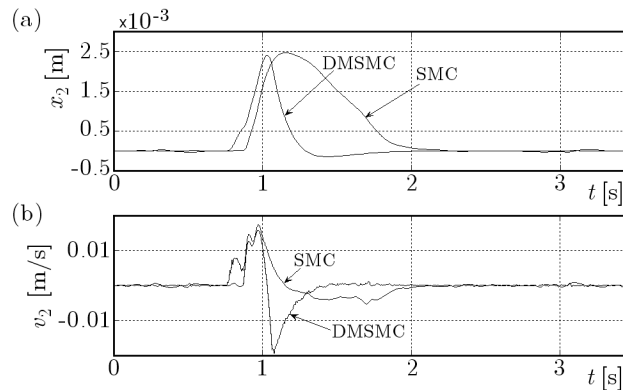


Fig. 10. Response to the impulse excitation – regulators: SMC ($\beta_x = \beta_v = 1$, $\gamma = 0.1$) and DMSMC ($\beta_x = \beta_v = 1$, $\gamma = 0.001$): (a) displacements, (b) velocities

In the considered example, if the value of γ is too high (for $\gamma > 0.01$, $\beta_x = 1$), the “chattering” effect occurs (Fig. 11). Apart from the additional high-frequency oscillations, the changes in the value are twice as high as for the system with optimally chosen parameters of control (Fig. 10a).

In addition to that, an increase in the value of β_x , causes the possibility of occurring of the chatter to be higher (at $\beta_x > 10$, the chattering can be observed for $\gamma = 0.001$).

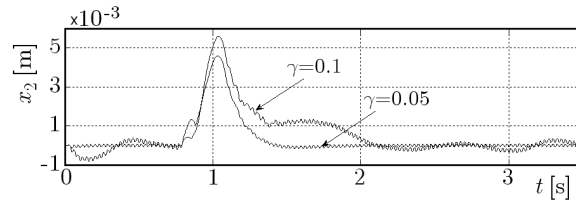


Fig. 11. Displacement plot with chattering ($\beta_x = \beta_v = 1$, $\gamma = 0.05, 0.1$, $\tau_s = 0.02$)

6. Summary

The analysis of the results allows formulating of the following conclusions:

- In all the considered active systems, the reduction of vibration is well enough, at least within the range that includes the first vibration mode. As this mode is significant, when considering vibration of the car body, it should be noted that making use of the presented regulators greatly increases the driving comfort.
- The continuous SMC regulator, for very high values of parameters β_x and γ , is theoretically more effective than discrete regulators. However, it is more susceptible to disturbances as well as the time delay present during control.
- From the two presented discrete regulators, the better one is definitely DMSMC. It is much more resistant to disturbances, and for small sampling times, its performance is comparable to SMC.
- When adjusting the parameters of sliding mode regulators, the possibility of the “chattering” effect to occur should be taken into consideration. Values of the regulator parameters should allow the optimal and regular operation of the regulator without undesirable high-frequency oscillations.

References

1. CHEN P.-C., HUANG A.-C., 2005, Adaptive sliding control of non-autonomous active suspension systems with time-varying loadings, *Journal of Sound and Vibration*, **282**, 1119-1135
2. HUANG S.-J., CHEN H.-Y., 2006, Adaptive sliding controller with self-tuning fuzzy compensation for vehicle suspension control, *Mechatronics*, **16**, 607-622
3. LEE H., UTKIN V.I., 2007, Chattering suppression methods in sliding mode control systems, *Annual Reviews in Control*, **31**, 179-188
4. LIN J., LIAN R.-J., HUANG C.-N., SIE W.-T., 2009, Enhanced fuzzy sliding mode controller for active suspension systems, *Mechatronics*, **19**, 1178-1190
5. ŁUCZKO J., FERDEK U., 2012, Comparison of different control strategies in a semi-active vehicle suspension system (in Polish), *Czasopismo Techniczne*, **11**, 6-M, 81-92
6. RAJESWARI K., LAKSHMI P., 2008, GA tuned distance based fuzzy sliding mode controller for vehicle suspension systems, *International Journal of Engineering and Technology*, **5**, 1, 36-47
7. SAM Y.M., OSMAN J.H.S., 2005, Modeling and control of the active suspension system using proportional integral sliding mode approach, *Asian Journal of Control*, **7**, 2, 91-98
8. SAM Y.M., OSMAN J.H.S., GHANI M.R.A., 2004, A class of proportional-integral sliding mode control with application to active suspension system, *Systems and Control Letters*, **51**, 217-223

9. SAM Y.M., SUAIB N.M., OSMAN J.H.S., 2008, Hydraulically actuated active suspension system with proportional integral sliding mode control, *WSEAS Transactions on Systems and Control*, **9**, 3, 859-868
10. SHEKHAR N.C., HATWAL H., MALLIK A.K., 1999, Performance of non-linear isolators and absorbers to shock excitations, *Journal of Sound and Vibration*, **227**, 2, 293-307
11. SNAMINA J., KOWAL J., WZOREK T., 2011, Analysis of energy dissipation in vehicle suspensions for selected control algorithms (in Polish), *Czasopismo Techniczne*, **2**, 1-M, 233-240
12. YAN M., FAN L., 2012, Discrete sliding mode control for DC-DC converters with uncertainties, *Przegląd Elektrotechniczny*, **88**, 5b, 60-63
13. YOSHIMURA T., KUME A., KURIMOTO M., HINO J., 2001, Construction of an active suspension system of a quarter car model using the concept of sliding mode control, *Journal of Sound and Vibration*, **239**, 2, 187-199
14. YU W.-C., WANG G.-J., CHANG C.-C., 2004, Discrete sliding mode control with forgetting dynamic sliding surface, *Mechatronics*, **14**, 737-755

Manuscript received December 12, 2014; accepted for print March 31, 2015

NUMERICAL ANALYSIS OF DYNAMICS OF AN AUTOMATICALLY TRACKED ANTI-TANK GUIDED MISSILE USING POLYNOMIAL FUNCTIONS

ZBIGNIEW KORUBA, ŁUKASZ NOCOŃ

Kielce University of Technology, Faculty of Mechatronics and Machine Design, Kielce, Poland

e-mail: ksmzko@tu.kielce.pl, waldek.afro@op.pl

The paper presents algorithms of automatic control of an intelligent anti-tank guided missile (ATGM) with possibility of attacking the target from the upper ceiling and with possibility of the missile flight through indicated points in space. The polynomial functions are used to designate the program trajectories. Numerical analysis of the operation of chosen algorithms is performed. The results are presented in a graphical form. As it results from the conducted tests, the proposed algorithms of automatic control of ATGM with the use of polynomial functions work properly during attack on the target from the upper ceiling, for both mobile and immobile targets.

Keywords: homing, direction algorithm, anti-tank guided missile

1. Introduction

This paper presents a medium-range anti-tank guided missile (ATGM) which is characterized by high maneuverability of flight, ability to attack a target from the upper hemisphere with the possibility to apply the feint. The passive guidance limits its tracking possibilities and the target can be selected from the battlefield during its flight.

High maneuverability of ATGM flight is directly used to bypass obstacles that appear on the flight trajectory of the missile. A special head is used to detect those obstacles. It is mounted on the deck of the ATGM, scanning the space in front of the ATGM (Nocoń, 2013). Detecting an obstacle is done in real time. It allows for a suitable adjustment of the flight trajectory depending on the appearing obstacles. In the case of occurring terrain obstacles (natural such as hills, and artificial such as buildings), it is possible to determine permanent points in space which delineate a safe flight path of ATGM between those obstacles. Introducing a map of the battlefield area to the on-deck computer of the missile will allow the auto-pilot to autonomously delineate the optimum flight trajectory to the target. Moreover, thanks to the possibilities of determining the points of flight, the flight of the missile may be designed in such a way that it reaches the target along a circular trajectory, for example along a circle and, as a result, attack it from the least expected direction. During the programmed flight the missile realizes the trajectory set before the start with simultaneous consideration of bypassing the obstacles. In the last flight stage, the missile detects and identifies the target and fulfils the process of self-guidance in accordance with the implemented algorithm. Depending on the situation on the battlefield, two ways of guiding the missile can be selected. The first is self-guidance (the missile type “fire and forget”). It is fully automatic. After firing, the shooter has no control over the ATGM flight. The second way is “fire-observe-correct”. In this case, the operator observes the actions on the battlefield in real time on the control panel. They operator can correct the flight path and choose targets. The image in real time is sent via a fiber-optic cable unwound behind the missile.

Thanks to the use of the Observation and Seeker Head coupled with the combat head EFP, the missile can very accurately determine the location of the target and hit it in the least armored place. In the paper, it is assumed that the ATGM is equipped with the modified scanning and tracking seeker which is presently undergoing intensive theoretical and experimental tests (Gapiński and Stefański, 2014; Krzysztofik, 2012).

During the attack, the flight of the missile is exposed to external disruptions in form of gusts of wind. Crosswinds surround the missile as a result of which the helm, flight stabilizers and the body of the missile are subject to additional, undesired carrying off forces and the moment of those forces. That results in flight trajectory errors. The auto-pilot with the proposed algorithm effectively compensates the occurring errors what was described in a separate paper by Nocoń and Stefański (2014). Even large gusts of wind of 17 m/s do not impact significantly the effectiveness of the programmed flight, not to mention the attack itself. That is why external disruptions were not considered in flight dynamics equations.

This paper presents a much simplified physical model and flight dynamics equations which by no means affect the preliminary analysis of correctness and effectiveness of the control algorithm. It should be emphasized that the developed algorithm of controlling the hypothetical anti-tank guided missile is the essence of the paper. On the other hand, the equations of flight dynamics of the missile are the tool to verify the correctness of its operation. They have been derived and analysed in more detail in other papers (Koruba and Osiecki, 2006; Baranowski, 2013).

It seems that it is not an overstatement to claim that the missile described herein is a part of the most recent trend of the fourth generation of anti-tank missiles.

2. Description of the tracking

Contemporary military actions more and more often take place in urban areas with high density of civilian objects. With regard to civil security, the fact that the attack on hostile armored units should take place with simultaneous consideration of avoidance of all obstacles: buildings and civilian vehicles, allied units and permanent natural objects is important, see Fig. 1 (Koruba and Nocoń, 2012). Military actions are also common on wooded, mountainous and desert areas – there are also a lot of obstacles interfering with the trajectory of the flight of ATGM.

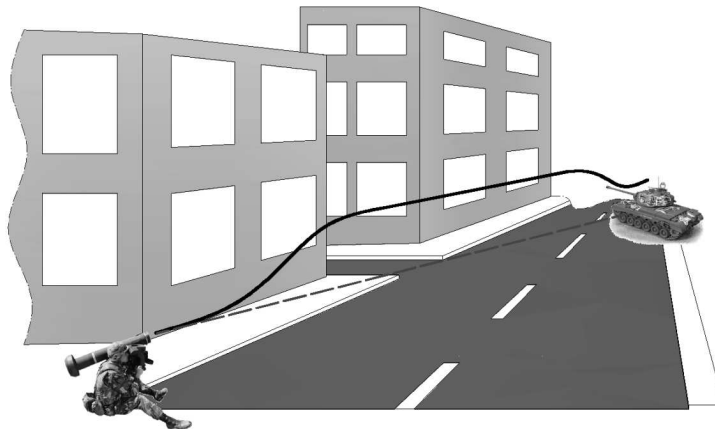


Fig. 1. General view of self-guidance of the third generation close-range ATGM in urban areas

The effectiveness of attack performance is influenced by the element of surprise, ability to avoid obstacles during the flight and the quality of armor of enemy's vehicles. It is commonly known that the weakest armor is the upper surface of the tank and its back, so it is best to direct the attack there. Based on the conditions presented above, the ATGM is required to enable efficient maneuvering between obstacles and precise hit on the selected target point.

Given that the tactical withdrawal of tanks is done in reverse gear, it is possible to set the flight trajectory with a surprise maneuver, which involves flying around the tank and attacking it from behind.

2.1. The modelling of ATGM motion

The equations of dynamics of flight of an anti-tank guided missile are derived in accordance with the adopted assumption that the ATGM performs maneuvers mainly in the horizontal plane. The consequence is the order of rotations in the transformation the ground-fixed system $Sx_gy_gz_g$ to the body-fixed system $Sxyz$ (Koruba and Osiecki, 2006; Siouris, 2004). The first rotation is performed in accordance with the plane of change of the direction of the flight of the ATGM. The second is in accordance with the plane of change of altitude of flight of the ATGM.

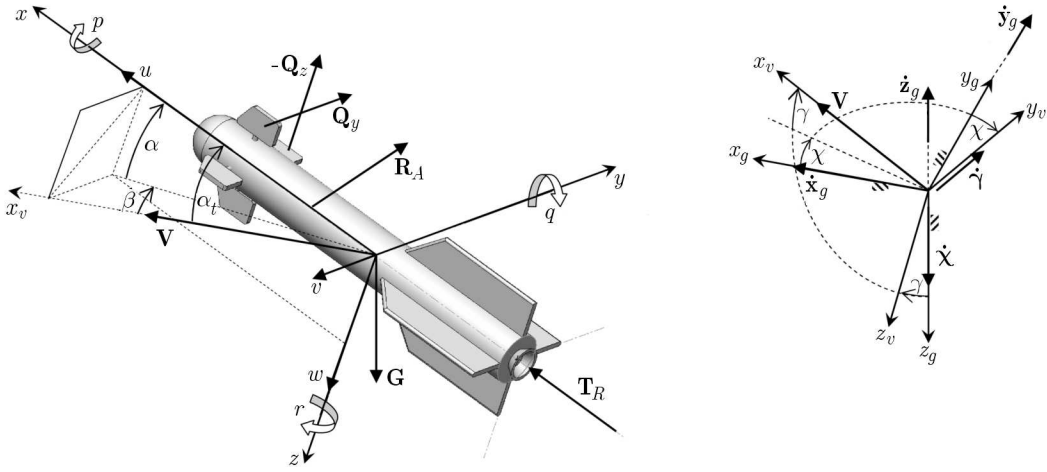
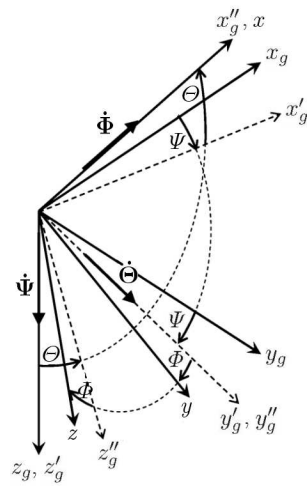


Fig. 2. The system of forces acting on the ATGM moving in the gravitational field and the Earth's atmosphere, together with the adopted coordinate systems

In Fig. 2, the following quantities and denotations are introduced: \mathbf{R}_A – vector of total aerodynamic forces; \mathbf{T}_R – total missile engine thrust; \mathbf{G} – vector of the gravity force; $\mathbf{Q}_y, \mathbf{Q}_z$ – controlling forces; \mathbf{V} – missile velocity vector; $Sxyz$ – system of coordinates connected with the missile (body-fixed system); $Sxgygzg$ – ground-fixed system; $Sxvyvzv$ – system of coordinates connected with the flow; α – missile angle of attack, $\alpha = \arctan(w/u)$; β – missile angle of sideslip, $\beta = \arcsin(v/V)$; α_t – missile total angle of attack; p, q, r – angular velocity components in the body reference frame; u, v, w – velocity components in the body-fixed system; γ, χ – flight-path angle in the vertical and horizontal plane (inclination and azimuth angles of the missile velocity vector); $\dot{x}_g, \dot{y}_g, \dot{z}_g$ – components of the velocity vector in the ground-fixed system.

The dynamical equations of motion can be presented in different coordinate systems. In this paper, the mathematical model is developed according to Polish and International Standard ISO 1151. A transformation matrix between the ground-fixed system $Sxgygzg$ and the body-fixed system $Sxyz$ is required to derive the equations of motion. The angular velocity is the sum of the rotation velocity with respect to the successive axes $\boldsymbol{\Omega} = \dot{\boldsymbol{\Theta}} + \dot{\boldsymbol{\Psi}} + \dot{\boldsymbol{\Phi}}$. The first rotation is around the vertical axis of the ground-fixed system Oz_g by the angle of azimuth Ψ , the second rotation is around the instantaneous horizontal axis Oy'_g by the angle of inclination Θ , and the third rotation is around the axis Ox by the angle of bank Φ .

In Fig. 3, the following quantities $\mathbf{L}_\Psi, \mathbf{L}_\Theta$ and \mathbf{L}_Φ represent the transformation matrix: \mathbf{L}_Ψ is the matrix of transformation of the rotation by the angle of azimuth Ψ , \mathbf{L}_Θ is the matrix of transformation of the rotation by the angle of inclination Θ , \mathbf{L}_Φ is the matrix of transformation of the rotation by the angle of bank Φ .



L_Ψ	x_g	y_g	z_g
x'_g	$\cos \Psi$	$\sin \Psi$	0
y'_g	$-\sin \Psi$	$\cos \Psi$	0
z'_g	0	0	1
L_Θ	x'_g	y'_g	z'_g
x''_g	$\cos \Theta$	0	$-\sin \Theta$
y''_g	0	1	0
z''_g	$\sin \Theta$	0	$\cos \Theta$
L_Φ	x''_g	y''_g	z''_g
x	1	0	0
y	0	$\cos \Phi$	$\sin \Phi$
z	0	$-\sin \Phi$	$\cos \Phi$

Fig. 3. Transformation the ground-fixed system $Sx_g y_g z_g$ to the body-fixed system $Sxyz$

The angular velocity components in the body-fixed system are calculated as follows

$$\begin{bmatrix} p \\ q \\ r \end{bmatrix} = \begin{bmatrix} \dot{\Phi} \\ 0 \\ 0 \end{bmatrix} + \mathbf{L}_\Phi \begin{bmatrix} 0 \\ \dot{\Theta} \\ 0 \end{bmatrix} + \mathbf{L}_\Phi \mathbf{L}_\Theta \begin{bmatrix} 0 \\ 0 \\ \dot{\Psi} \end{bmatrix} \quad (2.1)$$

The final form of the angular velocity is

$$\begin{aligned} p &= \dot{\Phi} - \dot{\Psi} \sin \Theta & q &= \dot{\Theta} \cos \Phi + \dot{\Psi} \sin \Phi \cos \Theta \\ r &= -\dot{\Theta} \sin \Phi + \dot{\Psi} \cos \Phi \cos \Theta \end{aligned} \quad (2.2)$$

The dynamical equations of motion based on the principles of classical mechanics are divided into the progressive part of the missile motion and the spherical part of the motion. The first part of the dynamical equations is

$$m\mathbf{a} = \sum \mathbf{F} \Rightarrow m \frac{\delta \mathbf{V}}{dt} = \sum \mathbf{F} \quad (2.3)$$

The total velocity vector is the sum of the velocity components lying in the body-fixed system. Then, the derivative is computed

$$\mathbf{V} = \mathbf{i}u + \mathbf{j}v + \mathbf{k}w \Rightarrow \frac{\delta \mathbf{V}}{dt} = \mathbf{i} \frac{\delta u}{dt} + \mathbf{j} \frac{\delta v}{dt} + \mathbf{k} \frac{\delta w}{dt} + u \frac{\delta \mathbf{i}}{dt} + v \frac{\delta \mathbf{j}}{dt} + w \frac{\delta \mathbf{k}}{dt}$$

or

$$\frac{\delta \mathbf{V}}{dt} = \mathbf{i}\dot{u} + \mathbf{j}\dot{v} + \mathbf{k}\dot{w} + \begin{vmatrix} \mathbf{i} & \mathbf{j} & \mathbf{k} \\ p & q & r \\ u & v & w \end{vmatrix} \quad (2.4)$$

The three dynamical equations of motion resulting from the progressive part of the motion are developed according with the body-fixed system

$$m(\dot{u} + wq - vr) = \sum F_x \quad m(\dot{v} + ur - wp) = \sum F_y \quad m(\dot{w} + vp - uq) = \sum F_z \quad (2.5)$$

The sum of the total forces acting on the missile is $\sum \mathbf{F} = \mathbf{T}_R + \mathbf{G} + \mathbf{R}_A + \mathbf{Q}_S$, where: m is mass of the missile; \mathbf{a} – total acceleration; $\mathbf{i}, \mathbf{j}, \mathbf{k}$ – unit vectors of the body-fixed system; $\mathbf{Q}_S = [0, Q_y, Q_z]$ – total vector of controlling forces.

Based on the principle of angular momentum, the other part of dynamical equations is the spherical part of motion

$$\frac{\delta \mathbf{K}}{dt} = \frac{\delta \mathbf{I} \boldsymbol{\Omega}}{dt} = \sum \mathbf{M} \quad (2.6)$$

The sum of the angular velocity in the body reference frame is the vector of the missile angular velocity $\boldsymbol{\Omega} = p\mathbf{i} + q\mathbf{j} + r\mathbf{k}$. The same case is with the angular momentum vector $\mathbf{K} = K_x\mathbf{i} + K_y\mathbf{j} + K_z\mathbf{k}$. The derivative of the angular momentum vector is

$$\frac{\delta \mathbf{K}}{dt} = \mathbf{i} \frac{\delta K_x}{dt} + \mathbf{j} \frac{\delta K_y}{dt} + \mathbf{k} \frac{\delta K_z}{dt} + K_x \frac{\delta \mathbf{i}}{dt} + K_y \frac{\delta \mathbf{j}}{dt} + K_z \frac{\delta \mathbf{k}}{dt}$$

or

$$\frac{\delta \mathbf{K}}{dt} = \mathbf{i} I_x \dot{p} + \mathbf{j} I_y \dot{q} + \mathbf{k} I_z \dot{r} + \begin{vmatrix} \mathbf{i} & \mathbf{j} & \mathbf{k} \\ p & q & r \\ I_x p & I_y q & I_z r \end{vmatrix} \quad (2.7)$$

The three dynamical equations of motion resulting from the spherical part of the motion are developed according with the body-fixed system

$$\begin{aligned} I_x \dot{p} + (I_z - I_y)qr &= \sum M_x & I_y \dot{q} + (I_x - I_z)pr &= \sum M_y \\ I_z \dot{r} + (I_y - I_x)pq &= \sum M_z \end{aligned} \quad (2.8)$$

The sum of the total moments acting on the missile is $\sum \mathbf{M} = \mathbf{M}_A + \mathbf{M}_Q$, where: $\mathbf{K} = [K_x, K_y, K_z]$ is the vector of the angular momentum components in the body-fixed system; $\boldsymbol{\Omega}$ – vector of the angular velocity; $bfI = [I_x, I_y, I_z]$ – moments of inertia; $\mathbf{M}_A = [L, M, N]$ – components of the total aerodynamic moment in the body-fixed system; \mathbf{M}_Q – total moment of the controlling force.

- Forces and moments needed in the equations of motion

The total missile thrust T_R is located in the axis Sx of the body-fixed system $Sxyz$

$$\begin{bmatrix} T_R^X \\ T_R^Y \\ T_R^Z \end{bmatrix} = \begin{bmatrix} T_R \\ 0 \\ 0 \end{bmatrix} \quad (2.9)$$

The vector of the gravity force $\mathbf{G} = [G_{xg}, G_{yg}, G_{zg}]$ is located in the axis Sz_g of the ground-fixed system $Sx_gy_gz_g$, so $\mathbf{G} = [0, 0, G]$ and thus it must be transformed to the body-fixed system $Sxyz$

$$\begin{bmatrix} G_X \\ G_Y \\ G_Z \end{bmatrix} = \mathbf{L}_\Phi \mathbf{L}_\Theta \mathbf{L}_\Psi \begin{bmatrix} 0 \\ 0 \\ G \end{bmatrix} = \begin{bmatrix} -G \sin \Theta \\ G \cos \Theta \sin \Phi \\ G \cos \Theta \cos \Phi \end{bmatrix} \quad (2.10)$$

- Simplified aerodynamic forces and moments

The total aerodynamic force \mathbf{R}_A is split into two components lying in plane of drag. The drag force $X_A = C_D \rho S V^2 / 2$ is the component parallel to the vector of velocity, whereas the lift force $P_A = C_L \rho S V^2 / 2$ is the component perpendicular to the vector of velocity.

The components of the total aerodynamic force $\mathbf{R}_A = [X, Y, Z]$ in the body-fixed system are

$$\begin{aligned} X &= -X_A \cos \alpha_t + P_A \sin \alpha_t & Y &= (X_A \sin \alpha_t + P_A \cos \alpha_t) \cos \varphi \\ Z &= -(X_A \sin \alpha_t + P_A \cos \alpha_t) \sin \varphi \end{aligned} \quad (2.11)$$

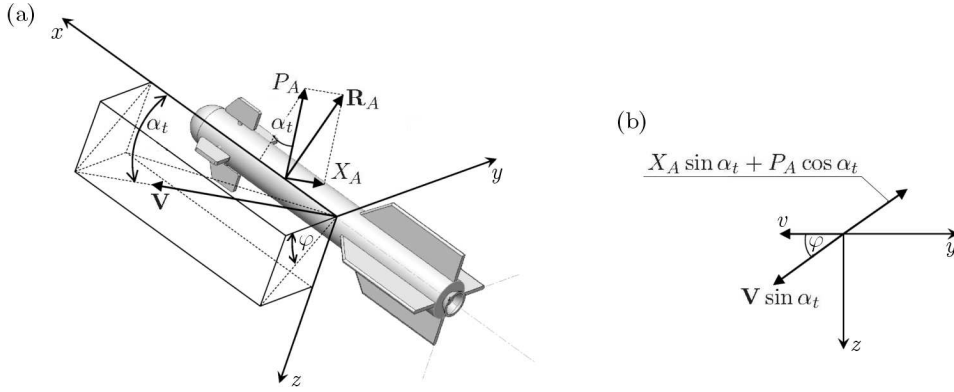


Fig. 4. The forces acting on the missile: (a) components and aerodynamic forces acting on the missile flight; (b) projections of the aerodynamic force vector \mathbf{R}_A and the velocity vector \mathbf{V} in the plane Syz

From obvious equations

$$v = V \sin \alpha_t \cos \varphi \Rightarrow \cos \varphi = \frac{v}{V \sin \alpha_t}$$

$$w = V \sin \alpha_t \sin \varphi \Rightarrow \sin \varphi = \frac{w}{V \sin \alpha_t}$$

the final form of the components of the total aerodynamic force is

$$\begin{aligned} X &= -\frac{C_D \cos \alpha_t - C_L \sin \alpha_t}{2} \rho S V^2 & Y &= \frac{C_D + C_L \cot \alpha_t}{2} \rho S V v \\ Z &= -\frac{C_D + C_L \cot \alpha_t}{2} \rho S V w \end{aligned} \quad (2.12)$$

where: C_D, C_L are coefficients of drag and lift; ρ – air density; S – cross sectional area of the missile; $\alpha_t = \arccos(u/V)$ – total angle of attack; $V = \sqrt{u^2 + v^2 + w^2}$ – missile velocity vector.

The vector of moments of the aerodynamic forces is $[L, M, N] = [0, -lZ, -lY]$ in the body-fixed system, where l is the distance from the center of gravity and the center of pressure of the aerodynamic forces.

The components of the total missile controlling forces Q_S are located in the body-fixed system $Sxyz$. In the axis Sy is the force of the directional control Q_y , in the axis Sz is the force of flight altitude control Q_z . The vector of moments of the controlling forces in the body-fixed system is $\mathbf{M}_Q = [0, eQ_z, -eQ_y]$, where e is the distance from the center of gravity and the control fins.

Based on a simplified physical model shown in Fig. 2 and on the assumption that the missile is axially symmetric $I_y = I_z$ and does not rotate around the longitudinal axis Sx , equations (2.13) of the flight dynamics of the missile are derived. The dynamical equations consist of the progressive part of ATGM motion and its spherical part (Harris and Slegers, 2009; Koruba and Osiecki, 2006; Siouris, 2004)

$$\begin{aligned} m(\dot{u} + wq - vr) &= T_R - G \sin \Theta - \frac{C_D \cos \alpha_t - C_L \sin \alpha_t}{2} S \rho V^2 \\ m(\dot{v} + ur - wp) &= G \cos \Theta \sin \Phi + \frac{C_D + C_L \cot \alpha_t}{2} S \rho V v + Q_y \\ m(\dot{w} + vp - uq) &= G \cos \Theta \cos \Phi - \frac{C_D + C_L \cot \alpha_t}{2} S \rho V w + Q_z \\ I_y \dot{q} + (I_x - I_z) pr &= -\frac{l}{2} (C_D + C_L \cot \alpha_t) \rho V w + e Q_z \\ I_z \dot{r} + (I_y - I_x) pq &= -\frac{l}{2} (C_D + C_L \cot \alpha_t) \rho V v - e Q_y \end{aligned} \quad (2.13)$$

The components of the velocity vector in the ground-fixed system (kinematic differential equations of motion of the missile center of mass) are as follows

$$\begin{bmatrix} \dot{x}_g \\ \dot{y}_g \\ \dot{z}_g \end{bmatrix} = (\mathbf{L}_\Phi \mathbf{L}_\Theta \mathbf{L}_\Psi)^T \begin{bmatrix} u \\ v \\ w \end{bmatrix} \quad (2.14)$$

For the missile stabilized around the longitudinal axis $\Phi = 0$, equation (2.14) takes the following form

$$\begin{aligned} \dot{x}_g &= u \cos \Theta \cos \Psi - v \sin \Psi + w \sin \Theta \cos \Psi \\ \dot{y}_g &= u \cos \Theta \sin \Psi + v \cos \Psi + w \sin \Theta \sin \Psi \\ \dot{z}_g &= -u \sin \Theta + w \cos \Theta \end{aligned} \quad (2.15)$$

The kinematic differential equations of rotational motion about the missile center of mass are as follows

$$\begin{aligned} \dot{\Phi} &= p + q \sin \Phi \tan \Theta + r \cos \Phi \tan \Theta \\ \dot{\Theta} &= q \cos \Phi - r \sin \Phi \quad \dot{\Psi} = q \frac{\sin \Phi}{\cos \Theta} + r \frac{\cos \Phi}{\cos \Theta} \end{aligned} \quad (2.16)$$

2.2. Algorithm of control of the ATGM

The control algorithm consists of two parts. The first part is a programmed trajectory that relates to the control in the vertical plane and the other part is a programmed trajectory in the horizontal plane. After combining both parts, we obtain the programmed trajectory of flight of the ATGM in space, running through the marked points (Fig. 5).

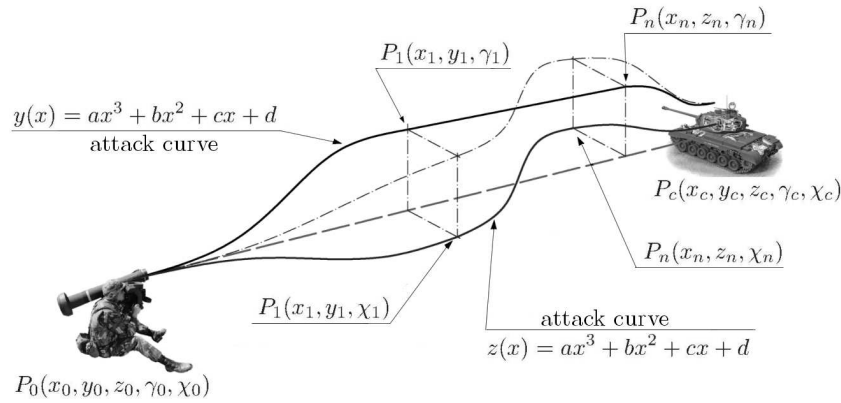


Fig. 5. A schematic depicting the gluing of the fragments of the trajectory by polynomial curves running through given points in space

A new fragment of both projections of the trajectory are calculated between the consecutive points. The program flight of the ATGM in each fragment is described by a third degree polynomial (Grzyb and Koruba, 2011)

$$y = ax^3 + bx^2 + cx + d \quad (2.17)$$

The program trajectory of flight of the ATGM consists of a finite number of sections – polynomial curves $y(x)$ and $z(x)$, glued with each other at predetermined points, see Fig. 5. Each curve is determined by the coordinates of the start and end point as well as angles of flight at these points. For the first section of the trajectory in the vertical plane, we can use the following data

$$(x_0, y_0, \gamma_0) \quad (x_k, y_k, \gamma_k) \quad (2.18)$$

From the system of four equations with four unknowns, which are the coefficients with the variables

$$\begin{aligned} ax_0^3 + bx_0^2 + cx_0 + d &= y_0 & 3ax_0^2 + 2bx_0 + c &= \tan \gamma_0 \\ ax_k^3 + bx_k^2 + cx_k + d &= y_k & 3ax_k^2 + 2bx_k + c &= \tan \gamma_k \end{aligned} \quad (2.19)$$

we obtain the following linear equation to solve (Grzyb and Koruba, 2011)

$$\begin{bmatrix} x_0^3 & x_0^2 & x_0 & 1 \\ 3x_0^2 & 2x_0 & 1 & 0 \\ x_k^3 & x_k^2 & x_k & 1 \\ 3x_k^2 & 2x_k & 1 & 0 \end{bmatrix} \begin{bmatrix} a \\ b \\ c \\ d \end{bmatrix} = \begin{bmatrix} y_0 \\ \tan \gamma_0 \\ y_k \\ \tan \gamma_k \end{bmatrix} \quad (2.20)$$

In the attack phase (Fig. 6), when the target is moving, the polynomial coefficients are calculated at any point in time, as the end point (target) of the curve keeps changing its coordinates.

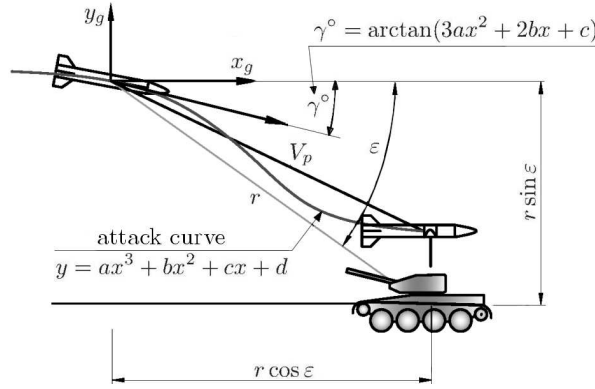


Fig. 6. View of the final stage of attack of the ATGM flying along a polynomial curve. The missile flight above the target

Due to the limited processing power of the system, the coefficients are presented in form of a cascade (next coefficient includes the previous one)

$$\begin{aligned} a &= -\frac{2y_k - 2y_0 + (x_0 - x_k)(\tan \gamma_k + \tan \gamma_0)}{(x_k - x_0)^3} & c &= \tan \gamma_k - 3x_k^2 a - 2x_k b \\ b &= \frac{\tan \gamma_0 - \tan \gamma_k - (3x_0^2 - 3x_k^2)a}{2x_0 - 2x_k} & d &= y_k - x_k^3 a - x_k^2 b - x_k c \end{aligned} \quad (2.21)$$

In the vertical plane, the program trajectory is described by the function $y = f(x)$

$$y = ax^3 + bx^2 + cx + d \quad (2.22)$$

The altitude control angle γ° is given by the formula

$$\gamma^\circ = \arctan(3ax^2 + 2bx + c) \quad (2.23)$$

The situation is analogous in the horizontal plane. By replacing the coordinate y with z and γ with χ , the program trajectory is described by the function $z = f(x)$

$$z = ax^3 + bx^2 + cx + d \quad (2.24)$$

and the direction control angle χ°

$$\chi^\circ = \arctan(3ax^2 + 2bx + c) \quad (2.25)$$

2.3. Selection of a regulator

To control the ATGM on the programmed trajectory in accordance with the implemented control algorithm, a double PID regulator is used in each plane separately

$$\begin{aligned}
 Q_y &= k_{y1}e_y + k_{y2}\frac{de_y}{dt} + k_{y3}\int_{t_0}^{t_k} e_y dt + h_{y1}f_y + h_{y2}\frac{df_y}{dt} + h_{y3}\int_{t_0}^{t_k} f_y dt \\
 Q_z &= k_{z1}e_z + k_{z2}\frac{de_z}{dt} + k_{z3}\int_{t_0}^{t_k} e_z dt + h_{z1}f_z + h_{z2}\frac{df_z}{dt} + h_{z3}\int_{t_0}^{t_k} f_z dt
 \end{aligned} \tag{2.26}$$

where

$$\begin{aligned}
 e_y &= \gamma^\circ - \gamma & e_z &= \chi^\circ - \chi \\
 f_y &= y - y_p & f_z &= z - z_p \\
 \gamma &= \arcsin \frac{\dot{z}_g}{V} & \chi &= \arctan \frac{\dot{y}_g}{\dot{x}_g}
 \end{aligned}$$

and where y_p is the current ceiling of the ATGM at a given moment of time; y – programmed altitude of ATGM at a given moment of time; z_p – factual location of ATGM; z – programmed location of the ATGM; γ, χ – flight-path angle in the vertical and horizontal plane (inclination and azimuth angles of the missile velocity vector); $\dot{x}_g, \dot{y}_g, \dot{z}_g$ – components of the velocity vector in the ground-fixed system.

The indicated control signals Q_y, Q_z for the purpose of simplification of the simulation can be considered as the controlling forces (Evans, 1990).

3. Results of simulation tests

Simulations are conducted for a hypothetical anti-tank guided missile whose mathematical model and equations of flight dynamics are presented in the previous Section. The data adopted for the missile are: $m = 12.9$ kg, $e = 0.45$ m, $l = 0.231$ m, $I_y, I_z = 1.53$ kg m², $I_x = 0.0324$ kg m², $T_R = 3700$ N (launch motor), $T_R = 400$ N (flight motor).

3.1. Simulation conducted for the ATGM flying through three points and attacking the target moving with a velocity of 30 m/s

The autopilot regulator parameters are selected as follows: $k_{y1} = 400, k_{y2} = 320, k_{y3} = 10, h_{y1} = 900, h_{y2} = 36, h_{y3} = 2300, k_{z1} = 400, k_{z2} = 170, k_{z3} = 1000, h_{z1} = 900, h_{z2} = 8, h_{z3} = 1000$.

3.2. Simulation conducted for the ATGM flying through four points and attacking the target moving with a velocity of 30 m/s

The autopilot regulator parameters are selected as follows: $k_{y1} = 400, k_{y2} = 320, k_{y3} = 10, h_{y1} = 900, h_{y2} = 36, h_{y3} = 2300, k_{z1} = 200, k_{z2} = 250, k_{z3} = 1000, h_{z1} = 900, h_{z2} = 23, h_{z3} = 1000$.

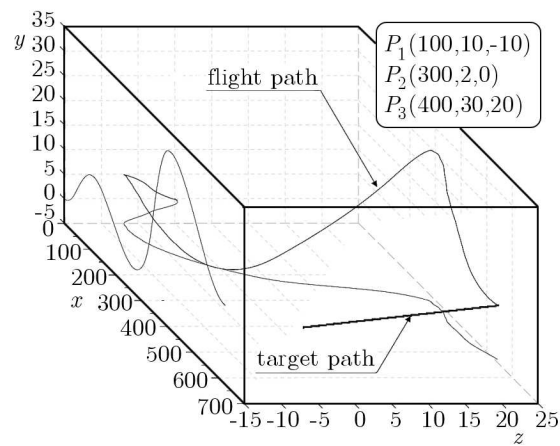


Fig. 7. Trajectory of the flight of the ATGM attacking the target moving with a velocity of 30 m/s. The target moves 100 to the left and 50 up

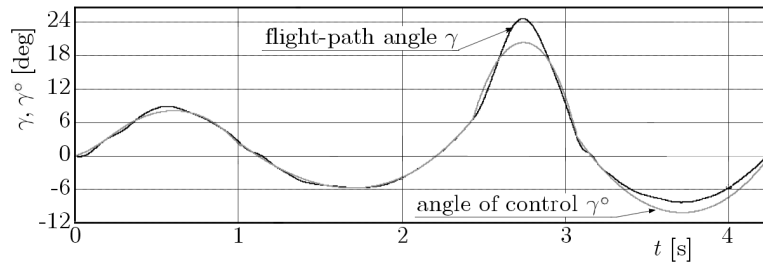


Fig. 8. The flight-path angle γ and the control angle γ° in function of time

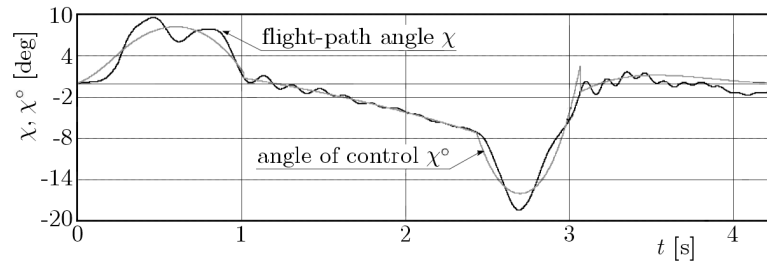


Fig. 9. The flight angle χ and the control angle χ° in function of time

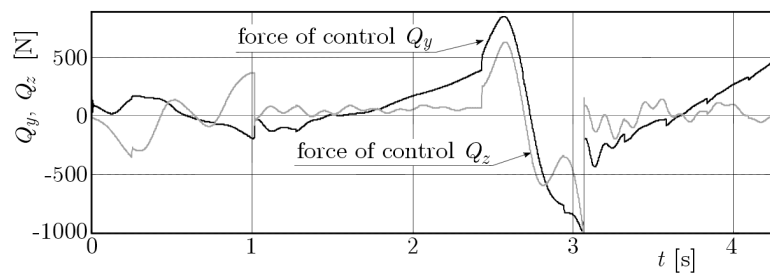


Fig. 10. Control signals of the ATGM: Q_y controlling the altitude in the vertical plane, Q_z controlling the direction in the horizontal plane

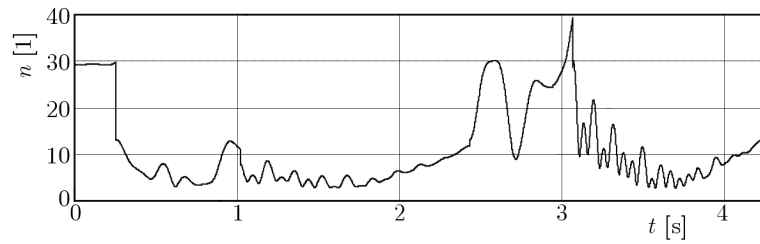


Fig. 11. Lateral overloads that affect the ATGM during the guidance

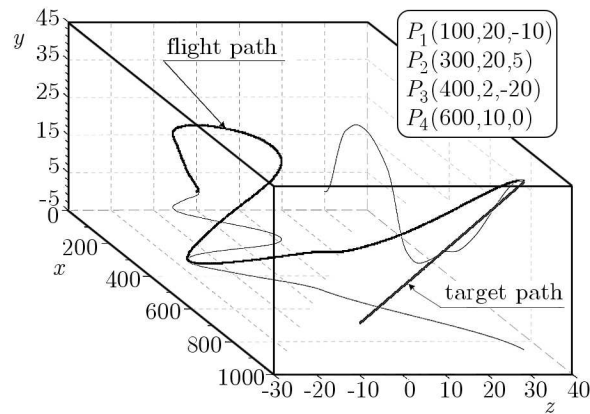
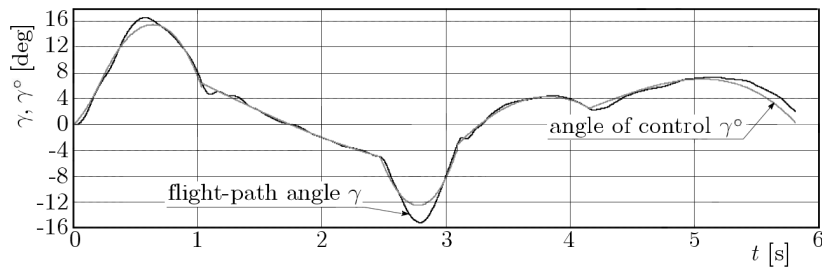
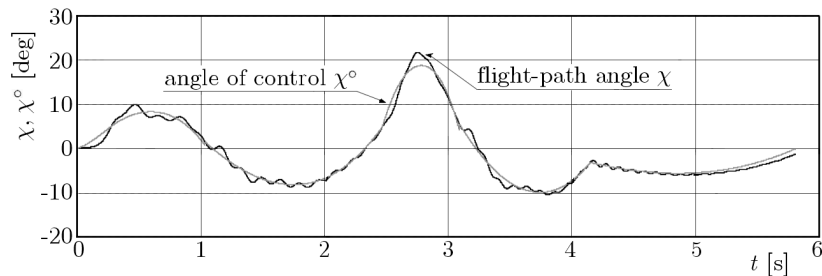


Fig. 12. Trajectory of the flight of the ATGM attacking the target moving with a velocity of 30 m/s. The target moves 150 to the left and 100 up


 Fig. 13. The flight-path angle γ and the control angle γ° in function of time

 Fig. 14. The flight angle χ and the control angle χ° in function of time

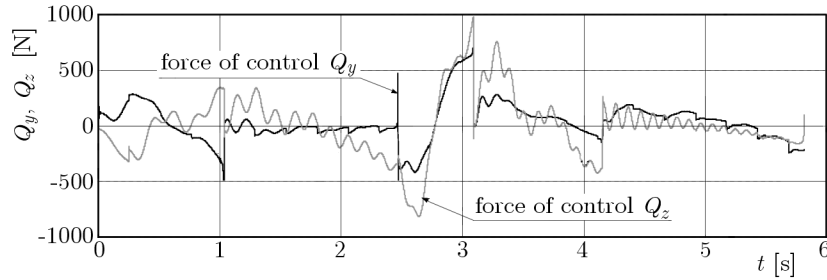


Fig. 15. Control signals of the ATGM: Q_y controlling the altitude in the vertical plane, Q_z controlling the direction in the horizontal plane

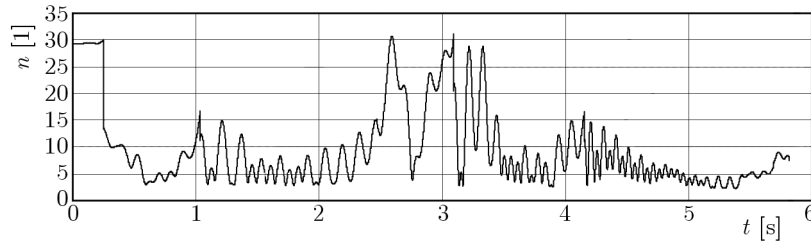


Fig. 16. Lateral overloads that affect the ATGM during the guidance

4. Conclusions and final remarks

From the conducted theoretical deliberations and simulation studies, one can draw the following conclusions:

- Proper selection of the regulator and its settings significantly affects not only the accuracy of mapping of the programmed trajectory, but also the optimal values of control signals as well as congestion during missile flight.
- Regulator settings are chosen in such a way so as to optimize the values of control signals and the existing congestions. It should be emphasized that the regulator gains assume values that are technically achievable. Admittedly, the angles of the missile flight do not coincide exactly with the control angles, and the trajectory does not perfectly map the trajectory of the program, however, it does not significantly affect the effectiveness of the attack.
- ATGM flies through designated points with a sufficient accuracy (one meter), and hits the target with a high accuracy (approx. half a meter). These results are satisfactory because of the fact that the target is moving at a relatively high velocity (about 30 m/s).
- In the points of gluing functions (subsequent parts of the trajectory), one can observe significant jumps of the control signals. This is due to the discontinuity of angular velocity functions in these points.

References

1. BARANOWSKI L., 2013, Equations of motion of spin-stabilized projectile for flight stability testing, *Journal of Theoretical and Applied Mechanics*, **51**, 1, 235-246
2. EVANS D.M., 1990, The direct-fire anti-armour capability of UK land forces, *Intern, Defense Review*, **7**, 739-742

3. GAPIŃSKI D., STEFAŃSKI K., 2014, Modified optical scanning and tracking head for identification and tracking air targets, *Solid State Phenomena*, **210**, 145-155, DOI: 10.4028/www.scientific.net/SSP.210.145
4. GRZYB M., KORUBA Z., 2011, Guiding a bomb to a sea target (in Polish), *Research Journal of Polish Naval Academy*, **185A**, ISSN 0860-889X, 189-195
5. HARRIS J., SLEGGERS N., 2009, Performance of a fire-and-forget anti-tank missile with a damaged wing, *Mathematical and Computer Modelling*, **50**, 1/2, 292-305
6. KORUBA Z., 2008, *The Elements of the Theory and Applications of the Controlled Gyroscope* (in Polish), Monographs, Studies, Dissertations M7, Kielce University of Technology, Kielce
7. KORUBA Z., NOCOŃ Ł., 2012, Selected algorithms of automatic guidance of anti-tank missiles attacking targets from upper ceiling (in Polish), *Pomiary, Automatyka, Robotyka*, **2**
8. KORUBA Z., OSIECKI J., 2006, *Structure, Dynamics and Navigation of Chosen Precision Kill Weapons*, Publishing House of Kielce University of Technology, ISBN 83-88906-17-8, Kielce, 50-209
9. KRZYSZTOFIK I., 2012, The dynamics of the controlled observation and tracking head located on a moving vehicle, *Solid State Phenomena*, **180**, 313-322, ISSN 1012-0394, DOI: 10.4028/www.scientific.net/SSP.180.313
10. NOCOŃ Ł., 2013, Detection control system of a missile safe distance trajectory, *Proceedings of the 10th European Conference of Young Researchers and Scientists*, EDIS – Žilina University Publisher, ISBN 978-80-554-0694-7, Transcom 2013, Žylina, 139-142
11. NOCOŃ Ł., STEFAŃSKI K., 2014, The analysis of anti-tank rocket dynamics including external disturbances (in Polish), [In:] *Mechanika w Lotnictwie, ML-XVI 2014*, K. Sibilski (edit.), PTMTS Warsaw, ISBN 978-83-932107-3-2, 409-426
12. STOURIS G.M., 2004, *Missile Guidance and Control Systems*, Springer, New York
13. YANUSHEVSKY R., 2008, *Modern Missile Guidance*, CRC Press Taylor & Francis Group, New York

Manuscript received November 29, 2014; accepted for print June 12, 2015

ANALYSIS OF AN EXPERIMENTAL SETUP FOR STRUCTURAL DAMPING IDENTIFICATION

OLAF P. HENTSCHEL, MARIUS BONHAGE, LARS PANNING-VON SCHEIDT, JÖRG WALLASCHEK

Leibniz Universität Hannover, Institute of Dynamics and Vibration Research, Hannover, Germany

e-mail: hentschel@ids.uni-hannover.de; bonhage@ids.uni-hannover.de; panning@ids.uni-hannover.de;

wallaschek@ids.uni-hannover.de

MARKUS DENK, PIERRE-ALAIN MASSEREY

ALSTOM Power, Steam Turbines and Generators, Baden, Switzerland; e-mail: markus.denk@power.alstom.com

In the present paper, an experimental setup for structural damping determination arising from energy dissipations within the material is presented. The experimental setup is developed in such a way that all unintended damping sources are eliminated. In this connection, priority is also given to the reproducibility of the experimental data. In addition, a vacuum chamber is developed to reduce the damping arising from the interaction with the surrounding medium. Furthermore, beam-shaped specimens are clamped in a suspended way, using screws with an apex to fix the specimens in their nodes of vibration. Then, the influence of test rig specific parameters on the damping value is analyzed. In this context, an ideal setup of the test rig is identified to measure structural damping values arising from dissipations within the material. Finally, a common model for material damping description is parameterized using the experimental data.

Keywords: damping determination, material damping, vacuum chamber, impact excitation, experimental setup

1. Introduction

In nearly all fields of mechanical engineering, the avoidance of High Cycle Fatigue (HCF) failures is of great importance. To reduce this risk, prediction and reduction of vibration amplitudes is a primary objective. One of the most important parameters for amplitude prediction is structural damping. In turbomachinery blading applications, for example aerodynamic, frictional and material damping are the most dominant damping mechanisms. In this paper, the latter one is in the focus of investigation.

During the last decades, the research mainly concentrated on the usage of nonlinear calculation tools to predict vibration amplitudes. Here, optimization of friction dampers in joints in dynamic systems is a superior criterion. Such calculations require specification of contact parameters as well as structural parameters. From this, many authors use low established material damping values to calculate transfer functions. Weiwei and Zili (2010) mention the material damping as low, using it for numerical blade calculation by means of a 3-D numerical contact model. Laborenz *et al.* (2010) also use a low material damping ratio ξ with $1.41 \cdot 10^{-4}$ for establishing their eddy current approach. Using the damping ratio ξ and the eigenfrequency ω_0 , the differential equation of a single degree of freedom (SDOF) system (displacement x) can be written as follows

$$\ddot{x} + 2\xi\omega_0\dot{x} + \omega_0^2x = 0 \tag{1.1}$$

Siewert and Stüer (2010) and Krack *et al.* (2012) only mention material damping as low and important for their nonlinear calculations. Petrov and Ewins (2006) use a collective loss factor η

for aerodynamic and material damping of 0.001. Regarding a linear SDOF-System it is possible to formulate the loss factor η in terms of damping ration ξ

$$\eta = 2\xi\sqrt{1 - \xi^2} \quad (1.2)$$

Resulting from the tendency to utilize blisks (blade integrated disks) to cut assembly costs and increase engine efficiency, the structural damping arising from the material is the most reasonable energy dissipation process. Therefore, quantification of mechanical damping (due to effects inside the material) is of essential relevance to predict and reduce vibration amplitudes in terms of HCF. Dealing with such low values, precise damping determination requires an appropriate experimental setup. To quantify material damping, an adequate experimental setup is elementary. For this purpose, a double reed cantilever beam is recommended as a test specimen by Gibson and Plunkett (1977), Granick and Stern (1965) as well as by Gudmundson and Wüthrich (1986). The disadvantage of using such a specimen is the necessity of frequency tuning with additional masses.

Regarding the adequate experimental setup, all other damping sources like frictional damping or damping due to the surrounding medium have to be minimized in order to identify the material damping only (see Granick and Stern, 1965; Gibert *et al.*, 2012). Therefore, measurements under vacuum are recommended.

For the identification of damping values, Plunkett (1959) gives an overview of possible methods for single degree of freedom systems, which can be classified in time and in frequency domain approaches. Concerning multi degree of freedom systems, the Rational Fractional Polynomial method based on a parameter fit in the frequency domain is presented by Richardson and Formenti (1982). Moreover, the Least-Squares Complex Exponential method is described by He and Fu (2001). This method is classified using time domain methods. Furthermore, Bert (1973) offers an overview of methods for modeling, experimental determination and parameter identification of material damping. Within this work, the method presented by Hentschel *et al.* (2015) is used for damping determination.

The objective of the present work is the development of an experimental setup for material damping determination, which serves the requirements for accuracy especially for expected low damping values. The reproducibility of the experimental data is a superior criterion within the development of the experimental setup. The experimental setup including the vacuum chamber and the specimen clamping mechanism is presented, documenting the constructional effort taken to minimize sources of unintended damping, as frictional damping within joints. Then the specimen excitation using a voice coil actuator and the data acquisition process are described. An automated impact excitation is used to enable the possibility of excitation in the vacuum chamber and to satisfy the criterion of reproducibility. A method for determining damping values including a short-term Fourier transform using resampling is briefly presented (see Hentschel *et al.*, 2015). The used test rig, in combination with the analysis method, offers the possibility to identify the decay curve of one mode shape in order to calculate the damping values. From this, decay fitting is used (see Rice *et al.*, 2007 and Siewert *et al.*, 2010). Then further experimental results are presented, which investigate in addition to the influence of ambient pressure also the influence of the clamping conditions on the determined specimen specific damping value of stainless steel. Using the measured data, a common model for material damping description (see Lazan, 1968 and Szwedowicz *et al.*, 2008) is parameterized. Conclusions are given at the end.

2. Experimental setup

Based on a common frequency range for turbine blades, the experimental setup is developed. Using a specific specimen length, plate-type specimens are manufactured for the frequency range of interest, corresponding to the mode shape of interest.

2.1. Specimen clamping

The specimens which are used for the material damping tests are beams with defined eigenfrequencies. The sample geometry (width and thickness) is selected in such a way that a wide gap between the eigenfrequencies of the test specimens is present. To reduce the influence of parasitic damping (i.e. frictional damping due to clamping), the specimens are clamped in a suspended way in their nodes of vibration (Fig. 1) corresponding to the mode shape of interest. Bolts with an apex (Fig. 1) are used to fix the specimens depending on the analyzed mode shape. This allows an evaluation of “free” modes and prevents rigid body mode shapes. In addition, the clamping mechanism design leaves a wide frequency gap between the specimen eigenfrequencies and those of the system consisting of the clamping device and the specimen (Fig. 1).

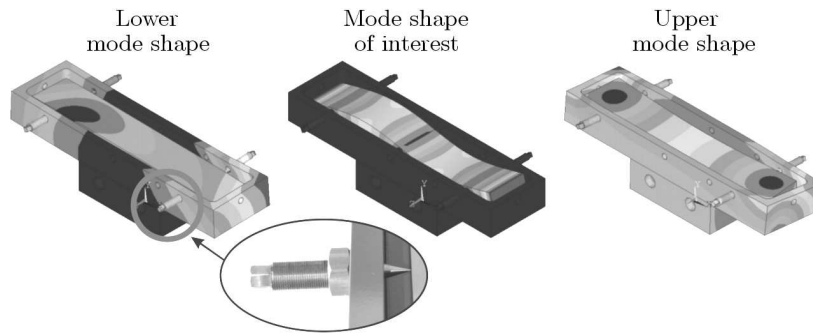


Fig. 1. Mode shapes of the clamping mechanism and the apex formed clamping screw

This avoids potential interactions between the specimen and clamping and helps one to eliminate unintended damping sources in the clamping mechanism. In Table 1, the normalized frequencies of interest $f_{s,i}$ (representing a common eigenfrequency range of turbine blades) chosen concerning the specimen and the nearest normalized eigenfrequencies of the system $f_{sy,l,i}$ and $f_{sy,u,i}$ are shown.

Table 1. Normalized frequencies

Specimen	Next lower normalized eigenfrequency	Normalized eigenfrequency of interest	Next upper normalized eigenfrequency
1	$f_{sy,l,a} = 0.031$	$f_{s,a} = 0.106$	$f_{sy,u,a} = 0.182$
2	$f_{sy,l,b} = 0.087$	$f_{s,b} = 0.32$	$f_{sy,u,b} = 0.511$
3	$f_{sy,l,c} = 0.9$	$f_{s,c} = 1$	$f_{sy,u,c} = 1.08$

2.2. Excitation and measurement

Specimens are excited by a force impact generated by a voice coil actuator. In this connection, an automated test sequence with a high reproducibility of the excitation force is realized. Based on this, a mechanical coupling of the structure and the excitation mechanism is avoided, which eliminates a potential source for data distortion. The voice coil actuator is operating in current mode. In this context, it is possible to control the acceleration of the actuator. A force sensor is used to monitor the behavior of the impact. Due to the used electrical device for specimen excitation, a high reproducibility of the impact force is realizable (see Fig. 2). Figure 2 shows in addition the relation of the preset current to the measured impact force.

The vibration is measured by a laser Doppler vibrometer. An optical measurement technique is used to avoid a coupling between structure and sensor, which may induce additional uninten-

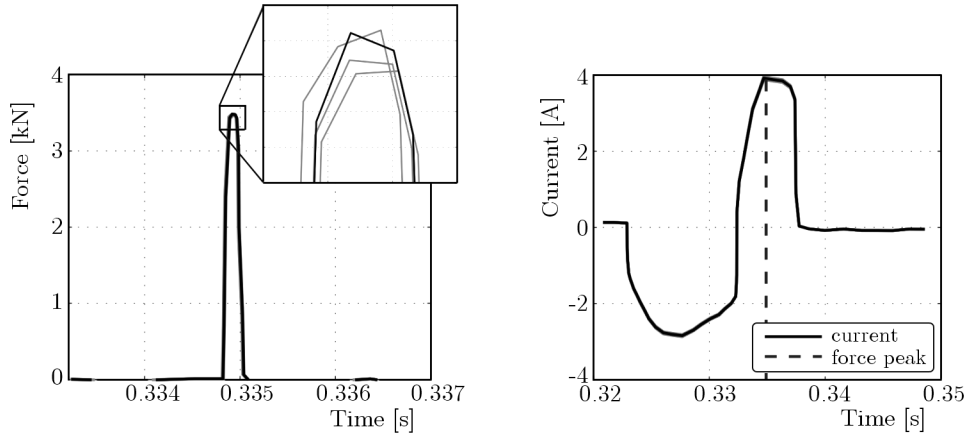


Fig. 2. Measured force with several executions of the excitation (left) and corresponding coil current (right)

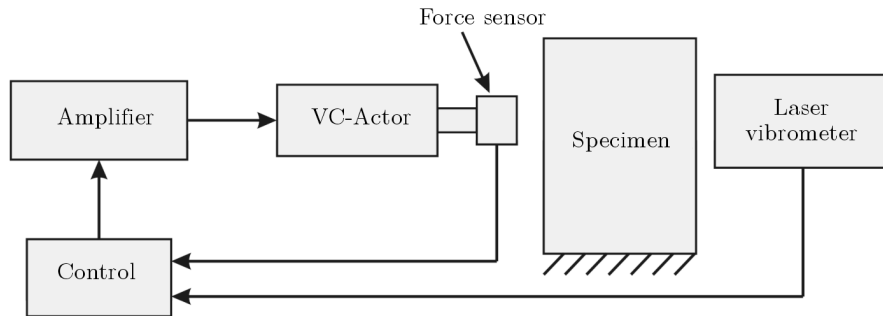


Fig. 3. Experimental setup (schematic)

ded damping. In Fig. 3, the schematic experimental setup is shown, also illustrating necessary supply and control units.

2.3. Vacuum chamber

The vacuum chamber is used to eliminate damping caused by the surrounding medium. The chamber is developed in two main design steps (Fig. 4). The first design step is focused on the ability to facilitate the whole experimental setup in the chamber. The specimen clamping and also the excitation mechanism are bolted to the bottom of the chamber. An electrical feed-through for the excitation mechanism and a window for vibration measurement are considered. On the basis of the first design step, the position of the flange, the flange height, the flange diameter and the wall thickness of the chamber are changed. This is ensured by frequency optimization with respect to a wide frequency range of interest (common eigenfrequency range of turbine blades). Being designed for vacuum conditions, a potential coupling of the specimen and the structure (via the remaining air in the chamber) is eliminated due to the performed frequency optimization. In this way, precise detection of the influence of the surrounding air on the damping value is also possible. Furthermore, additional masses are applicable on the chamber cap, to ensure a shift of the eigenfrequency range of the vacuum chamber. This enables a high variability of the analyzable eigenfrequencies of interest.

It is possible to define the optimization problem by maximizing the gap between the eigenfrequencies of the chamber and the eigenfrequencies of interest (representative eigenfrequency range for turbine blades). In Fig. 5, the frequency gaps are graphically presented.

The optimization variable Opt has to be calculated using the three frequency gaps (Δf_a , Δf_b , Δf_c). In this context, it has to be ensured that the frequency gaps reach their maximal

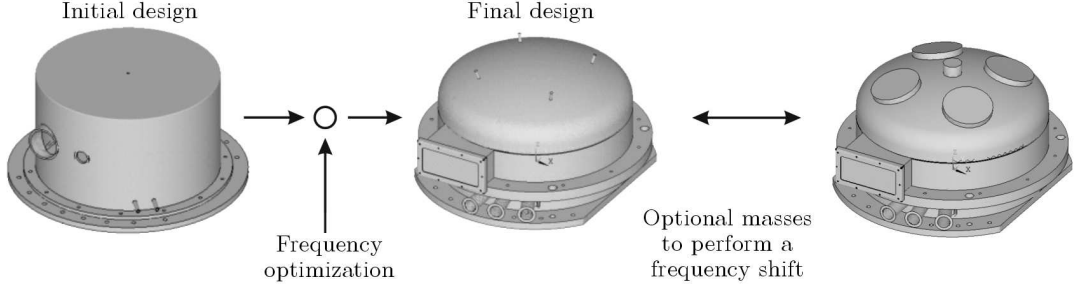


Fig. 4. Design steps of the vacuum chamber

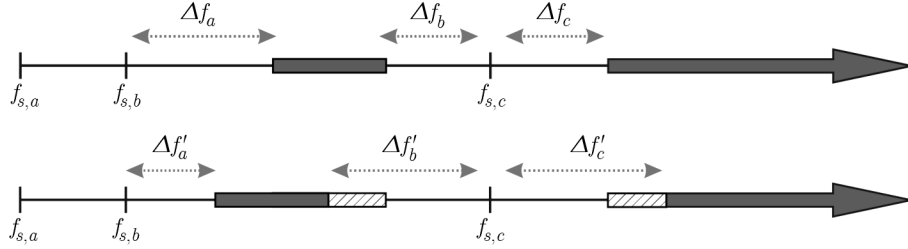


Fig. 5. Frequency gaps of the specimen and the vacuum chamber (bold: eigenfrequency range of the chamber), top: chamber without additional masses, bottom: chamber with additional masses

magnitudes. Furthermore, the magnitudes of Δf_b and Δf_c should be equal. As a consequence, the optimization variable can be defined as follows

$$Opt = e\Delta f_a + h(\Delta f_b, \Delta f_c) \quad (2.1)$$

The factor e represents a weight factor concerning the first frequency gap. To satisfy the criterion of maximal and equal magnitudes of the factors Δf_b and Δf_c , the function $h(\Delta f_b, \Delta f_c)$ is defined

$$h(\Delta f_b, \Delta f_c) = a|\cos(\alpha)\Delta f_b - \sin(\alpha)\Delta f_c|\sigma(\sin(\alpha)\Delta f_c - \cos(\alpha)\Delta f_b) \\ + b|\cos(\alpha)\Delta f_b - \sin(\alpha)\Delta f_c|\sigma(\cos(\alpha)\Delta f_b - \sin(\alpha)\Delta f_c) - c(\sin(\alpha)\Delta f_b + \cos(\alpha)\Delta f_c) \quad (2.2)$$

The factors a , b , c and α are additional weight factors concerning the two frequency gaps Δf_b and Δf_c . The several weight factors are used to ensure a high variability of the optimization process. Out of this, it is possible to repeat the optimization by changing the weighting factors to give e.g. priority to another frequency gap.

The influences of these factors on the frequency gaps are summarized in Table 2 and Fig. 6.

Table 2. Influences of the different weight factors

Factor	Influence
a	weight factor concerning the magnitude of Δf_c
b	weight factor concerning the magnitude of Δf_b
c	symmetric weight factor concerning Δf_b and Δf_c
α	weight factor concerning the relationship between Δf_b and Δf_c

The optimization is carried out by performing modal analysis using the finite element program ANSYS and its sub-problem approximation method (see ANSYS, 2009). The optimization process is presented in detail in Fig. 7.

Using the defined scalar optimization variable and the optimization process presented in Fig. 7, the ideal chamber geometry with a high magnitude of the frequency gaps is calculated. The

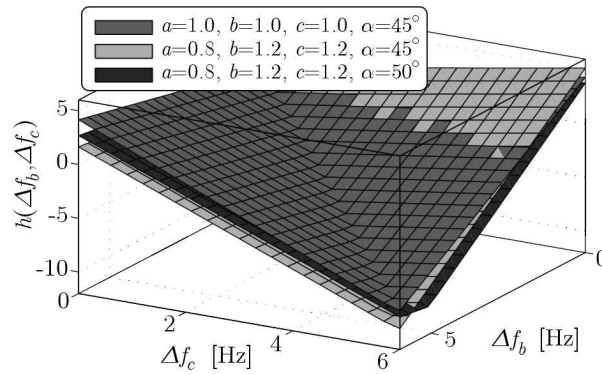


Fig. 6. Weight factors and their influences

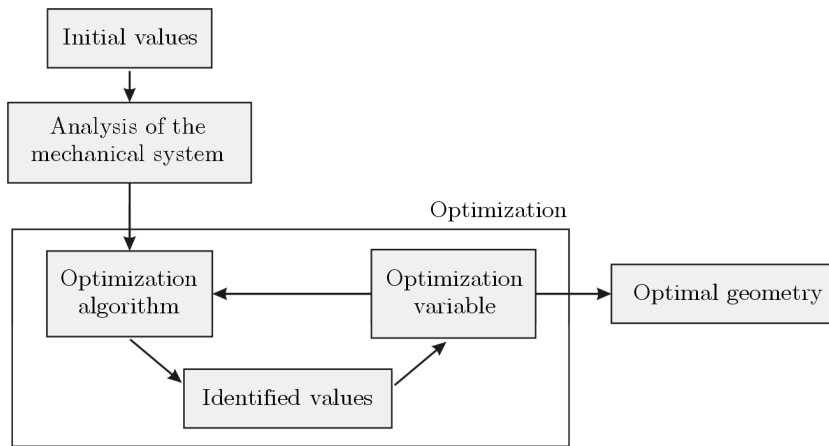


Fig. 7. Design steps of the vacuum chamber

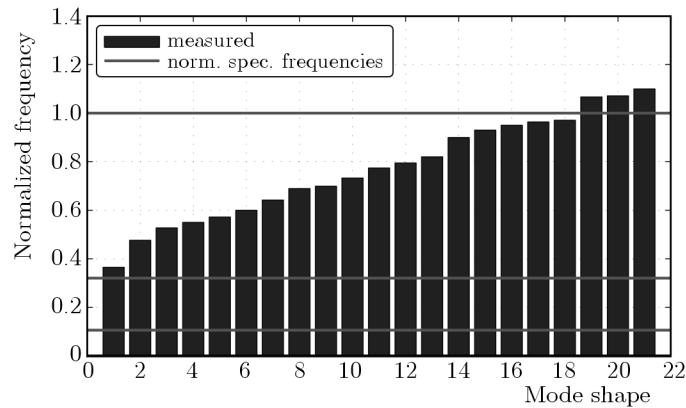


Fig. 8. Measured natural frequencies of the vacuum chamber

different eigenfrequencies measured for the manufactured chamber without additional masses are shown in Fig. 8.

It shall be pointed out that the requested frequency gaps are reached. Figure 9 shows the vacuum chamber with the integrated experimental setup.

Being equipped with a vacuum pump, low chamber pressures can be reached (see Fig. 10) and maintained during testing.

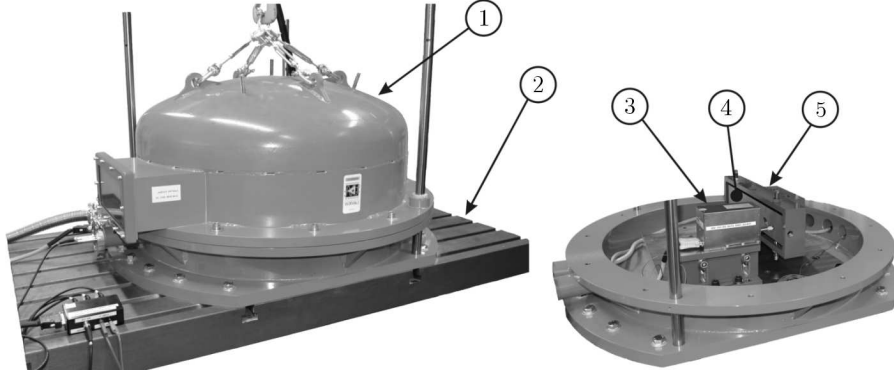


Fig. 9. Experimental setup: 1 – vacuum chamber, 2 – vibration desk, 3 – voice coil actuator, 4 – specimen, 5 – clamping device

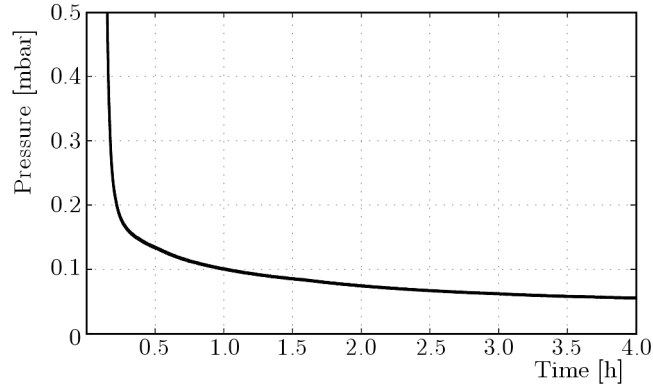


Fig. 10. Pressure-time dependency

3. Damping determination

The methodology of deriving damping values includes a Short-Term Fourier transform with an integrated Resampling (STFR) of the signal. The used methodology for damping identification was already presented by Hentschel *et al.* (2015). In this paper, only a short overview of the used methodology will be given. Using the mentioned STFR method, it is possible to get adequate information concerning vibration amplitude and eigenfrequency. This method is limited only to structures excited by a force impact (realized with the experimental setup). Here, the decaying signal $x_u[w]$, which is necessary for damping evaluation, is measured by a laser Doppler vibrometer. This signal can be specified by the following data sequence with N_w values regarding the signal parts u

$$x_u[w] = \begin{cases} x(t = (uN_w + w)T_0) & \text{for } 0 \leq w \leq N_w - 1 \\ 0 & \text{otherwise} \end{cases} \quad (3.1)$$

where w represents the signal point and T_0 the sampling time. The signal is equidistantly divided into

$$U = \frac{N_S}{N_w} - 1 \quad (3.2)$$

parts, and it is analyzed stepwise. N_S represents the number of all data values. In the next step, a Discrete Fourier Transform (DFT) is applied

$$X_u[k] = \sum_{w=0}^{N_w-1} x((uN_w + w)T_0) e^{-j2\pi \frac{kw}{N_w}} \quad (3.3)$$

where k describes the spectral line number. In the following, the measured signal is extracted with respect to the mode shape of interest. Using this formulation, the frequency resolution $\Delta\omega_f$ reads

$$\Delta\omega_f = \frac{2\pi}{T_0 N_w} \quad (3.4)$$

By analyzing weakly damped systems, the amplitude is underestimated at the eigenfrequency. To avoid this problem, resampling of the signal is performed. The goal in this context is the identification of the required sample rate in such a way that the frequency resolution $\Delta\omega_{f,n}$ is equal to an integer numbered multiple g of the eigenfrequency of interest $\omega_{d,int}$.

$$\omega_{d,int} = g\Delta\omega_{f,n} \quad (3.5)$$

To satisfy the required sample rate corresponding to the criteria in Eq. (3.5), real numbered alternation d of the sample rate T_0 is necessary

$$\Delta\omega_{f,n} = \frac{2\pi}{T_{0,n} N_w} = \frac{2\pi}{dT_0 N_w} \quad (3.6)$$

As the eigenfrequency is unknown (due to production tolerances), optimization (such as the Nelder-Mead algorithm, Nelder and Mead, 1965) of the resampling factor d is necessary. In this respect, the achievement of the maximal amplitude at eigenfrequency represents the optimization criterion.

After calculating the eigenfrequency, the modal amplitude for each part of the decay curve can be identified. Dividing the decay curve into several parts, it is possible to calculate the decay coefficient as a function of the mean amplitude.

4. Experimental results

In this Section, the influence of experimental setup specific parameters on the damping value is analyzed. For this purpose, an optimal setup of the test rig is identified, using the achievement of a minimal damping value as a criterion for test rig adjustment. In addition, the reproducibility of the measured data is also analyzed whereby the experimental setup is reassembled prior to each measurement. The measurements are realized four times per configuration. The tests are performed using beams with a reduced eigenfrequency for the 2-nd bending $f_{s,c}$ (see Table 1). As a result of this investigation, a quantification of the identified damping value concerning its quality is expected.

The first analyzed parameter is the ambient pressure. In Fig. 11, the normalized damping (ratio of the measured loss factor and the maximum measured loss factor) value versus the normalized displacement (ratio of the measured displacement and the maximum measured displacement) calculated from the measured velocity is shown.

To eliminate any possibility of an aerodynamic coupling between the vacuum chamber and the specimen, damping values are measured with and without the chamber cap under ambient conditions. Comparing the normalized damping course with and without the chamber cap (shown in Fig. 11), it can be seen, that there is no influence of the chamber cap on the measured damping value. Additionally, a decrease of the normalized damping value with decreasing pressure is visible. With regard to the ambient pressure conditions, the damping decreases to 17%. The mean standard deviation is in a range of about 0.02% of the measured damping value at the maximal amplitude with respect to the analyzed configuration. Herewith, an adequate reproducibility can be obtained. Due to the used scaling factor, the influence of normalized amplitude on the damping value cannot be recognized.

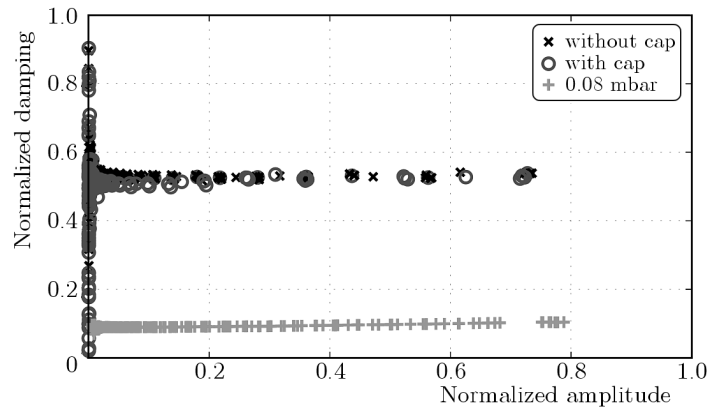


Fig. 11. Normalized damping as a function of normalized amplitude and pressure

The next analyzed parameter is the torque of the screws with the apex (see Fig. 1). This analysis is performed at 0.08 mbar (vacuum conditions). Five different torque magnitudes are analyzed. The normalized damping value versus the normalized amplitude is shown in Fig. 12.

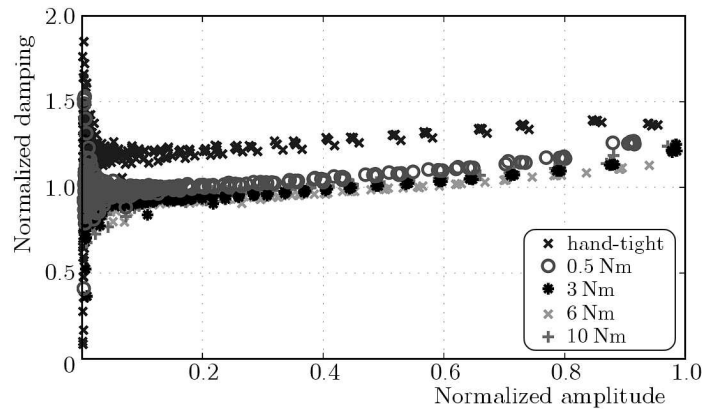


Fig. 12. Normalized damping as a function of normalized amplitude and torque

Based on this analysis, an amplitude-dependent damping value can be identified. Here, the damping value increases with the increasing amplitude. The maximal damping is measurable at the lowest torque (hand-tight). Under these conditions, the specimen is not completely fixed in its nodes of vibration, starting to rattle after the force impact. Frictional and impact effects are present and responsible for additional energy dissipations. In this respect, higher damping values are measurable. With an increasing torque magnitude, the damping value decreases to the lowest damping value at a torque magnitude of about 6 Nm. Assuming that the lowest measurable damping value course represents the energy dissipation due to dissipation within the material, the specimen-specific material damping value is measurable under these conditions. By a further increase of the torque value, the damping increases too. In this context, the apex geometry is discussed. The point of contact is plasticized, and the damaged apex lies flat on the specimen. Through these measurements, a mean standard deviation of about 0.03% of the measured damping value at the maximal amplitude with respect to the analyzed configuration is identifiable.

To check the influence of the apex variation on the damping value, different apex geometries are analyzed. From this, three different apex geometries are used (see Fig. 13), whereby the apex radius r is varied.

For specimen clamping, a torque of 6 Nm (identified before) is used. The tests are performed at 0.08 mbar (vacuum conditions). In Fig. 14, the influence of this variation on the damping value is presented.

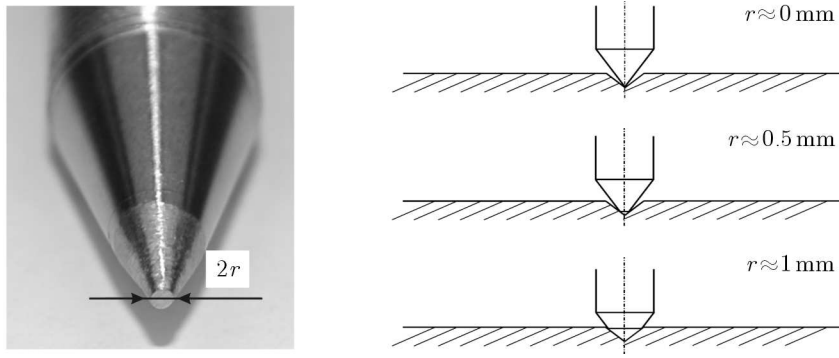


Fig. 13. Apex geometry

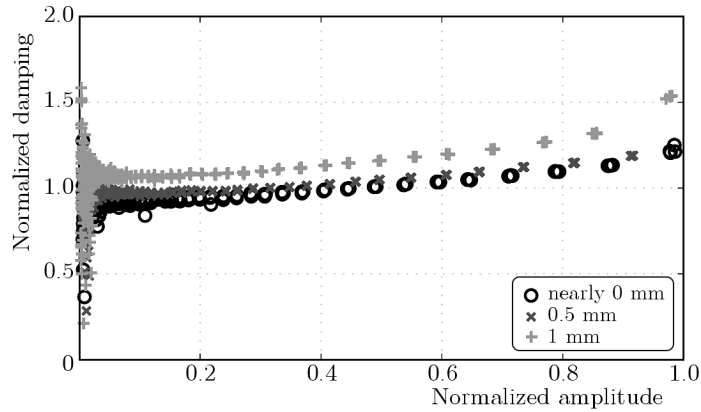


Fig. 14. Normalized damping as a function of normalized amplitude and apex geometry

The damping value increases with the increasing apex radius. This effect leads to an additional frictional damping within the contact area. Here, the lowest damping is identifiable at the lowest apex radius (approximately 0 mm). For these configurations, also a low standard deviation (0.028% of the measured damping value at the maximal amplitude) is identifiable. This is the basis for proving the adequate reproducibility of the measured values.

Based on this analysis, it can be seen that a sufficient adjustment of the experimental setup is necessary for sufficient structural damping identification arising from the material. In Table 3, the adjustment of different parameters regarding the experimental setup is summarized.

Table 3. Adjustment of the experimental setup

Parameter	Magnitude
Pressure	0.08 mbar
Clamping torque	6 Nm
Apex radius	≈ 0 mm

5. Model verification

To demonstrate further utilization of the experimental data, the measured values are used to parameterize a common model for material damping description. For this purpose, the test rig is adjusted with respect to the data presented in Table 3. It now becomes obvious that the measured normalized damping values correspond to the lowest measured values made in previous investigations (see Fig. 14, Fig. 12 and Fig. 11). These damping values, which arise

from dissipations within the material, are used for parameterization. In this connection, a static hysteresis model is utilized which was already recommended by Lazan (1968)

$$\Psi_S = \frac{\Delta W_S}{2\pi U_S} = \frac{1}{2\pi U_S} \int_{V=0}^{V_S} \Delta W_{loc} dV = \frac{1}{2\pi U_S} \int_{V=0}^{V_S} J\sigma^n dV \quad (5.1)$$

In Eq. (5.1), Ψ_S , ΔW_S , U_S and V_S represent the specimen-specific loss coefficient, the entire loss, the potential energy and the entire volume of the specimen. In this context, the local energy dissipation ΔW_{loc} is describable as a function of the local stress σ weighted by two material constants J and n . Analyzing the stress distribution by the Finite Element approach within the specimen, the parameters can be identified. From this, the least squares method is used to identify the magnitudes on the basis of the experimental data. In Fig. 15, the course of the normalized damping with respect to the maximal local stress σ_{max} is presented.

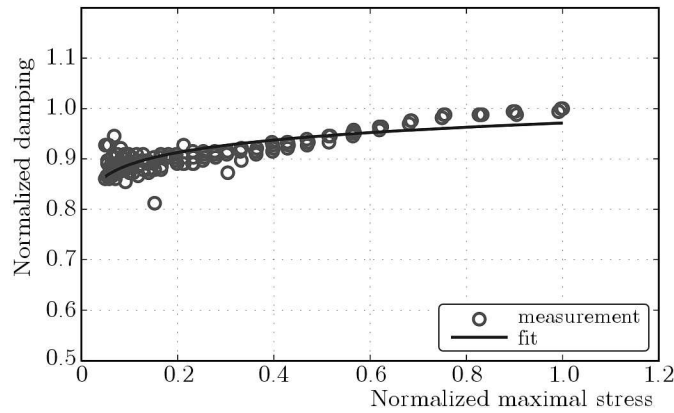


Fig. 15. Parameterization of a common model for material damping description

It is to be mentioned that the maximal local stress σ_{max} within the specimen corresponds to the measured amplitude. The magnitude of the maximal local stress is identified using the Finite Element approach. Finally, it can be seen that the experimental data presented in Fig. 15 are describable in a suitable way using the static hysteresis model presented by Lazan (1968). In this context, the coefficient of determination has a magnitude of $R^2 = 0.94$.

6. Conclusions

In the present paper, an experimental setup for specimen-specific material damping determination is developed. A design optimization with respect to the natural frequencies of a vacuum chamber and a frequency range of interest are performed. It could be shown that requested frequency gaps are achieved to avoid possible aerodynamic coupling between test specimen and vacuum chamber. In addition, test specimens are clamped in their nodes of vibration to avoid unintended frictional damping. The clamping device is also frequency optimized to avoid possible structural coupling. Moreover, a method for damping determination is discussed briefly. Subsequently, several parameters influencing the measured specimen-specific damping value using the analyzed setup are identified. It can be shown that a defined magnitude of the clamping torque as well as a defined geometry of the clamping apex is important to identify an accurate damping value. In this connection, an adjustment of the experimental setup is presented. In this context, the lowest identifiable damping value is used as a criterion for the adjustment of the experimental setup. Additionally, it can be shown that an adequate reproducibility of the

measured values is realizable. Finally, a model for material damping description is parameterized on the basis of the measured material-specific damping values.

Using the developed experimental setup, it is possible to identify influential parameters on structural damping values arising from dissipations within the material. Based on this, development and parameterization of material damping models is realizable. It should be mentioned, that the analyzable respectively excitable frequency range is limited by the impact force.

References

1. ANSYS Inc., 2009, Advanced Analysis Techniques Guide, *ANSYS Inc.*, Release 12.0, Canonsburg
2. BERT C.W., 1973, Material damping: an introductory review of mathematical models measures and experimental techniques, *Journal of Sound and Vibration*, **29**, 129-153
3. GIBERT C., BLANC L., ALMEIDA P., LEBLANCA X., OUSTYB J.P., THOUVEREZA F., LAÎNÉ J.-P., 2012, Modal tests and analysis of a radial impeller at rest: influence of surrounding air on damping, *Proceedings of ASME Turbo Expo 2012, Power for Land, Sea and Air*, Copenhagen Denmark, Paper GT2012-69577
4. GIBSON R.F., PLUNKETT R., 1977, A forced-vibration technique for measurement of material damping, *Journal of Experimental Mechanics*, **17**, 297-302
5. GRANICK N., STERN J.E., 1965, Material damping of aluminum by a resonant dwell technique, *NASA Technical Note, National Aeronautics and Space Administration*, Washington D.C., USA, NASA TN D-2893
6. GUDMUNDSON P., WÜTHRICH C., 1986, Die Werkstoffdämpfung von Stählen bei hohen Dehnungsamplituden, *Materialwissenschaft und Werkstofftechnik*, **17**, 286-292, Weinheim, Germany
7. HE J., FU Z.F., 2001, *Modal Analysis*, Butterworth Heinemann, Oxford Auckland Boston Johannesburg Melbourne New Dehli
8. HENTSCHEL O.P., PANNING-VON SCHEIDT L., WALLASCHEK J., DENK M., 2015, Introduction and evaluation of a damping determination method based on a short-term fourier transform and resampling (STFR), *Journal of Theoretical and Applied Mechanics*, **53**, 2, 395-407
9. KRACK M., PANNING L., WALLASCHEK J., SIEWERT C., HARTUNG A., 2012, Robust design of friction interfaces of bladed disks with respect to parameter uncertainties, *Proceedings of ASME Turbo Expo 2012, Power for Land, Sea and Air*, Copenhagen Denmark, Paper GT2010-68578
10. LABORENZ J., SIEWERT C., PANNING L., WALLASCHEK J., GERBER C., MASSEREY P.A., 2010, Eddy current damping: a concept study for steam turbine blading, *Journal of Engineering for Gas Turbines and Power*, **132**, 1-7
11. LAZAN B., 1968, *Damping of Materials and Members in Structural Mechanics*, Pergamon Press, Oxford London Edinburgh New York Toronto Sydney Paris Braunschweig
12. PETROV E.P., EWINS D.J., 2006, Effects of damping and varying contact area at blade-disk joints in forced response analysis of bladed disk assemblies, *Journal of Turbomachinery*, **128**, 403-410
13. PLUNKETT R., 1959, Measurement of damping, [In:] *Structural Damping*, Ruzicka J. (Edit.), ASME, 117-131, Atlantic City NJ USA
14. RICE T., BELL D., SINGH G., 2007, Identification of the stability margin between safe operation and the onset of blade flutter, *Proceedings of ASME Turbo Expo 2007, Power for Land, Sea and Air*, Montreal Canada, Paper GT2007-27462
15. RICHARDSON M.H., FORMENTI D.L., 1982, Parameter estimation from frequency response measurements using rational fraction polynomials, *Proceedings of the First International Modal Analysis Conference*, Orlando FL USA, 167-180

16. SIEWERT C., PANNING L., GERBER C., MASSEREY P.A., 2010, Numerical and experimental damping prediction of a nonlinearly coupled low pressure steam turbine blading, *Proceedings of ASME Turbo Expo 2008, Power for Land, Sea and Air*, Berlin Germany, Paper GT2010 51073
17. SIEWERT C., STÜER H., 2010, Forced response analysis of mistuned turbine bladings, *Proceedings of ASME Turbo Expo 2010, Power for Land, Sea and Air*, Glasgow UK, Paper GT2010-23782
18. SZWEDOWICZ J., SECALL-WIMMEL T., DNCK-KERST P., 2008, Damping performance of axial turbine stages with loosely assembled friction bolts, the non-linear dynamic assessment, *Journal of Engineering for Gas Turbines and Power*, **130**, 3, 1-14
19. WEIWEI G., ZILI X., 2010, 3D numerical friction contact model and its application to nonlinear blade damping, *Proceedings of ASME Turbo Expo 2010, Power for Land, Sea and Air*, Glasgow UK, Paper GT2010-22292

Manuscript received January 19, 2015; accepted for print June 12, 2015

ANALYTICAL AND EXPERIMENTAL VIBRATION ANALYSIS OF TELESCOPIC PLATFORMS

ADIL YUCEL, ALAEDDIN ARPACI

Istanbul Technical University, Department of Mechanical Engineering, Taksin, Istanbul, Turkey

e-mail: adil.yucel@itu.edu.tr; arpacial@itu.edu.tr

In this study, vibration analysis of a telescopic platform is conducted, and the platform structure is reconstructed to satisfy vibrational standards. The analysis is realised using solid modelling, finite elements and an analytical method. The results are verified using experimental modal techniques. Through the finite element and experimental modal approach free vibration analysis is carried out and natural frequencies are determined. Additionally, vibration accelerations of the structure are obtained by forced vibration analysis of the model. All calculations are performed on the new reconstructed structure, and it is determined whether the reconstructed structure satisfies the vibrational standards.

Keywords: telescopic platforms, modal analysis, Finite Element Method, vibration

1. Introduction

Platforms are crane-like machines that lift workers and their equipment to desired heights and over various distances. The word 'platform' was only used to describe static structures such as bridges and ladders until the second half of the twentieth century. However, over the past 30 years, various types of platforms have been specified:

- jointed platforms
- trussed platforms
- load platforms
- telescopic platforms
- vertical platforms

In this study, we examine vibrations of telescopic platforms, which are widely used in construction areas, airports and harbours. Telescopic platforms are structures that have at least two long beams, with one sliding within the other, called booms. Usually, the second boom operates through hydraulic cylinders, and the other subsequent booms operate through chains. An example of a telescopic platform with five booms is shown in Fig. 1.

A survey of the literature reveals that many studies have been conducted using the finite element method and three-dimensional modelling. Dayawansa *et al.* (2004) described cracks that grow in weld joints (called clusters), which protect the booms from catastrophic collapse, and the maintenance and repair techniques used to keep these joints in service. Karahan (2007) designed and analysed a two-level telescopic crane using the finite element method. The parts of the crane were designed in 3D using the Pro ENGINEER software program. The sheet thickness of the main stationary boom carrying the load was determined by performing stress analysis in the ANSYS workbench using the finite element method. Marjamaki and Makinen (2006) extended the idea of modelling a flexible telescopic boom using a non-linear finite element method in 3D. The boom was assembled using Reissner's geometrically exact beam elements. The sliding



Fig. 1. An example of a five-boom telescopic platform

boom parts were coupled together by the elements where the slide-spring was coupled to the beam with the aid of the master-slave technique. A special element with a revolute joint and an element with an offset were developed. Telescopic movement was achieved by varying the length of the element and the connecting chains. Ozkan (2005) analysed connection points of a frame crane and investigated stress distributions of the connection point components. The commercial finite element package ANSYS was used for finite element analysis. The main objectives of the study conducted by Rusiński *et al.* (2006) were to discuss design problems associated with machines used in underground mining and to investigate the reasons why these problems arise in the cracked boom of an underground mine machine. Numerical and experimental approaches were pursued. The finite element method was used for numerical simulation. Fractographic and microscopic evaluation, chemical analysis and hardness tests were used to evaluate the materials. The objectives were achieved by numerical simulation of a cracked loader boom, material evaluations of specimens and comparison of the results obtained from both approaches. Numerical simulations were performed based on a discrete model of a jib boom using predefined boundary conditions. The finite element analysis of the jib boom provided information regarding stress distribution under extreme load conditions. The study involved macroscopic and fractographic inspection, microscopic evaluation as well as hardness testing of the materials used for the jib boom. Erdol (2007) performed static finite element analysis and weight optimisation of a box girder, which constitutes approximately 50% of the total weight of gantry crane structures. Trabka (2014) presented ten variants of a computational model for a telescopic boom crane that differs in the number and selection of flexible components. Modelling and numerical simulations were conducted using the finite element method. In the study, the compatibility of the numerical simulation results and test results of a real structure was qualitatively and quantitatively assessed. Time characteristics and frequency characteristics after application of the discrete Fourier transformation were also analysed in the study. Posiadała and Cekus (2008) presented one degree of freedom discrete model representing vibration of the telescopic boom of a truck crane in the rotary plane. In the model, the influence of the hydraulic cylinder on the crane radius change was considered. Park and Chang (2004) applied time delay control and commandless input shaping technique, which is a modification-based on the concept of Input Shaping Technique to increase the productivity of the boom of the telescopic handler. Lastly, Sochacki (2007), considered the dynamic stability of a laboratory model of the truck crane. In the study, the results in form of frequency curves for changing the geometry of the system were presented. In this study, vibrational analyses of telescopic platforms are conducted, and these structures are optimised to satisfy vibrational standards.

2. Models

In this study, a telescopic platform with five booms and a maximum operating height of 24 m has been selected for modelling. The booms are modelled in two different cross-sections: rectangular and annular. The telescopic platform which is was constructed using annular cross sectional booms, is named the 'reconstructed structure' in the study. All of the components of the platform are modelled using the Pro/ENGINEER software. The model consists of the following main parts: foundation, tower, booms, basket joint and basket. The first part that is modelled is the foundation. The foundation is based on a 4920×2100 mm area, and profiles with cross-sections measuring $80 \times 160 \times 6$ mm are used for modelling where 80 mm represents height, 160 mm represents width and 6 mm represents thickness of the thin-walled rectangular section. The tower is mounted on the foundation using a group of gears located in the reduction gear box. The next part that is modelled is called the tower. The base flange of the tower has thickness of 20 mm. It consists of $16 \times \emptyset 17$ mm holes that are used to mount the gear box. The tower can rotate 360° around its axis, but its operation angle is limited to 180° . The piston that connects the first boom to the tower is also modelled. The properties of the five booms modelled in this study are presented in Tables 1 and 2 for the rectangular and annular cross-section, respectively. The solid models for the booms with rectangular and annular cross-sections are also presented in Figs. 2 and 3, respectively.

Table 1. Dimensions of the booms with thin-walled rectangular cross-sections

Boom No.	Length ℓ_i [mm]	Cross-section [mm]
1	4580	$292 \times 510 \times 8$
2	3600	$250 \times 422 \times 6$
3	3600	$210 \times 340 \times 5$
4	3600	$170 \times 260 \times 5$
5	3600	$132 \times 202 \times 5$

Table 2. Dimensions of the booms with thin-walled annular cross-sections

Boom No.	Length ℓ_i [mm]	Cross-section [mm]
1	4580	$\emptyset 340 \times 12$
2	3600	$\emptyset 280 \times 12$
3	3600	$\emptyset 232 \times 10$
4	3600	$\emptyset 184 \times 8$
5	3600	$\emptyset 132 \times 8$



Fig. 2. A boom with a rectangular cross-section

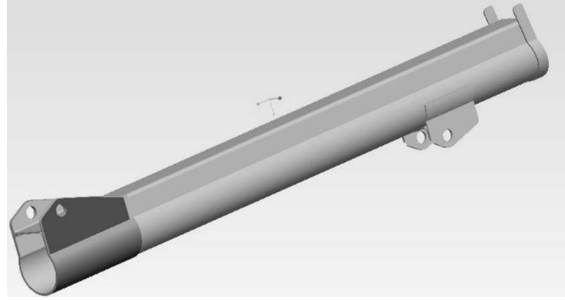


Fig. 3. A boom with an annular cross-section

One of the most important components of the model is the basket joint. The basket joint is the vital part that connects the last boom to the basket in which the worker operates. The last component of the model is the basket in which the work operates. The basket is modelled using $\emptyset 30 \times 2.5$ mm round profiles. It has base area of 900×1500 mm and height of 1120 mm. The assemblies are constructed both for rectangular and annular section booms.

3. Finite element analysis for full assemblies

After the assembled 3D solid model of the telescopic platform is obtained, it is imported into the commercial finite element analysis software program ABAQUS for natural frequency and mode shape analysis. The approximate mesh size of the finite element model is 100 mm. The meshed finite element model is shown in Fig. 4. Linear tetrahedral solid elements are used in the mesh and the material properties are taken as follows:

- density: 7850 kg/m^3
- Poisson's ratio: 0.3
- modulus of elasticity: 210000 MPa

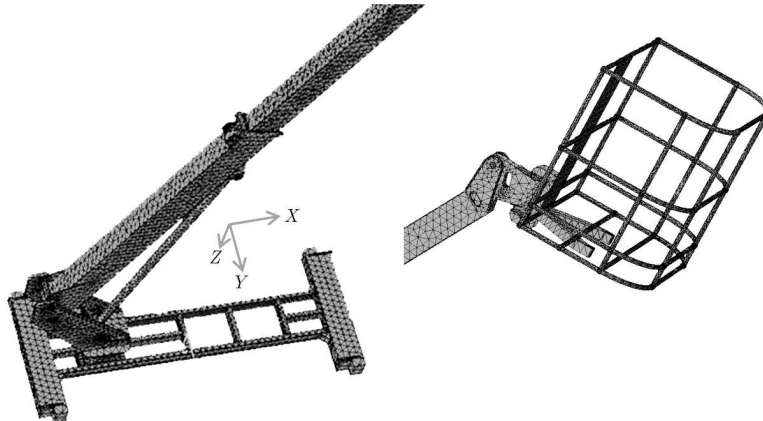


Fig. 4. Finite element model

The first 10 natural frequencies are presented in Table 3. In Table 3, 'ip' and 'op' stand for the in-plane (XZ plane) and out-of-plane (XY plane) mode shapes, respectively.

The source of the excitation is mainly the engine, and the origin of the excitation has been accepted as the foundation; therefore, we conducted the forced vibration finite element analysis by applying the force to the foundation of the platform. The operating (excitation) frequency of the system is 12.875 Hz. This is the frequency of the system when the engine runs idle and the

Table 3. Natural frequencies

Mode No.	Natural frequency [Hz] (rectangular section)	Natural frequency [Hz] (annular section)	Mode shape
1	0.2987	0.2515	ip
2	0.4196	0.2668	op
3	1.1249	1.0035	ip
4	1.6382	1.0812	op
5	4.9468	4.1055	ip
6	7.1794	4.4389	op
7	12.125	10.105	ip
8	16.929	10.988	op
9	21.803	18.631	ip
10	31.183	19.926	op

workers are working in the basket. As shown in Table 3, the natural frequency is $f = 12.125$ Hz, which is very close to the operating frequency of the system. This indicates a risk of resonance under operating conditions. Therefore, the model has been reconstructed. After reconstruction (annular boom profile), it has been clearly revealed that there is no natural frequency close to the operating frequency of the system, which validates the reconstruction.

4. Analytical solution for the five-boom model

For flexural modes, the boom is modelled as shown in Fig. 5.

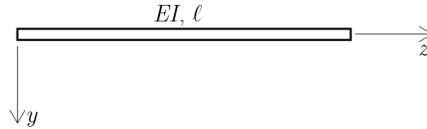


Fig. 5. Analytical model of the boom for flexural modes

Let the deflection in the y direction be $\nu(z, t)$. The equation of vibration for the beam element is given as

$$EI \frac{\partial^4 \nu}{\partial z^4} + \mu \frac{\partial^2 \nu}{\partial t^2} = 0 \quad (4.1)$$

where μ is mass per unit length, ρ is mass density, A is cross-sectional area, t is time and EI represents the flexural stiffness. As known

$$\mu = \rho A \quad (4.2)$$

and

$$\nu(z, t) = \phi(z) \sin(\omega t) \quad (4.3)$$

for harmonic motion. Substituting Eq. (4.3) into Eq. (4.1) gives

$$\frac{\partial^4 \phi}{\partial z^4} - \frac{\mu \omega^2}{EI} \phi = 0 \quad (4.4)$$

The solution is

$$\phi(z) = A \cosh \frac{\lambda z}{\ell} + B \sinh \frac{\lambda z}{\ell} + C \cos \frac{\lambda z}{\ell} + D \sin \frac{\lambda z}{\ell} \quad (4.5)$$

where A , B , C and D are the integration constants and

$$\lambda = \ell \sqrt[4]{\frac{\mu\omega^2}{EI}} \quad (4.6)$$

For a five-boom structure, the equations are arranged as below. The model of the booms of a telescopic platform with a point mass at the free end is shown in Fig. 6, where M is mass of the point mass, and J is mass moment of inertia of the point mass with respect to the x -axis for in-plane and the y -axis for out-of-plane analysis

$$\phi_i(z) = A_i \cosh \frac{\lambda_i z}{\ell_i} + B_i \sinh \frac{\lambda_i z}{\ell_i} + C_i \cos \frac{\lambda_i z}{\ell_i} + D_i \sin \frac{\lambda_i z}{\ell_i} \quad i = 1, 2, 3, 4, 5 \quad (4.7)$$

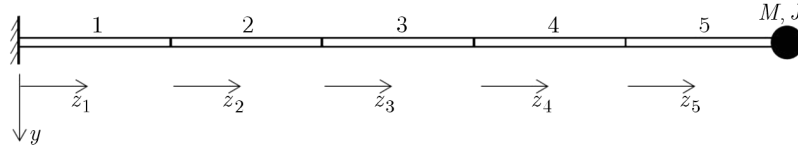


Fig. 6. Analytical model of the five-boom structure for flexural modes

Geometric boundary conditions are

$$\phi_1(0) = 0 \quad \frac{d\phi_1}{dz}(0) = 0 \quad (4.8)$$

Transition boundary conditions are ($i = 1, 2, 3, 4$)

$$\begin{aligned} \phi_i(\ell_i) &= \phi_{i+1}(0) & \frac{d\phi_i}{dz}(\ell_i) &= \frac{d\phi_{i+1}}{dz}(0) \\ EI_i \frac{d^2\phi_i}{dz^2}(\ell_i) &= EI_{i+1} \frac{d^2\phi_{i+1}}{dz^2}(0) & EI_i \frac{d^3\phi_i}{dz^3}(\ell_i) &= EI_{i+1} \frac{d^3\phi_{i+1}}{dz^3}(0) \end{aligned} \quad (4.9)$$

Natural boundary conditions are

$$EI_5 \frac{d^2\phi_5}{dz^2}(\ell_5) - \omega^2 J \frac{d\phi_5}{dz}(\ell_5) = 0 \quad EI_5 \frac{d^3\phi_5}{dz^3}(\ell_5) + \omega^2 M \phi_5(\ell_5) = 0 \quad (4.10)$$

For torsional modes, the boom is modelled as shown in Fig. 7.

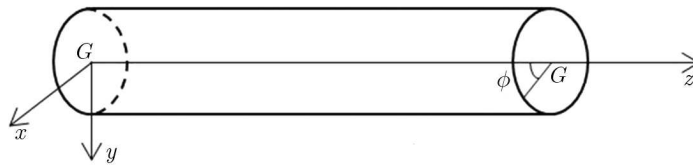


Fig. 7. Analytical model of the boom for torsional modes

Let the twist angle about the z -axis be $\varphi(z, t)$. The equation of vibration for the beam element is given as

$$\varphi = \varphi(z, t) \quad GC \frac{\partial^2 \varphi}{\partial z^2} = \rho I_p \frac{\partial^2 \varphi}{\partial t^2} \quad (4.11)$$

where GC is the torsional stiffness related to Saint-Venant's principle. For harmonic motion, substituting Eq. (4.12)₁ into Eq. (4.11)₂ gives Eq. (4.12)₂

$$\varphi = \theta(z) \sin(\omega t) \quad c^2 \frac{\partial^2 \theta}{\partial z^2} + \omega^2 \theta = 0 \quad (4.12)$$

where

$$c^2 = \frac{GC}{I_p} \quad (4.13)$$

The solution is

$$\theta(z) = A \sin \frac{\omega z}{c} + B \cos \frac{\omega z}{c} \quad (4.14)$$

where A and B are the integration constants. For the booms of the telescopic platform

$$\theta_i(z_i) = A_i \sin \frac{\omega z_i}{c_i} + B_i \cos \frac{\omega z_i}{c_i} \quad c_i^2 = \frac{GC_i}{\rho(I_p)_i} \quad i = 1, 2, 3, 4, 5 \quad (4.15)$$

Geometric boundary conditions are

$$\theta_1(0) = 0 \quad \theta_i(\ell_i) = \theta_{i+1}(0) \quad i = 1, 2, 3, 4 \quad (4.16)$$

Transition boundary conditions are

$$GC_i \frac{d\theta_i}{dz}(\ell_i) = GC_{i+1} \frac{d\theta_{i+1}}{dz}(0) \quad i = 1, 2, 3, 4 \quad GC_5 \frac{d\theta_5}{dz}(\ell_5) = 0 \quad (4.17)$$

The results of the finite element analysis and analytical solutions for both rectangular and annular cross-sectional five-boom systems are given in Tables 4-7. In Table 4, 'ip' and 'op' stand for the in-plane and out-of-plane mode shapes, respectively. The value of the point mass is 200 kg, which is the sum of masses of the basket and the worker. The discrepancies in Tables have been calculated according to the formula given below

$$\text{Dis. [\%]} = \frac{\text{Analytical} - \text{FEA}}{\text{Analytical}} \cdot 100$$

Table 4. Flexural natural frequencies for rectangular cross-sections

Rectangular section (five-boom without point mass)			Rectangular section (five-boom with point mass)			Rectangular section (full assembly)	Mode shape
FEA	Analytical	Dis. [%]	FEA	Analytical	Dis. [%]	FEA	
			0.3045	0.3134	2.84	0.2987	ip
			0.4286	0.4425	3.14	0.4196	op
1.3610	1.4180	4.02	1.1529	1.1924	3.31	1.1249	op
2.0196	2.1049	4.05	1.6864	1.7486	3.56	1.6382	op
5.1049	5.3411	4.42	5.1198	5.3358	4.05	4.9468	op
7.4014	7.7389	4.36	7.4375	7.7484	4.01	7.1794	op
12.027	12.649	4.92	12.291	12.884	4.60	12.125	op
17.324	18.258	5.12	17.714	18.629	4.91	16.929	op
22.285	23.643	5.74	22.862	24.182	5.46	21.803	op
31.995	34.076	6.11	32.811	34.881	5.93	31.183	op

Table 5. Flexural natural frequencies for annular cross-sections

Annular section (five-boom without point mass)			Annular cross-section (five-boom with point mass)			Annular cross-section (full assembly)
FEA	Analytical	Dis. [%]	FEA	Analytical	Dis. [%]	FEA
			0.2549	0.2691	5.28	0.2515
1.2790	1.3410	4.62	1.0224	1.0745	4.85	1.0035
4.4066	4.6309	4.84	4.2253	4.4469	4.98	4.1055
10.366	11.010	5.85	10.425	11.134	6.37	10.105
19.119	20.419	6.37	19.339	20.875	7.36	18.631
31.444	33.434	5.95	31.584	33.926	6.90	30.105
48.990	52.014	5.81	48.927	52.673	7.11	46.439
65.911	70.520	6.54	65.163	71.154	8.42	61.458

Table 6. Torsional natural frequencies for rectangular cross-sections

Rectangular cross-section (five-boom model)			Rectangular cross-section (full assembly)
FEA	Analytical	Dis. [%]	FEA
61.67	63.71	3.20	60.5784
110.96	112.10	1.02	105.988
167.98	169.81	1.08	156.036
214.76	230.28	6.74	190.169

Table 7. Torsional natural frequencies for annular cross-sections

Annular section (five-boom model)			Annular section (full assembly)
FEA	Analytical	Dis. [%]	FEA
76.44	79.47	3.81	74.7758
135.92	140.40	3.19	129.100
204.09	210.30	2.95	186.386
273.28	282.68	3.33	233.853

5. Experimental modal analysis

To conduct forced vibration analysis using the finite element method, we need to determine the excitation force of the system. Due to the restrictions regarding the construction of the telescopic platform, it is impossible to locate a force transducer to measure the excitation force of the system. Instead, we measure the acceleration values of the foundation and basket. Then, we conduct a series of forced vibration analyses using the finite element method to satisfy these acceleration values measured at certain points using sensors on the platform. Thus, we obtain the excitation force value required to further reconstruct the structure. The positions of the sensors on the system are shown in Fig. 8. A B&K 4524B triaxial CCLD piezoelectric accelerometer with frequency range of 0.25-3000 Hz and sensitivity of 100 mV/g has been used in the experiments. FFT analyses are conducted for 0-100 Hz (800 lines – 0.125 Hz resolution) with sampling rate of 256 Hz (256 samples per second).

The first triaxial accelerometer is located on the connection part between the foundation and the tower so we obtain the acceleration data for the foundation to create the simulation



Fig. 8. Locations of the sensors on the foundation and basket

of forced vibration analysis. Secondly, another triaxial accelerometer is located on the floor of the basket to obtain the acceleration data for the basket in order to use in the forced vibration simulation. These data obtained by the measurements on the foundation and basket are then used as reference values in the forced vibration analysis, and a series of forced vibration simulations are carried out to satisfy these reference values. The correct excitation force value is detected when we reach the same values on the foundation and basket as the reference values. This excitation force value which is obtained from forced vibration simulations is then used in the forced vibration simulation of the reconstructed platform model (annular boom profile). Thus, both models have been excited by the same and correct excitation force for the forced vibration simulations.

The results of spectral analyses of the acceleration data obtained by the sensors on the foundation and basket are shown in Figs. 9 and 10.

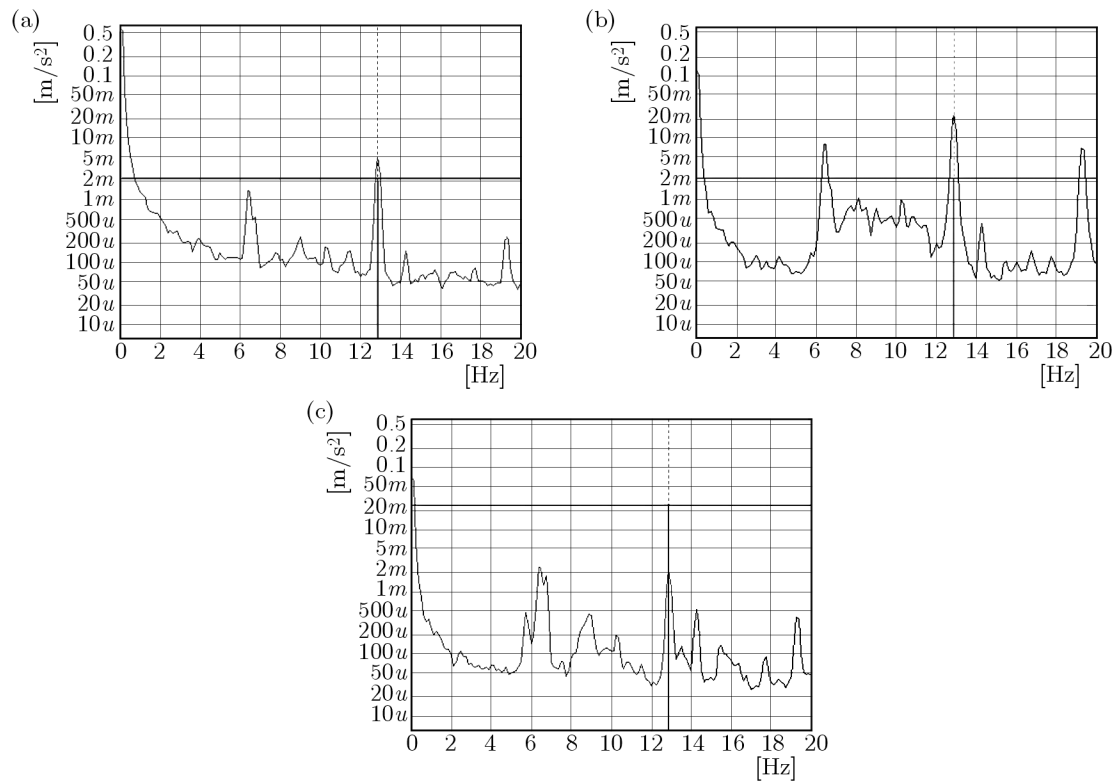


Fig. 9. Spectral analysis of foundation vibration of the telescopic platform: (a) X direction, (b) Y direction, (c) Z direction

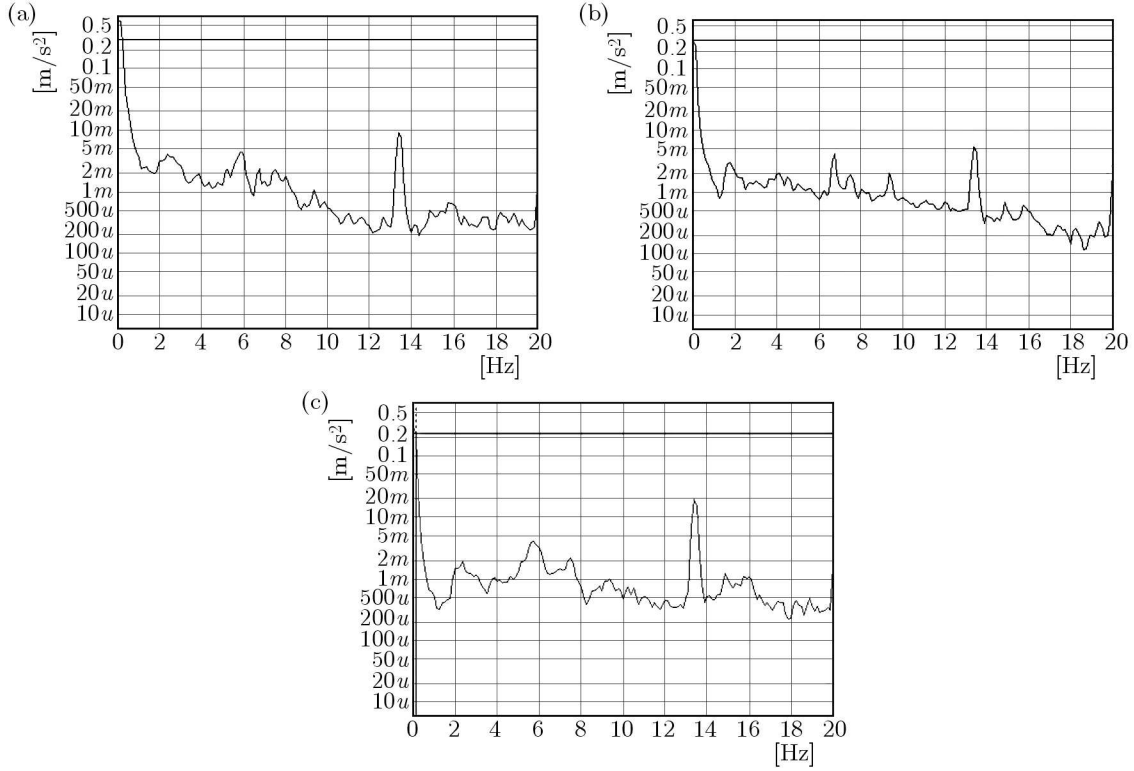


Fig. 10. Spectral analysis of basket vibration of the telescopic platform: (a) X direction, (b) Y direction, (c) Z direction

The main units written at the top of the axes in Fig. 9 and Fig. 10 are m/s^2 . $2m$ means $2\text{ mm}/s^2$ where m stands for mm . $500u$ means $500\text{ }\mu\text{m}/s^2$ where u stands for μm .

Using the results of spectral analysis, the acceleration values at the operating frequency have been determined. They are presented in Table 8.

Table 8. Experimentally obtained acceleration values at the operating frequency

Direction	Foundation [mm/s^2]	Basket [mm/s^2]
X	5.004	9.173
Y	24.455	5.494
Z	2.203	19.532

Having realised the forced vibration analysis using the finite element method to satisfy the acceleration values, the distributed excitation force is determined to be $8.52 \cdot 10^{-6}\text{ ton}/\text{mm}^2$ (0.0836 MPa). This force has been used to analyse both assembly models (with rectangular and annular boom profiles).

6. Conclusions

In this study, vibrational analysis of a telescopic platform has been conducted. This structure has been reconstructed to satisfy vibrational standards (applying to the industrial safety regulations) and shift resonance frequencies. The vibrational analyses are conducted using solid modelling, finite elements and an analytical method. The results of the analysis are also verified using the experimental modal technique.

The operating (excitation) frequency of the system is 12.875 Hz. The table of natural frequencies of the original model indicates that there is a natural frequency value of 12.125 Hz that is very close to the operating frequency of the system. This reveals a risk of resonance under operating conditions. After reconstruction, it has been clearly revealed that there is no natural frequency close to the operating frequency of the system, which validates the reconstruction.

Although it is impossible to locate a force transducer on the system and to measure the acting force, the distributed force has been determined to be $8.52 \cdot 10^{-6}$ ton/mm² (0.0836 MPa) using experimental modal analysis by taking the acceleration values obtained experimentally into account. We measured the accelerations in different points of the system and then conducted a series of forced vibration finite element analyses with different force values until we achieved the acceleration values obtained by the experiments. This force value can be used in any modal analysis of this model.

By examining the related standard, it has been observed that the acceleration values on the basket are very high for workers. After the reconstruction, we observed a significant reduction in the acceleration values. The acceleration values on the basket before and after reconstruction are presented in Table 9. According to the related standard (ISO 2631), which defines the maximum allowed acceleration values for a worker, the acceleration values on the basket after reconstruction stay considerably under the limits for the operating frequency.

Table 9. Comparison of acceleration values on the basket

Direction	Rectangular cross-ception (original) [mm/s ²]	Annular cross-section (reconstructed) [mm/s ²]
<i>X</i>	9.597	1.358
<i>Y</i>	5.709	1.267
<i>Z</i>	20.636	3.528

Tables 4-7 indicate that five-boom analytical models can be accepted instead of full assemblies because parts other than the booms have little effect on the frequencies. Therefore, we can agree that the telescopic platform can be taken as a connection of beams with varying cross-sections for frequency calculations. The results also show that the point mass, which replaces the masses of the basket and workers in the analytical model, causes very little difference on natural frequencies but only changes the mode shapes. The point mass has no effect on torsional modes.

Acknowledgments

We want to thank Ms. Elif Naz Aladag and Mr. Mehmet Ozaltinoglu for their supports in the preparation of solid models and analyses files.

References

1. DAYAWANSA P., CHITTY G., KEREZSI B., BARTOSIEWICZ H., PRICE J.W.H., 2004, Fracture mechanics of mining dragline booms, *Structural Integrity and Fracture: Proceedings of the International Conference, SIF2004*, Brisbane, Australia
2. ERDOL T., 2007, Design, analysis of the gantry crane with finite element method and box girder optimization, Master's Thesis, Gebze Institute of Technology, Gebze, Turkey
3. KARAHAN M., 2007, Design and finite element analysis of two levels telescopic crane, Master's Thesis, Ataturk University, Erzurum, Turkey
4. MARJAMAKI H., MAKINEN J., 2006, Modelling a telescopic boom – the 3D case: Part II, *Computers & Structures*, **84**, 29, 2001-2015

5. OZKAN I., 2005, Computer aided design and analysis of frame crane, Master's Thesis, Dokuz Eylul University, Izmir, Turkey
6. RUSIŃSKI E., CZMOCHOWSKI J. MOCZKO, P., 2006, Numerical and experimental analysis of a mine's loader boom crack, *Journal of Achievements in Materials and Manufacturing Engineering*, **17**, 1/2, 273-276
7. SOCHACKI W., 2007, The dynamic stability of a laboratory model of a truck crane, *Thin-Walled Structures*, **45**, 927-930
8. POSIADAŁA B., CEKUS D., 2008, Discrete model of vibration of truck crane telescopic boom with consideration of the hydraulic cylinder of crane radius change in the rotary plane, *Automation in Construction*, **17**, 245-250
9. PARK J.Y., CHANG P.H., 2004, Vibration control of a telescopic handler using time delay control and commandless input shaping technique, *Control Engineering Practice*, **12**, 769-780
10. TRABKA A., 2014, Dynamics of telescopic cranes with flexible structural components, *International Journal of Mechanical Sciences*, **88**, 162-174

Manuscript received July 16, 2014; accepted for print June 20, 2015

AN INVERSE KINEMATIC ALGORITHM FOR THE HUMAN LEG

SEBASTIAN GŁOWIŃSKI, TOMASZ KRZYŻYŃSKI

Koszalin University of Technology, Faculty of Technology and Education, Koszalin, Poland

e-mail: sebastian.glowinski@tu.koszalin.pl; tomasz.krzyzynski@tu.koszalin.pl

In this article, a 3-link kinematic model of a human leg is defined and analyzed with focus on optimizing the manipulability. The forward kinematics for the leg is used to define quantitative measures of the manipulability and workspace in a sagittal plane. Analytical results for different manipulability indices are derived. Using numerical optimization in Matlab package, the manipulability measure is optimized under different constraints. The range of motion and joint comfort zones of every joint is defined. The algorithm for redundant chain, based on analytical equations, is proposed in inverse kinematics.

Keywords: inverse kinematics, human leg, optimization

1. Introduction

The inverse kinematics of a human leg is the mapping that, given a goal position, calculates a set of joint positions so as to place the human leg effector (e.g. toe) in the specified goal. It is very important in the rehabilitation process. In this work, we present the main concerns on finding an inverse kinematics algorithm for a 3 link kinematic leg in plane. The work is divided into two parts: the first one, describing the analytical method for solving inverse kinematics, and the second one about the numerical method by using Matlab package. Inverse kinematics algorithms have been an issue to focus on since the first robots have been built. The most popular methods have been the analytical ones (Parker *et al.*, 1989), but an exact solution does not always exist. Therefore, sometimes alternative methods are used as interval methods (Rao *et al.*, 1998), based on distances (Porta *et al.*, 2006), genetic algorithms (Parker *et al.*, 1989), or based on neural networks (Tejomurtula and Kak, 1999). This paper presents a numerical approach to solve the problem of multiple inverse kinematic solutions of a 3-link redundant manipulators (like the model of a human leg) to find a single optimum solution. A simulation model of this approach has been developed and computer simulations have been conducted by using Matlab package. The movement of the hip joint has not been implemented in the proposed algorithm, whereas it can be significant and should be included in the future studies. For people with injured spinal cord, the most important is verticalization. The authors treated the hip as stationary. Future work can be done in this direction by extending this approach to the 3 dimensional model with an increased number of links and joints. The described approach is simple and very fast in nature while solving inverse kinematics in comparison with genetic algorithms.

2. Kinematic model of the leg

The human structure is constituted by a skeleton and a number of muscles, which are collectively called the human musculoskeletal system. The human skeleton is a framework that consists of more than 200 bones (Gu, 2013). The movements of parts of the human body are presented in Fig. 1. Circumduction is a circular movement that combines flexion/extension, abduction/adduction.

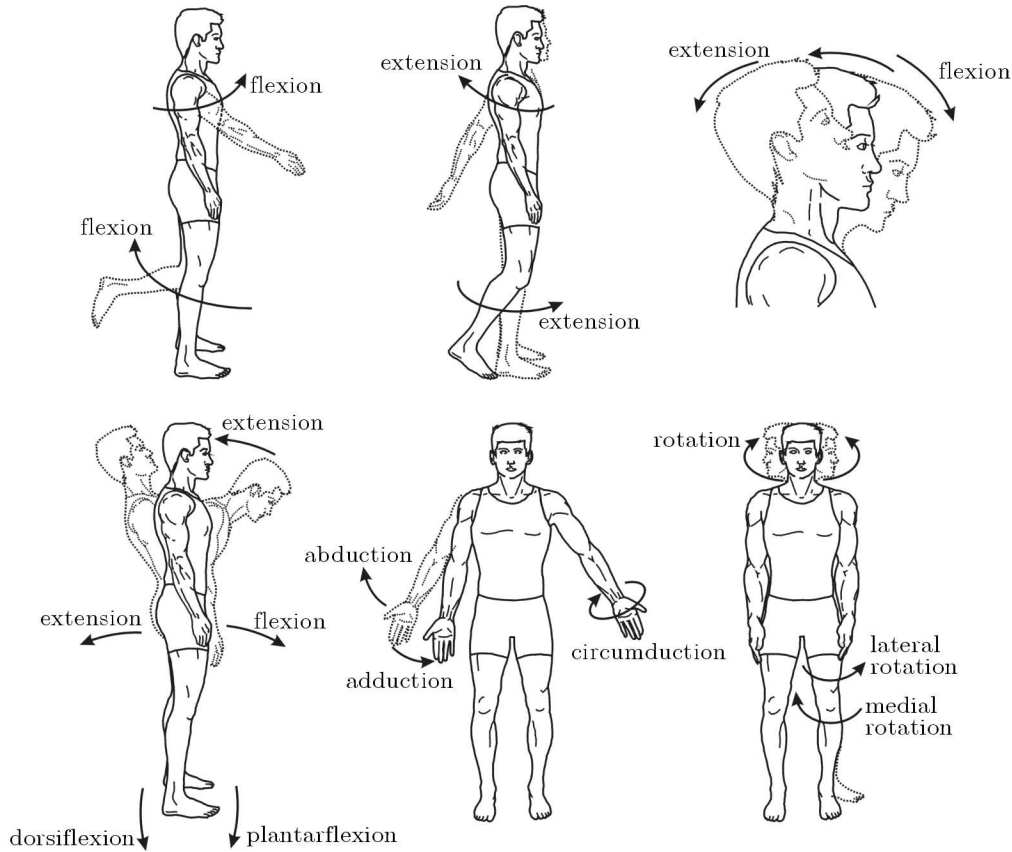


Fig. 1. Human joint movement. Reproduced from [9]

2.1. Model of the human leg

The proposed kinematic human leg model, in a sagittal plane, which passes from anterior to posterior, dividing the body into right and left halves, is presented in Fig. 2. The system of articulated links connected by rotatory joints are adopted to illustrate the human leg in this study. The leg is described as a system consisting of three segments, thigh, shank and foot as the length between ankle and metatarsal. The leg can be represented topologically using a kinematic chain structure in which links represent leg segments. The proposed model is kinematically redundant, because it possesses more degrees of freedom than those required to place the effector in a specified goal. To obtain the kinematic parameters, we make the following assumptions:

- The leg base is located at the origin $C(x_C, y_C)$ (hip joint), the knee joint $G(x_G, y_G)$, the ankle joint $K(x_K, y_K)$ and end effector (metatarsal) $O(x_O, y_O)$, respectively;
- Lengths of links are calculated as a function of human height H [m], thigh bone $l_t = 0.2450 H$, shank $l_l = 0.2460 H$, length from ankle to metatarsal $l_f = 0.0577 H$;
- Joints are revolute and the limitations $\theta_h, \theta_k, \theta_a$ are known;
- The initial joint angles $\theta_h, \theta_k, \theta_a$ are known;
- The coordinates of the goal are given.

2.2. The range of motion and comfort zone

The range of motion (ROM) of every joint is determined not only by the mechanical structure, but also by many human factors, such as the use, body build, gender, health condition, age and

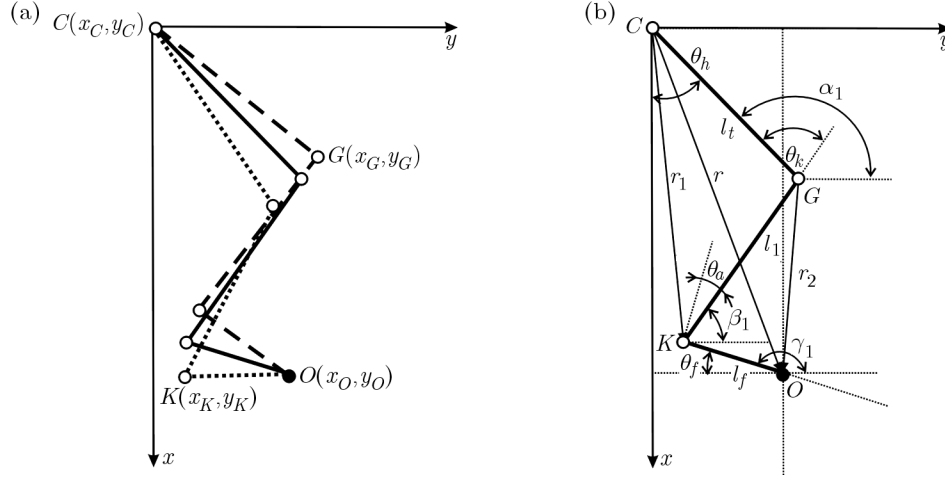


Fig. 2. Model of the human leg in a sagittal plane

many other factors (Chaffin and Andersson, 1991). The comfort zone (CZ) of each joint of the human leg, should be a subset of the corresponding joint ROM. Table 1 lists those average joint ROM's and the comfort zones just as a reference. The appropriate value of the upper-lower limit of each comfort zone is calculated by $0.35 \times$ the upper or lower limit of the corresponding human leg joint ROM. All the ROM data in the table are referred to the literature of biomechanics and kinesiology as average ranges (Tejomurtula and Kak, 1999). The comfort zone of each joint is determined by 35% of the ROM values, and the comfort center θ_i^C for each joint angle θ_i can be obtained as

$$\theta_i^C = \frac{1}{2}(\theta_{iCZ}^u - \theta_{iCZ}^l) + \theta_i^h \quad (2.1)$$

where θ_{iCZ}^u and θ_{iCZ}^l are the first and second angles of the comfort zone, respectively, for the corresponding joint i , and θ_i^h is the i -th joint home position. For example, θ_a is the joint angle of ankle plantarflexion/dorsiflexion with its home position $\theta_a^h = 0^\circ$ (knee neutral 0°). According to Table 1, $\theta_{aCZ}^u = 13.30^\circ$ and $\theta_{aCZ}^l = -12.25^\circ$. The ankle comfort zone plantarflexion/dorsiflexion joint can be calculated as $\theta_a^C = (13.30^\circ + 12.25^\circ)/2 - 0^\circ = 12.78^\circ$. This calculation can be useful to set up the joint comfort optimization criterion in trajectory generation.

Table 1. The average joint ROM's and joint comfort zones

Joint mobility	ROM [deg]	Comfort zone [deg]	Conditions when
Hip flexion/extension	113 / - 45	39.55 / - 15.75	knee neutral 0°
	90 / - 30	31.50 / - 10.5	knee flex 90°
Knee flexion	113 (stand)	39.55	hip neutral 0°
	125 (prone)	43.75	
	159 (knee)	55.65	hip flex 90°
	80 (stand)	28.00	
Ankle plantarflexion/dorsiflexion	38 / - 35	13.30 / - 12.25	knee neutral 0°
	36 / - 33	12.60 / - 11.55	knee flex 90°

2.3. The trajectory planning

Seeking the joint trajectories of the human leg is a wide research problem. In this article, the proposed method is based on the fifth degree polynomial. One of the advantages of this

polynomial is that the velocity and acceleration at the beginning and at the end of motion is zero. To start, it is necessary to determine the function for each natural coordinate in the initial position for the moment in time t_0 and end at the time t_k . By using the fifth degree polynomial, it is essential to plan the velocity and acceleration at the beginning and the end of the movement. The fifth degree polynomial takes the form

$$\theta(t) = s_0 + s_1t + s_2t^2 + s_3t^3 + s_4t^4 + s_5t^5 \quad (2.2)$$

with restrictions

$$\begin{aligned} \theta(0) &= \theta_p & \theta(t_k) &= \theta_k & \dot{\theta}(0) &= \dot{\theta}_p \\ \dot{\theta}(t_k) &= \dot{\theta}_k & \ddot{\theta}(0) &= \ddot{\theta}_p & \ddot{\theta}(t_k) &= \ddot{\theta}_k \end{aligned}$$

then we receive

$$\begin{aligned} \theta_p &= s_0 & \theta_k &= s_0 + s_1t_k + s_2t_k^2 + s_3t_k^3 + s_4t_k^4 + s_5t_k^5 \\ \dot{\theta}_p &= s_1 & \dot{\theta}_k &= s_1 + 2s_2t_k + 3s_3t_k^2 + 4s_4t_k^3 + 5s_5t_k^4 \\ \ddot{\theta}_p &= 2s_2 & \ddot{\theta}_k &= 2s_2 + 6s_3t_k + 12s_4t_k^2 + 20s_5t_k^3 \end{aligned} \quad (2.3)$$

where the final formula takes form of

$$\begin{bmatrix} s_0 \\ s_1 \\ s_2 \\ s_3 \\ s_4 \\ s_5 \end{bmatrix} = \begin{bmatrix} 1 & t_0 & t_0^2 & t_0^3 & t_0^4 & t_0^5 \\ 0 & 1 & 2t_0 & 3t_0^2 & 4t_0^3 & 5t_0^4 \\ 0 & 0 & 2 & 6t_0 & 12t_0^2 & 20t_0^3 \\ 1 & t_k & t_k^2 & t_k^3 & t_k^4 & t_k^5 \\ 0 & 1 & 2t_k & 3t_k^2 & 4t_k^3 & 5t_k^4 \\ 0 & 0 & 2 & 6t_k & 12t_k^2 & 20t_k^3 \end{bmatrix}^{-1} \begin{bmatrix} \theta_0 \\ \dot{\theta}_0 \\ \ddot{\theta}_0 \\ \theta_k \\ \dot{\theta}_k \\ \ddot{\theta}_k \end{bmatrix} \quad (2.4)$$

2.4. Forward kinematics and the workspace

By using the forward kinematics, it is possible to determine the position and orientation of the end effector. There are several methods to resolve this problem from geometrical to analytical by using homogeneous transformation matrices method and Denavit-Hartenberg's systematic representation of reference systems (Głowiński *et al.*, 2015). Our kinematic model of the leg is in the sagittal plane, then one can easily extract its direct kinematics parameters

$$\begin{aligned} x_O &= l_t \cos \theta_h + l_l \cos(\theta_h - \theta_k) - l_f \sin(\theta_h - \theta_k - \theta_a) \\ y_O &= l_t \sin \theta_h + l_l \sin(\theta_h - \theta_k) + l_f \cos(\theta_h - \theta_k - \theta_a) \\ r &= \sqrt{x_O^2 + y_O^2} & r_1 &= \sqrt{l_t^2 + l_l^2 + 2l_t l_l \cos \theta_k} & r_2 &= \sqrt{l_l^2 + l_f^2 + 2l_l l_f \sin \theta_a} \\ \theta_k &= \alpha_l - \beta_l & \theta_a &= \gamma_l - \beta_l - \frac{\pi}{2} & \theta_f &= \pi - \gamma_l \end{aligned} \quad (2.5)$$

The workspace is an important performance index of a human leg in the rehabilitation process. This workspace can be divided into two categories: the position workspace and the orientation angle workspace. The position workspace indicates the region reached by the reference point on the end-effector. The orientation angle workspace indicates a set of angle ranges by which the end-effector can reach with certain orientation for any point within the reachable position workspace. The workspace coordinates of the human leg including n -joints constraints can be obtained by using formulas

$$x = \sum_{i=1}^n l_i \cos \left(\sum_{p=1}^i \theta_p \right) \quad y = \sum_{i=1}^n l_i \sin \left(\sum_{p=1}^i \theta_p \right) \quad (2.6)$$

Figure 3 shows the leg workspace in the sagittal plane of a 1.75 m height person, with joint constraints. This workspace is characterized in a half cross-section by singular curves. The workspace topology is defined by the number of cusps and nodes that appear on these singular curves.

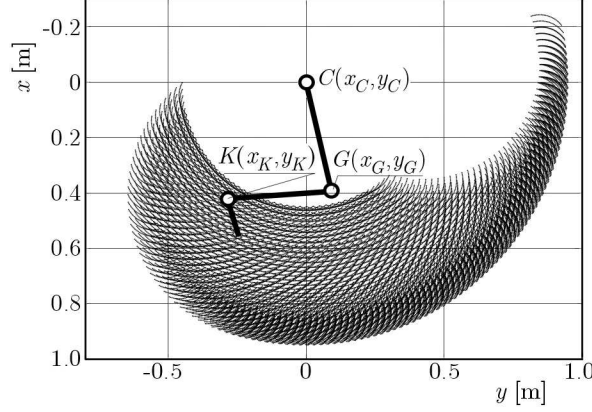


Fig. 3. The human leg workspace for the constrained optimization problem

3. Algorithm approach to solving the inverse kinematics and obtaining the trajectory of the human leg

In inverse kinematics we want to find the set of joint angles that produce a specific end-effector position. If we have a configuration of our model, and we want to move it to a new position, then, we want to compute the change in the joint angles needed to produce the change in endpoint position. In Fig. 2a it is assumed that it is not straightforward to obtain the inverse kinematics of a simple 3-joint leg model. If we know the orientation (e.g. the foot angle θ_f) and the final position, it is possible to obtain analytical solutions by using formulas

$$\begin{aligned}\theta_k &= \arccos \frac{(x_O - l_f \sin \theta_f)^2 + (y_O - l_f \cos \theta_f)^2 - l_t^2 - l_l^2}{2l_t l_l} \\ \theta_h &= \arctan \frac{y_O - l_f \cos \theta_f}{x_O - l_f \sin \theta_f} + \arccos \frac{l_t^2 - l_l^2 + (x_O - l_f \sin \theta_f)^2 + (y_O - l_f \cos \theta_f)^2}{2l_t \sqrt{(x_O - l_f \sin \theta_f)^2 + (y_O - l_f \cos \theta_f)^2}} \\ \theta_a &= \theta_h - \theta_k - \theta_f + \frac{\pi}{2}\end{aligned}\quad (3.1)$$

If we do not know the orientation, there is an infinite number of solutions. Thus, the numerical methods appears to be acceptable.

3.1. Formulation of the optimization problem

When dealing with a redundant manipulator, as the proposed leg model has more degrees of freedom than necessary to perform a certain task, the remaining degrees of freedom give a set of feasible solutions of the inverse kinematics. Among these solutions, it is recommended to choose that satisfying a certain criterion. The main goal is to find the compromising solutions between several criteria. The criteria can be formulated as ROM and the distance between the goal and end the effector. One of the criteria used in inverse kinematics algorithms is to restrict joint limits. This can be done by optimizing a potential function with very high values in the neighbourhood of a limit. This function can be expressed as

$$w(\theta) = \frac{1}{2n} \sum_{i=1}^n \frac{(\theta_{i,max} - \theta_{i,min})^2}{(\theta_{i,max} - \theta_i)(\theta_i - \theta_{i,min})}\quad (3.2)$$

where n is the number of joints. This function gives, as we can see in Fig. 4, a very high potential when approaching the knee joint limit, and the minimum value at the midpoint.

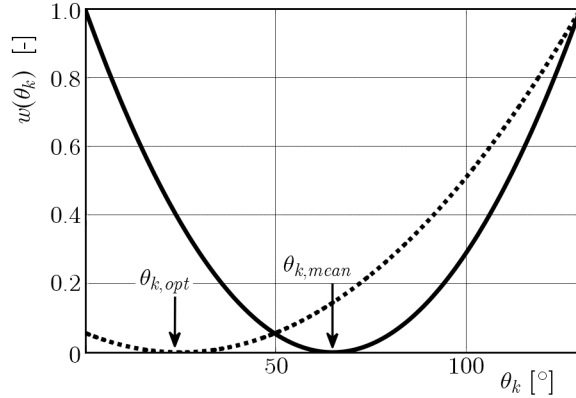


Fig. 4. The rise of the potential function when approaching knee joint limits

The next criterion can be formulated as a distance, where $O(x_O, y_O)$ represents the goal

$$\begin{aligned} x_O - [l_t \cos \theta_h + l_l \cos(\theta_h - \theta_k) - l_f \sin(\theta_h - \theta_k - \theta_a)] &< 0.0001 \\ y_O - [l_t \sin \theta_h + l_l \sin(\theta_h - \theta_k) + l_f \cos(\theta_h - \theta_k - \theta_a)] &< 0.0001 \end{aligned} \quad (3.3)$$

A general formulation of the optimization problem would be

$$\min_{\theta} f(\theta) \quad \text{such that} \quad c(\theta) < 0 \quad \text{and} \quad c_{eq}(\theta) = 0 \quad (3.4)$$

In formulation (4.4) θ is the vector of optimization variables, c and c_{eq} are vectorial functions involved in the inequality and equality constraints, respectively. The optimum angles of joints are defined as $\theta_{h,opt}, \theta_{k,opt}, \theta_{a,opt}$. They can be personalized for each person. Problems without any constraint c and c_{eq} are called unconstrained while the others are constrained. The objective function $f(\theta)$ should be minimized and it is based on the comfort zone of every joint, and can be expressed as

$$f(\theta) = \left(\frac{\theta_h - \theta_{h,opt}}{\theta_{h,min} - \theta_{h,max}} \right)^2 + \left(\frac{\theta_k - \theta_{k,opt}}{\theta_{k,min} - \theta_{k,max}} \right)^2 + \left(\frac{\theta_a - \theta_{a,opt}}{\theta_{a,min} - \theta_{a,max}} \right)^2 \quad (3.5)$$

By using Matlab package, it is possible to use different solvers depending on the objective function and constrains. In his problem, the constrains are nonlinear and the objective function is quadratic, then the best fit solver is *fmincon*.

3.2. Inverse kinematics algorithm

In Fig. 5, the inverse kinematics algorithm is illustrated. The algorithm is divided into four steps. The first step begins by initialization. It is necessary to determine the height H of a subject and calculate length of thigh l_t , shank l_l and foot l_f as the height function. The next part of this step is the determination of the initial hip, knee and ankle angles, respectively, $\theta_h, \theta_k, \theta_a$, and calculation of the initial effector position by using forward kinematics (3.1). Next, with joints constraints and formulas (3.2) the workspace and the comfort zone of each joint should be designated. In the second step, the end position coordinates should be given. The program checks whether the final coordinates are in the workspace. If not, it is necessary to find new coordinates. The third steps of the optimization begins by using Matlab package *fmincon* solver. The solution is a matrix with three angles in the final position. The angles are the most comfortable with taking into account the comfort zone of each joint. If the result is not satisfied,

the next optimization should be done, or the comfort zone calculated properly. In the fourth step, the maximum velocity, acceleration and the minimum time of movement is determined. After that step, the trajectory by using fifth degree polynomial (2.4) can be obtained.

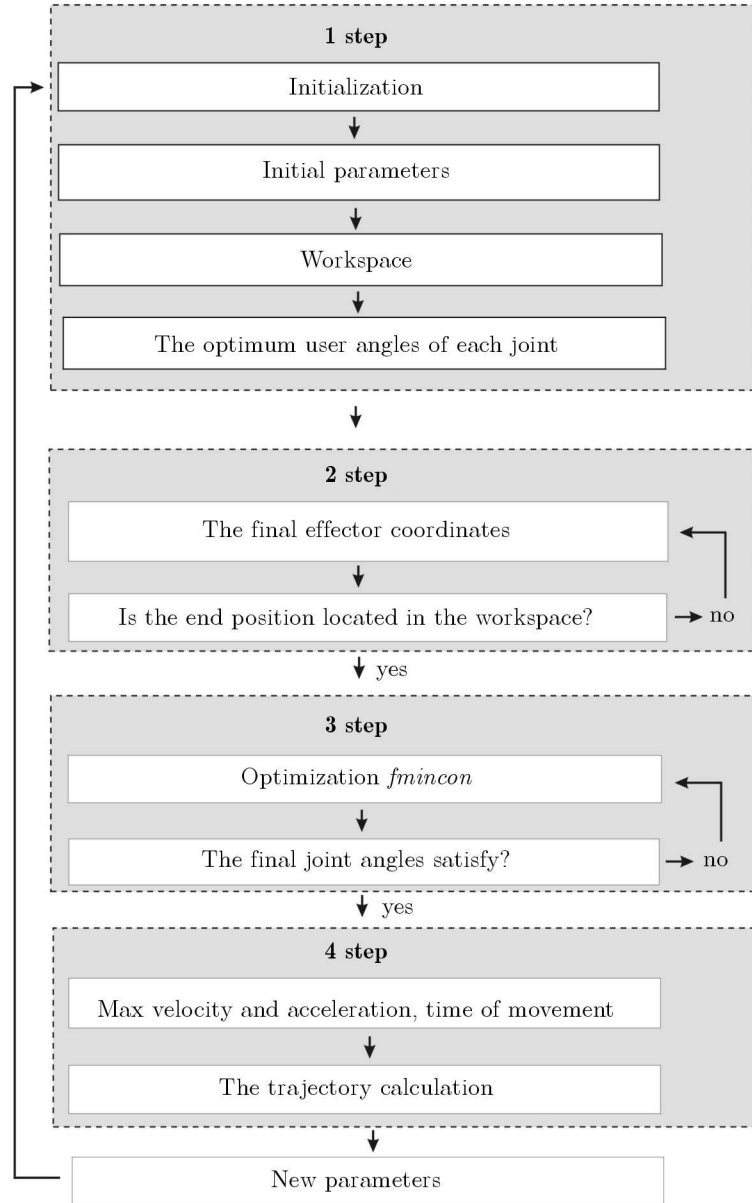


Fig. 5. The inverse kinematics algorithm

4. Results

For a 1.75 m person height, the initial angles are obtained as $\theta_{hi} = 86^\circ$, $\theta_{ki} = 17^\circ$, $\theta_{ai} = -6^\circ$. From forward kinematics (3.1), the end-effector coordinates are calculated as $A(x_O = 0.089, y_O = 0.856)$. If we know the final point as $C(x_f = 0.4, y_f = -0.4)$, based on the provided algorithm and the determined optimal angles, the final angles are calculated as $\theta_{hf} = 17^\circ$, $\theta_{kf} = 108^\circ$, $\theta_{af} = -6^\circ$. Then by using fifth degree polynomial (2.2), the trajectory can be determined. Figure 6 shows the visualization and the angles, angular velocity and acceleration of each joint. The time of motion is 2 s. The maximum angular knee joint velocity is about $80^\circ/\text{s}$, whereas acceleration $140^\circ/\text{s}^2$. It is acceptable from the biomechanical point of view (Głowiński

et al., 2015). The generated result shows high similarity between the model motion and the real human leg motion.

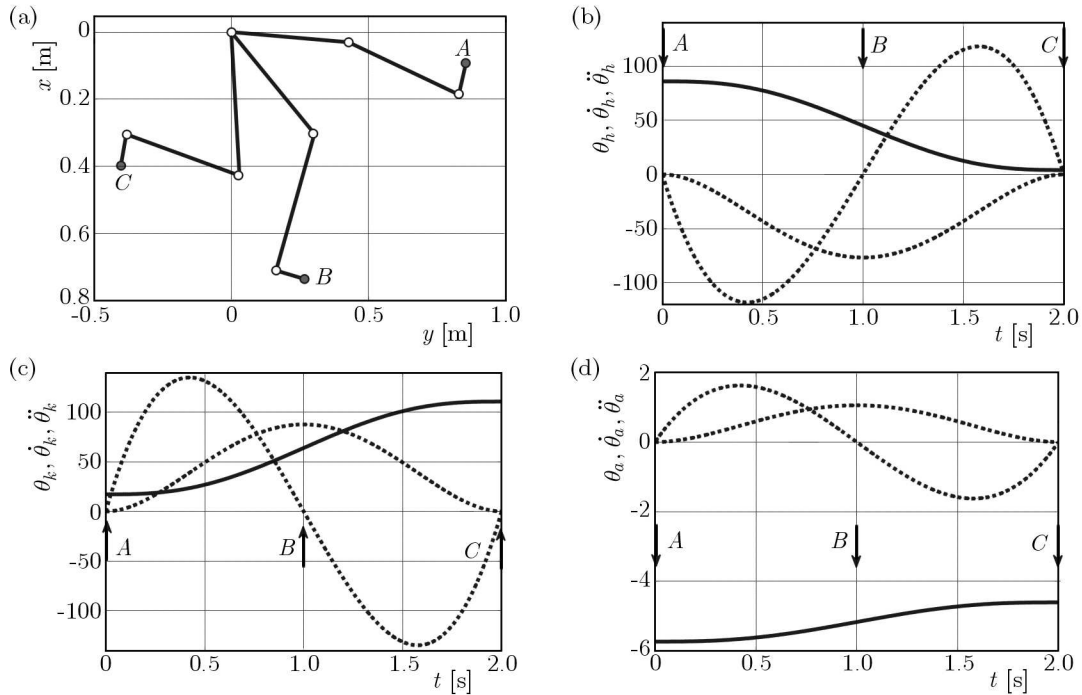


Fig. 6. Graph presenting displacement, angular velocity and acceleration for the fifth degree polynomial describing motion of the human leg between the two positions, human leg model displacement (a), hip (b), knee (c), foot (d)

From Fig. 6, it is observed that the final leg position is close to the target points $C(x_f = 0.4, y_f = -0.4)$. The proposed methodology has been validated for different starting points and the results satisfied the criteria. Repeatability is a significant issue in our algorithm. It is very important for the user that the Matlab solver behaves consistently and is not sensitive to changes in the starting point.

5. Conclusion

In this paper, an approach for modelling and simulation of the human leg inverse kinematics is presented. When planning the trajectory of the human leg, which will be used for rehabilitation, individual patient capabilities need to be taken into consideration. This can be done by a preliminary study. Subsequently, the physician selects exercises depending on disease. It is particularly important after stroke with spasticity. As mentioned earlier, it should be noted that this study is limited to analysis of movements in the sagittal plane. Further investigations are thus needed in order to generalize our findings to other planes.

When planning the trajectory, significant simplifications are being made by assuming the maximum acceleration values for each degree of freedom. If the maximum acceleration values are improperly selected, this can lead to the possibility of exceeding human joint limits. From the presented simulation results, the best method for path planning is a fifth degree polynomial. According to the simulation results, it is decided to improve the mechanical construction. In real situations, for particular real exercises, there are much more parameters needed to be considered in the modelling, for example, the inserted force or the stability criterion. Further experiments are to be carried out in order to verify the modelling results in experiments.

References

1. CHAFFIN D., ANDERSSON G., 1991, *Occupational Biomechanics*, 2nd edn., John Wiley & Sons
2. GŁOWIŃSKI S., KRZYŻYŃSKI T., PECOLT S., MACIEJEWSKI I., 2015, Kinematics and dynamics of an exoskeleton arm, *Archives of Applied Mechanics*, **85**, 75-87, DOI 10.1007/s00419-014-0900-8
3. GU E.Y.L., 2013, *A Journey from Robot to Digital Human, Mathematical Principles and Applications with MATLAB Programming*, Springer
4. NOCEDAL J., WRIGHT S.J., 1999, *Numerical Optimization*, Springer
5. PARKER J.A., KHOOGAR A.R., GOLDBERG D.E., 1989, Inverse kinematics of redundant robots using genetic algorithms, *Proceedings, IEEE International Conference on Robotics and Automation*, **1**, 271-276
6. PORTA J.M., ROS L., THOMAS F., 2005, Inverse kinematic solution of robot manipulators using interval analysis, *4th International Workshop on Computational Kinematics*
7. RAO R.S., ASAITHAMBI A., AGRAWAL S.K., 1998, Inverse kinematic solution of robot manipulators using interval analysis, *Journal of Mechanical Design*, **120**, 1, 147-150
8. TEJOMURTULA S., KAK S., 1999, Inverse kinematics in robotics using neural networks, *Information Sciences*, **116**, 2/4, 147-164
9. <http://philschatz.com/anatomy-book/contents/m46398.html>,
<http://creativecommons.org/licenses/by/4.0/> *Anatomy and Physiology Textbook* (access 10.02.2015)

Manuscript received April 8, 2015; accepted for print June 26, 2015

VERIFICATION OF ANALYTICAL MODELS OF THE S-N CURVE WITHIN LIMITED FATIGUE LIFE

PRZEMYSŁAW STRZELECKI, JANUSZ SEMPRUCH

University of Science and Technology, Faculty of Mechanical Engineering, Bydgoszcz, Poland
e-mail: p.strzelecki@utp.edu.pl; semjan@utp.edu.pl

This paper presents analytical methods for determination of the curve for a high-cycle fatigue. It has been found based on qualitative and quantitative verification that the error introduced by these methods can be as large as 3-fold length of the experimental life. In addition, the wrong result can lay on either the safe or the unsafe side with equal probability. Therefore, an analytical-and-experimental (hybrid) method has been proposed. Verification of computed characteristics vs. experimental data demonstrated that the “proprietary” proposal reduced the error. In addition, an approximate error depending on the number of experiments has been determined based on the computations.

Keywords: fatigue design, S-N curve, high-cycle fatigue, accelerated method

1. Introduction

While designing a new component of a machine, the designer has to give it correct dimensions. Typically, the part is exposed to loads variable in time, which can produce fatigue failure. This is why the fatigue life of the component is determined by means of computations. Before the computations can be made, fatigue characteristics of the material or component has to be available, such as that provided by Skibicki *et al.* (2012). Because this information is typically unavailable at the preliminary computation phase, analytical methods are used to determine these characteristics based on static properties of the material or based on characteristics available for a test specimen of different geometry, an example of which can be found in Tomaszewski *et al.* (2014). The references describe many such methods but their authors fail to describe the possible error inherent to the method. Note further that the resulting fatigue characteristics predict the point of destruction of the component with a 50% probability whereas, for design purposes, engineers use plots featuring a 95% or higher probability factor. An appropriate coefficient is used to bring the fatigue characteristics to the required level of reliability. The following points describe a method for determining this coefficient.

The approach described in the FITNET procedure, documented in the report by Kocak *et al.* (2006) is one of the latest analytical methods used to determine fatigue characteristics. The main assumption underlying the algorithm is the determination of the fatigue limit for a material consisting of multiplication of the material tensile strength by an appropriate coefficient. The basic number of cycles adopted for the method is 10^6 cycles (same as in the remaining methods described in the literature). However, for the limited life, the method uses slope coefficients $m = 5$ for normal stress and $m = 8$ for shear stress. See a diagram of the algorithm in Fig. 1a.

Another of the discussed methods is the one proposed by Lee *et al.* (2005). This approach assumes that 2 points on the plot are required for the determination of fatigue characteristics: the fatigue limit for the basic 10^6 cycles for steel and the fatigue for 10^3 cycles. See Fig. 1b for the illustration of the method.

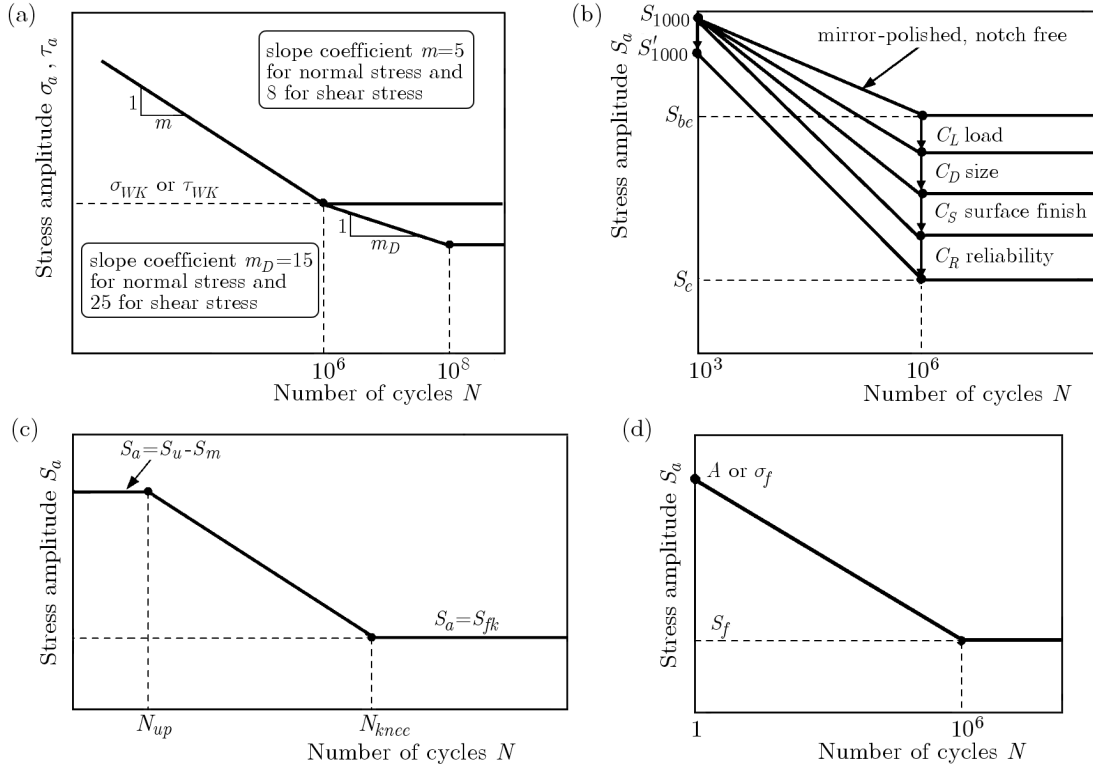


Fig. 1. S-N characteristics according to: (a) FITNET method, (b) Lee and Taylor's method, (c) Schijve's method and (d) method by Stephens *et al.* (2001)

Another approach described in the literature is the one proposed by Schijve (2009). As in the previous method, again, 2 points are required for the determination of fatigue characteristics: the fatigue limit S_{fk} for the basic 10^6 cycles (N_{knee}) for steel and the fatigue life for 10^2 cycles (N_{up}). The author of the method claimed that the value adopted as the material tensile strength S_u less than the mean stress S_m was a good approximation. See Fig. 1c for a schematic description of the procedure.

One more approach discussed in this paper is the method proposed by Stephens *et al.* (2001). It is based on setting 2 points: the fatigue life for an unlimited life S_f and the strength for one loading cycle A . The value of A can be determined experimentally using Basquin's equation or be adopted as the value of the actual tensile strength σ_f (breaking force on elongation divided by the minimum cross sectional area on rupture). If the foregoing information is not available, A can be equal to the material tensile strength (see Fig. 1d) for a schematic procedure for the estimation of the fatigue characteristics.

The last of the presented methods is the "proprietary" one. In this approach, the determination of the fatigue limit is based on the method described in the FITNET procedures while the value of the straight line slope coefficient within the limited life range is computed as follows

$$m_{e\sigma} = \frac{\log \frac{10^6}{N_{Re}}}{\log \frac{0.9R_e}{\sigma_{WK}}} \quad N_{Re} = 400 \left(\frac{R_e}{R_m} \right)^{-10} \quad (1.1)$$

where R_m is tensile strength, R_e – yield point.

The proprietary method of analytical determination of the Wöhler diagram is shown in Fig. 2. See the paper by Strzelecki and Sempuch (2012) for a more detailed description.

The solid line represents the fatigue plot for the 50% probability and the dashed line defines the characteristics for the target probability. A plot featuring the probability different than 50% is obtained by multiplying the fatigue limit (σ_{WK}, τ_{WK}) by the coefficient C_R (Table 1).

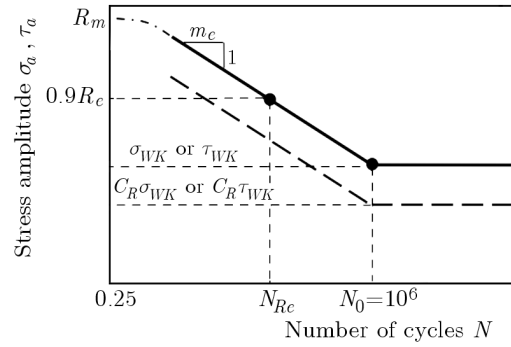


Fig. 2. S-N characteristics according to the proprietary method

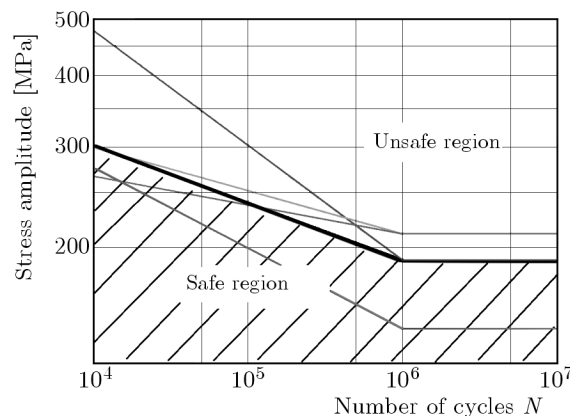
Table 1. Value of the coefficient of reliability for different levels of reliability

Reliability	C_R
0.9	0.897
0.95	0.868
0.98	0.836
0.99	0.814
0.999	0.753
0.9999	0.702

The method for obtaining these values is described in the paper by Strzelecki and Sempruch (2013). Note that the values of C_R obtained by the authors are based on the normal distribution of the fatigue limit and the coefficient of variation is equal to 0.08 (value proposed in the literature).

2. Analytical verification of methods for approximate determination of the characteristics

Because the literature is silent on the error made while using the analytical methods described in the foregoing Section, the authors decided to verify these algorithms. The qualitative verification was based on the determination whether the estimated characteristics fits within the safe zone or not. See Fig. 3 for a sample diagram used for the evaluation of these methods.


 Fig. 3. Diagram for steel S235JR (Robak *et al.*, 2012) (black line) vs. characteristics obtained by analytical methods: sample diagram illustrating the qualitative evaluation of the characteristics

Where the estimated characteristic was positioned within the safe zone (the dashed part of the diagram), the estimated life of the material was identified with the “+” sign. Otherwise, the

sign was negative (“−”). However, if the characteristics laid on the safe side but shifted to the unsafe side, it was marked with the “+/-” signs. If vice versa, the signs was reversed to “-/+”. For the “+/-” case, the fatigue limit was found to lay on the safe side but the slope coefficient of the analytical characteristics was smaller than the value determined based on the experimental data. But when the case was flagged with the “-/+” signs, the method overestimated the fatigue limit, but the resulting slope coefficient was larger than the experimental value. See Table 2 for the results of verification for smooth samples made of 71 grades of steel.

Table 2. Results of qualitative verification of analytical methods

Evaluation sign	Method				
	FITNET	Lee & Taylor	Schijve	Stephens <i>et al.</i>	Proprietary
+	6/8%	21/30%	17/24%	28/39%	32/45%
+/-	33/46%	20/28%	3/4%	0/0%	9/13%
-/+	0/0%	6/8%	8/11%	26/37%	6/8%
−	32/45%	24/34%	43/61%	17/24%	24/34%

In order to verify the procedural algorithm in quantitative terms, the authors determined the strength of the specified material for the life of 10^5 cycles based on the fatigue characteristics taken from the literature and, then, determined the material life for the known stress based on the characteristics determined using the specified method. See Fig. 4 for an illustration of the procedure.

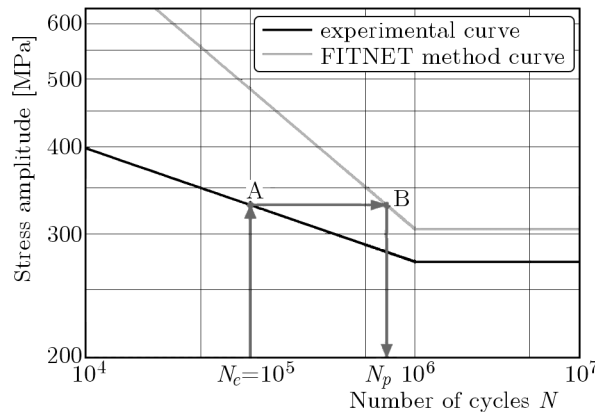


Fig. 4. Fatigue plot for steel S355J0 (Ligaj and Szala, 2010) and fatigue plot account to FITNET: presentation of the method of computation of the estimation error of the analytical method

The error was computed using the difference between the logarithmized life obtained for the experimental characteristics (N_e – value for 10^5 cycles) and the logarithmized life determined using the analytical method N_p . The determination of this value was written with

$$B_l = \log N_e - \log N_p \quad B_l = \log \frac{N_e}{N_p} \quad (2.1)$$

Note that there were cases when the value of the fatigue limit determined by the analytical method was larger than the material strength for 10^5 -cycle life based on the experimental characteristics. In this case, the straight line from the limited life range was extended until it provided the target stress value. In such a case, the life N_p was longer than 10^6 cycles.

Based on the value of the error computed using equation (2.1)₂, the authors determined the normal distribution (i.e., mean and standard deviation) for this error for each of the methods listed in Table 3. In addition, the table presents the results of the Shapiro-Wilk test for the normality of distribution performed using application *R*, v. 2.15.3, 64-bit.

Table 3. Quantitative verification results

Method	Normal distribution values		Values obtained by the Shapiro-Wilk test	
	μ -mean	σ -SD		μ -mean
FITNET	-0.4874	0.3920	0.9838	0.4744
Lee & Taylor	-0.1603	0.8597	0.9725	0.1208
Schijve	-0.5201	1.0915	0.9817	0.3888
Stephens <i>et al.</i>	0.0767	1.5589	0.9854	0.5821
Proprietary	0.1676	0.8574	0.9814	0.3760

To illustrate the distribution of the error generated by each method, the distributions were overlaid on the plot of the density of probability (Fig. 5).

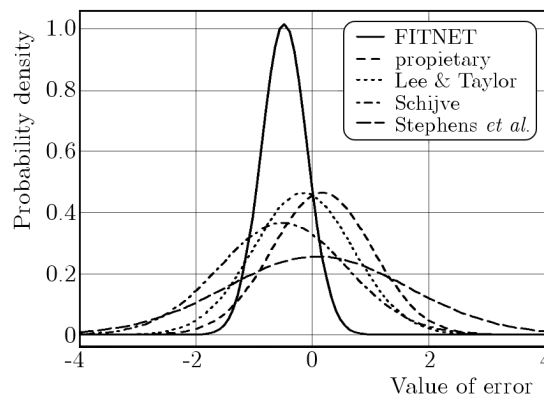


Fig. 5. Plot of the function of density of errors for the individual methods

3. Analytical and experimental method

Considering that the qualitative and quantitative verification presented in Section 2 showed that the analytical methods can generate significant errors, the authors decided to propose a hybrid solution. It consists of setting the characteristics using an analytical method and, then, correcting the accuracy of life determination by carrying out a “simplified” experiment. This simplified experiment consists of determining an experimental point within the limited life range for the strength corresponding to 10^5 cycles based on the analytical characteristics. The schematic procedure is illustrated in Fig. 6. Note that 3 fatigue tests were carried out and arithmetic mean was computed for the tests to determine the point in support of the analytical method.

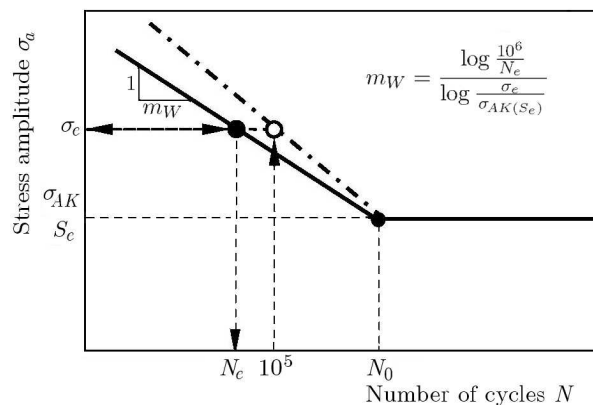


Fig. 6. Schematic presentation of the experimental support for the analytical method

4. Experimental verification of the proposals

To verify the proposals presented in the foregoing sections, the authors carried out an experiment consisting of plotting the fatigue of materials C45+C (as delivered) and 42CrMo4 (toughened). The static properties of the materials are presented in Table 4. The fatigue properties under high-cycle loading were determined using a device for rotating bending based on a proprietary design presented and verified in the authors' paper (2012).

Table 4. Static properties of the materials tested

Property	Material	
	C45+C	42CrMo4
R_m [MPa]	826	1172
R_e [MPa]	647	1095
HRC	21.1	32.7

The tests were conducted on smooth and circumferentially notched samples. The drawings of the samples are shown in Fig. 7 and the diagrams based on the data obtained from the experiments are presented in Fig. 8.

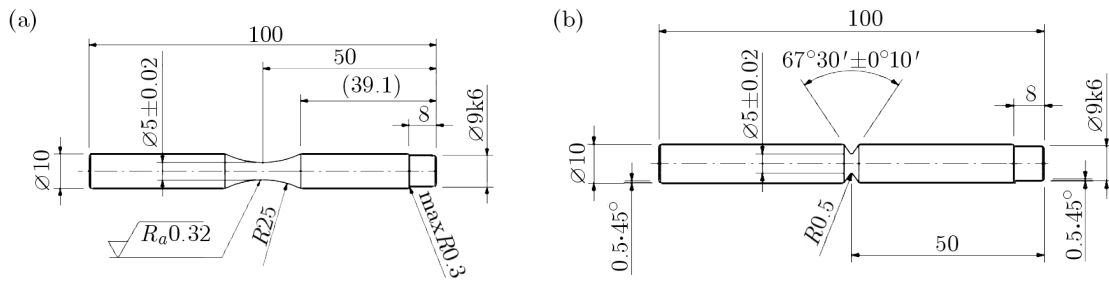


Fig. 7. Test samples: (a) smooth, (b) notched

5. Verification results

To verify the accuracy of application of the reliability factor described in Section 1 used to generate the fatigue plot by the analytical method for the required level of probability, Fig. 9 presents plots obtained for the experimental data and characteristics obtained by the analytical method for the 50% and 95% probabilities of survival.

The analytical and hybrid methods were verified in accordance with the methodology described by Park and Song (1995). The following equations (Park and Song, 1995) are used to estimate the quantitative conformity of the analytical characteristics to the experimental plot

$$E_f(s) = \frac{\frac{1}{s} \leq \frac{N_p}{N_f} \leq s}{n} \quad (5.1)$$

$$E_a = \frac{(1 - |\alpha|) + (1 - |1 - \beta|) + (1 - |1 - \alpha - \beta|) + (1 - |1 - r|)}{4}$$

where: N_p – life obtained by the application of the verified characteristics, n – number of experimental points, α – free term in the equation for simple regression for the verified method, β – slope coefficient for the regression line for the verified method, r – correlation coefficient for the regression line for the verified method.

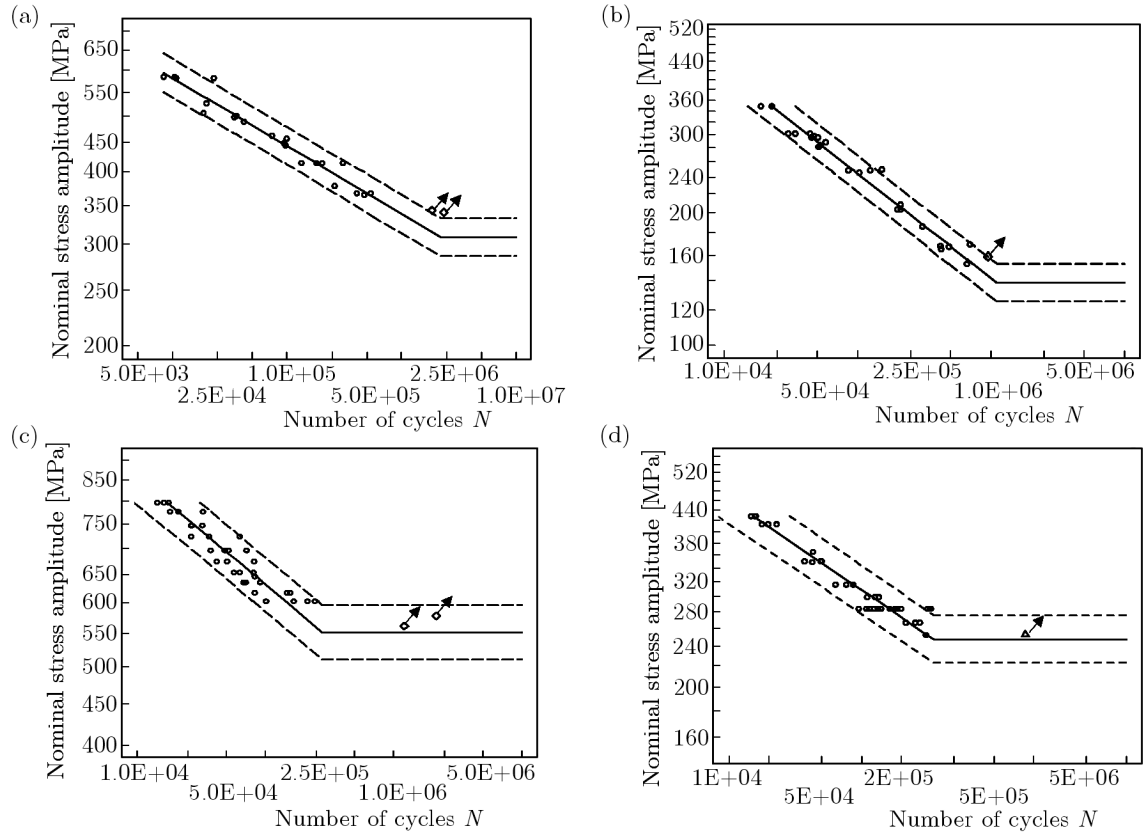


Fig. 8. The resulting fatigue characteristics for: (a) material C45+C, smooth sample, (b) material C45+C, notched sample, (c) material 42CrMo4, smooth sample, (d) material 42CrMo4, notched sample

The value of $E_f(s)$ ranges from 0 to 1 and stands for the number of points determined by the analytical method, located within the specified scatter band. On the other hand, the maximum value of E_a is 1 but the quantity has no lower limit. The last relation defines the matching of the straight line estimated from the points obtained by the analytical method to the ideal straight line assuming that the experimental life is equal to the estimated life. Table 5 shows the results of computations for the foregoing analytical methods.

For instance, Fig. 10 shows the subsequent plots based on the FITNET method and on the experimental characteristics.

The following equation (Jakubiec and Malinowski, 1996) was used to perform statistical analysis aiming at the determination of the error made using the analytical method and the analytical-experimental (hybrid) method based on experimental values, i.e., the measurement of hardness, tensile strength R_m , yield point R_e , life determined within the limited strength range (mean from 3 measurements) and fatigue limit determined with the LOCATI method

$$B_p = \sqrt{\left(\frac{\partial f}{\partial x_1}\right)^2 \Delta x_1^2 + \left(\frac{\partial f}{\partial x_2}\right)^2 \Delta x_2^2 + \dots + \left(\frac{\partial f}{\partial x_n}\right)^2 \Delta x_n^2} \quad (5.2)$$

where: f – equation of the function defining the value of the quantity being determined, Δx_n – standard deviation of the n -th measured value, x_n – n -th quantity measured in an intermediate measurement.

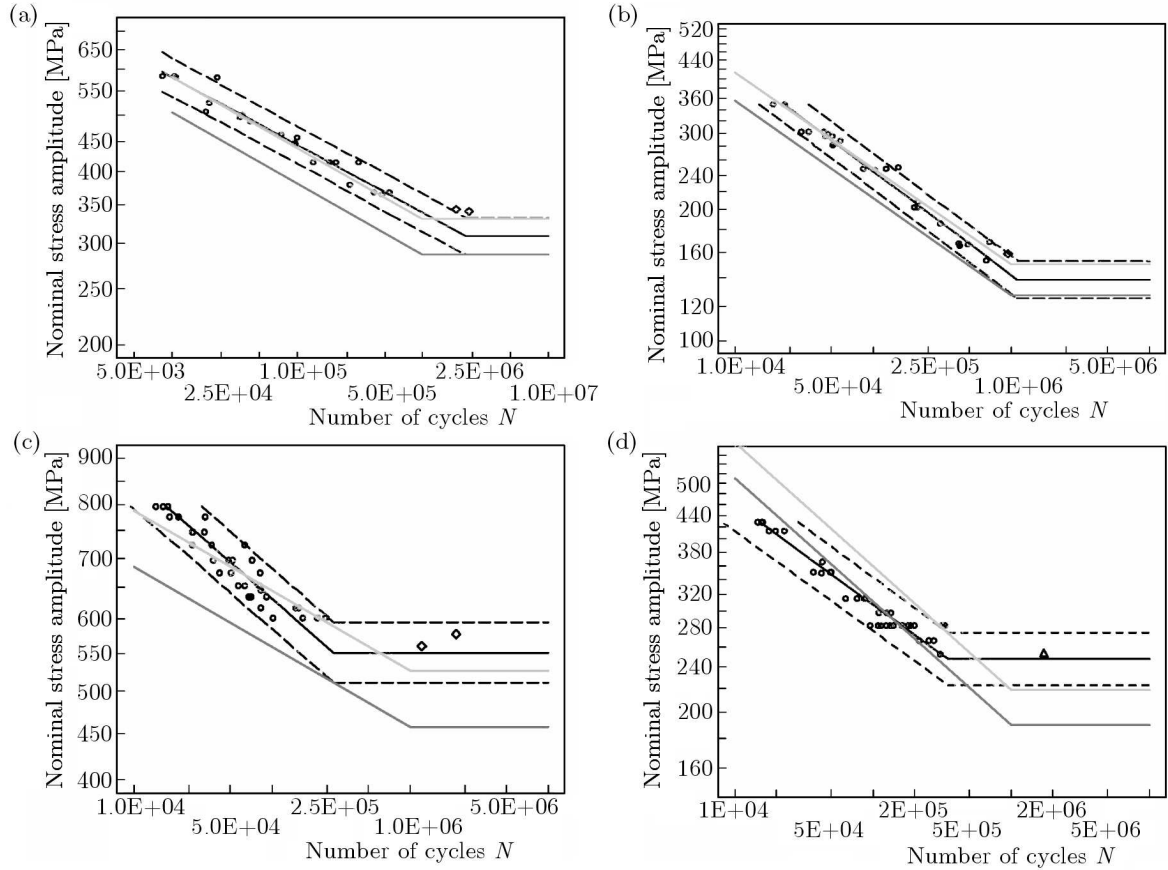


Fig. 9. Fatigue plots: experimental (black line), analytical (grey line) and set off to the 95% reliability level for the analytical method (dark grey line) for: (a) material C45+C, smooth sample, (b) material C45+C, notched sample, (c) material 42CrMo4, smooth sample, (d) material 42CrMo4, notched sample

Table 5. Values of coefficients E_f and E_a for the analytical and analytical-experimental methods for the tested materials

Material type	Method								
	Coefficient type	FITNET	FITNET with experimental support	Lee & Taylor	Lee & Taylor with experimental support	Stephens <i>et al.</i>	Stephens <i>et al.</i> with experimental support	Schijve	Schijve with experimental support
C45+C	$E_f(3)$	0.64	1.0	0.27	0.46	0.95	0.95	0.41	0.46
	E_a	-0.34	0.75	0.09	-0.83	0.46	0.73	-0.37	-0.83
42CrMo4	$E_f(3)$	0.09	1.0	0.06	0.36	0.82	1.0	0.58	0.58
	E_a	-0.91	0.7	-0.71	-2.38	0.41	0.79	-0.38	-0.37
C45+C notched	$E_f(3)$	0.0	0.39	0.44	0.56	0.5	0.56	0.5	0.56
	E_a	0.22	-2.2	-0.57	-2.1	-1.33	-2.46	-0.81	-2.10
42CrMo4 notched	$E_f(3)$	0.0	0.0	0.0	0.2	0.23	0.34	0.09	0.4
	E_a	-0.95	-1.6	0.05	-1.46	-0.05	-0.57	0.26	-0.35

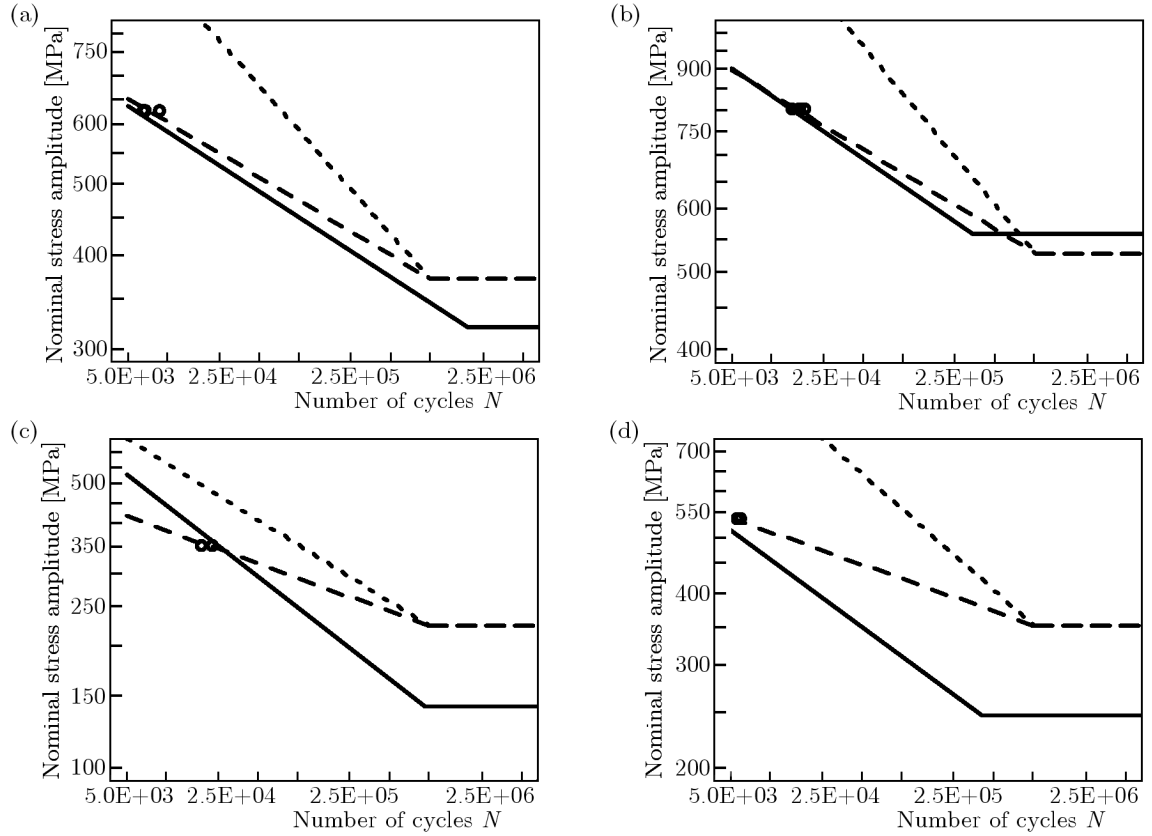


Fig. 10. Characteristics for: (a) material C45+C, smooth sample, (b) material 42CrMo4, smooth sample, (c) material C45+C, notched sample, (d) material 42CrMo4, notched sample; solid line – experimental characteristics, dotted line – FITNET method, dashed line – FITNET method with experimental support

The proposed method determining the material life is employed to make the computation using the foregoing equation based on the following relationship

$$N = \left(\frac{Z}{\sigma_a} \right)^{\frac{\log \frac{N_0}{400(R_e/R_m)^{-10}}}{\log \frac{0.9R_e}{Z}}} N_0 \quad (5.3)$$

For the notched samples, the method of determining the life is expressed as follows (Strzelecki and Sempruch, 2013)

$$N = \left(\frac{Z_k}{\sigma_a} \right)^{\frac{\log \frac{N_0}{10^3}}{\log Z + \frac{\log(0.9R_e/Z)}{\log(N_0/N_{Re})} \log \frac{N_0}{10^3} - \log Z_k}} N_0 \quad (5.4)$$

The values of errors depending on the quantity of experimental information for the tested materials are shown in Fig. 11. Figure 11 illustrates the determination of the relative error using the following formula

$$\xi_p = \left| \frac{N_e - B_p}{N_e} \right| \cdot 100\% \quad (5.5)$$

The time required for completing the measurement is assumed as the time of the experiment. The times for the preparation of measuring instruments, preparation of samples, etc. are not taken into account. It is assumed that the measurement of hardness would take 10 minutes (A)

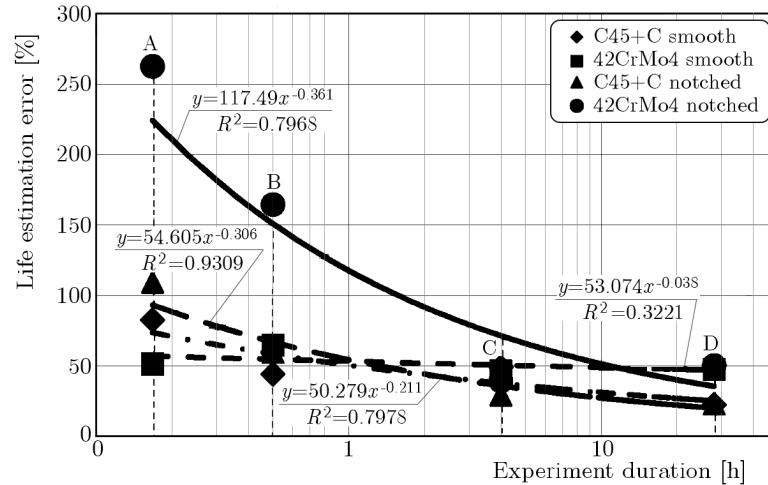


Fig. 11. Error of the analytical method error depending on the number of quantities determined experimentally

and the static tensile test 30 minutes (B). But the determination of life for a limited strength time for 3 samples takes 4 hours (C). For the experiment carried out using the Locati method, a 24-hour measurement time (D) is adopted.

6. Summary and conclusions

The verification of the methods for analytical determination of fatigue characteristics presented in Section 2 demonstrated that the value of the error can be 3 times larger than the experimental value. Further, the inaccuracy of determining the fatigue life using these methods can lay on either the safe or unsafe side with equal probability. Even if the proposed method provides better verification results, the accuracy of life determination carries a significant error. In addition, Section 5 presents the verification of the analytical method using the reliability coefficient C_R , which makes it possible to obtain characteristics featuring the desired probability. Based on the characteristics obtained, the results are satisfactory except for the plot for material 42CrMo4 and notched samples.

In order to improve the estimation of the fatigue life, the authors propose the analytical-and-experimental (hybrid) method. The experimental verification demonstrated that the error made while using this algorithm combined with laboratory testing can be significantly smaller, which is shown in Section 5. Therefore, whenever it is possible to conduct an experiment, it is recommended that the fatigue life is determined experimentally for 3 samples within the limited life range defined in Section 3.

References

1. BOYER E., 2003, *Atlas of Fatigue Curves*, Boyer E. (edit.), 5-th ed., American Society for Metals, Ohio
2. JAKUBIEC W., MALINOWSKI J., 1996, *Metrology of Geometrical Dimensions* (in Polish), 2-nd ed., Warszawa WNT
3. KOÇAK M., WEBSTER S., JANOSCH J.J., AINSWORTH R.A., KOERS R. (EDIT.), 2006, *FITNET Fitness-for-Service PROCEDURE – FINAL DRAFT MK7*, Vol. I: *FITNET FFS Procedure*, European Fitness-for-Service Thematic Network – FITNET

4. LEE Y.-L., PAN J., HATHAWAY R.B., BARKEY M.E., 2005, *Fatigue Testing and Analysis*, University of Alabama, Elsevier
5. LIGAJ B., SZALA G., 2010, Experimental verification of two-parametric models of fatigue characteristics by using the tests of S55J0 steel as an example, *Polish Maritime Research*, **17**, 1, 39-50
6. PARK J.H., SONG J.H., 1995, Detailed evaluation of methods for estimation of fatigue properties, *International Journal of Fatigue*, **17**, 5, 365-373
7. ROBAK G., SZYMANIEC M., ŁAGODA T., 2012, The fictitious radius as a tool for fatigue life estimation of notched elements, *Material Science Forum*, **726**, 27-32,
8. SCHIJVE J., 2009, *Fatigue of Structures and Materials*, 2-nd ed., Springer
9. SEMPRUCH J., STRZELECKI P., 2011, Error of fatigue life determined according to the FITNET method, *Engineering Mechanics*, 531-534
10. SKIBICKI D., SEMPRUCH J., PEJKOWSKI L., 2012, Steel X2CrNiMo17-12-2 testing for uniaxial, proportional and non-proportional loads as delivered and in the annealed condition, *Material Science Forum*, **726**, 171-180
11. STEPHENS R.I., FATEMI A., STEPHENS R.R., FUCHS H.O., 2001, *Metal Fatigue in Engineering*, 2-nd ed., New York Wiley
12. STRZELECKI P., SEMPRUCH J., 2012, Experimental verification of the analytical method for estimated S-N curve in limited fatigue life, *Material Science Forum*, **726**, 11-16
13. STRZELECKI P., SEMPRUCH J., 2013, Experimental verification of the analytical method for determining the S-N curve for alloy steel, *Key Engineering Materials*, **598**, 219-224
14. TOMASZEWSKI T., SEMPRUCH J., PIĄTKOWSKI T., 2014, Verification of selected models of size effect based on high-cycle fatigue testing on mini specimens made of EN AW-6063 aluminium alloy, *Journal of Theoretical and Applied Mechanics*, **52**, 2, 883-894

Manuscript received November 25, 2014; accepted for print June 27, 2015

KINEMATIC SYNTHESIS OF SPATIAL LINKAGES WITH SPHERICAL PAIRS

SERIKBAY KOSBOLOV, ALGAZY ZHAUYT, SERIKBOL KOSBOLOV

Kazakh National Technical University named after K.I. Satpayev, Department of Applied Mechanics and Basics of Machine Design, Almaty, Kazakhstan; e-mail: kosbolov@mail.ru; ali84jauit@mail.ru; serikbolk@mail.ru

A solution to the problem of synthesizing an initial three-dimensional kinematic chain with spherical and rotary kinematic pairs is presented. It is shown that this chain can be used as a structural module for structural-kinematic synthesis of motion of a three-dimensional four-link generating lever mechanisms by preset positions of the input and output links.

Keywords: mechanism, four-link, kinematic pairs, kinematic chains, synthesis

1. Introduction

Some papers demonstrate that four-link basic kinematic chains (BKC) may be used as a structural module with structural and kinematic synthesis of plain linkage mechanisms. Such an approach to the synthesis of plain mechanisms allows reducing the problem of their structural and kinematic synthesis to solution of the problem of BKC synthesis (Joldasbekov *et al.*, 1987), which is very useful for automation of mechanisms engineering. This paper testifies that a specified approach may be applied to the problem of structural and kinematic synthesis of spatial linkage mechanisms (Kosbolov and Rakhmatulina, 2012b). The solution of the problem of synthesis of spatial BKC of RSS type (R – rotational, S - spherical kinematic pairs) is represented, and its use as a structural module with structural and kinematic synthesis of spatial linkage mechanisms through predetermined positions of input and output links is shown (Kosbolov *et al.*, 2005). A method of solving the problem of BKC synthesis of RSS type is based on the introduction of two movable bodies invariably associated with the input and output links (Kosbolov and Rakhmatulina, 2013b).

2. On the existence of solution to the problem of initial kinematic chain synthesis with spherical kinematic pairs

Problem statement: given N of finite distant positions of two solids Q_1 and Q_2

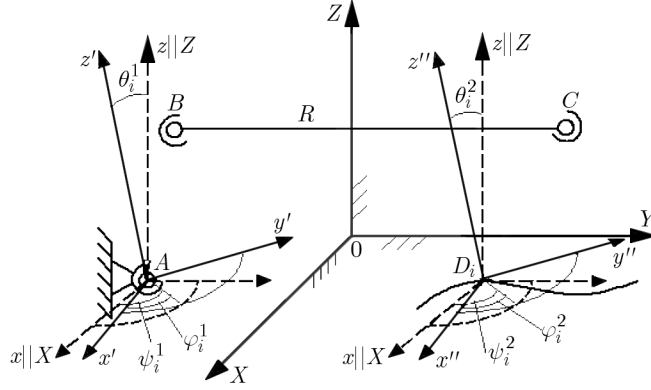
$$Q_1(\theta_i^1, \psi_i^1, \phi_i^1) \quad Q_2(X_{Di}, Y_{Di}, Z_{Di}, \theta_i^2, \psi_i^2, \phi_i^2) \quad i = \overline{1, N} \quad (2.1)$$

where $\theta_i^j, \psi_i^j, \phi_i^j$ are fixed axis Eulerian angles $OXYZ$ and X_{Di}, Y_{Di}, Z_{Di} are coordinates of the point D_i of the solid Q_2 .

It is required to find such points in the fixed axis as $A(X_A, Y_A, Z_A)$, of the solid Q_1 and $C(x_C, y_C, z_C)$ of the solid Q_2 , so that distance between the points B and C in all positions of the solids Q_1 and Q_2 is little different from some constant value R (Fig. 1).

Problem solution: Let us introduce a weighted difference for the i -th position of the solids in form

$$\Delta_{q_i} = |\overrightarrow{B_i C_i}|^2 - R^2 = (X_{C_i} - X_{B_i})^2 + (Y_{C_i} - Y_{B_i})^2 + (Z_{C_i} - Z_{B_i})^2 - R^2 \quad i = \overline{1, N} \quad (2.2)$$

Fig. 1. Equivalent four-link kinematic chain $ABCD$

where

$$\begin{aligned} \begin{bmatrix} X_{B_i} \\ Y_{B_i} \\ Z_{B_i} \\ 1 \end{bmatrix} &= \begin{bmatrix} & & X_A \\ & \mathbf{T}_{10}^i & Y_A \\ 0 & 0 & 0 & 1 \\ & & Z_A & \end{bmatrix} \begin{bmatrix} x_B \\ y_B \\ z_B \\ 1 \end{bmatrix} \\ \begin{bmatrix} X_{C_i} \\ Y_{C_i} \\ Z_{C_i} \\ 1 \end{bmatrix} &= \begin{bmatrix} & & X_{D_i} \\ & \mathbf{T}_{20}^i & Y_{D_i} \\ 0 & 0 & 0 & 1 \\ & & Z_{D_i} & \end{bmatrix} \begin{bmatrix} x_C \\ y_C \\ z_C \\ 1 \end{bmatrix} \end{aligned} \quad (2.3)$$

and

$$\mathbf{T}_{j0}^i = \begin{bmatrix} e'_{i1} & e'_{i2} & e'_{ic} \\ m'_{i1} & m'_{i2} & m'_{ic} \\ n'_{i1} & n'_{i2} & n'_{ic} \end{bmatrix} \quad \begin{array}{l} j = \overline{1, 2} \\ i = \overline{1, N} \end{array} \quad (2.4)$$

where

$$\begin{aligned} e_{i1}^j &= \cos \psi_i^j \cos \phi_i^j - \cos \theta_i^j \sin \psi_i^j \sin \phi_i^j \\ m_{i1}^j &= \sin \psi_i^j \cos \phi_i^j + \cos \theta_i^j \cos \psi_i^j \cos \phi_i^j \\ n_{i1}^j &= \sin \theta_i^j \sin \phi_i^j \\ e_{i2}^j &= -\cos \psi_i^j \sin \phi_i^j - \cos \theta_i^j \sin \psi_i^j \cos \phi_i^j \\ m_{i2}^j &= -\sin \psi_i^j \sin \phi_i^j + \cos \theta_i^j \cos \psi_i^j \sin \phi_i^j \\ n_{i2}^j &= \sin \theta_i^j \cos \phi_i^j \\ e_{i3}^j &= \sin \theta_i^j \sin \psi_i^j \\ m_{i3}^j &= -\sin \theta_i^j \cos \psi_i^j \\ n_{i3}^j &= \cos \phi_i^j \end{aligned} \quad (2.5)$$

It is a function of ten parameters: $X_A, Y_A, Z_A, x_B, y_B, z_B, R, x_C, y_C, z_C$. By grouping these parameters in fours with the common parameter R , let us represent the weighted difference in three different forms (McCarthy, 1995; Golynski, 1970; Innocenti, 1995; Kosbolov and Rakhmatulina, 2012b, 2013b,c; Kosbolov *et al.*, 2014)

$$\begin{aligned} \Delta_{q_i}^{(1)} &= (\tilde{X}_{A_i} - X_A)^2 + (\tilde{Y}_{A_i} - Y_A)^2 + (\tilde{Z}_{A_i} - Z_A)^2 - R^2 \\ \Delta_{q_i}^{(2)} &= (\tilde{x}_{B_i} - x_B)^2 + (\tilde{y}_{B_i} - y_B)^2 + (\tilde{z}_{B_i} - z_B)^2 - R^2 \\ \Delta_{q_i}^{(3)} &= (\tilde{x}_{C_i} - x_C)^2 + (\tilde{y}_{C_i} - y_C)^2 + (\tilde{z}_{C_i} - z_C)^2 - R^2 \end{aligned} \quad (2.6)$$

where

$$\begin{aligned}
\begin{bmatrix} \tilde{X}_{Ai} \\ \tilde{Y}_{Ai} \\ \tilde{Z}_{Ai} \\ 1 \end{bmatrix} &= \begin{bmatrix} & & 0 \\ & \mathbf{T}_{10}^i & \\ 0 & 0 & 0 & 1 \end{bmatrix} \begin{bmatrix} x_B \\ y_B \\ z_B \\ 1 \end{bmatrix} + \begin{bmatrix} & & X_{D_i} \\ & \mathbf{T}_{20}^i & Y_{D_i} \\ 0 & 0 & 0 & 1 \end{bmatrix} \begin{bmatrix} x_C \\ y_C \\ z_C \\ 1 \end{bmatrix} \\
\begin{bmatrix} \tilde{x}_{B_i} \\ \tilde{y}_{B_i} \\ \tilde{z}_{B_i} \\ 1 \end{bmatrix} &= \begin{bmatrix} & & 0 \\ & \mathbf{T}_{01}^i & \\ 0 & 0 & 0 & 1 \end{bmatrix} \begin{bmatrix} X_{D_i} - X_A \\ Y_{D_i} - Y_A \\ Z_{D_i} - Z_A \\ 1 \end{bmatrix} + \begin{bmatrix} & & 0 \\ & \mathbf{T}_{21}^i & \\ 0 & 0 & 0 & 1 \end{bmatrix} \begin{bmatrix} x_C \\ y_C \\ z_C \\ 1 \end{bmatrix} \\
\begin{bmatrix} \tilde{x}_{C_i} \\ \tilde{y}_{C_i} \\ \tilde{z}_{C_i} \\ 1 \end{bmatrix} &= - \begin{bmatrix} & & 0 \\ & \mathbf{T}_{02}^i & \\ 0 & 0 & 0 & 1 \end{bmatrix} \begin{bmatrix} X_A - X_{D_i} \\ Y_A - Y_{D_i} \\ Z_A - Z_{D_i} \\ 1 \end{bmatrix} + \begin{bmatrix} & & 0 \\ & \mathbf{T}_{12}^i & \\ 0 & 0 & 0 & 1 \end{bmatrix} \begin{bmatrix} x_B \\ y_B \\ z_B \\ 1 \end{bmatrix}
\end{aligned} \tag{2.7}$$

where \mathbf{T}_{kj}^i is the transfer matrix from the k coordinate system to the j system determined as

$$\mathbf{T}_{01}^i = [\mathbf{T}_{10}^i]^T \quad \mathbf{T}_{02}^i = [\mathbf{T}_{20}^i]^T \quad \mathbf{T}_{21}^i = \mathbf{T}_{01}^i \times \mathbf{T}_{20}^i \quad \mathbf{T}_{12}^i = \mathbf{T}_{02}^i \times \mathbf{T}_{10}^i \tag{2.8}$$

The necessary conditions for minimum of the sum of squares of the weighted difference

$$S = \sum_{i=1}^N [\Delta_{q_i}^{(k)}]^2 \quad k = 1, 2, 3 \tag{2.9}$$

may be written as the following system of equations

$$\begin{aligned}
\frac{\partial S}{\partial X_A} = 0 & \quad \frac{\partial S}{\partial Y_A} = 0 & \quad \frac{\partial S}{\partial Z_A} = 0 & \quad \frac{\partial S}{\partial R} = 0 \\
\frac{\partial S}{\partial x_B} = 0 & \quad \frac{\partial S}{\partial y_B} = 0 & \quad \frac{\partial S}{\partial z_B} = 0 & \quad \frac{\partial S}{\partial R} = 0 \\
\frac{\partial S}{\partial x_C} = 0 & \quad \frac{\partial S}{\partial y_C} = 0 & \quad \frac{\partial S}{\partial z_C} = 0 & \quad \frac{\partial S}{\partial R} = 0
\end{aligned} \tag{2.10}$$

From (2.10)₁, considering (2.6)₁ and (2.9), we obtain

$$\begin{aligned}
\sum_{i=1}^N \Delta_{q_i}^{(1)} (\tilde{X}_{A_i} - X_A) = 0 & \quad \sum_{i=1}^N \Delta_{q_i}^{(1)} (\tilde{Y}_{A_i} - Y_A) = 0 \\
\sum_{i=1}^N \Delta_{q_i}^{(1)} (\tilde{Z}_{A_i} - Z_A) = 0 & \quad \sum_{i=1}^N \Delta_{q_i}^{(1)} R = 0
\end{aligned} \tag{2.11}$$

Assume that $R \neq 0$. Then from the last equality of system (2.11), it follows that

$$\sum_{i=1}^N \Delta_{q_i}^{(1)} = 0 \tag{2.12}$$

With provision for (2.12), the system of equations (2.11) takes the form

$$\sum_{i=1}^N \Delta_{q_i}^{(1)} \tilde{X}_{A_i} = 0 \quad \sum_{i=1}^N \Delta_{q_i}^{(1)} \tilde{Y}_{A_i} = 0 \quad \sum_{i=1}^N \Delta_{q_i}^{(1)} \tilde{Z}_{A_i} = 0 \quad \sum_{i=1}^N \Delta_{q_i}^{(1)} = 0 \tag{2.13}$$

By substituting expressions for $\Delta_{q_i}^{(1)}$ from (2.6)₁ into system (2.13), we obtain

$$\begin{aligned}
& \sum_{i=1}^N \left[\tilde{X}_{Ai}^2 X_A + \tilde{X}_{Ai} \tilde{Y}_{Ai} Y_A + \tilde{Z}_{Ai} \tilde{X}_{Ai} Z_A + \frac{1}{2} (R^2 - X_A^2 - Y_A^2 - Z_A^2) \tilde{X}_{Ai} \right] \\
&= \frac{1}{2} \sum_{i=1}^N (\tilde{X}_{Ai}^2 + \tilde{Y}_{Ai}^2 + \tilde{Z}_{Ai}^2) \tilde{X}_{Ai} \\
& \sum_{i=1}^N \left[\tilde{X}_{Ai} \tilde{Y}_{Ai} X_A + \tilde{Y}_{Ai}^2 Y_A + \tilde{Z}_{Ai} \tilde{Y}_{Ai} Z_A + \frac{1}{2} (R^2 - X_A^2 - Y_A^2 - Z_A^2) \tilde{Y}_{Ai} \right] \\
&= \frac{1}{2} \sum_{i=1}^N (\tilde{X}_{Ai}^2 + \tilde{Y}_{Ai}^2 + \tilde{Z}_{Ai}^2) \tilde{Y}_{Ai} \\
& \sum_{i=1}^N \left[\tilde{Z}_{Ai} \tilde{X}_{Ai} X_A + \tilde{Y}_{Ai} \tilde{Z}_{Ai} Y_A + \tilde{Z}_{Ai}^2 Z_A + \frac{1}{2} (R^2 - X_A^2 - Y_A^2 - Z_A^2) \tilde{Z}_{Ai} \right] \\
&= \frac{1}{2} \sum_{i=1}^N (\tilde{X}_{Ai}^2 + \tilde{Y}_{Ai}^2 + \tilde{Z}_{Ai}^2) \tilde{Z}_{Ai} \\
& \sum_{i=1}^N \left[\tilde{X}_{Ai} X_A + \tilde{Y}_{Ai} Y_A + \tilde{Z}_{Ai} Z_A + \frac{1}{2} (R^2 - X_A^2 - Y_A^2 - Z_A^2) \tilde{X}_{Ai} \right] = \frac{1}{2} \sum_{i=1}^N (\tilde{X}_{Ai}^2 + \tilde{Y}_{Ai}^2 + \tilde{Z}_{Ai}^2)
\end{aligned} \tag{2.14}$$

System (2.14) is linear with respect to the variables X_A, Y_A, Z_A and $H_1 = (R^2 - X_A^2 - Y_A^2 - Z_A^2)/2$, thus it may be written as

$$\begin{bmatrix} \sum_{i=1}^N \tilde{X}_{Ai}^2 & \sum_{i=1}^N \tilde{X}_{Ai} \tilde{Y}_{Ai} & \sum_{i=1}^N \tilde{X}_{Ai} \tilde{Z}_{Ai} & \sum_{i=1}^N \tilde{X}_{Ai} \\ \sum_{i=1}^N \tilde{X}_{Ai} \tilde{Y}_{Ai} & \sum_{i=1}^N \tilde{Y}_{Ai}^2 & \sum_{i=1}^N \tilde{Y}_{Ai} \tilde{Z}_{Ai} & \sum_{i=1}^N \tilde{Y}_{Ai} \\ \sum_{i=1}^N \tilde{X}_{Ai} \tilde{Z}_{Ai} & \sum_{i=1}^N \tilde{Y}_{Ai} \tilde{Z}_{Ai} & \sum_{i=1}^N \tilde{Z}_{Ai}^2 & \sum_{i=1}^N \tilde{Z}_{Ai} \\ \sum_{i=1}^N \tilde{X}_{Ai} & \sum_{i=1}^N \tilde{Y}_{Ai} & \sum_{i=1}^N \tilde{Z}_{Ai} & N \end{bmatrix} \begin{bmatrix} X_A \\ Y_A \\ Z_A \\ H_1 \end{bmatrix} = \frac{1}{2} \begin{bmatrix} \sum_{i=1}^N R_{Ai}^2 \tilde{X}_{Ai} \\ \sum_{i=1}^N R_{Ai}^2 \tilde{Y}_{Ai} \\ \sum_{i=1}^N R_{Ai}^2 \tilde{Z}_{Ai} \\ \sum_{i=1}^N R_{Ai}^2 \end{bmatrix} \tag{2.15}$$

where $R_{Ai}^2 = \tilde{X}_{Ai}^2 + \tilde{Y}_{Ai}^2 + \tilde{Z}_{Ai}^2$.

The solution to this system by Cramer's rule is as follows

$$(X_A, Y_A, Z_A, H_1) = \frac{1}{D_1} (D_{X_A}, D_{Y_A}, D_{Z_A}, D_{H_1}) \quad D_1 \neq 0 \tag{2.16}$$

Similarly, from (2.10)₂, considering (2.6)₂ and (2.9), we obtain a system of linear equations in the unknowns x_B, y_B, z_B, H_2

$$\begin{bmatrix} \sum_{i=1}^N \tilde{x}_{Bi}^2 & \sum_{i=1}^N \tilde{x}_{Bi} \tilde{y}_{Bi} & \sum_{i=1}^N \tilde{x}_{Bi} \tilde{z}_{Bi} & \sum_{i=1}^N \tilde{x}_{Bi} \\ \sum_{i=1}^N \tilde{x}_{Bi} \tilde{y}_{Bi} & \sum_{i=1}^N \tilde{y}_{Bi}^2 & \sum_{i=1}^N \tilde{y}_{Bi} \tilde{z}_{Bi} & \sum_{i=1}^N \tilde{y}_{Bi} \\ \sum_{i=1}^N \tilde{x}_{Bi} \tilde{z}_{Bi} & \sum_{i=1}^N \tilde{y}_{Bi} \tilde{z}_{Bi} & \sum_{i=1}^N \tilde{z}_{Bi}^2 & \sum_{i=1}^N \tilde{z}_{Bi} \\ \sum_{i=1}^N \tilde{x}_{Bi} & \sum_{i=1}^N \tilde{y}_{Bi} & \sum_{i=1}^N \tilde{z}_{Bi} & N \end{bmatrix} \begin{bmatrix} x_B \\ y_B \\ z_B \\ H_2 \end{bmatrix} = \frac{1}{2} \begin{bmatrix} \sum_{i=1}^N R_{Bi}^2 \tilde{x}_{Bi} \\ \sum_{i=1}^N R_{Bi}^2 \tilde{y}_{Bi} \\ \sum_{i=1}^N R_{Bi}^2 \tilde{z}_{Bi} \\ \sum_{i=1}^N R_{Bi}^2 \end{bmatrix} \tag{2.17}$$

By solving this system by Cramer's rule, we obtain

$$(x_B, y_B, z_B, H_2) = \frac{1}{D_2} (D_{x_B}, D_{y_B}, D_{z_B}, D_{H_2}) \quad D_2 \neq 0 \tag{2.18}$$

From (2.10)₃, considering (2.6)₃ and (2.10)₁, we obtain a system of linear equations in the unknowns x_C, y_C, z_C, H_3

$$\begin{bmatrix} \sum_{i=1}^N \tilde{x}_{Ci}^2 & \sum_{i=1}^N \tilde{x}_{Ci}\tilde{y}_{Ci} & \sum_{i=1}^N \tilde{x}_{Ci}\tilde{z}_{Ci} & \sum_{i=1}^N \tilde{x}_{Ci} \\ \sum_{i=1}^N \tilde{x}_{Ci}\tilde{y}_{Ci} & \sum_{i=1}^N \tilde{y}_{Ci}^2 & \sum_{i=1}^N \tilde{y}_{Ci}\tilde{z}_{Ci} & \sum_{i=1}^N \tilde{y}_{Ci} \\ \sum_{i=1}^N \tilde{x}_{Ci}\tilde{z}_{Ci} & \sum_{i=1}^N \tilde{y}_{Ci}\tilde{z}_{Ci} & \sum_{i=1}^N \tilde{z}_{Ci}^2 & \sum_{i=1}^N \tilde{z}_{Ci} \\ \sum_{i=1}^N \tilde{x}_{Ci} & \sum_{i=1}^N \tilde{y}_{Ci} & \sum_{i=1}^N \tilde{z}_{Ci} & N \end{bmatrix} \begin{bmatrix} x_C \\ y_C \\ z_C \\ H_3 \end{bmatrix} = \frac{1}{2} \begin{bmatrix} \sum_{i=1}^N R_{Ci}^2 \tilde{x}_{Ci} \\ \sum_{i=1}^N R_{Ci}^2 \tilde{y}_{Ci} \\ \sum_{i=1}^N R_{Ci}^2 \tilde{z}_{Ci} \\ \sum_{i=1}^N R_{Ci}^2 \end{bmatrix} \quad (2.19)$$

From which we obtain x_C, y_C, z_C, H_3

$$(x_C, y_C, z_C, H_3) = \frac{1}{D_3} (D_{x_C}, D_{y_C}, D_{z_C}, D_{H_3}) \quad D_3 \neq 0 \quad (2.20)$$

Eliminating the first four unknowns X_A, Y_A, Z_A, R , based on formula (2.15), it is possible to bring system (2.10) to a system of six equations with six unknowns $x_B, y_B, z_B, x_C, y_C, z_C$, which is convenient to be given as

$$\begin{aligned} \sum_{i=1}^N \Delta_{qi}^{(1)} \frac{\partial \Delta_{qi}^{(2)}}{\partial x_B} = 0 & \quad \sum_{i=1}^N \Delta_{qi}^{(1)} \frac{\partial \Delta_{qi}^{(3)}}{\partial x_C} = 0 \\ \sum_{i=1}^N \Delta_{qi}^{(1)} \frac{\partial \Delta_{qi}^{(2)}}{\partial y_B} = 0 & \quad \sum_{i=1}^N \Delta_{qi}^{(1)} \frac{\partial \Delta_{qi}^{(3)}}{\partial y_C} = 0 \\ \sum_{i=1}^N \Delta_{qi}^{(1)} \frac{\partial \Delta_{qi}^{(2)}}{\partial z_B} = 0 & \quad \sum_{i=1}^N \Delta_{qi}^{(1)} \frac{\partial \Delta_{qi}^{(3)}}{\partial z_C} = 0 \end{aligned} \quad (2.21)$$

Apparently, equations of this system are the same as the three equations of the thirteen degree in the three unknown functions given in the work by Kosbolov *et al.* (2005), though in this case we have a system of six equations in six unknown functions. Solution of system (2.21) is labor-intensive task, so it is more effective to apply a search algorithm for the minimum of the function S stated below:

1. Give arbitrarily reference points $B^{(0)} \in Q_1, C^{(0)} \in Q_2$.
2. Solve the system of linear equations (2.16) and determine $X_A^{(1)}, Y_A^{(1)}, Z_A^{(1)}, R_1^{(1)}$.
3. Give points $A^{(1)} \in Q, C^{(0)} \in Q_2$.
4. Solve the system of equations (2.18) and determine $x_B^{(1)}, y_B^{(1)}, z_B^{(1)}, R_2^{(1)}$.
5. Give points $A^{(1)} \in Q, B^{(1)} \in Q_1$.
6. Solve the system of equations (2.20) and determine $x_C^{(1)}, y_C^{(1)}, z_C^{(1)}, R_3^{(1)}$.
7. Check $|X_A^{i+1} - X_A^i| \leq \varepsilon, |Y_A^{i+1} - Y_A^i| \leq \varepsilon, |Z_A^{i+1} - Z_A^i| \leq \varepsilon, |R^{i+1} - R^i| \leq \varepsilon$.
8. If this condition is satisfied, the iterating is completed.
9. If this condition is not satisfied, proceed to item 1 by replacing the reference points $B^{(0)}$ and $C^{(0)}$ for the found points $B^{(1)}$ and $C^{(0)}$.
10. Then check the accuracy of the prescribed function reproduction by analysis of the position RKC $ABCD$

$$\mathbf{r}_{D_0} = \mathbf{T}_{10} \mathbf{T}_{21} \mathbf{T}_{32} \mathbf{r}_{D_3}$$

11. The iterating is completed, if the accuracy of reproduction satisfies the prescribed function. If it does not satisfy the prescribed accuracy, it is necessary to proceed to item 1 of the given algorithm.

By applying the algorithm, we obtain a decreasing sequence of values of the objective function $S_1^{(1)}, S_2^{(1)}, S_3^{(1)}, S_1^{(2)}, S_2^{(2)}, S_3^{(2)}$ which has a limit equal to the value of the function S at the point of local minimum. When satisfying the inequality

$$\max\left(|R^{(i)} - R^{(i-1)}|, |X_A^{(i)} - X_A^{(i-1)}|, |Y_A^{(i)} - Y_A^{(i-1)}|, |Z_A^{(i)} - Z_A^{(i-1)}|\right) \leq \varepsilon$$

where ε is the prescribed calculation accuracy, the iterating is completed. Convergence of the suggested algorithm is proved by the Weierstrass theorem.

Weierstrass theorem: For each function $f(x)$ continuous over $[a, b]$ and any real number $\varepsilon > 0$, such a polynomial $p(x)$ may be found that $\|P(x) - f(x)\| < \varepsilon$.

As a result of the problem solution, the points $A(X_A, Y_A, Z_A)$ are determined in the fixed system of coordinates, $B^{(0)} \in Q_1$, $C^{(0)} \in Q_2$, such that when coinciding the link BC with them, we obtain the desired RKC in form of an open four-link chain $ABCD$.

Then we check the accuracy of the prescribed function reproduction by analysis of the position of RKC $ABCD$. If the accuracy of reproduction satisfies the prescribed function, the iteration is completed, and if it does not satisfy the prescribed accuracy, it is necessary to proceed to item 1 of the prescribed algorithm.

When specifying a part of the desired synthesis parameters in various combinations, we obtain different modifications of RKC (Kosbolov and Rakhmatulina, 2013b).

- If the coordinates of point $A(X_{A_i}, Y_{A_i}, Z_{A_i})$ and Eulerian angles $\theta_i^1, \psi_i^1, \phi_i^1$ of the solid Q_1 as well as the axes of point $D_i(X_{D_i}, Y_{D_i}, Z_{D_i})$ and Eulerian angles $\theta_i^1, \psi_i^1, \phi_i^1$ of the solid Q_2 are specified, we obtain a three-link open chain $ABCD$ (Fig. 1). The necessary conditions for the minimum of the sum S in this case takes the form

$$\frac{\partial S}{\partial j} = 0 \quad j = x_B, y_B, z_B, R, x_C, y_C, z_C \quad (2.22)$$

and to find the minimum S , we may use the algorithm given above, considering that the parameters X_A, Y_A, Z_A are specified.

If the points $A(X_A, Y_A, Z_A)$ and $D(X_D, Y_D, Z_D)$ are fixed, then, as a result of the synthesis of RKC, we obtain a spatial four-link chain $ABCD$.

- Given the coordinates $x_C = y_C = z_C = 0$ of the point $C \in Q_2$, coordinates $X_{D_i}, Y_{D_i}, Z_{D_i}$ of the point D of the solid Q_2 and Eulerian angles $\theta_i^1, \psi_i^1, \phi_i^1$ of the solid Q_1 , and the desired parameters $X_A, Y_A, Z_A, R, x_B, y_B, z_B$.

The necessary conditions for the minimum of the sum S takes the form

$$\frac{\partial S}{\partial j} = 0 \quad j = X_A, Y_A, Z_A, R, x_B, y_B, z_B \quad (2.23)$$

To find the minimum of the function S we may use again the algorithm given above, considering that $x_C = y_C = z_C = 0$.

- Given coordinates $x_B, y_B, z_B = 0$ of the point B of the solid Q_1 and Eulerian angles of the solid Q_2 , $\theta_i^2, \psi_i^2, \phi_i^2$. The original problem reduces to the definition of sphere of positions of the fixed point C of the solid Q_2 which is the least remote from N (Fig. 1).

The necessary conditions for the minimum of the sum S is

$$\frac{\partial S}{\partial j} = 0 \quad j = X_A, Y_A, Z_A, R, x_C, y_C, z_C \quad (2.24)$$

This problem was studied in detail in work by Kosbolov *et al.* (2013c). For its solution we may also use the algorithm given above, assuming $x_B, y_B, z_B = 0$, but in this special case, the algorithm of the minimum search is absolutely coinciding with the kinematic inversion method.

Thus, as we see, the problem of RKC with spherical kinematic pairs is solved, and their modifications may be used as modules of structural and kinematic synthesis of spatial linkage mechanisms through specified positions of the input and output links.

3. Example

Suppose that it is necessary to design a six-linkage mechanism with spherical pairs (Fig. 2), approximately reproducing seven body positions specified in Table 1 and the initial data in Table 2.

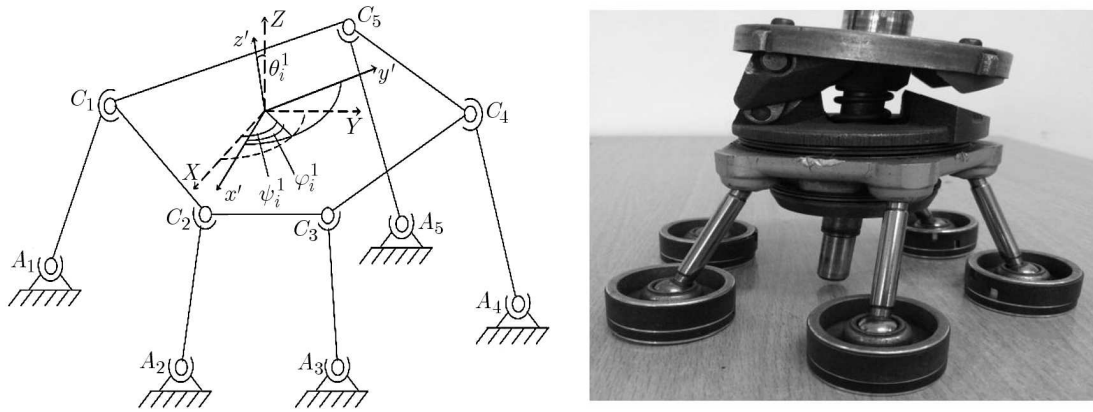


Fig. 2. Kinematic diagram of spatial linkage mechanisms with spherical pairs

Table 1. Assigned positions of the body for synthesis of a single movable mechanism – six-linkage mechanism with $N = 7$

Position No. (i)	X_{O_i}	Y_{O_i}	Z_{O_i}	Euler angles [deg]		
				θ_i^1	ψ_i^1	ϕ_i^1
1	0.30	0.12	0.01	0	0	0
2	0.35	0.17	0.24	28	35	17
3	0.44	0.21	0.25	34	38	5
4	0.51	0.15	0.32	17	24	12
5	0.50	0.30	0.45	50	50	21
6	0.60	0.25	0.41	45	33	24
7	0.55	0.32	0.35	0	0	0

When $N = 7$, as known in mobile spatial systems, there are points (not more than 20) with seven positions on one sphere. Furthermore, the points which are in the seven considered positions are approaching the sphere. As noted, the exact spherical points of a movable system correspond to an absolute minimum $S = 0$ of the sum $S = \sum \Delta_{q_i}^2$, because they make all Δ_{q_i}

Table 2. Initial data ($N = 7$)

$N = 7$	ZLL = 6, ZKK = 6, ZII = 6, dmj = 0.2		MJ0 = -1.2, NJ0 = -1.2, KJ0 = -1.2		
XS = 0.3	YS = 0.12	ZS = 0.01	F = 0	P = 0	T = 0
XS = 0.35	YS = 0.17	ZS = 0.24	F = 28	P = 35	T = 17
XS = 0.44	YS = 0.21	ZS = 0.25	F = 34	P = 38	T = 5
XS = 0.51	YS = 0.15	ZS = 0.32	F = 17	P = 24	T = 12
XS = 0.5	YS = 0.3	ZS = 0.45	F = 50	P = 50	T = 21
XS = 0.6	YS = 0.25	ZS = 0.41	F = 45	P = 33	T = 24
XS = 0.55	YS = 0.32	ZS = 0.35	F = 0	P = 0	T = 0

Table 3. Results of calculation ($N = 4$)

LL = 3, KK = 2, II = 1		MJ = -0.6, NJ = -0.8, KJ = -1	
$N = 1$	$A = 0.488270$	$C = -2.22103$	
$N = 2$	$A = 0.303894$	$C = 3.96393$	
$N = 3$	$A = 0.151985$	$C = -3.85753$	
$N = 4$	$A = 0.146845$	$C = 3.00599$	
$R0 = 0.245293$	$R01 = 0.245194$	$S = 4.296551E-0.3$	$S1 = 4.295576E-0.3$
LL = 3, KK = 2, II = 2		MJ = -0.6, NJ = -0.8, KJ = -0.8	
$N = 1$	$A = 0.488270$	$C = -3.42355$	
$N = 2$	$A = 0.303894$	$C = 2.28575$	
$N = 3$	$A = 0.151985$	$C = -2.95424$	
$N = 4$	$A = 0.146845$	$C = 3.00600$	
$R0 = 0.245216$	$R01 = 0.245194$	$S = 4.292136E-0.3$	$S1 = 4.295576E-0.3$
LL = 3, KK = 2, II = 3		MJ = -0.6, NJ = -0.8, KJ = -0.6	
$N = 1$	$A = 0.488174$	$C = -3.18222$	
$N = 2$	$A = 0.303906$	$C = 5.18244$	
$N = 3$	$A = 0.152115$	$C = -2.55608$	
$N = 4$	$A = -0.146845$	$C = 0.3006$	
$R0 = 0.245195$	$R01 = 0.245194$	$S = 4.294402E-0.3$	$S1 = 4.295576E-0.3$
LL = 3, KK = 2, II = 4		MJ = -0.6, NJ = -0.8, KJ = -0.6	
$N = 1$	$A = 0.488217$	$C = -2.74528$	
$N = 2$	$A = 0.303942$	$C = 8.77332$	
$N = 3$	$A = 0.152078$	$C = -2.92302$	
$N = 4$	$A = 0.146866$	$C = 3.00599$	
$R0 = 0.245217$	$R01 = 0.245194$	$S = 4.297097E-0.3$	$S1 = 4.295576E-0.3$

($i = 1, 2, \dots, 7$) vanish. The approximate spherical points of a movable system correspond to the local minima of the sum or are located in the vicinity of the local minimum of the function $S = F(x_C, y_C, z_C)$. Both these and other are common points of the surfaces $G_x = 0$, $G_y = 0$, $G_z = 0$, and they are determined based on the solution to system (2.21).

We are definitely interested not in all system solutions (2.24), but in those which correspond to the minimum of the sum S . These solutions in this case are a numerical method for searching of the minimum of the sum S , based on the searching algorithm for the minima of the function S . Since we need five spherical points of the movable system for construction of the six-linkage mechanism (Fig. 2) having analysed the results we selected five points of the minimum of the

surface $S = F(x_C, y_C, z_C)$. The coordinates of these points, the parameters of approaching spheres corresponding to them and the values Δ_{q_i} maximum per module are given in Table 3.

4. Research results

Judging from deviations, the points C_1, C_2, C_3 are the exact spherical points (found with the given measure of inaccuracy), and C_4 and C_5 – are approximate points.

To solve this problem, a Visual Basic program has been written. The results of the problem solution are given in Table 3.

The calculations have been made within the range

$$-1.2 < MJ < 0.6 \quad -1.2 < NJ < 0.6 \quad -1.2 < KJ < 0.6$$

with a pitch $dm_j = 0.2$.

In the entire range of calculations, the process of calculation is concurrent. The global minimum is equal to

$$S_{min} = 0.0042921$$

and it is achieved at

$$LL = 3 \quad KK = 2 \quad II = 2$$

In Table 3, only a part of results in the neighborhood of the global minimum is shown. Its value is highlighted in bold frame in Table 3.

Below, the results of calculation of the objective function in form of carpet plots and 3D plots (Figs. 3 and 4) are given.

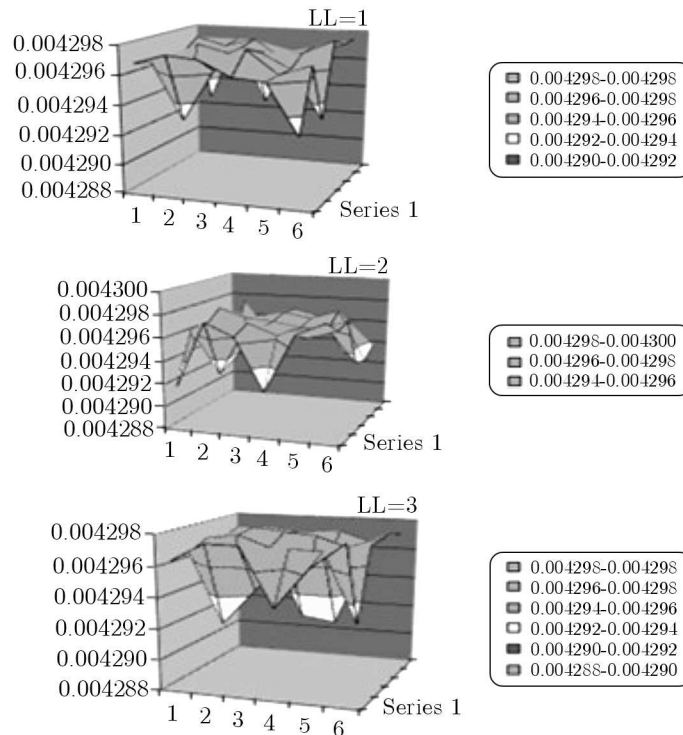


Fig. 3. $LL = 1, 2, 3$, $S_{min} = -0.0042921$, volume graphics

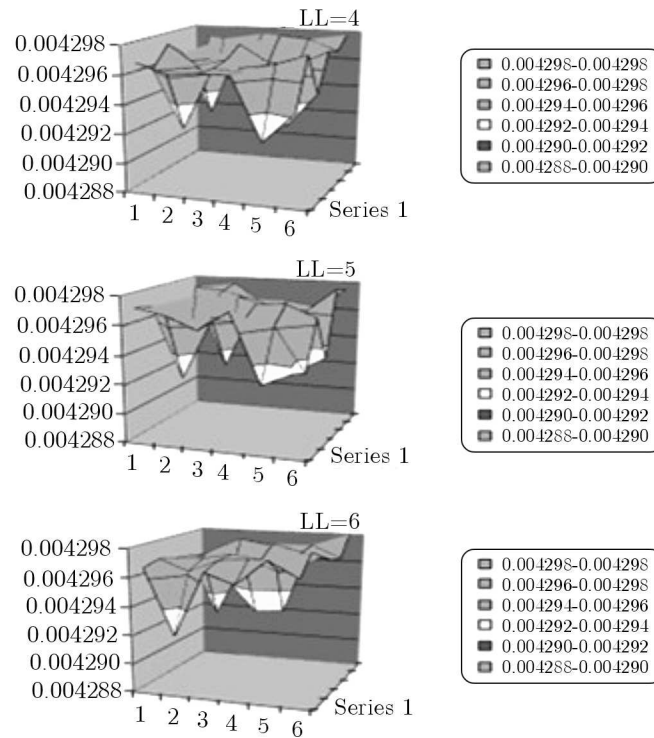


Fig. 4. LL = 4,5,6, $S_{min} = -0.0042921$, volume graphics

5. Discussion

As can be concluded, the use of one and the same objective function being generated for synthesis of BKC and its modification allows automating of the process of synthesis of spatial linkage mechanisms through predetermined positions of the input and output links of the mechanism.

6. Conclusions

In summary, in the synthesis of BKC with spherical kinematic pairs through predetermined positions of the input and output links of a mechanism when two adjacent links of BKC tend to infinity, it is necessary to replace the spherical kinematic pair for a plain or cylindrical one. In such a case, the synthesized mechanism takes form of a spatial link mechanism after determining the required parameters.

References

1. GOLYNSKI Z., 1970, Optimal synthesis problems solved by means of nonlinear programming and random methods, *Journal of Mechanisms*, **3**, 287-309
2. INNOCENTI C., 1995, Direct kinematics in analytical form of the 6-4 fully – parallel mechanisms, *Transactions of the ASME, Journal of Mechanical Design*, **1**, 85-95
3. JOLDASBEKOV W.A., DRAKUNOV Y.M., KOSBOLOV S.B., MOLDABEKOV M.M., 1987, Synthesis of starting kinematics mechanisms. High grade Math., *Academy of Sciences of the Kazakh SSR, series Science*, **3**, 65-70
4. KOSBOLOV S.B., BEKENOV E.T., 2013, Kinematic synthesis of spatial six-membered transfer mechanism based on the original kinematic chains, *Bulletin of Science and Technological*, **6**, 30-38

5. KOSBOLOV S., MOLDABEKOV M., BEKENOV E., 2005, Kinematic synthesis of spatial lever motion – generating mechanisms by use of initial kinematic chain, *The 9-th IFToMM, International Symposium on Theory of Machines and Mechanisms*, **4**, 245-250
6. KOSBOLOV S.B., RAKHMATULINA A.B., 2012a, Optimization flow of force of plane leverage mechanisms, *International Conference on European Science and Technology*, 271-276
7. KOSBOLOV S.B., RAKHMATULLINA A.B., 2012b, Parametric synthesis of spatial linkage based on the initial kinematic chain, *Modern Problems of Science and Education*, **2**, 207-215
8. KOSBOLOV S.B., RAKHMATULINA A.B., 2013a, Design of a new load lifting mechanism, *Procedia Social and Behavioral Sciences*, **83**, 689-692
9. KOSBOLOV S.B., RAKHMATULINA A.B., 2013b, Kinematic synthesis of three-dimensional six-link motion-generating mechanisms in the basis of initial kinematic chains, *Journal of Machinery Manufacture and Reliability*, **2**, 102-108
10. KOSBOLOV S.B., RAKHMATULINA A.B., 2013c, Synthesis mechanism to compensate weft threads on a multicolored weaving loom machine shuttleless, *Tekstil ve Konfeksiyon*, Turkey, **23**, 23-31
11. KOSBOLOV S.B., RAKHMATULINA A.B., IMANBAEVA N.C., ZHAUYT A., 2014, Optimal design of leading kinematical chain of eight linked planar load lifting linkage, *Mediterranean Journal of Social Sciences*, **23**, 2656-2660
12. MCCARTHY J.M., 1995, The synthesis of planar RR and spatial CC chains and the equation of a triangle, *Transactions of the ASME, Journal of Mechanical Design*, 101-106
13. VOROBYOV E.I., EGOROV O.D., POPOV S.A., 1988, Mechanics of industrial robots, *Calculation and Design of Mechanisms*, 366-376

Manuscript received January 10, 2015; accepted for print June 30, 2015

INCLUSION OF THE D-OPTIMALITY IN MULTISINE MANOEUVRE DESIGN FOR AIRCRAFT PARAMETER ESTIMATION

PIOTR LICHOTA

Warsaw University of Technology, Institute of Theoretical and Applied Mechanics, Warsaw, Poland
e-mail: plichota@meil.pw.edu.pl

This paper is concerned with the designing of simultaneous flight control deflections for aircraft system identification. The elevator, ailerons and rudder are excited with harmonically related multisine signals. The optimal deflections are designed when there is no information about the stability and control derivatives and when this information is available. The inclusion of the system dynamics in the inputs design phase is done with the D-optimality criterion. Both sets of optimal flight surface deflections are used as excitations of a nonlinear aircraft model which is identified through the maximum likelihood estimation method. Parameters accuracy for those maneuvers (designed with and without a-priori knowledge) is presented and compared.

Keywords: inputs design, system identification, flight dynamics

1. Introduction

To obtain precise information about aircraft dynamics, aerodynamic stability and control derivatives have to be determined. This can be done by various methods like wind tunnel tests (Hoe *et al.*, 2012), Computational Fluid Dynamics – CFD (Mader and Martins, 2011) and System Identification – Sys-ID (Jameson and Cooke, 2012; Jategaonkar, 2006; Lichota and Ohme, 2014). Among this group, the gathering of aerodynamic databases from flight test data is the most reliable as it is based on experiments made on real objects. On the other hand, as multiple flight tests are performed in the Sys-ID, it is of high cost and time consuming. CFD methods are the least expensive in this group, however final results of aerodynamic derivatives (regardless of the object) have to be compared with experiments (Rogowski and Maroński, 2015).

The Sys-ID approach consists of four main steps that are: designing and performing manoeuvres, measuring the data, modelling the object and estimating unknown parameters. Those steps are strictly connected, and if the registered data will be inaccurate or there will be not enough information about the aircraft dynamics in the output signals, reliable estimation will not be possible. As modern sensors allow one to obtain very high accuracy of the data and measurement techniques are well developed a strong emphasis should be put on designing inputs used for exciting the optimal aircraft response.

The research concerning excitations that were to maximize the information content in the measured data was extensively investigated in the seventies and eighties. Those studies showed that sine-sweep (linear or logarithmical) or typical multi-step inputs (pulse, doublet, 3-2-1-1) can be used to develop a good mathematical model of an aircraft if only one flight control surface is deflected through a manoeuvre. It has been shown recently that simultaneous multi-step excitations could be used for this purpose as well (Lichota and Ohme, 2014), but this requires *a priori* knowledge of the aerodynamic derivatives.

If the flight controls can be deflected at the same time, the use of harmonically related multisine signals is possible as well. This approach does not require the initial information about

the system and allows one to obtain estimates with the same quality (in terms of parameters accuracy) as the design with simultaneous multi-step inputs. If the inclusion of the *a priori* knowledge in the multisine inputs design phase would increase the quality of estimation, it would mean that multisine signals are more adequate for aircraft Sys-ID purposes than simultaneous multi-step excitations.

The incorporation of initial knowledge of aerodynamic parameters can be done by introducing the D-optimality criterion instead of the Relative Peak Factor in the multisine optimization phase. In the present study, a linear aircraft model is used for this purpose as it is less computationally demanding than the nonlinear representation. The designed set of simultaneous multisine excitations is used as inputs for a nonlinear aircraft model that has been created in Matlab. On the basis of recorded signals the unknown parameters of the object are estimated by applying the maximum likelihood principle.

A similar procedure is applied to multisine signals that are designed without *a priori* knowledge of the system dynamics. Evaluated ailerons, elevator and rudder deflections are used as excitations for the nonlinear aircraft model. The response of the object is recorded and then the unknown parameters of the system are identified. The results are compared with the estimates obtained from the manoeuvre in which initial values of the aerodynamic derivatives are available in the inputs design phase.

2. Multisine input signals

The multisine input is an excitation that is composed of summed harmonic sinusoids with individual amplitudes A_k and phase shifts ϕ_k (Morelli, 2012)

$$\delta = \sum_{k=1}^M A_k \sin(2\pi f_k t + \phi_k) \quad (2.1)$$

where $k = 1, \dots, M$ stands for the number of the harmonic, f_k is the frequency of the k -th component and δ is the input signal.

An important feature of the multisine signals is that they can be designed as mutually orthogonal in the time and frequency domain (Morelli, 2003). This means that simultaneous ailerons, elevator and rudder deflections can be independent. In order to achieve this aim, it is required to assign different harmonics to each flight control (e.g. $2f_0, 5f_0, 8f_0, \dots$ to ailerons, $3f_0, 6f_0, 9f_0, \dots$ to elevator, $4f_0, 7f_0, 10f_0, \dots$ to rudder). This assignment provides orthogonality in the frequency domain as distinct spectral lines form the frequency content of each input. In the time domain, the mutual orthogonality is achieved due to orthogonality properties of the sine function (Morelli, 2012). It is practicable to omit the first harmonic in this assignment in order to optimize the cost function effectively.

Frequencies of the consecutive components in the multisine signals are evenly spaced and based on the excitation time T : $f_k = k/T$. This also limits the minimum available frequency which must satisfy the condition: $f_{min} \geq 2/T$. The maximum available frequency is limited by the frequency range of interest in the investigated case.

Multisine input signals have wide-frequency band and the amplitudes of the different harmonics A_k are chosen to achieve desired power spectrum. If there is no need to put an emphasis on specific frequencies, a uniform power spectrum should be used. For simultaneous aileron, elevator and rudder deflections and flat power spectrum, the amplitudes A_k related to the j -th control are given by

$$A_{j,k} = \frac{A_j}{\sqrt{M_j}} \quad (2.2)$$

where A_j is the amplitude of the j -th flight control and M_j is the number of the harmonic components assigned to the j -th flight surface.

For each flight control, input energy maximization is done through proper selection of consecutive harmonics phase angles $\phi_{j,k}$. The phase angles should maximize the excitation effectiveness without unnecessary increase in each signal value as this can cause that aircraft will go too far from the trim conditions and will hinder the Sys-ID process. For this purpose, the Relative Peak Factor (RPF) can be used as it expresses the input amplitude range divided by the excitation energy. The RPF is also scaled so that for a single sinusoid it is equal to 1. For the j -th flight surface deflection δ_j , the RPF is given by

$$RPF(\delta_j) = \frac{\max \delta_j - \min \delta_j}{2\sqrt{2}\text{rms}(\delta_j)} \quad (2.3)$$

RPF minimization is equivalent to input effectiveness maximization and can be achieved with a simplex optimization algorithm. In our study, the Schroeder phase angles are used as initial values of the phase angles ϕ_k for the j -th flight control (Schroeder, 1970)

$$\phi_{j,k} = \phi_{j,k-1} + 2\pi(f_{j,k-1} - f_{j,k})t_{j,k-1} \quad t_{j,k} = T \sum_{l=1}^k p_{j,l} \quad (2.4)$$

where $f_{j,k}$ is the k -th harmonic frequency assigned to the j -th input and t_k is time epoch. For the flat power spectrum and the j -th flight control, the power of the k -th component is $p_{j,k} = 1/M_j$.

As deflections should start and end with zero amplitude, it is necessary to find a constant time offset for the components of each excitation. This is equivalent to sliding the inputs along the time axis until the zero crossing occurs at $t = 0$.

3. D-optimal criterion

The design process of multisine input signals does not require knowledge of the system dynamics in terms of stability and control derivatives. However, it is considered that inclusion of some information about aerodynamic parameters in the design phase could increase the quality of the aircraft response in terms of the Sys-ID. This requires introducing estimator based on the minimum mean squared error (Kay, 1993)

$$\text{MSE}(\hat{\Theta}) = E[(\hat{\Theta} - \Theta)^2] = \text{cov}(\hat{\Theta}) + \text{bias}^2(\Theta, \hat{\Theta}) \quad (3.1)$$

where Θ are the parameters of the model and $\hat{\Theta}$ are their estimates.

When the estimator is designed to be unbiased, the minimum mean squared error consists only of the covariance term. This part can be determined on the basis of Cramér-Rao inequality which states that the covariance of the unbiased estimator is at least as high as the inverse of the Fisher Information Matrix \mathcal{F}

$$\text{cov}(\hat{\Theta}) \geq \mathcal{F}^{-1} \quad (3.2)$$

The Fisher Information Matrix which is a measure of the amount of information that observable variables carry about the unknown system parameters is defined as

$$\mathcal{F} = E \left\{ \left[\frac{\partial \ln \mathcal{L}(\Theta|\mathbf{z})}{\partial \Theta} \right] \left[\frac{\partial \ln \mathcal{L}(\Theta|\mathbf{z})}{\partial \Theta} \right]^T \right\} \quad (3.3)$$

where the likelihood function $\mathcal{L}(\Theta|\mathbf{z})$ is equal to $p(\mathbf{z}|\Theta)$ – conditional probability that the measurement vector \mathbf{z} is observed for the model parameters Θ .

If the likelihood function is twice differentiable with respect to the model parameters, it can be shown that

$$\mathcal{F} = -\mathbb{E} \left[\frac{\partial^2 \ln \mathcal{L}(\Theta | \mathbf{z})}{\partial \Theta \Theta^T} \right] \quad (3.4)$$

Multivariate normal distribution is usually chosen to evaluate the probability density function at a certain time point t_k . Due to variables, independence the probability can be defined for all time points in the manoeuvre (Jategaonkar, 2006)

$$p(\mathbf{z} | \Theta) = \frac{1}{\sqrt{(2\pi)^n |\mathbf{R}|^N}} \exp \left(-\frac{1}{2} \sum_{k=1}^N [\mathbf{z}(t_k) - \mathbf{y}(t_k)]^T \mathbf{R}^{-1} [\mathbf{z}(t_k) - \mathbf{y}(t_k)] \right) \quad (3.5)$$

where n is the number of model outputs y , $k = 1, \dots, N$ is the index of time samples and \mathbf{R} is the measurement noise covariance matrix.

The described approach with neglecting small terms leads strictly to the Fisher Information Matrix sensitivity form

$$\mathcal{F} \approx \sum_{k=1}^N \left[\frac{\partial \mathbf{y}(t_k)}{\partial \Theta} \right]^T \mathbf{R}^{-1} \left[\frac{\partial \mathbf{y}(t_k)}{\partial \Theta} \right] \quad (3.6)$$

where the output signals gradients $\partial \mathbf{y}(t_k) / \partial \Theta$ can be obtained through forward difference formula. Introducing central differences does not increase the accuracy significantly and raises the computational time, therefore, it is not used in the evaluations.

The columns of the Fisher Information Matrix represent contributions of the model parameters, so if the columns are independent, the determinant reaches its maximum value. On the contrary, if the columns are linearly dependent, the determinant will accept the minimum value. Therefore, the optimality criterion (D-optimality) is expressed by maximization of the Fisher Information Matrix determinant what means that the estimation error ellipsoid volume is minimized.

Inclusion of the D-optimality criterion in the multisine design phase can be used in order to introduce the initial information about stability and control derivatives. This task can be achieved by incorporating the linear aircraft model and minimization of the Fisher Information Matrix inverse (Parameter Error Covariance Matrix \mathcal{P}) determinant. The linear representation has been selected because it well describes the object, and the computational time for single evaluation is relatively short.

4. Linear model

The aircraft dynamic equations of motion are derived in a vehicle carried coordinate system $Oxyz$ and linearised in accordance with Etkin (1972). The origin of the $Oxyz$ reference frame is located at the center of gravity. The Ox axis coincides with the longitudinal axis of the airplane. The Oy axis is normal to the aircraft symmetry plane and is pointing in the direction of the right wing. The Oz axis is oriented downward, so it completes the right-handed coordinate system.

The $Oxyz$ system is related to the vehicle carried $Ox_g y_g z_g$ reference frame through rotation angles: Φ (roll angle), Θ (pitch angle), Ψ (yaw angle) which are used to describe the orientation of the object. The $Ox_g y_g z_g$ coordinate system remains parallel to the earth fixed reference frame $O_1 x_1 y_1 z_1$, whose origin is located at an arbitrary point of the Earth with the Ox_1 axis pointed north, Oy_1 axis pointed east and the Oz_1 axis is directed toward center of the Earth. Relations between the described coordinate systems are shown in Fig. 1, and the transformations of linear

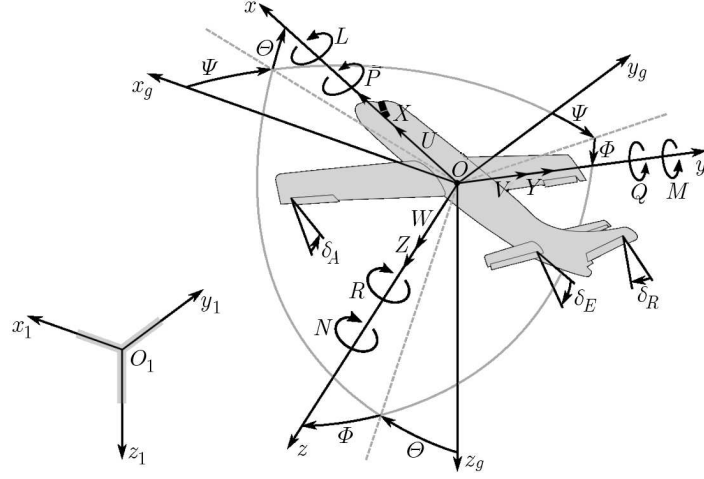


Fig. 1. Coordinate systems and motion variables

and angular quantities from the gravitational reference frame $Ox_gy_gz_g$ to the body coordinate system $Oxyz$ are given by the matrices

$$\mathbf{\Lambda}_V = \begin{bmatrix} 1 & 0 & 0 \\ 0 & \cos \Phi & \sin \Phi \\ 0 & -\sin \Phi & \cos \Phi \end{bmatrix} \begin{bmatrix} \cos \Theta & 0 & -\sin \Theta \\ 0 & 1 & 0 \\ \sin \Theta & 0 & \cos \Theta \end{bmatrix} \begin{bmatrix} \cos \Psi & \sin \Psi & 0 \\ -\sin \Psi & \cos \Psi & 0 \\ 0 & 0 & 1 \end{bmatrix} \quad (4.1)$$

$$\mathbf{\Lambda}_\Omega = \begin{bmatrix} 1 & 0 & -\sin \Theta \\ 0 & \cos \Phi & \sin \Phi \cos \Theta \\ 0 & -\sin \Phi & \cos \Phi \cos \Theta \end{bmatrix}$$

Dynamic equations of motion are derived from Newton's second law of motion in $Oxyz$ and kinematic relationships, which leads to

$$m(\dot{\mathbf{V}}_O + \mathbf{\Omega} \times \mathbf{V}_O) = \mathbf{F} \quad \mathbf{I}\dot{\mathbf{\Omega}} + \mathbf{\Omega} \times (\mathbf{I}\mathbf{\Omega}) = \mathbf{M}_O \quad \dot{\mathbf{\Phi}} = \mathbf{\Lambda}_\Omega^{-1}\mathbf{\Omega} \quad (4.2)$$

where $\mathbf{V}_O = [U \ V \ W]^T$ is the velocity of the origin, $\mathbf{\Omega} = [P \ Q \ R]^T$ is the angular velocity, $\mathbf{\Phi} = [\Phi \ \Theta \ \Psi]^T$ describes the aircraft orientation, m stands for mass, \mathbf{I} for inertia matrix, $\mathbf{F} = [X \ Y \ Z]^T$ and $\mathbf{M}_O = [L \ M \ N]^T$ are forces and moments acting on the object. The dot symbol is used to denote derivatives with respect to time.

When the level flight is the equilibrium state, it is possible to linearize the equations of motion and describe the system as follows

$$\begin{aligned} \dot{u} &= X_u u + X_\alpha \alpha + (X_q - u_0 \alpha_0) q + g \theta \cos \Theta_0 + X_{\delta_E} \delta_E \\ \dot{\beta} &= Y_\beta \beta + (Y_p + \alpha_0) p + (Y_r - 1) r + \frac{g}{|\mathbf{V}_0|} \cos \Theta_0 + Y_{\delta_A} \delta_A + Y_{\delta_R} \delta_R \\ \dot{\alpha} &= Z_u u + Z_\alpha \alpha + (Z_q + 1) q - \frac{g}{U_0} \sin \Theta_0 + Z_{\delta_E} \delta_E \\ \dot{p} &= L_\beta \beta + L_p p + L_r r + L_{\delta_A} \delta_A + L_{\delta_R} \delta_R \\ \dot{q} &= M_u u + M_\alpha \alpha + M_q q + M_{\delta_E} \delta_E \\ \dot{r} &= N_\beta \beta + N_p p + N_r r + N_{\delta_A} \delta_A + N_{\delta_R} \delta_R \\ \dot{\phi} &= p + r \tan \Theta_0 \\ \dot{\theta} &= q \end{aligned} \quad (4.3)$$

where small letters are used to describe the perturbations of the flight state from the trim condition which is denoted by subscript 0 (e.g. $U = u_0 + u$). Symbol g is used for gravitational

acceleration, α is the angle of attack, β is the angle of sideslip and δ_A , δ_E , δ_R are ailerons, elevator and rudder deflections respectively. The signs of flight control deflections are defined with accordance to Hopkin (1970) – a positive flight surface deflection causes a negative aircraft response. This means that: left aileron up, elevator down and rudder to left are considered as positive. The symbols that are not defined yet are known as dimensional stability and control derivatives, e.g. M_α is the pitching moment derivative with respect to the angle of attack.

5. D-optimal multisine inputs

Application of the D-optimality criterion for phase angles selection in multisine inputs design requires minimization of the Fisher Information Matrix inverse determinant (cost function)

$$\delta = \min_{\phi} \mathcal{F}^{-1} \quad (5.1)$$

The cost function has multiple local minima, therefore a genetic algorithm is selected for finding the optimal solution. The phase angles related with j -th flight surface and k -th harmonic $\phi_{j,k}$ are coded in a binary string that consists of fixed-length strings s . Base-2 floating point representation is used to determine phase angles for different aileron, elevator and rudder deflections

$$\phi_{j,k} = 2\pi \sum_s b_s 2^{-s} \quad (5.2)$$

where $s = 1, \dots, 12$ is a part of the string that contains bit values $b_s \in \{0, 1\}$ used for coding a specific phase angle $\phi_{j,k}$.

Genetic algorithms mimics the process of natural selection and require multiple executions of four steps that are: population generation, selection mating, exchange of the information and mutation (Mitchel, 1999).

The initial population contains P possible solutions that are randomly drawn. The solutions are decoded into input signals and sorted in descending order in accordance with the cost function. Then different selection probability is assigned for each solution. The binary string that represents simultaneous excitations and produces the highest cost function has the smallest drawing probability $p_{min} = 1/\sum_{i=1}^P i$. The binary string that represents excitations with the smallest cost function has the highest drawing probability $p_{max} = P/\sum_{i=1}^P i$. The probabilities are assigned with the linear scale. In the next step, solutions are drawn in accordance to their probabilities and combined in pairs.

Exchanging information between the solutions in each mated pair (parents) is done by applying uniform crossover which results in creating two new solutions (offspring). Applying uniform crossover requires drawing a mask of flags which has the same length as coded solutions and is filled with zeros and ones. The first offspring is formed from fields of the first parent when the flag of the mask is 0 and from fields of the second parent when the flag of the mask is 1. The second offspring is created in a similar way – from fields of the first parent when the flag of the mask is 1 and from fields of the second parent when the flag of the mask is 0. The uniform crossover idea is shown in Fig. 2. Fields of the first parent have white background and of the second parent – gray. The described procedure is carried for all mated pairs and results in creating a set of new solutions whose size is equal to the initial population.

To introduce more diversity in the newly created population, a mutation operator is used. This action requires drawing a number for each field of each solution. When this number is higher than the threshold (0.95), the value of the field is changed from 0 to 1 or from 1 to 0. After performing mutation for all solutions, the initial population is replaced by the new one. In order to preserve the best simultaneous inputs, the parent that has the lowest cost function is also included in this population.

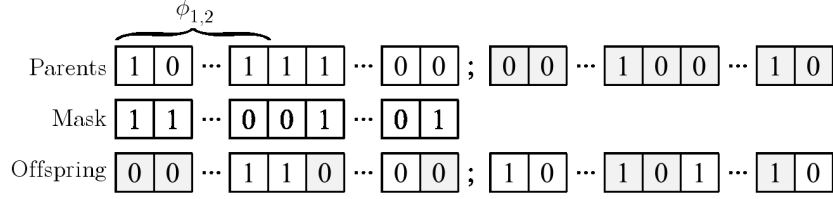


Fig. 2. Uniform crossover

The described steps: selection, crossing, mutation and population generation are performed until the global maximum is found.

6. Nonlinear model

Multisine input signals designed with and without *a priori* knowledge of stability and control derivatives are used as excitations of the nonlinear aircraft model (Lichota and Ohme, 2014; Raab, 2006). The dynamic equations of motion of the object are given by (4.2). The forces and moments that act on the aircraft consist of aerodynamic, gravitational and propulsion terms

$$\mathbf{F} = \mathbf{F}_a + \mathbf{F}_g + \mathbf{F}_t \quad \mathbf{M}_O = \mathbf{M}_a + \sum_{i=1}^4 \mathbf{r}_i \times \mathbf{F}_t \quad (6.1)$$

where \mathbf{r} is the thrust force arm and the indices a , g and t indices denote aerodynamic, gravitational and propulsion forces and moments.

The aerodynamic forces $\mathbf{F}_a = [X_a \ Y_a \ Z_a]$ and moments $\mathbf{M}_{aO} = [L_a \ M_a \ N_a]$ are obtained with the use of dimensionless force and moment coefficients (about quarter-chord point)

$$\begin{aligned} C_D &= C_{D0} + kC_L^2 \\ C_Y &= C_{Y0} + C_{Y\beta}\beta + (C_{Yp} + C_{Yp\alpha}\alpha)p^* + (C_{Yr} + C_{Yr\alpha}\alpha)r^* + C_{Y\delta_R}\delta_R \\ C_L &= C_{L0} + C_{LWB}\alpha + \frac{S_H}{S}(C_{LH\alpha_H}\alpha_H + C_{LH\delta_E}\delta_E) \\ C_{l_{25}} &= C_{l0} + C_{l\beta}\beta + (C_{lp} + C_{lp\alpha}\alpha)p^* + (C_{lr} + C_{lr\alpha}\alpha)r^* + C_{l\delta_A}\delta_A + C_{l\delta_R}\delta_R \\ C_{m_{25}} &= C_{m0} + C_{mWB}q^* - \frac{x_{LH}}{\bar{c}} \frac{S_H}{S}(C_{LH\alpha_H}\alpha_H + C_{LH\delta_E}\delta_E) \\ C_{n_{25}} &= C_{n0} + C_{n\beta}\beta + (C_{np} + C_{np\alpha}\alpha)p^* + (C_{nr} + C_{nr\alpha}\alpha)r^* + C_{n\delta_A}\delta_A + C_{n\delta_R}\delta_R \end{aligned} \quad (6.2)$$

where $p^* = pb/(2V_O)$, $q^* = q\bar{c}/(V_O)$ and $r^* = rb/(2V_O)$ are normalised angular rates, S is the wing area, S_H the horizontal tail area, x_{LH} is the horizontal tail arm and k is the drag polar coefficient. The indices WB and H in the equations for the lift force and pitching moment coefficients denote Wing-Body and Horizontal tail, respectively.

The angle of attack at the horizontal tail is given by

$$\alpha_H = \alpha - \frac{\partial \varepsilon}{\partial \alpha} \alpha \left(t - \frac{x_{LH}}{V_O} \right) + i_H + \alpha_{dyn} \quad (6.3)$$

where ε is the downwash angle, i_H is the horizontal tail setting angle and $\alpha_{dyn} = qx_{LH}/V_O$ is the dynamic angle of attack.

The force and moment coefficients are defined in the aerodynamic coordinate system $Ox_e y_e z_e$. The Ox_e axis has the direction of the flow, the Oy_e axis is directed towards the right wing and

the Oz_e axis is directed upwards. As the equations of motion are derived in the body fixed coordinate system $Oxyz$, the following transformation is required

$$\begin{aligned} C_x &= -C_D \cos \alpha + C_L \sin \alpha & C_y &= C_Y & C_z &= -C_D \sin \alpha - C_L \cos \alpha \\ C_l &= C_{l25} \cos \alpha - C_{n25} \sin \alpha & C_m &= C_{m25} & C_n &= C_{l25} \sin \alpha + C_{n25} \cos \alpha \end{aligned} \quad (6.4)$$

This allows one to obtain components of the aerodynamic forces and moments as

$$\begin{aligned} X_a &= C_x \bar{q} S & Y_a &= C_y \bar{q} S & Z_a &= C_z \bar{q} S \\ L_a &= C_l \bar{q} S b & M_a &= C_m \bar{q} S \bar{c} & N_a &= C_n \bar{q} S b \end{aligned} \quad (6.5)$$

The thrust force is a function of the throttle position, altitude and speed: $\mathbf{T}(\delta_{th}, h, V_O)$. It is stored in a 3D array and interpolated for specific flight conditions. The gravitational force $\mathbf{F}_g = m\mathbf{g}$ is defined in the $Ox_g y_g z_g$ coordinate system, therefore transformation to $Oxyz$ is required.

7. System Identification

The classical and most widely used definition of System Identification was given by Zadeh: “*Identification is the determination, on the basis on input and output, of a system within a specified class of systems, to which the system under test is equivalent*” (Zadeh, 1962). If the response of the dynamical system and input signals are recorded and the structure of the model is known then the Sys-ID is equal to adjusting the model parameters Θ so that the model outputs \mathbf{y} match the measured aircraft response \mathbf{z} when the inputs \mathbf{u} are the same. The process can be done either offline or online in real time (Hendzel and Trojnacki, 2014).

The structure of the model we used in the Sys-ID was nonlinear and the same as for generating the aircraft response what allowed us to eliminate modelling errors in the study. The adjusting of model parameters was done in the time domain when all data was collected (offline). To find the set of unknown model parameters we used the Output Error Method whose aim was to minimize the error between measured system outputs and estimated response.

When the Maximum Likelihood Estimation principle is selected for error minimization the task is equivalent to finding the parameters vector that maximize the conditional probability $p(\mathbf{z}|\Theta)$

$$\hat{\Theta} = \arg \max_{\Theta} p(\mathbf{z}|\Theta) \quad (7.1)$$

where the hat symbol denotes the estimates, and the conditional probability $p(\mathbf{z}|\Theta)$ is given by (3.5).

As it is frequently done, we replace the probability maximization task by an easier action – minimization of a negative log likelihood function (Jategaonkar, 2006)

$$\mathcal{L}(\Theta|\mathbf{z}) = \frac{1}{2} \sum_{k=1}^N [\mathbf{z}(t_k) - \mathbf{y}(t_k)]^T \mathbf{R}^{-1} [\mathbf{z}(t_k) - \mathbf{y}(t_k)] + \frac{nN}{2} \ln(2\pi) + \frac{N}{2} \ln(\det(\mathbf{R})) \quad (7.2)$$

The unknown measurement covariance matrix \mathbf{R} is estimated as

$$\hat{\mathbf{R}} = \frac{1}{N} \sum_{k=1}^N [\mathbf{z}(t_k) - \mathbf{y}(t_k)][\mathbf{z}(t_k) - \mathbf{y}(t_k)]^T \quad (7.3)$$

Substitution of the measurement covariance matrix estimate $\hat{\mathbf{R}}$ into the negative log likelihood function and rejection of the constant terms allows one to obtain the cost function

$$J(\Theta) = \det(\mathbf{R}) \quad (7.4)$$

The Gauss-Newton algorithm has been used for cost function minimization.

The accuracy of each estimated parameter is determined on the basis of the Parameter Error Covariance Matrix \mathcal{P}

$$\sigma(\Theta_i) = \sqrt{\mathcal{P}_{i,i}} \quad (7.5)$$

where σ is the standard deviation and $\mathcal{P}_{i,i}$ is the element of the Parameter Error Covariance Matrix $\mathcal{P} = \mathcal{F}^{-1}$.

8. Results

In the study, we investigate two designs with simultaneous multisine inputs: when there is no *a priori* knowledge of the system dynamics and when this information is available. The frequency range of interest upper bound is set to $f_{max} = 2$ Hz and the lower is determined on the basis of the excitation length $T = 20$ s. A total of 39 harmonics is evaluated and assigned to the elevator (f_2, f_5, \dots), aileron (f_3, f_6, \dots) and rudder deflections (f_4, f_7, \dots). The maximum values of all inputs are set to 1 deg. In the multisine design without *a priori* knowledge, the phase angles ϕ_k are optimized through Relative Peak Factor minimization. When additional information about the system is available, the D-optimality criterion is used for signal optimization. In this case, the cost function extreme is found by a genetic algorithm.

Both designed sets of excitations are used as input signals for a nonlinear aircraft model. In both cases, the response of the model is recorded. The gathered data is used to perform a Sys-ID for a model with unknown aerodynamic parameters. The results of the estimation are shown in Fig. 3, Fig. 4 and in Table 1.

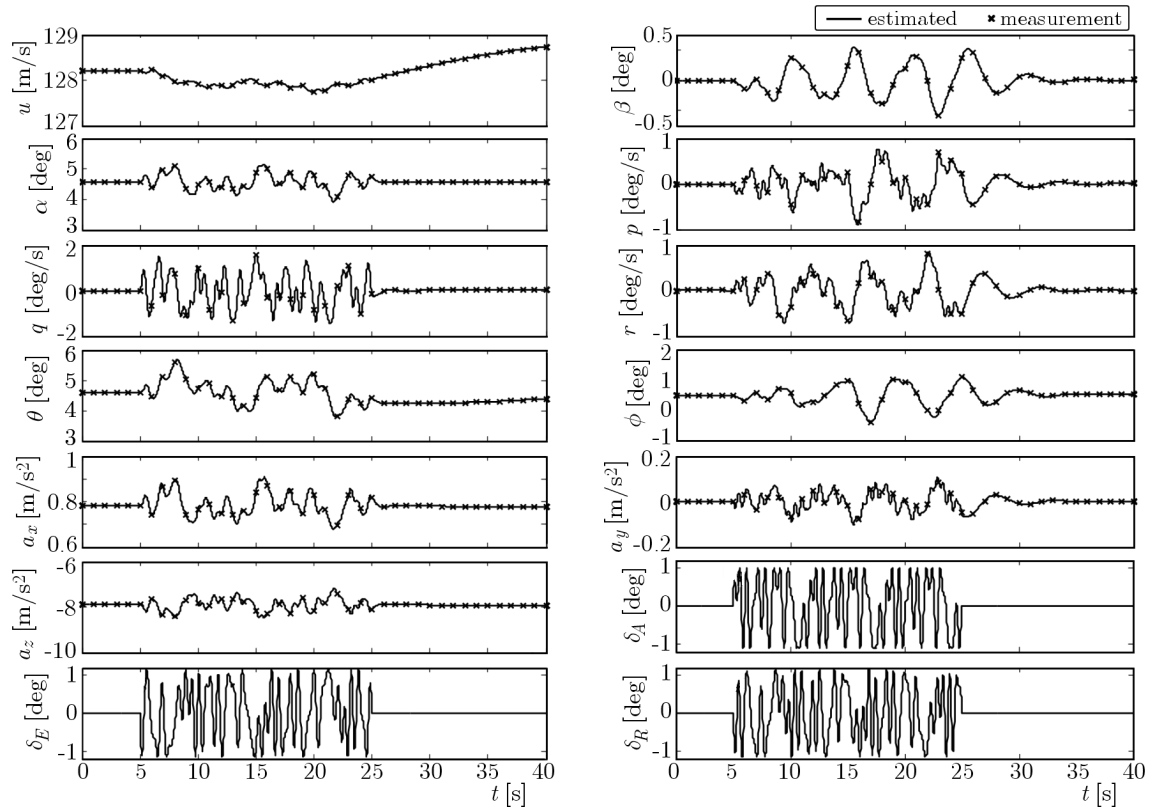


Fig. 3. Measured and estimated signals for multisine inputs

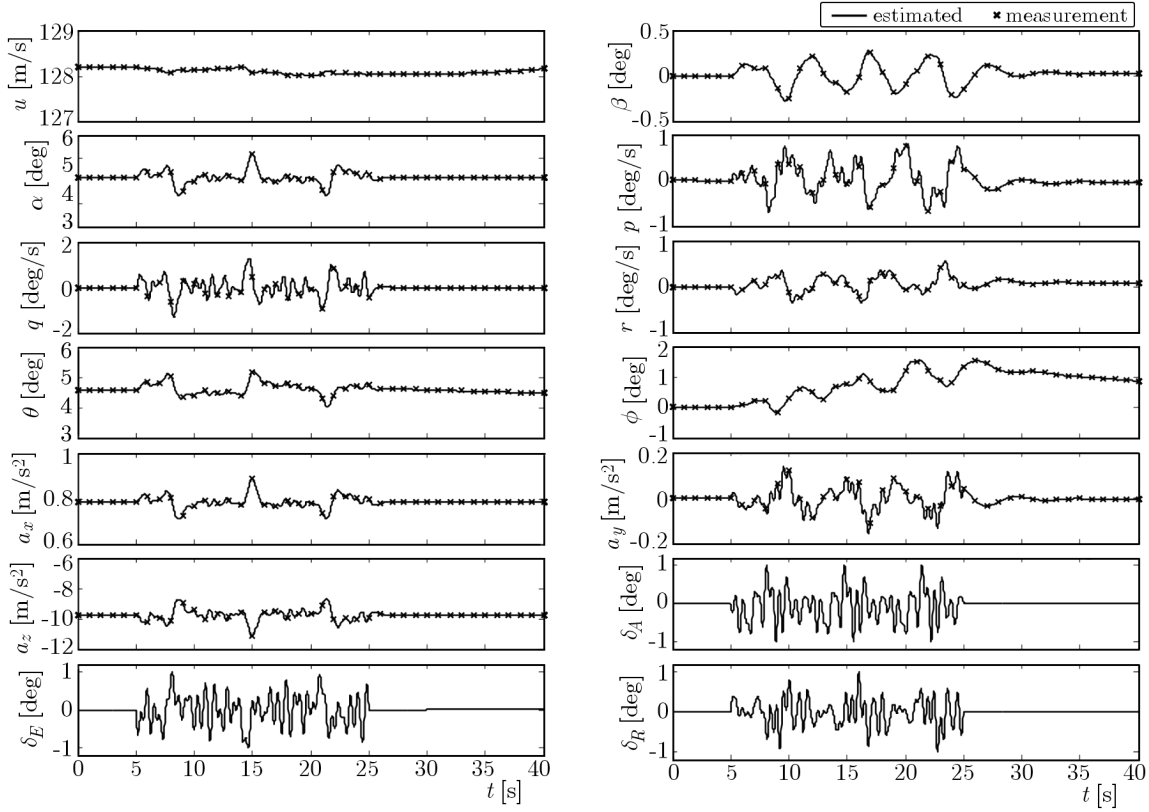


Fig. 4. Measured and estimated signals for the D-optimal multisine inputs

Table 1. Standard deviations

Parameter	Multisine	D-optimal multisine	Parameter	Multisine	D-optimal multisine
k	2.5440E-004	3.5897E-004	C_{l0}	2.2346E-009	7.2915E-010
C_{L0}	3.6488E-005	3.9050E-005	$C_{l\beta}$	2.6671E-006	9.9505E-007
$C_{L_{WB}\alpha}$	2.6817E-004	3.1839E-004	C_{lp}	1.3783E-004	2.1207E-004
$C_{L_H\alpha_H}$	1.1588E-003	1.3114E-003	$C_{lp\alpha}$	1.6153E-003	2.6471E-003
$C_{L_H\delta_E}$	6.8113E-005	8.6226E-005	C_{lr}	2.3736E-004	2.6195E-004
$\partial\varepsilon/\partial\alpha$	1.7339E-004	1.9543E-004	$C_{lr\alpha}$	3.0391E-003	3.2459E-003
C_{D0}	1.0919E-004	1.6787E-004	$C_{l\delta_A}$	1.2369E-006	4.8513E-007
C_{m0}	2.1883E-004	1.8874E-004	$C_{l\delta_R}$	9.6532E-007	4.0260E-007
$C_{m_{WB}q}$	1.0397E-002	1.1892E-002	C_{n0}	2.1906E-009	7.2876E-010
C_{Y0}	2.2318E-008	8.4724E-009	$C_{n\beta}$	2.5441E-006	1.6348E-006
$C_{Y\beta}$	1.3871E-005	5.2384E-006	C_{np}	1.1095E-004	2.1430E-004
C_{Yp}	1.0030E-003	1.6169E-003	$C_{np\alpha}$	1.3218E-003	2.6642E-003
$C_{Yp\alpha}$	1.2198E-002	2.0359E-002	C_{nr}	1.9973E-004	2.3221E-004
C_{Yr}	1.6164E-003	2.0590E-003	$C_{nr\alpha}$	2.5561E-003	2.8803E-003
$C_{Yr\alpha}$	2.0288E-002	2.5716E-002	$C_{n\delta_A}$	1.5451E-006	8.3159E-007
$C_{Y\delta_R}$	4.8513E-006	2.6505E-006	$C_{n\delta_R}$	1.2249E-006	7.7315E-007

In Figs. 3 and 4, solid lines are used to denote the estimated aircraft response and the input signals. The cross points denote the recorded values of flight parameters. For presenting the measurements, a 10-point data reduction is used. From Figs. 3 and 4 it can be seen that the obtained set of estimates allows one to obtain a good visual match for flight parameters whether

the D-optimality criterion is used or not. However, as more than one set of model parameters can produce a response that visually fits well the data, another quality of estimation indicator should be used – standard deviations.

Table 1 indicates that for both analysed designs the evaluated standard deviations are small (of the order of 1.0E-002 or lower) for all parameters what means that the estimation is successful. The standard deviations obtained for model parameters when the D-optimality is used in the design phase are of the same order as when the criterion is not used in the optimization. Therefore we consider that the inclusion of the D-optimality criterion for phase angles optimization in the simultaneous multisine inputs design does not increase significantly the quality of the Sys-ID manoeuvre. Moreover, as the Parameter Error Covariance Matrix determinant minimization is more computationally demanding than Relative Peak Factor optimization, we found the inclusion of the D-optimality criterion impractical.

Acknowledgments

This work has been supported by the European Union in the framework of European Social Fund through the “Didactic Development Program of the Faculty of Power and Aeronautical Engineering of the Warsaw University of Technology”.

The author would like to thank German Aerospace Center (DLR) for the support and guidance he received during his stay in the Institute of Flight Systems (FT) in Braunschweig.

References

1. ETKIN B., 1972, *Dynamics of Atmospheric Flight*, John Wiley and Sons, New York, USA
2. HENDZEL Z., TROJNACKI M., 2014, Neural network identifier of a four-wheeled mobile robot subject to heel slip, *Journal of Automation, Mobile Robotics & Intelligent Systems*, **8**, 4, 24-30
3. HOE G., OWENSAND D.B., DENHAM C., 2012, Forced oscillation wind tunnel testing for FASER flight research aircraft, *AIAA Atmospheric Flight Mechanics Conference*, Minneapolis, USA, AIAA 2012-4645
4. HOPKIN H.R., 1970, *A Scheme of Notation and Nomenclature for Aircraft Dynamics and Associated Aerodynamics*, Aeronautical Research Council, Report 3562
5. JAMESON P., COOKE A., 2012, Developing real-time system identification for UAVs, *UKACC International Conference on Control 2012*, Cardiff, UK, 958-963
6. JATEGAONKAR R.V., 2006, *Flight Vehicle System Identification: A Time Domain Methodology*, AIAA, Reston, USA
7. KAY S.M., 1993, *Fundamentals of Statistical Signal Process – Estimation Theory*, Prentice Hall, Upper Saddle River
8. LICHOTA P., OHME P., 2014, *Design and Analysis of new Multi Axis Input Manoeuvres for Aircraft Sys-ID*, Deutsches Zentrum für Luft- und Raumfahrt (DLR), Report DLR-IB 111-2014/46
9. MADER C.A., MARTINS J.R.R.A., 2011, Computation of aircraft stability derivatives using an automatic differentiation adjoint approach, *AIAA Journal*, **49**, 12, 2737-2750
10. MITCHEL M., 1999, *An Introduction to Genetic Algorithms*, MIT Press, Cambridge, USA
11. MORELLI E.A., 2003, Multiple input design for real-time parameter estimation in the frequency domain, *13th IFAC Symposium on System Identification*, Rotterdam, Netherlands, REG-360
12. MORELLI E.A., 2012, Efficient global aerodynamic modeling from flight data, *50th AIAA Aerospace Sciences Meeting*, Nashville, USA, AIAA-2012-1050
13. RAAB C., 2006, *A Versatile and Modular Architecture for Aircraft System Simulation and Test*, Deutsches Zentrum für Luft- und Raumfahrt (DLR), Report DLR-IB 111-2006/22

14. ROGOWSKI K., MAROŃSKI R., 2015, CFD computation of the Savonius rotor, *Journal of Theoretical and Applied Mechanics*, **53**, 1, 37-45
15. SCHROEDER M., 1970, Synthesis of low-peak-factor signals and binary sequences with low auto-correlation, *IEEE Transactions on Information Theory*, **16**, 1, 85-89
16. ZADEH L.A., 1962, From circuit theory to control theory, *Proceeding of the IRE*, **50**, 5, 856-865

Manuscript received February 25, 2015; accepted for print July 8, 2015

SPATIAL MOTION OF THE AIRCRAFT MANOEUVRING TO AVOID MOVING OBSTACLE

JERZY GRAFFSTEIN

Institute of Aviation, Centre of Space Technologies Department, Warsaw, Poland

e-mail: jgraff@ilot.edu.pl

In the paper, mathematical relationships which are used to describe kinematic variables of the aircraft-obstacles configuration and motion of the aircraft are presented. These define the base for the set of conditions enabling determination of the possibility and threat of collision. The second important aim of such a definition is creation of prerequisites for selection of an appropriate anti-collision manoeuvre, computation of reference signals and inequalities used as limitations on these signals in the automatic flight control process. Theoretical analysis is illustrated by an example of computer simulation of the flight of aircraft. Two anti-collision manoeuvres are studied in this experiment. The first one, performed in a vertical plane, consists in emergency climbing. The second one, performed in the horizontal plane, is shaped by three turns, each one of small radius, to go around the obstacle and then return to the previously realised flight path.

Keywords: anti-collision manoeuvre, obstacle avoidance, flight simulation

1. Introduction

Recently, one can notice the growing number of methods presented in accessible scientific materials aimed at solving the collision avoidance problem with several types of obstacles. This results from growing requirements for flight safety of piloted and unmanned flying objects. The proposed solutions and mathematical methods focused on the problem differ one from another due to geometrical representations of obstacles (Graffstein, 2012a; Park *et al.*, 2012), types of moving objects, types of obstacles, methods of getting information about obstacles (Ariyur *et al.*, 2005; Higuchi *et al.*, 2012), etc.

A safe preselected anti-collision manoeuvre is the most typical solution of the considered problem. Safety of such motion consists, among others, in keeping the minimum distance between any point of the object and any point of the obstacle above the assumed level, defined as the safety margin r_{CMB} . This value depends on a number of factors, some of them were described by Blajer and Graffstein (2012), Graffstein (2006, 2012b). The capability of avoiding the collision with previously unknown obstacles safely depends on many factors including, first of all manoeuvring capabilities of the flying object, configuration and dimension of obstacles, parameters of its motion, object-to-obstacle distance at the moment of obstacle detection and accuracy of accessible data characterising the obstacle.

The object-to-obstacle distance at the moment of obstacle detection is determined by technical means used in the obstacle detector, first of all by the type of sensor (Fasano *et al.*, 2010; Freeman and Moosbruggerb, 2010; Higuchi *et al.*, 2012). The knowledge of this distance and parameters of the object and obstacle motion enables determination of the most convenient anti-collision manoeuvre and its parameters (Becker *et al.*, 2006; Graffstein, 2012a; Schøler *et al.*, 2009). In the case of danger of collision with a moving obstacle, the situation appears to be more complex, because of possible and crucial variety of the obstacle motion. Four possible

scenarios of such a situation exist: continuation of the flight without any changes to motion parameters and the following three types of manoeuvres: a random one or according with rules and agreed with the pilot. This last scenario can be a solution in the case of collision threat with many moving obstacles (Carbone *et al.*, 2006; Lalish *et al.*, 2009; Seo *et al.*, 2012). Another scenario is assumed for an obstacle continuing its motion without any changes and reactions to the collision threat. In such a case, computation of necessary kinematic variables, described in further parts of the work, is obligatory as well as verification of collision threat conditions and choice of the appropriate manoeuvre. These operations are within the scope of tasks defined for anti-collision systems, which is described in the next Section. Presented results of computer flight simulation illustrate a practical solution of the described problem. In the numerical experiments, two different types of anti-collision manoeuvres have been simulated, both effective in avoiding collision with moving obstacle.

2. Structure of the anti-collision system

Preparation and execution of a manoeuvre to avoid a moving obstacle is a complex operation that constitutes considerable workload for the aircraft pilot. Thus, the structure of an anti-collision system is proposed, aiming at reduction of the workload of the pilot performing such tasks. The diagram (Fig. 1) presents the general idea of sub-system cooperation. The system is autonomous and makes use of two sources of data of obstacles: the detector of obstacles and the data base containing data of obstacles. The first source detects moving and fixed obstacles, delivers estimates of the object-to-obstacle distance and relative velocity. The data base contains information about fixed obstacles in the terrain covering the planned flight path and also about height of the terrain. This source of data plays a supplementary role in the system designed to avoid moving obstacles. During the process of searching for the appropriate anti-collision manoeuvre, the data base makes the system capable of eliminating manoeuvre candidates which make the risk of collision with one of the existing fixed obstacles and being too high.

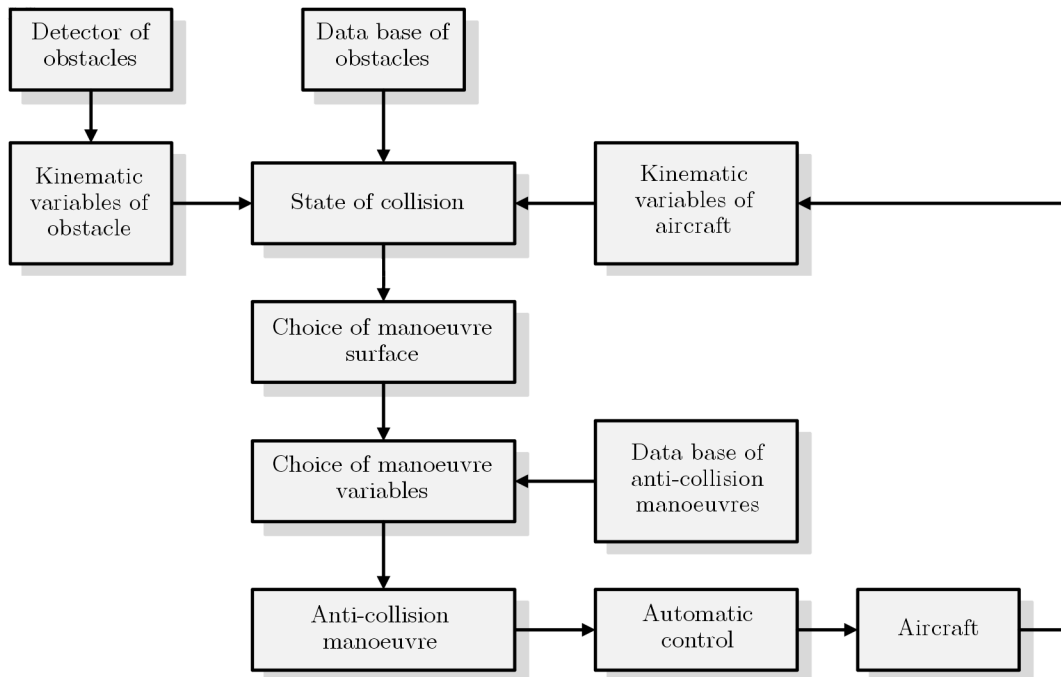


Fig. 1. Schematic diagram illustrating operation of the anti-collision system

In every time step, when new data of the obstacles are acquired, the process of new obstacles detection is executed as well as the estimation of risk of collision in one or both planes. If the threat is detected, the procedure of searching for possible and safe anti-collision manoeuvre is executed. Searching for parameters fulfilling the appropriate criteria is performed within the base of anti-collision manoeuvres prepared in advance. In the case when more than one manoeuvre is found (for example: performed within both planes), selection of one of them is necessary. Safety is the basic criterion for the final decision, so is the magnitude of safety margin, among others. On the other side, important conditions require minimisation of two values: the distance from the previously planned flight path and the time interval defined as becoming when the aircraft abandons this flight path and ends when returns. In addition, flight conditions have to be taken into account: the magnitude and type of disturbances, e.g. wind direction and speed, altitude, height of the obstacle, etc. The selected manoeuvre is executed by an automatic control system.

3. Variables describing motion of the aircraft and obstacles in airspace

The aircraft and the obstacle detected by the on-board sensing sub-system create the spatial aircraft-obstacle configuration (Becker *et al.*, 2006; Blajer and Graffstein, 2012; Graffstein, 2012b) similar to UAV-target (Koruba and Chatys, 2005) and Missile-target (Ładyżyńska-Kozdraś, 2009). Mutual relations in this configuration are described by physical quantities illustrated in Figs. 2 and 3. These quantities apply also to each moving object separately: the aircraft with geometric centre in the point O_S and the obstacle with geometric centre in the point O_P . Kinematic variables for the considered objects are described by mathematical relationships defined in the body axes reference system fixed to the aircraft and within the reference system fixed to the Earth. Further, the position of the aircraft towards the obstacle is considered separately (Carbone *et al.*, 2006; Smith and Harmon, 2009): in the horizontal plane, see Figs. 2 and 4 and in vertical plane, see Figs. 3 and 5.

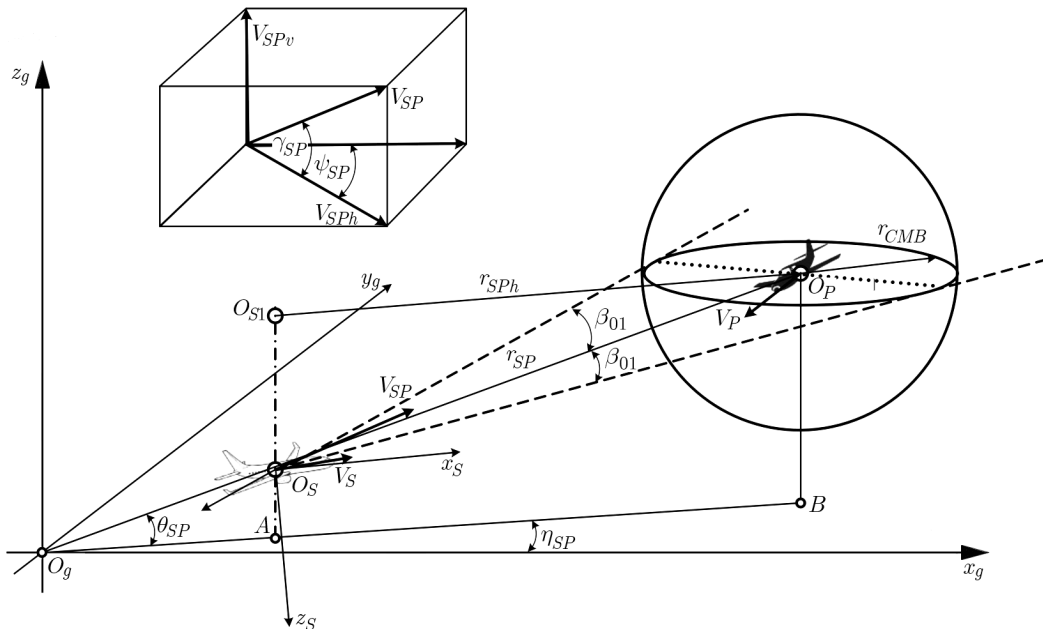


Fig. 2. The aircraft-obstacle spatial arrangement including elements contained in the horizontal plane

The linear position of the obstacle, determined in relation to the aircraft, is the important information for presented considerations. This position is described by the vector \mathbf{r}_{SP} which is computed with accordance to the relationship

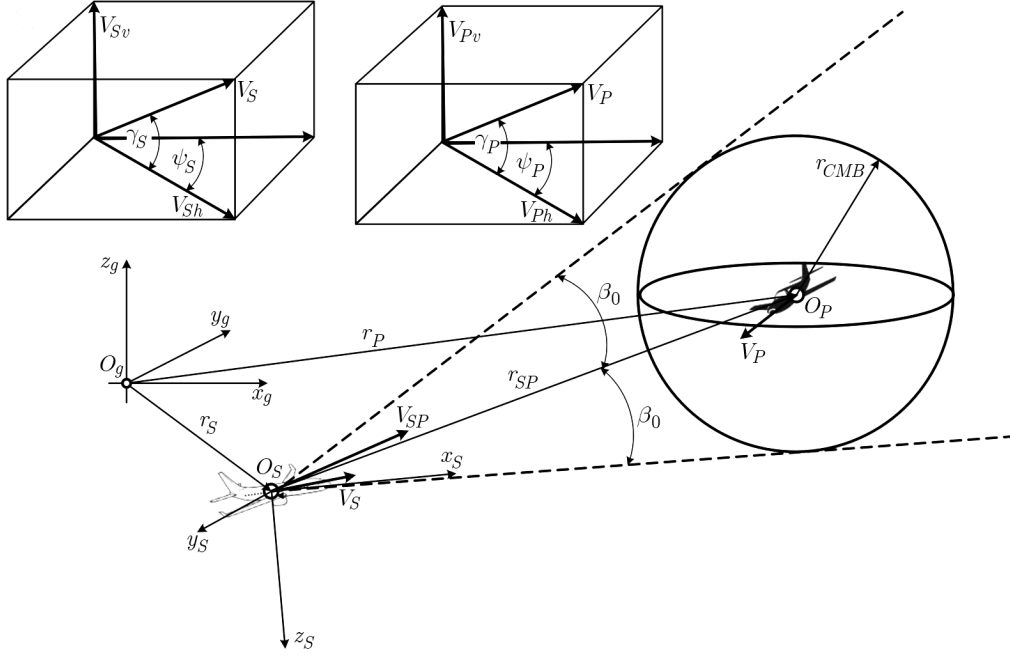


Fig. 3. The aircraft-obstacle spatial arrangement including elements contained in the vertical plane

$$\mathbf{r}_{SP} = \mathbf{r}_P - \mathbf{r}_S \quad \mathbf{r}_{SP} = |\mathbf{r}_{SP}| \mathbf{\Lambda}_r \quad (3.1)$$

where the matrix of transformation takes the form

$$\mathbf{\Lambda}_r = \begin{bmatrix} \cos \gamma_{SP} \cos \psi_{SP} & \cos \gamma_{SP} \sin \psi_{SP} & -\sin \gamma_{SP} \end{bmatrix}^T \quad (3.2)$$

The position of the aircraft and the obstacle in the Earth reference system are

$$\mathbf{r}_S = \begin{bmatrix} x_{1S} & y_{1S} & z_{1S} \end{bmatrix}^T \quad \mathbf{r}_P = \begin{bmatrix} x_{1P} & y_{1P} & z_{1P} \end{bmatrix}^T \quad (3.3)$$

The aircraft-to-obstacle distance is computed according to the relationship

$$|\mathbf{r}_{SP}| = \sqrt{(x_{1P} - x_{1S})^2 + (y_{1P} - y_{1S})^2 + (z_{1P} - z_{1S})^2} = \frac{r_{CMB}}{\sin \beta_0} \quad (3.4)$$

The components of linear velocity of the aircraft and velocity of the obstacle in the Earth reference systems and in body axes are

$$\mathbf{V}_i = \begin{bmatrix} \dot{x}_{1i} & \dot{y}_{1i} & \dot{z}_{1i} \end{bmatrix}^T = \mathbf{\Lambda}_V^{-1} \begin{bmatrix} U_i & V_i & W_i \end{bmatrix}^T \quad (3.5)$$

where $i = S$ for the aircraft or $i = P$ for the obstacle.

The matrix of transformation for the aircraft and the obstacle is

$$\mathbf{\Lambda}_{V_i} = \begin{bmatrix} \cos \Psi_i \cos \Theta_i & \sin \Psi_i \cos \Theta_i & -\sin \Theta_i \\ \sin \Phi_i \cos \Psi_i \sin \Theta_i - \cos \Phi_i \sin \Psi_i & \sin \Phi_i \sin \Psi_i \sin \Theta_i + \cos \Phi_i \cos \Psi_i & \sin \Phi_i \cos \Theta_i \\ \cos \Phi_i \cos \Psi_i \sin \Theta_i + \sin \Phi_i \sin \Psi_i & \cos \Phi_i \sin \Psi_i \sin \Theta_i - \sin \Phi_i \cos \Psi_i & \cos \Phi_i \cos \Theta_i \end{bmatrix} \quad (3.6)$$

The trajectory angles for the aircraft and the obstacle are

$$\gamma_i = \arcsin \frac{\dot{z}_{1i}}{V_i} \quad (3.7)$$

where

$$V_i = \sqrt{\dot{x}_{1i}^2 + \dot{y}_{1i}^2 + \dot{z}_{1i}^2} \quad (3.8)$$

The vector of relative velocity of the obstacle is

$$\mathbf{V}_{SP} = \mathbf{V}_S - \mathbf{V}_P \quad \dot{\mathbf{r}}_{SP} = \dot{\mathbf{r}}_{SP} \quad (3.9)$$

The components of relative velocity are (Choi and Kim, 2013)

$$\mathbf{V}_{SP} = \begin{bmatrix} V_{SPx} \\ V_{SPy} \\ V_{SPz} \end{bmatrix} = \begin{bmatrix} \cos \gamma_{SP} \cos \psi_{SP} & -r_{SP} \cos \gamma_{SP} \sin \psi_{SP} & -r_{SP} \sin \gamma_{SP} \cos \psi_{SP} \\ \cos \gamma_{SP} \sin \psi_{SP} & -r_{SP} \cos \gamma_{SP} \cos \psi_{SP} & -r_{SP} \sin \gamma_{SP} \sin \psi_{SP} \\ -\sin \gamma_{SP} & 0 & -r_{SP} \cos \gamma_{SP} \end{bmatrix} \begin{bmatrix} \dot{r}_{SP} \\ \dot{\gamma}_{SP} \\ \dot{\psi}_{SP} \end{bmatrix} \quad (3.10)$$

The components of angular velocity of the aircraft and angular velocity of the obstacle in the body axes and Earth reference systems are

$$\boldsymbol{\Omega}_i = [P_i \quad Q_i \quad R_i]^T = \mathbf{\Lambda}_{\Omega i} [\dot{\Phi}_i \quad \dot{\Theta}_i \quad \dot{\Psi}_i]^T \quad (3.11)$$

where the matrix of transformation is

$$\mathbf{\Lambda}_{\Omega i} = \begin{bmatrix} 1 & 0 & -\sin \Theta_i \\ 0 & \cos \Phi_i & \sin \Phi_i \cos \Theta_i \\ 0 & -\sin \Phi_i & \cos \Phi_i \cos \Theta_i \end{bmatrix} \quad (3.12)$$

4. Motion of the aircraft and the obstacle in the horizontal plane

The selected horizontal plane (parallel to the surface of the Earth) includes the geometrical centre of the aircraft shifted from the point O_S to the point O_{S1} along the straight line AO_{S1} . The distance r_{SPh} (in Fig. 2) to the obstacle is smaller in comparison with the real value. Physical quantities which appear to be important in the horizontal plane are illustrated in Fig. 4. The knowledge of values presented in this figure makes verification whether the threat of

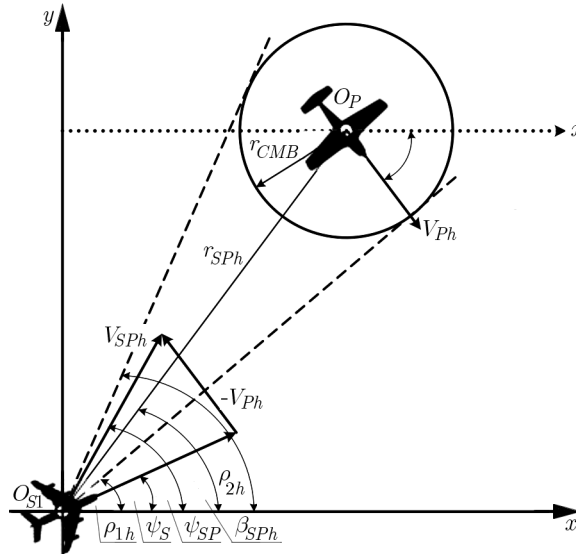


Fig. 4. The aircraft obstacle arrangement in horizontal plane

collision with the obstacle exists in the considered plane possible. This information is the basis of the procedure of searching for the anti-collision manoeuvre (series of appropriate turns). Using trigonometric identities, the angle of the aircraft velocity vector in the horizontal plane can be described by the relationship (Paielli, 2003)

$$\psi_S = \psi_{SP} + \arcsin\left[\frac{V_{Ph}}{V_{Sh}} \sin(\psi_P - \psi_{SP})\right] \quad (4.1)$$

The angle of relative velocity vector takes the form

$$\psi_{SP} = \arctan \frac{V_{Sh} \sin \psi_S - V_{Ph} \sin \psi_P}{V_{Sh} \cos \psi_S - V_{Ph} \cos \psi_P} \quad (4.2)$$

The relative velocity in the horizontal plane is equal to

$$V_{SPh} = \sqrt{V_{Sh}^2 + V_{Ph}^2 - V_{Sh}V_{Ph} \cos(\psi_S - \psi_P)} \quad (4.3)$$

where the velocity of the aircraft and obstacle in the horizontal plane is

$$V_{ih} = \sqrt{\dot{x}_{1i}^2 + \dot{y}_{1i}^2} \quad (4.4)$$

The time derivative of the angle of tangent

$$\dot{\rho}_{2h} = \dot{\beta}_{SPh} + \dot{\beta}_{0h} \quad (4.5)$$

Taking into account relationships (3.4) and (4.5), the derivative of the angle of tangent is determined

$$\dot{\rho}_{2h} = -\frac{V_{SPh} \sin \psi_{SP}}{r_{SPh} \cos \beta_{SPh}} - \frac{\dot{r}_{SPh}}{r_{SPh}} (\tan \beta_{SPh} + \tan \beta_{0h}) \quad (4.6)$$

where

$$\dot{r}_{SPh} = -\frac{r_{CMB}}{\sin \beta_{0h} \tan \beta_{0h}} \dot{\beta}_{0h}$$

and when $\theta_{SP} = \gamma_{SP}$ the equality holds $r_{SPh} = r_{SP} \cos \gamma_{SP}$.

The angle of line of sight in the horizontal plane is

$$\beta_{SPh} = \arctan \frac{y_{1P} - y_{1S}}{x_{1P} - x_{1S}} \quad (4.7)$$

The angles of straight lines tangent to the circle of diameter r_{CMB} and centre in the point O_P and coming through the point O_{SI} included in the horizontal plane are (Benayas *et al.*, 2002)

$$\rho_{1h}, \rho_{2h} = \beta_{SPh} \mp \arcsin \frac{r_{CMB}}{\sqrt{(x_{1P} - x_{1S})^2 + (y_{1P} - y_{1S})^2}} \quad (4.8)$$

The aircraft-to-obstacle distance in the horizontal plane is

$$r_{SPh} = \sqrt{(x_{1P} - x_{1S})^2 + (y_{1P} - y_{1S})^2} = \frac{r_{CMB}}{\sin \beta_{0h}} \quad (4.9)$$

Verification of the reliable condition enabling determination whether collision threat exists appears to be a significant element of safe flight. The case when first two (4.10) or the last one (4.10) of inequalities presented below are fulfilled proves that the threat occurs, so the procedure according to the diagram presented in Fig. 1 ought to be initiated

$$\psi_{SP} > \rho_{1h} \quad \wedge \quad \psi_{SP} < \rho_{2h} \quad \vee \quad r_{SPh} > r_{CMB} \quad (4.10)$$

To avoid the collision in the horizontal plane, it is necessary to perform a turn of radius r_{zs} . During this turning, conditions regarding the derivative of the angle of relative velocity vector have to be fulfilled simultaneously. The first one of them follows from the change of the tangent angle

$$\dot{\psi}_{SP} > \dot{\rho}_{2h} \quad (4.11)$$

The second condition follows from the necessity to reach the desired value of the angle of relative velocity vector before the aircraft enters the dangerous area in which the threat of collision exists

$$\dot{\psi}_{SP} > \frac{1}{t_Z}(\psi_{SP} - \rho_{2h}) \quad (4.12)$$

The desired value of yaw angle is

$$\Psi_{SZ} = \rho_{2h} + \arcsin\left[\frac{V_P}{V_S} \sin(\psi_P - \rho_{2h})\right] \quad (4.13)$$

The desired value of roll angle (Schøler *et al.*, 2009) is

$$\Phi_Z = \arctan \frac{V_S^2 \cos \gamma_S}{gr_{zs}} \quad (4.14)$$

5. Motion of the aircraft and the obstacle in the vertical plane

The spatial configuration of the vertical plane is presented in Fig. 3. Physical values, found to be necessary for considerations within this plane (Thippavong, 2009), are shown in Fig. 5. The presented relationships have form analogous to those discussed in the previous Section, but due to different kind of aircraft motion, serious discrepancies occur in some mathematical formulas. The definition of kinematic variables enables formulation of the second condition for the collision threat. This makes it possible to prepare an anti-collision manoeuvre resulting in a change in the altitude of flight.

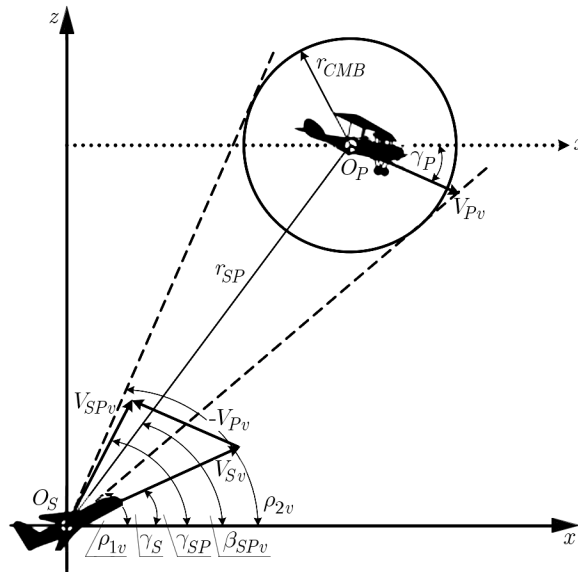


Fig. 5. The aircraft-obstacle arrangement in vertical plane

The angle of the vector of aircraft linear velocity in the vertical plane is described by a relationship analogous to (4.1)

$$\gamma_S = \gamma_{SP} + \arcsin \left[\frac{V_{Pv}}{V_{Sv}} \sin(\gamma_P - \gamma_{SP}) \right] \quad (5.1)$$

The angle of linear relative velocity vector takes the form

$$\gamma_{SP} = \arctan \frac{V_{Sv} \sin \gamma_S - V_{Pv} \sin \gamma_P}{V_{Sv} \cos \gamma_S - V_{Pv} \cos \gamma_P} \quad (5.2)$$

The relative velocity in the vertical plane is

$$V_{SPv} = \sqrt{V_{Sv}^2 + V_{Pv}^2 - V_{Sv}V_{Pv} \cos(\gamma_S - \gamma_P)} \quad (5.3)$$

where the velocity of the aircraft and the obstacle in the vertical plane is

$$V_{iv} = \sqrt{\dot{x}_{1i}^2 + \dot{z}_{1i}^2} \quad (5.4)$$

The time-derivative of the angle of tangential line is

$$\dot{\rho}_{2v} = \dot{\beta}_{SPv} + \dot{\beta}_0 \quad (5.5)$$

Taking into account relationships (3.4) and (5.5), the derivative of the angle of the tangent line is defined by the relationship

$$\dot{\rho}_{2v} = -\frac{V_{SPv} \sin \gamma_{SP}}{r_{SP} \cos \beta_{SPv}} - \frac{\dot{r}_{SP}}{r_{SP}} (\tan \beta_{SPv} + \tan \beta_0) \quad (5.6)$$

where

$$\dot{r}_{SP} = -\frac{r_{CMB}}{\sin \beta_0 \tan \beta_0} \dot{\beta}_0 \quad (5.7)$$

The angle of the line of sight in the vertical plane is

$$\beta_{SPv} = \arctan \frac{z_{1P} - z_{1S}}{x_{1P} - x_{1S}} \quad (5.8)$$

The angles of lines tangential to the circle of diameter r_{CMB} and centre O_P , which are going through the point O_S within the vertical plane (Benayas *et al.*, 2002) are

$$\rho_{1v}, \rho_{2v} = \beta_{SPv} \mp \arcsin \frac{r_{CMB}}{\sqrt{(x_{1P} - x_{1S})^2 + (z_{1P} - z_{1S})^2}} \quad (5.9)$$

Just like in the previous discussion, it is important to verify the condition of collision threat in the vertical plane. The fulfilment of first two (5.10) or the last one (5.10) of inequalities, points out that the collision threat exists, and the procedure illustrated in diagram (Fig. 1) ought to be started

$$\gamma_{SP} > \rho_{1v} \quad \wedge \quad \gamma_{SP} < \rho_{2v} \quad \vee \quad r_{SPv} > r_{CMB} \quad (5.10)$$

It is important to notice that the fulfilment of only one of logical conditions (5.10) proves that the collision threat with the obstacle exists. In the vertical plane, it is possible to avoid the collision by the climb (or descent) manoeuvre with conditions regarding the derivative of the angle of relative velocity vector $\dot{\gamma}_{SP}$ fulfilled. The first condition follows from the change of the angle of the tangent line

$$\dot{\gamma}_{SP} > \dot{\rho}_{2hv} \quad (5.11)$$

The second one follows from the necessity of reaching the desired value of the angle of relative velocity before the aircraft enters the dangerous area, where the threat of collision with the obstacle is considerable

$$\dot{\gamma}_{SP} > \frac{1}{t_Z}(\gamma_{SP} - \rho_{2v}) \quad (5.12)$$

The desired value of the trajectory angle is

$$\gamma_{SZ} = \rho_{2v} + \arcsin \left[\frac{V_P}{V_S} \sin(\gamma_P - \rho_{2v}) \right] \quad (5.13)$$

The desired pitch angle is

$$\Theta_{SZ} = \gamma_{SZ} + \alpha_S \quad (5.14)$$

where the angle of attack is computed by the relationship

$$\alpha_S = \arctan \frac{W_S}{U_S} \quad (5.15)$$

6. Results of computer simulation

The mathematical model of the I23 Manager aircraft dynamics has been used in simulations according to (Maryniak, 1992; Phillips, 2010). This model meets general, typical simplifying assumptions that were mentioned in (Maryniak, 1987).

The system of differential equations describing the aircraft motion is solved numerically within the Matlab package by the *rk4* procedure with a 0.01 s time-step.

The simulated motion of the aircraft contains two manoeuvres performed to avoid moving obstacles: climbing (within the vertical plane) and a series of turns (within the horizontal plane). A number of variables describing this motion are obtained. Appropriate time histories illustrating some selected variables describing the aircraft position, motion and control signals are also presented graphically.

Pre-determined scenarios describing motion of the objects taking part in the numerical experiment have been assumed. The obstacles are moving at constant altitudes: the first one at 160 m, and the second one at 220 m, respectively. Both of them perform steady, constant level motion with constant speeds with respect to the ground: 40 m/s for the first one, 60 m/s for the second one. The first anti-collision manoeuvre consists in climbing from the altitude of 200 m up to the altitude of 250 m. The second one is composed of three turns, each one performed with the same 60° roll angle. In both cases, the speed of the aircraft with respect to the ground is 50 m/s.

The aircraft and obstacle trajectories are chosen to make the considered objects come closer one to another: for the first obstacle – along perpendicular trajectories, for the second one – along trajectories crossing at the angle of 40°. The initial positions and speeds of these objects at the moment when the evasive manoeuvring starts, guaranteed that the aircraft could perform this manoeuvres safely.

To avoid collision with an obstacle for the assumed conditions, it is required either to climb with a considerable value of the trajectory angle or to perform an alternative manoeuvre – a series of turns of appropriately small radius. In order to minimise the time needed to fly by the obstacle and return to the previous leg of trajectory, the aircraft completes the series of turns with the same pre-determined roll angle.

The flight path in the airspace is presented in Fig. 6 with symbolic representations of obstacle positions and projection of the flight path on the horizontal plane. The trajectory of the climb

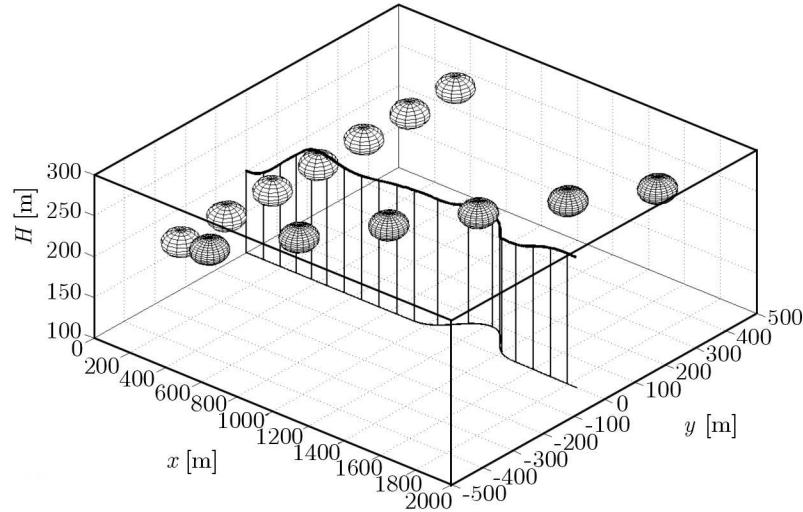


Fig. 6. Trajectories of the aircraft and obstacles in airspace

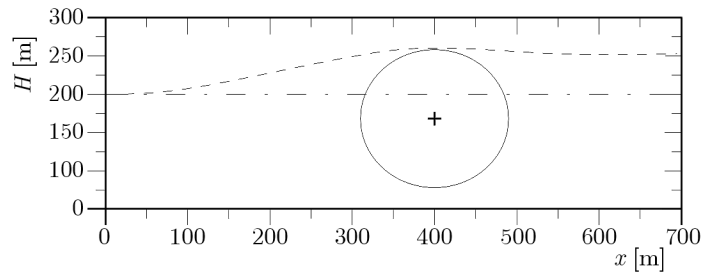


Fig. 7. The segment aircraft trajectory in the vertical plane

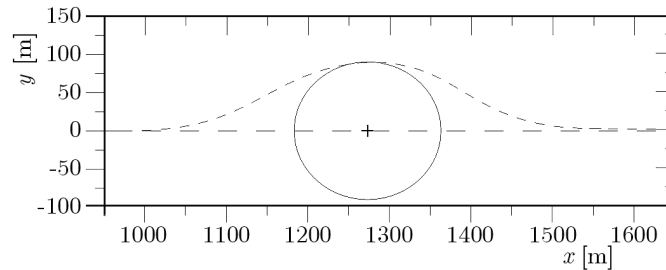


Fig. 8. The segment aircraft trajectory in the horizontal plane

manoeuvre is shown in the vertical plane in Fig. 7. The circle of 90 m radius represents the sum of dimensions of the aircraft, obstacle and pre-defined safety margin.

The minimum distance between the aircraft and contour of the obstacle in the vertical plane is 60 m what corresponds to the pre-defined safety margin. The diagram presented in Fig. 9 illustrates the time histories of pitch angle and pitch rate obtained during simulated climb. Nature of these changes follows from the elevator deflection, which is illustrated in Fig. 9. Extreme values of the elevator deflection are not exceeded.

Three turns (the first one and third to the right and the second one to the left) are necessary to omit the obstacle in the horizontal plane and then to return to the previously realised flight path (Figs. 6 and 8).

The first turn ensures avoidance of collision, the second turn – safe bypassing the obstacle, the third one – returning to the leg of the flight path realised before the anti-collision manoeuvre. The flight trajectory in the horizontal plane during the complex manoeuvre is presented in space in Fig. 6 and in the plane in Fig. 8. The safety margin has the same value: 60 m as in the previous

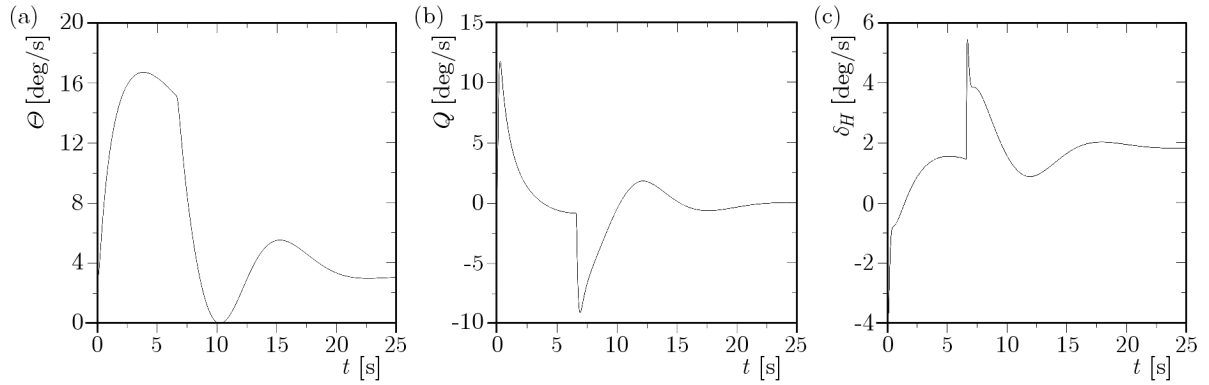


Fig. 9. The time history of pitch angle, pitch rate and the elevator deflection during the manoeuvre in vertical plane

example. The described motion of the aircraft is characterised by presented variations of the angle of the velocity vector and roll rate (Fig. 10). Aileron movements, necessary to complete the discussed complex manoeuvre, are shown in Fig. 11. Extreme values of aileron deflections vary within the range of $+15^\circ$ and -15° . For ailerons, it is the full range of displacement. The maximum rate of the change is equal to $50^{circ}/s$.

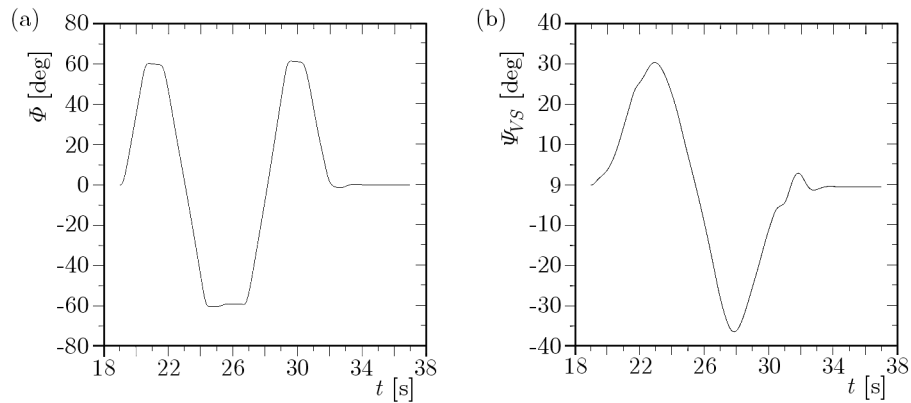


Fig. 10. The time history of roll angle and angle of velocity vector during the manoeuvre in the horizontal plane

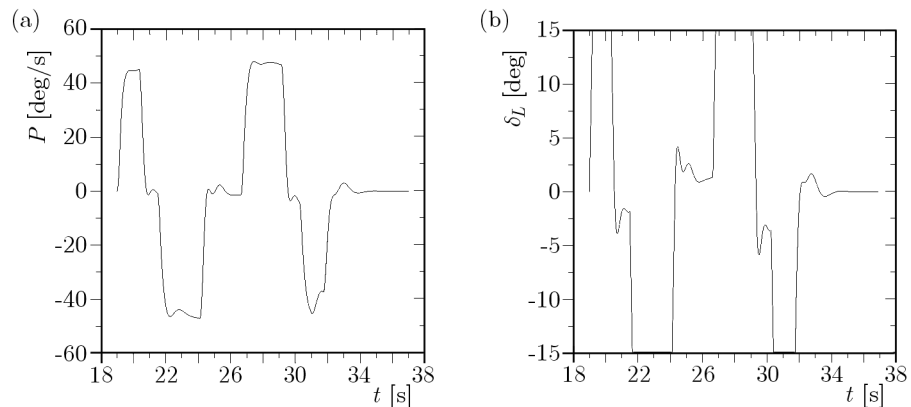


Fig. 11. The time history roll rate and aileron deflections during the manoeuvre in the horizontal plane

7. Concluding remarks

In the paper, two selected scenarios of the threat of collision with a moving obstacle as well as appropriate different manoeuvres as a reaction to this threat have been presented. Discussion has been carried out on the base of the spatial scenario of the flight of the aircraft and motion of the obstacle.

During the simulated flight, two different anti-collision manoeuvres have been performed to bypass moving obstacles. Transients of state variables of the aircraft performing the anti-collision manoeuvre serve as the basis for the assessment of the object behaviour during the examined phases of flight.

Results obtained from these simulations have led to the following conclusions:

- The simulated anti-collision manoeuvres guide the aircraft to the safe state of motion keeping the accepted safety margin.
- The manoeuvre proposed in the vertical plane avoids the collision threat within 8.8 s, whereas the manoeuvre in the horizontal plane – within 6.9 s.
- It should be assumed that the anti-collision manoeuvre performed in the vertical plane has to be started earlier than the manoeuvre performed in the horizontal plane.
- Solution of the collision avoidance problem in the case of moving, manoeuvring obstacle may require introducing of some modifications to the presented method.

Various scenarios of motion of the aircraft and obstacle as well as their relative positions will be analysed in the future. For the assessment of the impact of disturbances typical for wind on the anti-collision manoeuvre, more results of numerical simulations are needed.

References

1. ARIYUR K.B., LOMMEL P., ENNS D.F., 2005, Reactive in flight obstacle avoidance via radar feedback, *American Control Conference*, Portland, 2978-2982
2. BECKER M., DANTAS C., MACEDO W.P., 2006, Obstacle avoidance procedure for mobile robots, *International Congress of Mechanical Engineering*, Ouro Preto, 250-257
3. BENAYAS J.A., FERNÁNDEZ J.L., SANZ R., DIÉGUEZ A.R., 2002, The beam-curvature method: a new approach for improving local real time obstacle avoidance, *The International Federation of Automatic Control*, Barcelona
4. BLAJER W., GRAFFSTEIN J., 2012, Anti-collision manoeuvre in programmed motion theory context (in Polish), [In:] *Mechanika w Lotnictwie, ML-XV 2012*, K. Sibilski (Ed.), PTMTS, Warszawa, 597-613
5. CARBONE C., CINIGLIO U., CORRARO F., LUONGO S., 2006, A novel 3D geometric algorithm for aircraft autonomous collision avoidance, *IEEE Conference on Decision and Control*, San Diego, 1580-1585
6. CHOI H., KIM T.Y., 2013, Reactive collision avoidance of unmanned aerial vehicles using a single vision sensor, *Journal of Guidance, Control, and Dynamics*, **36**, 4, 1234-1240
7. FASANO G., FORLENZA L., ACCARDO D., MOCCIA A., 2010, Integrated obstacle detection system based on radar and optical sensors, *AIAA Infotech and Aerospace Conference*, Atlanta, 1-17
8. FREEMAN P., MOOSBRUGGER P., 2010, A low cost phased array solution for UAV collision avoidance, *AIAA Infotech and Aerospace Conference*, Atlanta, 1-4
9. GRAFFSTEIN J., 2006, Changes in automatically controlled object motion caused by selected perturbations (in Polish), [In:] *Mechanika w Lotnictwie, ML-XII 2006*, J. Maryniak (Ed.), PTMTS, Warszawa, 103-119

10. GRAFFSTEIN J., 2012a, Anti-collision manoeuvre: process and parameters selection (in Polish), *Transaction of the Institute of Aviation*, **224**, 32-45
11. GRAFFSTEIN J., 2012b, Elements of collision threat detection process and automatically controlled emergency manoeuvre (in Polish), *Measurements, Automation, Robotics*, **2**, 383-387
12. HIGUCHI T., TORATANI D., UENO S., 2012, Double tetrahedron hexa-rotorcraft collision avoidance of indoor flying, *International Congress of the Aeronautical Sciences ICAS*, 1-7
13. KORUBA Z., CHATYS R., 2005, Gyroscope-based control and stabilization of unmanned aerial mini-vehicle (mini-UAV), *Aviation*, **9**, 10-16
14. LALISH E., MORGANSEN K.A., TSUKAMAKI T., 2009, Decentralized reactive collision avoidance for multiple unicycle-type vehicles, *American Control Conference*, Seattle, 5055-5061
15. ŁADYŻYŃSKA-KOZDRAŚ E., 2009, The control laws having a form of kinematic relations between deviations in the automatic control of a flying object, *Journal of Theoretical and Applied Mechanics*, **47**, 2, 363-381
16. MARYNIAK J., 1987, The system of airplane flight simulation for homing and air combat (in Polish), *Journal of Theoretical and Applied Mechanics*, **25**, 1/2, 189-214.
17. MARYNIAK J., 1992, General mathematical model of controlled aircraft (in Polish), [In:] *Mechanika w Lotnictwie*, J. Maryniak (Ed.), PTMTS, Warszawa, 575-592
18. PAIELLI R.A., 2003, Modeling maneuver dynamics in air traffic conflict resolution, *Journal of Guidance, Control, and Dynamics*, **26**, 3, 407-415
19. PARK J.-W., KIM J.-H., TAHK M.-J., 2012, UAV collision avoidance via optimal trajectory generation method, *International Congress of the Aeronautical Sciences ICAS*, Brisbane, 1-7
20. PHILLIPS W.F., 2010, *Mechanics of Flight*, John Willey & Sons, Inc.
21. SCHØLER F., LA COUR-HARBO A., BISGAARD M., 2009, Collision Free path generation in 3D with turning and pitch radius constraints for aerial vehicles, *AIAA Guidance, Navigation, and Control Conference*, Chicago, 1-11
22. SEO J., KIM Y., TSOURDOS A., WHITE B.A., 2012, Multiple UAV formation reconfiguration with collision avoidance guidance via differential geometry concept, *International Congress of the Aeronautical Sciences ICAS*, Brisbane, 1-8
23. SMITH A.L., HARMON F.G., 2009, UAS collision avoidance algorithm minimizing impact on route surveillance, *AIAA Guidance, Navigation, and Control Conference*, Chicago, 1-20
24. THIPPHAVONG D., 2009, Analysis of a multi-trajectory conflict detection algorithm, for climbing flights, *AIAA Aviation Technology, Integration, and Operations Conference*, Hilton Head, 1-13

ELASTIC-PLASTIC ANALYSIS OF PRESSURE VESSELS AND ROTATING DISKS MADE OF FUNCTIONALLY GRADED MATERIALS USING THE ISOGEOMETRIC APPROACH

AMIR T. KALALI, BEHROOZ HASSANI, SAIED HADIDI-MOUD

Mechanical Engineering Department, Ferdowsi University of Mashhad, Iran

e-mail: amir.kalali.121@stu-mail.um.ac.ir; b_hassani@um.ac.ir; hadidi@um.ac.ir

An NURBS-based isogeometric analysis for elastic-plastic stress in a cylindrical pressure vessel is presented. The vessel is made of a ceramic/metal functionally graded material, i.e. a particle-reinforced composite. It is assumed that the material plastic deformation follows an isotropic strain-hardening rule based on the von Mises yield criterion. The mechanical properties of the graded material are modelled by the modified rule of mixtures. Selected finite element results are also presented to establish the supporting evidence for validation of the isogeometric analysis. Similar analyses are performed and solutions for spherical pressure vessel and rotating disk made of FGMs are also provided.

Keywords: isogeometric analysis, NURBS, functionally graded material, modified rule of mixtures

1. Introduction

The intensity and variation of stress distributions due to large mismatch in material properties can be substantially reduced if micro-structural transition behaviour, i.e. a graded material model, is used. Advances in material synthesis technologies have spurred the development of functionally graded materials (FGM) with promising applications in aerospace, transportation, energy, cutting tools, electronics, and biomedical engineering (Chakraborty *et al.*, 2003). An FGM comprises a multi-phase material with volume fractions of the constituents varying gradually in a predetermined profile, thus yielding a non-uniform microstructure in the material with continuously graded properties (Jin *et al.*, 2003).

Elastic and elastic-plastic analyses of thick-walled pressure vessels have always attracted a lot of research interest because of their importance in engineering applications. Figueiredo *et al.* (2008) proposed a numerical methodology in order to predict the elastic-plastic stress behaviour of functionally graded cylindrical vessels subjected to internal pressure. It was assumed that the structures undergo small strain and that the material properties of the graded layer were modelled by the modified rule of mixtures approximation. Furthermore, the plastic domain for ductile phases was defined through the von Mises yield criterion. They proposed an iterative method for solving the nonlinear system combining a finite element approximation and an incremental-iterative scheme. Haghpanah Jahromi *et al.* (2009, 2010) extended the Variable Material Property (VMP) method developed by Jahed and Dubey (1997) for materials with varying elastic and plastic properties. In the VMP method, the linear elastic solution to the boundary value problem was used as a basis to generate the inelastic solution. Through iterative analysis, the VMP method was used to obtain the distribution of material parameters which were considered as field variables. The application of the VMP method, generally applied to homogeneous elastic-plastic materials (Jahed and Shirazi, 2001; Jahed *et al.*, 2005, 2006), was extended to materials with varying elastic-plastic properties in order to calculate the residual stresses in an autofrettaged FGM cylindrical vessel.

Although there are several papers on the elastic analysis of FGM spherical pressure vessels in the literature (You *et al.*, 2005; Dai *et al.*, 2006; Chen and Lin, 2008), elastic-plastic stress analysis of FGM spherical pressure vessels is not such a customary study. Sadeghian and Ekhteraei (2011) studied thermal stress field for an FGM spherical pressure vessel made of an elastic-perfectly plastic and a power law material model.

Similar to the FGM cylindrical and spherical vessels, much of the studies on FGM rotating disks has been carried out in elasticity cases (Durodola and Attia, 2000; Bayat *et al.*, 2008). Haghpanah Jahromi *et al.* (2012) applied the VMP method to estimate the elasto-plastic stresses in a rotating disk with varying elastic and plastic properties in the radial direction.

In this paper, isogeometric analysis is proposed for predicting stress components of a strain-hardening cylinder based on the von Mises yield criterion under plane stress conditions. Isogeometric analysis was introduced by Hughes *et al.* (2005) as a generalisation of the standard finite element analysis. In isogeometric analysis, the solution space for dependent variables is represented in terms of the same functions which represent the geometry. The geometric representation is typically smooth, whereas the solution space for the standard finite element analysis is continuous but not smooth. Adoption of the isogeometric concept has shown computational advantages over the standard finite element analysis in terms of accuracy and analysis time in many application areas, including solid and structural mechanics. Most CAD systems use spline basis functions and often Non-Uniform Rational B-Splines (NURBS) of different polynomial orders to represent geometry. Results obtained from finite element analysis using the commercial software ABAQUS (v. 6.10) were used to validate the results from the isogeometric analysis. The analysis was further extended to obtain solutions for FGM spherical vessels and rotating disks.

A brief review of the isogeometric analysis based on NURBS is presented in Section 2. This is followed in Section 3 by describing the details of isogeometric analysis formulation for elastic-plastic cases (functionally graded cylindrical and spherical vessels and rotating disks). In Section 4, we describe material properties of the graded layer modelled by the modified rule of mixtures, whereas in Section 5 the results of elastic-plastic analyses are presented. Finally, in Section 6, key conclusions are pointed out.

2. Fundamentals of NURBS-based isogeometric analysis

2.1. B-splines and NURBS

Non-uniform rational B-splines (NURBS) are a standard tool for describing and modelling curves and surfaces in the computer aided design and computer graphics.

B-splines are piecewise polynomial curves composed of linear combinations of B-spline basis functions. The piecewise definition allows approximation of a large number of control points using lower order polynomials. The coefficients are points in space, referred to as the control points. A knot vector Ξ is a set of non-decreasing real numbers representing coordinates in the parametric space of the curve

$$\Xi = [\xi_1, \xi_2, \xi_3, \dots, \xi_i, \dots, \xi_{n+p+1}] \quad (2.1)$$

where p is the order of the B-spline and n refers to the number of the basis functions (also control points). The interval $[\xi_1, \xi_{n+p+1}]$ is called a patch.

The B-spline basis functions for a given degree p are defined recursively over the parametric domain by the knot vector. The piecewise constants are first defined as

$$N_{i,0}(\xi) = \begin{cases} 1 & \text{if } \xi_i \leq \xi < \xi_{i+1} \\ 0 & \text{otherwise} \end{cases} \quad (2.2)$$

For $p > 0$, the basis functions are defined by the following recursion formula

$$N_{i,p}(\xi) = \frac{\xi - \xi_i}{\xi_{i+p} - \xi_i} N_{i,p-1}(\xi) + \frac{\xi_{i+p+1} - \xi}{\xi_{i+p+1} - \xi_{i+1}} N_{i+1,p-1}(\xi) \quad (2.3)$$

A B-spline surface is constructed by the basis functions in two directions, $N_{i,p}(\xi)$ and $M_{j,q}(\eta)$, and a set of control points P_{ij} , $i = 1, 2, \dots, n$, $j = 1, 2, \dots, m$. Similar to the first parametric direction ξ , $M_{j,q}(\eta)$ is also defined by Eqs. (2.2) and (2.3), but another knot vector $\mathbf{H} = [\eta_1, \eta_2, \eta_3, \dots, \eta_j, \dots, \eta_{m+q+1}]$ constitutes the foundation. Often, the B-spline order is the same in both directions, i.e. $p = q$.

The surface is to be drawn in the two-dimensional space, $P_{ij} \in R^2$. The B-spline surface is then interpolated by

$$S(\xi, \eta) = \sum_{i=1}^n \sum_{j=1}^m N_{i,p}(\xi) M_{j,q}(\eta) P_{ij} \quad (2.4)$$

The B-spline surface is the result of a tensor product. The patch for the surface is now the domain $[\xi_1, \xi_{n+p+1}] \times [\eta_1, \eta_{m+q+1}]$. Identifying the logical coordinates (i, j) of the B-spline surface with the traditional notation of the node A and the Cartesian product of the associated basis functions with the shape function $N_A(\xi, \eta) = N_{i,p}(\xi) M_{j,q}(\eta)$, the familiar finite element notation is recovered, namely

$$S(\xi, \eta) = \sum_{A=1}^{nm} N_A(\xi, \eta) P_A \quad (2.5)$$

B-splines are non-rational functions that form non-rational B-spline curves and surfaces. A rational curve or surface can represent conical sections in an exact manner. Non-uniform rational B-splines (NURBS) are therefore introduced by including weights on the control points. The NURBS basis functions will differ from the B-spline basis functions, but the knot vectors, the tensor product nature, and refinement mechanisms are unchanged.

The NURBS surface is given by

$$S(\xi, \eta) = \frac{1}{w(\xi, \eta)} \sum_{A=1}^{nm} N_A(\xi, \eta) w_A P_A = \sum_{A=1}^{nm} \bar{N}_A(\xi, \eta) P_A \quad (2.6)$$

where

$$w(\xi, \eta) = \sum_{A=1}^{nm} N_A(\xi, \eta) w_A \quad \bar{N}_A(\xi, \eta) = \frac{N_A(\xi, \eta) w_A}{w(\xi, \eta)}$$

2.2. Fundamentals of the isogeometric analysis

The isogeometric analysis was defined by Hughes *et al.* (2005) and means that the analysis model uses the same mathematical description as the geometry model. This notion of using the same basis for geometry and analysis is called the isoparametric concept, and it is quite common in the classical finite element analysis. The fundamental difference between the isogeometric analysis and the finite element analysis is that, in the FEA, the basis chosen for the approximation of the unknown solution fields is used to approximate known geometry whereas the isogeometric analysis turns this idea around and selects a basis capable of exactly representing the known geometry, and uses it as a basis for the fields we wish to approximate (Cottrell *et al.*, 2009).

The main advantages of the isogeometrical method, compared to other numerical methods, can be summarised as below:

- reduction in size of the system of equations,

- flexibility and accuracy in the definition of geometry and its boundaries,
- the possibility of keeping the original model in the whole process without several remeshing in problems with a varying domain of interest,
- considerable ease in implementing adaptively and mesh refinement,
- accuracy in satisfaction of the essential boundary conditions,
- applicability of the method in problems of functionally graded materials (Hassani *et al.*, 2011).

And the main disadvantages of the isogeometric analysis can be mentioned as in the following:

- the control points of geometry commonly are not a part of the physical domain of the problem,
- the relative difficulty of establishing a correspondence between the point in the domain and the solution.

3. Isogeometric analysis formulation for the elastic-plastic case

3.1. Elastic formulation

We use the principle of virtual displacement applied to a plane elastic body

$$0 = \int_V (\sigma_{ij} \delta \varepsilon_{ij} + \rho \ddot{u}_i \delta u_i) dV - \int_V f_i \delta u_i dV - \oint_S t_i \delta u_i ds \quad (3.1)$$

where σ_{ij} is the Cauchy stress, ε_{ij} is strain, ρ is density, \ddot{u}_i is the acceleration component, u_i is the displacement component (i.e. u, v, w), f_i is the body force component, t_i is the traction component (i.e. t_x, t_y, t_z), V is volume and S is surface area corresponding to the volume.

In the cylindrical coordinate system and axisymmetric condition, Eq. (3.1) can be rewritten as follows

$$0 = 2\pi \iint (\sigma_{ij} \delta \varepsilon_{ij} + \rho \ddot{u}_i \delta u_i) r dr dz - 2\pi \iint f_i \delta u_i r dr - \oint_S t_i \delta u_i ds \quad (3.2)$$

By using the NURBS basis functions, the approximated displacement functions can be written as

$$\begin{aligned} r(\xi, \eta) &= \sum_{A=1}^{nm} N_A(\xi, \eta) r_A = [N_1(\xi, \eta), N_2(\xi, \eta), \dots, N_{nm}(\xi, \eta)] \begin{bmatrix} r_1 \\ r_2 \\ \vdots \\ r_{nm} \end{bmatrix} = \mathbf{N} \mathbf{r} \\ z(\xi, \eta) &= \sum_{A=1}^{nm} N_A(\xi, \eta) z_A = \mathbf{N} \mathbf{z} \\ u(\xi, \eta) &= \sum_{A=1}^{nm} N_A(\xi, \eta) u_A = \mathbf{N} \mathbf{u} & w(\xi, \eta) &= \sum_{A=1}^{nm} N_A(\xi, \eta) w_A = \mathbf{N} \mathbf{w} \\ \delta u(\xi, \eta) &= \sum_{A=1}^{nm} N_A(\xi, \eta) \delta u_A = \mathbf{N} \delta \mathbf{u} & \delta w(\xi, \eta) &= \sum_{A=1}^{nm} N_A(\xi, \eta) \delta w_A = \mathbf{N} \delta \mathbf{w} \end{aligned} \quad (3.3)$$

where r_A and z_A are the x - and y -coordinates of the control points of the surface, u_A and w_A are the control points of the displacement.

The stress and strain relationships are given by

$$\boldsymbol{\varepsilon} = \mathbf{T}\mathbf{N} \begin{bmatrix} u \\ w \end{bmatrix} = \mathbf{B} \begin{bmatrix} u \\ w \end{bmatrix} \quad \boldsymbol{\sigma} = \mathbf{C}\boldsymbol{\varepsilon} = \mathbf{C}\mathbf{B} \begin{bmatrix} u \\ w \end{bmatrix} \quad (3.4)$$

where \mathbf{T} is the matrix of differential operators, \mathbf{C} is the constitutive matrix (constitutive matrix is calculated via Young's modulus and Poisson's ratio) and $\mathbf{B} = \mathbf{T}\mathbf{N}$. In this study it is assumed that Poisson's ratio ν is a material constant while Young's modulus $E(r)$ varies with the position across the wall thickness of the vessel (disk).

Substituting Eqs. (3.3) and (3.4) into Eq. (3.2), and in the absence of inertia forces, we obtain

$$0 = 2\pi \iint \left(\mathbf{B}^T \mathbf{C} \mathbf{B} \begin{bmatrix} u \\ w \end{bmatrix} \right) r \, dr \, dz - 2\pi \iint \mathbf{N}^T \begin{bmatrix} f_r \\ f_z \end{bmatrix} r \, dr \, dz - \oint_S \mathbf{N}^T \begin{bmatrix} t_r \\ t_z \end{bmatrix} ds \quad (3.5)$$

Note that in Eq. (3.5) all variables are written in terms of the parameters ξ and η which is similar to mapping in the standard finite element method where the base or unit elements are used

$$\begin{aligned} 0 = 2\pi & \int_{\xi_1}^{\xi_{n+p+1}} \int_{\eta_1}^{\eta_{m+q+1}} \mathbf{B}^T \mathbf{C} \mathbf{B} \begin{bmatrix} u \\ w \end{bmatrix} r(\det \mathbf{J}) \, d\eta \, d\xi \\ & - 2\pi \int_{\xi_1}^{\xi_{n+p+1}} \int_{\eta_1}^{\eta_{m+q+1}} \mathbf{N}^T \begin{bmatrix} f_r \\ f_z \end{bmatrix} r(\det \mathbf{J}) \, d\eta \, d\xi - \oint_S \mathbf{N}^T \begin{bmatrix} t_r \\ t_z \end{bmatrix} ds \end{aligned} \quad (3.6)$$

where

$$\mathbf{J} = \begin{bmatrix} \partial r / \partial \xi & \partial z / \partial \xi \\ \partial r / \partial \eta & \partial z / \partial \eta \end{bmatrix}$$

and the matrix form is as follows

$$\mathbf{K}\mathbf{u} = \mathbf{F} + \mathbf{T} \quad (3.7)$$

where

$$\begin{aligned} \mathbf{K} &= 2\pi \int_{\xi_1}^{\xi_{n+p+1}} \int_{\eta_1}^{\eta_{m+q+1}} \mathbf{B}^T \mathbf{C} \mathbf{B} \begin{bmatrix} u \\ w \end{bmatrix} r(\det \mathbf{J}) \, d\eta \, d\xi \\ \mathbf{F} &= 2\pi \int_{\xi_1}^{\xi_{n+p+1}} \int_{\eta_1}^{\eta_{m+q+1}} \mathbf{N}^T \begin{bmatrix} f_r \\ f_z \end{bmatrix} r(\det \mathbf{J}) \, d\eta \, d\xi \\ \mathbf{T} &= \oint_S \mathbf{N}^T \begin{bmatrix} t_r \\ t_z \end{bmatrix} ds \end{aligned} \quad (3.8)$$

Integrals in Eq. (3.8) can be calculated using the Gauss-Legendre method of numerical integration.

In order to obtain stress distributions for a spherical thick-walled functionally graded pressure vessel, the isogeometric analysis formulation is rewritten in the spherical coordinate system (r, θ, φ) .

3.2. Plastic formulation

In order to formulate a theory which models elasto-plastic material deformation, three requirements have to be met:

- before the onset of plastic deformation, an explicit relationship between stress and strain must be formulated to describe material behaviour under elastic conditions,
- a yield criterion must be postulated to indicate the stress level at which plastic flow commences,
- a relationship between stress and strain must be developed for post yield behaviour, when the deformation is made up of both elastic and plastic components (Owen and Hinton, 1980).

According to the normality hypothesis of plasticity, the plastic strain increment $d\varepsilon^p$ is defined as:

$$d\varepsilon^p = d\lambda \frac{\partial Q}{\partial \sigma} \quad (3.9)$$

where Q is the yield function and $d\lambda$ is called the plastic multiplier.

Assuming that the material plastic deformation follows the isotropic strain-hardening rule based on the von Mises yield criterion $\mathbf{n} \equiv \partial Q / \partial \sigma = [3/(2\sigma_e)]\mathbf{S}$ and $d\lambda = d\varepsilon_e^p$, Eq. (3.9) may be rewritten as

$$d\varepsilon^p = \frac{3}{2} \frac{d\varepsilon_e^p}{\sigma_e} \mathbf{S} \quad (3.10)$$

where $d\varepsilon_e^p$ is the equivalent plastic strain increment. The superscripts p and e denote plasticity and elasticity conditions respectively, also the subscript e denotes equivalent (effective) parameters (stress or plastic strain).

The equivalent stress σ_e and the deviatoric stress S for the plane stress field are defined as

$$\sigma_e = \sqrt{\sigma_r^2 + \sigma_\theta^2 - \sigma_r \sigma_\theta} \quad \mathbf{S} = \begin{bmatrix} S_r \\ S_\theta \\ S_z \end{bmatrix} = \begin{bmatrix} \frac{2\sigma_r - \sigma_\theta}{3} \\ \frac{2\sigma_\theta - \sigma_r}{3} \\ -\frac{\sigma_r + \sigma_\theta}{3} \end{bmatrix} \quad (3.11)$$

where σ_r and σ_θ are the radial and hoop stresses, respectively. For a linear strain hardening material (Fig. 1), the yield stress σ_y and the plastic multiplier $d\lambda$ are determined by

$$\sigma_y = \sigma_{y0}(r) + h_p(r)\varepsilon_e^p \quad d\lambda = \frac{\mathbf{n}^T \mathbf{C} d\varepsilon}{\mathbf{n}^T \mathbf{C} \mathbf{n} + h_p} \quad (3.12)$$

where $h_p(r)$ is the plasticity modulus (i.e. the gradient of the stress-plastic strain curve) and $\sigma_{y0}(r)$ is the initial yield stress of the FGM material. Both $h_p(r)$ and $\sigma_{y0}(r)$ are functions dependent on the radial position r . The stress increment is given by

$$d\boldsymbol{\sigma} = \mathbf{C} d\varepsilon^e = \mathbf{C}(d\varepsilon - d\varepsilon^p) = \mathbf{C}(d\varepsilon - d\lambda \mathbf{n}) \quad (3.13)$$

by substituting Eq. (3.12)₂ into Eq. (3.13), we can obtain the complete elasto-plastic incremental stress-strain relation

$$d\boldsymbol{\sigma} = \mathbf{C}^{ep} d\varepsilon \quad \mathbf{C}^{ep} = \mathbf{C} - \frac{\mathbf{C} \mathbf{n} \mathbf{n}^T \mathbf{C}}{\mathbf{n}^T \mathbf{C} \mathbf{n} + h_p} \quad (3.14)$$

where the superscripts ep denote the elasto-plastic behaviour.

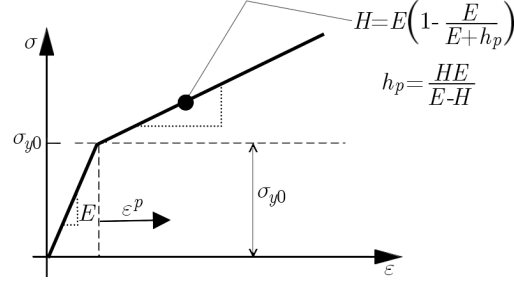


Fig. 1. Stress-strain curve for linear strain hardening

If we denote all quantities at the iteration k with a superscript k , and those at the next increment by $k+1$ in a similar way, then we may write

$$d\lambda^k = \frac{\mathbf{n}^k{}^T \mathbf{C} d\boldsymbol{\varepsilon}^k}{\mathbf{n}^k{}^T \mathbf{C} \mathbf{n}^k + h_p} \quad d\boldsymbol{\sigma}^k = \mathbf{C} (d\boldsymbol{\varepsilon}^k - d\lambda^k \mathbf{n}^k) \quad (3.15)$$

The integration to obtain the quantity at the end of the time step Δt may be then written as

$$\boldsymbol{\sigma}^{k+1} = \boldsymbol{\sigma}^k + d\boldsymbol{\sigma}^k \quad (3.16)$$

If relatively large load increments are to be permitted, the process described can lead to an inaccurate prediction of the stresses. Two parameters R (reduction factor) and m (the excess of the yield stress is divided into m parts) can help to minimize the error (Owen and Hinton, 1980). The algorithm for plasticity isogeometric analysis is summarized in Fig. 2.

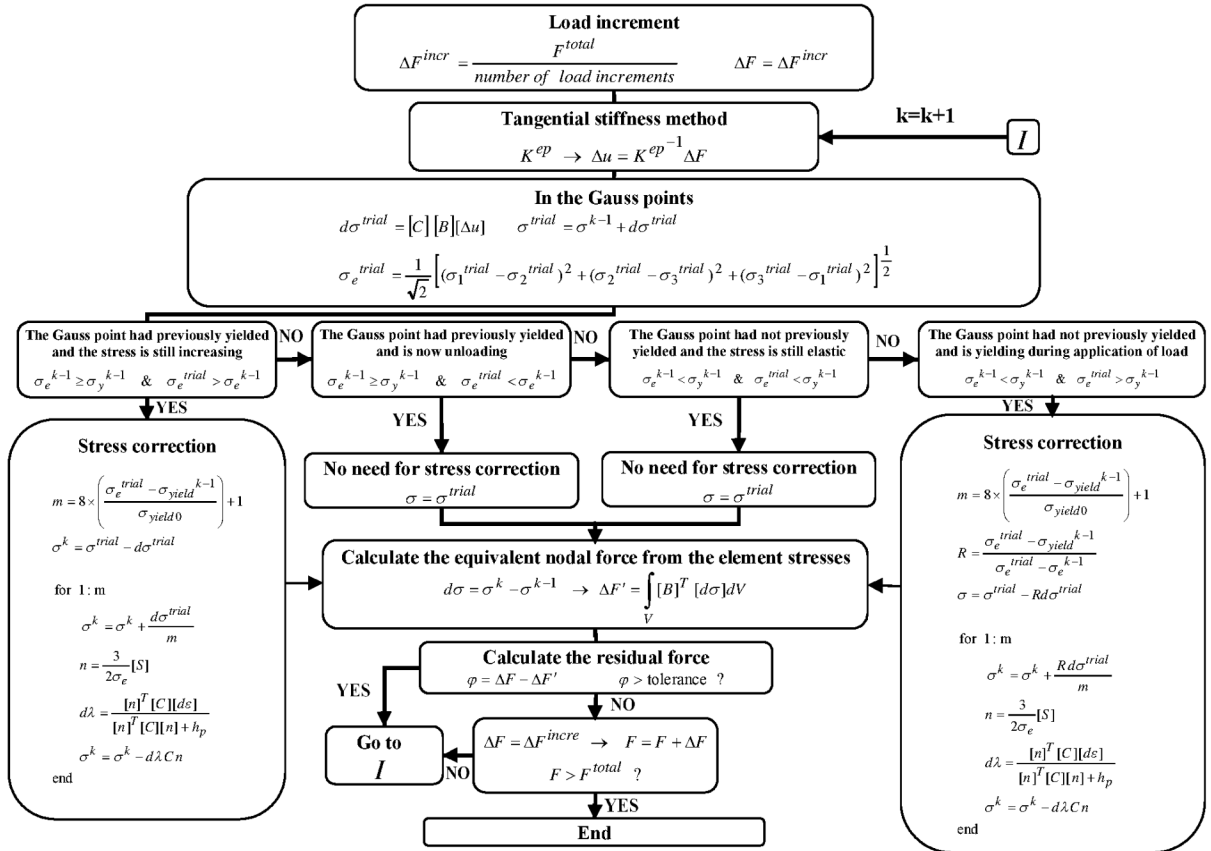


Fig. 2. Flow chart of the algorithm for the elastic-plastic analysis

4. Mechanical behaviour of FGM

It is assumed that the functionally graded metal-ceramic composite is locally isotropic and follows the von Mises yield criterion. The three important material properties for elastic-plastic analysis are the elastic modulus $E(r)$, the initial yield stress $\sigma_{y0}(r)$, and the tangent modulus $H(r)$. These properties can be calculated using the modified rule of mixtures for composites (Suresh and Mortensen, 1998). Note that the modified rule of mixtures is appropriate for modeling of isotropic materials

$$\begin{aligned}
 E &= \left[(1 - f_c) E_m \frac{q + E_c}{q + E_m} + f_c E_c \right] \left[(1 - f_c) \frac{q + E_c}{q + E_m} + f_c \right]^{-1} \\
 \sigma_{y0} &= \sigma_{y0m} \left[(1 - f_c) + \frac{q + E_m}{q + E_c} \frac{E_c}{E_m} f_c \right] \\
 H &= \left[(1 - f_c) H_m \frac{q + E_c}{q + H_m} + f_c E_c \right] \left[(1 - f_c) \frac{q + E_c}{q + H_m} + f_c \right]^{-1} \\
 h_p &= \frac{EH}{E - H}
 \end{aligned} \tag{4.1}$$

where the subscripts c and m indicate the ceramic and metal material, respectively. The volume fraction of ceramic particles is denoted by f_c , and q is the ratio of the stress to strain transfer, where σ_c , ε_c and σ_m , ε_m are the average stresses and strains in ceramic and metal, respectively (see Fig. 3)

$$q = \frac{\sigma_c - \sigma_m}{|\varepsilon_c - \varepsilon_m|} \quad 0 < q < \infty \tag{4.2}$$

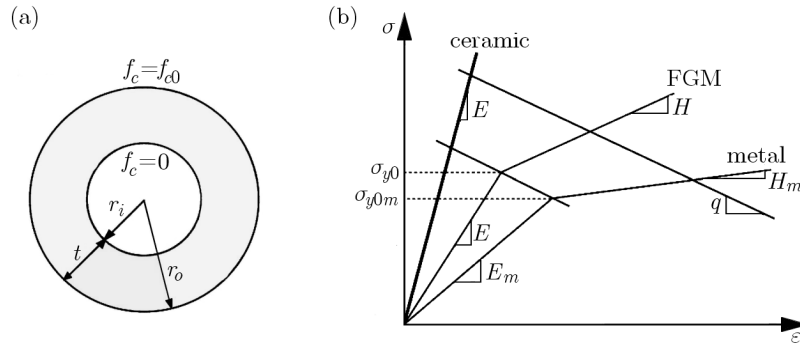


Fig. 3. (a) Schematic representation of a thick FGM vessel (rotating disk) with internal radius r_i and external radius r_o . (b) Schematic representation of the modified rule of mixtures used to estimate the behaviour of the ceramic particle-reinforced metal composite

The empirical parameter q depends on many factors including material composition, microstructural arrangements and internal constraints. For example, $q \rightarrow \infty$ if the constituent elements deform identically in the loading direction, while $q = 0$ if the constituent elements experience the same stress level. In the present analysis, the ceramic particle reinforcement is assumed to have a volume fraction that varies from 0 at the inner radius r_i to f_{c0} at the outer radius r_o according to the following relationship

$$f_c(r) = f_{c0} \left(\frac{r - r_i}{r_o - r_i} \right)^n \tag{4.3}$$

where n is the reinforcement distribution exponent $n = 0$ denotes uniformly-reinforced metal-ceramic). The material properties for each constituent phase are listed in Table 1. The parameter q may be approximated by calibration of experimental data from tensile tests performed on monolithic composite specimens. For example, a value of $q = 4.5$ GPa is used for a TiB/Ti FGM (Carpenter *et al.*, 1999), whereas Poisson's ratio is taken constant and equal to 0.3.

Table 1. Material properties (Jin *et al.*, 2003)

Materials	Young's modulus [GPa]	Yield stress [MPa]	Tangent modulus [GPa]
Ti	107	450	10
TiB	373		

5. Results

In this Section, we study three cases, a cylindrical and spherical pressure vessel as well as a rotating disk made of FGMs. The elastic-plastic isogeometric analysis code is written in MATLAB (2008). The cylinder (disk) B-spline model includes 50 control points (10 points in the r -direction and 5 points in the z -direction), and the assumed knot vectors are $\Xi = [0, 0, 0, 0, 0.142, 0.285, 0.428, 0.571, 0.714, 0.857, 1, 1, 1, 1]$ and $\mathbf{H} = [0, 0, 0, 0, 0.5, 1, 1, 1, 1]$ (cubic NURBS). In all the cases, the second order Gauss quadrature is used for numerical integrations (156 Gauss points in the r -direction and 8 Gauss point in the z -direction). The knot vectors and the number of control points in the sphere model is similar to that in the cylinder model. The geometries in this study are modeling with a single patch (the patch for the surface is the domain $[\xi_1 = 0, \xi_{n+p+1} = 1] \times [\eta_1 = 0, \eta_{n+p+1} = 1]$), and we have no need to assemble the stiffness matrices and force vectors. By removing the assemble step, we reduce the overall analysis time by about 10% (at the same number of degrees-of-freedom in the isogeometric method and FEM).

To verify the accuracy of the isogeometric analysis, finite element analyses have been performed using the commercial finite element code ABAQUS (Karlsson, Hibbitt, Sorensen Inc., 2008). The conventional method of modelling FGMs in the software is to subdivide the thick wall into several thin layers with equal thickness. This method of modelling leads to discontinuity in the mechanical properties of FGM materials and is both difficult and time-consuming. Setoodeh *et al.* (2008) proposed a new approach for analysing the FGM material in the elastic zone without the need for dividing the thickness into thin strips. They applied a virtual temperature distribution in the cylinder wall using the facility available within the software to assign continuously variable properties across the wall thickness and then created a one-to-one relationship between the temperature and mechanical properties. The correlation of the distribution of temperature and mechanical properties of the FGM material allowed one to model the variation of FGM properties in the cylinder. Note that the conductivity factor and other thermal parameters are set to zero, and the temperature does not change during analysis. Indeed, the analysis is solely mechanical and no thermomechanical examination is carried out. This method allows the analysis of the elastic-plastic FGM cylindrical and spherical vessels as well as the rotating disk. The three-dimensional 8-noded linear coupled temperature displacement family of finite elements in ABAQUS has been used to model the cylinder. Sensitivity analysis of the mesh has also been performed to ensure the results remained insensitive to the element size.

In order to evaluate the isogeometric analysis code, a set of results from finite element calculations and the VMP method (Haghpanah Jahromi *et al.*, 2009) obtained for the plane strain conditions have been compared with the results obtained from the isogeometric analysis for the FGM cylindrical vessel subjected to autofrettage internal pressure 100 MPa (Fig. 4). The results indicated that the isogeometric analysis method has some influence on the accuracy. Figure 5 illustrates the distribution of von Mises stresses across the thickness in the cylindrical vessel subjected to internal pressure 300 MPa with $n = 2$ and different reinforcement distribution coefficients f_{c0} . The results show that because $E_c/E_m > 1$, an increase in f_{c0} elevates von Mises stress in the outer surface, and the plastic region decreases in the inner surface.

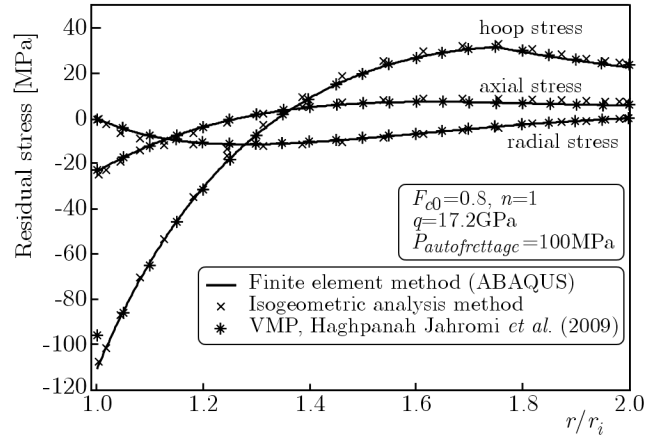


Fig. 4. Comparison of the VMP method (Haghpanah Jahromi *et al.*, 2009) with the finite element analysis. The results show the residual stresses in the autofrettaged vessel. In this calculation: $E_m = 56$ GPa, $E_c = 20$ GPa, $\sigma_{y0m} = 106$ MPa, $H_m = 12$ GPa and $\nu_m = \nu_c = 0.25$. The vessel undergoes a plane-strain condition

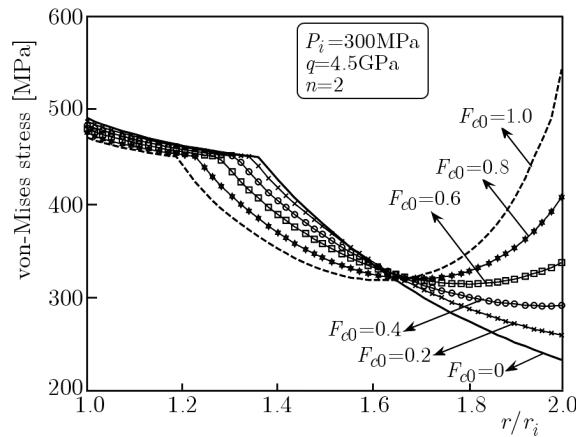


Fig. 5. Von Mises stress along the thickness in the FGM cylindrical vessel subjected to internal pressure 300 MPa with $q = 4.5$ GPa and $n = 2$ for different f_{c0} . The vessel has $t/r_i = 1$ and plane-stress condition (properties listed in Table 1)

For the spherical vessel subjected to internal pressure of 600 MPa, the results obtained from the isogeometric analysis method have been compared with the finite element results. Excellent agreement is observed as shown in Fig. 6. For the purpose to investigate the effect of n on the initiation of yielding, we introduce two parameters P_{v1} (pressures corresponding to the initiation of yielding at the inner radius) and P_{v2} (pressures corresponding to the initiation of yielding at the outer radius). Figure 7 shows that P_{v1} and P_{v2} decrease with growing n . Also, in the cylinder subjected to P_{v2} , by increasing n , the plastic region gradually spreads from the inner surface. Note that by increasing n , the metal properties dominate overcoming the ceramic properties and, therefore, the plastic behaviour of the material becomes more evident.

Similar to the previous cases, the excellent agreement of the isogeometric analysis with the finite element predictions of elastic-plastic stresses for the rotating disc is shown in Fig. 8. The distribution of von Mises stresses across the thickness in the disk rotating at different angular velocities with $n = 2$ and $f_{c0} = 0.8$ is presented in Fig. 9. The results clearly indicate that the growth of the plastic zone across the thickness is initiated from both sides of the disc. In this study, density of metal is $\rho_m = 4420$ kg/m³ and density of ceramic is $\rho_c = 2000$ kg/m³.

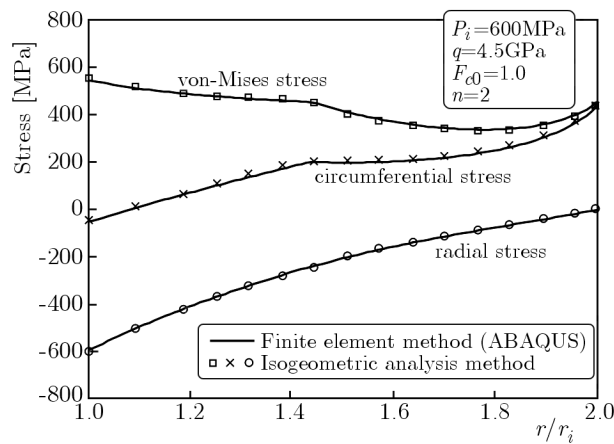


Fig. 6. Comparison with the finite element method. The results show the stress components in the spherical vessel with $f_{c0} = 1$ and $n = 2$ subjected to internal pressure 600 MPa. In this calculation $q = 4.5$ GPa. The vessel has $t/r_i = 1$ (properties listed in Table 1)

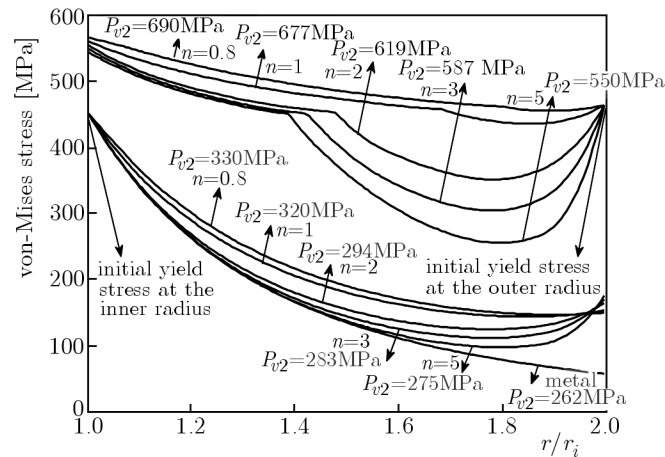


Fig. 7. Von Mises stress along the thickness in the FGM spherical vessel subjected to P_{v1} and P_{v2} with $f_{c0} = 1$ and different n . In this calculation $q = 4.5$ GPa. The vessel has $t/r_i = 1$ (properties listed in Table 1)

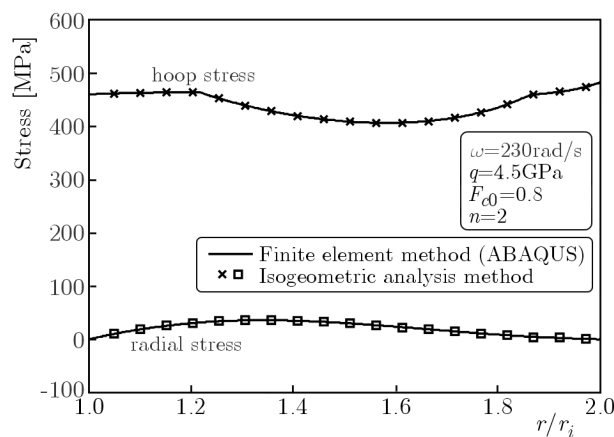


Fig. 8. Comparison with the finite element method. The results show the stress components in the rotating disk with $f_{c0} = 0.8$ and $n = 2$ at the angular velocity $\omega = 230$ rad/s. In this calculation $q = 4.5$ GPa. The disk has $t/r_i = 1$ (properties listed in Table 1)

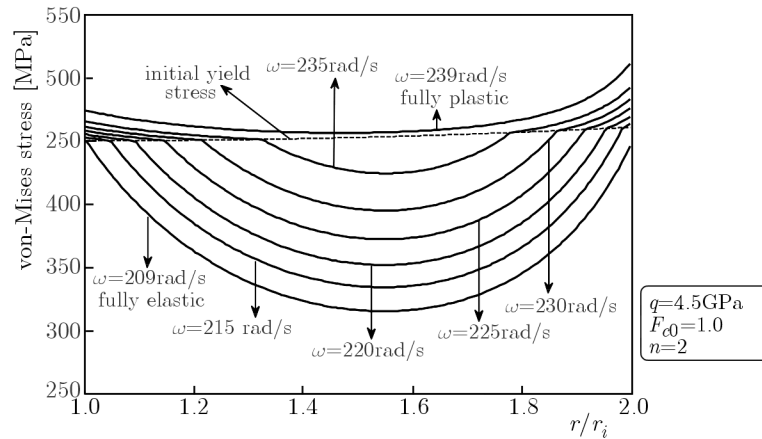


Fig. 9. Von Mises stress along the thickness in the FGM rotating disk at different angular velocities with $f_{c0} = 0.8$ and $n = 2$. In this calculation $q = 4.5$ GPa. The disk has $t/r_i = 1$ (properties listed in Table 1)

6. Conclusion

Using the isogeometric analysis method, elastic-plastic stress distributions in a cylindrical and spherical pressurized vessels and rotating disks made of an FGM material have been determined. As expected, this approach to the plasticity problem is computationally cost effective and results in a much smaller system of equations to solve. Finite element analysis of the problem using ABAQUS commercial code has been used for verification of the isogeometric method. The numerical analysis within the software has been performed by the application of a “virtual thermal load” that enabled continuous variation of the material behaviour through the wall thickness. The analysis results obtained in this work also indicate the possibility of formation and growth of a plastic region within the wall thickness from the external surface of the FGM vessels or rotating disks whereas in cylindrical (spherical) vessels and rotating disks made of homogeneous materials, the plasticity essentially starts from the inner surface.

References

1. BAYAT M., SALEEM M., SAHARI B.B., HAMOUDA A.S.M., MAHDI E., 2008, Analysis of functionally graded rotating disks with variable thickness, *Mechanics Research Communications*, **35**, 283-309
2. CARPENTER R.D., LIANG W.W., PAULINO G.H., GIBELING J.C., MUNIR Z.A., 1999, Fracture testing and analysis of a layered functionally graded Ti/TiB beam in 3-point bending, *Materials Science Forum*, **308**, 837-842
3. CHAKRABORTY A., GOPALAKRISHNAN S., REDDY J., 2003, A new beam finite element for the analysis of functionally graded materials, *International Journal of Mechanical Sciences*, **45**, 519-539
4. CHEN Y.Z., LIN X.Y., 2008, Elastic analysis for thick cylinders and spherical pressure vessels made of functionally graded materials, *Computational Materials Science*, **44**, 581-587
5. COTTRELL J.A., HUGHES T.J.R., BAZILEVS Y., 2009, *Isogeometric Analysis: Toward Integration of CAD and FEA*, John Wiley, U.K.
6. DAI H.L., FU Y.M., DONG Z.M., 2006, Exact solutions for functionally graded pressure vessels in a uniform magnetic field, *International Journal of Solids and Structures*, **43**, 5570-5580
7. DURODOLA J.F., ATTIA O., 2006, Deformation and stresses in functionally graded rotating disks, *Composites Science and Technology*, **60**, 987-995

8. FIGUEIREDO F., BORGES L., ROCHINHA F., 2008, Elasto-plastic stress analysis of thick-walled FGM pipes, *AIP Conference Proceedings*, 147-152
9. HAGHPANAH JAHROMI B., AJDARI A., NAYEB-HASHEMI H., VAZIRI A., 2010, Autofrettage of layered and functionally graded metal-ceramic composite vessels, *Composite Structures*, **92**, 1813-1822
10. HAGHPANAH JAHROMI B., FARRAHI G.H., MALEKI M., NAYEB-HASHEMI H., VAZIRI A., 2009, Residual stresses in autofrettaged vessel made of functionally graded material, *Engineering Structures*, **31**, 2930-2935
11. HAGHPANAH JAHROMI B., NAYEB-HASHEMI H., VAZIRI A., 2012, Elasto-plastic stresses in a functionally graded rotating disk, *ASME Journal of Engineering Materials and Technology*, **134**, 21004-21015
12. HASSANI B., TAVAKKOLIN S.M., MOGHADAMA N.Z., 2011, Application of isogeometric analysis in structural shape optimization, *Scientia Iranica*, **18**, 864-852
13. HUGHES T.J.R., COTTRELL J.A., BAZILEVS Y., 2005, Isogeometric analysis: CAD, finite elements, NURBS, exact geometry and mesh refinement, *Computer Methods in Applied Mechanics and Engineering*, **194**, 4135-4195
14. JAHED H., DUBEY R.N., 1997, An axisymmetric method of elastic-plastic analysis capable of predicting residual stress field, *Journal of Pressure Vessel Technology*, **119**, 264-273
15. JAHED H., FARSHI B., BIDABADI J., 2005, Minimum weight design of inhomogeneous rotating discs, *International Journal of Pressure Vessels and Piping*, **82**, 35-41
16. JAHED H., FARSHI B., KARIMI M., 2006, Optimum autofrettage and shrink-fit combination in multi-layer cylinders, *Journal of Pressure Vessel Technology*, **128**, 196-201
17. JAHED H., SHIRAZI R., 2001, Loading and unloading behaviour of a thermoplastic disc, *International Journal of Pressure Vessels and Piping*, **78**, 637-645
18. JIN Z.H., PAULINO G.H., DODDS JR R.H., 2003, Cohesive fracture modelling of elastic-plastic crack growth in functionally graded materials, *Engineering Fracture Mechanics*, **70**, 1885-1912
19. Karlsson, Hibbitt, Sorensen, 2008, ABAQUS/CAE, v. 6.8-1.
20. OWEN D.R.J., HINTON E. 1980, *Finite Elements in Plasticity: Theory and Practice*, Pineridge Press, U.K.
21. SADEGHIAN M., EKHTERAEEI H., 2011, Axisymmetric yielding of functionally graded spherical vessel under thermo-mechanical loading, *Computational Materials Science*, **50**, 975-981
22. SETOODEH A., KALALI A., HOSSEINI A., 2008, Numerical analysis of FGM plate by applying virtual temperature distribution, *Proceedings of 7th Conference of Iranian Aerospace Society*, Tehran
23. SURESH S., MORTENSEN A., 1998, *Fundamentals of Functionally Graded Materials*, IOM Communications Ltd.
24. YOU L.H., ZHANG J.J., YOU X.Y., 2005, Elastic analysis of internally pressurized thick-walled spherical pressure vessels of functionally graded materials, *International Journal of Pressure Vessels and Piping*, **82**, 374-345

VORTICITY TRANSPORT ANALYSIS IN MAGNETIC VISCOELASTIC FLUID

PARDEEP KUMAR, HARI MOHAN

Department of Mathematics, ICDEOL, Himachal Pradesh University, Shimla, India

e-mail: pkdureja@gmail.com

GAMAL HOSHOUDY

Department of Applied Mathematics, Faculty of Science, South Valley University, Kena, Egypt

e-mail: g_hoshoudy@yahoo.com

Results of investigation on the transport of vorticity in Rivlin-Ericksen viscoelastic fluid in the presence of suspended magnetic particles is presented here. Equations governing the transport of vorticity in Rivlin-Ericksen viscoelastic fluid in the presence of suspended magnetic particles are obtained from the equations of magnetic fluid flow. From these equations it follows that the transport of solid vorticity is coupled with the transport of fluid vorticity. Further, we find that because of thermokinetic process, fluid vorticity may exist in the absence of solid vorticity, but when fluid vorticity is zero, then solid vorticity is necessarily zero. A two-dimensional case is also studied and found that the fluid vorticity is indirectly influenced by the temperature and the magnetic field gradient.

Keywords: Rivlin-Ericksen viscoelastic fluid, suspended magnetic particles, vorticity

1. Introduction

A magneto-rheological fluid contains particles of magnetic materials mixed in a liquid that acts as a carrier. Under normal conditions, the material behaves like a viscous fluid. When it is exposed to a magnetic field, the particles inside align and it responds to the field, exhibiting magnetized behaviour. There are a number of uses for magnetic fluids, ranging from medicine to industrial manufacturing. It is, therefore, a two-phase system consisting of solid and liquid phases. We assume that the liquid phase is non-magnetic in nature and magnetic force acts only on the magnetic particles. Thus, the magnetic force changes the velocity of the magnetic particles. Consequently, the dragging force acting on the carrier liquid is changed and thus the flow of carrier liquid is also influenced by the magnetic force. Because of the relative velocity between the solid and liquid particles, the net effect of the particles suspended in the fluid is extra dragging force acting on the system. Taking this force into consideration, Saffman (1962) proposed the equations of the flow of suspension of non-magnetic particles. These equations were subsequently modified to describe the flow of magnetic fluid with the magnetic body force $\mu_0 M \nabla H$ taken into account by Wagh (1991). Wagh and Jawandhia (1996) have studied the transport of vorticity in a magnetic fluid. Yan and Koplik (2009) have studied the transport and sedimentation of suspended particles in inertial pressure-driven flow.

In all the above studies, the fluid was considered as Newtonian, but many industrially important fluids (molten plastics, polymers, pulps and foods) exhibit a non-Newtonian fluid behaviour. Many common materials (paints and plastics) and more exotic ones (silicic magma, saturated soils, and the Earth's lithosphere) behave as viscoelastic fluids. With the growing importance of non-Newtonian materials in various manufacturing and processing industries, considerable effort has been directed towards understanding their flow. The stability of a horizontal layer of

Maxwell's viscoelastic fluid heated from below has been investigated by Vest and Arpaci (1969). The nature of the instability and other factors can affect viscoelastic fluids differently than Newtonian fluids. For example, Bhatia and Steiner (1972) have considered the effect of a uniform rotation on the thermal instability of Maxwellian viscoelastic fluid, where rotation is found to have a destabilizing effect. This is in contrast to the thermal instability of a Newtonian fluid where rotation has a stabilizing effect. The thermal instability of an Oldroydian viscoelastic fluid acted on by a uniform rotation has been studied by Sharma (1976). There are many viscoelastic fluids that cannot be characterized by Maxwell's or Oldroyd's constitutive relations. One such fluid is Rivlin-Ericksen viscoelastic fluid, having relevance and importance in geophysical fluid dynamics, chemical technology and petroleum industry. Rivlin and Ericksen (1955) have studied the stress-deformation relaxation for isotropic materials. Garg *et al.* (1994) have studied the drag on a sphere oscillating in conducting dusty Rivlin-Ericksen viscoelastic fluid. Thermal instability in Rivlin-Ericksen viscoelastic fluid in the presence of rotation and magnetic field, separately, has been investigated by Sharma and Kumar (1996, 1997b). Sharma and Kumar (1997a) have studied the hydromagnetic stability of two Rivlin-Ericksen viscoelastic superposed conducting fluids and the analysis has been carried out, for two highly viscous fluids of equal kinematic viscosities and equal kinematic viscoelasticities wherein it was found that the stability criterion is independent of the effects of viscosity and viscoelasticity and is dependent on the orientation and magnitude of the magnetic field. The stability of two superposed Rivlin-Ericksen viscoelastic fluids in the presence of suspended particles has been considered by Kumar and Singh (2006). Kumar *et al.* (2007) have studied the hydrodynamic and hydromagnetic stability of two stratified Rivlin-Ericksen viscoelastic superposed fluids.

Keeping in mind the importance of viscoelastic fluids in modern technology and industries, the present paper attempts to study the transport of vorticity in magnetic Rivlin-Ericksen viscoelastic fluid-particle mixtures by using the equations proposed by Wagh and Jawandhia (1996).

2. Basic assumptions and magnetic body force

The particles of magnetic material are much larger than the molecules of the carrier liquid. Accordingly, we consider the limit of a microscopic volume element in which the fluid can be assumed to be a continuous medium and the magnetic particles must be treated as discrete entities. If we consider a cell of magnetic fluid containing a larger number of magnetic particles, then we must consider the microrotation of the cell in addition to its translations as a point mass. We must, therefore, assign average velocity \mathbf{q}_d and the average angular velocity $\boldsymbol{\omega}$ to the cell. But, here as an approximation, we neglect the effect of microrotation. We also assume the following:

- (i) The free current density \mathbf{J} is negligible, and $\mathbf{J} \times \mathbf{B}$ is insignificant.
- (ii) The magnetic field is curl free i.e. $\nabla \times \mathbf{H} = \mathbf{0}$.
- (iii) The liquid compressibility is unimportant in many practical situations. Hence, the contribution due to magnetic friction can be neglected. The remaining force of the magnetic field is referred as magnetization force.
- (iv) All time-dependent magnetization effects in the fluid (such as hysteresis) are negligible, and the magnetization \mathbf{M} is collinear with \mathbf{H} .

From electromagnetic theory, the force per unit volume (in MKS units) on a piece of magnetized material of magnetization \mathbf{M} (i.e. dipole moment per unit volume) in the field of magnetic intensity \mathbf{H} is $\mu_0(\mathbf{M} \cdot \nabla)\mathbf{H}$, where μ_0 is the free space permeability.

Here we note that

$$\nabla \cdot \mathbf{a} = \frac{\partial a_1}{\partial x} + \frac{\partial a_2}{\partial y} + \frac{\partial a_3}{\partial z} \quad \mathbf{a} \cdot \nabla = a_1 \frac{\partial}{\partial x} + a_2 \frac{\partial}{\partial y} + a_3 \frac{\partial}{\partial z}$$

where $\mathbf{a} = a_1 \mathbf{i} + a_2 \mathbf{j} + a_3 \mathbf{k}$.

Using assumption (iv), we obtain

$$\mu_0(\mathbf{M} \cdot \nabla)\mathbf{H} = \frac{\mu_0 M}{H}(\mathbf{H} \cdot \nabla)\mathbf{H} \quad (2.1)$$

where $M = |\mathbf{M}|$ and $H = |\mathbf{H}|$.

But by assumption (ii), we have

$$(\mathbf{H} \cdot \nabla)\mathbf{H} = \frac{1}{2}\nabla(\mathbf{H} \cdot \mathbf{H}) - \mathbf{H} \times (\nabla \times \mathbf{H}) = \frac{1}{2}\nabla(\mathbf{H} \cdot \mathbf{H}) \quad (2.2)$$

Hence

$$\mu_0(\mathbf{M} \cdot \nabla)\mathbf{H} = \left(\frac{\mu_0 M}{H}\right)\frac{1}{2}\nabla(\mathbf{H} \cdot \mathbf{H}) = \mu_0 M \nabla H$$

The magnetic body force therefore becomes (Rosensweig, 1997)

$$\mathbf{f}_m = \mu_0 M \nabla H \quad (2.3)$$

3. Derivation of the equations governing the vorticity transport in a magnetic Rivlin-Ericksen viscoelastic fluid

Let Γ_{ij} , τ_{ij} , e_{ij} , δ_{ij} , u_i , x_i , p , μ and μ' denote the stress tensor, shear stress tensor, rate-of-strain tensor, Kronecker delta, velocity vector, position vector, isotropic pressure, viscosity and viscoelasticity, respectively. The constitutive relations for the Rivlin-Ericksen viscoelastic fluid (Rivlin and Ericksen, 1955; Sharma and Kumar, 1997a) are

$$\Gamma_{ij} = -p\delta_{ij} + \tau_{ij} \quad \tau_{ij} = 2\left(\mu + \mu' \frac{\partial}{\partial t}\right)e_{ij} \quad e_{ij} = \frac{1}{2}\left(\frac{\partial u_i}{\partial x_j} + \frac{\partial u_j}{\partial x_i}\right)$$

To describe the flow of a magnetic fluid by including the body force $\mu_0 M \nabla H$ acting on the suspended magnetic particles, Wagh (1991) modified the Saffman's equations for flow of suspension. The equations for the flow of suspended magnetic particles and the flow of Rivlin-Ericksen viscoelastic fluid in which magnetic particles are suspended are therefore written as

$$\begin{aligned} mN\left(\frac{\partial \mathbf{V}}{\partial t} + (\mathbf{V} \cdot \nabla)\mathbf{V}\right) &= mN\mathbf{g} + \mu_0 M \nabla H + KN(\mathbf{u} - \mathbf{V}) \\ \rho\left(\frac{\partial \mathbf{u}}{\partial t} + (\mathbf{u} \cdot \nabla)\mathbf{u}\right) &= -\nabla P + \rho\mathbf{g} + \left(\mu + \mu' \frac{\partial}{\partial t}\right)\nabla^2 \mathbf{u} + KN(\mathbf{V} - \mathbf{u}) \end{aligned} \quad (3.1)$$

where P , ρ , $\mathbf{u}(u_x, u_y, u_z)$, $\mathbf{g}(0, 0, -g)$, $\mathbf{V}(l, r, s)$, m and $N(\bar{x}, t)$ respectively denote the pressure minus hydrostatic pressure, density, velocity of fluid particles, gravity force, velocity of solid particles, particle mass and particle number density. Moreover, $\bar{x} = (x, y, z)$, and $K = 6\pi\mu\eta$, where η is the particle radius, is the Stokes' drag coefficient.

If we assume that the particle has a uniform spherical shape and that the velocity relative to the fluid is small, then in the equations of motion for the viscoelastic fluid, because of the presence of suspended particles, an additional force term appears proportional to the velocity difference between the suspended particles and the fluid. Since the force exerted by the fluid

on the suspended particles is equal and opposite to that exerted by the particles on the fluid, an additional force term equal in magnitude but opposite in sign appears in the equations of motion for the suspended particles. We neglect the buoyancy force on the particles. This force is proportional to the quotient of ρ and the particle density, and an analysis in the case of free-free boundary conditions (no tangential stresses) shows that its small stabilizing effect is negligible. We also assume that the distances between particles are quite large compared with their diameter, and we therefore also ignore particle interactions.

By making use of the Lagrange's vector identities

$$(\mathbf{q}_d \cdot \nabla) \mathbf{q}_d = \frac{1}{2} \nabla q_d^2 - \mathbf{q}_d \times \boldsymbol{\Omega} \quad (\mathbf{q} \cdot \nabla) \mathbf{q} = \frac{1}{2} \nabla q^2 - \mathbf{q} \times \boldsymbol{\Omega}_1 \quad (3.2)$$

Equations (3.1) become

$$\begin{aligned} mN \left[\frac{\partial \mathbf{V}}{\partial t} - (\mathbf{V} \times \boldsymbol{\Omega}) \right] &= -\nabla mNgz - \frac{1}{2} mN \nabla V^2 + \mu_0 M \nabla H + KN(\mathbf{u} - \mathbf{V}) \\ \rho \left[\frac{\partial \mathbf{u}}{\partial t} - (\mathbf{u} \times \boldsymbol{\Omega}_1) \right] &= -\nabla P - \nabla \rho gz - \frac{1}{2} \rho \nabla u^2 + \left(\mu + \mu' \frac{\partial}{\partial t} \right) \nabla^2 \mathbf{u} + KN(\mathbf{V} - \mathbf{u}) \end{aligned} \quad (3.3)$$

where $\boldsymbol{\Omega} = \nabla \times \mathbf{V}$ and $\boldsymbol{\Omega}_1 = \nabla \times \mathbf{u}$ are solid vorticity and fluid vorticity.

Taking the curl of these equations and recalling that the curl of a gradient is identically equal to zero, we obtain

$$\begin{aligned} mN \left[\frac{\partial \boldsymbol{\Omega}}{\partial t} - (\nabla \times \mathbf{V} \times \boldsymbol{\Omega}) \right] &= \mu_0 \nabla \times M \nabla H + KN(\boldsymbol{\Omega}_1 - \boldsymbol{\Omega}) \\ \rho \left[\frac{\partial \boldsymbol{\Omega}_1}{\partial t} - (\nabla \times \mathbf{u} \times \boldsymbol{\Omega}_1) \right] &= \left(\mu + \mu' \frac{\partial}{\partial t} \right) \nabla^2 \boldsymbol{\Omega}_1 + KN(\boldsymbol{\Omega} - \boldsymbol{\Omega}_1) \end{aligned} \quad (3.4)$$

By making use of the vector identities

$$\begin{aligned} \nabla \times (\mathbf{V} \times \boldsymbol{\Omega}) &= (\boldsymbol{\Omega} \cdot \nabla) \mathbf{V} - (\mathbf{V} \cdot \nabla) \boldsymbol{\Omega} + \mathbf{V} \nabla \cdot \boldsymbol{\Omega} - \boldsymbol{\Omega} \nabla \cdot \mathbf{V} = (\boldsymbol{\Omega} \cdot \nabla) \mathbf{V} - (\mathbf{V} \cdot \nabla) \boldsymbol{\Omega} \\ \nabla \times (\mathbf{u} \times \boldsymbol{\Omega}_1) &= (\boldsymbol{\Omega}_1 \cdot \nabla) \mathbf{u} - (\mathbf{u} \cdot \nabla) \boldsymbol{\Omega}_1 + \mathbf{u} \nabla \cdot \boldsymbol{\Omega}_1 - \boldsymbol{\Omega}_1 \nabla \cdot \mathbf{u} = (\boldsymbol{\Omega}_1 \cdot \nabla) \mathbf{u} - (\mathbf{u} \cdot \nabla) \boldsymbol{\Omega}_1 \end{aligned} \quad (3.5)$$

Equations (3.4) become

$$\begin{aligned} mN \frac{D\boldsymbol{\Omega}}{Dt} &= \mu_0 \nabla \times M \nabla H + mN(\boldsymbol{\Omega} \cdot \nabla) \mathbf{V} + KN(\boldsymbol{\Omega}_1 - \boldsymbol{\Omega}) \\ \frac{D\boldsymbol{\Omega}_1}{Dt} &= \left(\nu + \nu' \frac{\partial}{\partial t} \right) \nabla^2 \boldsymbol{\Omega}_1 + (\boldsymbol{\Omega}_1 \cdot \nabla) \mathbf{u} + \frac{KN}{\rho} (\boldsymbol{\Omega} - \boldsymbol{\Omega}_1) \end{aligned} \quad (3.6)$$

where ν and ν' are kinematic viscosity and kinematic viscoelasticity, respectively and $\frac{D}{Dt} \equiv \frac{\partial}{\partial t} + (\mathbf{V} \cdot \nabla)$ is the convective derivative.

In equation (3.6)₁

$$\nabla \times (M \nabla H) = (\nabla M \times \nabla H) + (M \nabla \times \nabla H) \quad (3.7)$$

Since the curl of the gradient is zero, the last term in equation (3.7) is zero. Also since $M = M(H, T)$.

Therefore

$$\nabla M = \left(\frac{\partial M}{\partial H} \right) \nabla H + \left(\frac{\partial M}{\partial T} \right) \nabla T \quad (3.8)$$

By making use of (3.8), equation (3.7) becomes

$$\nabla \times (M \nabla H) = \left(\frac{\partial M}{\partial H} \right) \nabla H \times \nabla H + \left(\frac{\partial M}{\partial T} \right) \nabla T \times \nabla H \quad (3.9)$$

The first term on the right hand side of this equation is clearly zero, hence we get

$$\nabla \times (M\nabla H) = \left(\frac{\partial M}{\partial T}\right) \nabla T \times \nabla H \quad (3.10)$$

Substituting this expression in equation (3.6)₁, we obtain

$$mN \frac{D\boldsymbol{\Omega}}{Dt} = \mu_0 \left(\frac{\partial M}{\partial T}\right) \nabla T \times \nabla H + mN(\boldsymbol{\Omega} \cdot \nabla) \mathbf{V} + KN(\boldsymbol{\Omega}_1 - \boldsymbol{\Omega}) \quad (3.11)$$

Here (3.6)₂ and (3.11) are the equations governing the transport of vorticity in magnetic Rivlin-Ericksen viscoelastic fluid-particle mixtures.

In equation (3.11), the first term in the right-hand side i.e. $\mu_0(\partial M/\partial T)\nabla T \times \nabla H$ describes the production of vorticity due to thermo-kinetic processes. The last term $KN(\boldsymbol{\Omega}_1 - \boldsymbol{\Omega})$ gives the change in solid vorticity on account of the exchange of vorticity between the liquid and solid.

It follows from equations (3.6)₂ and (3.11) that the transport of solid vorticity $\boldsymbol{\Omega}$ is coupled with the transport of fluid vorticity $\boldsymbol{\Omega}_1$.

From equation (3.11), we see that if solid vorticity $\boldsymbol{\Omega}$ is zero, then the fluid vorticity $\boldsymbol{\Omega}_1$ is not-zero and it is given by

$$\boldsymbol{\Omega}_1 = -\frac{\mu_0}{KN} \left(\frac{\partial M}{\partial T}\right) \nabla T \times \nabla H \quad (3.12)$$

This implies that due to thermo-kinetic processes, fluid vorticity can exist in the absence of solid vorticity.

From equation (3.6)₂, we find that if $\boldsymbol{\Omega}_1$ is zero, then $\boldsymbol{\Omega}$ is also zero. This implies that when fluid vorticity is zero, then solid vorticity is necessarily zero.

In the absence of suspended magnetic particles, N is zero and magnetization M is also zero. Then, equation (3.11) is identically satisfied and equation (3.6)₂ reduces to

$$\frac{D\boldsymbol{\Omega}_1}{Dt} = \left(\nu + \nu' \frac{\partial}{\partial t}\right) \nabla^2 \boldsymbol{\Omega}_1 + (\boldsymbol{\Omega}_1 \cdot \nabla) \mathbf{q} \quad (3.13)$$

This equation is the vorticity transport equation. The last term on the right hand side of equation (3.13) represents the rate at which $\boldsymbol{\Omega}_1$ varies for a given particle, when the vortex lines move with the fluid, the strengths of the vortices remaining constant. The first term represents the rate of dissipation of vorticity through friction (resistance) and rate of change of vorticity due to fluid viscoelasticity.

3.1. Two-dimensional case

Here we consider the two-dimensional case:

Let

$$\mathbf{V} = v_x(x, y)\mathbf{i} + v_y(x, y)\mathbf{j} \quad \mathbf{u} = u_x(x, y)\mathbf{i} + u_y(x, y)\mathbf{j} \quad (3.14)$$

where components v_x , v_y and u_x , u_y are functions of x , y and t , then

$$\boldsymbol{\Omega} = \Omega_z \mathbf{k} \quad \boldsymbol{\Omega}_1 = \Omega_{1z} \mathbf{k} \quad (3.15)$$

In two-dimensional case, equation (3.11) becomes

$$\frac{D\Omega_z}{Dt} = \frac{\mu_0}{mN} \left(\frac{\partial M}{\partial T}\right) \left(\frac{\partial T}{\partial x} \frac{\partial H}{\partial y} - \frac{\partial H}{\partial x} \frac{\partial T}{\partial y}\right) + \frac{K}{m} (\Omega_{1z} - \Omega_z) \quad (3.16)$$

and equation (3.6)₂ similarly becomes

$$\frac{D\Omega_{1z}}{Dt} = \nu \nabla^2(\Omega_{1z}) + \nu' \frac{\partial}{\partial t} \nabla^2(\Omega_{1z}) + \frac{KN}{\rho}(\Omega_z - \Omega_{1z}) \quad (3.17)$$

since it can be easily verified that

$$(\boldsymbol{\Omega} \cdot \nabla)\mathbf{V} = 0 \quad (\boldsymbol{\Omega}_1 \cdot \nabla)\mathbf{u} = 0 \quad (3.18)$$

The first term on the right hand side of equation (3.17) is the change of fluid vorticity due to internal friction (resistance). The second term is the rate of change of fluid vorticity due to fluid viscoelasticity and the third term is change in fluid vorticity due to the exchange of vorticity between solid and liquid. Equation (3.17) does not explicitly involve the term representing change of vorticity due to magnetic field gradient and/or temperature gradient. But equation (3.16) shows that solid vorticity Ω_z depends on these factors. Hence, it follows that the fluid vorticity is indirectly influenced by the temperature and the magnetic field gradient.

In the absence of magnetic particles, N is zero and magnetization M is also zero. Equation (3.16) is therefore satisfied identically, and equation (3.17) reduces to the classical equation for the transport of fluid vorticity. If we consider a suspension of non-magnetic particles instead of a magnetic fluid, then the corresponding equation for the transport of vorticity may be obtained by setting M equal to zero in the equations governing the transport of vorticity in magnetic fluids. If magnetization M of the magnetic particles is independent of temperature, then the first term of equations (3.11) and (3.16) vanishes, and the equations governing the transport of vorticity in a magnetic fluid become the same as those governing the transport of vorticity in non-magnetic suspensions.

If the temperature gradient ∇T vanishes or if the magnetic field gradient ∇H vanishes or if ∇T is parallel to ∇H , then also the first term in (3.11) and (3.16) vanishes. We thus see that the transport of vorticity in a magnetic fluid is also the same as the transport of vorticity in non-magnetic suspension.

Acknowledgements

The authors are grateful to the learned referee for his useful technical comments and valuable suggestions, which led to a significant improvement of the paper.

References

1. BHATIA P.K., STEINER J.M., 1972, Convective instability in a rotating viscoelastic fluid layer, *Zeitschrift für Angewandte Mathematik und Mechanik*, **52**, 321-324
2. GARG A., SRIVASTAVA R.K., SINGH K.K., 1994, Drag on a sphere oscillating in conducting dusty Rivlin-Ericksen elastico-viscous liquid, *Proceedings of the National Academy of Sciences, India*, **64A**, 355-361
3. KUMAR P., LAL R., SINGH M., 2007, Hydrodynamic and hydromagnetic stability of two stratified Rivlin-Ericksen elastico-viscous superposed fluids, *International Journal of Applied Mechanics and Engineering*, **12**, 645-653
4. KUMAR P., SINGH G.J., 2006, Stability of two superposed Rivlin-Ericksen viscoelastic fluids in the presence of suspended particles, *Romanian Journal of Physics*, **51**, 927-935
5. RIVLIN R.S., ERICKSEN J.L., 1955, Stress-deformation relaxations for isotropic materials, *Archive for Rational Mechanics and Analysis*, **4**, 323-425
6. ROSENSWEIG R.E., 1997, *Ferrohydrodynamics*, Dover Publications, Inc. Mineola, New York
7. SAFFMAN P., 1962, On the stability of a laminar flow of a dusty gas, *Journal of Fluid Mechanics*, **13**, 120-128

8. SHARMA R.C., 1976, Effect of rotation on thermal instability of a viscoelastic fluid, *Acta Physica Hungarica*, **40**, 11-17
9. SHARMA R.C., KUMAR P., 1996, Effect of rotation on thermal instability in Rivlin-Ericksen elastico-viscous fluid, *Zeitschrift für Naturforschung*, **51a**, 821-824
10. SHARMA R.C., KUMAR P., 1997a, Hydromagnetic stability of Rivlin-Ericksen elastico-viscous superposed conducting fluids, *Zeitschrift für Naturforschung*, **52a**, 528-532
11. SHARMA R.C., KUMAR P., 1997b, Thermal instability in Rivlin-Ericksen elastico-viscous fluid in hydromagnetics, *Zeitschrift für Naturforschung*, **52a**, 369-371
12. VEST C.M., ARPACI V.S., 1969, Overstability of a viscoelastic fluid layer heated from below, *Journal of Fluid Mechanics*, **36**, 613-619
13. WAGH D.K., 1991, A mathematical model of magnetic fluid considered as two-phase system, *Proceedings of International Symposium on Magnetic Fluids*, R.E.C. Kurukshetra (Edit.), India, Sept. 21-23, 182
14. WAGH D.K., JAWANDHIA A., 1996, Transport of vorticity in magnetic fluid, *Indian Journal of Pure and Applied Physics*, **34**, 338-340
15. YAN Y., KOPLIK J., 2009, Transport and sedimentation of suspended particles in inertial pressure-driven flow, *Physics of Fluids*, **21**, 013301

Manuscript received December 24, 2014; accepted for print July 13, 2015

THREE-DIMENSIONAL THERMAL BUCKLING ANALYSIS OF FUNCTIONALLY GRADED CYLINDRICAL PANELS USING DIFFERENTIAL QUADRATURE METHOD (DQM)

SEYED A. AHMADI, HADI POURSHAHSAVARI

Babol University of Technology, Department of Mechanical Engineering, Babol, Iran

e-mail: ali_ahmadi1366@yahoo.com

Thermal buckling analysis of functionally graded cylindrical panels subjected to various conditions is discussed in this paper. Buckling governing equations are solved using the differential quadrature method. It is assumed that the mechanical properties of the panel are graded through thickness according to a power function of the thickness variable. The panel is assumed to be under the action of three types of thermal loading including uniform temperature rise and variable temperature rise in the axial and radial direction. In the present study, the effects of power law index, panel angle, different thermal load conditions and geometric parameters on the buckling behavior of functionally graded curved panels are studied. The results obtained through the present method are compared to the finite element solutions and the reported results in the literature. A desirable compatibility is concluded.

Keywords: thermal buckling, curved panel, functionally graded material, differential quadrature method

1. Introduction

Due to special mechanical properties, circular cylindrical panels are widely used in engineering structures such as pressure vessels, nuclear reactors, spacecrafts and jet engine exhausts. Due to the increasing demands for heat-resisting, energy absorbing, light-weight elements and high structural performance requirements in extremely high temperature environments and high-speed industries such as fusion reactors, aircraft and aerospace structures the use of special materials with high thermal and mechanical resistance has gained much popularity by many researchers. The applications of functionally graded materials (FGMs) have attracted much attention in the past two decades since they were first reported by Koizumi (1993). FGMs are composite materials, microscopically inhomogeneous, in which mechanical properties vary smoothly and continuously from one surface to the other. The main advantage of FGMs is that the ceramic component provides high temperature resistance due to its low thermal conductivity while the metal component prevents fracture induced by thermal stresses due to the high-temperature gradient in a very short period of time. When these are subjected to a thermal loading, the determination of thermal buckling capacity of these structures is important to achieve an optimized design in cost and weight.

Buckling analyses of various structures were carried out by many researchers. A review of research on the buckling response of plates and shells in a temperature environment was presented by Thornton (1993). He did some research on thermal buckling of plates and shells. In his work, he described elastic thermal buckling of metallic as well as composite plates and shells. Murphy and Ferreira (2001) investigated thermal buckling analysis of imperfect flat plates based on the energy consideration. They showed the ratio of the critical temperature for a perfect rectangular plate to that of an imperfect plate as a function of the initial imperfection amplitude. Mahayni (1966) studied thermal buckling behavior of doubly curved isotropic panels using Galerkin's

method. Chang and Chui (1991) carried out bifurcation buckling analysis of composites under the action of uniform temperature change using higher order transverse shear deformation theory and the finite element method. Earlier, the Differential Quadrature Method introduced by Jang *et al.* (1989), was applied only to rectangular plates and lately it was considered for shells. Mirfakhraei and Redekop (1998) used the Differential Quadrature Method to study buckling behavior of circular cylindrical shells. Alibeigloo and Kani (2010) and Haftchenari *et al.* (2007) used this method to study cylindrical shells as well.

The study of structures of functionally graded materials has received considerable attention in recent years. Buckling of functionally graded plates under thermal loads was studied by Javaheri and Eslami (2002b). They used classical plate theory and obtained nonlinear equilibrium and linear stability equations using variational formulations. Shahsiah and Eslami (2003) considered effects of various temperature distributions on thermal buckling of simply supported FG cylindrical shells, using the first order shear deformation theory, however the temperature dependency of material properties was not included. Thermoelastic stability of FG cylindrical shells subjected to various thermal load conditions was studied by Wu *et al.* (2005). Thermal buckling analysis of functionally graded plates considering simply supported boundary conditions by using the first shear deformation theory was carried out by Wu (2004). He reached the stability equation of functionally graded shells using Donnell's shell theory and presented its closed-form solution. Buckling analysis of FG plates using a higher order theory was presented by Javaheri and Eslami (2002a). It was shown that higher order shear deformation theory accurately predicts the buckling behavior, whereas the classical plate theory overestimates the critical loads. Breivik (1997) discussed the buckling response of composite cylindrical panels under the action of mechanical and thermal loading. Zhao *et al.* (2007) and Zhao and Liew (2010) used the element-free kp-Ritz method for thermal and mechanical buckling analysis of functionally graded cylindrical shells. They obtained three-dimensional buckling equations of the shell based on the Donnell shell theory and presented a closed form solution to predict buckling loads caused by thermal loads and critical edge displacement in the longitudinal direction.

In this paper, buckling analysis of cylindrical panels made of a functionally graded material subjected to three types of thermal loading is investigated. To obtain the buckling load of the cylindrical panels, the Differential Quadrature Method (DQM) is used to discretize differential equations obtained based on the second Piola-Kirchhoff stress tensor using three-dimensional theory of elasticity by Akbari Alashti and Ahmadi (2014). The material properties are assumed to be temperature independent and vary continuously along the thickness according to a power law function while Poisson's ratio of the material is taken to be constant. Effects of various parameters including panel curvature, grading index, various thermal load conditions and geometric ratios on the buckling behavior of the curved panels are investigated. Numerical results are validated against finite element calculations and results that are available in the offered literature.

2. Governing equation for buckling

Consider a thick cylindrical panel made of ceramic and metallic materials with the inner radius R_1 , mid-surface radius a , thickness h and length L . The geometric parameters and the cylindrical coordinate system. i.e. r , θ and x -coordinates are shown in Fig. 1.

The components of the displacement field in this coordinate system are expressed as w , v and u , respectively. Assume that the material is isotropic, inhomogeneous with Young's modulus varying continuously in the thickness direction, i.e. from ceramic in the inner layer to metallic in the outer layer according to the following formula

$$V_m = \left(\frac{2z + h}{2h} \right)^K \quad V_c + V_m = 1 \quad (2.1)$$

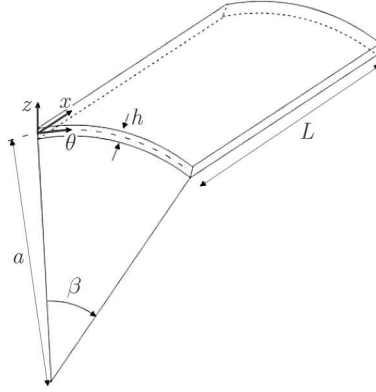


Fig. 1. Geometry of a cylindrical panel

where V_c and V_m represent the volume fractions of the ceramic and metallic constituent and K denotes the volume fraction index that indicates the material variation profile through the FG shell thickness. Thus, the Young modulus in the radial direction is assumed to vary according to the power law in the following forms

$$E(z) = E_c + E_{mc} \left(\frac{2z + h}{2h} \right)^K \quad E_{mc} = E_m - E_c \quad (2.2)$$

where E_m and E_c denote the elastic modulus of the metal and ceramic, respectively. The material composition varies smoothly from the outer surface ($z = h/2$) of the shell as metal to the inner surface ($z = -h/2$) as ceramic. Material properties of the shell are assumed to be independent of the temperature field and Poisson's ratio is considered to be constant throughout the thickness of the shell.

In order to calculate buckling loads of panels, the buckling equations obtained by Akbari Alashti and Ahmadi (2014) are used.

In this work, also the finite element linear or bifurcation buckling analysis of the cylindrical panel using ANSYS suite of program is carried out. The eigen buckling analysis predicts theoretical buckling strength of a shell made of a linear elastic material. This analysis is used to predict the bifurcation point on an $F-U$ diagram using a linearized model of the elastic structure. It is a technique used to determine buckling pressures at which the structure becomes unstable and their corresponding buckling mode shapes. The basic form of the eigen buckling analysis is

$$\mathbf{K}\phi = \lambda_i \mathbf{S}\phi \quad (2.3)$$

where \mathbf{K} , ϕ_i , λ_i and \mathbf{S} are the structural stiffness matrix, eigenvector, eigenvalues and stress stiffness matrix, respectively.

Eight noded quadrilateral shell elements, namely Shell281, are used to model the thick cylindrical shell. The elements can handle membrane, bending and transverse shear effects and are able to form the curvilinear surface satisfactorily. The elements are suitable for modeling of the layer and have the stress stiffening, large deflection and large strain capabilities.

Boundary conditions of shell panels are defined using equilibrium equations. For the initial and perturbed equilibrium positions, we have

$$\begin{aligned} \sigma_{rr} \left(a + \frac{h}{2}, \theta \right) = \sigma_{rr} \left(a - \frac{h}{2}, \theta \right) = 0 & \quad \tau_{r\theta} \left(a + \frac{h}{2}, \theta \right) = \tau_{r\theta} \left(a - \frac{h}{2}, \theta \right) = 0 \\ \tau_{rx} \left(a + \frac{h}{2}, \theta \right) = \tau_{rx} \left(a - \frac{h}{2}, \theta \right) = 0 & \end{aligned} \quad (2.4)$$

Boundary conditions at the panel edges are defined as:

— up and down edge, $x = 0, L$

$$\begin{aligned} \text{Simply supported:} \quad & w = v = \sigma'_{xx} = 0 \\ \text{Clamped:} \quad & w = v = u = 0 \end{aligned} \quad (2.5)$$

— lateral edges, $\theta = 0, \beta$

$$\begin{aligned} \text{Simply supported:} \quad & w = \sigma'_{\theta\theta} = u = 0 \\ \text{Clamped:} \quad & w = v = u = 0 \end{aligned} \quad (2.6)$$

3. Calculation of buckling load

In this work, two types of panels are considered:

Case 1. The panel is assumed to be simply supported at lateral edges and clamped at two ends. Therefore, thermal variation causes no axial stress on the panel, $N_\theta = 0$.

Case 2. We assume that the panel has clamped boundary conditions at all edges. For this case thermal loading cause axial and circumferential stresses at the panel walls, $N_x \neq 0$, $N_\theta \neq 0$.

By substituting the components of the displacement field in the stress-strain and linear strain-displacement equations and the resulted expression in the buckling equations, the equilibrium equations are defined in terms of components of the displacement field.

In the present work, a polynomial expansion based on the Differential Quadrature Method applied by Bellman and Casti (1971) is used to discretize and solve the obtained buckling equations. According to this method, the first order derivative of the function $f(x)$ can be approximated as a linear sum of all functional values in the domain

$$\left. \frac{df}{dx} \right|_{x=x_i} = \sum_{j=1}^N w_{ij}^{(1)} f(x_j) \quad \text{for } i = 1, 2, \dots, N \quad (3.1)$$

where $w_{ij}^{(1)}$ is the weighting coefficient and N denotes the number of grid points x_i in the domain. There are different methods for calculation of the weighting coefficients matrix, see Shu (2000). Here, the weighting coefficients of the first order derivatives are defined based on the Lagrange interpolation polynomials as

$$w_{ij}^{(1)} = \frac{M^{(1)}(x_i)}{(x_i - x_j)M^{(1)}(x_j)} \quad \text{for } i \neq j \quad w_{ii}^{(1)} = \frac{M^{(2)}(x_i)}{2M^{(1)}(x_j)} \quad (3.2)$$

where

$$M^{(1)}(x_i) = \prod_{\substack{k=1 \\ k \neq i, j}}^N (x_i - x_k) \quad N(x_i, x_j) = M^{(1)}(x_i)\delta_{ij} \quad (3.3)$$

$$M^{(2)}(x) = N^{(2)}(x, x_k)(x - x_k) + 2N^{(1)}(x, x_k)$$

and for higher order derivatives, we have

$$\begin{aligned} w_{ij}^{(r)} &= r \left(w_{ij}^{(1)} w_{ii}^{(r-1)} - \frac{w_{ij}^{(r-1)}}{x_i - x_j} \right) \quad \text{for } i, j = 1, 2, \dots, N \quad r = 2, 3, \dots, N - 1 \\ w^{(r)}_{ii} &= - \sum_{j=1, j \neq i}^N w^{(r)}_{ij} \end{aligned} \quad (3.4)$$

Now, applying the above formulation to the buckling equations, we have

$$\begin{aligned}
 & \mathcal{G}_2 \sum_{l=1}^N a_{i,l}^{(2)} w_{l,j,k} + \frac{\mathcal{G}_2}{r} \sum_{l=1}^N a_{i,l}^{(1)} w_{l,j,k} + G(z) \sum_{n=1}^Q b_{j,n}^{(2)} w_{i,n,k} + \mathcal{G}_1 \sum_{l=1}^N \sum_{n=1}^Q a_{i,l}^{(1)} b_{j,n}^{(1)} u_{l,n,k} \\
 & - \frac{\mathcal{G}_2}{r^2} w_{i,j,k} + \frac{\mathcal{G}_1}{r} \sum_{l=1}^N \sum_{m=1}^M a_{i,l}^{(1)} c_{k,m}^{(1)} v_{l,j,m} + \frac{G(z)}{r^2} \sum_{m=1}^M c_{k,m}^{(2)} w_{i,j,m} + \frac{\mathcal{G}_3}{r^2} \sum_{m=1}^M c_{k,m}^{(1)} v_{i,j,m} \\
 & + \sigma_x^0 \sum_{n=1}^Q b_{j,n}^{(2)} w_{i,n,k} + \sigma_{\theta\theta}^0 \frac{2}{r^2} \sum_{m=1}^M c_{k,m}^{(1)} v_{i,j,m} + \sigma_{\theta\theta}^0 \frac{1}{r^2} B_{i,j,k} - \sigma_{\theta\theta}^0 \frac{1}{r^2} \sum_{m=1}^M c_{k,m}^{(2)} w_{i,j,m} = 0 \\
 & G(z) \sum_{l=1}^N a_{i,l}^{(2)} v_{l,j,k} + \frac{\mathcal{G}_1}{r} \sum_{l=1}^N \sum_{m=1}^M c_{k,m}^{(1)} a_{i,l}^{(1)} w_{l,j,m} + \frac{\mathcal{G}_3}{r^2} \sum_{m=1}^M c_{k,m}^{(1)} w_{i,j,m} + G(z) \sum_{n=1}^Q b_{j,n}^{(2)} v_{i,n,k} \\
 & + \frac{G(z)}{r} \sum_{l=1}^N a_{i,l}^{(1)} v_{l,j,k} - \frac{G(z)}{r^2} v_{i,j,k} + \frac{\mathcal{G}_2}{r^2} \sum_{m=1}^M c_{k,m}^{(2)} v_{i,j,m} + \frac{\mathcal{G}_1}{r} \sum_{n=1}^Q \sum_{m=1}^M c_{k,m}^{(1)} b_{j,n}^{(1)} u_{i,n,m} \quad (3.5) \\
 & + \sigma_x^0 \sum_{n=1}^Q b_{j,n}^{(2)} v_{i,n,k} - \sigma_{\theta\theta}^0 \frac{2}{r^2} \sum_{m=1}^M c_{k,m}^{(1)} w_{i,j,m} + \sigma_{\theta\theta}^0 \frac{1}{r^2} v_{i,j,k} - \sigma_{\theta\theta}^0 \frac{1}{r^2} \sum_{m=1}^M c_{k,m}^{(2)} v_{i,j,m} = 0 \\
 & G(z) \sum_{l=1}^N a_{i,l}^{(2)} u_{l,j,k} + \mathcal{G}_2 \sum_{n=1}^Q b_{j,n}^{(2)} v_{i,n,k} + \mathcal{G}_1 \sum_{l=1}^N \sum_{n=1}^Q b_{j,n}^{(1)} a_{i,l}^{(1)} w_{l,n,k} + \frac{G(z)}{r} \sum_{l=1}^N a_{i,l}^{(1)} u_{l,j,k} \\
 & + \frac{G(z)}{r^2} \sum_{m=1}^M c_{k,m}^{(2)} u_{i,j,m} + \frac{\mathcal{G}_1}{r} \sum_{m=1}^M c_{k,m}^{(1)} v_{i,j,m} + \frac{\mathcal{G}_1}{r} \sum_{n=1}^Q b_{j,n}^{(1)} w_{i,n,k} \\
 & + \sigma_x^0 \sum_{n=1}^Q b_{j,n}^{(2)} u_{i,n,k} - \sigma_{\theta\theta}^0 \frac{1}{r^2} \sum_{m=1}^M c_{k,m}^{(2)} u_{i,j,m} = 0
 \end{aligned}$$

where

$$\mathcal{G}_1 = G(z) + \lambda(z) \quad \mathcal{G}_2 = 2G(z) + \lambda(z) \quad \mathcal{G}_3 = 3G(z) + \lambda(z)$$

and $a_{ij}^{(k)}$, $b_{ij}^{(k)}$ and $c_{ij}^{(k)}$ denote the weighting coefficients of the k -th order derivative in the r , θ and x -direction, respectively; N , Q and M are grid point numbers in the r , θ and x -direction, respectively. The critical value of the buckling load is obtained by solving the set of equations presented in the matrix form as

$$\begin{bmatrix} \mathbf{B}_B & \mathbf{B}_D \\ \mathbf{D}_B & \mathbf{D}_D \end{bmatrix} \begin{bmatrix} d_b \\ u \\ v \\ w \end{bmatrix} = \sigma \begin{bmatrix} 0 & 0 \\ \mathbf{D}_{BG} & \mathbf{D}_{DG} \end{bmatrix} \quad (3.6)$$

where the sub-matrices \mathbf{B}_B , \mathbf{B}_D and \mathbf{D}_{BG} , \mathbf{D}_D , \mathbf{D}_B , \mathbf{D}_{DG} are found from the boundary conditions and governing equations, respectively. Equation (3.6) is transformed into the standard eigenvalue equation, as

$$\left(-\mathbf{D}_{BG} \mathbf{B}_B^{-1} \mathbf{B}_D + \mathbf{D}_{DG} \right)^{-1} \left(-\mathbf{D}_B \mathbf{B}_B^{-1} \mathbf{B}_D + \mathbf{D}_D \right) [u \ v \ w]^T - \sigma \mathbf{I} [u \ v \ w]^T = 0 \quad (3.7)$$

from which, the eigenvalues of σ can be found. The smallest value of σ is found to be the buckling load.

4. Thermal loading

4.1. Uniform temperature rise

The temperature changes uniformly through the thickness and remains constant in the longitudinal and circumferential directions of the panel. This thermal variations induces only normal stress, and the parameter Φ is defined as

$$\sigma = \frac{N}{h} \quad N = -\frac{\Phi}{1-\nu} \quad (4.1)$$

and

$$\begin{aligned} \Phi &= \int_{-\frac{h}{2}}^{\frac{h}{2}} \left[E_m + E_{cm} \left(\frac{2z+h}{2h} \right)^K \right] \left[\alpha_m + \alpha_{cm} \left(\frac{2z+h}{2h} \right)^K \right] \Delta T(x, \theta, z) dz \\ \Rightarrow \Phi &= \left(E_c \alpha_c h + \frac{[E_c(\alpha_m - \alpha_c) + \alpha_c(E_m - E_c)]h}{K+1} + \frac{(\alpha_m - \alpha_c)(E_m - E_c)h}{2K+1} \right) \Delta T_{cr} \end{aligned} \quad (4.2)$$

Substituting buckling stress obtained by numerical solution into Eq. (4.1) and (4.2), helps us to obtain the thermal buckling load ΔT_{cr} .

4.2. Non-uniform temperature rise in the axial direction

In this case, the assumed temperature varies in the longitudinal direction according to the following formula

$$T = \Delta T \left(\frac{x}{L} \right)^n + T_m \quad \Delta T = T_c - T_m \quad n > 0 \quad (4.3)$$

where T_m is the temperature at the metal surface of the panels. According to the above equations, axial stresses caused by the temperature rise have the same variation in this direction. The critical stresses are obtained by considering the effects of this loading in the discretized governing equations and then, the buckling temperatures are achieved using equations (4.1) and (4.2).

4.3. Non-uniform temperature rise in the radial direction

The functionally graded materials are designed in order to resist against high temperature rise by ceramic, so the temperature change will be quite different at the two sides of FGM structures. The temperature distribution across the thickness is a function of the z coordinate as follows

$$T = \Delta T \left(-\frac{z}{h} + \frac{1}{2} \right)^q + T_m \quad -\frac{h}{2} < z < \frac{h}{2} \quad \Delta T = T_c - T_m \quad (4.4)$$

The parameter Φ is defined as

$$\Phi = \int_{-\frac{h}{2}}^{\frac{h}{2}} \left[E_m + E_{cm} \left(\frac{2z+h}{2h} \right)^K \right] \left[\alpha_m + \alpha_{cm} \left(\frac{2z+h}{2h} \right)^K \right] \left[\Delta T \left(-\frac{z}{h} + \frac{1}{2} \right)^q + T_m \right] dz \quad (4.5)$$

The buckling temperature rise will be obtained using equation (4.1). For example, for $q = 1$, the parameter Φ is given as

$$\begin{aligned} \Phi &= \left(E_c \alpha_c h + \frac{[E_c(\alpha_m - \alpha_c) + \alpha_c(E_m - E_c)]h}{K+1} + \frac{(\alpha_m - \alpha_c)(E_m - E_c)h}{2K+1} \right) T_m \\ &+ \frac{h}{(K+1)(K+2)(2K+1)} \left\{ E_c \alpha_c K^3 + \frac{7}{2} E_c \alpha_c K^2 \right. \\ &\left. + \alpha_c K \left[2 \left(\frac{E_m - E_c}{4} + E_c \right) (\alpha_m - \alpha_c) + \left(2(E_m - E_c) + \frac{7}{2} E_m \right) \right] + E_m \alpha_m \right\} \Delta T_{cr} \end{aligned} \quad (4.6)$$

5. Numerical results and discussion

In order to illustrate the results of the presented method for an inhomogeneous shell, a functionally graded cylindrical shell made of aluminum and alumina is considered. Young's modulus is assumed to be temperature independent and vary smoothly in the radial direction according to a power law distribution of the volume fraction of the constituent materials. Young's modulus for alumina at the inner surface and for aluminum at the outer surface is assumed to be $E_c = 380$ GPa and $E_m = 70$ GPa, respectively. It is also assumed that Possion's ratios of the constituent materials are constant and equal to 0.3. At the first step, the buckling temperatures calculated by the present study are validated against the results reported in the literature.

Figures 2 and 3 plot the critical temperature changes of the complete shell with $L = a = 1$ against the ratio of the thickness to mid surface radius of the shell h/a for the uniform temperature rise loading. The results are compared to the finite element results and those reported by Breivik (1997).

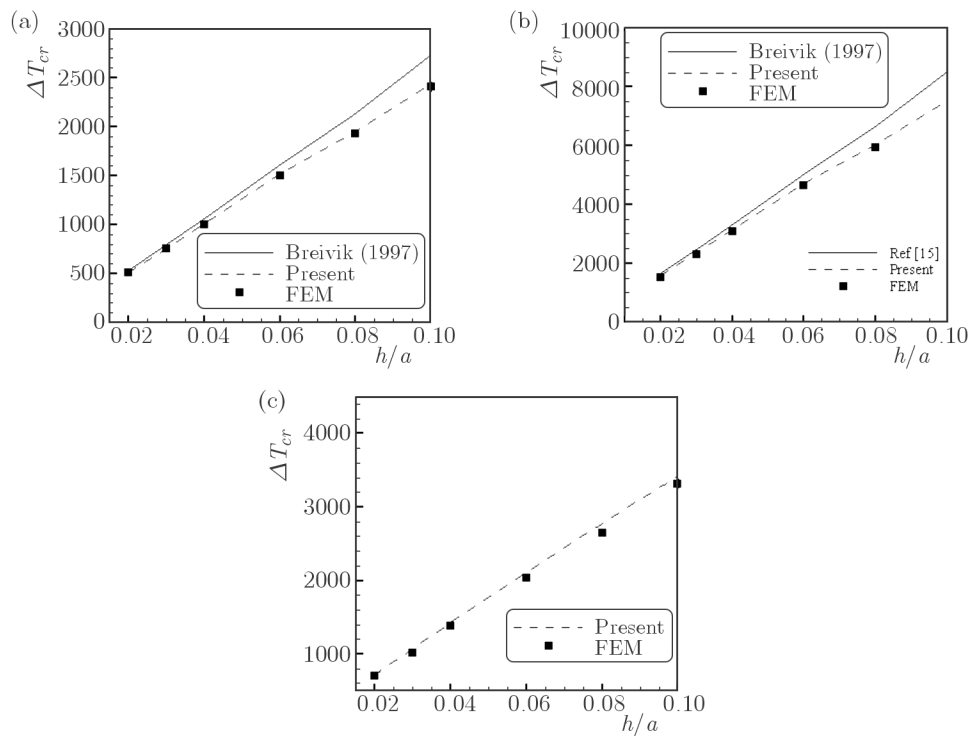


Fig. 2. Comparisons of the critical temperature of the complete shell under uniform temperature rise, (a) aluminum, (b) alumina, (c) functionally graded shell $K = 1$

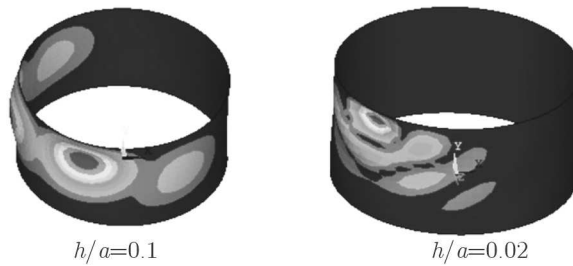


Fig. 3. Buckling mode shapes of complete shells made of aluminum under uniform temperature rise

It is evident that the results of the presented method are in good agreement with the finite element results and those of Breivik (1997). It can be seen from these figures that the critical

buckling temperature increases linearly as the ratio of h/a increases, and also the difference between the results increases when the relative thickness grows. It is because of the fact that Breivik (1997) used Donnell's theory to obtain the buckling equation of the thin shell. This equation creates an overestimation in the prediction of buckling load for a thick shell. The effects of panel angle on the buckling temperature are shown in Fig. 4. The results are compared to the results reported by Wu *et al.* (2005). The results are obtained for the panel (case 1) under uniform and non-uniform temperature rise in the radial direction, and the panel is assumed to be made of aluminum with $a = 1$ m, $L/a = 1$ and $h/a = 0.02$.

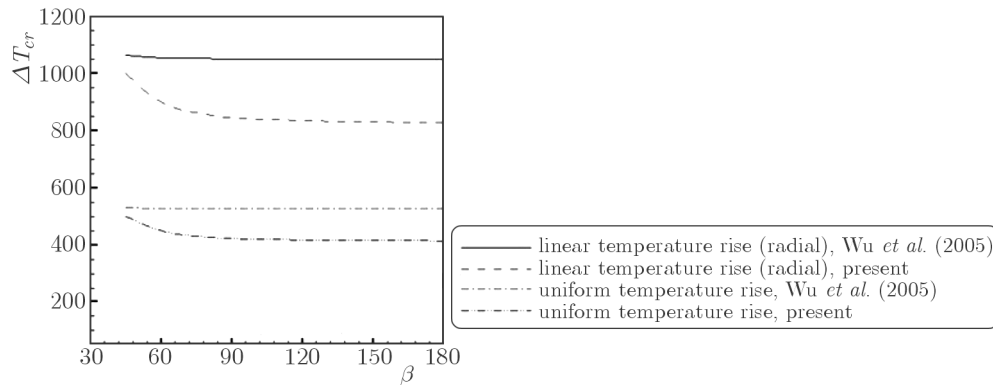


Fig. 4. Comparisons of the critical temperature of the homogeneous panel (case 1) made of aluminum with different angles ($T_m = 0$)

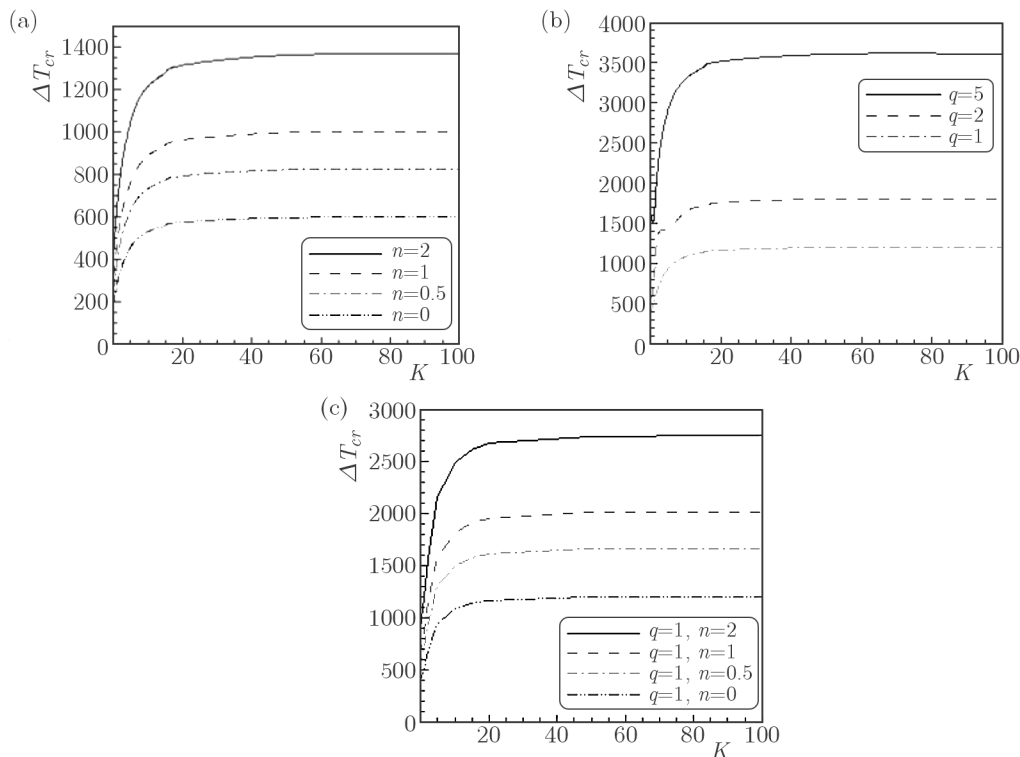


Fig. 5. Effect of the volume fraction index K on the buckling temperature of the panel (case 1), non-uniform temperature rise in: (a) axial direction, (b) radial direction, (c) combined loading ($T_m = 0$)

To make calculations following Wu *et al.* (2005), the critical stress is obtained first through the given formula and then substituted into Eq. (4.6). It can be inferred from Fig. 4 that the buckling temperature changes decrease when the panel angle increases, and for higher angles the

results approach constant values. The results obtained based on Donnell's theory and obtained by Wu *et al.* (2005), show low variation of the buckling load versus panel angles.

Next, variation of the critical buckling temperature for the panel (case 1) with $L = a = 1$ m, $h = 0.01$ m and $\beta = 1$ rad under non-uniform temperature loading versus material gradient index K , are presented.

It is obvious from Fig. 5 that as the material gradient index K increases from 1 to 10, the critical buckling temperature grows rapidly and, for higher values, the results approach constant values. It is also evident that the critical buckling temperatures increase as the value of K increases. The main reason for such an increase is the fact that a higher value of K corresponds to a ceramic-rich panel, which usually has a higher thermal strength than a metal-rich one. Figure 6 shows the buckling temperature versus the ratio of h/a for the panel (case 1) with $L = 1$ m and $\beta = 1$ rad for three types of loading, i.e. uniform temperature rise and non-uniform temperature rise in the axial and radial direction. Buckling modes obtained through the finite element program for the uniform temperature rise are illustrated in Fig. 7.

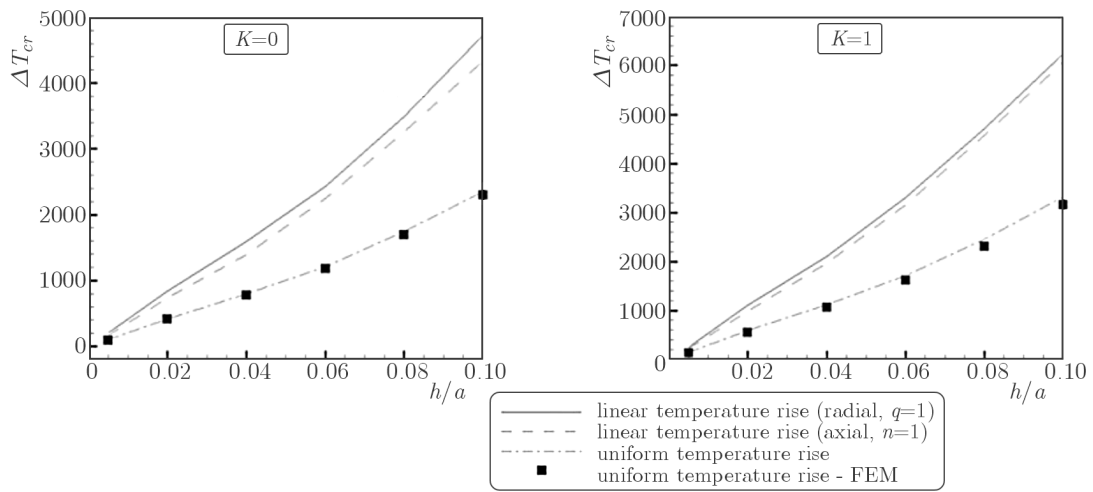


Fig. 6. Buckling temperature of the panel (case 1) versus h/a ($T_m = 0$)

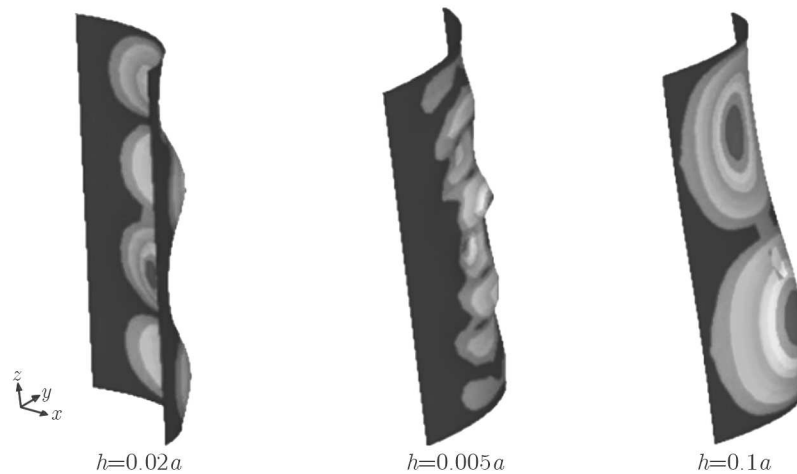


Fig. 7. Buckling mode shapes of the inhomogeneous ($K = 1$) panel (case 1)

It can be observed in Fig. 7 that when the thermal loading has a linear variation, the buckling temperature rises significantly. Then, the critical buckling temperatures with respect to the panel are plotted for the cylindrical panel with different temperatures at the outer surface under the action of non-uniform temperature rise in the radial direction. Assuming that the panel has

$L = a = 1$ m, $h = 0.01$ m and $\beta = 1$ rad, it is found that the variation of the outer surface temperature has a significant effect on the buckling temperature of the panel.

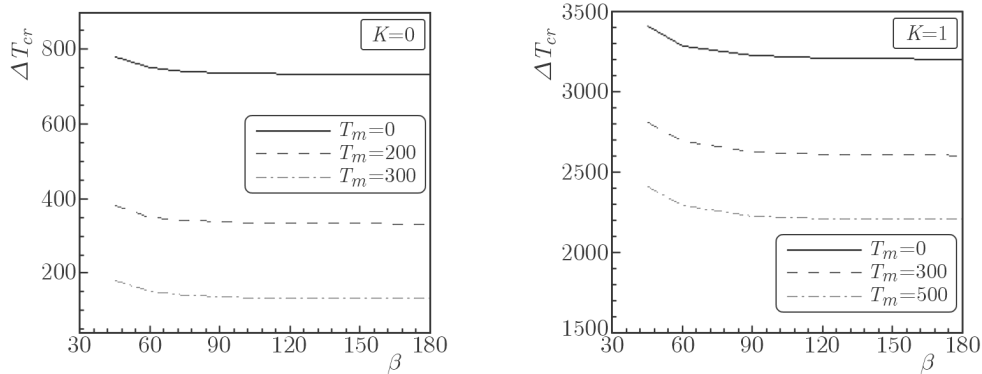


Fig. 8. Buckling temperature of the panel (case 1) versus β for various values of T_m

Figure 9 demonstrates variation of the buckling temperature change versus aspect ratio h/a of the panel (case 2). The results obtained through the present method are compared with the results obtained through the given governing equations in Breivik (1997). It should be noted that the buckling equations presented by Breivik (1997) are only solved for the shell (case 1), and here we resolve it for the panel (case 2) using equation (4.1).

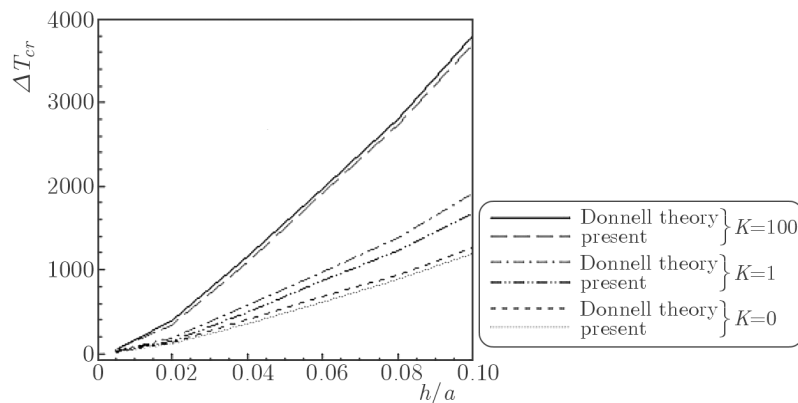


Fig. 9. Comparisons of the critical temperature of the panel (case 2) with different gradient indices under uniform temperature rise loading, $L = a = 1$ m, $\beta = 1$ rad ($T_m = 0$)

It is obvious that the results of the presented numerical method are in good agreement with the results issuing from Donnell's shell theory. As concluded above, the difference between the present results and those obtained based on Donnell's theory increase as the thickness of the panel grows. Buckling temperature changes against the thickness ratio for the panel (case 2) under the action of various loading conditions are illustrated in Figs. 10 and 11.

It can be found from Figs. 10 and 11 that the buckling temperature rises linearly when thickness of the panel increases. It is also clear that the critical buckling temperatures increase as the volume fractions of the ceramic increase. To study the effects of thermal loading variation in several directions and buckling temperature rises for the panel (case 2) with $L = a = 1$ m, $\beta = 0.8$ rad, $h = 0.005$ m versus the index K under combined temperature loadings are given in Table 1.

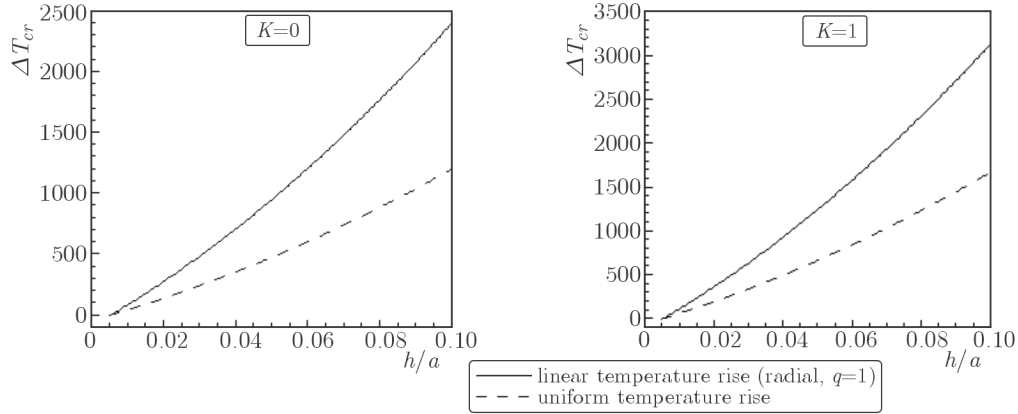


Fig. 10. Buckling temperature of panel (case 2) versus h/a for uniform temperature rise and non-uniform loading in the radial direction, $\beta = 0.8$ rad, $L/a = 1$

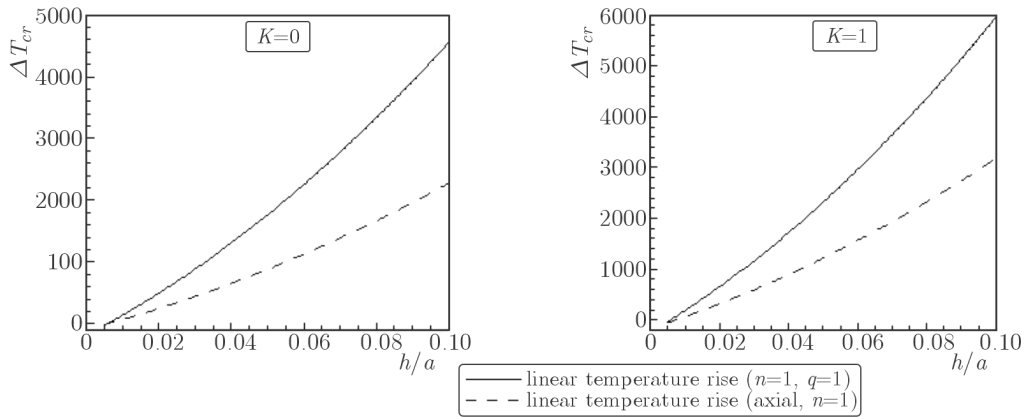


Fig. 11. Buckling temperature of the panel (case 2) versus h/a for non-uniform temperature rise in the axial and radial direction, $\beta = 0.8$ rad, $L/a = 1$

Table 1. Buckling temperature of the panel (case 2) versus K for combined load conditions

K	$n = 0$		$n = 0.5$		$n = 1$	
	$q = 0$	$q = 1$	$q = 0$	$q = 1$	$q = 0$	$q = 1$
0	13.8	27.6	19	38	24.9	49.8
1	18.7	35.1	26	48.9	34.1	64
2	14.2	47	33.4	65.8	43.7	86
5	31.9	65.6	44.3	89.8	57.6	118.8
10	37.7	77.3	52.9	107.5	68.7	140.1
20	41.5	84	57.8	117.3	75	152.5
50	42.9	86.5	59.4	119.7	77.3	156.1
100	43.2	87.6	59.8	119.8	77.6	156.8

6. Conclusion

In this paper, buckling analysis of FG cylindrical panels under the action of thermal loading is carried out. Material properties are assumed to be temperature-independent and graded through the simple power law distribution in terms of the volume fractions of the constituents. The Differential Quadrature Method is used to discretize and solve buckling equations. The buckling analysis of such panels under the action of three types of thermal loadings, i.e. uniform temperature rise and non-uniform temperature rise in the axial and radial direction considering two

types of boundary conditions, is carried out. From the present study, the following conclusions are drawn:

- Determination the critical loads by the use of equations extracted from Donnell's theory cause an overestimation when thickness of the panel increases. The results obtained by the three-dimensional buckling equations, as presented in this work, are more accurate in comparison with the results based on the Donnell shell theory.
- The critical buckling temperature T_{cr} increases linearly with an increase in the thickness to mid-surface radius ratio h/a .
- For functionally graded cylindrical panels under various thermal loads, an increase in the volume fraction of the ceramic constituent increases the critical load.

References

1. AKBARI ALASHTI R., AHMADI S.A., 2014, Buckling of imperfect thick cylindrical shells and curved panels with different boundary conditions under external pressure, *Journal of Theoretical and Applied Mechanics*, **52**, 1, 25-36
2. ALIBEIGLOO A., KANI A.M., 2010, 3D free vibration analysis of laminated cylindrical shell integrated piezoelectric layers using differential quadrature method, *Applied Mathematical Modeling*, **34**, 4123-4137
3. BELLMAN R.E., CASTI J., 1971, Differential quadrature and long term integration, *Journal of Mathematical Analysis and Applications*, **34**, 1, 235-238
4. BREIVIK N.L., 1997, Thermal and mechanical response of curved composite panels, Dissertation submitted to the Faculty of the Virginia Polytechnic Institute and State University in partial fulfillment of the requirements for the degree of doctor of Philosophy in engineering mechanics
5. CHANG J.S., CHUI W.C., 1991, Thermal buckling analysis of antisymmetric laminated cylindrical shell panels, *International Journal of Solids and Structures*, **27**, 1, 1295-1309
6. HAFTCHENARI H., DARVIZEH M., DARVIZEH A., ANSARI R., SHARMA C.B., 2007, Dynamic analysis of composite cylindrical shells using Differential Quadrature Method (DQM), *Composite Structures*, **78**, 292-298
7. JANG S.K., BERT C.W., STRIZ A.G., 1989, Application of differential quadrature to static analysis of structure components, *International Journal for Numerical Methods in Engineering*, **28**, 261-577
8. JAVAHERI R., ESLAMI M.R., 2002a, Thermal buckling of functionally graded plates based on higher order theory, *Journal of Thermal Stresses*, **25**, 603-625
9. JAVAHERI R., ESLAMI M.R., 2002b, Thermal buckling of functionally graded plates, *AIAA Journal*, **40**, 1, 162-169
10. KOIZUMI M., 1993, The concept of FGM, *Ceramic Transactions, Functionally Gradient Materials*, **34**, 3-10
11. MAHAYNI M.A., 1966, Thermal buckling of shallow shells, *International Journal of Solids and Structures*, **2**, 167-180
12. MIRFAKHRAEI P., AND REDEKOP D., 1998, Buckling of circular cylindrical shells by the differential quadrature method, *International Journal of Pressure Vessels and Piping*, **75**, 347-353
13. MURPHY K.D., FERREIRA D., 2001, Thermal buckling of rectangular plates, *International Journal of Solids and Structures*, **38**, 22/23, 3979-3994
14. SHAHSIAH R., ESLAMI M.R., 2003, Thermal buckling of functionally graded cylindrical shell, *Journal of Thermal Stresses*, **26**, 277-294
15. SHU C., 2000, *Differential Quadrature and its Application in Engineering*, Springer-Verlag, London, UK

16. THORNTON E.A., 1993, Thermal buckling of plates and shells, *Applied Mechanics Review*, **46**, 10, 485-506
17. WU L.H., 2004, Thermal buckling of a simply supported moderately thick rectangular FGM plate, *Composite Structures*, **64**, 2, 211-218
18. WU L., JIANG Z., LIU J., 2005, Thermoelastic stability of functionally graded cylindrical shells, *Composite Structures*, **70**, 60-68
19. ZHAO X., LIEW K.M., 2010, A mesh-free method for analysis of the thermal and mechanical buckling of functionally graded cylindrical shell panels, *Computational Mechanics*, **45**, 297-310
20. ZHAO X., YANG Y., LIEW K.M., 2007, Geometrically nonlinear analysis of cylindrical shells using the element-free kp-Ritz method, *Engineering Analysis with Boundary Elements*, **31**, 783-792

Manuscript received May 13, 2014; accepted for print July 15, 2015

MODELLING AND SIMULATION STUDIES ON THE MOBILE ROBOT WITH SELF-LEVELING CHASSIS

JACEK BAŁCHANOWSKI

Wrocław University of Technology, Faculty of Mechanical Engineering, Wrocław, Poland
e-mail: jacek.balchanowski@pwr.edu.pl

The mobile robot presented in the article is a hybrid system combining efficient travel on wheels on a flat terrain with the capability of surmounting obstacles by walking. The research is focused on designing a control system maintaining the robot chassis at a constant position to the ground. The aims of this research are: creation of the computational model of the control system for the levelling system of designed mobile robots and realization of simulation studies on the robots travel in terrain with obstacles. The simulations aimed at determination of basic dynamic and kinematic properties.

Keywords: mobile robot, simulation studies, self-leveling chassis

1. Introduction

The research on mobile robots has intensified in the recent years, especially to meet the demand for automating the transport process and for inspection (chemically, biologically) of contaminated areas and those exposed to hazard of fire explosions (Tchoń *et al.*, 2000; Trojnacki *et al.*, 2008).

Studies focused on mobile robots have been carried out in many research centers (universities, military and industrial centers). They deal with wheeled robots, walking robots, tracking robots, crawling robots, flying robots, floating robots and their hybrids. The research has been calculated on variety of such vehicles differing in their way of traveling: wheeled systems (WalkPartner, see Halme *et al.*, 2003), tracked systems (INSPECTOR Robot, see Hołdanowicz, 2008), walking systems (PetMan, see Boston Dynamic, 2014), floating and flying systems (Hermes® 900, see Elbit Systems, 2014).

The dominant contemporary form of vehicles motion is riding on wheels. In an urban area, where the surface is smooth, the wheels are the most effective. However, the biggest disadvantage is that they have no ability to overcome obstacles in form of a substrate discontinuity – curbs, stairs, slopes. The most common form of motion by living organisms of the Earth is treading. This type of transportation is especially effective with moving around non-urbanized irregular surfaces containing obstacles (Bałchanowski and Gronowicz, 2012a,b; Zielińska, 2003).

Mobile wheel-legged robots are hybrids that combine efficient travelling on a flat terrain by wheels with the capability of surmounting obstacles by walking. A major challenge in designing such systems is to develop its wheel suspension allowing the robot both to move on wheels and to walk, and automatically level its chassis during travelling on an uneven surface (Bałchanowski and Gronowicz, 2012a,b; Gronowicz and Szrek, 2009a,b; Szrek and Wójtowicz, 2010).

One such system is a wheel-legged mobile robot (Fig. 1) designed and built at Wrocław University of Technology (Bałchanowski, 2012; Bałchanowski and Gronowicz, 2012a,b). The robot is equipped with a unique wheel suspension which allows it to drive, walk, rise, lower and self-level the chassis. In this paper, the design of this device is described.

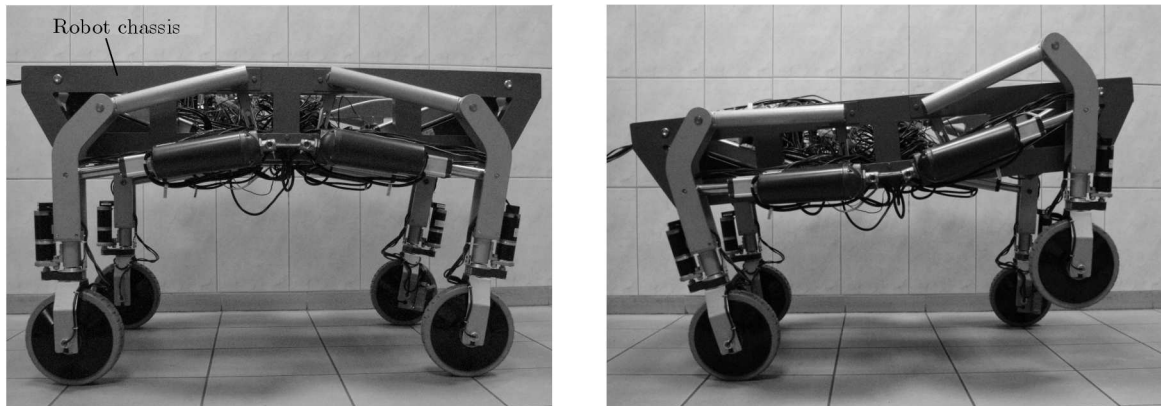


Fig. 1. A general view of a mobile robot and a view of the walking phase

2. Design of a mobile robot

In the framework of the project realized at Wrocław University of Technology the design of a robot whose schematic is shown in Fig. 2 has been developed. It is assumed that the wheels with suspensions are symmetrically arranged in relation to the longitudinal and transverse axis of the robot. Such a position of the wheels ensures a level playing field for driving of the front and rear axles. The major design challenge was to develop a suspension mechanism which should provide the robot with ability to walk with a view system to overcome obstacles on the track and enabling automatic self-levelling of the chassis (Fig. 3).

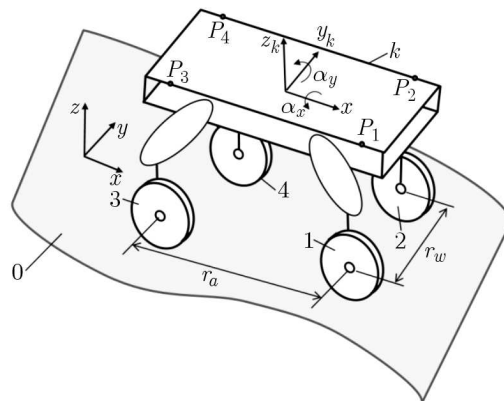


Fig. 2. A general scheme of the wheel-legged mobile robot (1-4 – wheel suspensions, 0 – ground, k – chassis)

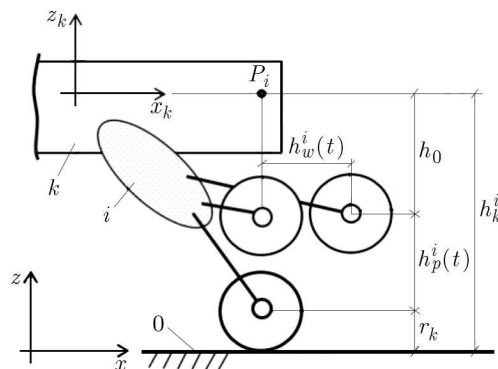


Fig. 3. A schematic showing the execution of suspension i motions: h_p^i – lifting, h_w^i – ejecting

Table 2. Main parameters of the drives

Actuator LINAK LA36		
	q_w, q_p (stroke length)	0.35-0.5 m
	v_w, v_p (speed)	0.068 m/s
	F_w, F_p (force)	1700 N
	m_s (mass)	4.9 kg
Wheel GOLDENMOTOR HUB24		
	dq_n/dt (angular velocity)	13.08 rad/s (125 rpm)
	M_n (nominal torque)	13.5 Nm
	k_r (radial stiffness)	$9.5 \cdot 10^5$ N/m
	m_k (mass)	5 kg
	r_k (radius of wheel)	0.105 m

the robot body above the ground according to the scheme shown in Figs. 2 and 3, which means maintaining the value of the given angles of orientation

$$\alpha_x = 0 \quad \alpha_y = 0$$

Raising or lowering the individual wheels can bring the robot to the assumed level. This function can be accomplished solely by lifting the chassis by means of the lifting actuators q_p^i (Fig. 4), while the other drives (ejection, turn and rolling) remain fixed.

For the given values of wheels radii r_k and suspension height h_0 , the height h_k^i of the robot chassis above the ground may be presented in the form (Fig. 3)

$$h_k^i = r_k + h_0 + h_p^i(q_p^i) \quad (2.1)$$

The graph in Fig. 5 shows changes of the height h_p^i for the suspension as a function of the actuator extension q_p^i (Bałchanowski and Gronowicz, 2012a,b,c). For the adopted actuator stroke $q_p^i = 0.35-0.5$ m (Table 2), the defined range of changes of the wheel lifting h_p^i is

$$0 \leq h_p^i \leq 0.26 \text{ m} = h_p \quad (2.2)$$

where h_p is the maximum height of the suspension lifting.

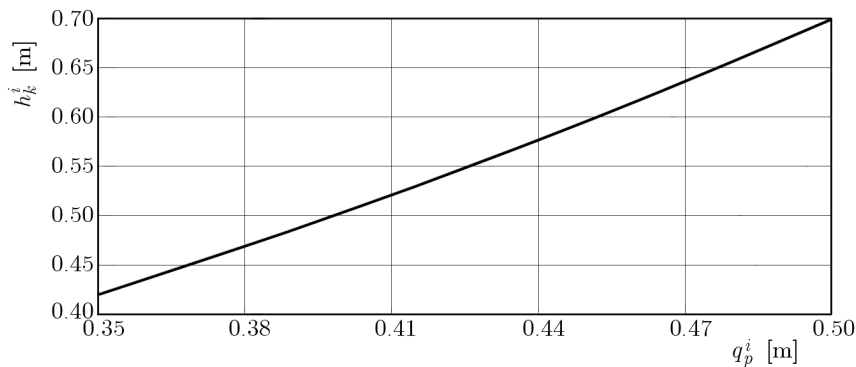


Fig. 5. Elevation of the robot chassis h_k^i versus extension of the lifting actuator q_p^i

The maximum value of the wheel lifting height h_p determines the possibility of overcoming a certain unevenness. The mechanism shown in side and front views on uneven ground is presented in Fig. 6. The maximum angles of the ground inclination α_x^{max} along the robot longitudinal x axis as well as α_y^{max} along the robot transverse y axis, can be determined from the relationship

$$\alpha_x^{max} = \arctan \frac{h_p}{r_w} = 21.8^\circ \quad \alpha_y^{max} = \arctan \frac{h_p}{r_a} = 18.0^\circ$$

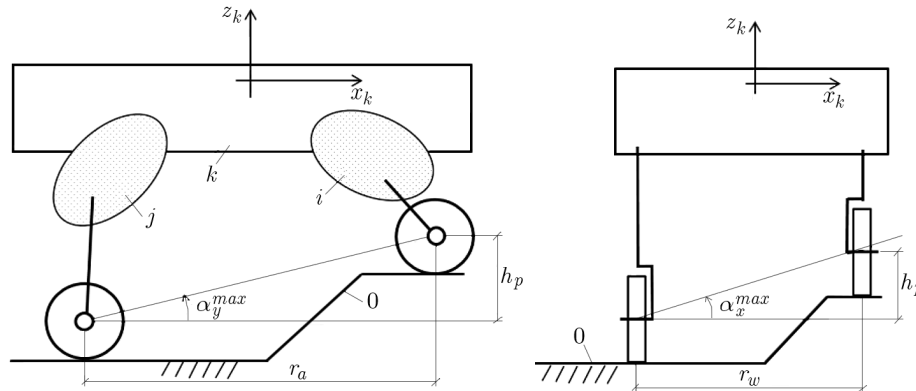


Fig. 6. Side and front views of the robot on uneven ground. The schematic shows the maximum angles of the ground inclination α_x^{max} and α_y^{max} along the robot longitudinal x and transverse y axis

If the area has larger values of the inclination angles, then the lifting mechanisms do not provide sufficient levelling of the chassis.

3. Numerical model of the mobile robot

In order to perform simulations, a computational model of the wheel-legged robot shown in Fig. 7, has been created in the LMS DADS (Haug, 1989) dynamic analysis system. The robot has 22 DOF, with the body having 6 DOF and each wheel suspension having 4 DOF relative to the body. Sixteen kinematic excitations are defined in the robot: 8 rotational excitations q_n^i and q_s^i (wheel rolling and turning) as well as 8 linear excitations q_p^i and q_w^i (wheel lifting and ejecting) for each suspension ($i = 1, 2, 3, 4$) (Bałchanowski, 2012; Bałchanowski and Gronowicz, 2012a,b).

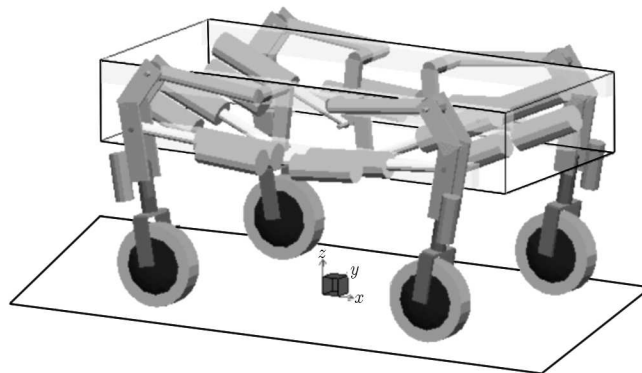


Fig. 7. The model of the wheel-legged mobile robot (main view)

The wheel/base interactions are modelled using a tire/ground interaction force model (TIRE) (Haug, 1989). The mass of the wheels is quite large due to the fact that the motor and gear are incorporated in the hub, and because of their high radial and longitudinal stiffness (Table 2).

The total weight (deadweight + payload) of the wheeled-legged robot is estimated at 100 kg. The mass and geometry of the suspension, wheel and actuator parts are assumed as in the design. The weight of the body (comprising deadweight of the frame bearer, steering system, batteries, current generator as well as payload) is appropriately matched to obtain the assumed total weight of 100 kg, with the center of gravity located in the body center.

3.1. Design of the control system for the levelling mechanism of the robot chassis

When the robot travels on an uneven substrate, the robot chassis changes its orientation relative to the ground. The changes in orientation of the chassis are described by the angles of inclination α_x (the angle of the body rotation relative to the robot transverse axis) and the steering angle α_y (the angle of the body rotation relative to the robot longitudinal axis, Fig. 2). In a real robot, both angles (Fig. 1) are measured using inclinometers (Bałchanowski and Gronowicz, 2012b; Gronowicz and Szrek, 2009a,b; Szrek and Wójtowicz, 2010).

The plane of the robot chassis will be twisted as a result of rotations α_x and α_y . The twisting can be described by means of h_1, h_2, h_3 and h_4 vertical displacements of points P_1, P_2, P_3 and P_4 (Figs. 2 and 8). For angles α_x, α_y , the position of points P_i in the global coordinate system xyz , described by the vector $\mathbf{r}_{P_i} = [x_{P_i}, y_{P_i}, z_{P_i}]^T$, can be calculated using the following formula

$$\mathbf{r}_{P_i} = \mathbf{A}_x \mathbf{A}_y {}^k \mathbf{r}_{P_i} \quad (3.1)$$

where i is the number of suspension, $i = 1, \dots, 4$, \mathbf{A}_x – matrices of rotation from the k -th system to the xyz system about the angle α_x along the x' axis, \mathbf{A}_y – matrices of rotation from the k -th system to the xyz system about the angle α_y along the y axis

$$\mathbf{A}_x = \begin{bmatrix} 1 & 0 & 0 & 0 \\ 0 & \cos \alpha_x & -\sin \alpha_x & 0 \\ 0 & \sin \alpha_x & \cos \alpha_x & 0 \\ 0 & 0 & 0 & 1 \end{bmatrix} \quad \mathbf{A}_y = \begin{bmatrix} \cos \alpha_y & 0 & \sin \alpha_y & 0 \\ 0 & 1 & 0 & 0 \\ -\sin \alpha_y & 0 & \cos \alpha_y & 0 \\ 0 & 0 & 0 & 1 \end{bmatrix}$$

and ${}^k \mathbf{r}_{P_i}$ – position vector of point P_i on the chassis in the $x_k y_k z_k$ coordinate system

$$\begin{aligned} {}^k \mathbf{r}_{P_1} &= [r_a/2, r_w/2, 0, 1]^T & {}^k \mathbf{r}_{P_2} &= [r_a/2, -r_w/2, 0, 1]^T \\ {}^k \mathbf{r}_{P_3} &= [-r_a/2, r_w/2, 0, 1]^T & {}^k \mathbf{r}_{P_4} &= [-r_a/2, -r_w/2, 0, 1]^T \end{aligned}$$

Finally, the value of h_i is described by the z_{P_i} coordinate of the vector \mathbf{r}_{P_i} from formula (3.1)

$$h_i = z_{P_i} \quad i = 1, \dots, 4 \quad (3.2)$$

In order to bring the robot chassis plane to the level, the points P_1, P_2, P_3 and P_4 need to be moved to the designated values of h_1, h_2, h_3, h_4 . The displacements h_i are the disruptions for the leveling control system of the robot chassis. The control system has to set the proper wheel elevation h_i using the linear actuators q_p^i to bring the robot chassis to the level ($\alpha_x = 0$ and $\alpha_y = 0$).

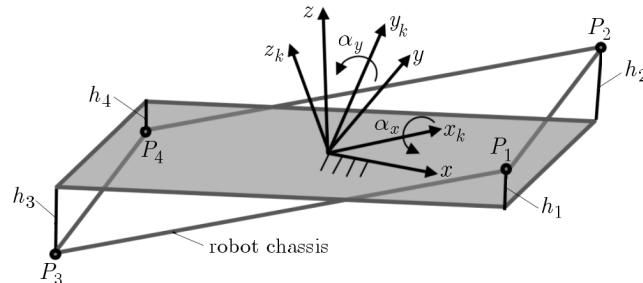


Fig. 8. The scheme of the robot chassis orientation angles

This requires controlling of only wheel lifting drives q_p^i i.e., forcing the suspension displacement of q_p^i by using forces F_p^i from the actuators.

For a mobile robot on four wheels equipped with mechanisms for raising and lowering, the all-wheel task of setting a specific orientation of the chassis for uneven ground can be realized in

many ways (Fig. 9) for different settings of the wheel height h_k^i in the permissible range of the stroke h_p . In the proposed algorithm of automatic positioning and orientation of the chassis, in order to obtain one solution, it is assumed that the suspensions of three wheels are active and the fourth one is the leading wheel with a predetermined height h_l (Fig. 10).

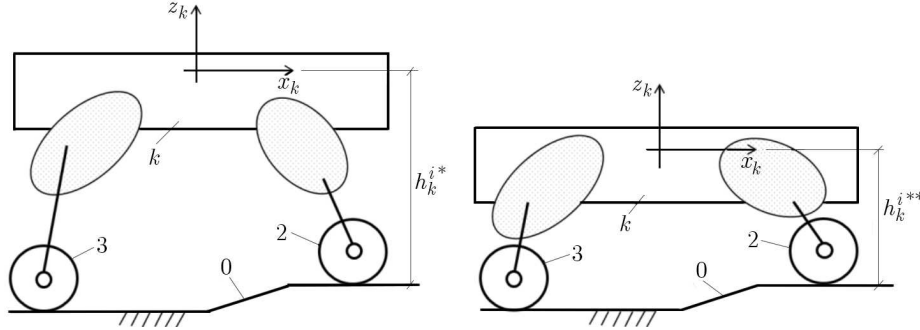


Fig. 9. A schematic showing examples of robot positions on uneven ground for different settings of the wheel heights h_k^{i*} and h_k^{i**}

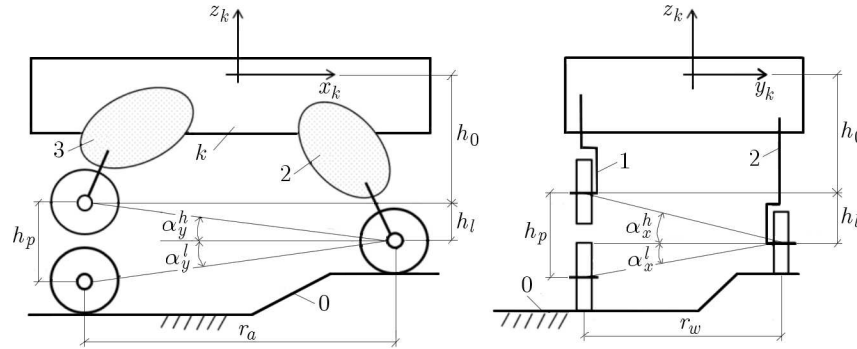


Fig. 10. The robot on the uneven ground with leading wheel 2 in side and front views. A schematic showing the maximum angles of ground inclination α_x^h , α_x^l and α_y^h , α_y^l

In the work, it is assumed that the leading wheel is wheel 2 (left front). For such a proposed method of levelling, only one solution of searched heights h_i will always be obtained for a given position of the body. The height h_l of the leading wheel can be set in the range of

$$0 \leq h_l \leq h_p \quad (3.3)$$

For the adopted height h_l , the leading wheel possible changes in the orientation angles can be determined by formulas (Fig. 10)

$$\begin{aligned} \alpha_y^h &= \arctan \frac{h_l}{r_a} & \alpha_y^l &= \arctan \frac{h_p - h_l}{r_a} \\ \alpha_x^h &= \arctan \frac{h_l}{r_w} & \alpha_x^l &= \arctan \frac{h_p - h_l}{r_w} \end{aligned} \quad (3.4)$$

The height h_l can be dynamically determined depending on the nature of the mobile robot ride and the existing uneven ground. In driving the robot on grounds with a positive angle (uphill), in order to increase the possibility of levelling the body, h_l should have values close to zero in order to get the angle α_y^l according to (3.4), reaching its maximum value.

When driving the robot on the ground with a negative angle (down), h_l value should be close to h_p to obtain the angle α_y^h reaching the maximum value. When driving in the area with an undetermined uneven ground, h_l should have a value of $h_p/2$.

As a result of the control model with leading wheel 2 (front left) having the fixed height h_l while levelling displacement of the body, the values h_i should be corrected about the value h_l

$$h_1^c = h_1 - h_l \quad h_3^c = h_3 - h_l \quad h_4^c = h_4 - h_l \quad (3.5)$$

The corrected values h_i^c will be disruptions to the regulators which control the raising of active wheel 1, 3 and 4 (front right, rear left and right). The regulators of the active wheels will reset the disruption h_i^c to zero. In the structure of the levelling algorithm, there are three active regulators that control the raising and lowering of the active wheels 1, 3 and 4. In Fig. 11, a block algorithm of the platform levelling system of the robot chassis is shown.

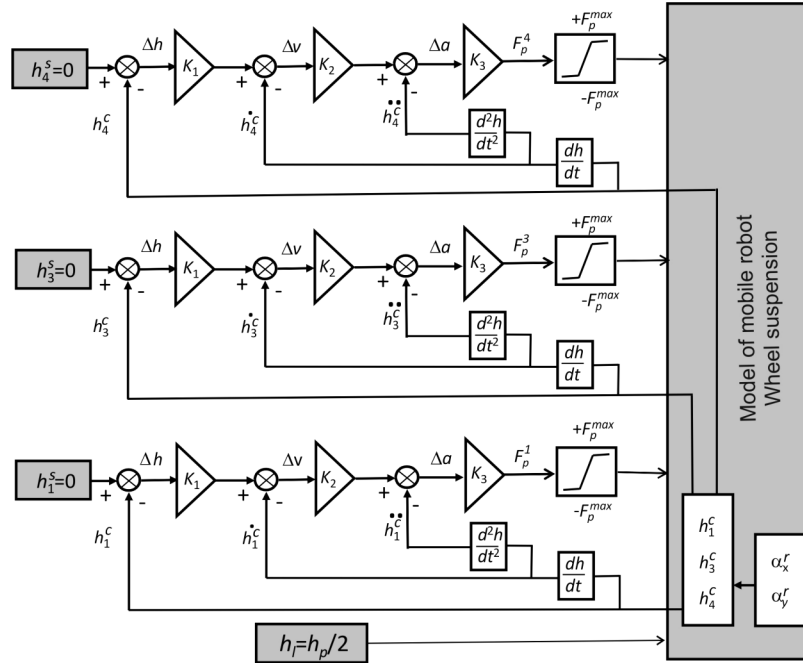


Fig. 11. A general diagram of the levelling control system

The inclinometers mounted on the robot body measure the distortions in form of orientation angles α_x^r, α_y^r of twisting of the chassis while driving. These values will be used for calculation from formula (3.5) the displacement h_i^c needed to bring the chassis to the level. The output of the regulator wheel is the force F_p^i which causes the displacement q_p^i of the actuator which controls raising and lowering of the active wheel i . The proposed control system has a closed structure with three feedback loops controlling the elevation h_i^c . The regulators control the actuators q_p^i by determination of the active force F_p^i . The heights h_1^c, h_3^c, h_4^c of the active wheels 1, 3, 4 relative to the chassis will be controlled in closed loops.

In this control system, an external control loop computes the difference between the prescribed robot chassis elevation h_i^s ($h_i^s = 0$ in the case of levelling) and the actual chassis elevation h_i^c calculated on the basis of the angles α_x^r, α_y^r read from the chassis location. The computed elevation deviation Δh passes through proportional controllers with constants K_1, K_2, K_3 , generating a signal specifying the required demand for the active lifting force F_p^i , which is applied to the driving link of the robot. The control system incorporates blocks limiting the generated value of the force F_p^i to the maximum values ($-F_p^{max} < F_p < F_p^{max} = 1700$ N) which the lifting actuator is capable of generating. Besides the robot, a computational model of the designed control system has been created in LMS DADS in order to study its dynamics.

The control parameters, i.e. constants K_1, K_2 and K_3 of the controllers need to be defined and matched. The parameters depend on the character of the object (the controlled mechanism). In

control theory, there are many methods of matching such parameters. In this work, a numerical parameter matching procedure based on the Ziegler-Nichols method has been carried out. The simulations have been run in LMS DADS. The results of the controller parameter matching are: $K_1 = 600$, $K_2 = 100$ and $K_3 = 100$.

4. Simulation examinations of the mobile robot with a leveling control system

In order to determine dynamical properties of the mechanism and to verify the control system matching, motion of the system on an uneven surface has been simulated. A schematic of the simulation is shown in Fig. 12. The surface bumps are built of wedge-shaped obstacle drive-ons and drive-offs. The variation in the route height along the direction of motion for left and right side wheels is shown in Fig. 13.

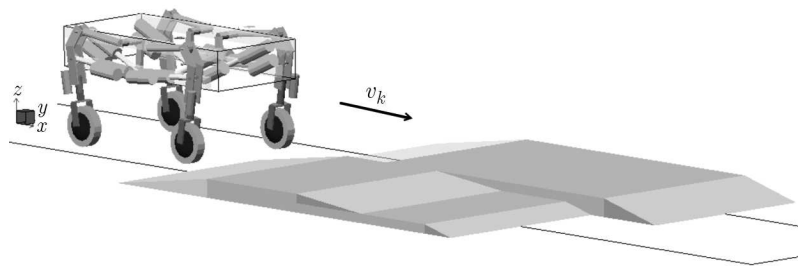


Fig. 12. The model of the mobile robot and a general scheme of simulation

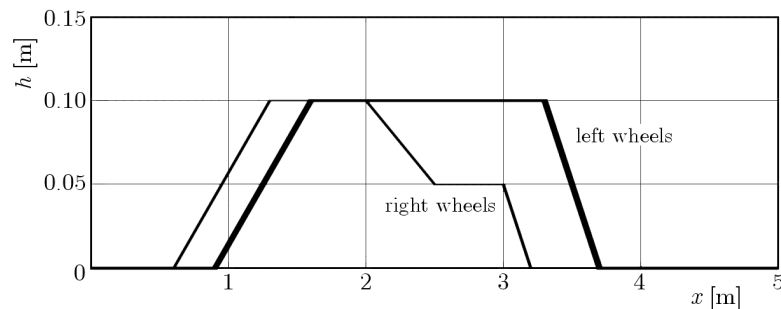


Fig. 13. Variation of heights h of the uneven ground under the left and right wheel along the axis of motion

The parameters of the control system are orientation angles $\alpha_x = \alpha_y = 0$ of the robot chassis with respect to the ground. They are constant during movement. It is assumed that the system would move at constant speed $v_k = 1.0$ m/s (3.6 km/h). Wheel 2 is adopted as the leading wheel with the height $h_l = h_p/2$. The terrain unevenness does not exceed the range of possible changes in the orientation angles α_x^h , α_x^l , α_y^h and α_y^l defined by formula (3.4). It is expected that during driving, the robot chassis will be kept at a given level. One of the aims of the simulations is to determine the control system response for the adopted excitations of motion. In particular, the accuracy of setting the orientations α_x , α_y and the determination of active forces F_p^i in the actuators q_p^i have been ensured and executed.

The diagrams in Figs. 14 to 20 show the results of simulations in LMS DADS. Figures 14 and 15 show the variation in the real elevation h_k^i of the robot chassis (coordinates z of points P_i – Fig. 2 and 8) and the trajectories of the centres z_s^i of wheels 1, 2, 3 and 4.

The quality of the control is illustrated in the next diagram where the errors α_x and α_y in the execution of the chassis levelling are shown (Fig. 16). The accuracy of the chassis orientation angles α_x and α_y below 0.5 deg has been achieved. The control system quickly reacts to

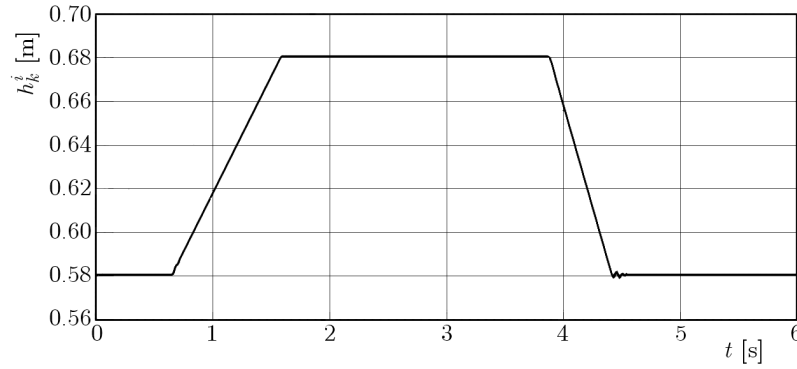


Fig. 14. Variation of the real elevations h_k^i of the robot chassis during movement

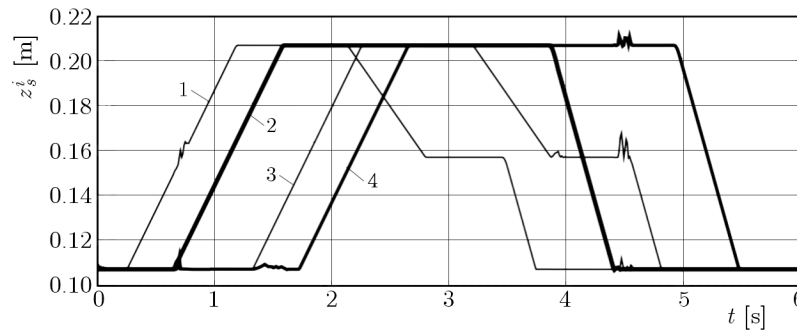


Fig. 15. Displacements of the centers z_s^i of wheels 1, 2, 3 and 4 during movement

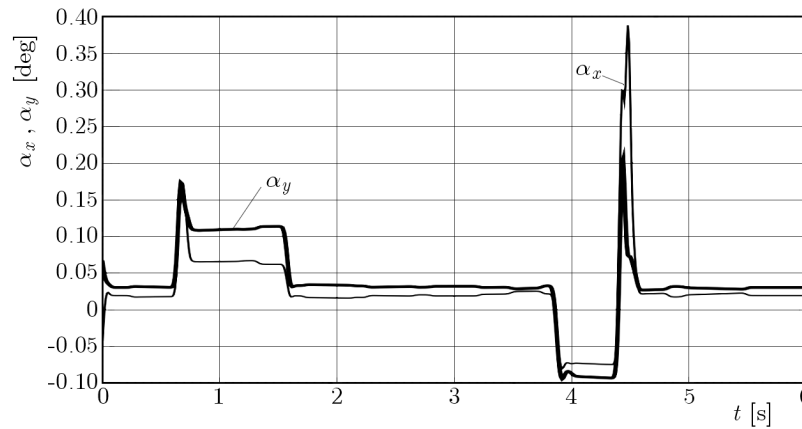


Fig. 16. Angles of orientation α_x, α_y of the robot chassis found from simulations

disturbances in the surface bumps (points for $t = 0.3, 0.6, 1.4, 1.7, 2.6, 3.4, 4.4, 4.8, 4.9, 5.1$ s in figures). The control system handles well the uneven ground, quickly stabilizing the robot.

The next figures show parameters of the lifting actuator. Figures 17 and 18 show the variation in length q_p^i and velocity v_p^i of the lifting actuator while Fig. 19 shows diagrams of the computed active force F_p^i in these actuators. The wheel-ground interaction forces F_k^i ($i = 1, 2, 3, 4$) are presented in Fig. 20.

The analysis of the levelling system reveals that its performance of the latter mainly depends on height of the obstacle and robot travelling speed v_k . These quantities determine the vertical velocity component z of the wheel which must be cancelled out by the opposite vertical motion of the chassis effected by the lifting actuator q_p^i moving with an appropriate velocity v_p^i (Fig. 17) and generating an appropriate active force F_p^i (Fig. 19). The choice of a proper lifting actuator

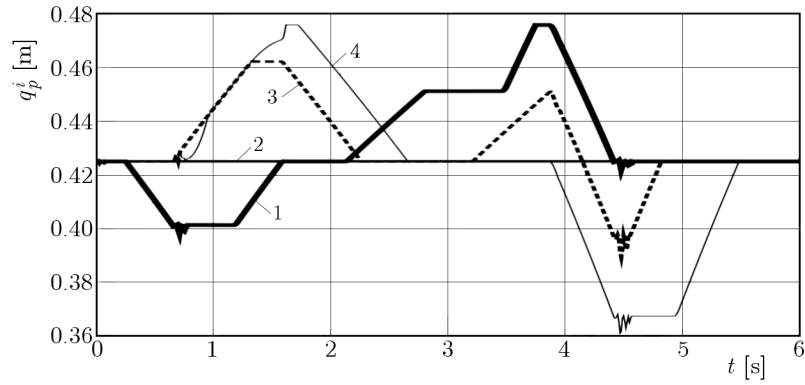


Fig. 17. Extension q_p^i of the lifting actuators ($i = 1, 2, 3, 4$)

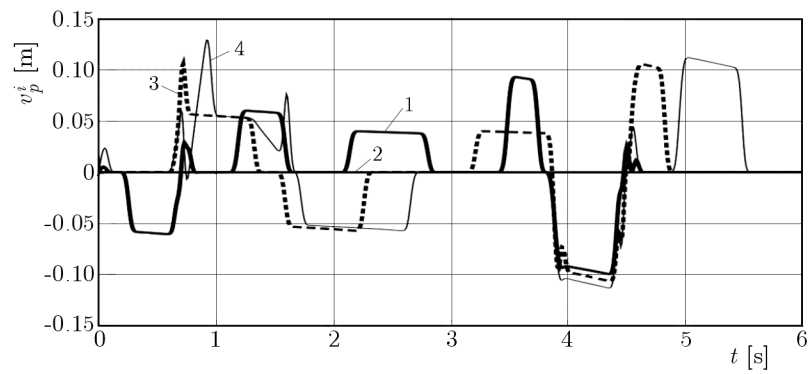


Fig. 18. Velocity v_p^i of the lifting actuators ($i = 1, 2, 3, 4$)

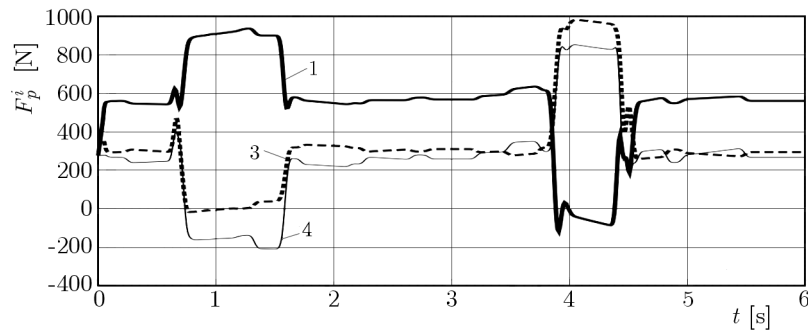


Fig. 19. Active forces F_p^i in the actuators q_p ($i = 1, 3, 4$) determined by the control system

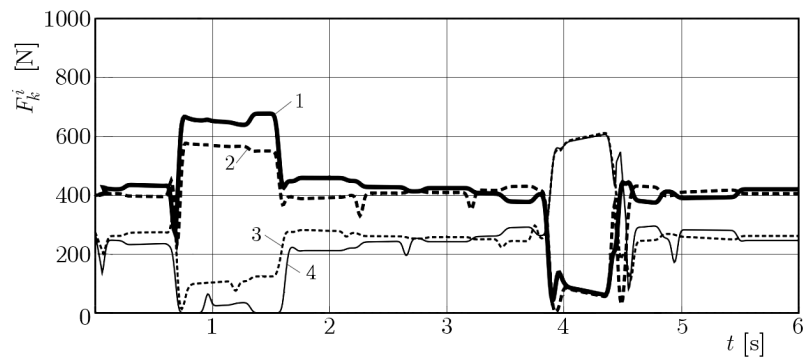


Fig. 20. Wheel-base interaction forces F_k^i ($i = 1, 2, 3, 4$)

whose dynamics would ensure that the required operating parameters can be exceeded is the guarantee for correct operation of the robot levelling system. As it appears from Table 2, the electric drives LINAK LA36 adopted for lifting and ejecting meet dynamic requirements since the driving forces F_p^i (Fig. 19) do not exceed the nominal forces specified by the manufacturer, even during overcoming of extreme obstacles.

5. Final remarks

Dynamic and kinematic parameters of a wheel-legged mobile robot have been determined as a result of simulation studies. For that purpose, a numerical model of the robot and a model of the levelling control system in a computer system have been built. Robots of this kind are subject to considerable loads generated during travel on a bumpy surface. In order to build an efficient and reliable suspension system, one needs to identify the state of loading of the robot. The research has concentrated on the modelling of the leveling control system maintaining a constant orientation of the robot chassis during travel on an uneven terrain.

The analysis of the levelling system has revealed that its performance mainly depends on height of the obstacle and robot travelling velocity. The simulations validated the structure of the control system adopted for the levelling of the robot chassis and confirmed the controller parameter values to be correct. The numerical results have been used to design and build a wheel-legged robot.

References

1. BALCHANOWSKI J., 2012, Mobile wheel-legged robot: researching of suspension leveling system, *Advances in Mechanisms Design*, J. Beran (Edit.), Dordrecht, Springer
2. BALCHANOWSKI J., GRONOWICZ A., 2012a, Design and simulations of wheel-legged mobile robot, *Acta Mechanica et Automatica*, **6**, 2
3. BALCHANOWSKI J., GRONOWICZ A., 2012b, Designing, building and dynamic studies of the autonomous wheel-legged robot (in Polish), The Project No. NN502271037, funded by Polish Ministry of Science and Higher Education in the years 2009-2012, SPR 24/2012, Wrocław
4. BALCHANOWSKI J., GRONOWICZ A., 2012c, Designing and simulation examinations of a wheel-legged suspension of the wheel (in Polish), *Journal of Transdisciplinary Systems Science*, **16**, 2
5. GRONOWICZ A., SZREK J., 2009a, Design of LegVan wheel-legged robot's mechanical and control system, [In:] *SYROM 2009*, Ion Visa (Edit.), Springer Netherlands, 145-158
6. GRONOWICZ A., SZREK J., 2009b, Idea of a quadruped wheel-legged robot, *Archive of Mechanical Engineering*, **56**, 3, 263-278
7. GRONOWICZ A., SZREK J., WUDARCZYK S., 2012, A rig for testing the leg of a wheel-legged robot, *Acta Mechanica et Automatica*, **6**, 10
8. HALME A., LEPPÄNEN I., SUOMELA J., YLÖNEN S., 2003, WorkPartner: interactive human-like service robot for outdoor applications, *The International Journal of Robotics Research*, **22**, 7-8
9. HAUG E.J., 1989, *Computer Aided Kinematics and Dynamics of Mechanical Systems*, Allyn and Bacon, Boston
10. HOŁDANOWICZ G., 2008, PIAP Robots eyes combat role, *Jane's International Defence Review*, July
11. http://www.bostondynamics.com/robot_petman.html
12. <http://www.elbitsystems.com/elbitmain/areain2.asp?parent=3&num=31&num2=31>

13. SPERZYŃSKI P., SZREK J. GRONOWICZ A., 2010, The geometric synthesis of a mechanism for realization of a rectilinear trajectory (in Polish), *Acta Mechanica et Automatica*, **4**, 2
14. SZREK J., WÓJTOWICZ P., 2010, Idea of wheel-legged robot and its control system design, *Bulletin of the Polish Academy of Sciences. Technical Sciences*, **58**, 1, 43-50
15. TCHOŃ K., MAZUR A., DULĘBA I., HOSSA R., MUSZYŃSKI R., 2000, *Manipulators and Mobile Robots* (in Polish), Akademicka Oficyna Wydawnicza, Warszawa
16. TROJNACKI M., SZYNKARCZYK P., ANDRZEJUK A., 2008, Tendencje rozwoju mobilnych robotów lądowych, *Pomiary Automatyka Robotyka*, 6/08
17. ZIELIŃSKA T., 2003, *Walkingmachine* (in Polish), PWN, Warszawa

Manuscript received August 5, 2014; accepted for print July 15, 2015

CONCEPT OF THE MAGNETIC LAUNCHER FOR MEDIUM CLASS UNMANNED AERIAL VEHICLES DESIGNED ON THE BASIS OF NUMERICAL CALCULATIONS

MIROSLAW KONDRATIUK, LESZEK AMBROZIAK

Faculty of Mechanical Engineering, Bialystok University of Technology (BUT), Bialystok, Poland

e-mail: m.kondratiuk@pb.edu.pl; l.ambroziak@pb.edu.pl

The paper presents a concept of a magnetic coil launcher for unmanned aerial vehicles of mass up to 25 kg. The idea is not new, nevertheless in the paper, an innovative application of magnetic launcher technology for selected class of unmanned aerial vehicles is presented. So far, at Bialystok University of Technology, a magnetic coil launcher for micro aerial vehicles of mass up to 2.5 kg has been investigated. In the article, simulations of a conceptual multi-coil launcher with a magnetic core system are presented. The finite element method has been used in calculations. Moreover, in the paper, the concept of a magnetic support for transmission of mechanical power from the magnetic core to the launched payload is proposed. The applied methodology, computational results and potential technical difficulties of practical applications are also widely discussed.

Keywords: electromagnetic launcher, EML, magnetic support, permanent magnet, FEM

1. Introduction

Fast development and constantly increasing industrial applicability of unmanned aerial vehicles (UAVs) require new solutions as far as their operation systems are concerned. For instance, modern engineering associated with UAVs focuses especially on developing innovative navigation systems (Gosiewski *et al.*, 2011; Kownacki, 2013), robust control of flight (Mystkowski, 2014), reliable security solutions, efficient electrical engines and power cells, formation of flight control algorithms (Gosiewski and Ambroziak, 2012), adaptive aerodynamics structures (Mystkowski, 2013), applications of so-called intelligent materials, etc. Generally speaking, most works are being carried out in order to increase the level of UAVs autonomy. There is also a major need for applying systems of assisted take-off and landing.

Starting launchers are used for many classes of UAVs from micro planes of mass up to a few kilograms to large military drones. Systems assisting take-off procedures increase the level of operators' safety, ensure recurrence of starts, decrease periods of time between consecutive starts, protect onboard equipment and UAV construction from undesired vibration and acceleration pulses. Employment of automatic launchers for UAV may also considerably increase the level of their autonomy and gives new possible applications, for example to autonomous systems for monitoring of countries borders as well as unmanned systems of forest fire protection or unmanned aerial post services.

Presently, many different constructions are used as launching devices. Main solutions involve devices based on pneumatic (Perkowski, 2008) and hydraulic technology or are equipped with rubber or steam drive systems. Since the early 50's, advanced research on electromagnetic launchers (EML) have been conducted in the world. In some publications, the knowledge of magnetic launchers was clearly systematised, e.g. Kolm *et al.* (1980). Electromagnetic launchers are a completely different group of starting devices basing on conversion of stored electrical

energy into kinetic energy of the launched object. Generally, there are two main types of EMLs: rail launchers and coil launchers. Moreover, coil launchers can be divided into synchronous and asynchronous (inductive) devices. More specified nomenclature and theory were presented in the following publications by Kondratiuk (2013), Tomczuk and Waindok (2009), Tomczuk *et al.* (2012). The idea of application of magnetic technology for aircraft launch is not new. Interesting papers concerning such topics have been already published (Patterson *et al.*, 2002; McNab, 2007). Among others, very innovative research was carried out on electromagnetic launch systems for large airplanes. The investigations were conducted in the frame of big European project called GABRIEL (Sibilski *et al.*, 2014). GABRIEL's research team proposed a system based on phenomena of superconducting levitation. As a result, the system can be capable of launching airliners such as Airbus A320. In the frame of the project, a magnetic drive system has been developed. The investigations involved numerical models, vibration analysis, CAD and design optimization procedures. Moreover, successful laboratory tests of a small scale launch system have been carried out and the outcomes were published, see Ładyżyńska-Kozdraś *et al.* (2014a,b). Consequently, system GABRIEL has been designed for a large class of planes – commercial airliners. The concept of an electromagnetic linear drive for launching a medium class of UAVs significantly differs from solutions proposed by GABRIEL's research team. Main differences involve the type of magnetic linear drives, scale of the device, target performance, field of applications and approach to design.

In this paper, investigations on a synchronous coil launcher are described. Such a device consists of several serially located driving coils (usually made of a copper isolated wire) and a cylindrical core moving inside those coils. The core may be made of a ferromagnetic material, or a permanent magnet may be used. Comparing to pneumatic and rubber catapults, the synchronous coil launcher has many advantages, for instance, a quick recharging process and readiness for another shot, control of the launching force, modular construction and lack of complicated constructional parts exposed to damage.

So far, at Bialystok University of Technology (BUT) the electromagnetic launcher for micro-unmanned aerial vehicles (MAVs) has been developed and investigated (Kondratiuk, 2013). The construction of this device consists of ten serially located copper coils with a ferromagnetic core placed inside. The controlled magnetic field of the solenoids affects the core, and, in that way, the magnetic driving force is produced. The core is connected by means of a diamagnetic pusher to the carriage to which the launched plane is attached. The whole system is controlled by the open-source Arduino MEGA platform (ATMEGA2560) with the implemented algorithm of feedback control of MAV's position and acceleration. The construction, conducted design works and control structure were widely described in the previous papers by Kondratiuk and Gosiewski (2013a,b, 2014).

The main goal of the present work is to investigate and test some technical concepts of a multi-coil EML for middle class of UAVs. As tools for the testing, numerical simulations have been applied. Moreover, the article involves modifications, adaptation and scaling procedures of the previously constructed coil EML in order to launch objects of mass up to 25 kg.

2. Main assumptions

Among different types of UAVs, there are various requirements for start conditions. The most important one is connected with the initial speed which is necessary to generate a proper lift force. Because of different UAVs geometries (shape, wing configuration, wingspan, etc.) different initial speed values are required. For instance, 25 kg delta wing planes require much greater velocity (about 25 m/s) than 25 kg gliders (about 15 m/s). In the paper, the design of an EML for 25 kg UAVs which ensure starting speed on the level of at least 20 m/s is described. That value has been chosen arbitrarily as the goal to achieve.

Another aspect connected with UAVs catapults concerns the source of power. In pneumatic and hydraulic launchers, the working fluid is accumulated under pressure in special tanks or containers. On the other hand, rubber launchers require an external force to stretch the elastic material while steam catapults need a whole complex system for preparing vapour of proper parameters. In EMLs, electrical energy should be accumulated in a suitably large storage from which it can be rapidly released by the launcher driving system. Previous investigations clearly showed that the capacitor bank perfectly meets this requirement.

In the proposed EML for 25 kg UAVs there can appear the necessity of switching very high currents flowing through driving coils (even up to 200 A). From the practical point of view, for current control, IGBT transistors can be used in electronic switching circuits. During FEM simulations, data sheets of such electronic devices as transistors and capacitors are strictly taken into account.

Launchers for UAVs should also ensure sufficient stability, vibration and a safety level under take-off circumstances. These factors should be taken into account during design procedures.

One of the main assumptions connected with the coil EML for 25 kg UAVs is that initial investigations will be carried out on the already existing EML model for micro UAVs. Thus, this paper starts from possible modifications of the construction described in the PhD Thesis by Kondratiuk (2013).

3. Model of the coil-core system

The first possible modification is connected with the application of a permanent magnet as a driving core instead of the ferromagnetic one. Force characteristics of the coil-core system with the ferromagnetic and with the magnetic cores were computed by means of the finite element method, (Tomczuk *et al.*, 2007). COMSOL Multiphysics software is employed as the ready-made computer program for electromagnetic computations. In the FEM model of the coil-core system, the advantage of the axial symmetry is used. The partial differential equation (PDE) describing the distribution of static magnetic field in the coil-core system is called Ampère's law, and in the ferromagnetic core domain it takes the following form

$$\nabla \times \left(\frac{\nabla \times \mathbf{A}}{\mu_0 \mu_r(|\mathbf{B}|)} \right) = \mathbf{J}_e \quad (3.1)$$

where ∇ denotes the nabla operator; \mathbf{A} – magnetic vector potential, [Wb/m]; $\mu_0 = 4\pi \cdot 10^{-7}$ H/m – permeability of vacuum; $\mu_r(|\mathbf{B}|)$ – relative permeability of a nonlinear ferromagnetic material, [dimensionless]; $|\mathbf{B}|$ – magnetic flux density, [T]; \mathbf{J}_e – external current density, [A/m²].

In the cylindrical coordinate system, the vector \mathbf{A} can be written as

$$\mathbf{A} = A_r \hat{\mathbf{r}} + A_\varphi \hat{\boldsymbol{\varphi}} + A_z \hat{\mathbf{z}} \quad (3.2)$$

where A_r , A_φ , A_z are components of the vector \mathbf{A} , [Wb/m]; $\hat{\mathbf{r}}$, $\hat{\boldsymbol{\varphi}}$, $\hat{\mathbf{z}}$ – unit vectors.

Thus, rotation of \mathbf{A} is equal

$$\nabla \times \mathbf{A} = \left(\frac{1}{r} \frac{\partial A_z}{\partial \varphi} - \frac{\partial A_\varphi}{\partial z} \right) \hat{\mathbf{r}} + \left(\frac{\partial A_r}{\partial z} - \frac{\partial A_z}{\partial r} \right) \hat{\boldsymbol{\varphi}} + \frac{1}{r} \left(\frac{\partial(r A_\varphi)}{\partial r} - \frac{\partial A_r}{\partial \varphi} \right) \hat{\mathbf{z}} \quad (3.3)$$

Ampère's law for the magnet domain has a different form than (3.1)

$$\nabla \times \left(\frac{\nabla \times \mathbf{A}}{\mu_0 \mu_r} - \mathbf{B}_r \right) = \mathbf{J}_e \quad (3.4)$$

where \mathbf{B}_r is the magnet remanent flux density vector, [T].

Coil and ferromagnetic core parameters used in the simulation are taken from the real EML model previously described by Kondratiuk (2013), Kondratiuk and Gosiewski (2013a,b, 2014). The catalogue value of remanent magnetic flux density of the simulated magnet is equal to 1.24 T. Relative permeability of the magnet material is equal to $\mu_r \approx 1.05$, but it can be modelled as close to 1 because, in order to generate a magnetic force, the magnet should be remagnetized so the external magnetic field produced by the coils increases magnetic induction in the magnet according to the following constitutive relation

$$\mathbf{B} = \mu_0\mu_r\mathbf{H} + \mathbf{B}_r \quad (3.5)$$

where \mathbf{H} is the magnetic field vector, [A/m].

Differences in the values of magnetic flux density for $\mu_r = 1$ and $\mu_r = 1.05$ obtained in a freely chosen point located inside the magnet are shown in Fig. 1.

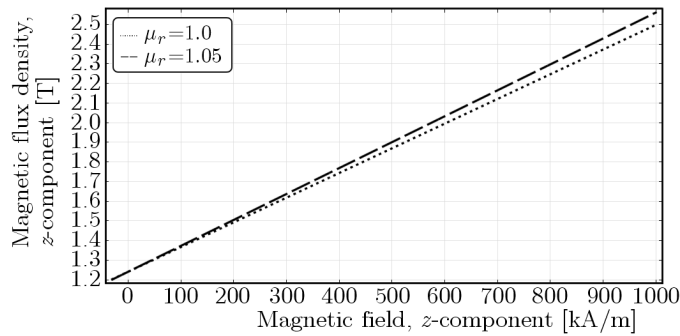


Fig. 1. Magnetic flux density in the magnet material during remagnetization

In fact, relative permeability of a permanent magnet decreases under influence of very strong external field and finally achieves the value of 1. Then, both lines in Fig. 1 line up parallelly. In the model, this effect is neglected.

A permanent magnet has been proposed instead of a ferromagnetic one in order to increase the magnetic force. In the FEM model, the Maxwell surface stress tensor method (MSST) and the virtual work (VW) method have been tested. Generally, both methods give similar results and they are applied alternatively. In order to present the advantage of application of a permanent magnet, the computed magnetic forces acting on both cores (magnetic and ferromagnetic) under influence of coil current $i_c = 1$ A and $i_c = 3$ A are compared in Fig. 2.

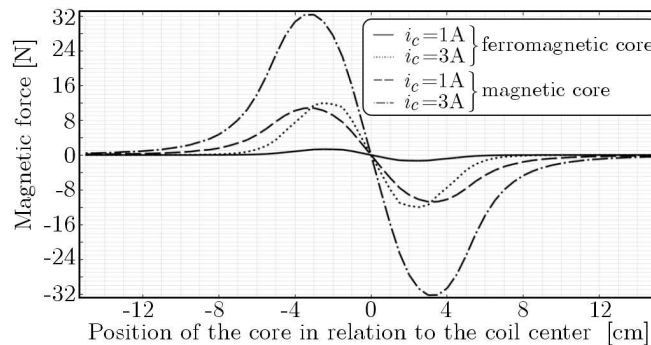


Fig. 2. Comparison of magnetic forces acting on the ferromagnetic and magnetic core

The calculations clearly show that the magnetic core can provide much greater magnetic force than the ferromagnetic core. The computed results for the ferromagnetic core have been experimentally verified and high level data similarity has been revealed (Kondratiuk, 2013).

In Fig. 3, 3D and 2D views of the modelled coil-magnet system are presented. Both representations are developed from the 2D axi-symmetric model by 2D revolution and 2D mirror functions respectively applied to the FEM solution.

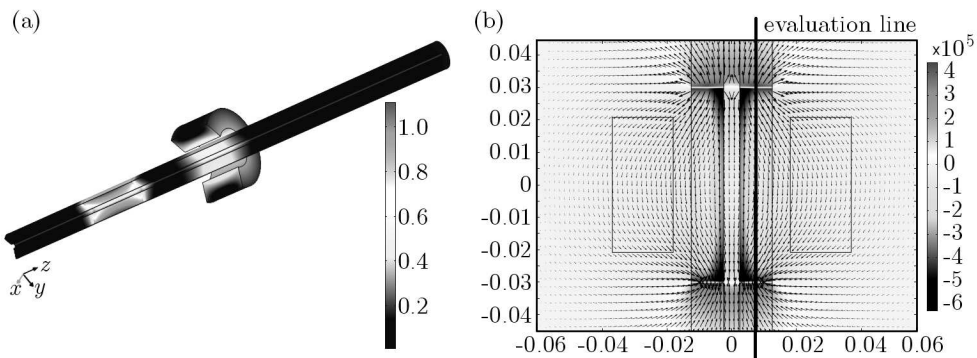


Fig. 3. Development of the FEM axi-symmetric solution for the coil-magnet system into 3D and 2D views: (a) magnetic flux density for the system under coil current $i_c = 10$ A and with the magnet position $z_m = -12$ cm, (b) magnetic field distribution (z -coordinate) around the system without current and with the magnet inside

In order to model motions of the core along the coil z -axis the Euler method has been applied (Kondratiuk, 2013). In the FEM model, a function of core length has been introduced. That function multiplied by remanent magnetic flux density, magnet permeability or conductivity describes properties of the core along the z -coordinate. In the model, isotropy of the above mentioned parameters has been assumed. In Fig. 3b, the evaluation line is drawn. Along this line, some crucial model parameters have been calculated and the results are presented in Fig. 4.

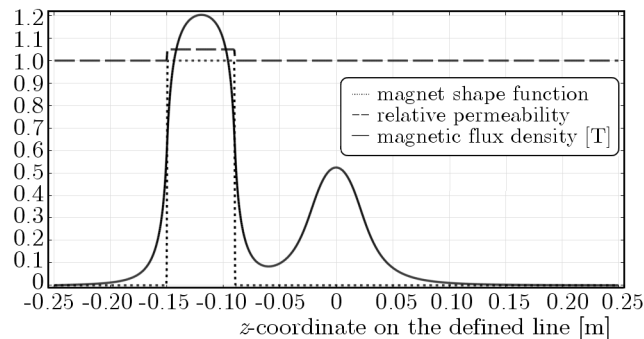


Fig. 4. Distribution of crucial parameters of the model along a selected line in the z -coordinate (coil current $i_c = 20$ A, coil position $p_c = 0$, magnet position $z_m = -12$ cm)

Positions of the core/magnet (z_m) or the coil (p_c) are defined as locations of their centres in the global coordinate system. The magnetic flux density distribution presented in Fig. 4 comes from the magnet (higher pick) and from the coil (lower pick). This also explains from where the magnetic force comes from. The magnetic field tries to retain uniformity and always acts in the opposite way to any changes, for example in the coil current value or in the system geometry. When the coil generates an external field, the magnet and solenoid are attracted to each other because only in that way the total magnetic field can become more uniform.

4. Multi-coil EML model

The model of a multi-coil EML can be divided into two strongly related parts: electromagnetic and mechanical.

4.1. Electromagnetic part of the multi-coil EML

The first model of EML with a permanent magnet as the core is based on the previously constructed and widely investigated 10-coil EML with a ferromagnetic core. Parameters of that construction were presented in previous publications by Kondratiuk (2013), Kondratiuk and Gosiewski (2013a,b, 2014). It is worth noticing that the investigated coils were made of a 0.8 mm isolated copper wire in configuration 27 per 52 turns (1391 turns in total). In the paper, a code for coils description was proposed. For instance, the aforementioned solenoid can be coded as $0.8 \times 27 \times 52$.

Each coil in the model affects the magnetic core through magnetic field. Strength and distribution of the field depend on coils configuration and currents intensity flowing through the wires. However, the magnetic force is directly proportional to the current value, so in order to simplify the model, it is possible to compute the magnetic force distribution for different core positions in relation to the coil centre and only for one current value $i_c = 1$ A. It incorporates the function $F(1 \text{ A}, [z_m - p_n])$ in the multi-coil EML model as follows

$$F_n(i_n, z_m) = i_n F(1 \text{ A}, [z_m - p_n]) \quad (4.1)$$

where $F_n(i_n, z_m)$ is the magnetic force generated by the n -th coil, [N]; i_n – coil current flowing through the n -th coil, [A]; p_n – n -th coil position, [m].

The total force acting on the magnet can be defined as

$$F_m = \sum_{n=1}^N F_n(i_n, z_m) \quad (4.2)$$

where N is the number of coils located serially.

As the core, an assembly of 6 ring-shaped magnets of remanence $B_r = 1.24$ T made of material N38 (Arnold, 2014) is proposed. Dimensions of selected magnets are the following: 27 mm – outer diameter, 5 mm – inner diameter, 10 mm – magnet height. Each magnet is magnetized along 10 mm dimension. The assembled core is 60 mm long. The number and shape of magnets are selected arbitrarily. Similarly to the coils, in the paper, a code for core description is proposed. The above described core can be coded as $6 \times \text{RSM}-27 \times 5 \times 10\text{-N38}$ where RSM means a ring-shaped magnet. Visualization of the proposed core in front of two coils $0.8 \times 27 \times 52$ is presented in Fig. 5.

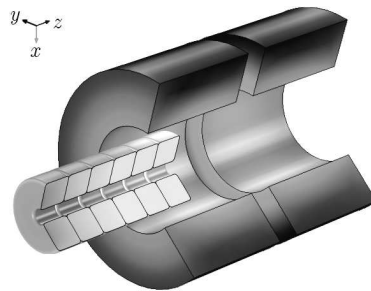


Fig. 5. Cross-sectional visualization of the core $6 \times \text{RSM}-27 \times 5 \times 10\text{-N38}$ in front of the two coils $0.8 \times 27 \times 52$

Stationary calculations for the coil $0.8 \times 27 \times 52$ and the assembled magnetic core $6 \times \text{RSM}-27 \times 5 \times 10\text{-N38}$ have been carried out and the function $F(1 \text{ A}, [z_m - p_n])$ calculated (Fig. 6). The function presented in Fig. 6 has been used according to equation (4.1) in the 10-coil EML model.

Regarding the power source in the model, a single bank of capacitors connected parallelly has been applied. First calculations have been conducted for the system voltage of 340 V and the

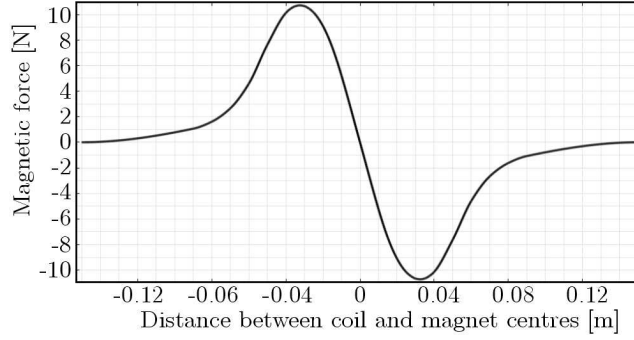


Fig. 6. Function $F(1 \text{ A}, [z_m - p_n])$ calculated for $p_n = 0$

total capacity of 94 mF. In the simulation, the capacitor discharging process has been modelled according to the following equations

$$u_c(t) = u_{c0} - \frac{1}{C} \int_0^t i_c(t) dt \quad i_c(t) = \sum_{n=1}^N i_n(t) \quad (4.3)$$

where $u_c(t)$ is capacitor voltage, [V]; u_{c0} – initial capacitor voltage, [V]; C – capacity of the bank, [F]; $i_c(t)$ – total capacitor discharging current, [A]; $i_n(t)$ – current flowing through n -th coil, [A].

4.2. Mechanical part of the multi-coil EML

In the mechanical part of the model, the damping force (F_d) is introduced

$$F_d(v_m) = \underbrace{b_d v_m}_{\text{holds always}} \quad \text{or} \quad F_d(v_p) = \underbrace{b_d v_p}_{\substack{\text{holds during} \\ \text{acceleration} \\ (v_m = v_p)}} \quad (4.4)$$

where b_d denoted the damping coefficient, [N·s/m]; v_m , v_p – magnet and payload (UAV) velocities, respectively, [m/s].

A simplified mechanical scheme of the system is presented in Fig. 7.

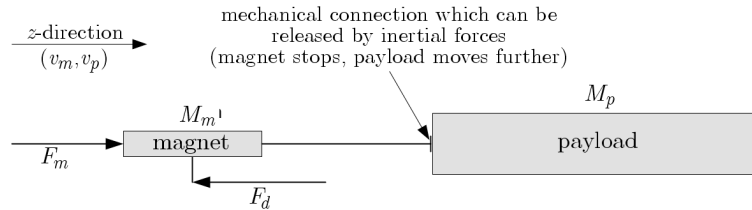


Fig. 7. Mechanical scheme of the investigated system

During simulations, the damping coefficient value has been arbitrarily chosen as constant $b_d = 5 \text{ N·s/m}$. Dynamic behaviour of the multi-coil EML with magnetic core and a 25 kg payload (launching UAV) is described by the following equations:

— for $z_p < \text{braking coil centre}$

$$\frac{d^2 z_m}{dt^2} = \frac{d^2 z_p}{dt^2} = \frac{F_m - F_d(v_m)}{M_m + M_p} \quad (4.5)$$

— for $z_p \geq$ braking coil centre

$$\frac{d^2 z_m}{dt^2} = \frac{F_m - F_d(v_m)}{M_m} \quad \frac{d^2 z_p}{dt^2} = 0 \quad (4.6)$$

where z_m, z_p are magnet and payload positions, [m]; M_m, M_p – magnet and payload masses, [kg]; F_m – magnetic force, [N].

Equations (4.5) and (4.6) mean that during the launch phase both magnet and UAV masses are accelerated. When the acceleration changes its sign to minus, the braking phase starts. The UAV disconnects from the magnet and after that, only the magnetic core mass takes part in the braking process (no acceleration acts on the payload). Mass of the core 6×RSM-27×5×10-N38 is equal to 0.25 kg, but in the model $M_m = 1$ kg. In that way, any masses contained in necessary constructional pushers, screws, fixings, etc., are taken into account.

4.3. Characteristics of the non-modified multi-coil EML model

In this Subsection, the results of simulations conducted on the non-modified multi-coil EML are presented. ‘Non-modified’ means that the calculations have been carried out for a construction consisting of 10 serially located coils $0.8 \times 27 \times 52$ designed for micro UAVs and widely described by Kondratiuk (2013), Kondratiuk and Gosiewski, 2013a,b, 2014). The core 6×RSM-27×5×10-N38 has been applied. In Fig. 8, the power source characteristics come from simulation of the EML with the magnetic core and launching a 25 kg UAV are presented.

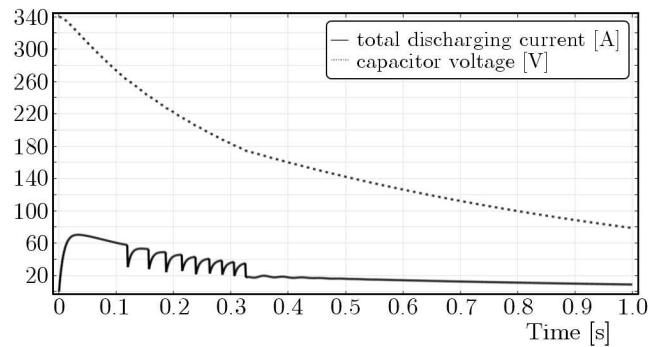


Fig. 8. Characteristic of the capacitors bank voltage (340 V/94 mF) and characteristic of the total discharging current from simulation of the launch of a 25 kg UAV by means of the EML with magnet core

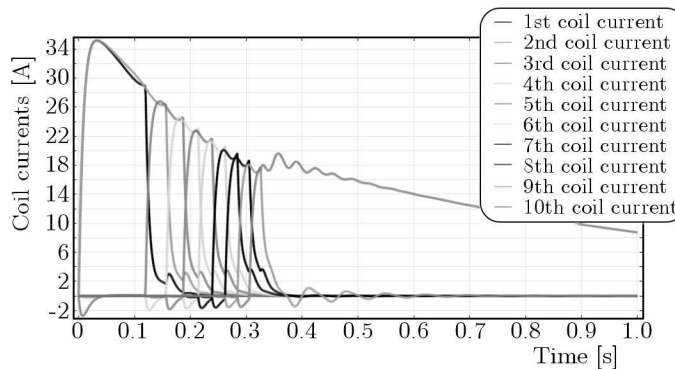


Fig. 9. Currents flowing through particular coils of the EML during simulation of the 25 kg UAV launch

In Fig. 9, the time evolutions of coil currents are presented. The last coil works until the magnetic core stops in its centre. The characteristics show that in the model electromagnetic

induction is taken into account. Changing currents in particular coils generate electromotive force in the neighbouring solenoids.

In the model, current can flow through wires in both directions. In reality it can be compensated by introducing switching transistors (IGBT) and safety rectifying diodes into control electronic systems. In the model, a semi-coil system has been applied. Two neighbouring coils are powered on simultaneously. When the core achieves the centre of the first coil, it is turned off and the next is powered on. This method is directly visible on the current characteristics in Fig. 9. Moreover, an influence of the capacitor power source can also be noticed because the maximum amplitude of currents decreases with time like as the capacitor voltage. This effect is caused by the finite capacity introduced into the model and directly shows how the power source parameters are significant.

In Fig. 10, characteristics of the magnetic force acting on the moving system of the magnet with payload are presented. The last coil can be recognized as a magnetic brake. Moreover, the damping force (F_d) value is also shown. That force can reach considerable values for higher velocities.

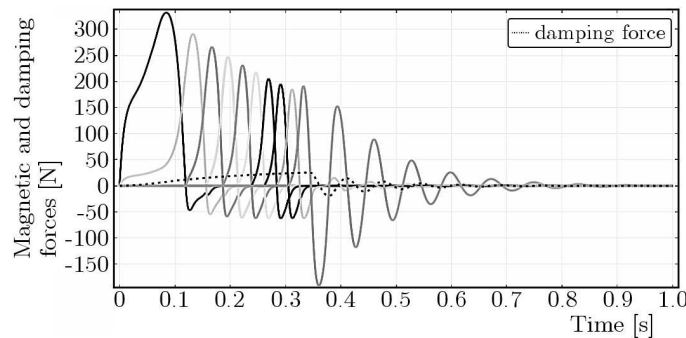


Fig. 10. Forces generated by particular coils of the EML during simulation of the 25 kg UAV launch

In Fig. 11, velocity characteristics are presented. The simulation reveals that the construction of 10 serially located coils $0.8 \times 27 \times 52$ with the core $6 \times \text{RSM-}27 \times 5 \times 10\text{-N38}$ can ensure a 25 kg UAV only a 2.5 m/s initial speed. It is less by an order than the assumed 20 m/s.

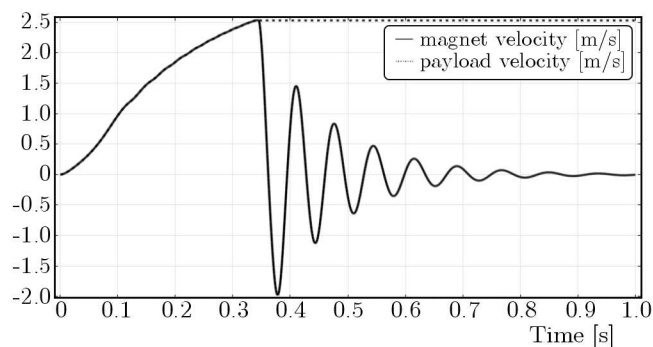


Fig. 11. Velocity characteristics from simulation of the 25 kg UAV launch

5. Modification of the EML

The computed results presented in the previous Section indicate that in order to increase the starting velocity, some modifications in the structure of the investigated EML should be introduced.

5.1. EML consisting of 4 parallel 20-coil ($0.8 \times 27 \times 52$) modules

As the first natural improvement, an increase in the coil number has been proposed (up to 20). Another modification is based on the parallel connection of a few of 20-coil modules (mechanical and electrical connection). In the modified FEM model, a single capacitor bank is used as the power source for all coils and modules. Thus, the capacitor voltage is increased up to 1 kV. Four modules consisting of 20 coils $0.8 \times 27 \times 52$ and mechanically connected in parallel have been investigated. The magnetic force generated by the module and coil currents are totalized. The electromagnetic interaction between each module is neglected. The whole system of 4 driving modules is coupled by common dynamic equations (4.5) and (4.6).

In Fig. 12, simulation characteristics of the capacitor bank (1 kV/94 mF) of four modules consisting of 20 $0.8 \times 27 \times 52$ coils each and connected in parallel as shown. It is worth noticing that the maximum value of the total discarding current increased by factor of 2.5.

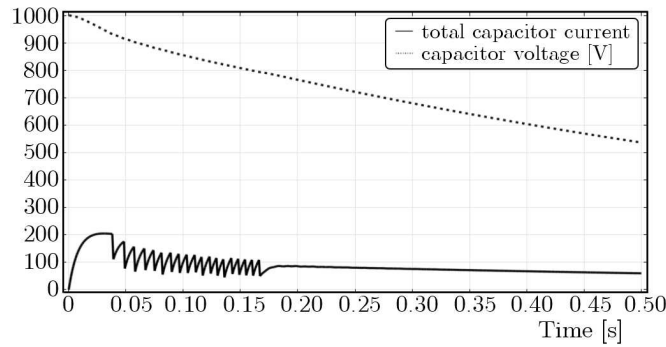


Fig. 12. Simulation characteristics of the capacitors bank (1 kV/94 mF) of four modules consisting of 20 $0.8 \times 27 \times 52$ coils each connected in parallel

Velocity characteristics of the modified EML are presented in Fig. 13. Improvements introduced into the model give an increase in the starting velocity up to 8.5 m/s. It is still not enough. The decision of coils configuration and the core structure modification has been made.

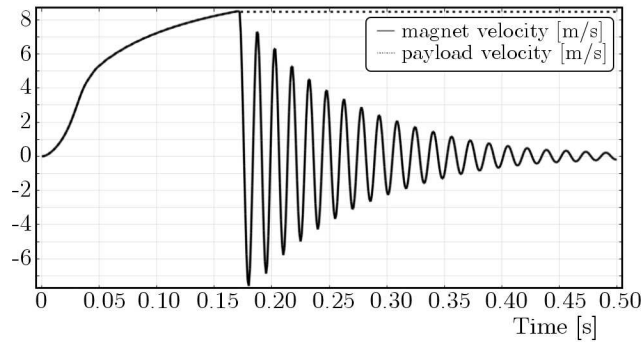


Fig. 13. Velocity characteristics from simulation of the launch of 25 kg UAV by means of the 4 EML module with magnet core connected in parallel

5.2. EML consisting of 6 parallel 20-coil ($1.0 \times 10 \times 150$) modules and the core $17 \times \text{RSM-28} \times 10 \times 10\text{-N52}$

In order to achieve the previously assumed velocity of 20 m/s a few modifications in the coils configuration and the core (magnet) structure have been proposed.

Firstly, the core $6 \times \text{RSM-27} \times 5 \times 10\text{-N38}$ has been replaced by $17 \times \text{RSM-28} \times 10 \times 10\text{-N52}$. It comprises 17 ring-shaped magnets made of material N52 (Arnold, 2014) and with remanence $B_r = 1.45$ T. Secondly, the coils $0.8 \times 27 \times 57$ have been replaced by $1.0 \times 10 \times 150$ made of an

isolated copper wire of 1 mm diameter. The distance between the coils is set to 1 cm, thus the driving part of the EML is about 3.3 m in length. The core and coils configurations are chosen arbitrarily. Thirdly, the number of parallel modules is increased up to 6. Finally, the capacity of the electrical energy bank is changed to 825 mF. It is a high value but can be simply achieved by the parallel and serial connection of a few hundreds of electrolytic capacitors (450 V/3.3 mF). In the new model of the EML capacitor bank, the voltage is set to 1 kV. Initial simulations reveal that more than one coil should be used to stop the core. In the final model, the last three solenoids act as magnetic brakes.

In Fig. 14, simulation characteristics of the capacitor bank (1 kV/825 mF) of six modules consisting of 20 $1.0 \times 10 \times 150$ coils each and connected in parallel are presented. The maximum value of the total discharging current significantly has increased up to 2.2 kA. However, currents of that value flow only in a short period of time, so it can be practically applied in the real device. Moreover, the currents flowing out from the electrical energy bank are spread over all capacitors. The simulated currents flowing through particular coils are shown in Fig. 15. Their maximum values are not higher than 190 A.

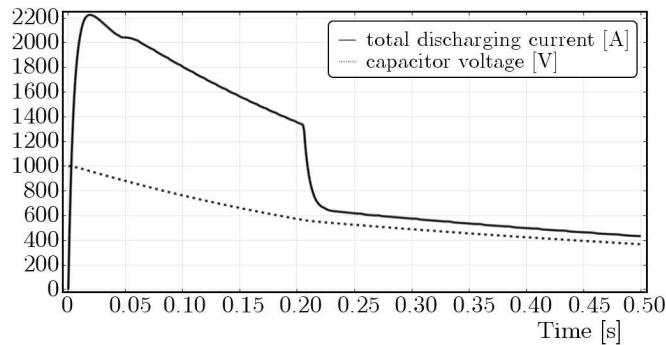


Fig. 14. Characteristics of the capacitor bank (1 kV/825 mF) supplying six modules consisting of 20 $1.0 \times 10 \times 150$ coils each and connected in parallel

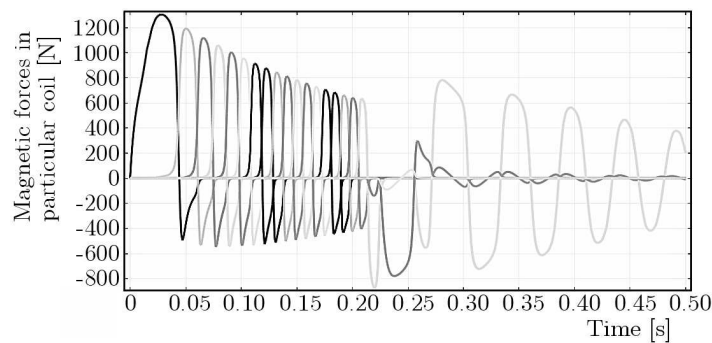


Fig. 15. Forces generated by particular coils of the single EML module (20 coils $1.0 \times 10 \times 150$)

In Figs. 16 and 17, the force characteristics are presented. They clearly show that the last three coils act as a magnetic brake. Influence of the introduced damping force is also visible. In Fig. 18, the velocity characteristics are shown. The modification introduced into the EML model enables the starting velocity to achieve the previously assumed value of 20 m/s.

6. Magnetic support

In the paper, a project of the magnetic slideway track for launched objects is also proposed. During the start, the supporting UAV of mass up to 25 kg may be a challenging task because of

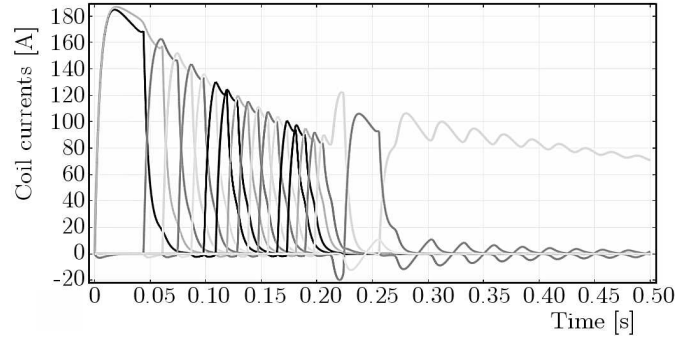


Fig. 16. Currents in particular coils of each module

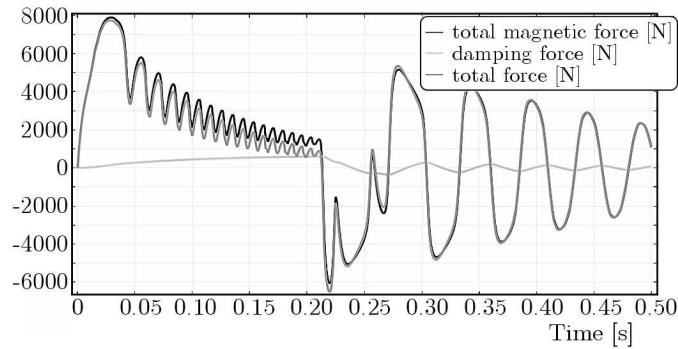


Fig. 17. Forces of the modified EML (6 modules)

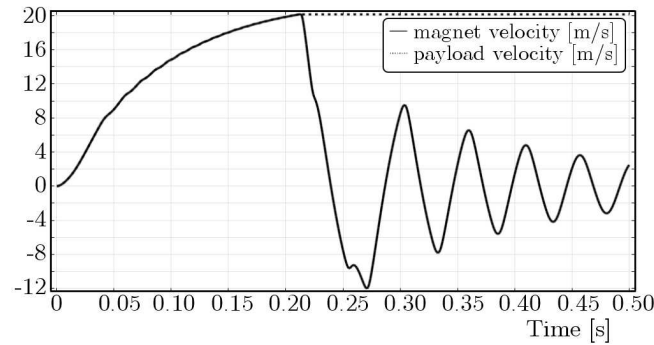


Fig. 18. Velocity characteristics of the modified EML (6 modules)

gravity, friction and material elastic buckling. The designed support solution consists of several permanent magnets of different sizes. The proposed solution creates a magnetic spring on which friction forces are minimized and the gravity is compensated for by magnetic repulsion. This system has also been modelled by means of FEM. The calculations have been conducted for different magnets and, as a result, the geometry configuration and magnet properties suitable for this particular type of support have been determined.

In Fig. 19, the concept of a magnetic track is presented. The construction consists of six downside (main) magnets BM-80×20×10-N35H (BM – board magnets, length [mm] × width [mm] × height [mm], N35H – magnet material (Arnold, 2014)) and ten upside (stabilizing) magnets BM-40×10×4-N35. The carriage moving in the x -direction comprises four magnets BM-80×20×10-N35H.

From the FEM models, the magnetic forces acting on the carriage consisting of 4-magnet have been computed. In Fig. 20, the force acting in the z -direction is presented as a function of the carriage position in the z -direction (zero position means contact between the carriage and

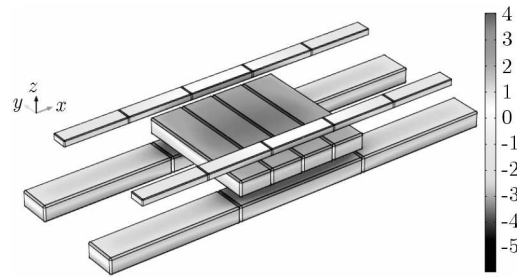


Fig. 19. The proposed magnetic track with the distribution of magnetic vector potential

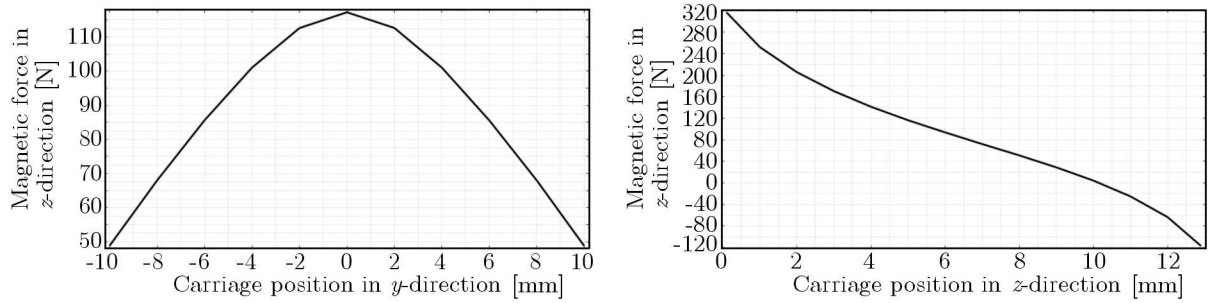


Fig. 20. Magnetic force acting on the 4-magnet carriage in the z -direction

downside magnets, 13 mm means contact with the upside magnets) and in the y -direction (zero means central location of the carriage).

In Fig. 21, the magnetic force acting on the 4-magnet carriage in the y -direction is presented as a function of the carriage position in the y -direction.

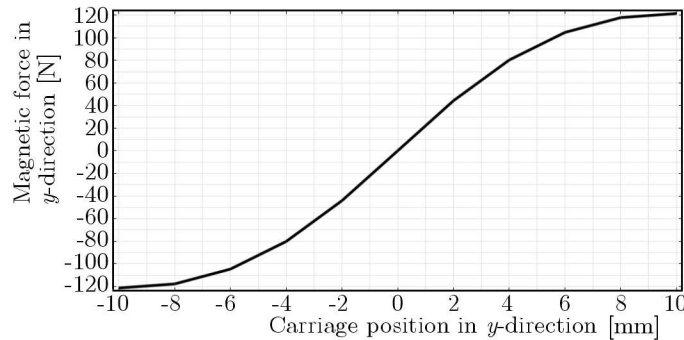


Fig. 21. Magnetic force acting on the 4-magnet carriage in the y -direction

The computed results are very optimistic and prove that the proposed magnetic support can be an applicable part in the real model of the coil EML for UAVs of mass up to 25 kg. Nevertheless, the magnetic force is strongly dependent on the carriage position and may cause instability of the slideway. In real objects, a bearing system in the y -direction should be applied.

7. Remarks and future works

The nearest future works should be connected with experimental verification of the magnetic forces generated by the investigated coils and acting on the proposed magnetic core. The important part is also CAD design of the EML construction consisting of six driving modules (each having 20 coils). The problems of power transmission from the core to the carriage and

the launched UAV should also be deeply investigated and solved. Moreover, other constructional aspects should be taken into design considerations, for instance, shape and materials of the frame, transport possibilities, system assembly and disassembly, power system connections, electronic control systems, safety conditions, fixing UAV on the launcher, mechanical strength of the crucial elements, etc. So far, the conducted research has revealed that the described project is quite challenging and very multidisciplinary. The obtained results and designed solutions are optimistic and give a real chance for practical realisation of the magnetic coil EML for UAVs of mass up to 25 kg.

Works conducted so far on magnetic launchers, assisted start procedures and UAVs autonomy inspired authors to think on the design of a fully operational autonomous system for observation and inspection of extensive territories and regions such as forests, swamps, deserts or even border zones. The main assumption is that the proposed system should operate and perform its missions without any human assistance. Such a system should consist of an operational micro or medium class wing-plane adjusted to particular missions, coil magnetic launcher, landing subsystem, generator or battery used as the power source and control system. An airplane with wings can cover much longer distance than quadco-, hexa- or octocopters in the same amount of time and with lower energy cost. In order to carry out a mission, such an UAV can be launched in precisely defined periods of time, for example, minutes, hours or days. A hard and challenging task is to accomplish the UAV landing process after which the airplane should almost instantly be prepared for another launch without any human assistance. In our opinion, development of the landing subsystem is crucial for practical application of the proposed autonomous system. First conceptual ideas have been already born and they will be investigated in the near future.

Acknowledgement

The study has been financed by Bialystok University of Technology as the own research work MB/WM/11/2013.

References

1. Arnold Magnetic Technologies Co., 2014, www.arnoldmagnetic.com (15.06.2014)
2. GOSIEWSKI Z., AMBROZIAK L., 2012, Formation flight control scheme for unmanned aerial vehicles, *Lecture Notes in Control and Information Science*, **422**, 331-340
3. GOSIEWSKI Z., CIEŚLUK J., AMBROZIAK L., 2011, Vision-based obstacle avoidance for Unmanned Aerial Vehicles, *4th International Congress on Image and Signal Processing*, P. Qiu, Y. Xiang, Y. Ding, D. Li, L. Wang (Edit.), IEEE, 2053-2058
4. KOLM H., MONGEAU P., WILLIAMS F., 1980, Electromagnetic launchers, *IEEE Transactions on Magnetism*, **Mag-16**, 5, 719-721
5. KONDRATIUK M., 2013, Designing and investigating of the magnetic coil launcher with controlled acceleration of the launching object (in Polish), PhD thesis, BUT
6. KONDRATIUK M., GOSIEWSKI Z., 2013a, Laboratory stand of an electromagnetic multi-coil launcher for micro aerial vehicles, *Mechatronic Systems and Materials IV*, Z. Gosiewski, Z. Kulesza (Edit.), Durnten-Zurich, Trans-Tech Publications, Solid State Phenomena, 334-339
7. KONDRATIUK M., GOSIEWSKI Z., 2013b, Simulation model of an electromagnetic multi-coil launcher for micro aerial vehicles, *Mechatronic Systems and Materials IV*, Z. Gosiewski, Z. Kulesza, Durnten-Zurich, Solid State Phenomena, 406-411
8. KONDRATIUK M., GOSIEWSKI Z., 2014, Comparison of electromagnetic coil launcher model with real-device characteristics, *Solid State Phenomena*, **214**, 58-66
9. KOWNACKI C., 2013, Successful application of miniature laser rangefinders in obstacle avoidance method for fixed wing MAV, *International Journal of Robotics and Automation*, **28**, 3, 292-298

10. ŁADYŻYŃSKA-KOZDRAŚ E., FALKOWSKI K., SIBILSKA-MROZIEWICZ A., 2014a, Physical model of the cart of an UAV catapult using Meissner effect (in Polish), [In:] *Mechanika w Lotnictwie, ML-XVI 2014*, t. II, K. Sibilski (Edit.), PTMTS Warsaw, 231-241
11. ŁADYŻYŃSKA-KOZDRAŚ E., FALKOWSKI K., SIBILSKA-MROZIEWICZ A., 2014b, Vibration analysis of a levitating cart of a magnetic catapult (in Polish), [In:] *Mechanika w Lotnictwie, ML-XVI 2014*, t. II, K. Sibilski (Edit.), PTMTS Warsaw, 243-250
12. McNAB I., 2007, A research program to study airborne launch to space, *IEEE Transactions on Magnetics*, **43**, 1, 486-490
13. MYSTKOWSKI A., 2013, Piezo-stack vortex generators for boundary layer control of a delta wing micro-aerial vehicle, *Mechanical Systems and Signal Processing*, **40**, 783-790
14. MYSTKOWSKI A., 2014, Implementation and investigation of a robust control algorithm for an unmanned micro-aerial vehicle, *Robotics and Autonomous Systems*, **62**, 1187-1196
15. PATTERSON D., MONTI A., BRICE C., DOUGAL R., PETTUS R., SRINIVAS D., DILIPCHANDRA K., BERTONCELLI T., 2002, Design and simulation of an electromagnetic aircraft launch system, *Industry Applications Conference, 37th IAS Annual Meeting*, 1950-1957
16. PERKOWSKI W., 2008, Pneumatic launcher for unmanned aerial vehicles, *Transport and Engineering*, **27**, 181
17. SIBILSKI K., FALKOWSKI K., OLEJNIK A., 2014, Magnetic take-off and landing system of airplanes – project GABRIEL (in Polish), [In:] *Mechanika w Lotnictwie, ML-XVI 2014*, t. II, K. Sibilski (Edit.), PTMTS Warsaw, 216-229
18. TOMCZUK B., SCHRÖDER G., WAINDOK A., 2007, Finite element analysis of the magnetic field and electromechanical parameters calculation for a slotted permanent magnet tubular linear motor, *IEEE Transactions on Magnetics*, **43**, 7, 3229-3236
19. TOMCZUK B., WAINDOK A., 2009, Linear motors in mechatronics – achievements and open problems, Transfer of innovation to the interdisciplinary teaching of mechatronics for the advanced technology needs, Opole University of Technology, 343-360
20. TOMCZUK B., WAINDOK A., WAJNERT D., 2012, Transients in the electromagnetic actuator with the controlled supplier, *Journal of Vibroengineering*, **14**, 1, 39-44

OPTIMAL POINT TO POINT PATH PLANNING OF FLEXIBLE MANIPULATOR UNDER LARGE DEFORMATION BY USING HARMONY SEARCH METHOD

HABIB ESFANDIAR

Department of Mechanical and Aerospace Engineering, Science and Research Branch, Islamic Azad University, Tehran, Iran; e-mail: habibesfandiar2014@gmail.com

MOHARAM HABIBNEJAD KORAYEM

Department of Mechanical and Aerospace Engineering, Science and Research Branch, Islamic Azad University, Tehran, and Robotic Research Laboratory, Center of Excellence in Experimental Solid, Mechanics and Dynamics, School of Mechanical Engineering, Iran University of Science and Technology, Tehran, Iran; e-mail: hkorayem@iust.ac.ir

This paper aims at planning an optimal point to point path for a flexible manipulator under large deformation. For this purpose, the researchers use a direct method and meta-heuristic optimization process. In this paper, the maximum load carried by the manipulator and the minimum transmission time are taken as objective functions of the optimization process to get optimal path profiles. Kinematic constraints, the maximum velocity and acceleration, the dynamic constraint of the maximum torque applied to the arms and also the constraint of final point accuracy are discussed. For the optimization process, the Harmony Search (HS) method is used. To evaluate the effectiveness of the approach proposed, simulation studies are reviewed by considering a two-link flexible manipulator with the fixed base. The findings indicate that the proposed method is in power of dealing with nonlinear dynamics of the system. Furthermore, the results obtained by rigid, small and large deformation models are compared with each other.

Keywords: meta-heuristic optimization, harmony search, large deformation, flexible manipulator

1. Introduction

In order to increase the efficiency and economy of manipulators, finding an optimal trajectory by maximum dynamic load capacity and minimum transmission time between two points is of particular and high importance. When planning a point to point path, there are many complexities, so different methods should be used to solve the problem. All used methods are a subset of two main methods, namely direct and indirect methods. In general, the indirect methods are based on the optimal control theory and the minimum principle of Pontryagin. The planning of a two-link rigid manipulator is done via using the optimal control by Korayem *et al.* (2009). To calculate Dynamic Load Carrying Capacity (DLCC) in a manipulator, the optimal control method is studied through considering complete dynamics of the system and nonlinear terms. Boundary conditions are exactly satisfied and the optimization problem is numerically solved with sufficient accuracy. Korayem and Nikoobin (2009) studied the optimal path planning for rigid and fixed-base two-link manipulators with the help of the optimal control method. By using Pontryagin optimality conditions, the determination of the maximum load capacity will be changed to the standard two-point boundary value problem (Korayem and Nikoobin, 2009). Korayem *et al.* (2011) planned an optimal path for a two-link mobile manipulator by using the indirect method. They proved that the implementation of the optimal control considering full

nonlinear dynamics of the system caused by Hamiltonian gradient calculation, the existence of a two-point boundary value problem and the use of a multiple shooting numerical method are not so easy.

In all activities mentioned using the indirect methods and the optimal control theory to plan the optimal path, there are the following limitations. Path planning by the optimal control needs nonlinear numerical techniques such as multiple shooting methods. These techniques require a good initial guess and are sensitive to it. These methods also require an analytical form of the Hamiltonian gradient and an optimum value of state variables obtained by using the Hamiltonian gradient. In these methods, the state variables are used to solve the problem that in the general case (especially by considering the flexibility) it is very difficult to estimate them. Furthermore, precise determination of weight functions for different objective functions will make some problems in the implementation of the methods presented. To resolve the defects, direct approaches are recommended to plan the path. Direct methods are based on discretization of dynamic variables of the system (state variables and control variables) in which ultimately, to provide the parameters, the problem of planning a path will result in a parametric optimization problem. In these methods, the profile of joints motion is represented directly by polynomial, Spline and B-spline functions. By the profile of joints motion, the path planning will be changed to the optimization problem to determine the optimality of profile constant coefficients. To solve the optimization problem, meta-heuristic approaches speeding up the convergence and decreasing the sensitivity to the initial guess can be used. To implement these methods, there is no requirement for linearization and simplification of dynamic equations of the system, and so complete dynamics of the system can be considered.

When planning a trajectory, different functions are considered as objective functions in optimization. The most important ones are the minimum transmission time (Haddad *et al.*, 2005), minimum energy consumption (Spangelo and Egeland, 1992) and minimum jerk in joints (Piazzi and Visoli, 2000). Different methods are developed to study the path planning by the direct method presented such as Genetic Algorithm method (GA) (Garg and Kumar, 2002; Saravanan and Ramabalan, 2008; Saravanan *et al.*, 2008), Simulated Annealing (SA), Sequential Weight Increasing Factor Technique (SWIFT) and Sequential Quadratic Programming (SQP) method (Chettibi *et al.*, 2004). In (Chettibi *et al.*, 2004), SQP method is used to plan the path. It is clear that SQP may get a local optimum, and for convergence of this optimal solution, it is necessary to select the initial guess appropriately. Haddad *et al.* (2007) studied a point to point path planning problem for a mobile base manipulator. They used the direct method and random optimization to plan the path. The path was generated based on the objective function of minimum transmission time and the kinematic constraints of velocity, acceleration as well as the dynamic constraint of torque of the motors. Furthermore, the path planning was also done based on the stability constraint of the manipulator by ZMP method. Tangpattanakul and Artrit (2009) paid attention to path planning of the manipulator based on the objective function of minimum transmission time in the point to point case. The optimization problem was solved by considering kinematic constraints using Harmony Search. The simulation results showed that HS method converged faster than SQP method to the optimal solution, and the sensitivity of this method was less toward the initial guess. Tangpattanakul *et al.* (2010) investigated the problem of point to point path planning by using HS optimization method. The simulation results proved that HS was a better method for solving the problem of robot path planning. Zanotto *et al.* (2011) considered the minimum transmission time and jerk as the objective function in the optimization problem. Experimental results were also elaborated to compare with the theoretical results. Chettibi and Lemoine (2007) planned a point to point path by using SQP. They offered a single-link manipulator considering full dynamics of the manipulator and the driving motor. To solve the problem of optimization, the objective function of minimum transmission time and electro-mechanic constraints were used.

This paper includes the following aspects of innovations. An optimal path is designed for a manipulator by considering the most complete nonlinear dynamics, large deformation model and Timoshenko beam model. In previous papers, direct methods were used and the effects of the flexibility with the large deformation model were rarely considered in manipulators. In addition, by using the optimal control method, simplification of non-linear equations is non-avoidable due to the excessive complexity of the solution process. In most papers employing direct methods, the minimum transmission time, minimum energy consumption and minimum jerk are considered as the objective function. However, in this paper, the minimum transfer time besides the maximum load carrying capacity of manipulators is assumed as the objective function. In this paper, the Harmony Search method is used to determine the load carrying capacity of the manipulators that have no restrictions to nonlinear dynamics of the systems. The methods like the optimal control have some difficulties when dealing with such issues. So, here, the most complete process is used to design an optimal path using HS method. The proposed optimization method has the following advantages: (1) a global optimal solution is possible, (2) it is easy to program and implement efficiently, (3) it ensures that the resulting optimized trajectory is smoother, faster, and nonsingular, (4) it can also be extended to get optimized trajectories for other types of robots, (5) it considers both kinematic and dynamic aspects of the robot, (6) it considers the payload constraint, and (7) it is computationally superior and faster. The paper is thus organized in the following Sections. In Section 2, dynamic modeling of the manipulator is investigated in the large deformation case. In Section 3, the problem of path planning is discussed by a direct method. Section 4 deals with the extraction of the optimization problem arising from path planning. The method proposed for solving the optimization problem and a flowchart of optimal path planning are presented in Section 5. Finally, the simulation results are presented for a two-link flexible manipulator.

2. Dynamic analysis of a flexible manipulator under large deformation

Consider an m -link manipulator (Fig. 1) by n degrees of freedom ($n > m$) that should move from the initial position X^{ini} to the final position X^{fin} in space of end effector (assume q_r^{fin} , q_r^{ini} are corresponding joint variables). For dynamic modeling, arms are based on the Timoshenko beam model, and also shear effects are considered. The movement of the arms will be described by the rotation angle of the links θ_i , flexible displacement $w_i(x_i, t)$ and rotation caused by the flexible displacement ψ_i .

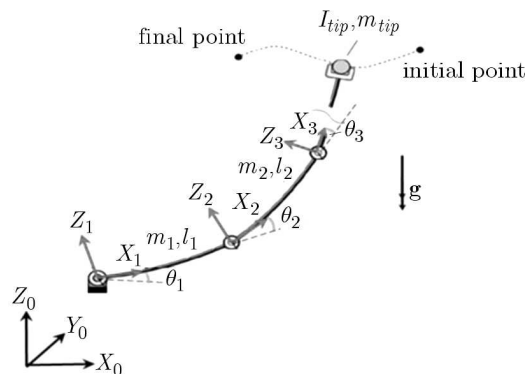


Fig. 1. m -link flexible manipulator with a fixed base

The displacement field for the Timoshenko beam with large deformation is as follows

$$u_x = -Z \sin \psi(x, t) \quad u_z = w(x, t) + Z \cos \psi(x, t) \quad (2.1)$$

where Z is the distance to the neutral axis of the beam. Non-zero elements of the Green strain tensor in the case of large deformation can be written as follows

$$E_{11} = E_0 + ZK_b = \underbrace{\frac{1}{2}(w_{,x}^2)}_{E_0} + \underbrace{Z[-\psi_{,x}(\cos\psi + w_{,x}\sin\psi)]}_{K_b} \quad (2.2)$$

$$E_{12} = \frac{1}{2}(-\sin\psi + w_{,x}\cos\psi) = \Lambda$$

where E_0 is axial strain, K_b – curve occurred in the beam element by large deformation, Λ – shear strain.

In the above expression, $w_{,x} = \partial w(x, t)/\partial x$. Kinetic energy of the system equals to kinetic energy of the arms KE_{arm} and tip KE_{tip} mass

$$KE = KE_{arm} + KE_{tip} \quad (2.3)$$

where

$$KE_{arm} = \sum_{i=1}^m KE_{i,arm} \quad KE_{i,arm} = \frac{1}{2} \int \rho_i [\dot{\mathbf{p}}_i^T(x_i, t) \dot{\mathbf{p}}_i(x_i, t)] dv_i$$

$$KE_{tip} = \frac{1}{2} m_{tip} (\dot{\mathbf{p}}_{tip}^T \dot{\mathbf{p}}_{tip}) + \frac{1}{2} I_{tip} \left(\sum_{j=1}^m \dot{\theta}_j \right)^2$$

where $\mathbf{p}_i(x_i, t)$ is the position of a small element on the i -th flexible arm and \mathbf{p}_{tip} is the position vector of tip mass with respect to the absolute coordinates $\{X_0, Y_0, Z_0\}$ defined as follows

$$\mathbf{p}_i(x_i, t) = \sum_{j=0}^{i-1} \mathbf{B}_j(l_j, t) + \mathbf{B}_i(x_i, t)$$

$$\mathbf{B}_i(x_i, t) = [x_i \cos(\theta_{i-1} + \theta_i) - w_i(x_i, t) \sin(\theta_{i-1} + \theta_i)] \mathbf{I} \quad (2.4)$$

$$+ [x_i \sin(\theta_{i-1} + \theta_i) + w_i(x_i, t) \cos(\theta_{i-1} + \theta_i)] \mathbf{K}$$

$$\mathbf{p}_{tip} = \sum_{j=1}^m \mathbf{B}_j(l_j, t) \quad (i = 1, 2, \dots, m) \quad \mathbf{B}_0 = \mathbf{0} \quad \theta_0 = 0$$

Potential energy of the system consists of strain energy and gravitational potential energy

$$PE = \frac{1}{2} \sum_{i=1}^m \int_0^{l_i} (E_i A_i E_{i,0}^2 + E_i I_i K_{i,b}^2 + k G_i A_i \Lambda_i^2) dx_i \quad (2.5)$$

$$+ \sum_{i=1}^m \rho_i A_i g \left(\sum_{j=0}^{i-1} H_j(l_j, t) + \int_0^{l_i} H_i(x_i, t) dx_i \right) + m_{tip} g \sum_{j=1}^m H_j(l_j, t)$$

$$H_i(x_i, t) = x_i \sin(\theta_{i-1} + \theta_i) + w_i(x_i, t) \cos(\theta_{i-1} + \theta_i) \quad H_0 = 0 \quad \theta_0 = 0$$

where g is the acceleration of gravity.

3. Problem statement

By separating the joint and flexibility variables and applying the extended Hamilton method, the general form of the m -link manipulator equations is as follows

$$\begin{bmatrix} \mathbf{M}_f & \mathbf{M}_r \end{bmatrix} \begin{bmatrix} \ddot{\mathbf{q}}_f \\ \ddot{\mathbf{q}}_r \end{bmatrix} + \begin{bmatrix} \mathbf{C}_f(\mathbf{q}, \dot{\mathbf{q}}) \\ \mathbf{C}_r(\mathbf{q}, \dot{\mathbf{q}}) \end{bmatrix} + \begin{bmatrix} \mathbf{Q}_f(\mathbf{q}) \\ \mathbf{Q}_r(\mathbf{q}) \end{bmatrix} = \begin{bmatrix} \mathbf{0} \\ \boldsymbol{\tau} \end{bmatrix} \quad (3.1)$$

where \mathbf{M}_f is the inertia matrix for flexibility degrees of freedom in the manipulator, \mathbf{M}_r – inertia matrix for rigid degrees of freedom, the vector \mathbf{q} contains generalized coordinates, $\mathbf{q}_r, \mathbf{q}_f$ are vectors of the flexibility coordinates and joint coordinates, respectively, $\mathbf{C}_f(\mathbf{q}, \dot{\mathbf{q}}), \mathbf{C}_r(\mathbf{q}, \dot{\mathbf{q}})$ – Coriolis and centrifugal force vector for flexible and for rigid degrees of freedom, $\mathbf{Q}_f(\mathbf{q}), \mathbf{Q}_r(\mathbf{q})$ – gravity vector for flexible and for rigid degrees of freedom, $\boldsymbol{\tau}$ – torque applied to the joints. By having both initial and final points of the end effector, the main purpose is to determine the maximum load capacity, transmission time, joint variables vector, the corresponding velocity and torque vector applied to the manipulator so that to satisfy all the constraints in the system. To solve the problem by the direct method, the profile of the joints path will be approximated directly through interpolation functions such as polynomial, Spline and B-Spline functions, and the problem of path planning will be changed to a parametric optimization problem in order to calculate the constants of interpolation functions. Then, the optimization problem can be solved by using meta-heuristic optimization.

3.1. Optimization by the objective function of maximum load carrying capacity

In this case, the objective of path planning in the point to point case is to calculate a trajectory for the robot end effector in which the manipulator can carry the maximum dynamic load and the kinematic constraints of the joints, velocity and acceleration, torque dynamic constraint and end point accuracy constraint will be satisfied. In addition, the optimal path must be planned not to meet manipulator singularity configurations. The problem of planning an optimal path by considering the objective function and above the constraints will be presented in the form of an optimization problem as follows

$$f_{obj} = \max(m_{tip}, I_{tip})$$

$$\text{subject to } (i = 1, 2, \dots, m) \begin{cases} |q_{r,i}(t)| \leq q_{r,i}^{max} & |\dot{q}_{r,i}(t)| \leq k_{vi} & |\ddot{q}_{r,i}(t)| \leq k_{ai} \\ |\tau_i(t)| \leq \tau_i^{max} & |q_{r,i}^{fin} - q_{r,i}(T)| \leq \varepsilon \end{cases} \quad (3.2)$$

where m_{tip}, I_{tip} are the concentrated mass and moment inertia of the end manipulator, τ_i^{max} – maximum torque applied to the joints.

3.2. Optimization by the objective function of minimum transmission time

In this case, minimization of the transmission time between the initial and final points is the aim of optimal path planning. Assume $\tilde{q}_r(t)$ as a candidate selected for the profile of the joints path. By using a change in the variable $\zeta = t/T$ ($0 \leq \zeta \leq 1$), any kinematic and dynamic constraints presented in the previous Section are discussed as bands of the transmission time. The constraints governing joint velocity and acceleration can be converted into the following formulas by applying the derivation chain rule

$$T \geq T_v \Rightarrow T_v = \max_{i=1,2,\dots,m} \left[\max_{\zeta \in [0,1]} \frac{|\tilde{q}'_{r,i}(\zeta)|}{k_{vi}} \right] \quad \tilde{q}'_{r,i}(\zeta) = \frac{d\tilde{q}_{r,i}(\zeta)}{d\zeta}$$

$$T \geq T_A \Rightarrow T_A = \max_{i=1,2,\dots,m} \left[\max_{\zeta \in [0,1]} \frac{|\tilde{q}''_{r,i}(\zeta)|}{k_{ai}} \right]^{\frac{1}{2}} \quad \tilde{q}''_{r,i}(\zeta) = \frac{d^2\tilde{q}_{r,i}(\zeta)}{d\zeta^2} \quad (3.3)$$

Dynamic constraints determination the motors torque may be changed to constraints of two bands in terms of the transmission time so that $T \in [T_L, T_R]$. By examining the bands time obtained, finally, the end band $[T_{lower}, T_{upper}]$ will be found for the transmission time. The optimal transmission time for each profile of the trajectory can be obtained by minimizing the objective function based on the transmission time of the period. By using a change in the variable $\zeta = t/T$,

the differential equation of motion for the i -th variable of the joint in the m -link manipulator will be as below

$$\begin{aligned}\bar{\tau}_i(\zeta) &= \frac{1}{T^2}\bar{h}_{r,i}(\zeta) + \bar{Q}_{r,i}(\zeta) & \zeta \in [0, 1] & & i = 1, 2, \dots, m \\ h_{r,i}(\zeta) &= \sum_{j=1}^m M_{r,ij}\tilde{q}_{r,j}''(\zeta) + C_{r,i}(\tilde{q}(\zeta), \tilde{q}'(\zeta)) \\ \bar{h}_{r,i}(\zeta) &= \frac{h_{r,i}(\zeta)}{\tau_i^{max}} & \bar{Q}_{r,i}(\zeta) &= \frac{Q_{r,i}(\tilde{q}(\zeta))}{\tau_i^{max}} & \bar{\tau}_i(\zeta) &= \frac{\tau_i(\zeta)}{\tau_i^{max}}\end{aligned}\quad (3.4)$$

So, the dynamic constraints will be changed to the following equation

$$\begin{aligned}-1 \leq \frac{1}{T^2}\bar{h}_{r,i}(\zeta) + \bar{Q}_{r,i}(\zeta) \leq 1 & & -b_i(\zeta) \leq \frac{1}{T^2}\bar{h}_{r,i}(\zeta) \leq a_i(\zeta) \\ a_i(\zeta) = 1 - \bar{Q}_{r,i}(\zeta) & & b_i(\zeta) = 1 + \bar{Q}_{r,i}(\zeta)\end{aligned}\quad (3.5)$$

Thus, for any $\zeta \in [0, 1]$, the time bands T related to the torque constraint are given in Table 1.

Table 1. Transmission time bands of the path profile selected for dynamic constraints

$\bar{h}_{r,i}(\zeta) \geq 0$			$\bar{h}_{r,i}(\zeta) < 0$		
$a_i(\zeta) < 0$	$a_i(\zeta) \geq 0$		$b_i(\zeta) < 0$	$b_i(\zeta) \geq 0$	
	$b_i(\zeta) < 0$	$b_i(\zeta) \geq 0$		$a_i(\zeta) < 0$	$a_i(\zeta) \geq 0$
\emptyset	$T_{L,i} = \sqrt{\frac{\bar{h}_{r,i}(\zeta)}{a_i}}$	$T_{L,i} = \sqrt{\frac{\bar{h}_{r,i}(\zeta)}{a_i}}$	\emptyset	$T_{L,i} = \sqrt{\frac{\bar{h}_{r,i}(\zeta)}{a_i}}$	$T_{L,i} = \sqrt{\frac{\bar{h}_{r,i}(\zeta)}{-b_i}}$
	$T_{R,i} = \sqrt{\frac{\bar{h}_{r,i}(\zeta)}{-b_i}}$	$T_{R,i} \rightarrow +\infty$		$T_{R,i} = \sqrt{\frac{\bar{h}_{r,i}(\zeta)}{-b_i}}$	$T_{R,i} \rightarrow +\infty$

In general, the problem of optimal path planning by objective function of minimum transmission time and the presented constraints are developed in the form of the optimization problem

$$\begin{aligned}f_{obj} &= \min(T) \\ \text{subject to} & \begin{cases} T \geq T_v & T_v = \max_{i=1,2,\dots,m} \left[\max_{\zeta \in [0,1]} \frac{|\tilde{q}_{r,i}'(\zeta)|}{k_{vi}} \right] \\ T \geq T_A & T_A = \max_{i=1,2,\dots,m} \left[\max_{\zeta \in [0,1]} \frac{|\tilde{q}_{r,i}''(\zeta)|}{k_{ai}} \right]^{\frac{1}{2}} \\ T_L \leq T \leq T_R & \text{Table 1} \\ |\tilde{q}_{r,i}^{fin} - \tilde{q}_{r,i}(T)| \leq \varepsilon \end{cases}\end{aligned}\quad (3.6)$$

4. The method of solving the optimization problem

To solve the problem of optimization, HS meta-heuristic method will be used. For designing the end effector trajectory, it is necessary to model the path profile for any joint by using the profile of a smooth trapezoid or a cubic Spline. For example, the overall form of a smooth trapezoidal profile is always as follows

$$\tilde{q}_{r,j} = \begin{cases} q_{r,j}^{ini} + D_j \frac{1}{1 + \zeta_b - \zeta_a} \left(\frac{2\zeta^3}{\zeta_a^2} - \frac{\zeta^4}{\zeta_a^3} \right) & 0 \leq \zeta < \zeta_a \\ q_{r,j}^{ini} + D_j \frac{2\zeta - \zeta_a}{1 + \zeta_b - \zeta_a} & \zeta_a \leq \zeta < \zeta_b \\ q_{r,j}^{ini} + D_j \left[1 - \frac{1}{1 + \zeta_b - \zeta_a} \left(\frac{2(1 - \zeta)^3}{(1 - \zeta_b)^2} - \frac{(1 - \zeta)^4}{(1 - \zeta_b)^3} \right) \right] & \zeta_b \leq \zeta \leq 1 \end{cases} \quad (4.1)$$

where

$$D_j = q_{r,j}^{fin} - q_{r,j}^{ini}$$

Therefore, by the initial and final points of the trajectory and optimal determination of the variables (ζ_b, ζ_a) (by observing the condition $0 \leq \zeta_a, \zeta_b \leq 1$), the optimal form of joint motion will be determined. A flowchart of optimal path planning is represented in Fig. 2 with the help of Harmony Search for the m -link manipulator.

5. Numerical simulation

Generalized coordinates of a two-link flexible manipulator with a fixed base is considered as the vector $\mathbf{q} = [\theta_1, \theta_2, w_1, \psi_1, w_2, \psi_2]$. w_1 and w_2 are transverse vibration variables of the first and second arm, respectively. Also, ψ_1 and ψ_2 are rotations caused by transverse vibrations of the first and second arm. By using the finite element method and dividing the arms into multiple elements, the flexibility variables of the i -th element of the first arm and the flexibility variables of the j -th element of the second arm are presented as follows

$$\begin{aligned} w_{1i} &= [N_1(x), N_2(x)] \{ \tilde{w}_{1i}(t) \} & \psi_{1i} &= [N_1(x), N_2(x)] \{ \tilde{\psi}_{1i}(t) \} & i &= 1, 2, \dots, n_1 \\ w_{2j} &= [N_1(x), N_2(x)] \{ \tilde{w}_{2j}(t) \} & \psi_{2j} &= [N_1(x), N_2(x)] \{ \tilde{\psi}_{2j}(t) \} & j &= 1, 2, \dots, n_2 \\ [N_1(x), N_2(x)] &= \left[1 - \frac{x}{l}, \frac{x}{l} \right] \end{aligned} \quad (5.1)$$

where n_1 and n_2 are equal to the nodes of the elements network of the first and second arm. So, the closed form of dynamic equations of the flexible two-link manipulator is as follows

$$\begin{bmatrix} m_{11} & m_{12} & m_{13} & m_{14} & m_{15} & m_{16} \\ & m_{22} & m_{23} & m_{24} & m_{25} & m_{26} \\ & & m_{33} & m_{34} & m_{35} & m_{36} \\ & & & m_{44} & m_{45} & m_{46} \\ \text{sym} & & & & m_{55} & m_{56} \\ & & & & & m_{66} \end{bmatrix} \begin{bmatrix} \ddot{\theta}_1 \\ \ddot{\theta}_2 \\ \tilde{w}_{1i} \\ \tilde{\psi}_{1i} \\ \tilde{w}_{2j} \\ \tilde{\psi}_{2j} \end{bmatrix} + \begin{bmatrix} C_1 \\ C_2 \\ C_{3i} \\ 0 \\ C_{5j} \\ 0 \end{bmatrix} + \begin{bmatrix} Q_1 \\ Q_2 \\ Q_{3i} \\ Q_{4i} \\ Q_{5j} \\ Q_{6j} \end{bmatrix} + \begin{bmatrix} D_1 \\ D_2 \\ D_{3i} \\ D_{4i} \\ D_{5j} \\ D_{6j} \end{bmatrix} = \begin{bmatrix} \tau_1 \\ \tau_2 \\ 0 \\ 0 \\ 0 \\ 0 \end{bmatrix} \quad (5.2)$$

$i = 1, 2, \dots, n_1 \quad j = 1, 2, \dots, n_2$

where the vector \mathbf{Q} represents the effects of gravitational and potential energy of the system. The vector \mathbf{D} is a disturbance torque or a force vector. It should be noted that \mathbf{D} has different meanings. For example, it can be a friction and reaction torque or force. The end effector position can be offered by the following equation

$$X_e = [l_1 \cos \theta_1 + l_2 \cos(\theta_1 + \theta_2)]\mathbf{i} + [l_1 \sin \theta_1 + l_2 \sin(\theta_1 + \theta_2)]\mathbf{j} \quad (5.3)$$

To optimally plan a path for a two-link manipulator in the point to point case, the optimization problems should be solved as follows:

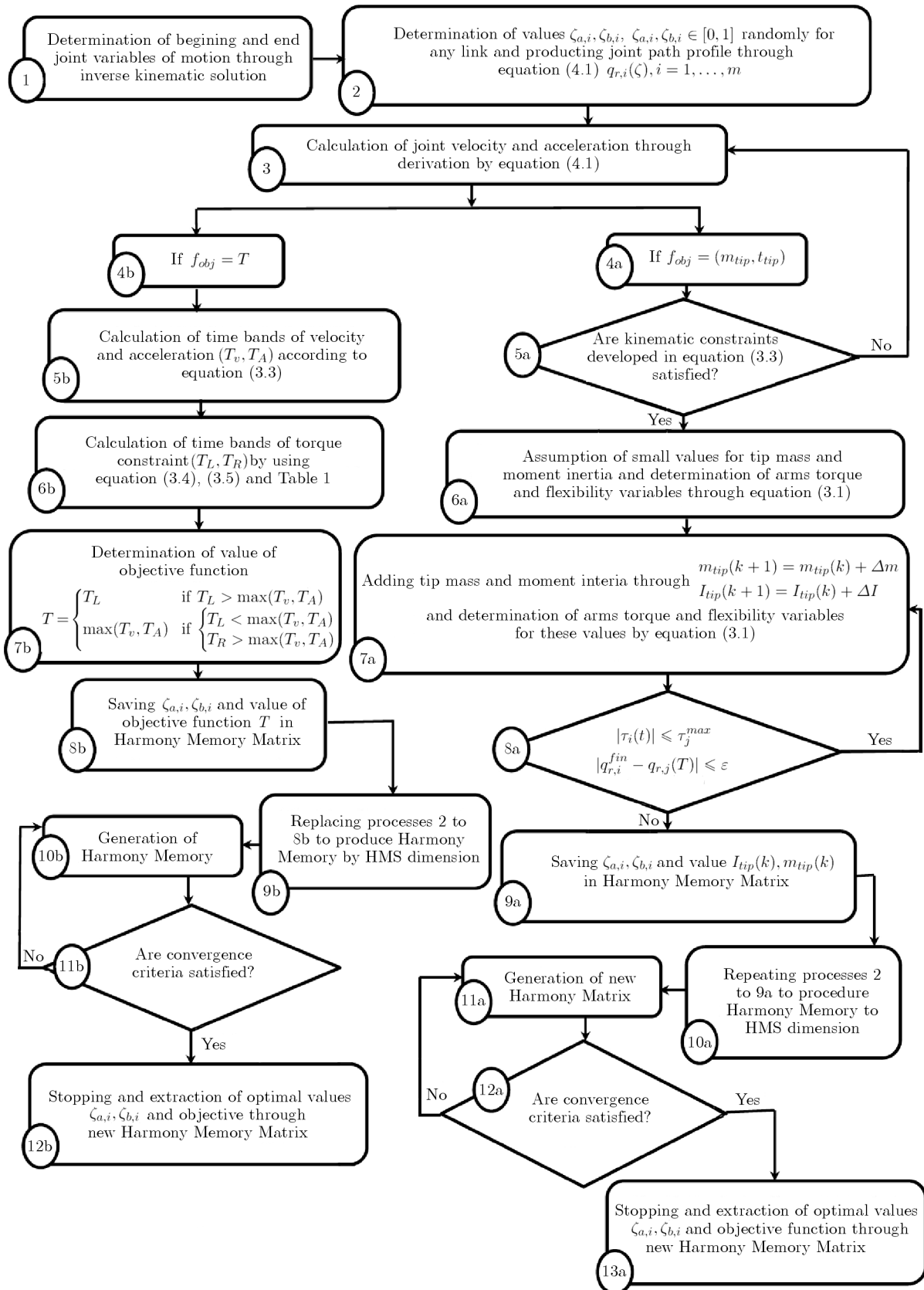


Fig. 2. Optimal path planning flowchart by Harmony Search method

— Path planning based on the minimum transmission time

$$f_{obj} = \min(T)$$

$$\text{design variables} = (\zeta_{a1}, \zeta_{b1}, \zeta_{a2}, \zeta_{b2})$$

$$\theta_i(t) = \tilde{q}_{r,i} \quad \text{from Eq. (4.2)}$$

$$\begin{bmatrix} \tau_1 \\ \tau_2 \end{bmatrix} = \begin{bmatrix} m_{11} & \cdots & m_{16} \\ m_{21} & \cdots & m_{26} \end{bmatrix} \begin{bmatrix} \ddot{\theta}_1 \\ \ddot{\theta}_2 \end{bmatrix} + \begin{bmatrix} C_1 \\ C_2 \end{bmatrix} + \begin{bmatrix} Q_1 \\ Q_2 \end{bmatrix} \quad \text{from Eq. (5.2)}$$

$$\text{subject to} \begin{cases} T \geq T_v & T_v = \max_{i=1,2} \left[\max_{\zeta \in [0,1]} \frac{|\tilde{q}'_{r,i}(\zeta)|}{k_{vi}} \right] \\ T \geq T_A & T_A = \max_{i=1,2} \left[\max_{\zeta \in [0,1]} \frac{|\tilde{q}''_{r,i}(\zeta)|}{k_{ai}} \right]^{\frac{1}{2}} \\ T_L \leq T \leq T_R & \text{from Eq. (3.6) and Table 1} \\ |X_e(T) - X^{fin}| \leq \varepsilon \end{cases}$$

— Path planning based on the maximum load capacity

$$f_{obj} = \max(m_{tip})$$

$$\text{design variables} = (\zeta_{a1}, \zeta_{b1}, \zeta_{a2}, \zeta_{b2})$$

$$\theta_i(t) = \tilde{q}_{r,i} \quad \text{from Eq. (4.2)}$$

$$\begin{bmatrix} \tau_1 \\ \tau_2 \end{bmatrix} = \begin{bmatrix} m_{11} & \cdots & m_{16} \\ m_{21} & \cdots & m_{26} \end{bmatrix} \begin{bmatrix} \ddot{\theta}_1 \\ \ddot{\theta}_2 \end{bmatrix} + \begin{bmatrix} C_1 \\ C_2 \end{bmatrix} + \begin{bmatrix} Q_1 \\ Q_2 \end{bmatrix} \quad \text{from Eq. (5.2)}$$

$$\text{subject to} \begin{cases} |\theta_i(t)| \leq \theta_i^{max} \\ |\dot{\theta}_i(t)| \leq k_{vi} \\ |\ddot{\theta}_i(t)| \leq k_{ai} & i = 1, 2 \\ |\tau_i(t)| \leq \tau_i^{max} \\ |X_e(T) - X^{fin}| \leq \varepsilon \end{cases}$$

To validate the results, simulation of a planar two-link manipulator described by Heidari (2011) will be done and compared with the results obtained by the optimal control method. Table 2 shows the parameters of the manipulator assumed.

Table 2. Parameters of the flexible two-link manipulator (Heidari, 2011)

Parameter (unit)	Value	Parameter (unit)	Value
Length of links [m]	$l_1 = l_2 = 0.5$	Moment of inertia [m ⁴]	$I_1 = I_2 = 2.5 \cdot 10^{-9}$
Mass [kg]	$m_1 = m_2 = 3$	Young's modulus of material [N/m ²]	$E_1 = E_2 = 2 \cdot 10^{10}$

The initial position of the end effectors, when $t = 0$, is at the point (0.5, 0) and when $t = 1$ s, is at the point (0.5, 0.5). The end effector velocity at the beginning and end of the path is also assumed to be zero. To get rid of the singularity case in the manipulator, the constraint $\theta_2(t) \neq 0^\circ$ and 180° is considered in the optimization problem. The maximum torque of the motors is equal to $\tau_{max} = 8$ Nm. The results of joints torque and the path paved by the end effector by considering the minimum of torque as the objective function for three cases including rigid arms, arm with small deformation and an arm with large deformation are shown in Figs.3 and 4. Figures 3a,b indicate that by taking the effect of flexibility of the arms into account, the torques resulting from the large and small deformation exhibit fluctuation behavior to the rigidity, and the torque resulting from large deformation is slightly greater than that from small deformation. Figure 4 indicates that the paths obtained by small and large deformation models

do not reach the end point and deviation occurs. The deviation at the start point is large, and the fluctuations of the end effector path are increased by greater flexibility. The results obtained are in good agreement with the results reported by Heidari (2011).

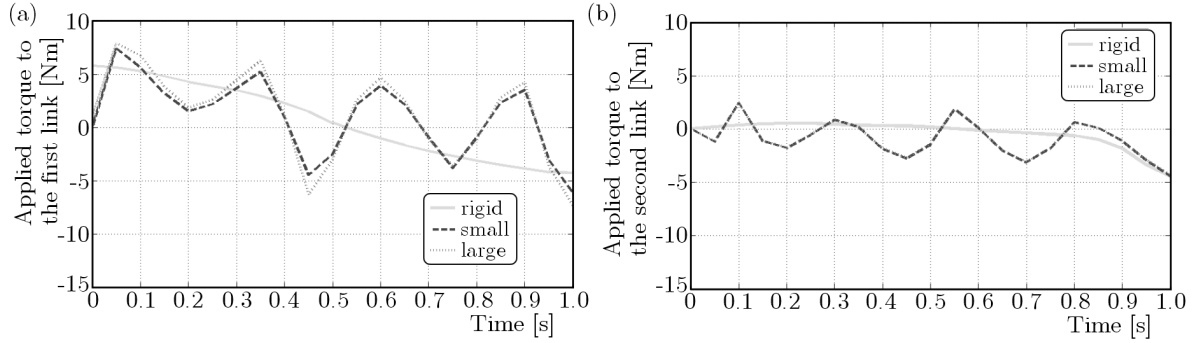


Fig. 3. Torque applied to the (a) first link and (b) second link

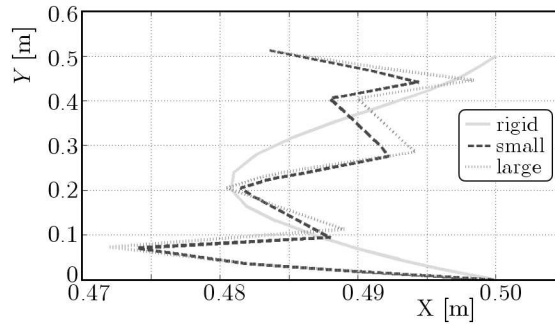


Fig. 4. End effector trajectory for the planar two-link manipulator

5.1. Results of path planning by the maximum load carrying capacity

This Section addresses the planning of an optimal path by considering the maximum load capacity as the objective function. For this purpose, a two-link manipulator is taken on the plane XZ in which the end effector moves from $x_1 = 1.6$ m, $z_1 = 0$ m and after the time $t = 2$ s stops in the point $x_2 = 1.2$ m, $z_2 = 1.2$ m. For HS optimization method, harmony memory size also is $HMS = 10$, the harmony memory considering rate is $HMCR = 0.75$ and the pitch adjustment rate is $PAR = 0.25$. The maximum velocity and acceleration equal to $k_v = 3$ rad/s, $k_a = 10$ rad/s² respectively, and the maximum torque is $\tau_{max} = 230$ Nm. The allowed error from the final point is $\varepsilon = 2$ cm as well. Manipulator parameters specified in this Section is are given in Table 3. In all following figures, a smooth trapezoidal profile is considered as profile 1 and a cubic Spline profile as profile 2. By solving inverse kinematics, the values of position and joints velocity at the beginning and end of the path are obtained as follows

$$\begin{aligned}
 \theta_1(0) &= -1.4455 \text{ rad} & \theta_2(0) &= -0.4240 \text{ rad} \\
 \theta_1(2) &= 1.6961 \text{ rad} & \theta_2(2) &= 1.4455 \text{ rad} \\
 \dot{\theta}_1(0) &= \dot{\theta}_2(0) = \dot{\theta}_1(2) = \dot{\theta}_2(2) = 0
 \end{aligned} \tag{5.4}$$

The results of these three cases including rigid arms, arms with small deformation and arms with large deformation are presented. The results of the maximum load by considering kinematic and dynamic constraints for both profiles are presented in Table 4. By studying the figures related to the angular displacement and arms torque, it is clear that wherever the slope of torque figure is greater, the corresponding angular displacements will change more quickly, and any change

Table 3. Parameters of the two-flexible link manipulator

Parameter	Value (unit)	Parameter	Value (unit)
Length of links	$l_1 = 0.4 \text{ m}, l_2 = 1.6 \text{ m}$	Cross-section area	$A_1 = A_2 = 2.5 \cdot 10^{-3} \text{ m}^2$
Density of links	$\rho_1 = \rho_2 = 3000 \text{ kg/m}^3$	Moment of inertia	$I_1 = I_2 = 5.2 \cdot 10^{-7} \text{ m}^4$
Young's modulus of material	$E_1 = E_2 = 0.3 \cdot 10^{11} \text{ N/m}^2$	Shear modulus	$G_1 = G_2 = 16 \cdot 10^5 \text{ N/m}^2$

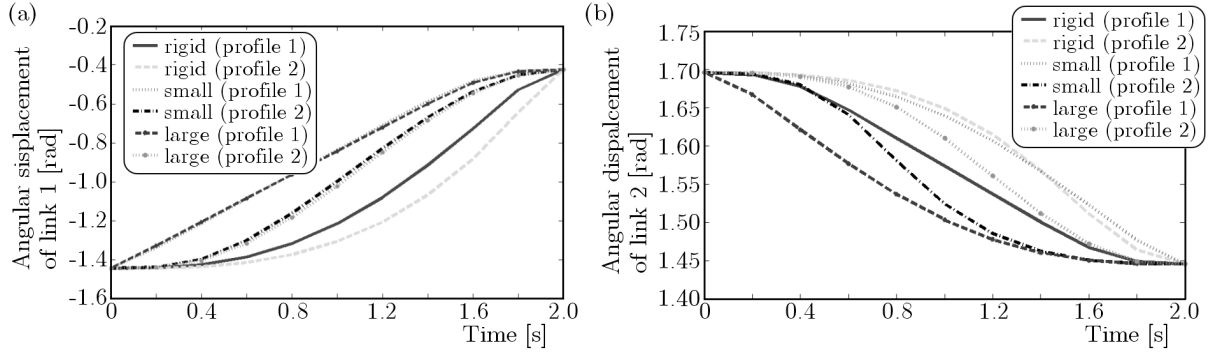


Fig. 5. Angular displacement of the (a) first link and (b) second link

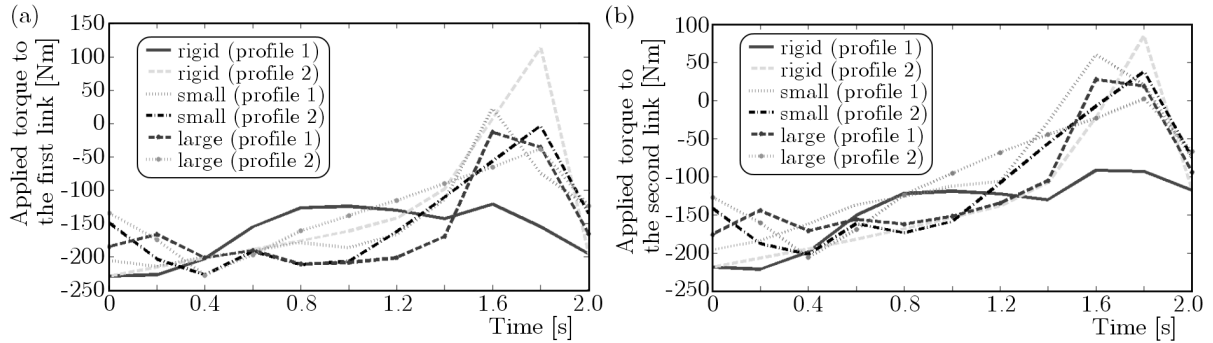


Fig. 6. Torque applied to the (a) first link and (b) second link

in the torque direction will alter the angular displacement of the arms. Figure 7 indicates that the path obtained for profiles in different cases are smooth. By studying the figures and the results obtained in this Section, it can be seen that the flexibility of the arms has a significant effect on the problem of manipulator path planning so that the load capacity of the manipulator for both profiles is less than the rigid one by taking into account the flexibility of the arms. This difference is due to the limitation of the engine torque caused by torque fluctuations in the small and large deformation models. A more careful flexibility analysis of the model developed to be carried out and more complete nonlinear terms to be considered makes the results for the load carrying capacity to decrease. Therefore, small deformation is no longer a complete model for studying the effects of flexibility. Harmony Search method is appropriately consistent with nonlinear dynamics of the system and for implementing this method. There is no need to simplify the dynamic equations of the system. The results indicate superiority of the smooth trapezoidal profile over the cubic Spline profile. Since, the load carrying capacity for the smooth trapezoidal profile is greater than that for the cubic Spline profile. According to the results obtained, it can be said as far as the capabilities of the method proposed are concerned that this method has no problem with nonlinear dynamics of the manipulator, and the optimal path will be obtained with appropriate convergence speed. It has potential to consider all kinematic, dynamic, and singularity constraints as well as the end point accuracy constraint at the same time in the optimization process.

Table 4. Results of optimally path planning by the maximum load capacity

Profile	Model	DLCC [kg]
Smooth trapezoidal	rigid	8.4
	small	6.9
	large	5.6
Cubic spline	rigid	8.4
	small	3.3
	large	2.4

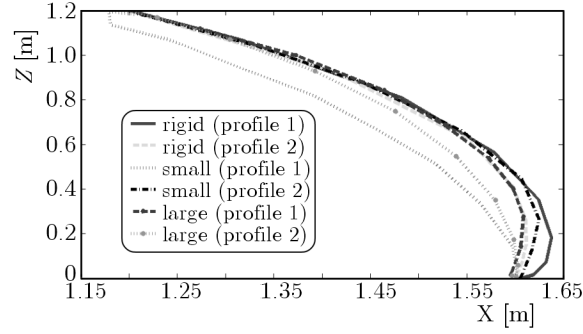


Fig. 7. The end effector trajectory in rigid, small and large deformation models

5.2. The results of planning the optimal path by minimum transmission time

The planning of an optimal path will be investigated here by considering the minimum transmission time as the objective function. The results are presented in form of a figure for the cubic Spline profile only. By reviewing the previous Section and taking $m_{tip} = 1.5$ kg, the results of path planning are presented in Figs. 8 and 9 for arms corresponding to the large deformation model. Since, the angular displacement of the first arm during motion is larger than the angular displacement of the second arm, as shown in Fig. 8b, the angular velocity of the first arm is greater than that of the second arm. Similarly, the torque applied to the first arm is greater than

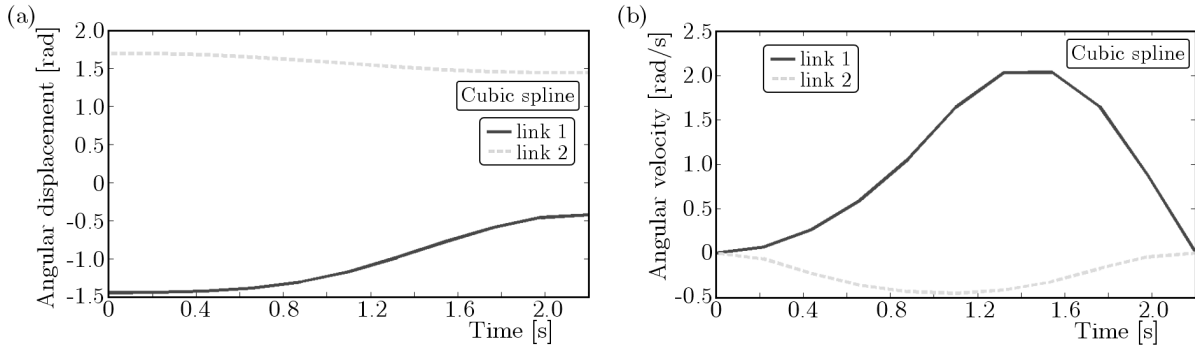


Fig. 8. Angular displacement (a) and angular velocity (b) of the first and second links in the large deformation model

that in the second arm, and the engine of the first arm will reach its saturation point sooner. The optimal path planned for all three models are shown in Fig. 10. By studying this figure, it is clear that the path planned for the small and large deformation models does not reach the end point, and there is a distance equal to the allowed amount $\varepsilon = 2$ cm. The results of the transmission time by considering kinematic and dynamic constraints and HS method for both profiles are given in Table 5. It shows that HS method is efficient enough to solve the optimal robot trajectory planning. What is presented in the table indicates that the flexibility of the

arms increases the time of transmission for both profiles. The transmission times obtained for the manipulator through the rigid and small deformation models are not much different. But, the value of this parameter in the large deformation model is greater than that in rigid and small deformation models. In this case, the results obtained from the smooth trapezoidal profile are even better than the results of the cubic Spline profile.

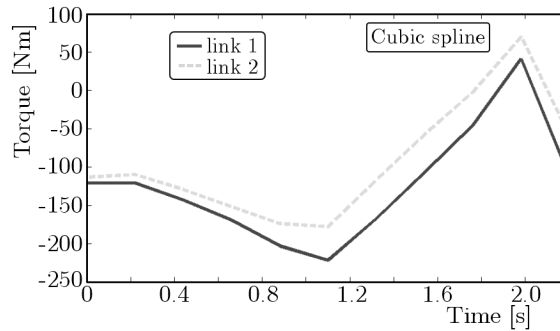


Fig. 9. Torque applied to the first and second links in the large deformation model

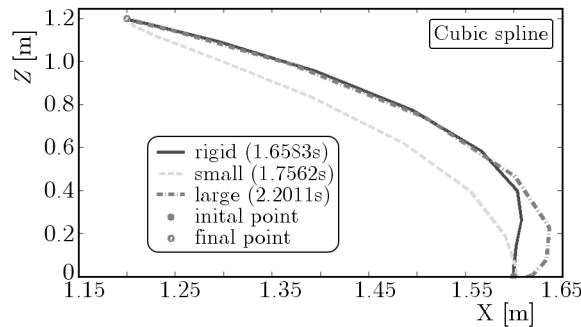


Fig. 10. Optimal path paved by the end effector for the minimum transmission time in rigid, small and large deformation models

Table 5. Results of the optimal path planning by the minimum transmission time

Profile	Model	Minimum transmission time [s]
Smooth trapezoidal	rigid	0.8794
	small	0.9152
	large	1.5603
Cubic spline	rigid	1.6583
	small	1.7562
	large	2.2011

6. Conclusion

The problem of optimal path planning for a flexible manipulator has been studied by using the direct process and HS meta-heuristic optimization method in the point to point case and the open-loop mode. The maximum of dynamic load capacity and the minimum transmission time as two criterions determining the efficiency of manipulators have been considered as objective functions in path planning of end the effector. Full dynamics of the manipulator has been studied

by taking large deformation of the arms into account. By using smooth trapezoidal and cubic Spline profiles as joint path profiles, the planning of the optimal path has changed to a nonlinear optimization problem through the direct process. To solve the problem of nonlinear optimization, HS efficient method has been used as being appropriate for optimization problems with multiple dimensions and having a high speed of convergence. The proposed method is more effective for path planning than indirect methods (optimal control theory). This is because there is no need to linearize and simplify nonlinear equations of motion which enables the dynamics of the system to be considered completely. The limitation of selecting appropriate weight functions does not exist in the proposed method, and there is no need for suitable initial guess to get faster convergence. To evaluate the effectiveness of the proposed method, optimal path planning for a two-link flexible manipulator has been performed for a trajectory between two points given. Also, comparison has been made between the results obtained for the arms of the rigid, small deformation and large deformation models. The results prove that the proposed method has a good compatibility with all models, and is also applicable to multi-link manipulators.

References

1. CHETTIBI T., LEHTIHET H.E., HADDAD M., 2004, Minimum cost trajectory planning for industrial robots, *European Journal of Mechanics A/Solids*, **23**, 703-715
2. CHETTIBI T., LEMOINE P., 2007, Generation of point to point trajectories for robotic manipulators under electro-mechanical constraints, *International Review of Mechanical Engineering, IREME*, 131-143
3. GARG D.P., KUMAR M., 2002, Optimization techniques applied to multiple manipulators for path planning and torque minimization, *Engineering Applications of Artificial Intelligence*, **15**, 241-252
4. HADDAD M., CHETTIBI T., HANCI S., LEHTIHET H.S., 2005, A new approach for minimum time motion planning problem of wheeled mobile robots, *16th IFAC World Congress*, Prague
5. HADDAD M., HANCI S., LEHTIHET H.E., 2007, Sub-optimal motion planner of a mobile manipulator with end-effector's specified path, *IFTToMM World Congress*
6. HEIDARI H., 2011, Maximum allowable dynamic load of flexible manipulators undergoing large deformation, PhD Thesis, Iran University of Science and Technology, Iran
7. KORAYEM M.H., NIKOUBIN A., 2009, Formulation and numerical solution of robot manipulators in point-to-point motion with maximum load carrying capacity, *Robotica*, **16**, 101-109
8. KORAYEM M.H., NIKOUBIN A., AZIMIRAD V., 2009, Maximum load carrying capacity of mobile manipulators: Optimal control approach, *Robotica*, **27**, 147-159
9. KORAYEM M.H., RAHIMI NOHOJHI H., NIKOUBIN A., 2011, Path planning of mobile elastic robotic arms by indirect approach of optimal control, *International Journal of Advanced Robotic Systems*, **8**, 10-20
10. PIAZZI A., VISIOLI A., 2000, Global minimum-jerk trajectory planning of robot manipulators, *IEEE Transactions on Industrial Electronics*, **47**, 140-149
11. SARAVANAN R., RAMABALAN S., 2008, Evolutionary minimum cost trajectory planning for industrial robots, *Journal of Intelligent and Robotic Systems*, **52**, 45-77
12. SARAVANAN R., RAMABALAN S., BALAMURUGAN C., 2008, Evolutionary optimal trajectory planning for industrial robot with payload constraints, *International Journal of Advanced Manufacturing Technology*, **38**, 1213-1226
13. SPANGELO I., EGELAND O., 1992, Generation of energy-optimal trajectories for an autonomous underwater vehicle, *Proceedings of the 1992 IEEE International Conference on Robotics and Automation*, Nice, France, May 12-14

14. TANGPATTANAKUL P., ARTRIT P., 2009, Minimum-time trajectory of robot manipulator using Harmony Search algorithm, *6th International Conference on Electrical Engineering/Electronics, Computer, Telecommunication and Information Technology (ECTICON)*, Chonburi, Thailand
15. TANGPATTANAKUL P., MEESOMBOON A., ARTRIT P., 2010, Optimal trajectory of robot manipulator using Harmony search algorithms, *SCI*, **270**, 23-36
16. ZANOTTO V., GASPARETTO A., LANZUTTI A., BOSCARIOL P., VIDONI R., 2011, Experimental validation of minimum time-jerk algorithms for industrial robots, *Journal of Intelligent and Robotic Systems*, **64**, 197-219

Manuscript received January 5, 2015; accepted for print July 19, 2015

POST-CRITICAL DEFORMATION STATES OF COMPOSITE THIN-WALLED AIRCRAFT LOAD-BEARING STRUCTURES

TOMASZ KOPECKI, JERZY BAKUNOWICZ, TOMASZ LIS

Rzeszów University of Technology, Faculty of Mechanical Engineering and Aeronautics, Rzeszów, Poland

e-mail: kopecki@prz.edu.pl; bakun@prz.edu.pl; list@prz.edu.pl

The study presents results of experimental examination of a model representing a fragment of an aircraft wing structure with the skin made of a glass fibre/epoxy composite. For such a system, the deformation pattern has been found and the representative equilibrium path determined. The finite element method has been used to develop the corresponding numerical model, the correctness of which has been then verified by comparing the obtained results with the course of the relevant experiment. Conformity of the results allowed one to determine usefulness of the applied methods in the assessment of mechanical properties of modified solutions involving integral skin stiffening elements.

Keywords: skin, loss of stability, finite element method, composite, equilibrium path

1. Introduction

Contemporary aircraft structures represent a group of devices that are, and, for many years have been invariably expected to meet the highest requirements in the area of their properties, fulfil exorbitant economical criteria and comply with particularly rigorous safety-related rules. To meet the latter, design engineers are compelled to continuously improve the design processes the fundamental portion of which is nowadays realised in the space of virtual objects by using sophisticated numerical tools. Among a number of software types utilised commonly in various stages of designing and fabrication of new structures, a specially important role should be attributed to programs based on the finite element method (FEM).

One of the problems related to application of such programs that, despite continuous progress in the aircraft technology, still lacks the ultimate solution, consists in imperfections of the utilised numerical models and the resulting divergences between the results obtained by means of them and behaviour of actual objects (Ramm and Wall, 2004). While the general knowledge and available databases containing results of experimental research for typical isotropic materials used in the aviation industry, such as e.g. titanium and aluminium alloys, allow one to define the above-mentioned models with sufficient precision, the structures based on composites of various types, although utilised more and more frequently, are still particularly troublesome objects to analyse (Seresta, 2007). It follows from the fact that results pertaining to experimental studies on composite structures, especially those dealing with their behaviour under cyclic load conditions and at occurrence of large deformations, are in general considered trade secrets of aerospace corporations and are disclosed only in a fragmentary scope in commonly available scientific publications.

A feature that is highly distinctive for aircraft structures in comparison with other groups of thin-walled systems is the admissibility of occurrence of post-critical deformation in their elements (Dow *et al.*, 1954), provided that the related loss of stability has an elastic nature and occurs locally within the area of skin segments limited by components of the skeleton (Taylor and Eckford, 1968). The principle is used commonly with respect to metal structures (Niu, 1988).

In the case of composite structures, the rule applicable for many years provided the obligatory use of solutions making the occurrence of skin buckling impossible, e.g. by means of using interlayers in the form of foamed plastics or cellular cores (Federal Aviation Administration, 2009). The above-mentioned rule in combination with the stiffness-based composite structure designing criterion can be applied to light aircraft structures (gliders, light-sports aircraft), but it must be considered inapplicable to extensive structures such as wings of large transportation aeroplanes in which large deformations are inevitable. In the process of designing contemporary transportation aircraft, in aspiration to minimise the overall mass of the structure, the use of composite skins are becoming more and more popular among designers constructing load-bearing demanding elements in the case of which a local stability loss is admissible. Examples of such solutions can be found in such aeroplanes as American Boeing 787 and European Airbus 350. In the case of the former, the main cause of delay in realisation of the project were problems with finding an appropriate design solution for the composite bearing structure. The scale of research projects necessary to realise undertakings of that scope can be partially illustrated by the input provided by projects POSICOSS and COCOMAT financed within the European Commission Framework Programme. However, there is always a serious fear that as a result of bending, relative high stress gradients may appear in outer layers of the skin that in turn may become a cause of its premature destruction (Arborcz, 1985; Nemeth, 2013).

Application of the above design principle involves therefore absolute necessity to perform experiments aimed at precise determination of mechanical properties of individual components of the structure in cyclic post-critical deformation conditions (Kopecki, 2019; Kopecki and Mazurek, 2013). It should be noted at this point that the results obtained in the case of composites may depend both on the skin thickness resulting from the number of fabric layers and the manufacturing process, type and properties of components as well as and fibre orientation. In view of multitude of such factors having the effect on the structure properties, the possibility to generalise experimental results concerning mechanical properties of composites is very limited.

Regardless of the composite type, advisability to strive after limitation of magnitude of post-critical deformations occurring in operating conditions seems to be obvious. Solutions aspiring to obtain such a target include employment of integral stiffening elements of various types as well as changing proportions and reducing dimensions of skin segments at risk of losing stability.

Realisation of relevant experiments with the use of models representing selected variants of solutions of that type can constitute a basis for development and making more specific numerical models formulated in terms of the finite element method thanks to which it would be possible to determine effects of a number of further modifications of the examined structures.

2. Purpose and scope of the research

Considerations presented in this study represent the first stage of a planned series of experimental-numerical analyses of thin-walled composite aircraft structures. The research program is aimed at determination of the effect of selected variants of integral skin stiffening elements on the critical load value and post-critical deformation magnitude in combination with mass analysis, the effect of which should be a structure with the most effective total mass/durability ratio.

The research stage described in this paper involves realisation of an experiment with the use of a model of a representative aircraft structure, and then the development of an adequate numerical model of the structure the nonlinear analysis of which, carried out with the use of the finite element method, would allow one to obtain a distribution of deformations corresponding to actual ones both qualitatively and quantitatively.

The subject of the analysis was a fragment of a monospar wing structure with a constant chord along the whole span and the stiffened front torsion box (Fig. 1). The examined variant constituted the simplest possible system of that type and lacked any integrated longitudinal skin stiffening elements, playing the role of a reference structure for subsequent variants with modified geometry and stiffness planned to be examined.

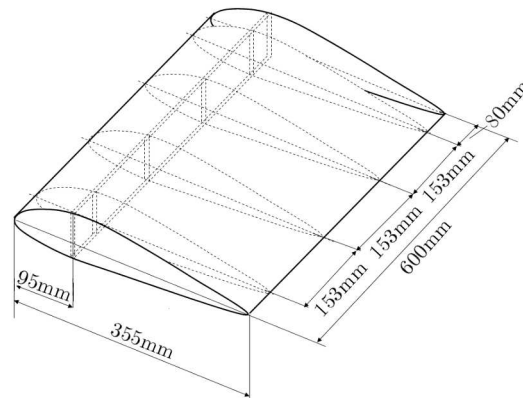


Fig. 1. An overall outline of the examined structure

The model was manufactured in the wet lay-up method and handmade formed in moulds. The composite consisted of Interglass 02037 and 92110 glass fabrics and MGS L285/H286 epoxy resin and was characterised by $E_{11} = 22000$ MPa, $E_{22} = 22000$ MPa, $\nu_{12} = 0.11$, $G_{12} = 4600$ constants. The upper and lower wing surfaces were connected to the spruce box spar and plywood web of 1mm thickness. Additionally, the roots were reinforced by plywood ribs with joints. The whole wing was manufactured from two halves attached together in mouldings and then cured in the LPC process.

3. Experimental research

The skeleton portion of the model used in the experiment was made of plywood and wooden slats with known mechanical parameters. The skin was an epoxy composite reinforced with glass fibre (GFRP).

As the composite reinforcement, Interglass glass fibre fabrics were used with the weight ratios of 50 g/m^2 and 163 g/m^2 . The matrix was a permeating mix based on epoxy resin MGSL285. The skin of the model in the torsion box zone was made as a laminar structure comprising three layers of a symmetric fabric. The main directions of the composite orthotropy were oriented at the angle of 45 degrees with respect to the direction of the spar flanges. The remaining portion of the structure contained two layers of the fabric (Fig. 2). Such a solution was aimed at protecting the torsion box surface against the loss of stability and creation of conditions favourable to the occurrence of post-critical deformations in the skin part between the spar and the trailing edge. The reinforcement coefficient of the composite was 50% in mass. The “mother” specimen for each composite type was fabricated in the same process, additionally. Analysis of the specimen weight allowed one to calculate the reinforcement coefficient, knowing weight of the fabric prior to fabrication.

In the course of experiment, the model was subjected to simultaneous bending and torsional deflection (Fig. 3) on a specially constructed experimental set-up (Fig. 4). Influence of friction in the bearing roller was neglected.

The load was applied gravitationally. In the course of the experiment, displacements of selected reference points were measured for subsequent stationary deformation states of the structure.

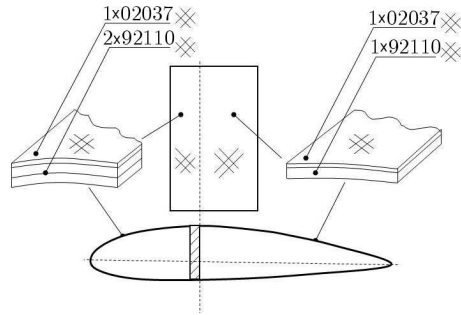


Fig. 2. Schematic representation of lamination of the considered structure

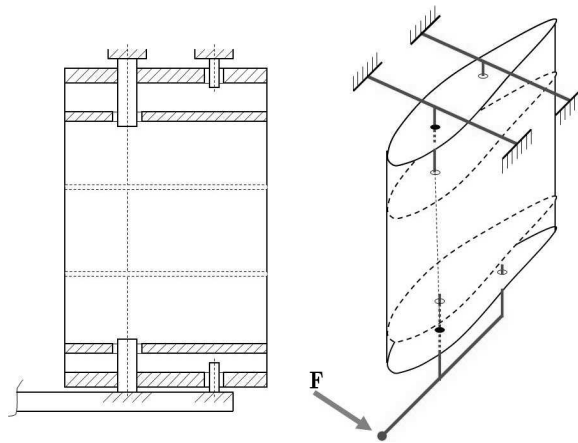


Fig. 3. An outline of the model fastening and load application (TL)

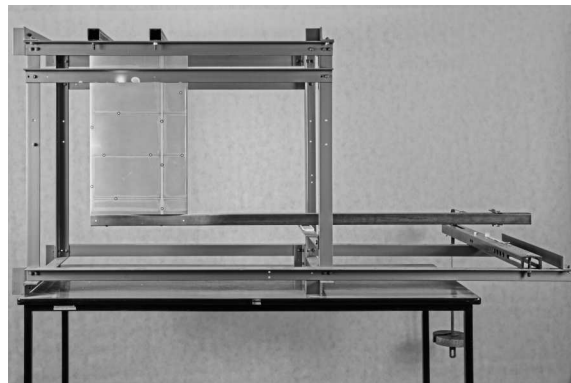


Fig. 4. The research set-up

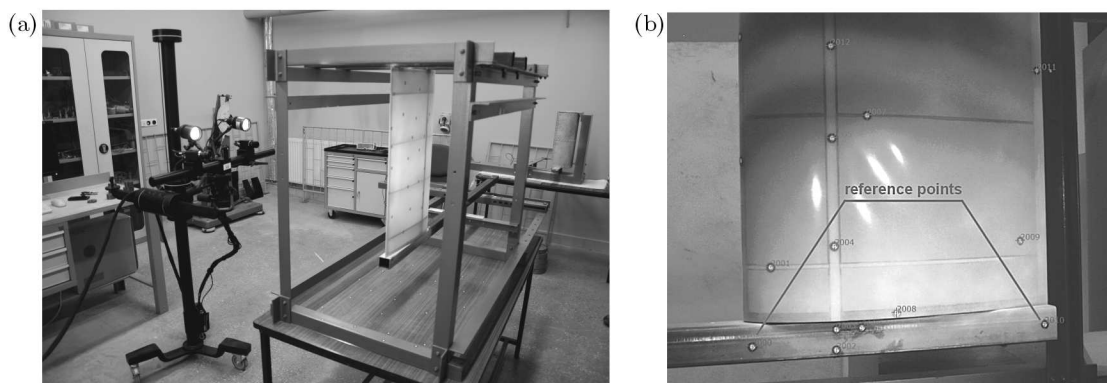


Fig. 5. (a) PONTOS measuring system; (b) selected reference points

To measure the displacements, PONTOS measuring system by GOM Optical Measuring Techniques was used (Fig. 5). As a result, a representative equilibrium path was obtained constituting a relationship between the structure total torsion angle and the load value (Fig. 6).

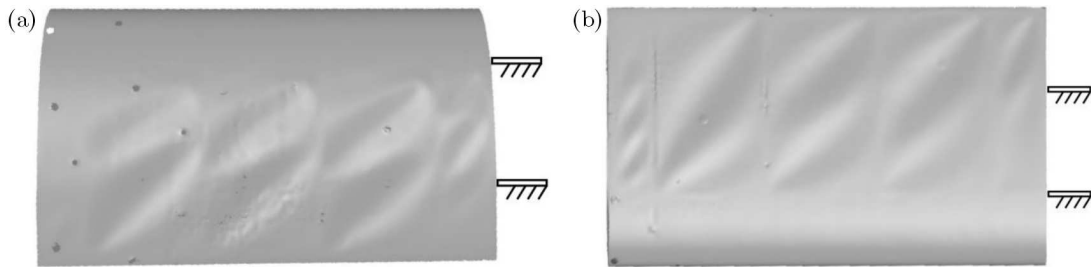


Fig. 6. Model deformations determined by means of ATOS scanner; (a) upper skin, (b) lower skin

Moreover, for the target load value, the whole surface of the deformed model was scanned with the use of ATOS scanner. As a result, the deformation fields was obtained (Fig. 6) constituting the base for qualitative verification of the results obtained numerically.

4. Numerical analyses

During the computational stage of the study the necessary question to be answered was, with the nature of deformations taken into account, the possibility of developing an adequate numerical model of a composite structure with the use of commercially available software. The decisive phase of the model creation stage is the use of an algorithm the purpose of which is to determine properties of the laminate based on sets of constants corresponding to its individual layers. In the case of MSC PATRAN/MARC software used in this study, any interference of the user to the structure of the program is not possible.

A distinctive feature of composite structures making the development of their numerical representation very difficult is their inhomogeneity resulting not only from conditions in which individual layers are laminated but also from assembling operations, i.e. presence of local excesses of resin and diversified thickness of bonded joints. Such factors can induce local skin stiffness variations and have an effect on post-critical deformation patterns. Even small errors in selection of geometric parameters for the numerical model, introducing definite deviations from actual boundary conditions characterising a skin segment, generate significant errors in the course of nonlinear analyses.

The fundamental relationship in the numerical problem determining quantitatively the link between conditions of a structure and the load applied to it is the so-called equilibrium path of the system in question constituting, in general, a hypersurface in the hyperspace of states (Ramm, 1987). The relationship fulfils the matrix equation of residual forces (Felippa, 1976)

$$\mathbf{r}(\mathbf{u}, A) = \mathbf{0} \quad (4.1)$$

where \mathbf{u} is the state vector containing components of displacements of nodes of the structure corresponding to its current geometrical configuration, A is the control parameter corresponding to the current load level, and \mathbf{r} is the residual vector containing non-balanced force components related to the current system deformation state. The set of control parameters can be represented by a single parameter being a function of the load. Equation (4.1) takes then the form

$$\mathbf{r}(\mathbf{u}, \lambda) = \mathbf{0} \quad (4.2)$$

called the single-parameter equation of residual forces.

The prediction-correction methods of determining the consecutive points of the equilibrium path used in contemporary software routines contain also a correction phase based on the requirement that the system satisfies an additional equation called the increment control equation or the constraints equation (Bathe, 1996; Kopecki and Mazurek, 2014)

$$c(\Delta \mathbf{u}_n, \Delta \lambda_n) = 0 \quad (4.3)$$

where the increments

$$\Delta \mathbf{u}_n = \mathbf{u}_{n+1} - \mathbf{u}_n \quad \Delta \lambda_n = \lambda_{n+1} - \lambda_n \quad (4.4)$$

correspond to transition from the state n to the state $n + 1$.

In view of the lack of possibility to represent equilibrium paths for systems with more than 2 degrees of freedom in a form of easily readable plots, in practice, for the purpose of comparison, the so-called representative equilibrium paths are used which represent a functional relationship between a selected parameter characterising deformation of the system and a single control parameter related to the applied load. Reliability of results obtained from FEM-based nonlinear numerical analyses is usually accepted when a satisfactory convergence is found between two representative equilibrium paths, namely the actual one determined in the course of an experiment and that obtained numerically. It is also necessary to obtain convergence between the forms of deformations following from calculations (Ramm and Wall, 2004) with the results of a corresponding experiment. On the grounds of the solution uniqueness rule, according to which a specific deformation pattern may correspond to one and only one stress distribution pattern, the reliability can be then attributed also to the reduced stress distributions in the deformed skin (Marcinowski, 1999).

As the nonlinear numerical analysis is an iterative process aimed at finding successive equilibrium states, its correctness is to a large degree determined by correct choice of the prognostic method, the correction strategy, and a number of control parameters. In the case described here, the Newton-Raphson method has been used in combination with the Crisfield hyperspherical correction strategy.

By contrast with numerical analyses where the goal is to obtain the number of finite elements as high as possible, the use of an excessively dense grid of elements in nonlinear analyses leads sometimes to faulty results with the calculation time becoming significantly longer. After a series of numerical tests aimed at selection of a proper topology of the model, it has been decided to use a model comprising 4838 bilinear, four-node shell elements. The necessity to employ such an element resulted from the fact that other types available in the MSC MARC software library, to which the properties of laminated composites could be assigned, do not offer the possibility to reproduce geometrically complex objects, in view of the type and number of degrees of freedom.

Mechanical properties of the numerical model have been taken from the experimental data set, as described in Section 3. Boundary conditions of the numerical model have been simulated by fixed degrees of freedom in certain nodes of the root rib. Moreover, the loading has been simulated by a relevant beam, as in the experimental setup (Fig. 7).

The first version of the model, reproducing faithfully geometry of the actual object, turned out to lead to an incorrect form of post-critical deformations despite appropriate selection of the set of nodes and correct application of the load (Fig. 8).

In the case of the obtained results, although the representative equilibrium path of the system proved to be satisfactorily similar to this determined in the course of the experiment, it was no longer possible to rely on the above-mentioned solution uniqueness rule.

Usually, the reasons of incorrect determination of deformation pattern corresponding to the minimum energy states can be usually sought in excessively idealised reproduction of geometrical parameters of the structure. The encountered problem can be attributed to the above-discussed

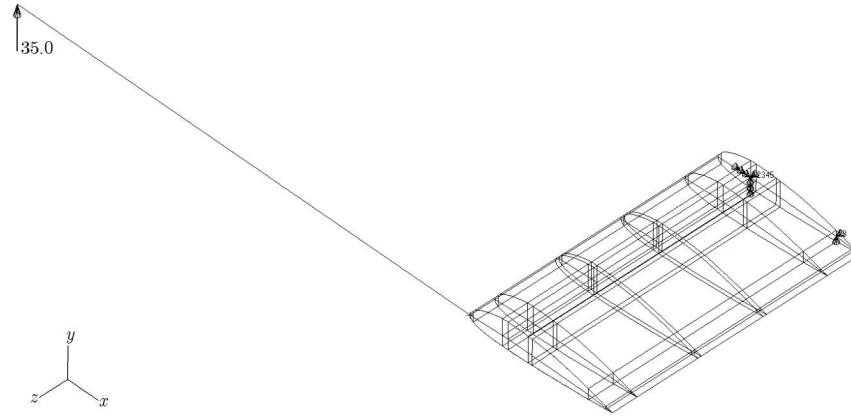


Fig. 7. Boundary conditions and load application of the numerical model

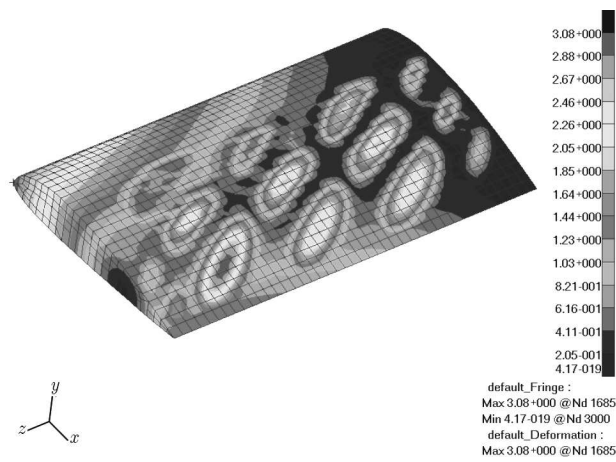


Fig. 8. Resultant displacement distribution in the first version of the numerical model found to be inconsistent with real behaviour (in mm)

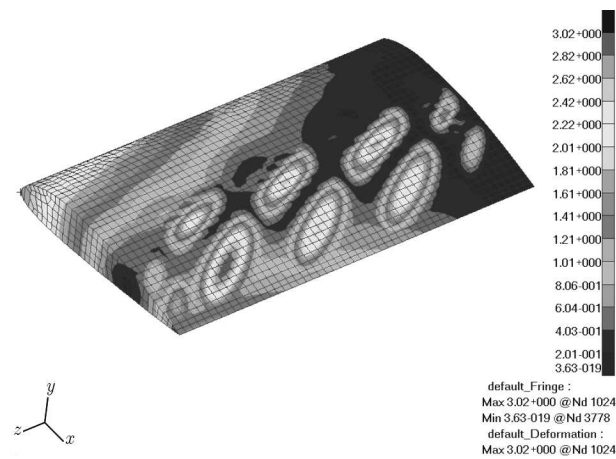


Fig. 9. Resultant displacement distribution in the corrected version of the model - the upper surface (in mm)

issue of geometrical inhomogeneity of the real object. In the analysed case, it turned out that the source of error consisted in too low stiffness of the rear fragments of the skin located in the vicinity of the spar. In the actual object, the feature resulting in additional stiffening of this fragment of the structure is the epoxy resin joint connecting the spar with the skin and contributing to a local increase in skin thickness.

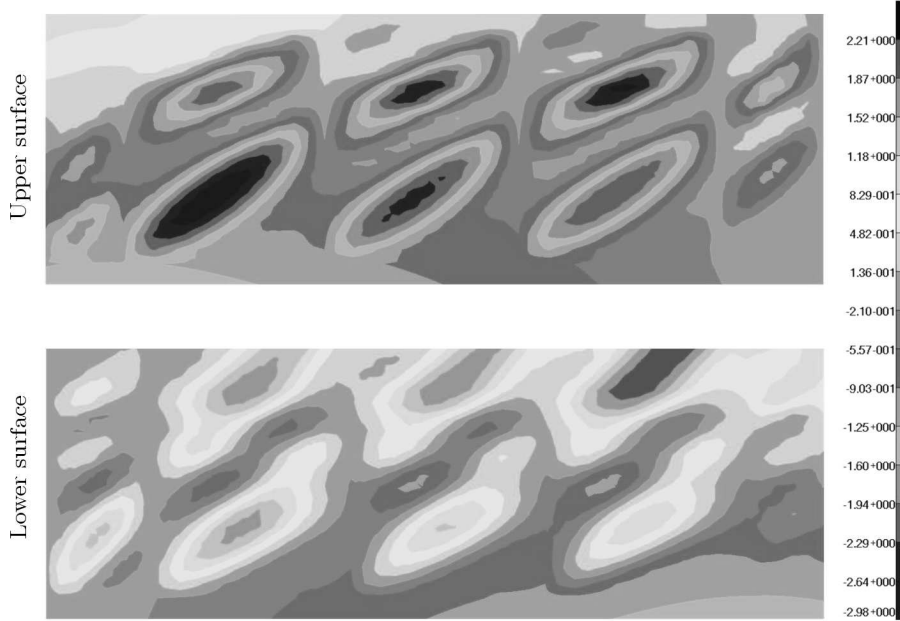


Fig. 10. Displacements in the direction normal to the surface – the skin area between the girder and the trailing edge (in mm)

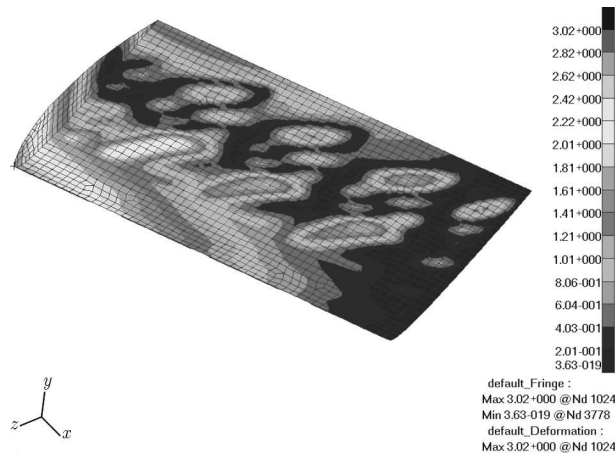


Fig. 11. Resultant displacement distribution in the corrected version of the model - the lower surface (in mm)

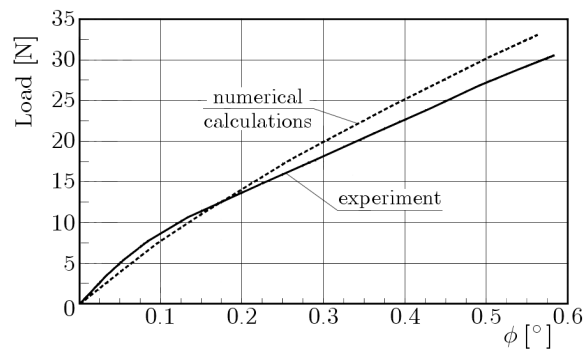


Fig. 12. A comparison of the representative equilibrium paths

After application of appropriate corrections, the displacement distribution satisfactorily consistent with the actual one has been finally obtained (Fig. 9).

At the same time, a satisfactory conformity has been observed of the equilibrium path obtained numerically with that determined in the course of the experiment (Fig. 12). The difference in the representative parameter value has not exceed 23%. Therefore, on the grounds of the rule of uniqueness of the solutions, the calculated stress distributions can be considered sufficiently reliable (Fig. 13).

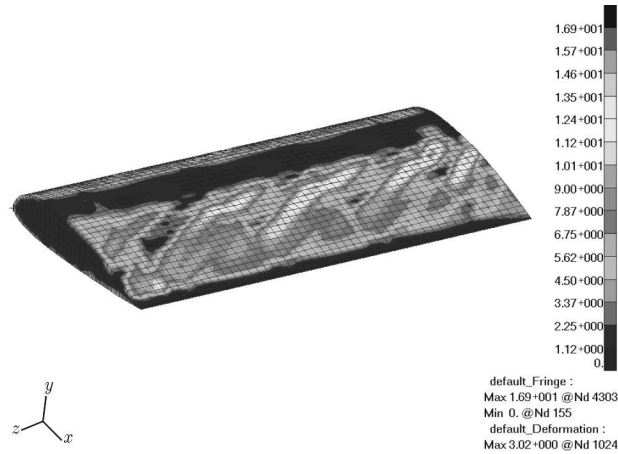


Fig. 13. Equivalent stress distributions according to σ_{max} hypothesis (in MPa)

5. Summary and conclusions

The results presented above and observations based on them should be considered in the context of a wider research program aimed at determination of properties of a series of aircraft composite skins subjected to post-critical deformation under permissible load conditions. A necessary complement to the experimental phase allowing one to obtain information about stress distribution patterns in the examined skins consists in the development of appropriate and effective FEM-based calculation models.

The satisfactory similarity found in this study between the deformations patterns and the courses of representative equilibrium paths obtained from the experiment on one hand and numerically on the other allows one to apply the rule of uniqueness of the solutions and consider the obtained stress distributions reliable. This way it can be stated that the properties of composites attributed to finite elements by PATRAN software, determined by the program based on data for individual layers of the composite, may be considered correct and corresponding to actual characteristics. However, it should be emphasised that in the case of occurrence of any defects in the real structure that may arise in the process of lamination, it is necessary to introduce an appropriate correction in the numerical model accounting for the effect of such flaws on the local stiffness of the skin.

Once a verified reference numerical model is at disposal, it is possible to apply a methodology constituting in introducing design changes to it by employing different stiffening variants. A criterion for selection of the target solution can be the highest possible value of the critical load or the lowest possible magnitude of critical deformation adopted as the representative one. The last step must consist in performing an experiment with the use of a model corresponding to the selected variant. This follows from the absolute necessity to verify the numerical model. However, this way of conduct allows one to eliminate the experimental phase involving intermediate solutions identified as failing to meet the selected criteria.

References

1. ARBORCZ J., 1985, Post-buckling behavior of structures. Numerical techniques for more complicated structures, *Lecture Notes in Physics*, **228**, USA
2. BATHE K.J., 1996, *Finite Element Procedures*, Prentice Hall, USA
3. BRZOSKA Z., 1965, *Statics and Stability of Bar and Thin-Walled Structures*, PWN, Warszawa, Poland
4. DOW N.F., HICKMAN W.A., ROSEN B.W., 1954, *Data on the Compressive Strength of Skin-Stringer Panels of Various Materials*, NACA TN 3064
5. Federal Aviation Administration, 2009, *Composite Aircraft Structure*, Advisory Circular 20-107B
6. FELIPPA C.A., 1976, *Procedures for Computer Analysis of Large Nonlinear Structural System in Large Engineering Systems*, edit. by A. Wexler, Pergamon Press, London, UK
7. KOPECKI T., 2010, *Advanced Deformation States In Thin-Walled Load-Bearing Structure Design Work* (in Polish), Publishing House of Rzeszów University of Technology, Rzeszów, Poland
8. KOPECKI T., MAZUREK P., 2013, Problems of numerical bifurcation reproducing in post-critical deformation states of aircraft structures, *Journal of Theoretical and Applied Mechanics*, **51**, 4, 969-977
9. KOPECKI T., MAZUREK P., 2014, Numerical representation of post-critical deformations in the processes of determining stress distributions in closed multi-segment thin-walled aircraft load-bearing structures, *Maintenance and Reliability*, **16**, 1, 164-169
10. MARCINOWSKI J., 1999, *Nonlinear Stability of Elastic Shells*, Publishing House of Technical University of Wrocław, Poland
11. NEMETH M.P., 2013, *A Leonard-Sanders-Budiansky-Koiter-Type Nonlinear Shell Theory with a Hierarchy of Transverse-Shearing Deformations*, NASA TP-2013-218025
12. NIU M.C., 1988, *Airframe Structural Design*, Conmilit Press Ltd., Hong Kong
13. RAKOWSKI G., KACPRZYK Z., 2005, *Finite Elements Method in Structure Mechanics*, Publishing House of Technical University of Warszawa, Warszawa, Poland
14. RAMM E., 1987, *The Riks/Wempner Approach – an Extension of the Displacement Control Method in Nonlinear Analysis*, Pineridge Press, Swensea, UK
15. RAMM E., WALL W.A., 2004, Shell structures – a sensitive interrelation between physics and numerics, *International Journal for Numerical Methods in Engineering*, **60**, 381-427
16. SERESTA O., 2007, Buckling, flutter and postbuckling optimization of composite structures, PhD Thesis, Virginia State University, Blacksburg
17. TAYLOR A.S., ECKFORD D.J., EDIT., 1968, *Aircraft Loading Actions Problems – Proceedings of a Symposium Held at Farnborough*, London

Manuscript received September 4, 2014; accepted for print July 20, 2015

FINITE ELEMENT ANALYSIS OF THE 3D THERMAL STRESS STATE IN A BRAKE DISK

ADAM ADAMOWICZ

Bialystok University of Technology (BUT), Faculty of Mechanical Engineering, Bialystok, Poland

e-mail: a.adamowicz@pb.edu.pl

The quasi-static thermal stress state within the linear uncoupled elasticity is studied. The calculations were performed using the finite element method (MSC.Patran/MSC.Nastran). In order to examine smooth stress changes in a brake disk during braking, based on the temperature fields at particular time steps, additionally the script using Python programming language was developed. The numerical three-dimensional FE model of the brake disk for calculation of the transient temperature field was adopted from the previous author's study. A single braking process at linear deceleration and constant contact pressure was simulated. The evolutions and the contours of the components of the stress tensor as well as the equivalent Huber-Mises stress were examined. The most important aspects of the stress state during braking were discussed.

Keywords: frictional heating, temperature, thermal stresses, pad-disk brake system, finite element method

Nomenclature

B, D, K	–	matrix of differential operators, elasticity matrix and stiffness matrix
c, h	–	specific heat [J/(kg K)] and heat transfer coefficient [W/(m ² K)]
e	–	dilatation
E	–	Young's modulus [MPa]
f	–	coefficient of friction
F	–	nodal force vector due to initial strain
J_2	–	second invariant of the deviatoric stress tensor [MPa ²]
k, K	–	thermal diffusivity [m ² /s] and thermal conductivity [W/(m K)]
p_0	–	contact pressure [MPa]
q	–	heat flux density [W/m ²]
r, z	–	radial and axial coordinate, respectively [m]
r, R	–	inner and outer radius, respectively [m]
t, t_s	–	time and braking time [s]
T, T_a, T_0	–	temperature, ambient temperature and initial temperature [°C]
T	–	temperature vector
u	–	column vector including components of displacements of the point
u_r, u_z	–	displacement components in radial r and axial z direction, respectively [m]

Greek symbols

α_T	–	thermal expansion coefficient [K ⁻¹]
Γ	–	area of the friction surface on the disk (within the pad)
δ	–	thickness [m]

ε	– strain
$\varepsilon_{rr}, \varepsilon_{\theta\theta}, \varepsilon_{zz}$	– shear strain components in cylindrical coordinates
ε_T	– column vector of initial strain due to non-uniform temperature distributions
η	– heat partition ratio
θ	– circumferential coordinate
θ_0	– cover angle of the pad [deg]
λ, μ	– Lamé’s first parameter and the shear modulus (Lamé’s second parameter)
ν	– Poisson’s ratio
ρ	– density [kg/m ³]
σ	– stress vector
$\sigma_{r\theta}, \sigma_{\theta z}, \sigma_{rz}$	– shear stress components in cylindrical coordinates [MPa]
$\sigma_r, \sigma_\theta, \sigma_z$	– normal stress components in cylindrical coordinates [MPa]
σ_{HM}	– equivalent Huber-Mises stress, $\sigma_{HM} = \sqrt{3J_2}$ [MPa]
ω, ω_0	– relative and initial relative angular slip speed, respectively [s ⁻¹]
Ω_i	– areas on the disk, $i = 1, 2, 3, 4$

Subscripts

d – disk, p – pad

1. Introduction

Temperature due to friction is one of the utmost importance factors affecting performance of brake systems. A review of studies on the methods of numerical evaluation of temperature field in a pad-disk brake system encloses the work by Yevtushenko and Grzes (2010). In that paper, the drawn conclusions indicated that numerical analysis by using FEM most frequently refers to two different models. The first of them is an axisymmetric (2D) model, allowing, in particular, determination of the average temperature on the friction surface of the disk (Talati and Jalalifar, 2008; 2009; Grześ, 2010; Yevtushenko and Grzes, 2012). The advantage of using two dimensionality is the ability of immediate evaluation of the average (axisymmetric) temperature field and the corresponding thermal stresses. The drawback of the model is lack of possibility of accounting for the oscillating behavior of the contact temperature change of the brake disk during operation, which means impossibility of calculation of its maximum value. In order to determine the highest value attained, spatial FE models of the brake disk were developed (Adamowicz and Grzes, 2011a,b, 2013).

Non-uniformity of the time-spatial temperature field induces thermal stresses due to thermal expansion (Ranaker, 2001). It may, in turn, initiate micro-cracks on the friction surface of the disk, their growth and the disabling of proper and safe exploitation of a disk brake system (Mackin *et al.*, 2002).

A review of studies on FE modeling of thermal stresses in disk brakes and clutches was given by Yevtushenko *et al.* (2014). It was shown that the vast majority of papers was devoted to the equivalent stress (Huber-Mises) only. However, the application of some fracture criterions enforces estimation of the evolution and spatial distribution of each component of the stress tensor in the disc brake (Norlander, 2005).

The axisymmetric quasi-static thermal stress state induced in the disk was studied using the finite element method in the first part of that research (Adamowicz, 2015). Accordingly, some papers on the development of 3D models of calculation of thermal stresses will be enclosed in this study.

Thermal fatigue fracture mechanisms of brake disks using FEM were studied by Gao *et al.* (2007). Temperature and thermal stresses based on the thermomechanical 3D contact model of

a pad-disk brake system were calculated using the FE based software ANSYS 8.1. The authors discussed in detail the correlations between the obtained results and the outcomes of other studies on FE calculations of thermal stresses in disk brakes. An attempt was made to identify the cause of the thermal fatigue. Temperature distributions on the contact surface of the disk at specific time steps were shown. Radial, circumferential and equivalent Huber-Mises stresses versus braking time were presented and analyzed.

Other FE calculations for a brake disk of a high speed rail (TGV) were carried out by Tirovic (1998). Shape optimization preventing from excessive deformations was conducted. A linear elastic range of material behavior and temperature-dependent properties were imposed in the computations. A three-dimensional section (7.5°) of a ventilated type of a disk brake was analyzed. Spatial temperature, displacement, and equivalent Huber-Mises stress distributions for one specific point time were shown.

A coupled thermoelasticity problem for a pad-disk brake system during multiple braking at a constant deceleration was considered by Choi and Lee (2004). Normal stress components were determined. The influence of physical (specific heat, thermal expansion coefficient, thermal conductivity) and mechanical properties (Young's modulus) of materials on the temperature field and the real contact area were studied. It was found that the maximum value among the stress components was reached for circumferential stress which increased with temperature and the number of brake applications.

The problem of thermal cracking of cast-iron disks of trucks was studied by Bagnoli *et al.* (2009). Based on macro-fractography, optical and scanning electron microscopes, several radial cracks were identified. In order to eliminate one of the source of cracking originated from material defects, measurements of chemical composition, structure and hardness were made. Further numerical calculations using the finite element method also revealed a relatively high temperature and the equivalent Huber-Mises stress. It was established that the dominant factor leading to the propagation of radial macro-cracks in the heating area of semi-elliptic shape, which grew from the contact surface into the disk, was the thermal fatigue mechanism.

Thermal stresses in a ventilated brake disk induced at a uniform and non-uniform distribution of the contact pressure were analyzed by Kim *et al.* (2008). The contact three-dimensional computational model incorporating only mechanical interactions was developed to calculate contact pressure distributions. Further analysis of the stress field revealed that the highest values of the equivalent stress occurring for the case of the nonuniform pressure distribution was attained in the contact region. At the uniform pressure distribution, the maximum equivalent stresses were slightly higher (about 3%) and were reached in the contact surface near the inner cylindrical surface of the disk.

Spatial FE models of three different types of ventilated and one solid disks were developed to analyze the stress field during braking (Yildiz and Duzgun, 2010). For each of the studied geometrical types of the disk, the influence of variable loading on the brake pads was also analyzed. The stresses resulted from nonuniform temperature distribution were not taken into account. In order to minimize the resulting stress, modifications of the loading of the pad were made.

Temperature distributions, equivalent Huber-Mises stresses and strains in a mine hoist brake disc were studied by Scieszka and Zolnierz (2014). The calculations were carried out both for a solid and divided disc (2, 4 and 8 sections) using a 3D thermomechanical finite element contact model. The model was validated by infrared measurements of the temperature field in real industrial conditions.

In this paper FE analysis of thermal stresses induced in a brake disk using fully three-dimensional model is carried out. The emphasis is placed on comprehensive examination of spatial distributions of each component of the stress tensor as well as their changes throughout the entire braking process. In order to simulate nonuniform heating of the rubbing path of the

disk due to the fact that the cover angle of the pad is smaller than 2π , an approach to program the boundary conditions has been adopted from the previous authors' study (Yevtushenko and Grzes, 2011). Quasi-static thermal stresses are determined based on the computed transient temperature fields at the specified time moments to obtain their smooth changes during braking. The script code has been written using Python programming language and the input files to the FE based software (MSC.Nastran) have been generated. Relevant conclusions regarding thermal fatigue cracking are drawn and discussed.

2. Statement of the problem

A scheme of a pad-disk system given in cylindrical coordinates r, θ, z is shown in Fig. 1. All of the values and parameters, which refer to the pad and the disk in the following considerations will have subscripts p and d , respectively. It is assumed that:

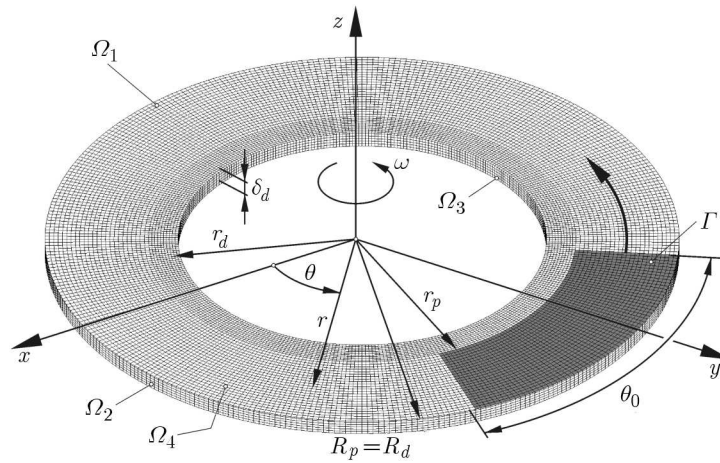


Fig. 1. A schematic diagram of a pad-disk brake system with boundary conditions and a section of the 3D FE mesh

- initially ($t = 0$), the pad is pressed to the rubbing path of the disk within the region $\Gamma = \{r_p \leq r \leq R_p, 0 \leq \theta \leq \theta_0, z = 0\}$. The distribution of pressure in the contact area Γ is uniform and equals p_0 ;
- angular speed of the disk decreases linearly from the speed of ω_0 at the initial time moment $t = 0$ to standstill at $t = t_s$

$$\omega(t) = \omega_0(1 - t/t_s) \quad 0 \leq t \leq t_s \quad (2.1)$$

- due to friction, heat generation takes place in the contact region Γ . The heat flux densities directed along the normal into the pad and the disk (within Γ) are equal to $q_p(r, t) = (1 - \eta)f\omega(t)rp_0$ and $q_d(r, t) = \eta f\omega(t)rp_0$, respectively. Thus, the sum of these densities is equal to the specific power of friction $q(r, t) = f\omega(t)rp_0$, $r_p \leq r \leq R_p$, $0 \leq t \leq t_s$ (Ling, 1959);
- influence of the pad on temperature of the disk is incorporated through the heat partition ratio η , while calculating this parameter in pad-disk brake systems, Charron's formula can be used (Charron, 1943)

$$\eta = \frac{\sqrt{K_d \rho_d c_d}}{\sqrt{K_d \rho_d c_d} + \sqrt{K_p \rho_p c_p}} \quad (2.2)$$

- during single braking, the heat transfer through convection and radiation on the free surfaces of the disk is negligibly small (Adamowicz and Grzes, 2011a,b). Therefore, in this study, convective cooling and thermal radiation was omitted;
- due to geometric and loading symmetry of the problem about the mid-plane of the disk, the computational region is restricted to the half δ_d of the disk thickness;
- materials of the pad and the disk are homogeneous and isotropic. Their physical and mechanical properties are temperature independent.

On these assumptions, the distribution of the transient 3D temperature field $T(r, \theta, z, t)$ in the disk was obtained on the basis of the FE solution to the spatial boundary heat conduction problem of the parabolic type in the paper by Adamowicz and Grzes (2013). The objective of that study was to evaluate the corresponding components of thermal stress σ_{ij} , $i, j = r, \theta, z$ in the disk volume from the solution to Navier's equations for uncoupled thermoelasticity given in the cylindrical coordinate system (Noda *et al.*, 2003)

$$\begin{aligned} (\lambda + 2\mu) \frac{\partial e}{\partial r} - 2\mu \left(\frac{1}{r} \frac{\partial \omega_z}{\partial \theta} - \frac{\partial \omega_\theta}{\partial z} \right) &= \alpha_T \frac{\partial T}{\partial r} \\ (\lambda + 2\mu) \frac{1}{r} \frac{\partial e}{\partial \theta} - 2\mu \left(\frac{\partial \omega_r}{\partial z} - \frac{\partial \omega_z}{\partial r} \right) &= \alpha_T \frac{1}{r} \frac{\partial T}{\partial \theta} \\ (\lambda + 2\mu) \frac{\partial e}{\partial z} - \frac{2\mu}{r} \left(\frac{\partial(r\omega_\theta)}{\partial r} - \frac{\partial \omega_r}{\partial \theta} \right) &= \alpha_T \frac{\partial T}{\partial z} \end{aligned} \quad (2.3)$$

where

$$\begin{aligned} e &\equiv \varepsilon_{rr} + \varepsilon_{\theta\theta} + \varepsilon_{zz} = \frac{\partial u_r}{\partial r} + \frac{u_r}{r} + \frac{1}{r} \frac{\partial u_\theta}{\partial \theta} + \frac{\partial u_z}{\partial z} \\ \omega_r &= \frac{1}{2} \left(\frac{1}{r} \frac{\partial u_z}{\partial \theta} - \frac{\partial u_\theta}{\partial z} \right) & \omega_\theta &= \frac{1}{2} \left(\frac{\partial u_r}{\partial z} - \frac{\partial u_z}{\partial r} \right) & \omega_z &= \frac{1}{2} \left(\frac{\partial(ru_\theta)}{\partial r} - \frac{\partial u_r}{\partial \theta} \right) \\ \lambda &= \frac{\nu E}{(1+\nu)(1-2\nu)} & \mu &= \frac{E}{2(1+\nu)} & \alpha_T &= \frac{\alpha E}{1-2\nu} \end{aligned} \quad (2.4)$$

A system of partial differential equations (2.3) and (2.4) will be solved for the following homogeneous (tractions free) boundary conditions (Fig. 1):

— on the surface of friction (the working surface) $\Gamma \cup \Omega_1 = \{r_d \leq r \leq R_d, 0 \leq \theta \leq 2\pi, z = 0\}$

$$\sigma_z = \sigma_{rz} = \sigma_{z\theta} = 0 \quad (2.5)$$

— on the outer cylindrical surface of the disk $\Omega_2 = \{r = R_d, 0 \leq \theta \leq 2\pi, 0 \leq z \leq \delta_d\}$

$$\sigma_r = \sigma_{r\theta} = \sigma_{rz} = 0 \quad (2.6)$$

— on the inner cylindrical surface of the disk $\Omega_3 = \{r = r_d, 0 \leq \theta \leq 2\pi, 0 \leq z \leq \delta_d\}$

$$\sigma_r = \sigma_{r\theta} = \sigma_{rz} = 0 \quad (2.7)$$

— on the plane of symmetry $\Omega_4 = \{r_d \leq r \leq R_d, 0 \leq \theta \leq 2\pi, z = -\delta_d\}$

$$u_z = 0 \quad \sigma_{rz} = \sigma_{z\theta} = 0 \quad (2.8)$$

where (Noda *et al.*, 2003)

$$\begin{aligned} \sigma_{ii} &= 2\mu\varepsilon_{ii} + \lambda e - \alpha_T T, & \sigma_{ij} &= 2\mu\varepsilon_{ij} & i, j &= r, \theta, z & i \neq j \\ \varepsilon_{rr} &= \frac{\partial u_r}{\partial r} & \varepsilon_{\theta\theta} &= \frac{u_r}{r} + \frac{1}{r} \frac{\partial u_\theta}{\partial \theta} & \varepsilon_{zz} &= \frac{\partial u_z}{\partial z} \\ \varepsilon_{rz} &= \frac{1}{2} \left(\frac{\partial u_r}{\partial z} + \frac{\partial u_z}{\partial r} \right) & \varepsilon_{r\theta} &= \frac{1}{2} \left(\frac{1}{r} \frac{\partial u_r}{\partial \theta} + \frac{\partial u_\theta}{\partial r} + \frac{u_\theta}{r} \right) & \varepsilon_{z\theta} &= \frac{1}{2} \left(\frac{\partial u_\theta}{\partial z} + \frac{1}{r} \frac{\partial u_z}{\partial \theta} \right) \end{aligned} \quad (2.9)$$

The solution to the boundary-value problem of quasi-static thermoelasticity, Eqs. (2.3) and (2.9)-(2.12) has been obtained using the finite element method.

3. FE discretization

A general FE procedure to obtain the solution to the boundary-value heat conduction problem under consideration was presented by Adamowicz and Grzes (2013). Therefore, below we shall present in general the form of the computational scheme of the solution by means of FEM for the corresponding problem of thermoelasticity.

Taking into account formula (2.4)₃, relationships between stress and strain for Eqs. (2.9), may be written in the following matrix notation (Huebner and Thornton, 1982)

$$\boldsymbol{\sigma} = \mathbf{D}\mathbf{B}\mathbf{u} - \mathbf{D}\boldsymbol{\varepsilon}_T \quad (3.1)$$

where

$$\mathbf{D} = \frac{\lambda}{a} \begin{bmatrix} 1 & a & a & 0 & 0 & 0 \\ a & 1 & a & 0 & 0 & 0 \\ a & a & 1 & 0 & 0 & 0 \\ 0 & 0 & 0 & b & 0 & 0 \\ 0 & 0 & 0 & 0 & b & 0 \\ 0 & 0 & 0 & 0 & 0 & b \end{bmatrix} \quad \mathbf{B} = \begin{bmatrix} \partial/\partial r & 0 & 0 \\ 0 & \partial/\partial z & 0 \\ r^{-1} & 0 & r^{-1}\partial/\partial\theta \\ \partial/\partial z & \partial/\partial r & 0 \\ 0 & r^{-1}\partial/\partial\theta & \partial/\partial z \\ r^{-1}\partial/\partial\theta & 0 & \partial/\partial r - r^{-1} \end{bmatrix} \quad (3.2)$$

$$\boldsymbol{\sigma} = [\sigma_r, \sigma_z, \sigma_\theta, \sigma_{rz}, \sigma_{z\theta}, \sigma_{r\theta}]^T \quad \mathbf{u} = [u_r, u_z, u_\theta]^T \quad \boldsymbol{\varepsilon}_T = \alpha_T T [1, 1, 1, 0, 0, 0]^T$$

and

$$a = \frac{\nu}{1 - \nu} \quad b = \frac{1 - 2\nu}{2(1 - \nu)} \quad (3.3)$$

and T is the temperature increase relative to the reference temperature T_0 for which thermal strains are zero. Taking into account Eqs. (2.4) and using the variational principle of minimization of the functional of total potential energy, the boundary problem, Eqs. (2.3) and (2.5)-(2.8), leads to the system of linear algebraic equations (Zienkiewicz *et al.*, 2005)

$$\mathbf{K}\mathbf{u} = \mathbf{F} \quad (3.4)$$

where \mathbf{K} is the stiffness matrix, \mathbf{F} – nodal force vector due to initial strain.

Thermal FE analysis contrary to the foregoing structural analysis is a scalar field problem. The temperature field of the FE model is continuous within elements and across interelement boundaries. Temperature gradients, similarly to strains in the stress analysis, are typically not interelement-continuous (Cook, 1995). Therefore, the mesh adequate for thermal analysis might not be adequate for stress analysis unless sufficient refinement of the grid or higher order elements are imposed. In this study, to assure appropriate accuracy of the solution using the same mesh for two studied problems, a relatively fine mesh using ‘CHEXA8’ type eight-node finite elements has been generated. The total overall mesh consists of 86040 elements and 102960 nodes (Fig. 1).

In the preliminary analysis, two FE meshes have been tested. Robust thermal load transferred through the pad-disk interface during a short time results in a high axial component of the temperature gradient. Thus, to assure precise and reliable outcomes, a reasonably small dimension of the element in the axial direction near the friction surface (plane) ought to be used. However, an increase in the overall total number of elements of the model obviously requires larger computational resources and lengthens the time of computations. Accordingly, different meshes have been constructed and the differences between the obtained temperature changes on the contact surface during braking have been analyzed. Figure 2 shows the results determined using two grids consisting of 360 and 1080 elements in the circumferential direction. The number of the elements in the radial direction is chosen so as to maintain the square shape of an element.

As can be seen, an increase in the number of elements does not cause significant temperature differences for the grid, therefore, its smaller number is chosen.

However, the FE based software chosen (MSC.Patran/MSC.Nastran, 2002) allowed one to conduct transient thermal analysis, it did not provide a possibility to automatically calculate stress changes based on the previously calculated temperature fields. In order to obtain stress distribution at the specified time step of the braking process, individual static stress analysis for each time step is necessary. Aiming at obtaining smooth changes of the stress fields, extremely large amount of data ought to be processed. Thus, the original code consistent with the commands used in MSC.Patran to automatize the calculations has been developed using Python programming language. The computations have been performed without the interference of MSC.Patran at the pre-processing stage. Finished input files to the FE solver (MSC.Nastran) with temperature fields at specific time steps have been generated based on the reports derived from thermal analysis.

4. Numerical analysis

Calculations are made for a metal-ceramic (FMC-11) pad and a cast iron (ChNMKh) disk (Chichinadze, 1967). Dimensions, properties of the components of the brake system and operating parameters of the process are listed in Table 1.

Table 1. Dimensions (Adamowicz and Grzes, 2011b), properties of materials (Yildiz and Duzgun, 2010) of the pad-disk system and operating parameters

Parameter	Disk (cast iron ChNMKh)	Pad (FMC-11)
inner radius, r [mm]	66	76.5
outer radius, R [mm]	113.5	
thickness, δ [mm]	5.5	10
pad arc length, θ_0 [deg]		64.5
thermal conductivity, K [W/(mK)]	51	34.3
density, ρ [kg/m ³]	7100	4700
thermal diffusivity, $k \cdot 10^5$ [m ² /s]	1.44	1.46
Young's modulus, E [GPa]	99.97	
Poisson's ratio, ν [-]	0.29	
thermal expansion coefficient, α_T [K ⁻¹]	$1.08 \cdot 10^{-5}$	
initial angular speed of the disk, ω_0 [s ⁻¹]	88.464	
braking time, t_s [s]	3.96	
contact pressure, p_0 [MPa]	1.47	
coefficient of friction, f	0.5	
initial temperature, T_0 [°C]	20	
ambient temperature, T_a [°C]	20	

The FE model of the brake disk is shown in Fig. 1. The mesh shown has been generated automatically by the code developed to evaluate boundary conditions prescribed on the rubbing path of the disk. As can be seen, the established time step for FE analysis of temperatures (Figs. 2a and 3a) as well as thermal stress components (Figs. 2bcd and 3bcd) give sufficient smoothness of their changes during the entire braking process. Therefore, neither the mesh refinement nor time step reduction has been necessary.

The time profiles of temperature in Fig. 2a as well as the non-zero components of the stress tensor in Figs. 2b,c and Huber-Mises stress in Fig. 2d are presented for four specific radial locations on the friction surface ($z = 0$) of the disk at $\theta = 0$: $r_d = 66$ mm – inner radius of

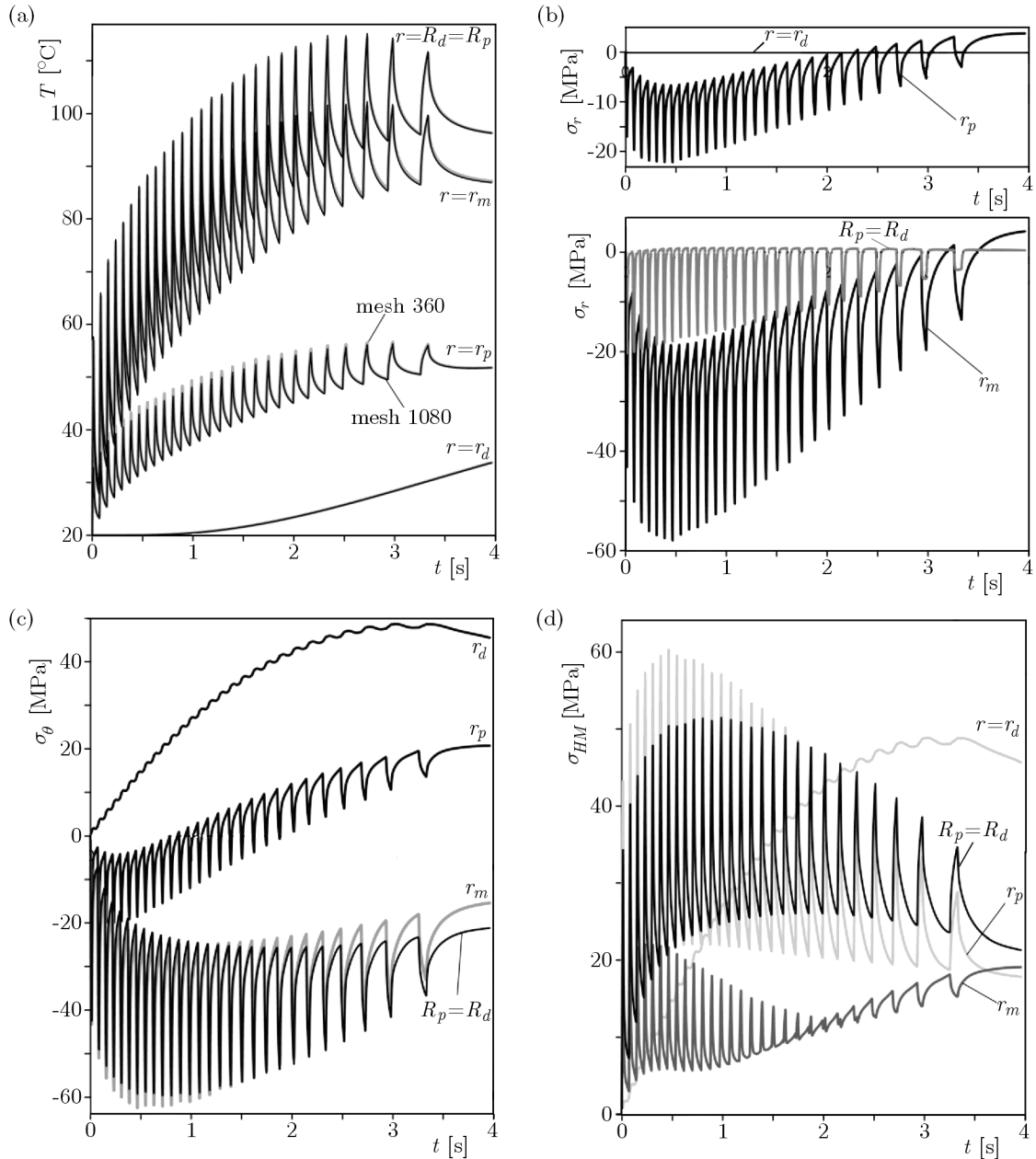


Fig. 2. Temperature (a), radial stress (b), circumferential stress (c) and equivalent Huber-Mises stress (d) changes for fixed locations on the contact surface of the disc $r \in \{r_d, r_p, r_m, R_d = R_p\}$, $\theta = 0$, $z = 0$ during braking

the disk, $r_p = 76.5$ mm – inner radius of the pad, $r_m = 95$ mm – mean radius of the pad, and $R_p = R_d = 113.5$ mm – outer radius of the pad and the disk.

Since the pad covers the rubbing path of the disk partly, as expected and seen in Fig. 2a, the temperature evolutions on the contact surface for fixed positions reveal fluctuations of the temperature. Only the temperature change on the inner edge of the disk varies uniformly. The average values of temperature within the rubbing path increase gradually until the maximum temperature is reached, then its slight decrease takes place. The amplitude of temperature variation during one disk revolution is attained at the beginning of the process $\Delta T = 37.6^\circ\text{C}$. The maximum temperature of the entire process occurs on the outer edge of the disk and equals $T = 115.1^\circ\text{C}$ ($t = 2.728$ s).

The evolutions of thermal stresses corresponding with the temporal temperature profiles from Fig. 2a, are shown in Figs. 2bcd.

The radial stress σ_r is negative during almost the entire period of braking, and only while approaching the stop moment, the stress changes sign to positive (Fig. 2b). The highest value $\sigma_r = -57.80$ MPa is reached for the mean radius $r_m = 95$ mm at $t = 0.466$ s. According to boundary conditions (2.7), the radial stress σ_r on the inner radius of the disk ($r = 66$ mm) equals zero. The non-zero values of σ_r at $r = 113.5$ mm stem from deformations of the outer surface of the disk.

The circumferential stress σ_θ is negative on the outer edge ($r = 113.5$ mm) and inside ($r = 95$ mm) the area of heating (Fig. 2c). While approaching the inner edge $r = 76.5$ mm of this area in a certain moment of time, there is a change in sign of this stress to positive. Note that the lack of the change in the sign in the article by Gao *et al.* (2007) was explained by insufficient decrease in temperature of the disk. In contrast to the radial stress, the circumferential stress reaches significant (≈ 40 MPa) positive (tensile) values on the inner radius $r = 66$ mm of the disk. The maximum absolute values of the radial and circumferential stresses are approximately the same (≈ 60 MPa).

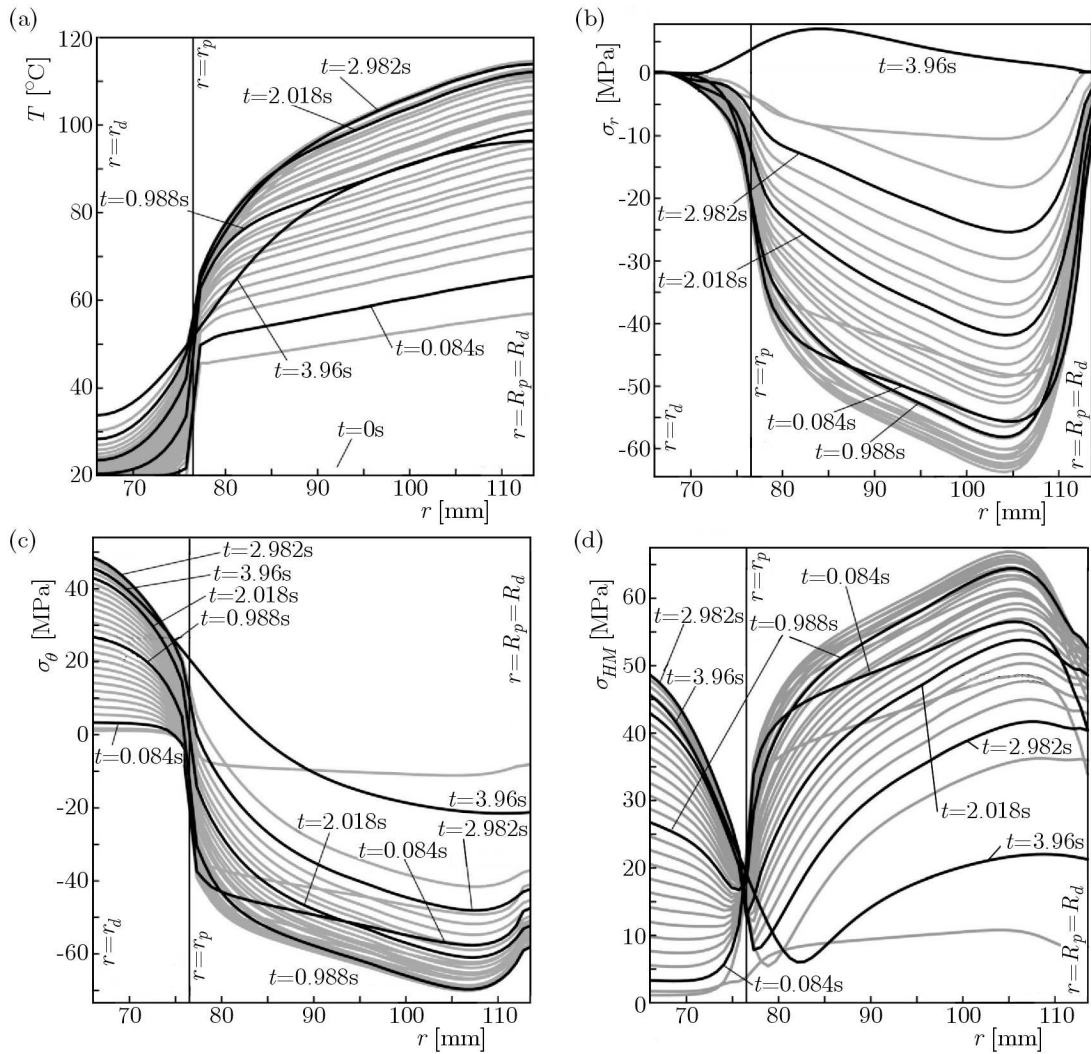


Fig. 3. Temperature (a), radial stress (b), circumferential stress (c) and equivalent Huber-Mises stress (d) distributions in the radial direction on the contact surface of disc distributions, $r_d \leq r \leq R_d$, $\theta = 0$, $z = 0$

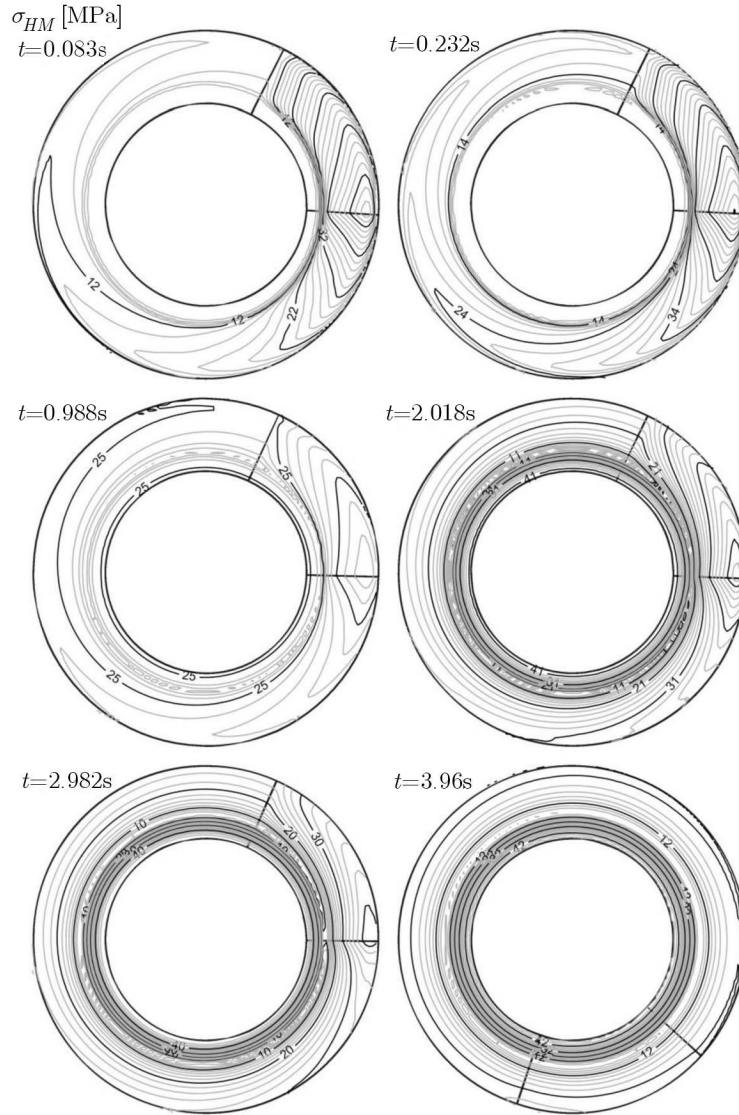


Fig. 4. Equivalent Huber-Mises stress contours on the contact surface of the disc $z = 0$ at specific time moments during braking: $t = 0.084$ s, 0.232 s, 0.988 s, 2.018 s, 2.982 s and 3.96 s

The Huber-Mises stress σ_{HM} rises rapidly at the beginning of the process and fluctuates according to rotations of the disk/wheel (Fig. 2d). The heating (the pad covers the considered node) and cooling (the pad out of the considered node) periods may be distinguished similarly to the time profiles of temperature from Fig. 2a. Out of the rubbing path but on the friction surface ($66 \text{ mm} \leq r \leq 76.5 \text{ mm}$) that effect weakens. An interesting fact is that while the average values of the stress σ_{HM} on the rubbing path decrease after reaching the maximum value at $t \approx 0.5$ s, the average values σ_{HM} on the inner radius of the disk increase steadily almost to standstill. The maximum value $\sigma_{HM} \approx 60 \text{ MPa}$ on the friction surface is reached at $r = 95 \text{ mm}$ and the time moment $t \approx 0.5$ s. Comparable qualitative results, namely the evolutions of stresses on the friction surface and the location of the maximum value, are obtained for the thermomechanical contact FE model of the pad-disk brake system analyzed by Gao *et al.* (2007). However, the stress near the inner radius of the disk, unlike the considered FE model of the brake disk is relatively insignificant. This, among other things (e.g. contact pressure, properties of materials, operating parameters) may be attributed to different inner radii of the disk, since other dimensions of the pad and the disk are similar (Fig. 3a).

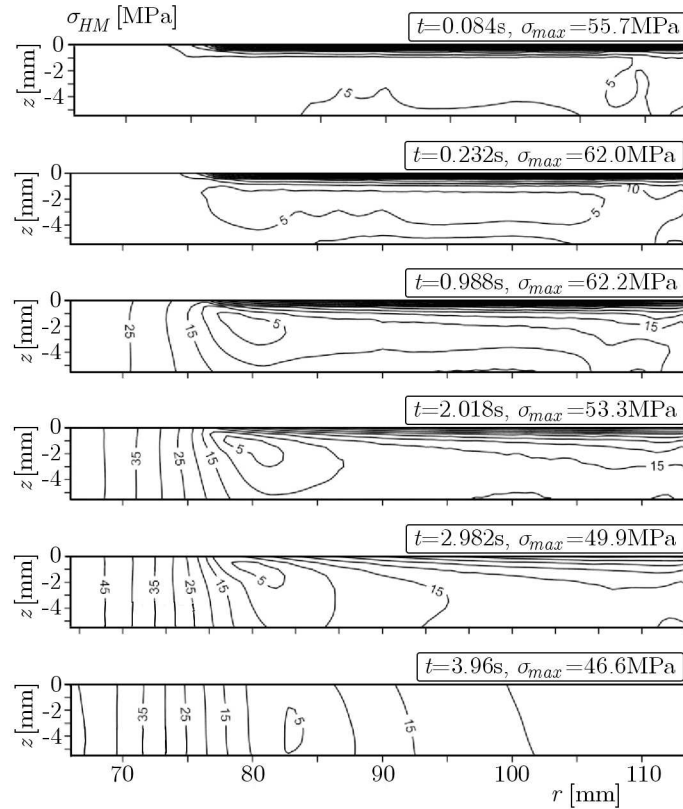


Fig. 5. Equivalent Huber-Mises stress contours in the cross-section (rz plane) of the disc at specific time moments during braking: $t = 0.084$ s, 0.232 s, 0.988 s, 2.018 s, 2.982 s and 3.96 s

Temperature distributions and thermal stresses on the friction surface of the disk in the radial direction at selected time moments ($t = 0.084$ s, 0.232 s, 0.988 s, 2.018 s, 2.982 s, 3.96 s) are shown in Fig. 3. Since the relative sliding speed of the pad and disk varies with distance from the axis of revolution z , the heat flux density applied on the contact surface $q = fVp$ affects the temperature distribution in the radial direction.

The distributions of stress component σ_r in radial direction r for the abovementioned time moments are shown in Fig. 3b. According to the imposed boundary conditions at the outer, Eq. (2.6), and inner, Eq. (2.7), cylindrical surface of the disk, the computed radial stresses should be zero. Some inconsistencies appear only on the outer edge. This is due to the software which does not use the coordinate system attached to normal directions of a deformed surface. Thus, the effect is noticeable for large stresses and deformations (from the beginning to the half of the braking process, Fig. 2b). As expected, outside these boundaries the distribution is in approximate agreement with the thermal load expressed by the product fVp . Additionally, it should be noted that the radial stress except the time of standstill is compressive.

In the similar way as for the radial stress distribution (within the range of the rubbing path $76.5 \text{ mm} \leq r \leq 113.5 \text{ mm}$), circumferential stresses in the radial direction reflect the influence of the thermal load on the friction surface of the disk manifested by a higher value of stress for a larger distance from the axis of revolution z (Fig. 3c). The circumferential stresses depicted, however, in contrast to the radial stresses (Fig. 3b) for the area free from heating on the contact surface are tensile and slightly lower than the highest compressive circumferential stresses (near the outer disk edge).

The distribution of equivalent Huber-Mises stress in the radial direction for several time moments are shown in Fig. 3d. The distribution for each time step reveals a minimum near the

internal edge of the contact region. The location of the minimum slightly moves in the direction of the outer edge of the disk after reaching a half of the braking time.

Huber-Mises stress contours on the friction surface of the disk at certain time moments ($t = 0.084$ s, 0.232 s, 0.988 s, 2.018 s, 2.982 s, 3.96 s) are depicted in Fig. 4. Concentration of the stresses follows the motion of the heating area (pad) which is particularly evident at the beginning of the process. The distribution of σ_{HM} equalizes in the circumferential direction after about 3 s.

Distributions of the Huber-Mises stress in the rz plane at selected time moments ($t = 0.084$ s, 0.232 s, 0.988 s, 2.018 s, 2.982 s, 3.96 s) are shown in Fig. 5. As can be seen, the highest values of the equivalent stress occur on the friction surface $z = 0$. Accordingly, these values are consistent with the results shown in Fig. 2d (the maximum stress is reached at $r = 95$ mm and $t \approx 0.5$ s. We can see also that some abrupt changes in the contour directions would suggest a slight mesh refinement in these areas.

5. Conclusions

The three-dimensional quasi-static thermal stresses in the brake disk using the finite element method are evaluated. Based on the obtained results general conclusions about the usefulness of the developed computational 3D FE model are drawn. This approach allows correct identification of the most strenuous disk areas. It is proved that these are: the region between the average and the outer radius of the rubbing path at the beginning of braking and the inner radius of the disk at the end of braking. Unlike the axisymmetric models, the developed spatial computational model provides valid and useful information about the stress state not only for one cycle of braking, but also distinguishes the phases of each disk rotation against the stationary pads. This may be suitable for predicting fatigue cracking processes occurring near in the zone near the contact surface of the brake disk. The periodic heating and cooling of the surface layer of the disk results in cyclic changes in the thermal stress with an amplitude of about 40 MPa, which gives the basis for the use of fatigue cracking criteria. It may be therefore established that the full thermal and mechanical stress state can only be given using a three-dimensional model.

Acknowledgement

The present paper has been financially supported by the National Science Centre in Poland (research project No. 2011/01/B/ST8/07446).

References

1. ADAMOWICZ A., 2015, Axisymmetric FE model to analysis of thermal stresses in a brake disk, *Journal of Theoretical and Applied Mechanics*, **53**, 2, 357-370
2. ADAMOWICZ A., GRZES P., 2011a, Analysis of disc brake temperature distribution during single braking under non-axisymmetric load, *Applied Thermal Engineering*, **31**, 1003-1012
3. ADAMOWICZ A., GRZES P., 2011b, Influence of convective cooling on a disc brake temperature distribution during repetitive braking, *Applied Thermal Engineering*, **31**, 2177-2185
4. ADAMOWICZ A., GRZES P., 2013, Three-dimensional FE model for calculation of temperature of a thermosensitive disc, *Applied Thermal Engineering*, **50**, 572-581
5. BAGNOLI F., DOLCE F., BERNABEI M., 2009, Thermal fatigue cracks of fire fighting vehicles gray iron brake discs, *Engineering Failure Analysis*, **16**, 152-163

6. CHARRON F., 1943, Partage de la chaleur entre deux corps frottants, *Publications Scientifiques et Techniques du Ministere de l'Air*, Paris, **182**
7. CHICHINADZE A.V., 1967, *Calculation and Investigation of External Friction During Braking* (in Russian), Nauka, Moscow
8. CHOI J.-H., LEE I., 2004, Finite element analysis of transient thermoelastic behaviors in disk brakes, *Wear*, **257**, 47-58
9. COOK R.D., 1995, *Finite Element Modeling for Stress Analysis*, John Wiley & Sons, Inc., New York
10. GAO C.H., HUANG J.M., LIN X.Z., TANG X.S., 2007, Stress analysis of thermal fatigue fracture of brake disks based on thermomechanical coupling, *Journal of Tribology, Transactions of the ASME*, **129**, 536-543
11. GRZES P., 2010, Finite element analysis of temperature distribution in axisymmetric model of disc brake, *Acta Mechanica et Automatica*, **4**, 4, 23-28
12. HUEBNER K.H., THORNTON E.A., 1982, *The Finite Element Method for Engineers*, John Wiley & Sons, New York
13. KIM D.-J., LEE Y.-M., PARK J.-S., SEOK C.-S., 2008, Thermal stress analysis for a disk brake of railway vehicles with consideration of the pressure distribution on a frictional surface, *Materials Science and Engineering, A – Structural Materials Properties*, **483/484**, 456-459
14. LING F.F., 1959, A quasi-iterative method for computing interface temperature distribution, *Zeitschrift für angewandte Mathematik und Physik (ZAMP)*, **10**, 5, 461-475
15. MACKIN T.J., NOE S.C., BALL K.J., 2002, Thermal cracking in disk brakes, *Engineering Failure Analysis*, **9**, 63-76
16. MSC.Nastran Thermal Analysis User's Guide, 2002
17. NODA N., HETNARSKI R.B., TANIGAWA Y., 2003, *Thermal Stresses*, 2nd ed., Taylor and Francis, New York
18. NORLANDER M., 2005, Crack propagation in fixed caliper brake discs, Master's Dissertation, Division of Solid Mechanics, Lund University, Sweden
19. RANAKER M., 2001, Non-linear behaviour of cast iron in disc brakes – survey and calculations, Division of Machine Design, Design Sciences, LTH, Lund
20. SCIESZKA S.F., ZOLNIERZ M., 2014, Experimental and numerical investigations of thermo-mechanical instability of the industrial disc brakes, *Proceedings of the Institution of Mechanical Engineers, Part J: Journal of Engineering Tribology*, **228**, 5, 567-576
21. TALATI F., JALALIFAR S., 2008, Investigation of heat transfer phenomena in a ventilated disk brake rotor with straight radial rounded vanes, *Journal of Applied Sciences*, **8**, 20, 3583-3592
22. TALATI F., JALALIFAR S., 2009, Analysis of heat conduction in a disk brake system, *Heat Mass Transfer*, **45**, 8, 1047-1059
23. TIROVIC M., 1998, Development of a wheel mounted disc brake for a high-speed train, *Proceedings of the Institution of Mechanical Engineers, Part F: Journal of Rail and Rapid Transit*, **212**, 2, 113-121
24. YEVTUSHENKO A.A., GRZES P., 2010, FEM-modeling of the frictional heating phenomenon in the pad/disc tribosystem (a review), *Numerical Heat Transfer, Part A: Applications*, **58**, 207-226
25. YEVTUSHENKO A., GRZES P., 2011, Finite element analysis of heat partition in a pad/disc brake system, *Numerical Heat Transfer, Part A: Applications*, **59**, 521-542
26. YEVTUSHENKO A.A., GRZES P., 2012, Axisymmetric FEA of temperature in a pad/disc brake system at temperature-dependent coefficient of friction and wear, *International Communications in Heat and Mass Transfer*, **39**, 8, 1045-1053

27. YEVTUSHENKO A.A., GRZES P., ADAMOWICZ A., 2014, Numerical analysis of thermal stresses in disk brakes and clutches (a review), *Numerical Heat Transfer, Part A: Applications*, ID: 923221 DOI: 10.1080/10407782.2014.923221
28. YILDIZ Y., DUZGUN M., 2010, Stress analysis of ventilated brake discs using the finite element method, *International Journal of Automotive Technology*, **11**, 133-138
29. ZIENKIEWICZ O.C., TAYLOR R.L., ZHU J.Z., 2005, *The Finite Element Method: its Basis and Fundamentals*, Elsevier Butterworth-Heinemann, Amsterdam

Manuscript received October 17, 2014; accepted for print July 26, 2015

LIFTING CAPACITY ENHANCEMENT OF A CRAWLER CRANE BY IMPROVING STABILITY

A.A. SHAIKH

*Sardar Vallabhbhai National Institute of Technology, Department of Mechanical Engineering, Surat, Gujarat, India
e-mail: aas@med.svmit.ac.in*

DINEESH KUMAR D

S.D. Material Handlers Pvt. Ltd., Surat, Gujarat, India; e-mail: dineesh@syamadynamic.com

The lifting capacity of a crawler crane is limited by its stability and structural strength. This paper analyzes the stability factor by calculating tipping loads at various load radii for a particular boom length. It shows that the tipping load decreases with an increase in the load radius. A new structural frame is proposed to extend out the superstructure counterweight of the crane. With such a proposed arrangement, it is shown that the lifting capacity of the crane, limited by stability, increases. Static structural analysis of the proposed structural frame is performed using ANSYS workbench software.

Keywords: crawler crane, stability, tipping load, lifting capacity

1. Introduction

The requirement for lifting in the construction industry is ever increasing. Crane manufacturers are constantly working on at achieving new heights in the lifting industry. Although higher capacity cranes are available, capacity enhancement of the existing cranes especially at longer radii will reduce the dependency on higher capacity cranes, which in turn will reduce costs of project construction. This will also cut down the capital investment of construction companies by avoiding the necessity of purchasing higher capacity cranes and, thereby, having an option to invest in other areas.

The load lifting capacity of a crawler crane is determined by the crane stability and its structural strength. There have been previous investigations on the tip over stability of the cranes and on the crane dynamics. Rauch *et al.* (2013) investigated the tip over stability analysis of mobile boom cranes with swinging payloads and presented the process for conducting stability analysis. Klinger (2014) studied the failure of cranes attributable to wind induced vibrations of tension bars leading to fatigue fractures. Wang *et al.* (2015) investigated stability of geometrically nonlinear slender frame structures of crawler cranes. Trąbka (2014) analyzed the influence of change in the number of flexible structural components of telescopic cranes. Savkovic *et al.* (2014) studied the stress distribution and deformation in the contact zone between segments of the telescopic boom of a hydraulic truck crane. Kiliclan *et al.* (1999) determined the maximum possible payload for a mobile crane that was kept in a fixed position by stabilizing arms while transferring the payload. Towarek (1998) studied dynamic stability of a boom crane influenced by flexible soil foundation. Chin *et al.* (2001) investigated effects of platform motion on the dynamic stability of a boom crane. Research studies on dynamic responses of a crane during various motions were demonstrated by Posiadała *et al.* (1990, 1991), Posiadała (1997), Sun and Kleeberger *et al.* (2003), Sun *et al.* (2005), Sun and Liu (2006), Jerman *et al.* (2004). However, it was found that the research study in the area of improving the lifting capacity of cranes had not developed appreciably.

In this paper, an effort is made to improve the lifting capacity of a crawler crane limited by stability conditions. The stability analysis of an 80MT crawler crane with a 18 m lattice boom is carried out to find out the standing moment of the crane. The proposed structural frame attached to the crane superstructure is modeled to support the counterweight, which can be extended or retracted. The new lifting capacity of the crane with the extended counterweight is calculated, and static structural analysis is done for the proposed structural frame using ANSYS workbench software.

2. Design aspects

2.1. Stability calculations

A three dimensional model of an 80 MT Demag CC280 crawler crane is made using modeling software ProE as depicted in Fig. 1. To do this, the field work has been carried out to collect the dimensional data of major structural parts of the machine and two dimensional drawings have been made using Autodesk Autocad software.

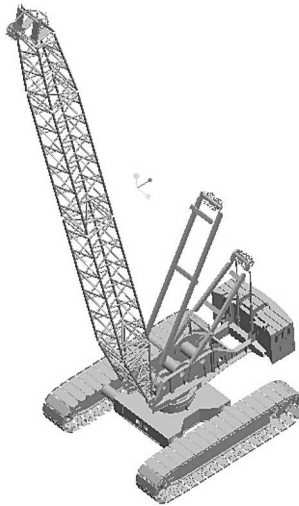


Fig. 1. 3D model of 80MT Demag CC 280 crawler crane

The predominant factor controlling load ratings for cranes is stability against tipping. The tipping load is the hook load at a specified radius about a line called the tipping fulcrum, which causes the crane to tip. A crane will tip when the overturning moment (moment of the load and boom about the tipping fulcrum) becomes close to or equal to the crane resisting moment (moment of the machine weight about the tipping fulcrum). The crane rating is based on taking the percentage of the tipping load. As per standard ASME (B30.5, 2011), the crawler crane load rating is 75 percent of the tipping load.

The crawler tracks are loose cast steel and their purpose is to provide runways for the track rollers and distribute the machine weight and load to the supporting surfaces. The track rollers define the position of the side fulcrum. When operating over the front and rear, the tipping fulcrum is located on the tilting edges defined by the connecting lines between the front and rear driving or idler sprockets. The sideways tilting edges are the connecting lines between the outer rollers. For calculation of 360° crane working operation, the tilting fulcrum is considered to be on the tipping circle having radius of the shortest distance between the crane slewing centre and various tipping edges.

The weight and centre of gravity locations of various crane components are obtained from the 3D model of the crane. The tilting edges and tipping circle of the crane are obtained as shown in Fig. 2.

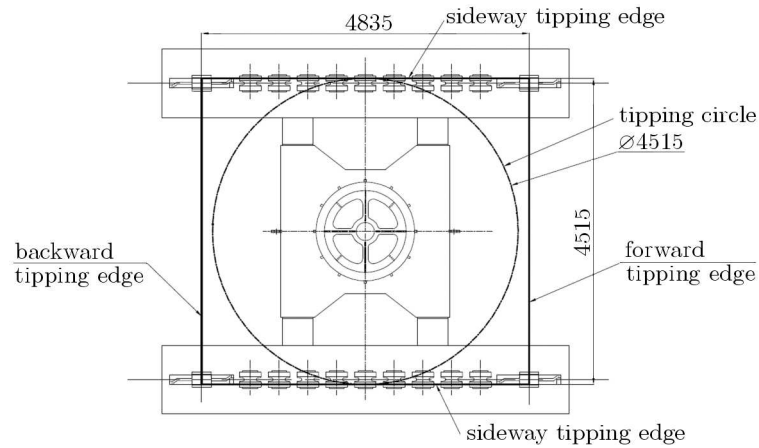


Fig. 2. Tipping edges and tipping circle of the crane – plan view

The selected crane can be configured with a boom length ranging from the minimum of 9 m to the maximum 54 m. For performing stability analysis and considering the complexity of the larger boom, a boom length of 18 m is selected, which is two times basic boom length. Crane standing moments and stability load ratings are calculated at seven different load radii (R) using the weights of crane parts and its centre of gravity (C.G.) locations as shown in Fig. 3.

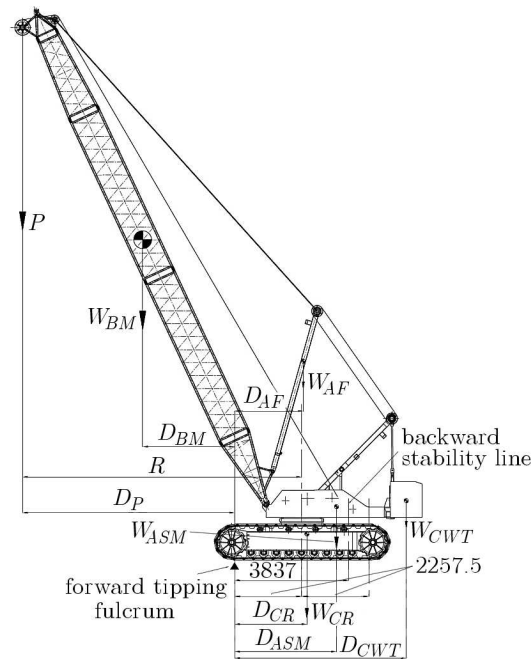


Fig. 3. Weights and centre of gravity (C.G.) locations of various crane parts

Standing moment (M_{CR} [kN m]) of the crane is calculated from the following formula

$$M_{CR} = W_{CR}D_{CR} + W_{CWT}D_{CWT} + W_{AF}D_{AF} + W_{BM}D_{BM} \quad (2.1)$$

where W_{CR} is the weight of the crane superstructure and carbody, D_{CR} – distance between the tipping fulcrum and C.G. of the crane superstructure and carbody, W_{CWT} – weight of the counterweight, D_{CWT} – distance between the tipping fulcrum and C.G. of the counterweight, W_{AF} – weight of the A-frame, D_{AF} – distance between the tipping fulcrum and C.G. of A-frame, W_{BM} – weight of the boom, D_{BM} – distance between the tipping fulcrum and C.G. of the boom.

The distance (D_{ASM} [m]) between the tipping fulcrum and C.G. of the total crane assembly is obtained from

$$D_{ASM} = \frac{M_{CR}}{W_{ASM}} \quad (2.2)$$

where W_{ASM} denotes the weight of the total crane assembly.

The tipping load (TL [kN]) of the crane is

$$TL = \frac{M_{CR}}{D_P} \quad (2.3)$$

where D_P is the distance between the tipping fulcrum and Hook load centre.

The rated load (P [kN]) limited by stability of the crane is obtained from

$$P = 75\%TL \quad (2.4)$$

The calculated values of the tipping load (TL) and rated load (P) are shown in Table 1.

Table 1. Tipping and rated loads of the crane in the red arrangement

Case		Unit	1	2	3	4	5	6	7	
Boom length		m	18	18	18	18	18	18	18	
Load radius (R)		m	4	5	7	9	11	14	16	
AAA	Crane super-structure and carbody	W_{CR}	kN	355.5	355.5	355.5	355.5	355.5	355.5	355.5
		D_{CR}	m	2.529	2.529	2.529	2.529	2.529	2.529	2.529
	Counter-weight	W_{CWT}	kN	208.3	208.3	208.3	208.3	208.3	208.3	208.3
		D_{CWT}	m	5.712	5.712	5.712	5.712	5.712	5.712	5.712
	A-frame	W_{AF}	kN	7.64	7.64	7.64	7.64	7.64	7.64	7.64
		D_{AF}	m	3.747	3.507	2.992	2.429	1.81	0.742	-0.113
	Boom	W_{BM}	kN	29.6	29.6	29.6	29.6	29.6	29.6	29.6
		D_{BM}	m	-0.12	-0.67	-1.77	-2.88	-3.99	-5.671	-6.808
Standing moment M_{CR}		kN m	2114	2096	2059	2022	1985	1927	1886	
Crane assembly	W_{ASM}	kN	601.1	601.1	601.1	601.1	601.1	601.1	601.1	
	D_{ASM}	m	3.517	3.487	3.426	3.365	3.302	3.205	3.138	
Load distance from tipping fulcrum D_P		m	1.742	2.742	4.742	6.742	8.742	11.742	13.742	
Tipping load (TL)		kN	1213.6	764.4	434.3	300.0	227.0	164.1	137.3	
Rated load (P)		kN	910.2	573.3	325.7	225.0	170.3	123.1	103.0	

AAA – Weight of the assembly and C.G. distance from tipping line

The stability of a crawler crane is governed by the standing moment of the crane. To increase the standing moment of the crane, counterweights (ballasts) are arranged at the rear end of the slewing platform or superstructure of the crane. The limit of the maximum counterweight is determined by the backward stability of the free standing crane. The backward stability of a crane is its ability to resist overturning in the direction opposite to the boom point while in the unloaded condition. The resistance to backward overturning is reflected in the margin of backward stability. According to standard ASME (B30.5, 2011), the minimum backward stability condition for crawler cranes is that the horizontal distance between the centre of gravity of the crane assembly and the axis of rotation shall not exceed 70% of the radial distance from the axis of rotation to the backward tipping fulcrum in the least stable direction. Since the counterweight is designed based on the backward stability of the crane at the minimum possible boom length

and maximum possible boom angle, the backward stability of the crane increases with an increase in the boom length and load radius as C.G. of the crane assembly moves towards the forward tipping fulcrum.

The maximum allowable standing moment (M_{CR}^{max} [kNm]) is obtained when the centre of gravity of the crane lies at the backward stability line

$$M_{CR}^{max} = W_{ASM} D_{BS} \quad (2.5)$$

where D_{BS} is the distance between the forward tipping fulcrum and the backward stability line, [m].

The backward stability line lies at a distance of 70% of the radial distance from the axis of rotation to the backward tipping fulcrum

$$D_{BS} = 2.2575 + 2.2575 \cdot 70\% = 3.837 \quad (2.6)$$

2.2. Stability calculations with the proposed structural frame

In the existing form, the counterweight of the crane is fixed at the rear end of the crane superstructure. The proposed structural frame is modeled using ProE software, which is attached to the bottom of the crane superstructure, wherein the counterweight is placed on top of it as shown in Fig. 4.

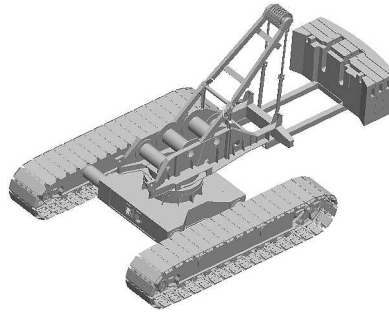


Fig. 4. 3D model of the crane assembly with an extended counterweight on the structural frame

This structural frame along with the counterweight is extendable and retractable. For a particular load radius, the structural frame along with the counterweight is extended correspondingly to the load radius so as to obtain the maximum possible standing moment considering the backward stability conditions. With an increase in the load radius, the counterweight is extended outwards and, if the load radius is decreased, the counterweight is retracted to the position corresponding to that load radius. The structural frame can be extended or retracted using a hydraulic cylinder with controls correlated with the safe load indicator or load moment indicator device of the crane. The position of the counterweight can be accurately controlled using length sensors and load moment indicator devices of the crane.

Considering the proposed structural frame and C.G. of various crane parts as shown in Fig. 5, where W'_{CWT} is the weight of the counterweight including the weight of the structural frame, D'_{CWT} [m] – distance between the tipping fulcrum and C.G. of the counterweight including the structural frame, W'_{ASM} – weight of the crane assembly including the weight of the structural frame, D'_{ASM} – distance between the tipping fulcrum and C.G. of the crane assembly including the structural frame.

To obtain the maximum possible standing moment, the counterweight is extended outwards to a distance corresponding to the load radius as shown in Fig. 5.

It is obtained by the following formula

$$D'_{CWT} = \frac{M_{CR}^{max} - (M_{CR} - W_{CWT} D_{CWT})}{W'_{CWT}} \quad (2.7)$$

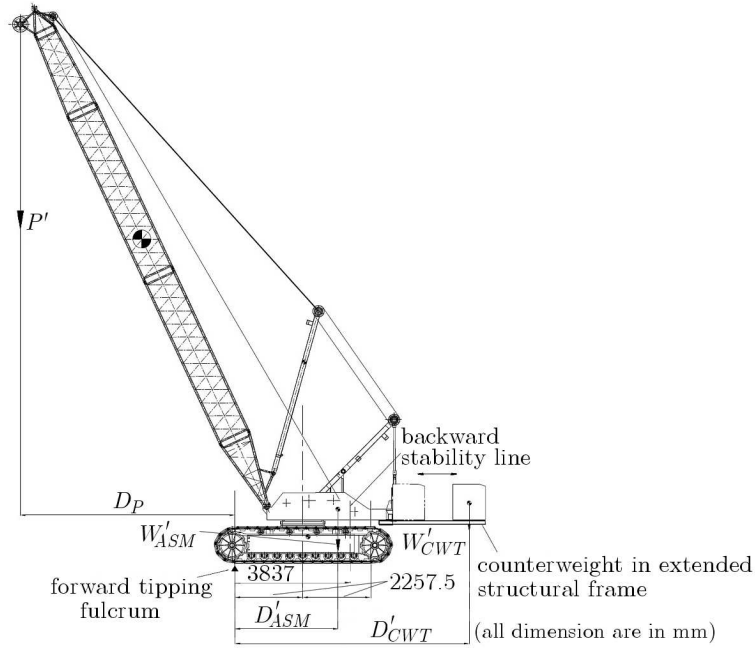


Fig. 5. Weights and C.G. of various crane parts in an extended counterweight position

The distance D'_{CWT} obtained from Eq. (2.7) satisfies the backward stability condition from standard ASME B30.5. The centre of gravity of the crane will be inside the backward stability line when the counterweight is in extended position. When there is a sudden release of load while the counterweight is in extended position, the backward stability margin will provide the overturning resistance to withstand the impact of the sudden release of load.

With the counterweight in an extended position, new tipping loads (TL') and new rated load (P') limited by stability are recalculated as shown in Table 2. The graph showing a comparison of the new rated load (P') with the extended counterweight and rated load (P) without the extended counterweight for various load radius (R) is plotted in Fig. 6.

The calculations are performed for seven cases where the load radius of the crane changes from 4 m to 16 m.

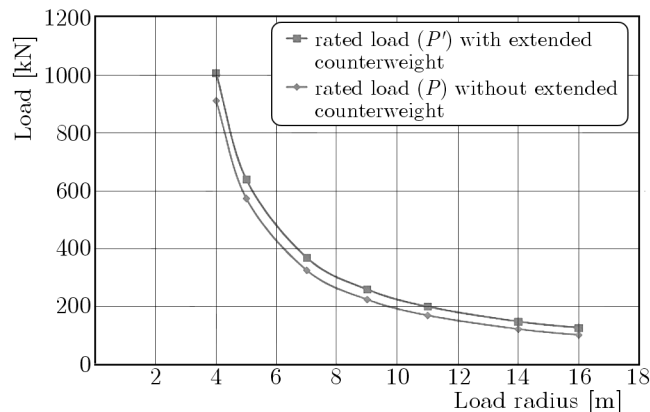


Fig. 6. Rated load versus load radius (R) with and without the extended counterweight

2.3. Static structural analysis

The proposed structural frame will be under maximum loading when it is extended completely outwards with the counterweight as in case 7. The static structural analysis of the structural

Table 2. Tipping and rated loads of the crane with the extended counterweight

Case		Unit	1	2	3	4	5	6	7	
Boom length		m	18	18	18	18	18	18	18	
Load radius (R)		m	4	5	7	9	11	14	16	
AAA	Crane super-structure and carbody	W_{CR}	kN	355.5	355.5	355.5	355.5	355.5	355.5	355.5
		D_{CR}	m	2.529	2.529	2.529	2.529	2.529	2.529	2.529
	BBB	W'_{CWT}	kN	215.6	215.6	215.6	215.6	215.6	215.6	215.6
		D'_{CWT}	m	5.667	5.667	5.667	5.667	5.667	5.667	5.667
	A-frame	W_{AF}	kN	7.6	7.6	7.6	7.6	7.6	7.6	7.6
		D_{AF}	m	3.747	3.507	2.992	2.429	1.81	0.742	-0.113
	Boom	W_{BM}	kN	29.6	29.6	29.6	29.6	29.6	29.6	29.6
		D_{BM}	m	-0.12	-0.669	-1.77	-2.876	-3.988	-5.671	-6.808
	Crane assembly	W_{ASM}	kN	608.4	608.4	608.4	608.4	608.4	608.4	608.4
		D_{ASM}	m	3.528	3.498	3.438	3.377	3.315	3.219	3.153
Load distance from tipping fulcrum D_P		m	1.742	2.742	4.742	6.742	8.742	11.742	13.742	
Max. possible standing moment (M_{CR}^{max})		kN m	2334.3	2334.3	2334.3	2334.3	2334.3	2334.3	2334.3	
New counterweight distance w.r.t max. standing moment (D'_{CWT})		m	6.540	6.624	6.794	6.966	7.140	7.409	7.596	
New tipping load with exten. counterweight (TL')		kN	1340.0	851.3	492.3	346.2	267.0	198.8	169.9	
Rated load with extended counterweight (P')		kN	1005.0	638.5	369.2	259.7	200.3	149.1	127.4	

AAA – Weight of the assembly and C.G. distance from tipping line

BBB – Counterweight with extendable frame

frame is performed in this condition using ANSYS workbench software. The material properties of the structural frame are described in Table 3 (ThyssenKrupp Steel, 2005). The stress analysis of the structural frame is shown in Fig. 7.

Table 3. Material properties of the structural frame

Steel grade	Minimum yield strength [MPa]	Tensile strength [MPa]	Modulus of elasticity [kN/mm ²]	Density [10 ³ kg/m ³]
N-A-XTRA (M) 700	700	770-940	210	7.85

3. Results and discussions

Table 1 reveals that the rated load limited by stability of the crane decreases with an increase in the load radius. As the load radius increases, the moment from the weight of the boom reduces the standing moment of the crane. Proportionately, the tipping load also decreases resulting in a reduction in the rated load capacity.

The calculated values described in Table 1 show that the standing moment of the crane is much below the maximum allowable standing moment calculated from Eq. (2.5). The difference between the maximum allowable standing moment (M_{CR}^{max}) and the standing moment (M_{CR})

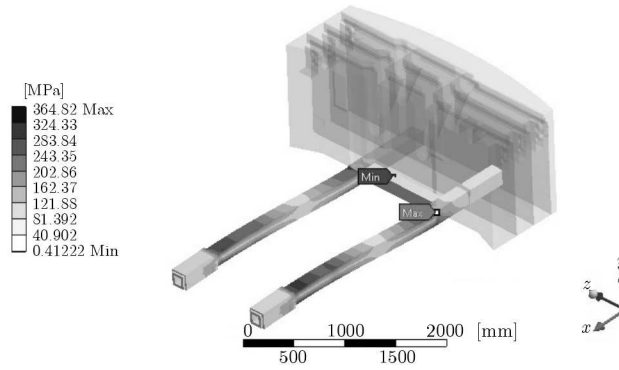


Fig. 7. Stress analysis of the proposed structural frame

of the crane increases with the load radius (R) and boom length. It is mainly due to fact that the counterweight is designed and optimized to obtain the maximum possible standing moment when the crane is equipped with the minimum boom length and maximum boom angle. The difference in this case is due to the same reason that the counterweight has been designed for the crane boom length of 9 m, which is the basic boom length of this crane, and at the maximum angle. In the present case, the crane is equipped with a 18 m boom length. Hence, the moment due to the weight of the additional 9 m boom reduces the standing moment of the crane, and it is further reduced with an increase in the load radius.

The graph shown in Fig. 6 reveals that the rated load of the crane, limited by the stability, increases by using a sliding structural frame. The structural frame is extended or retracted with respect to the corresponding load radius. When the counterweight is extended outwards using the structural frame, C.G. of the crane assembly moves backwards closer to the backward stability line. It is observed that the standing moment of the crane increases to the maximum allowable standing moment by extending the structural frame with the counterweight. Finally, the tipping load and rated load are increased due to improvement of the standing moment of the crane.

The structural stress analysis of the proposed structural frame shown in Fig. 8 reveals that the maximum value of stress obtained is 365 N/mm^2 , which is below the permissible limit of 466 N/mm^2 according to standard SAE J987 (2003).

4. Conclusions

Based on the three dimensional model of a crawler crane and standard ASME B30.5 (2011), the standing moment and tipping loads of the crane are obtained. The maximum allowable standing moment of the crane is obtained from the backward stability condition specified in standard ASME B30.5. The proposed structural frame is modeled for extending and retracting the crane counterweight corresponding to the particular load radius. The tipping loads and lifting capacities of the crane with the extended counterweight at various radii are recalculated.

It is shown that the lifting capacity limited by the stability increases with making use of the proposed structural frame. By changing the fixed counterweight into a movable counterweight placed on the proposed sliding structural frame, the standing moment of the crane is improved to the maximum allowable standing moment. This furtherly enhances the tipping load and finally the lifting capacity of the crane. The lifting capacity of the crane, limited by stability, increases to the range of 10% to 24% with the use of the extended counterweight. It is also found that the percentage of the lifting capacity enhancement increases with increase of load radius. The compliance of the backward stability condition, according to standard ASME B30.5, ensures safety and stability of the crane with the extended counterweight.

Acknowledgements

The authors appreciate the support provided by M/s. S. D. Material Handlers Pvt. Ltd. for this work.

References

1. CHIN C., NAYFEH A.H., ABDEL-RAHMAN E., 2001, Nonlinear dynamics of a boom crane, *Journal of Vibration and Control*, **7**, 199-220
2. JERMAN B., PODRZAJ P., KRAMAR J., 2004, An investigation of slewing-crane dynamics during slewing motion-development and verification of a mathematical model, *International Journal of Mechanical Sciences*, **46**, 729-750
3. KILICSLAN S., BALKAN T., IDER S.K., 1999, Tipping load of mobile cranes with flexible booms, *Journal of Sound and Vibration*, **223**, 4, 645-657
4. KLINGER C., 2014, Failure of cranes due to wind induced vibrations, *Engineering Failure Analysis*, **43**, 198-220
5. POSIADAŁA B., 1997, Influence of crane support system on motion of the lifted load, *Mechanism and Machine Theory*, **32**, 1, 9-20
6. POSIADAŁA B., SKALMIERSKI B., TOMSKI L., 1990, Motion of the lifted load brought by a kinematic forcing of the crane telescopic boom, *Mechanism and Machine Theory*, **25**, 547-555
7. POSIADAŁA B., SKALMIERSKI B., TOMSKI L., 1991, Vibration of load lifted by a truck crane with consideration of physical properties of rope, *Machine Dynamics Problems*, **2**, 85-104
8. RAUCH A., SIGHOSE W., FUJIOKA D., JONES T., 2013, Tip – over stability analysis of mobile boom cranes with swinging payloads, *Journal of Dynamic Systems, Measurement, and Control*, **135**, 3, 0310081-6
9. SAVKOVIC M., GASIC M., PAVLOVIC G., BULATOVIC R., ZDRAVKOVIC N., 2014, Stress analysis in contact zone between the segments of telescopic booms of hydraulic truck cranes, *Thin-Walled Structures*, **85**, 332-340
10. Standard ASME B30.5-2011, Mobile and Locomotive cranes, Safety standard for Cable-ways, Cranes, Derricks, Hoists, Hooks, Jacks, and Slings
11. Standard SAE J987, 2003, Lattice Boom Cranes – Method of Test
12. SUN G., KLEEBERGER M., 2003, Dynamic responses of hydraulic mobile crane with consideration of the drive system, *Mechanism and Machine Theory*, **38**, 1489-1508
13. SUN G., KLEEBERGER M., LIU J., 2005, Complete dynamic calculation of mobile crane during hoisting motion, *Mechanism and Machine Theory*, **40**, 447-466
14. SUN G., LIU J., 2006, Dynamic responses of hydraulic crane during luffing motion, *Mechanism and Machine Theory*, **41**, 1273-1288
15. ThyssenKrupp Steel, Material Specification 215, 2005-12, 1-4
16. TOWAREK Z., 1998, The dynamic stability of a crane standing on soil during the rotation of the boom, *International Journal of Mechanical Sciences*, **40**, 557-574
17. TRĄBKA A., 2014, Dynamics of telescopic cranes with flexible structural components, *International Journal of Mechanical Sciences*, **88**, 162-174
18. WANG G., QI Z., KONG X., 2015, Geometrical nonlinear and stability analysis for slender frame structures of crawler cranes, *Engineering Structures*, **83**, 209-222

DELAMINATION PROPERTIES OF THE HUMAN THORACIC ARTERIAL WALL WITH EARLY STAGE OF ATHEROSCLEROSIS LESIONS

MARTA KOZUŃ

Wrocław University of Technology, Faculty of Mechanical Engineering, Wrocław, Poland
e-mail: marta.kozun@pwr.edu.pl

The aim of this work is to determine mechanical properties of interfaces between layers of the human thoracic aortic wall with early stages of atherosclerosis lesions. Circumferential ($n = 48$) and axial ($n = 15$) specimens have been prepared and the mechanical properties of the interfaces between the layers have been determined on the basis of the peeling test. The results show that the mechanical and dissection properties of the interfaces between the layers depend on the direction of the tests. The results confirm that the early stage of atherosclerosis does not affect the mechanical parameters of the layer interfaces and does not affect resistance of the vessel wall to delamination.

Keywords: peeling test, human arterial wall, thoracic artery, mechanical properties, atherosclerosis

1. Introduction

Human arterial wall is a three-layer (the intima, media, and adventitia) laminate reinforced with long fibres (collagen and elastin fibres), which play a key role in the transfer of mechanical stress. Collagen and elastin fibres are held together by the extracellular matrix.

Each layer of the arterial wall is characterized by a different structure, orientation of collagen and elastic fibres, mechanical properties, and function performed in the vessel wall (Holzapfel *et al.*, 2004). The intimal layer is built mostly of connective tissue (Shekhonin *et al.*, 1985), and in young and healthy people it is not involved in the transfer of mechanical stress. In the physiological range of blood pressure, this process is carried out by the media (collagen fibres, elastin fibres, and smooth muscle cells, see Kobielarz *et al.* (2013), Gašior-Głogowska *et al.* (2011), Schriebl *et al.* (2012). The collagen fibres in this layer are arranged circumferentially (Schriebl *et al.*, 2012). In the case of arterial hypertension, the process of transfer of stress also involves the adventitia (collagen fibres) (Shekhonin *et al.*, 1985), which protects the vessel against overstretching and rupture (Holzapfel 2008; Schulze-Bauer *et al.*, 2001). In the adventitia, collagen fibres are dispersed, and only individual fibres are arranged circumferentially (Schriebl *et al.*, 2012). The cohesive composite structure of the human thoracic aortic wall ensures its high mechanical strength and determines its proper functioning, i.e. transfer of mechanical stress resulting from blood pressure and the ability to deform reversibly (Sommer *et al.*, 2010).

Delamination of the vessel wall may occur spontaneously or as a result of trauma. Spontaneous dissection occurs in 5-30 cases per million people/year and depends on a number of factors (hypertension, atherosclerosis, aortic dilatation, and Marfans and Ehlers-Danlos syndromes (Tong *et al.*, 2011). This kind of dissection is usually the result of structural remodelling of the aortic wall, which progresses along with the development of vascular diseases, including atherosclerosis. Degenerative changes that develop along with the progression of atherosclerosis, in particular the formation of atherosclerotic plaque (Kot *et al.*, 2011), lead to changes in the mechanical properties of the individual layers of the aortic wall (Teng *et al.*, 2009; Weisbecker

et al., 2012) and affect the adhesion between them (Karimi *et al.*, 2013). This leads to a loss of integrity of the vessel wall and, consequently, to its delamination. Aortic dissection of traumatic origin is, in most cases, the result of a diagnostic or therapeutic procedure performed on the vascular system, for example insertion of a stent graft or aortic stents. This treatment causes denudation of the endothelium, disruption of the intima and the atherosclerotic plaque with frequent separation from or dissection of the media, and overstretching of non-diseased portions of the arterial wall (Sommer *et al.*, 2008). These intimal defects can cause an imbalance of distribution of mechanical stress on the arterial wall and may be the trigger for propagation of the aortic dissection. Due to its dynamic progression, diagnostic difficulties, and high mortality, aortic dissection is a difficult clinical issue. According to statistics, in the first 48 hours of the onset of dissection, the mortality rate is 1% per hour among untreated patients, about 16-20% of patients survive 14 days, and only 5% survive 12 months (Szpakowski *et al.*, 2006). Although arterial dissection is a frequently occurring phenomenon, the underlying biomechanical properties of arterial dissection remain largely unclear.

The research carried out in recent years on cardiovascular biomechanics has concerned mainly the analysis of the impact of pressure on the vessel wall. The interaction between the aortic wall and blood is also modelled, and the mechanical properties of the vessel wall and its layers are determined. The mechanical properties (maximum strain, tensile strength, and Young's modulus) are determined mostly by a uniaxial tension test (Kobielarz and Jankowski, 2013; Vorp *et al.*, 1996, 2003) in radial, circumferential, and axial directions (Sommer *et al.*, 2008). The results of experimental research obtained in this regard are important for description of the mechanism of vessel wall destruction but they are insufficient to determine pathogenesis of its dissection. Delamination of the vessel wall as a three-layer laminate reinforced with collagen and elastin fibres was considered by Sommer *et al.* (2008) and Tong *et al.* (2011). The authors proposed a new experimental method (peeling test), which allows them to determine the mechanical parameters of the interfaces between the layers of the vessel wall and the energy required to initiate and propagate dissection. Sommer *et al.* (2008) investigated the human abdominal aorta. Only the medial layer of the vessel wall was assessed in circumferential and axial directions. Tong *et al.* (2011) conducted a peeling test of human carotid bifurcations. The authors determined the mechanical properties and the energy dissipated during the dissection of adventitia-media and media-intima composites in circumferential and axial directions. Research conducted by Sommer *et al.* (2008) and Tong *et al.* (2011) focused on normal specimens while the problem of dissection concerned vessel walls with lesions arising due to development of atherosclerosis. Therefore, in the opinion of the author, the results of the studies on vessel wall delamination conducted so far have not fully explained the mechanism of this process.

Based on the above, the aim of the study is to determine the mechanical parameters of the interfaces between the layers of the human thoracic aortic wall in the early stage of atherosclerosis, including energy dissipated during the process of delamination (cracking) of the aortic wall. The obtained results may serve as the basis for the development of constitutive models of the arterial wall. None of the currently existing models takes into account the problem of delamination of the arterial wall, which is a major limitation because many diagnostic procedures as well as flow-related issues are based on the aforementioned models.

2. Material and method

The study has been conducted on human thoracic aortas collected at autopsy within 24 hours of death. A total of 14 specimens qualified for the study (male; age range: 29 ± 12) showing early atherosclerotic lesions (stage II of the development of atherosclerosis according to the classification proposed by Stary (2000, 2004)). Each specimen was dissected parallel to the long

axis of the vessel with a pair of surgical scissors. Next, a blanking tool was used on each aorta to punch out flat rectangular specimens with fixed dimensions of 5 mm (width) by 25 mm (length). The specimens were cut out in two orthogonal directions: in the circumferential direction (C) ($n = 48$) and in the axial direction (A) ($n = 15$) (Fig. 1).

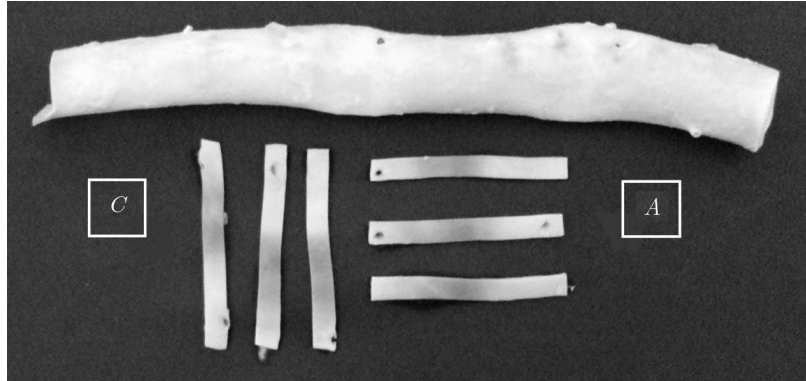


Fig. 1. Directions of specimen preparation: axial (A) and circumferential (C)

The specimens were initially dissected over a length of about 5 mm. This way two “tongues” were obtained for mounting the specimen into the testing machine (Fig. 2). Dissection was introduced between the following interfaces:

- adventitia (A) \rightarrow media (M) + intima (I) (interface 1)
- adventitia (A) + media (M) \rightarrow intima (I) (interface 2)

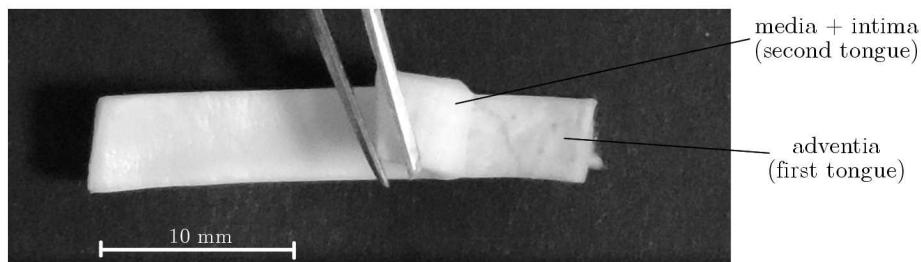


Fig. 2. Preparation of the material for tests of the mechanical properties – initial dissection of the axial specimen of the vessel wall. Width was measured for each specimen

The number of specimens prepared for tests is presented in Table 1. Until the performance of the tests, the specimens were stored in saline solution (0.9% NaCl) at room temperature (15 minutes).

Table 1. The number of specimens prepared for testing of the mechanical properties

Type of interface	Number of specimens
Circumferential direction	
interface 1	26
interface 2	22
Axial direction	
interface 1	7
interface 2	8

Both sides of the two “tongues” of each specimen were fixed to two grips of the testing machine. The study used the material testing system (MTS) Synergie 100 machine. The mechanical properties of the interfaces between vessel wall layers were determined on the basis of the

research methodology proposed by Sommer in 2008, the so-called peeling test (Sommer *et al.*, 2008, 2010). The load was applied perpendicular to the specimen dissection plane (T-peel test configuration) (Fig. 3). The test was conducted at a constant crosshead speed of 2 mm/min in two directions: axial and circumferential. The testing was carried out under repeatable conditions at a constant ambient temperature. During the test, changes were recorded in the value of force (F) as a function of displacement (d) in the direction of the applied load.

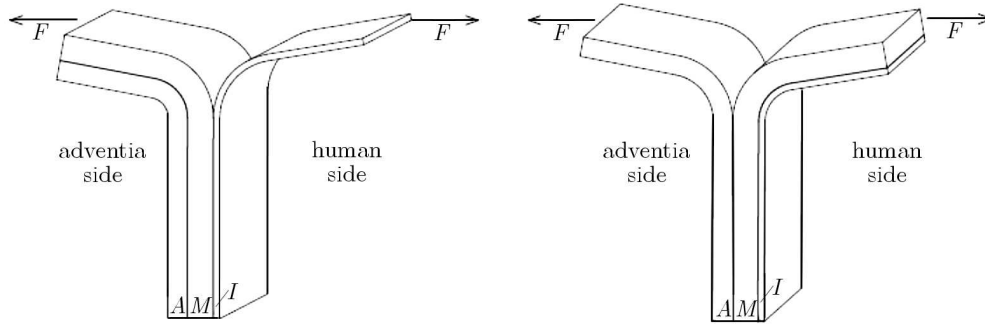


Fig. 3. Schematic illustration of the peeling test: (a) for interface No. 1 and (b) for interface No. 2. The letters A , M , and I mark layers of the vessel wall: A – adventitia, M – media, and I – intima

2.1. Statistical analysis

A statistical analysis was performed using the nonparametric Wilcoxon test (Statistica 10.0, StatSoft). This test was performed at a statistically significant level of $p = 0.05$. The values of mechanical parameters are presented as median values (Me). Additionally, in order to compare these results with the data presented in the literature, the values of mechanical parameters are also presented as arithmetic mean with standard deviation ($X_{mean} \pm SD$).

3. Results

The peeling test causes slow and controlled delamination propagation of human arteries. Figure 4 shows an example of the force per width [mN/mm] vs the dissection path curve [mm] (Fig. 5) determined on the basis of the peeling test. All curves obtained for both circumferential and

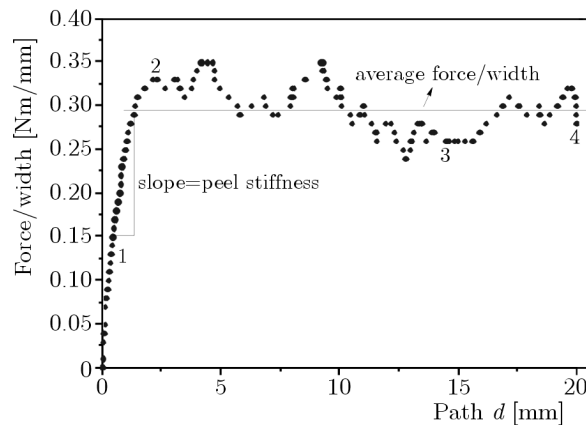


Fig. 4. The force/width vs the path curve obtained on the basis of the peeling test for interface No. 2 in the axial direction with the marked method of determining the mechanical properties, i.e. the stiffness (k) and the average value of the force in relation to the width of the specimen (F/W) during dissection

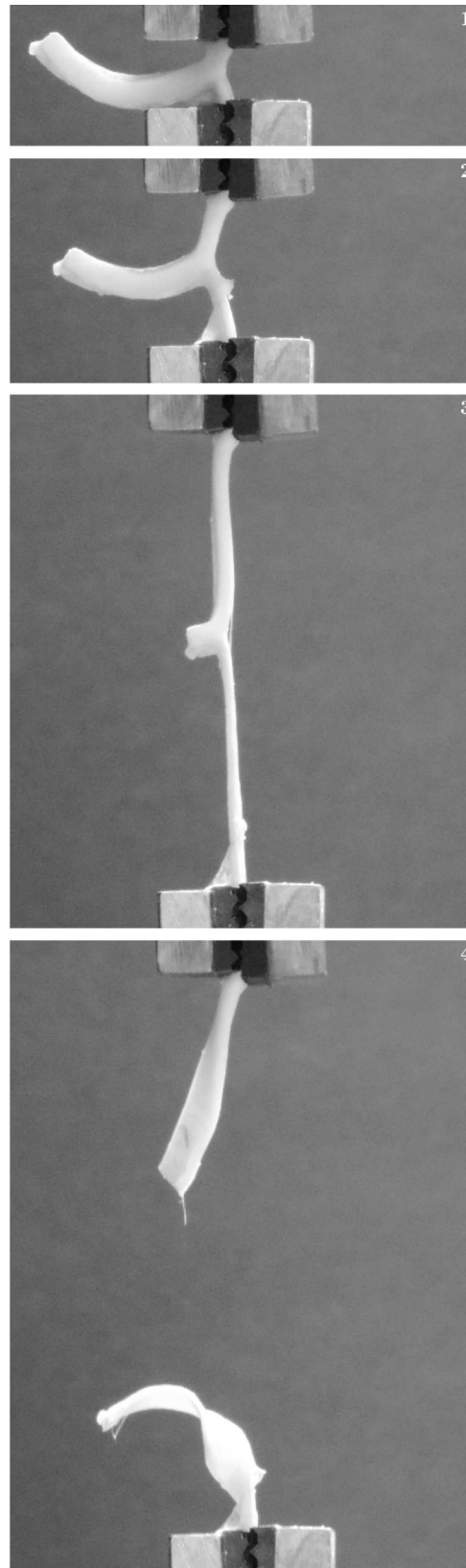


Fig. 5. Axial specimen of the arterial wall (interface No. 2) tested in the T-peel test configuration; four images (1,2,3,4) show progression of the peel test until complete separation of the tissue (4). Examples of where each image (1-4) could fall on the force/width vs path curve (Fig. 4) are indicated by numbers 1, 2, 3, and 4

axial specimens are characterized by a jagged plateau region. Those curves were divided into two stages. Stage I is the linear part of the curve, which is characterized by high dynamics of the change in the force in relation to the change in displacement. This part was used to determine stiffness (k) (Gregory *et al.*, 2012) of the interfaces between the layers of the human thoracic aortic wall (Fig. 4). During stage I, the strength of the tested interface is exceeded, and then stage II begins. At this stage, the aortic wall dissection is propagated as a result of tearing of individual collagen and elastin fibres, as evidenced by local increases and decreases in the value of the force (Fig. 4). For stage II, the average force value was determined, obtained during the process of aortic wall dissection in relation to the initial width of the specimen (F/W) (Fig. 2), which was motivated by assuming ideal rectangular geometries and homogeneous mechanical properties of each specimen (Sommer *et al.*, 2008).

The mechanical properties of both soft tissues (Maksymowicz *et al.*, 2011; Pezowicz, 2010; Żak *et al.*, 2011) and hard tissues (Nikodem, 2012) are analysed in the literature on the basis of the power criterion (Żak, 2014). In the presented work, the process of dissection of thoracic arterial wall has been described as cracking of the three-layer laminate using the energy balance, as previously proposed by Sommer *et al.* (2008) and Tong *et al.* (2011)

$$W_C = \frac{W_C^{ext} - W_C^{stor}}{L_C} \quad W_A = \frac{W_A^{ext} - W_A^{stor}}{L_A} \quad (3.1)$$

where C, A are indications of the direction: C – circumferential, A – axial, L is reference length of the specimen, W^{ext} – external energy supplied to the system, W^{stor} – energy stored in the system.

External energy is defined as follows (Tong *et al.*, 2011)

$$W_C^{ext} = 2.0F_C l_C \quad W_A^{ext} = 2.0F_A l_A \quad (3.2)$$

where: F – ratio of the force recorded during the test to the specimen width, l – length of the specimen prior to dissection (before mounting in the grips of the material testing machine).

The energy stored in the system was calculated as follows (Tong *et al.*, 2011)

$$W_C^{stor} = F_C(l_C - L_C) \quad W_A^{stor} = F_A(l_A - L_A) \quad (3.3)$$

where: F – ratio of the force recorded during the test to the specimen width, L – length of the specimen after dissection (after mounting in the grips of the material testing machine).

Table 2. The value (Me) of dissipated energy (W) during dissection of the human thoracic arterial wall

Type of interface	W [mJ/cm ²]
Circumferential direction	
interface 1	4.9
interface 2	4.5
Axial direction	
interface 1	7.2
interface 2	6.2

Both the stiffness values as well as force/width are significantly higher for axial specimens. Regardless of the analysed direction, statistically significant differences have been found between the stiffness of the tested interfaces. For axial specimens, the stiffness values Me are, respectively, $k = 0.17$ N/mm and $k = 0.11$ N/mm. The energy dissipated during propagation of aortic wall dissection is higher for axial specimens in the case of both interface No. 1 and interface No. 2 (6). These values (Me) are, respectively, as follows: $W = 7.2$ mJ/cm² and $W = 6.2$ mJ/cm² ($X_{mean} \pm SD$: 7.6 ± 1.7 mJ/cm² and 4.7 ± 0.9 mJ/cm²). In the case of both axial and circumferential specimens, higher energy values were obtained for interface No. 1 (Fig. 6).

4. Discussion

The present study has been conducted to explain delamination of the human thoracic artery with stage II atherosclerotic lesions according to Stary (2000, 2004). The study included a peeling test which was used to determine the force per width, stiffness, and dissection energy of the adventitia-media+intima interface and the adventitia+media-intima interface in the circumferential and axial directions. The obtained results were used to characterise the resistance of the thoracic aortic wall as a three-layer laminate to propagation of delamination. The problem of delamination of the vessel wall is a new issue in the literature and only two papers (Sommer *et al.*, 2008; Tong *et al.*, 2011) attempted to describe the mechanism of this process.

Sommer *et al.* (2008) and Tong *et al.* (2011) determined the force per width and the energy dissipated during the process of delamination of the media of normal vessels: human abdominal artery and human carotid bifurcation. The analysis was conducted in the circumferential and axial directions relative to the long axis of the vessel. The results obtained by Sommer *et al.* (2008) and Tong *et al.* (2011) are higher for axial specimens. In this work, the obtained values of energy and force per width are comparable to the values obtained by Sommer *et al.* (2008) and Tong *et al.* (2011). In each of the analysed cases, the adventitia-media+intima interface is characterised by higher values of the mechanical parameters (Table 3). These differences are statistically significant ($p = 0.05$). None of the previous papers have analysed the values of stiffness of the interfaces between vessel wall layers, which in this paper, as in the case of other parameters, is higher for longitudinal specimens. In each of the analysed directions, statistically significant differences have been found between the stiffness of interface No. 1 and interface No. 2, with the higher values of this parameter obtained in the second case (Table 3).

Table 3. Comparison of the average values of mechanical parameters: energy (W), force per width (F/W), and stiffness (k) obtained by Sommer *et al.* (2008) and Tong *et al.* (2011) and the results of own research in two directions: axial (A) and circumferential (C)

Type of interface	W [mJ/cm ²]		F/W [mN/mm]		k [N/mm]		Source
	A	C	A	C	A	C	
$A-MI$	6.5 ± 2.7	5.0 ± 1.0	29.1 ± 12.2	22.7 ± 4.5	–	–	[25]
	7.6 ± 1.7	5.6 ± 0.9	32.4 ± 6.5	24.5 ± 7.5	0.20 ± 0.08	0.13 ± 0.05	own research
$AM-I$	5.2 ± 3.1	3.6 ± 0.7	23.3 ± 13.8	16.4 ± 3.3	–	–	[25]
	4.7 ± 0.9	4.1 ± 1.0	34.2 ± 3.5	26.5 ± 6.7	0.19 ± 0.07	0.013 ± 0.07	own research
M	7.6 ± 2.7	5.1 ± 0.6	34.8 ± 15.5	22.9 ± 2.9	–	–	[18]

[18] – Sommer *et al.* (2008), [25] – Tong *et al.* (2011)

Studies of the mechanical properties of the interfaces between vessel wall layers, conducted by Sommer *et al.* (2008) and Tong *et al.* (2011), concerned normal vessels, while dissection of the vessel wall is related to the occurrence of lesions, e.g. atherosclerosis. Hypothetically, structural remodelling of the aortic wall, which occurs even in the early stages of the disease, changes the mechanical parameters of vessel wall layers (Holzapfel, 2008; Teng *et al.*, 2009; Weisbecker *et al.*, 2012) and affects the adhesion between them. Consequently, atherosclerosis is believed to increase the risk of dissection. In the present study, mechanical parameters were designated for blood vessels in stage II of the development of atherosclerosis. The obtained results are similar to the distribution characteristics and values of the results obtained for normal vessels (Sommer *et al.*, 2008; Tong *et al.*, 2011).

On this basis, it can be concluded that the early stage of atherosclerosis does not affect the mechanical parameters of the interfaces between the layers of the aortic wall and, consequently, does not affect vessel the wall resistance to delamination. The test results show that the

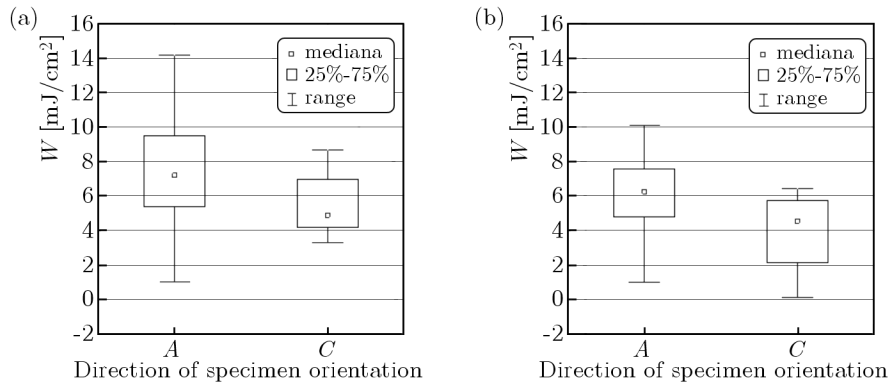


Fig. 6. The energy values obtained during dissection of the human thoracic aortic wall depending on the peeling test direction (*A* – axial direction, *C* – circumferential direction): (a) for interface 1 and (b) for interface 2

mechanical and dissection properties of the interfaces between the layers of the human thoracic aortic wall depend on the specimen orientation. It is worth noting, however, that in contrast to the mechanical properties of the vessel wall, lower values of those parameters were obtained for circumferential specimens. This study demonstrated that lower dissection energy is required in the circumferential peeling test compared with the axial peeling tests, which may be related to the multiphase structure of the vessel wall and alignment of collagen and elastin fibres and smooth muscle cells. Dissection disseminates in the circumferential direction along elastic laminae, while in the axial direction it crosses elastic layers and the external or internal elastic laminae. In addition, circumferential alignment of smooth muscle cells and collagen and elastin fibres in the media of the vessel wall leads to stronger resistance to dissection during the peeling test in the axial direction (Tong *et al.*, 2011). Circumferential specimens are also characterized by a lower stiffness value. Regardless of the analysed direction, lower dissection energy is needed to propagate dissection of the adventitia+media-intima interface. The energy values obtained for the interface between these layers are lower by 38% (axial specimens) and 27% (circumferential specimens) compared with the dissection energy obtained for the adventitia-media+intima interface. This shows that the adventitia+media-intima interface is most prone to delamination. In the case of stiffness, regardless of the analysed direction, both interfaces have the same value of the parameter.

In the experiment conducted in the study, the process of thoracic aortic wall dissection progressed in a controlled manner, while clinical circumstances of the dissection were more diverse. As a result, the obtained values of the mechanical and dissection properties might not be representative for *in vivo* aortic dissection. Despite this, in the opinion of the author, the obtained results of the experiments may be useful for the estimation of the response to the artery dissection and may improve clinical assessment, diagnosis, balloon angioplasty, and cardiovascular medicine.

Acknowledgement

This work has been part of the project "WROVASC – Integrated Cardiovascular Centre", co-financed by the European Regional Development Fund within Innovative Economy Operational Programme 2007-2013.

References

1. BECKER A, EPPLE M., MULLER K.M., SCHMITZ J., 2004, A comparative study of clinically well-characterized human atherosclerotic plaques with histological, chemical and ultrastructural methods, *Journal of Inorganic Biochemistry*, **98**, 12, 2032-2038

2. CARMO M., COLOMBO L., BRUNO A., CORSI F.R., RONCORONI L., CUTTIN M.S., RADICE F., MUSSINI E., SETTEMBRINI P.G., 2002, Alteration of elastin, collagen and their cross-links in abdominal aortic aneurysm, *European Journal of Vascular and Endovascular Surgery*, **23**, 6, 543-549
3. GAŚIOR-GŁOGOWSKA M., KOMOROWSKA M., HANUZA J., PTAK M., KOBIELARZ M., 2011, Structural alteration of collagen fibers-spectroscopic and mechanical studies, *Acta of Bioengineering and Biomechanics*, **12**, 4, 55-62
4. GREGORY D.E., BAE W.C., SAH R.L., MASUDA K., 2012, Annular delamination strength of human lumbar intervertebral disc, *European Spine Journal*, **21**, 1716-1723
5. HOLZAPFEL G.A., 2008a, Arterial Tissue in Health and Disease: Experimental Data, Collagen-Based Modeling and Simulation, Including Aortic Dissection, Lecture Notes, Graz University of Technology, Austria,
6. HOLZAPFEL G.A., 2008b, Chapter no. 11, Collagen in arterial walls: biomechanical aspects, [In:] *Collagen Structure and Mechanics*, Peter Fratzl (Edit.), LLC, 285-324
7. HOLZAPFEL G.A., GASSER TH.C., OGDEN R.W., 2004, Comparison of a multi-layer structural model for arterial walls with a Fung-type model for arterial walls with a Fung-type model and issues of material stability, *Journal of Biomechanical Engineering*, **126**, 2, 264-275
8. HOLZAPFEL G.A., OGDEN R.W., 2003, *Biomechanics of Soft Tissue in Cardiovascular Systems*, Springer Wien New York
9. KARIMI A., NAVIDBAKHS M., SHOJAEI A., FAGHIHI S., 2013, Measurement of the uniaxial mechanical properties of healthy and atherosclerotic human coronary arteries, *Materials Science and Engineering*, **33**, 5, 2550-2554
10. KOBIELARZ M., JANKOWSKI L., 2013, Experimental characterization of the mechanical properties of the abdominal aortic aneurysm wall under uniaxial tension, *Journal of Theoretical and Applied Mechanics*, **51**, 4, 949-958
11. KOT M., KOBIELARZ M., MAKSYMOWICZ K., 2011, Assessment of mechanical properties of arterial calcium deposition, *Transactions of FAMENA*, **35**, 3, 49-56
12. MAKSYMOWICZ K., KOBIELARZ M., CZOŁGAŁA J., 2011, Potential indicators of the degree of abdominal aortic aneurysm development in rupture risk estimation, *Advances in Clinical and Experimental Medicine*, **20**, 2, 221-225
13. NIKODEM A., 2012, Correlations between structural and mechanical properties of human trabecular femur bone, *Acta of Bioengineering and Biomechanics*, **14**, 2, 37-46
14. PEZOWICZ C., 2010, Analysis of selected mechanical properties of intervertebral disc annulus fibrosus in macro and microscopic scale, *Journal of Theoretical and Applied Mechanics*, **48**, 4, 917-932
15. SCHRIEFL A.J., ZEINDLINGER G., PIERCE D.M., 2012, Determination of the layer-specific distributed collagen fibre orientations in human thoracic and abdominal aortas and common iliac arteries, *Journal of the Royal Society Interface*, **9**, 1275-1286
16. SCHULZE-BAUER C., REGITNIG P., HOLZAPFEL G.A., 2001, Mechanics of the human femoral adventitia including high-pressure response, *American Journal of Physiology*, **282**, 6, H2427-2440
17. SHEKHONIN B.V., DOMOGATSKY S.P., MUZYKANTOV V.R., IDELSON G.L., RUKOSUEV V.S., 1985, Distribution of type I, III, IV and V collagen in normal and atherosclerotic human arterial wall: Immunomorphological characteristics, *Coll. Relat. Res.*, **5**, 355-368
18. SOMMER G., GASSER T.C., REGITNIG P., AUER M., HOLZAPFEL G.A., 2008, Dissection properties of the human aortic media: an experimental study, *Journal of Biomechanical Engineering*, **130**, 2, 1-12
19. SOMMER G., REGITNIG P., KLTRINGER L., HOLZAPFEL G.A., 2010, Biaxial mechanical properties of intact and layer-dissected human carotid arteries at physiological and suprphysiological loadings, *Heart and Circulatory Physiology – American Journal of Physiology*, **298**, 3, H898-H912

20. STARY H.C., 2000a, Natural history of calcium deposits in atherosclerosis progression and regression, *Cardiology Journal*, **89**, (Suppl 2): II/28-II/35
21. STARY H.C., 2000b, Natural history and histological classification of atherosclerotic lesions: an update, *Arteriosclerosis, Thrombosis and Vascular Biology*, **20**, 1177-1178
22. STARY H.C., 2004, *Atlas of Atherosclerosis Progression and Regression*, CD-ROM, 2nd Edition
23. SZPAKOWSKI E., KOTLIŃSKI K., JANASZEK-SITKOWSKA H., 2006, Acute aortic dissection type A with concomitant myocardial infarction, *Folia Cardiologica*, **13**, 1, 68-72
24. TENG Z., TANG D., ZHENG J., WOODARD P.K., HOFFMAN A.H., 2009, An experimental study on the ultimate strength of the adventitia and media of human atherosclerotic carotid arteries in circumferential and axial direction, *Journal of Biomechanics*, **42**, 15, 2535-2539
25. TONG J., SOMMER G., REGITNIG P., HOLZAPFEL G.A., 2011, Dissection properties and mechanical strength of tissue components in human carotid bifurcation, *Annals of Biomedical Engineering*, **39**, 6, 1703-1719
26. VORP D.A., RAGHAVAN M.L., MULUK S.C., MAKAROUN M.S., STEED D.L., SHAPIRO R., WEBSTER M.W., 1996, Wall strength and stiffness of aneurysmal and nonaneurysmal aorta, *Annals of the New York Academy of Science*, **18**, 800, 274-276
27. VORP D.A., SCHIRO B.J., EHRLICH M.P., JUVONEN T.S., ERGIN M.A., GRIFFITH B.P., 2003, Effect of aneurysm on the tensile strength and biomechanical behavior of the ascending thoracic aorta, *The Annals of Thoracic Surgery*, **75**, 4, 1210-1214
28. WEISBECKER H., PIERCE D.M., REGITING P., HOLZAPFEL G.A., 2012, Layer – specific damage experiments and modeling of human thoracic and abdominal aortas with non-atherosclerotic intimal thickening, *Journal of the Mechanical Behavior of Biomedical Materials*, **12**, 93-106
29. ŻAK M., 2014, Effect of support on mechanical properties of the intervertebral disc in long-term compression testing, *Journal of Theoretical and Applied Mechanics*, **52**, 3, 677-686
30. ŻAK M., KUROPKA P., KOBIELARZ M., DUDEK A., KALETA-KURATEWICZ K., SZOTEK S., 2011, Determination of the mechanical properties of the skin of pig fetuses with respect to its structure, *Acta of Bioengineering and Biomechanics*, **13**, 2, 37-43

Manuscript received December 23, 2014; accepted for print August 12, 2015

MAGNETO-THERMO-MECHANICAL CREEP BEHAVIOR OF NANO-COMPOSITE ROTATING CYLINDER MADE OF POLYPROPYLENE REINFORCED BY MWCNTS

ABBAS LOGHMAN, HOSSEIN SHAYESTEMOGHADAM

Faculty of Mechanical Engineering, Department of Solid Mechanics, University of Kashan, Kashan, Iran

e-mail: aloghman@kashanu.ac.ir; h.shayestemoghadam@gmail.com

History of strains, stresses and displacements of a rotating cylinder made of polypropylene reinforced by multi-walled carbon nanotubes (MWCNTs) subjected to magneto-thermo-mechanical loading is investigated using Burgers viscoelastic creep model. By making use of equations of equilibrium, stress-strain and strain-displacement, a constitutive differential equation containing creep strains is obtained which is solved semi analytically. It has been found that radial displacement, tangential strain and absolute values of radial strain are increasing with time at a decreasing rate so that they finally approach the steady state condition. Effective stresses are decreasing at the inner and increasing at the outer surface of the cylinder.

Keywords: nano-composite cylinder, creep analysis, MWCNTs, polypropylene, Burgers model

1. Introduction

Composite cylinders subjected to thermo-mechanical load are extensively used in aerospace, pressure vessels and petrochemical industries. Carbon nanotubes reinforced polymer matrix composites have shown high strength properties and are widely used in manufacturing of components exposed to high pressure environment. Even at room temperature, significant creep deformation is observed for polypropylene tubes. Therefore, creep analysis and creep life assessment of such components are very important. When such vessels are loaded, thermo-elastic stresses will be developed in the cylinder at zero time. However, because of creep evolution, stress redistribution occur during life of the component, which can affect its long-time performance.

The analysis of an internally pressurized, homogeneous, orthotropic rotating cylinder subjected to a steady state creep condition was investigated by Bhatnagar *et al.* (1984). In another work, they considered an orthotropic thick-walled cylinder under primary creep conditions (Bhatnagar *et al.*, 1986). In their second work, the authors presented the analysis of an orthotropic, thick-walled cylinder undergoing creep due to combined action of internal and external pressures and rotary inertia. As a result, they found that the material which is strong in the radial direction may be beneficial for design of the cylinder as it gives lower values of the effective stress. Evaluation of creep compliances of unidirectional fiber-reinforced composites was done by Moal and Perreux (1994). In that paper, a method based on the model of Laws and McLaughlin was proposed for the determination of viscoelastic behavior of unidirectional fiber-reinforced composites. Moreover, the interface problem was taken into account by using anisotropic elastic coefficients for the reinforcement fiber. The suggested procedure allowed the viscoelasticity of the resin to be characterized. A variational method was developed by Ohno *et al.* (2002) for analyzing the matrix creep induced time-dependent change in fiber stress profiles in unidirectional composites. They verified the solutions on the basis of an energy balance equation and a finite

difference computation. They also showed that the solution for the fiber pull-out model agreed well with an experiment on a single carbon fiber/acrylic model composite if the initial slip at fiber/matrix interface was taken into account. Singh and Ray (2002) modeled anisotropy and creep in an orthotropic aluminum-silicon carbide composite rotating disc. They observed that the anisotropy helped reduction of the tangential strain rate significantly, more near the inner radius. It was also found the strain rate distribution in the orthotropic disc was lower than that of isotropic disc following von Misses criterion. Creep deformations and stresses in thick-walled cylindrical vessels of functionally graded materials subjected to internal pressure were investigated by You *et al.* (2007). They examined how variations of material parameters along the radial direction affect the stresses in the vessels. Yang *et al.* (2006) carried out characterization of tensile creep resistance of polyamide 66 nano-composites. To develop their works, they presented both a viscoelastic creep model named Burgers model and an empirical method called Findley power law. They revealed that the simulation results from both models agreed quite well with the experimental data. Jia *et al.* (2011) studied the creep and recovery of polypropylene/multi-walled carbon nanotube composites. They showed that the creep strain reduces with a decrease in temperature and an increase in the content of carbon nanotubes. Magneto-thermo-elastic creep analysis of functionally graded cylinders was presented by Loghman *et al.* (2010). The paper describes time-dependent creep stress redistribution analysis of a thick-walled FGM cylinder subjected to a uniform magnetic field, temperature field and internal pressure. They calculated stress redistributions iteratively using magneto-thermo-elastic stresses as initial values for stress redistributions. The result indicated that the radial stress redistributions were not significant for different material properties, while major redistributions occurred for circumferential and effective stresses. A semi analytical solution of magneto-thermo-elastic stresses was suggested for functionally graded variable thickness rotating disks by Ghorbanpour Arani *et al.* (2010). In the paper, stresses and perturbation of magnetic field vector in FG rotating disks were determined using infinitesimal theory of magneto-thermo elasticity under plane stress conditions. It was found that imposing a magnetic field significantly decreases tensile circumferential stresses. Thus, the fatigue life of the disk would be significantly improved by applying the magnetic field. They suggested that the results of that investigation could be applied for optimum design of FG hollow rotating disks with variable thickness. Theory of plasticity for carbon nanotube reinforced composites was mentioned by Barai and Weng (2011). It was found that, with perfect interface contact, the decreasing of the CNT radius would improve the overall stiffness and plastic strength, but with an imperfect interface the size effect was reversed. Time-dependent thermo-elastic creep analysis of a rotating disk made of Al-SiC composite using Mendelson's method of successive elastic solution was presented by Loghman *et al.* (2011). They found that the stresses, displacement, and creep strains were changing with time at a decreasing rate so that after almost 50 years the solution approached the steady-state condition.

The main objective of this paper is to obtain history of creep stresses and deformations of a nano-composite rotating cylinder made of polypropylene reinforced by MWCNTs using Burgers viscoelastic creep model under magneto-thermo-mechanical loadings.

2. Geometry, loading condition and material properties

2.1. Geometry and loading condition

A long rotating thick-walled nano-composite cylinder made of polypropylene reinforced by MWCNTs with inner radius r_i and outer radius r_o is considered (Fig. 1). The cylinder is subjected to a uniform magnetic field in the axial direction and a uniform temperature field. The following data for geometry and loading conditions are used in this paper: $r_o/r_i = 2$,

MWCNTs content = 4.5%, $\nu = 0.45$, $T = 80^\circ\text{C}$, $\omega = 52.35 \text{ rad/s}$, $\mu_0 = 4\pi \cdot 10^{-7} \text{ H/m}$, $H_Z = 1 \cdot 10^8 \text{ A/m}$.

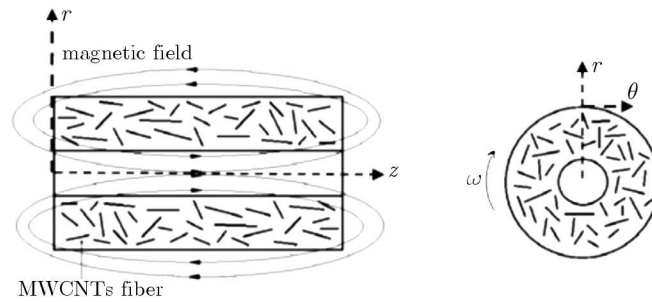


Fig. 1. Schematic of the rotating thick-walled composite cylinder subjected to uniform magnetic and thermal fields

2.2. Material properties

Young's modulus of the polymeric composite cylinder reinforced with different MWCNT contents is given in Table 1 based on experimental results reported by Jia *et al.* (2011).

Table 1. Young's modulus of propylene nano-composite with different MWCNT contents (Jia *et al.*, 2011)

MWCNTs content [vol.%]	Young's modulus [GPa]
0	1.83 ± 0.11
0.3	2.10 ± 0.11
0.6	2.12 ± 0.03
2.8	2.33 ± 0.14
4.5	2.42 ± 0.13

3. Burgers viscoelastic creep model

Burgers four-element model can be used to predict the viscoelastic creep behavior of polymer based nano-composites. This model is shown in Fig. 2 with Maxwell and Kelvin rheological elements connected in series.

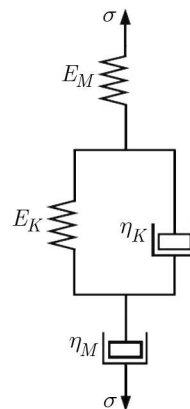


Fig. 2. Schematic diagram of Burgers four-element model (Yang *et al.*, 2006)

The creep constitutive model based on the Burgers law is written as follows (Yang *et al.*, 2006)

$$\varepsilon = \frac{\sigma_0}{E_M} + \frac{\sigma_0}{E_K} \left(1 - e^{-\frac{t}{\tau}}\right) + \frac{\sigma_0}{\eta_M} t \quad \tau = \frac{\eta_K}{E_K} \quad (3.1)$$

in which σ_0 is the initially applied stress, τ is the retardation time taken to produce 63.2% or $(1 - e^{-1})$ of the total deformation in the Kelvin element, E_M and η_M are the elastic modulus and viscosity of the Maxwell spring and dashpot model, E_k and η_k are the elastic modulus and the viscosity of the Kelvin spring and dashpot model. The Burgers model which includes the essential elements can be satisfactorily applied to describe behavior of viscoelastic materials practically. Differentiating Eq. (3.1) with respect to time gives the strain rate constitutive equation of the Burgers model as

$$\dot{\varepsilon} = \frac{\sigma_0}{\eta_M} + \frac{\sigma_0}{\eta_K} e^{-\frac{t}{\tau}} \quad (3.2)$$

The material parameters, η_m , E_K and η_k are simulated from the experimental data (Jia *et al.*, 2011).

Table 2. The simulated parameters of the Burger model with different MWCNT contents for long term prediction (Jia *et al.*, 2011)

MWCNTs [vol.%]	E_k [MPa]	η_k [MPa s]	η_m [s]	τ [s]
0	5.7	9.00E+07	1.50E+10	1.49E+07
0.3	8.5	1.00E+08	2.10E+10	1.53E+07
0.6	9.2	1.50E+08	2.60E+10	1.63E+07
2.8	9.6	1.70E+08	2.70E+10	1.77E+07
4.5	10.4	2.00E+08	2.80E+10	1.92E+07

4. Theoretical analysis

The strain-displacement relationship for a long cylinder under an axisymmetric loading condition is written as

$$\varepsilon_r = \frac{\partial u_r}{\partial r} \quad \varepsilon_\theta = \frac{u_r}{r} \quad (4.1)$$

where ε_r and ε_θ are the radial and circumferential total strains, and u_r is the radial displacement.

Considering the total strains to be the sum of elastic, thermal and creep strains, the stress-strain relations may be written as follows

$$\begin{aligned} \sigma_r &= C_{11}\varepsilon_r + C_{12}\varepsilon_\theta - \lambda_r T_r - (C_{11}\varepsilon_r^c + C_{12}\varepsilon_\theta^c) \\ \sigma_\theta &= C_{21}\varepsilon_r + C_{22}\varepsilon_\theta - \lambda_\theta T_r - (C_{21}\varepsilon_r^c + C_{22}\varepsilon_\theta^c) \end{aligned} \quad (4.2)$$

where σ_r and σ_θ are the radial and circumferential stresses, ε_r^c and ε_θ^c are the radial and circumferential creep strains, T_r is the temperature field. and the other coefficients are defined as

$$\begin{aligned} C_{11} &= \frac{E(1-\nu)}{(1+\nu)(1-2\nu)} & C_{12} &= \frac{E\nu}{(1+\nu)(1-2\nu)} & C_{21} &= C_{12} \\ C_{22} &= C_{11} & \lambda_r &= \frac{E\alpha}{1-2\nu} & \lambda_\theta &= \frac{E}{1+\nu} \end{aligned} \quad (4.3)$$

in which E , ν and α are Young's modulus, Poisson's ratio and the coefficient of thermal expansion of nano-composite, respectively.

The equilibrium equation of a thick-walled composite hollow cylinder subjected to a uniform magnetic field is written as (Loghman *et al.*, 2010)

$$\frac{\partial \sigma_r}{\partial r} + \frac{\sigma_r - \sigma_\theta}{r} + f_r + \rho r \omega^2 = 0 \quad (4.4)$$

in which $\rho r \omega^2$ is the centrifugal body force per unit volume, and f_r is the Lorentz force written as

$$f_r = \mu_{(r)} H_z^2 \frac{\partial}{\partial r} \left(\frac{\partial u_r}{\partial r} + \frac{u_r}{r} \right) \quad (4.5)$$

where $\mu_{(r)}$ is the magnetic permeability and H_z is the magnetic field intensity in the axial direction. Substituting the strains from Eqs. (4.1) into Eqs. (4.2), and then substituting the radial and circumferential stresses into equilibrium Eq. (4.4) and substituting f_r from Eq. (4.5), the following constitutive differential equation for displacement is obtained

$$\begin{aligned} & (C_{11} + \mu_{(r)} H_z^2) \frac{\partial^2 u_r}{\partial r^2} + \left(\frac{C_{11}}{r} + \frac{\mu_{(r)} H_z^2}{r} \right) \frac{\partial u_r}{\partial r} + \left(\frac{C_{22}}{r^2} - \frac{H_z^2}{r^2} \mu_{(r)} \right) u_r \\ & = \frac{\lambda_r - \lambda_\theta}{r} T_r + \lambda_r \frac{\partial T_r}{\partial r} + \frac{\varepsilon_r^c (C_{11} - C_{21})}{r} + \frac{\varepsilon_\theta^c (C_{12} - C_{22})}{r} + \frac{\partial}{\partial r} (C_{11} \varepsilon_r^c + C_{22} \varepsilon_\theta^c) - \rho r \omega^2 \end{aligned} \quad (4.6)$$

The above differential equation is summarized as

$$D_{11} \frac{\partial^2 u_r}{\partial r^2} + D_{12} \frac{\partial u_r}{\partial r} + D_{13} u_r + D_{14} = 0 \quad (4.7)$$

in which

$$\begin{aligned} D_{11} &= C_{11} + \mu_{(r)} H_z^2 & D_{12} &= \frac{C_{11}}{r} + \frac{\mu_{(r)} H_z^2}{r} & D_{13} &= \frac{C_{22}}{r^2} - \frac{H_z^2}{r^2} \mu_{(r)} \\ D_{14} &= \frac{\lambda_r - \lambda_\theta}{r} T_r + \lambda_r \frac{\partial T_r}{\partial r} + \frac{\varepsilon_r^c (C_{11} - C_{21})}{r} + \frac{\varepsilon_\theta^c (C_{12} - C_{22})}{r} + \frac{\partial}{\partial r} (C_{11} \varepsilon_r^c + C_{22} \varepsilon_\theta^c) - \rho r \omega^2 \end{aligned} \quad (4.8)$$

D_{14} contains creep strains which are time, temperature and stress dependent.

If we ignore the time-dependent creep strains in the coefficient D_{14} , then differential Eq. (4.7) becomes Navier's equation, a non-homogenous second-order ordinary differential equation with variable coefficients the solution to which can be found from magneto-thermo-elastic analysis. This analysis is done by making use of the division method (Hosseini Kordkheili and Naghdabai, 2007). In this method, the cylinder thickness is divided into a finite number of divisions. Then Navier's equation for k -th division yields the following differential equation with constant coefficients

$$\left(D_{11}^{(k)} \frac{\partial^2}{\partial r^2} + D_{12}^{(k)} \frac{\partial}{\partial r} + D_{13}^{(k)} \right) u_r^k + D_{14}^k = 0 \quad (4.9)$$

The coefficients of Eq. (4.9) are evaluated in each division in terms of constants and the radius of k th division. The exact solution to Eq. (4.9) can be written in the form of

$$u_r^{(k)} = X_1^{(k)} \exp(\eta_1^{(k)} r^{(k)}) + X_2^{(k)} \exp(\eta_2^{(k)} r^{(k)}) - \frac{D_{14}^{(k)}}{D_{13}^{(k)}} \quad (4.10)$$

where

$$\eta_1^{(k)}, \eta_2^{(k)} = \frac{D_{12}^{(k)} \pm \sqrt{(D_{12}^{(k)})^2 - 4D_{13}^{(k)} D_{11}^{(k)}}}{2D_{11}^{(k)}} \quad (4.11)$$

It is noted that this solution to Eq. (4.9) is valid in the following sub-domain

$$r^{(k)} - \frac{t^{(k)}}{2} \leq r \leq r^{(k)} + \frac{t^{(k)}}{2} \quad (4.12)$$

where $t^{(k)}$ is the thickness of k th division and $X_1^{(k)}$, $X_2^{(k)}$ are unknown constants for k -th division. The unknowns $X_1^{(k)}$ and $X_2^{(k)}$ are determined by applying the necessary boundary conditions between two adjacent sub-domains. For this purpose, the continuity of the radial displacement u as well as the radial stress σ_r is imposed at the interfaces of the adjacent sub-domains. These continuity conditions at the interfaces are written as

$$\begin{aligned} u_r^{(k)} \Big|_{r=r^{(k)}} + \frac{t^{(k)}}{2} &= u_r^{(k+1)} \Big|_{r=r^{(k+1)}} - \frac{t^{(k+1)}}{2} \\ \sigma_r^{(k)} \Big|_{r=r^{(k)}} + \frac{t^{(k)}}{2} &= \sigma_r^{(k+1)} \Big|_{r=r^{(k+1)}} - \frac{t^{(k+1)}}{2} \end{aligned} \quad (4.13)$$

and the global boundary conditions are

$$\sigma_r = 0 \quad \text{at} \quad r = r_i \quad \sigma_r = 0 \quad \text{at} \quad r = r_o \quad (4.14)$$

Continuity conditions Eqs. (4.13) together with global boundary conditions Eqs. (4.14) yield a set of linear algebraic equations in terms of $X_1^{(k)}$ and $X_2^{(k)}$. Solving the resultant linear algebraic equations for $X_1^{(k)}$ and $X_2^{(k)}$, the unknown coefficients of Eq. (4.10) are calculated. Then, the displacement component u_r and the stresses are determined in each radial sub-domain. Accuracy of the results will be improved by increasing number of divisions.

5. Time-dependent creep analysis

For time-dependent creep analysis, the creep strains in the coefficient D_{14} must be considered. The creep strains are time, temperature, and stress dependent. Creep strain increments are related to the current stresses and the material uni-axial creep behavior by Prandtl-Reuss relations. For problems of a rotating thick-walled composite cylinder with axial symmetry, these relations (Loghman *et al.*, 2010) are written as follows

$$\begin{aligned} \dot{\epsilon}_r^c &= \frac{\dot{\epsilon}_c}{2\sigma_e} [2\sigma_r - (\sigma_\theta + \sigma_z)] & \dot{\epsilon}_\theta^c &= \frac{\dot{\epsilon}_c}{2\sigma_e} [2\sigma_\theta - (\sigma_r + \sigma_z)] \\ \dot{\epsilon}_z^c &= \frac{\dot{\epsilon}_c}{2\sigma_e} [2\sigma_z - (\sigma_r + \sigma_\theta)] \end{aligned} \quad (5.1)$$

where $\dot{\epsilon}_r^c$, $\dot{\epsilon}_\theta^c$ and $\dot{\epsilon}_z^c$ are the radial, circumferential, and axial creep strain rates, $\dot{\epsilon}_c$ and σ_e are the equivalent creep strain rate and equivalent stress, respectively. These equivalent or effective variables are defined as follows

$$\begin{aligned} \dot{\epsilon}_c &= \frac{2}{\sqrt{3}} \sqrt{(\dot{\epsilon}_r^c)^2 + (\dot{\epsilon}_\theta^c)^2 + (\dot{\epsilon}_z^c)^2} & \sigma_e &= \sqrt{\frac{1}{2} [(\sigma_r - \sigma_\theta)^2 + (\sigma_r - \sigma_z)^2 + (\sigma_\theta - \sigma_z)^2]} \\ \dot{\epsilon}_z^c &= 0 \rightarrow \sigma_z = \frac{1}{2}(\sigma_r + \sigma_\theta) \end{aligned} \quad (5.2)$$

The material creep constitutive model can be rewritten in terms of the equivalent creep strain rate and equivalent stress as

$$\dot{\epsilon}_c = \frac{\sigma_0}{\eta_M} + \frac{\sigma_0}{\eta_K} e^{-\frac{t}{\tau}} \quad (5.3)$$

Equations (5.1), (5.2), and (5.3) together with differential Eq. (4.9) are used in a numerical procedure based on Mendelson's method of successive elastic solution (Mendelson, 1968) to obtain history of stresses and deformations during creep process. The numerical procedure is explained by Loghman *et al.* (2011).

6. Numerical results and discussion

The results presented in this study are based on the data presented in Section 2 for geometry, material properties and loading conditions. The elastic properties are dependent on the volume percent of MWCNTs content and are given in Table 1. In this research, a 4.5% volume content of MWCNTs is considered.

The history of radial displacement, radial and circumferential stresses, effective stress, radial and circumferential strains, radial and circumferential creep strains are plotted with and without the effect of magnetic field in Figs. 3 to 10.

Figures 3a and 3b show the radial displacement histories. Generally, the radial displacements are increasing with time at a decreasing rate during life of the cylinder so that finally approach the steady state condition. However, in the presence of a magnetic field, the radial displacements are lower in magnitude.

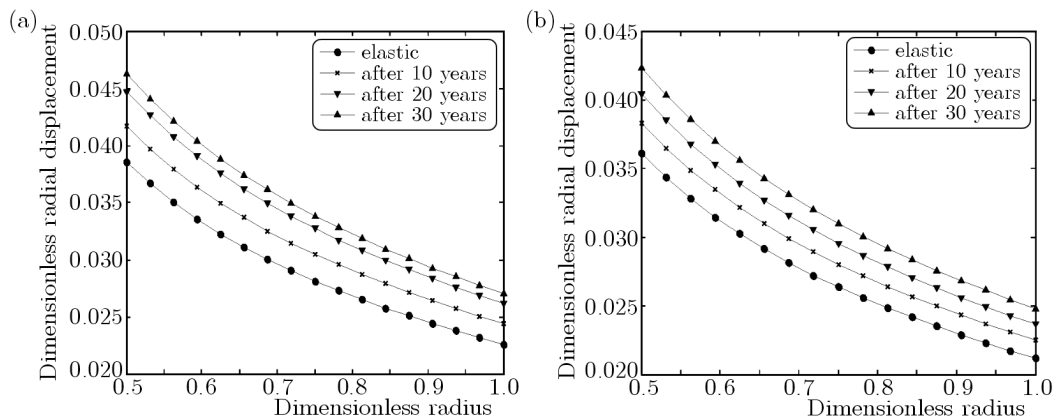


Fig. 3. Radial displacement of the nano-composite cylinder (a) without and (b) with the effect of magnetic field ($H = 1E + 8$)

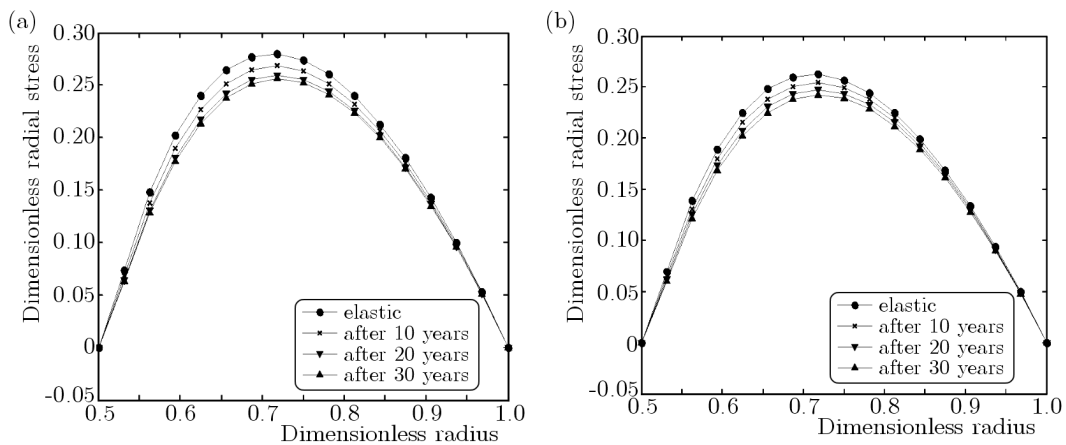


Fig. 4. Radial stress of the nano-composite cylinder (a) without and (b) with the effect of magnetic field ($H = 1E + 8$)

Histories of the radial stress are illustrated in Figs. 4a and 4b in which the boundary conditions at the inner and outer surfaces of the cylinder are satisfied. The radial stresses are decreasing with time during life of the cylinder. The radial stresses with the effect of magnetic field are of lower magnitudes.

Histories of the circumferential stress are illustrated in Figs. 5a and 5b. The circumferential stresses are decreasing at the inner surface of the cylinder and are increasing at the outer surface so that the reference point can be identified where the circumferential stress is not changing with time.

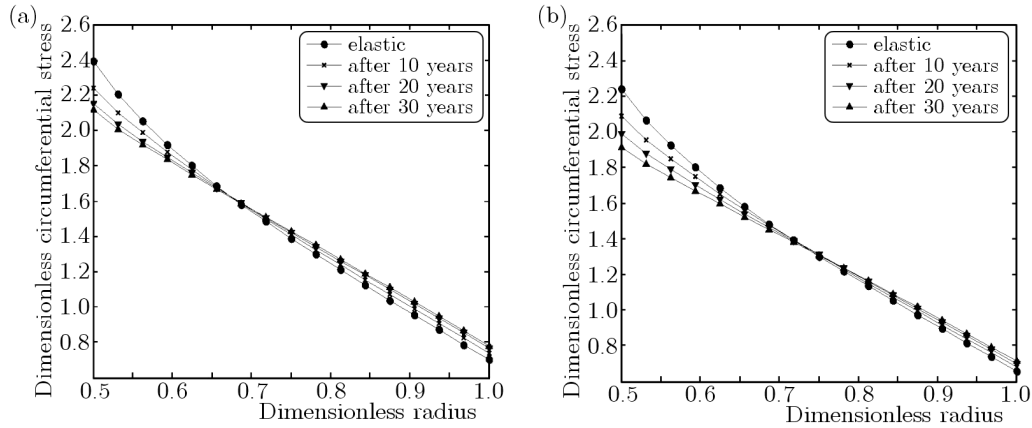


Fig. 5. Circumferential stress of the nano-composite cylinder (a) without and (b) with the effect of magnetic field ($H = 1E + 8$)

Histories of the effective stress are demonstrated in Figs. 6a and 6b. The effective stresses are very similar to circumferential stresses. This is because the circumferential stresses are almost ten times greater than the radial stresses and therefore are dominant.

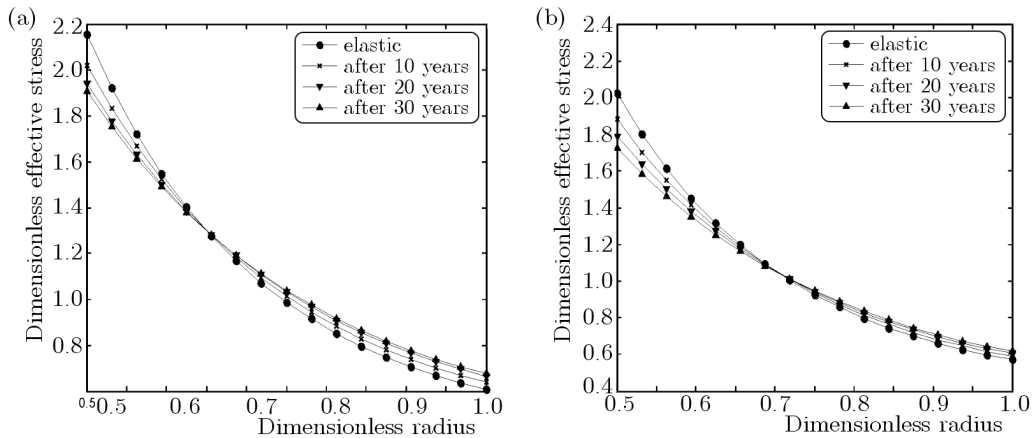


Fig. 6. Effective stress of the nano-composite cylinder (a) without and (b) with the effect of magnetic field ($H = 1E + 8$)

Histories of the radial strain are shown in Figs. 7a and 7b. The radial strains are compressive because of highly tensile circumferential stresses.

Histories of the circumferential strain are shown in Figs. 8a and 8b. The circumferential strains are positive due to highly tensile circumferential stresses.

Histories of the radial creep strain are shown in Figs. 9a and 9b. It is clear that the radial creep strains at zero time are zero, however, their absolute values are increasing with time due to creep. The creep strains are negative because of highly tensile circumferential stresses.

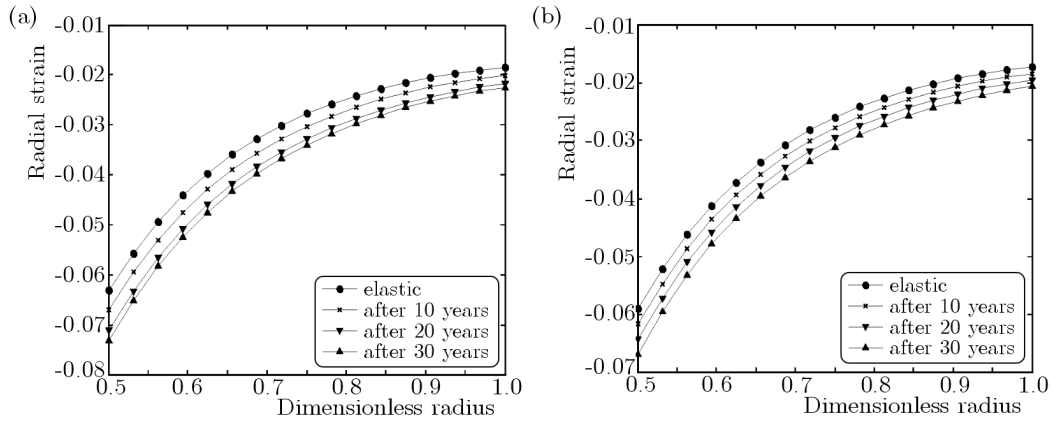


Fig. 7. Radial strain of the nano-composite cylinder (a) without and (b) with the effect of magnetic field ($H = 1E + 8$)

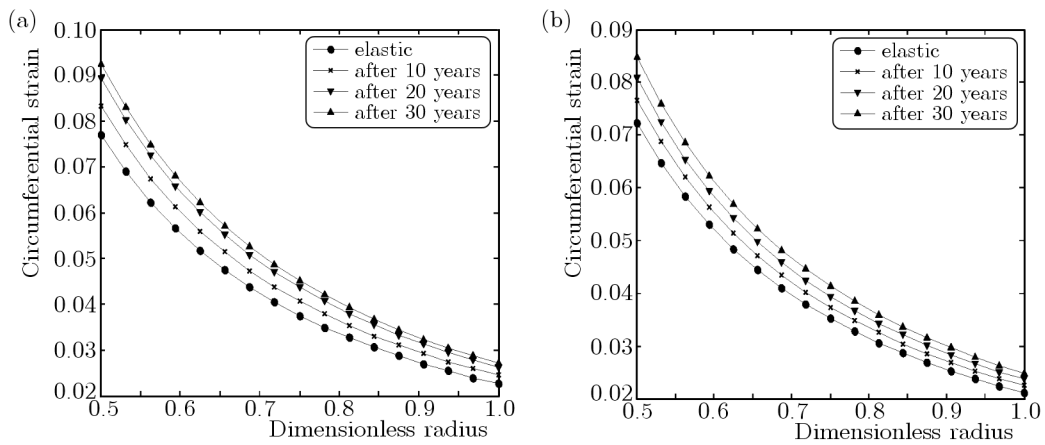


Fig. 8. Circumferential strain of the nano-composite cylinder (a) without and (b) with the effect of magnetic field ($H = 1E + 8$)

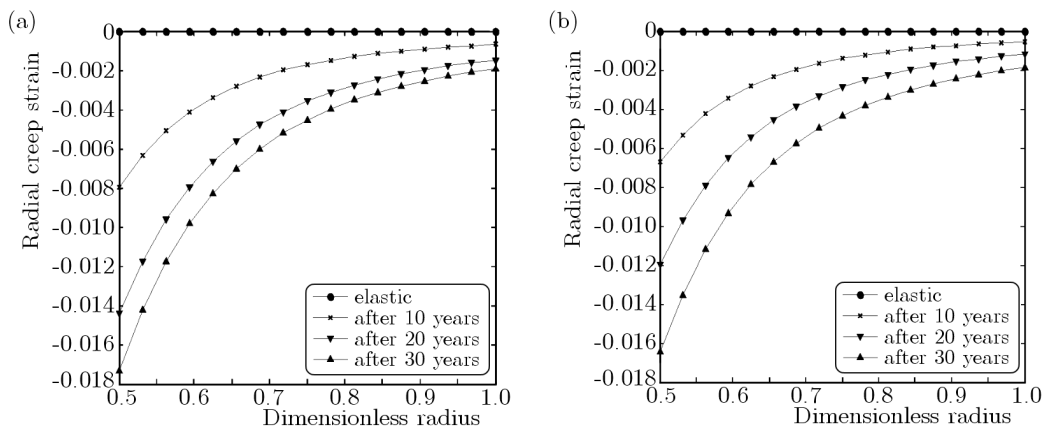


Fig. 9. Radial creep strain of the nano-composite cylinder (a) without and (b) with the effect of magnetic field ($H = 1E + 8$)

Histories of the circumferential creep strain are shown in Figs. 10a and 10b. Due to the incompressibility condition of the material, the circumferential strains are positive. They are also increasing with time due to creep deformation.

Generally, the stresses, strains and displacements are changing with time at a decreasing rate during life of the cylinder so that they finally approach the steady state condition. However, in the presence of a magnetic field they are all lower in magnitude.

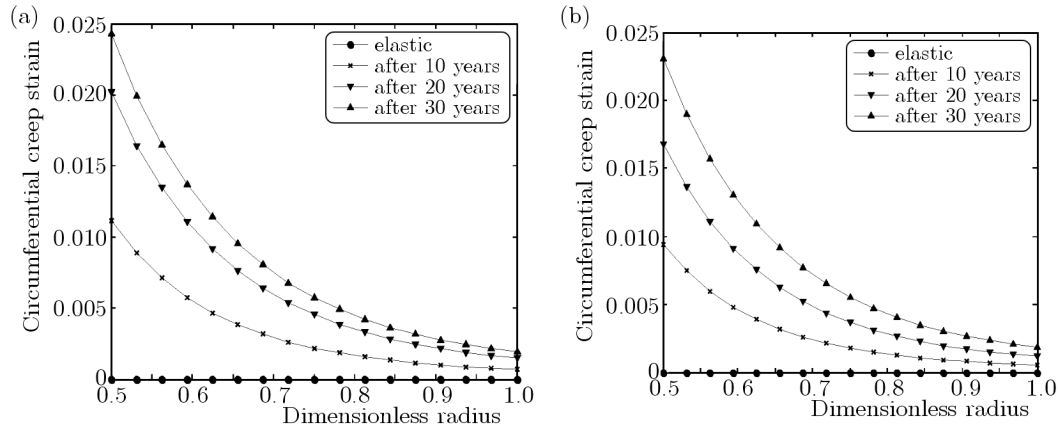


Fig. 10. Circumferential creep strain of the nano-composite cylinder (a) without and (b) with the effect of magnetic field ($H = 1E + 8$)

7. Conclusion

Time-dependent creep stress, strain and displacement analysis of a rotating thick-walled nano-composite cylinder made of polypropylene reinforced by multi-walled carbon nanotubes (MWCNTs) subjected to magnetic, thermal and mechanical load is investigated using Burgers viscoelastic creep model. The results are presented with and without the effect of magnetic field. It has been found that the radial displacement, tangential strain and absolute values of the radial strain are increasing with time at a decreasing rate so that they finally approach the steady state condition. The effective stresses are decreasing at the inner surface and increasing at the outer surface of the cylinder and approach their steady state condition after 30 years. In the presence of magnetic field stresses, the strains and radial displacement are lower in magnitude.

Acknowledgement

The authors are grateful to University of Kashan for supporting this work by giving research grant.

References

1. BARAI P., WENG G.J., 2011, A theory of plasticity for carbon nanotube reinforced composites, *International Journal of Plasticity*, **27**, 539-559
2. BHATNAGAR N.S., KULKARNI P.S., ARYA V.K., 1984, Creep analysis of an internally pressurized orthotropic rotating cylinder, *Nuclear Engineering and Design*, **83**, 379-388
3. BHATNAGAR N.S., KULKARNI P.S., ARYA V.K., 1986, Analysis of an orthotropic thick-walled cylinder under primary creep conditions, *International Journal of Pressure Vessels and Piping*, **23**, 165-185
4. GHORBANPOUR ARANI A., LOGHMAN A., SHAJARI A.R., AMIR S., 2010, Semi-analytical solution of magneto-thermo-elastic stresses for functionally graded variable thickness rotating disks, *Journal of Mechanical Science and Technology*, **24**, 2107-2117
5. HOSSEINI KORDKHEILI S.A., NAGHDABADI R., 2007, Thermo-elastic analysis of a functionally graded rotating disk, *Composite Structures*, **79**, 508-516
6. JIA Y., PENG K., GONG X.L., ZHANG Z., 2011, Creep and recovery of polypropylene/carbon nanotube composites, *International Journal of Plasticity*, **27**, 1239-1251
7. LOGHMAN A., GHORBANPOUR ARANI A., AMIR S., VAJEDI A., 2010, Magneto-thermo-elastic creep analysis of functionally graded cylinders, *International Journal of Pressure Vessels and Piping*, **87**, 389-395

8. LOGHMAN A., GHORBANPOUR ARANI A., SHAJARI A.R., AND AMIR S., 2011, Time-dependent thermo-elastic creep analysis of rotating disk made of Al-SiC composite, *Archive of Applied Mechanics*, **81**, 1853-1864
9. MENDELSON A., 1968, *Plasticity Theory and Applications*, The Macmillan Company, New York
10. MOAL P.L., PERREUX D., 1994, Evaluation of creep compliances of unidirectional fiber-reinforced composites, *Composites Science and Technology*, **51**, 469-477
11. OHNO N., ANDO T., MIYAKE T., BIWA S., 2002, A variational method for unidirectional fiber-reinforced composites with matrix creep, *International Journal of Solid and Structures*, **39**, 159-174
12. SINGH S.B., RAY S., 2002, Modeling the anisotropy and creep in orthotropic aluminum-silicon carbide composite rotating disc, *Mechanics of Materials*, **34**, 363-372
13. YANG J.L., ZHANG Z., SCHLARB A.K., FRIEDRICH K., 2006, On the characterization of tensile creep resistance of polyamide 66, *Polymer*, **47**, 6745-6758
14. YOU L.H., OU Z.Y., ZHENG H., 2007, Creep deformations and stresses in thick-walled cylindrical vessels, *Composite Structures*, **78**, 285-291

Manuscript received November 17, 2014; accepted for print August 13, 2015

STRENGTH CALCULATIONS OF AN ELEMENT COMPENSATING CIRCUMFERENTIAL BACKLASH IN THE EXTERNAL GEAR PUMP

PIOTR OSIŃSKI, GRZEGORZ CHRUSCIELSKI

Wroclaw University of Technology, Faculty of Mechanical Engineering, Wroclaw, Poland

e-mail: piotr.osinski@pwr.edu.pl; grzegorz.chruscielski@pwr.edu.pl

The aim of the article is to discuss the issue of strength of the circumferential backlash compensating beam in a high-efficiency gear pump. Three geometric versions of the compensating beam structure differing in the wrapping angle are analyzed. The mechanical model is solved assuming the curved beam model supported at the contact points between the beam and the gear teeth. The assumed mechanical structure is statically indeterminate. In order to determine the reactions in the supports and in the beam fixing, the Menabrei and Castigliano theorems are used. Based on analytical calculation results, the cause of compensation structure damage during experimental tests of prototype units is identified and the most favorable variant of beam structure, from the mechanical strength point of view, is determined.

Keywords: external gear pump, strength calculation, circumferential backlash compensation

1. Introduction

The efficiency of a gear pump is to a large extent determined by clearances between the gears and the elements limiting the displacement chamber volume of the pump (Chrobot *et al.*, 1997; Judin, 1958; Kollek, 1996, 2004; Osiński *et al.*, 2013; Osiński and Kollek, 2007; Rangunathan and Manoharan, 2012; Vacca and Guidetti, 2011; Wang *et al.*, 2011). Two types of clearance, i.e. radial clearance and frontal clearance, are distinguished. The former is also referred to as circumferential clearance (backlash). The circumferential gap is formed by the surface of casing concavities and that of the cylinder with the radius of the addendum circle of toothed displacement elements. The gap is not constant along the whole circumference the gears often move within the bearing slackness limits towards the suction space. In conventional pumps without radial backlash compensation, the circumferential gap assumes the shape of a crescent widening towards the delivery side. In such a pump design, the gap ranges from 0.01 to 0.3 mm. The circumferential clearance is a gap with one fixed wall and one movable wall moving in the direction opposite to that of the pressure drop. This is an advantageous configuration as a result of the rotational motion of the gear the liquid is lifted from the suction space to the delivery space, thereby reducing the leakages due to the pressure difference between the gap ends (Singal *et al.*, 2009; Stryczek, 1995).

Frontal clearances have the shape of a ring limited by the diameter of the dedendum circle and that of the gear shaft. Most of the leakages are used to cool and lubricate the bearings. After they pass through the bearings, the leakages are directed via special grooves to the suction chamber, but some of the volume losses pass directly through the gap into the suction space. The frontal clearance values are by one order of magnitude lower than the radial clearance values. In typical pumps, frontal clearances are in a range of 0.01-0.05 mm. The recommended clearance also depends on the pump size. Lower values are recommended for units with a lower specific output.

Nowadays backlash compensation is used to improve the efficiency of gear pumps (Kollek and Radziwanowska, 2015). In addition, this treatment contributes to better running in of the interacting parts and maintenance of a constant gap despite the wear of the parts. In the currently produced pumps, mainly the axial backlash compensation is carried out. However, if higher efficiency is required, it is necessary to compensate also the circumferential gap. The latter can be compensated in two ways. One way consists in compensating backlash locally along a short distance. It is further referred to as *radial backlash compensation* (Fig. 1a). Another method, developed by the authors, consists in ensuring a constant gap along the whole circumference (Osiński, 2012a,b; Wiczowski, 2012). The method is called circumferential backlash compensation (Fig. 1c).

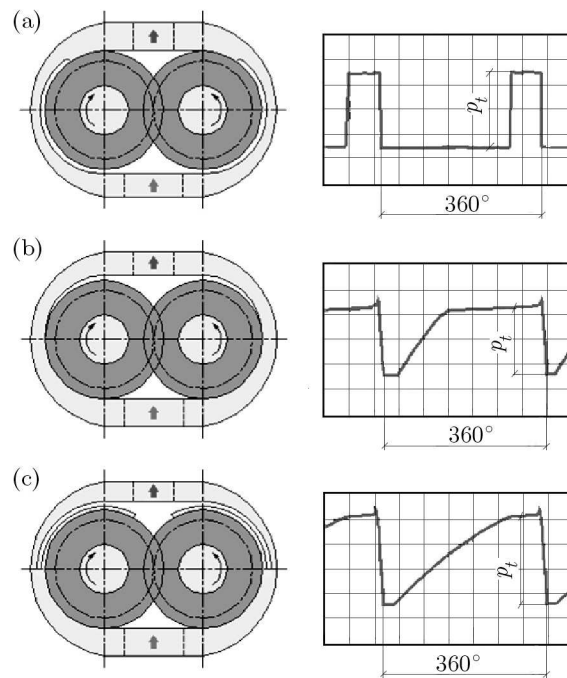


Fig. 1. Schematic showing the way of sealing gears along circumference plus graph of circumferential pressure measured in the gear root: (a) pump with radial backlash compensation, (b) pump with axial backlash compensation, (c) pump with circumferential backlash compensation (Osiński *et al.*, 2012a)

The influence of the applied compensation on the overall efficiency of the pump is shown in Fig. 2. The comparative diagram is based on specifications found in the manufacturer catalogues of Bosch, Casappa, Marzocchi, Hamworthy, Hidroirma, Orsta, Parker, PZL-Hydral, Rexroth, WPH, VPS and on the authors' own studies of prototype pumps with circumferential backlash compensation (Osiński, 2013).

It appears from the diagram that the application of different methods of backlash compensation considerably increases the efficiency and working pressure of gear pumps. The currently produced pumps reach working pressures as high as 32 MPa. The innovative circumferential backlash compensation method enables one to increase the pressures by nearly 20%, i.e. to the level of 40 MPa. The increasing of the internal tightness also makes it possible to increase the total efficiency by about 5% on average.

2. Circumferential compensation structure

There are three versions of the displacement pump structure with a compensating pressure chamber (Osiński, 2013; Osiński *et al.*, 2012), differing in the design of the compensating chamber

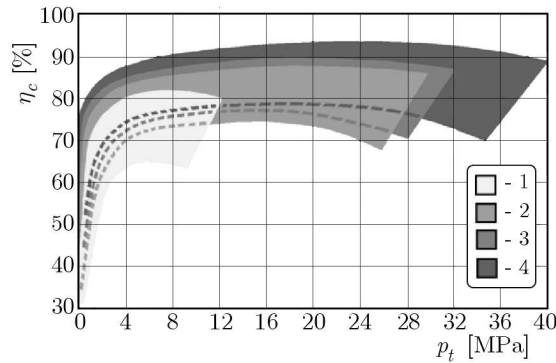


Fig. 2. Comparison of total efficiency η_c of gear pumps with regard to forcing pressure p_t and backlash compensation (based on catalogues of major manufacturers + own research): 1 – without compensation, 2 – with axial compensation, 3 – with axial and radial compensation, 4 – with axial and circumferential compensation

(Fig. 3). In this pump, two interacting gears perform rotations in the directions marked in Fig. 3, forcing the working liquid (oil) from the suction chamber on the left side of the pump (Fig. 3) through the inter tooth spaces into the delivery chamber on the right side of the pump.

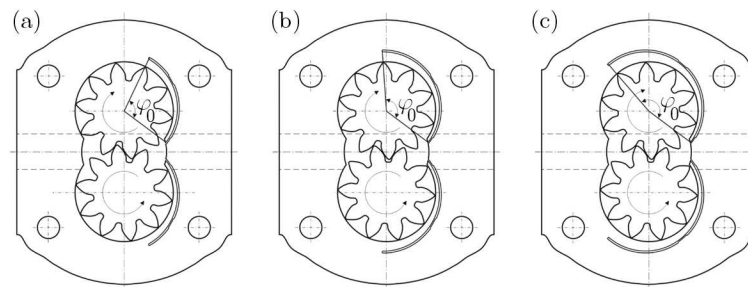


Fig. 3. Schematic of the displacement pump with different compensating beam designs: (a) beam with a wrapping angle $\varphi_0 = 102^\circ$, (b) $\varphi_0 = 132^\circ$, (c) $\varphi_0 = 169^\circ$

Experimental studies of prototypes of such pumps have shown that during operation under heavy loads (at pressures p above 20 MPa) the beam closing the compensating pressure chamber is susceptible to failure in the place of its fixing because of too small beam thickness. The aim of the calculations presented in this paper is to determine (from the strength condition) the minimum thickness h in the fixed cross section of the beam ensuring that the stresses in this cross section are carried.

Three geometric versions of the compensating beam structure have been designed. The most optimal version will be selected on the basis of theoretical calculations and experiments. The versions differ in the beam length, i.e. its wrapping angle, and so in the number of teeth interacting with the beam. For the statical analysis, a fixed gear position in which one of the teeth is in contact with the beam fixing cross section is assumed in each of the cases. The versions include:

- a beam with a wrapping angle $\varphi_0 = 102^\circ$, interacting with three teeth of the gear, one of which is in contact with the beam fixing cross section (Fig. 3a);
- a beam with a wrapping angle $\varphi_0 = 132^\circ$, interacting with four teeth of the gear, one of which is in contact with the beam fixing cross section (Fig. 3b);
- a beam with a wrapping angle $\varphi_0 = 169^\circ$, interacting with five teeth of the gear, one of which is in contact with the beam fixing cross section (Fig. 3c).

3. Static calculations for the pressure chamber beam

3.1. Beam with a wrapping angle $\varphi_0 = 102^\circ$

3.1.1. Beam geometry and loading diagram

During the operation of the pump, the compensating chamber beam is loaded from the outside with compensating pressure p_2 constant along the whole length of the beam, and from the inside with working pressure p_1 (Fig. 4a). The pressure p_1 decreases in the successive intertooth spaces from the initial value $p_{1p} = p_2$ at the inlet to the compensating chamber up to end value $p_{1k} = 0.5p_2$ in the tooth space at the beam fixing. Thus the pressure difference $\Delta p = p_2 - p_{1k}$ constitutes a linearly variable continuous load $q(\varphi)$ for the beam, whose initial value is $q(\varphi = 0) = 0$ and its end value is $q(\varphi = 2\varphi_1 + \alpha) = q_0 = \Delta pb$, where b is the beam width (Fig. 4b). Then the beam load can be reduced to a flat system.

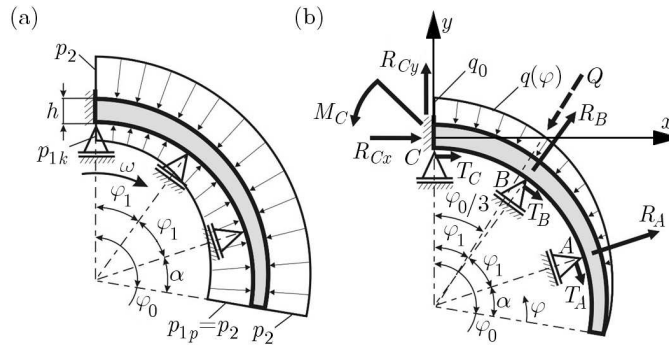


Fig. 4. (a) Static diagram of the beam with the wrapping angle of 102° , loaded with working pressure p_1 and compensating pressure p_2 , (b) diagram after introduction of continuous load replacing the action of pressures p_1 and p_2

As a result of the difference between the pressure p_2 and p_1 , the beam comes into contact with the pump gear teeth, constituting movable supports of the beam, in points A and B (Fig. 2b). Respective reactions R_A and R_B and friction forces T_A and T_B , whose sense is consistent with the direction of the rotational motion of the pump gear, occur in the supports. Two reactions: R_{Cx} and R_{Cy} and fixing moment M_C occur in the beam fixing place (point C). The directions of reactions R_{Cx} and R_{Cy} correspond to the adopted flat reference system (xy) whose origin is in the centre of gravity of the fixed cross section and which is connected with the normal and tangent direction of this cross section (Fig. 4b).

The angles φ_1 (marked in Fig. 4) between the central surfaces of the teeth amount to $\varphi_1 = 360^\circ/10 = 36^\circ$ (the pump gears have 10 teeth) while the complementary angle between point A and the beginning of the beam amounts to $\alpha = 30^\circ$. The beam width (in the direction perpendicular to the load surface) is constant and amounts to $b = 26.3$ mm.

3.1.2. Solutions for beam static load system

For the assumed beam loading diagram (Fig. 4b), the static equilibrium equations have the form

$$\begin{aligned}
 \sum P_x &= R_{Cx} - Q_x + R_{Bx} + R_{Ax} + T_C + T_{Bx} + T_{Ax} = 0 \\
 \sum P_y &= R_{Cy} - Q_y + R_{By} + R_{Ay} - T_{By} - T_{Ay} = 0 \\
 \sum M^C &= M_C + R_B r \sin \varphi_1 + R_A r \sin 2\varphi_1 - T_B(r - r \cos \varphi_1) - T_A(r - r \cos 2\varphi_1) \\
 &\quad - Qr \sin(\varphi_c/3) = 0
 \end{aligned} \tag{3.1}$$

The equations include the reaction force and friction force components amounting to: $R_{Ax} = R_A \sin 2\varphi_1$, $R_{Ay} = R_A \cos 2\varphi_1$, $R_{Bx} = R_B \sin \varphi$, $R_{By} = R_B \cos \varphi$, $T_{Ax} = T_A \cos 2\varphi_1$, $T_{Ay} = T_A \sin 2\varphi_1$, $T_{Bx} = T_B \cos \varphi_1$, $T_{By} = T_B \sin \varphi_1$. Moreover, the action of continuous load $q(\varphi)$ has been replaced with the concentrated force Q applied to the point corresponding to angle $\varphi = 2/3\varphi_0$, where: $\varphi_0 = (2\varphi_1 + \alpha)$ is the maximum angle φ value (for the whole beam span). Then the value of force Q can be calculated from the formula

$$Q = \frac{1}{2}q_0r\varphi_0 \quad (3.2)$$

and the force components for the axes x and y amount to $Q_x = Q \sin(\varphi_0/3)$ and $Q_y = Q \cos(\varphi_0/3)$.

It appears from Eqs. (3.1) that the analyzed static system is a double hyperstatic system. The Menabrei energy method, according to which the derivative of the system elastic energy relative to the hyperstatic reaction amounts to zero (Zakrzewski and Zawadzki, 1983; Niezgodziński and Niezgodziński, 1996; Dyląg *et al.*, 1999), will be used to determine reactions in the supports and in the beam fixing.

The bending moment equations and their derivatives over hyperstatic reactions R_A and R_B depending on the angle φ for particular beam intervals are as follows:

— interval I ($0 < \varphi \leq \alpha$)

$$M_g^I(\varphi) = -\frac{qr^2\varphi^2}{2\varphi_0} \sin \frac{\varphi}{3} \quad \frac{\partial M_g^I}{\partial R_A} = 0 \quad \frac{\partial M_g^I}{\partial R_B} = 0 \quad (3.3)$$

— interval II ($\alpha < \varphi \leq \alpha_2 = \alpha + \varphi_1$)

$$M_g^{II}(\varphi) = -\frac{qr^2\varphi^2}{2\varphi_0} \sin \frac{\varphi}{3} + R_A r \sin(\varphi - \alpha) - T_A[r - r \cos(\varphi - \alpha)] \quad (3.4)$$

$$\frac{\partial M_g^{II}}{\partial R_A} = r \sin(\varphi - \alpha) \quad \frac{\partial M_g^{II}}{\partial R_B} = 0$$

— interval III ($\alpha_2 < \varphi \leq \varphi_0$)

$$M_g^{III}(\varphi) = -\frac{qr^2\varphi^2}{2\varphi_0} \sin \frac{\varphi}{3} + R_A r \sin(\varphi - \alpha) - T_A[r - r \cos(\varphi - \alpha)]$$

$$+ R_B r \sin(\varphi - \alpha_2) - T_B[r - r \cos(\varphi - \alpha_2)] \quad (3.5)$$

$$\frac{\partial M_g^{III}}{\partial R_A} = r \sin(\varphi - \alpha) \quad \frac{\partial M_g^{III}}{\partial R_B} = r \sin(\varphi - \alpha_2)$$

In the above equations, the expression for the bending moment produced by continuous load $q(\varphi) = q_0\varphi/\varphi_0$ takes into account equation (3.2): $Q(\varphi) = 0.5r\varphi q(\varphi) = q_0r\varphi^2/(2\varphi_0)$, assuming that for any cross section defined by angle φ the substitute force $Q(\varphi)$ is applied to the point situated relative to this cross section at angle $\varphi/3$: $M_{Q(\varphi)} = -Q(\varphi)r \sin(\varphi/3) = [-qr^2\varphi^2/(2\varphi_0)] \sin(\varphi/3)$. Moreover, in order to simplify the notation, the angle $\alpha_2 = \alpha + \varphi_1$ is introduced for determination of the range of variation of angle φ in intervals II and III.

According to the Menabrei theorem, hyperstatic reactions R_A and R_B can be calculated from the following system of equations

$$\begin{aligned} \frac{\partial V}{\partial R_A} = & \left[\int_{\alpha}^{\alpha_2} \left(-\frac{q_C r^2 \varphi^2}{2\varphi_0} \sin \frac{\varphi}{3} + R_A r \sin(\varphi - \alpha) - T_A r [1 - \cos(\varphi - \alpha)] \right) [r \sin(\varphi - \alpha)] d\varphi \right] \\ & + \frac{1}{EI} \left[\int_{\alpha_2}^{\varphi_C} \left(-\frac{q_C r^2 \varphi^2}{2\varphi_0} \sin \frac{\varphi}{3} + R_A r \sin(\varphi - \alpha) - T_A r [1 - \cos(\varphi - \alpha)] \right) \right. \\ & \left. + R_B r \sin(\varphi - \alpha_2) - T_B r [1 - \cos(\varphi - \alpha_2)] \right) [r \sin(\varphi - \alpha)] d\varphi \Big] = 0 \end{aligned} \quad (3.6)$$

$$\begin{aligned} \frac{\partial V}{\partial R_B} = & \frac{1}{EI} \left[\int_{\alpha_2}^{\varphi_0} \left(-\frac{q_C r^2 \varphi^2}{2\varphi_0} \sin \frac{\varphi}{3} + R_A r \sin(\varphi - \alpha) - T_A r [1 - \cos(\varphi - \alpha)] \right) \right. \\ & \left. + R_B r \sin(\varphi - \alpha_2) - T_B r [1 - \cos(\varphi - \alpha_2)] \right) [r \sin(\varphi - \alpha_2)] d\varphi \Big] = 0 \end{aligned}$$

Having solved the system of equations (3.6), one can calculate reactions R_A and R_B

$$\begin{aligned} R_A &= 0.2316 \Delta p b r + 0.1915 T_A - 0.0283 T_B = 2376.7 \text{ N} \\ R_B &= 0.3870 \Delta p b r + 0.8494 T_A + 0.2997 T_B = 3978.1 \text{ N} \end{aligned} \quad (3.7)$$

Then using static equilibrium equations (3.1) one can calculate the reactions in the beam fixing

$$\begin{aligned} R_{Cx} &= Q_{Cx} - R_{Bx} - R_{Ax} - T_C - T_{Bx} - T_{Ax} = 490.4 \text{ N} \\ R_{Cy} &= Q_{Cy} - R_{By} - R_{Ay} + T_{By} + T_{Ay} = 3628.1 \text{ N} \\ M_C &= Q_r \sin \varphi_0 3 - R_B r \sin \varphi_1 - R_A r \sin 2\varphi_1 + T_B (r - r \cos \varphi_1) \\ &+ T_A (r - r \cos 2\varphi_1) = 13.35 \text{ N} \end{aligned} \quad (3.8)$$

3.2. Beam with the wrapping angle $\varphi_0 = 132^\circ$

3.2.1. Beam geometry and loading diagram

The loading diagram for the beam with the wrapping angle $\varphi_0 = 132^\circ$ is shown in Fig. 5a, while its modified version (having pressures replaced with the continuous load) is shown in Fig. 3b. In the latter version, the beam interacts with four teeth of the gear and the working pressure p_1 decreases from the initial value $p_{1p} = p_2$ for $\varphi = 0$ up to end value $p_{1k} = 0.33p_2$ for $\varphi = \varphi_0$. The continuous load acting on the beam, arising due to the pressure difference, and the resultant substitute force Q is defined the same as for the beam with the wrapping angle 102° . Besides the continuous load also the friction forces T_A, T_B, T_C, T_D , reactions in the supports (at the contact with the pump teeth) R_A, R_B, R_C and the reactions in the fixing R_{Dx}, R_{Dy}, M_D (Fig. 5b) act on the beam.

3.2.2. Solution for beam load static system

For the loading diagram shown in Fig. 5b, the static equilibrium equations have the form

$$\begin{aligned} \sum P_x &= R_{Dx} + R_{Cx} + R_{Bx} + R_{Ax} + T_D + T_{Cx} + T_{Bx} - T_{Ax} - Q_x = 0 \\ \sum P_y &= R_{Dy} + R_{Cy} + R_{By} - R_{Ay} - T_{Cy} - T_{By} - T_{Ay} - Q_y = 0 \\ \sum M^D &= M_D + R_C r \sin \varphi_1 + R_B r \sin 2\varphi_1 + R_A r \cos \frac{\varphi_1}{2} - T_C (r - r \cos \varphi_1) \\ &- T_B (r - r \cos 2\varphi_1) - T_A \left(r + r \sin \frac{\varphi_1}{2} \right) - Q r \sin \frac{\varphi_0}{3} = 0 \end{aligned} \quad (3.9)$$

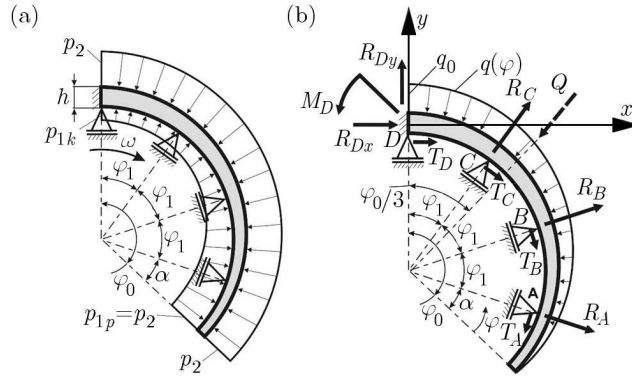


Fig. 5. (a) Static diagram of the beam with the wrapping angle of 132° , loaded with working pressure p_1 and compensating pressure p_2 , (b) diagram after introduction of continuous load replacing the action of pressures p_1 and p_2

The equilibrium equations include the reaction and friction force components amounting to: $R_{Ax} = R_A \cos(\varphi_1/2)$, $R_{Ay} = R_A \sin(\varphi_1/2)$, $R_{Bx} = R_B \sin 2\varphi_1$, $R_{By} = R_B \cos 2\varphi_1$, $R_{Cx} = R_C \sin \varphi_1$, $R_{Cy} = R_C \cos \varphi_1$, $T_{Ax} = T_A \sin(\varphi_1/2)$, $T_{Ay} = T_A \cos(\varphi_1/2)$, $T_{Bx} = T_B \cos 2\varphi_1$, $T_{By} = T_B \sin 2\varphi_1$, $T_{Cx} = T_C \cos \varphi_1$, $T_{Cy} = T_C \sin \varphi_1$, $Q_x = Q \sin(\varphi_0/3)$, $Q_y = Q \cos(\varphi_0/3)$.

Since the considered beam is a triple hyperstatic system, in order to calculate the reactions occurring in the supports and in the beam fixing one should formulate three equations based on the Menabrei method. Assuming R_A , R_B and R_C as hyperstatic reactions occurring in the supports, the equations become

$$\begin{aligned}
 \frac{\partial V}{\partial R_A} &= \frac{1}{EI} \left[\int_{\alpha}^{\alpha_2} \left(-\frac{q_0 r^2 \varphi^2}{2\varphi_0} \sin \frac{\varphi}{3} + R_A r \sin(\varphi - \alpha) - T_A r [1 - \cos(\varphi - \alpha)] \right) [r \sin(\varphi - \alpha)] d\varphi \right] \\
 &+ \frac{1}{EI} \left[\int_{\alpha_2}^{\alpha_3} \left(-\frac{q_0 r^2 \varphi^2}{2\varphi_0} \sin \frac{\varphi}{3} + R_A r \sin(\varphi - \alpha) - T_A r [1 - \cos(\varphi - \alpha)] \right. \right. \\
 &\left. \left. + R_B r \sin(\varphi - \alpha_2) - T_B r [1 - \cos(\varphi - \alpha_2)] \right) [r \sin(\varphi - \alpha)] d\varphi \right] \\
 &+ \frac{1}{EI} \left[\int_{\alpha_3}^{\varphi_0} \left(-\frac{q_0 r^2 \varphi^2}{2\varphi_C} \sin \frac{\varphi}{3} + R_A r \sin(\varphi - \alpha) - T_A r [1 - \cos(\varphi - \alpha)] + R_B r \sin(\varphi - \alpha_2) \right. \right. \\
 &\left. \left. - T_B r [1 - \cos(\varphi - \alpha_2)] + R_C r \sin(\varphi - \alpha_3) - T_C r [1 - \cos(\varphi - \alpha_3)] \right) [r \sin(\varphi - \alpha)] d\varphi \right] = 0 \\
 \frac{\partial V}{\partial R_B} &= \frac{1}{EI} \left[\int_{\alpha_2}^{\alpha_3} \left(-\frac{q_0 r^2 \varphi^2}{2\varphi_0} \sin \frac{\varphi}{3} + R_A r \sin(\varphi - \alpha) - T_A r [1 - \cos(\varphi - \alpha)] \right. \right. \\
 &\left. \left. + R_B r \sin(\varphi - \alpha_2) - T_B r [1 - \cos(\varphi - \alpha_2)] \right) [r \sin(\varphi - \alpha_2)] d\varphi \right] \\
 &+ \frac{1}{EI} \left[\int_{\alpha_3}^{\varphi_0} \left(-\frac{q_0 r^2 \varphi^2}{2\varphi_C} \sin \frac{\varphi}{3} + R_A r \sin(\varphi - \alpha) - T_A r [1 - \cos(\varphi - \alpha)] + R_B r \sin(\varphi - \alpha_2) \right. \right. \\
 &\left. \left. - T_B r [1 - \cos(\varphi - \alpha_2)] + R_C r \sin(\varphi - \alpha_3) - T_C r [1 - \cos(\varphi - \alpha_3)] \right) [r \sin(\varphi - \alpha_2)] d\varphi \right] = 0
 \end{aligned} \tag{3.10}$$

$$\frac{\partial V}{\partial R_C} = \frac{1}{EI} \left[\int_{\alpha_3}^{\varphi_0} \left(-\frac{q_0 r^2 \varphi^2}{2\varphi_0} \sin \frac{\varphi}{3} + R_{Ar} \sin(\varphi - \alpha) - T_{Ar} [1 - \cos(\varphi - \alpha)] + R_{Br} \sin(\varphi - \alpha_2) - T_{Br} [1 - \cos(\varphi - \alpha_2)] + R_{Cr} \sin(\varphi - \alpha_3) - T_{Cr} [1 - \cos(\varphi - \alpha_3)] \right) [r \sin(\varphi - \alpha_3)] d\varphi \right] = 0$$

Having solved equations (3.10), one can calculate reactions R_A , R_B and R_C

$$\begin{aligned} R_A &= 0.1103\Delta pbr + 0.2522T_A - 0.0259T_B + 0.0067T_C = 1510.2 \text{ N} \\ R_B &= 0.3164\Delta pbr + 0.7156T_A - 0.3009T_B - 0.0369T_C = 4334.5 \text{ N} \\ R_C &= 0.5946\Delta pbr + 0.6019T_A - 0.6787T_B + 0.3009T_C = 8144.1 \text{ N} \end{aligned} \quad (3.11)$$

Finally, using static equilibrium equations (3.9), one gets the values of reactions in the beam fixing

$$\begin{aligned} R_{Dx} &= Q_x - R_{Cx} - R_{Bx} - R_{Ax} - T_D - T_{Cx} - T_{Bx} + T_{Ax} = 583.8 \text{ N} \\ R_{Dy} &= Q_y - R_{Cy} - R_{By} + R_{Ay} + T_{Cy} + T_{By} + T_{Ay} = 3889.9 \text{ N} \\ M_D &= Qr \sin \frac{\varphi_0}{3} - R_C r \sin \varphi_1 - R_B r \sin 2\varphi_1 - R_A r \cos \frac{\varphi_1}{2} + T_C (r - r \cos \varphi_1) \\ &\quad + T_B (r - r \cos 2\varphi_1) + T_A \left(r + r \sin \frac{\varphi_1}{2} \right) = 15.98 \text{ N} \end{aligned} \quad (3.12)$$

3.3. Beam with the wrapping angle $\varphi_0 = 169^\circ$

3.3.1. Beam geometry and loading diagram

Figures 6a and 6b show the loading diagram and the diagram which takes into account the replacement of pressures p_1 and p_2 (acting on both sides of the beam) with continuous load q for the pump with the compensating chamber with the wrapping angle $\varphi_0 = 169^\circ$.

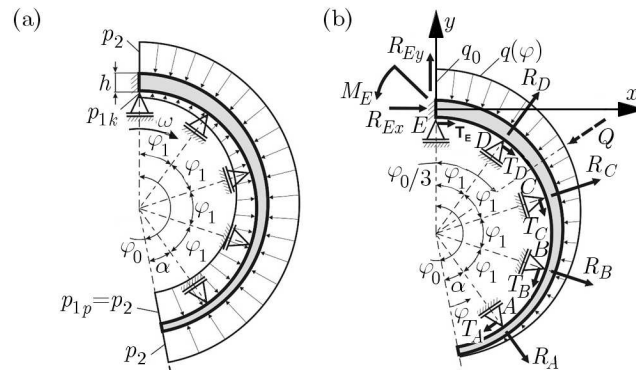


Fig. 6. (a) Static diagram of the beam with the wrapping angle $\varphi_0 = 169^\circ$, loaded with working pressure p_1 and compensating pressure p_2 , (b) diagram after introduction of continuous load replacing the action of pressures p_1 and p_2

In this case, the chamber beam is in contact with five teeth of the gear and the working pressure p_1 decreases from the initial value $p_{1p} = p_2$ for $\varphi = 0$ down to the end value $p_{1k} = 0.166p_2$ for $\varphi = \varphi_0$. Besides the continuous load, as shown in Fig. 4b, the friction forces T_A, T_B, T_C, T_D, T_E , reaction forces in the supports R_A, R_B, R_C, R_D and the forces in the beam fixing R_{Ex}, R_{Ey}, M_E act on the beam.

3.3.2. Solutions for the beam subject to load static scheme

The static equilibrium equations for the considered beam assume the form

$$\begin{aligned}
\sum P_x &= R_{Ex} + R_{Dx} + R_{Cx} + R_{Bx} + R_{Ax} + T_E + T_{Dx} + T_{Cx} - T_{Bx} - T_{Ax} - Q_x = 0 \\
\sum P_y &= R_{Ey} + R_{Dy} + R_{Cy} - R_{By} - R_{Ay} - T_{Dy} - T_{Cy} - T_{By} - T_{Ay} - Q_y = 0 \\
\sum M^E &= M_E + R_D r \sin \varphi_1 + R_C r \sin 2\varphi_1 + R_B r \cos \frac{\varphi_1}{2} + R_A r \cos \frac{3\varphi_1}{2} \\
&\quad - T_D(r - r \cos \varphi_1) - T_C(r - r \cos 2\varphi_1) - T_B\left(r + r \sin \frac{\varphi_1}{2}\right) \\
&\quad - T_A\left(r + r \sin \frac{3\varphi_1}{2}\right) - Qr \sin \frac{\varphi_c}{3} = 0
\end{aligned} \tag{3.13}$$

The reaction and friction force components in equations (3.13) are described by the formulas: $R_{Ax} = R_A \cos(3\varphi_1/2)$, $R_{Ay} = R_A \sin(3\varphi_1/2)$, $R_{Bx} = R_B \cos(\varphi_1/2)$, $R_{By} = R_B \sin(\varphi_1/2)$, $R_{Cx} = R_C \sin 2\varphi_1$, $R_{Cy} = R_C \cos 2\varphi_1$, $R_{Dx} = R_D \sin \varphi_1$, $R_{Dy} = R_D \cos \varphi_1$, $T_{Ax} = T_A \sin(3\varphi_1/2)$, $T_{Ay} = T_A \cos(3\varphi_1/2)$, $T_{Bx} = T_B \sin(\varphi_1/2)$, $T_{By} = T_B \cos(\varphi_1/2)$, $T_{Cx} = T_C \cos 2\varphi_1$, $T_{Cy} = T_C \sin 2\varphi_1$, $T_{Dx} = T_D \cos \varphi_1$, $T_{Dy} = T_D \sin \varphi_1$, $Q_x = Q \sin(\varphi_0/3)$, $Q_y = Q \cos(\varphi_0/3)$.

In order to determine the four hyperstatic reactions (assumed here as the reactions in the supports) one should formulate four Menabrei equations

$$\begin{aligned}
\frac{\partial V}{\partial R_A} &= \frac{1}{EI} \left[\int_{\alpha}^{\alpha_2} \left(-\frac{q_0 r^2 \varphi^2}{2\varphi_0} \sin \frac{\varphi}{3} + R_A r \sin(\varphi - \alpha) - T_A r [1 - \cos(\varphi - \alpha)] \right) [r \sin(\varphi - \alpha)] d\varphi \right] \\
&\quad + \frac{1}{EI} \left[\int_{\alpha_2}^{\alpha_3} \left(-\frac{q_0 r^2 \varphi^2}{2\varphi_0} \sin \frac{\varphi}{3} + R_A r \sin(\varphi - \alpha) - T_A r [1 - \cos(\varphi - \alpha)] \right. \right. \\
&\quad \left. \left. + R_B r \sin(\varphi - \alpha_2) - T_B r [1 - \cos(\varphi - \alpha_2)] \right) [r \sin(\varphi - \alpha)] d\varphi \right] \\
&\quad + \frac{1}{EI} \left[\int_{\alpha_3}^{\alpha_4} \left(-\frac{q_0 r^2 \varphi^2}{2\varphi_0} \sin \frac{\varphi}{3} + R_A r \sin(\varphi - \alpha) - T_A r [1 - \cos(\varphi - \alpha)] + R_B r \sin(\varphi - \alpha_2) \right. \right. \\
&\quad \left. \left. - T_B r [1 - \cos(\varphi - \alpha_2)] + R_C r \sin(\varphi - \alpha_3) - T_C r [1 - \cos(\varphi - \alpha_3)] \right) [r \sin(\varphi - \alpha)] d\varphi \right] \\
&\quad + \frac{1}{EI} \left[\int_{\alpha_4}^{\varphi_0} \left(-\frac{q_0 r^2 \varphi^2}{2\varphi_0} \sin \frac{\varphi}{3} + R_A r \sin(\varphi - \alpha) - T_A r [1 - \cos(\varphi - \alpha)] \right. \right. \\
&\quad \left. \left. + R_B r \sin(\varphi - \alpha_2) - T_B r [1 - \cos(\varphi - \alpha_2)] + R_C r \sin(\varphi - \alpha_3) - T_C r [1 - \cos(\varphi - \alpha_3)] \right. \right. \\
&\quad \left. \left. + R_D r \sin(\varphi - \alpha_4) - T_D r [1 - \cos(\varphi - \alpha_4)] \right) [r \sin(\varphi - \alpha)] d\varphi \right] = 0 \\
\frac{\partial V}{\partial R_B} &= \frac{1}{EI} \left[\int_{\alpha_2}^{\alpha_3} \left(-\frac{q_0 r^2 \varphi^2}{2\varphi_0} \sin \frac{\varphi}{3} + R_A r \sin(\varphi - \alpha) - T_A r [1 - \cos(\varphi - \alpha)] \right. \right. \\
&\quad \left. \left. + R_B r \sin(\varphi - \alpha_2) - T_B r [1 - \cos(\varphi - \alpha_2)] \right) [r \sin(\varphi - \alpha_2)] d\varphi \right] \\
&\quad + \frac{1}{EI} \left[\int_{\alpha_3}^{\alpha_4} \left(-\frac{q_0 r^2 \varphi^2}{2\varphi_0} \sin \frac{\varphi}{3} + R_A r \sin(\varphi - \alpha) - T_A r [1 - \cos(\varphi - \alpha)] + R_B r \sin(\varphi - \alpha_2) \right. \right.
\end{aligned}$$

$$\begin{aligned}
& -T_B r [1 - \cos(\varphi - \alpha_2)] + R_C r \sin(\varphi - \alpha_3) - T_C r [1 - \cos(\varphi - \alpha_3)] \Big) [r \sin(\varphi - \alpha_2)] d\varphi \Big] \\
& + \frac{1}{EI} \left[\int_{\alpha_4}^{\varphi_0} \left(-\frac{q_0 r^2 \varphi^2}{2\varphi_0} \sin \frac{\varphi}{3} + R_{Ar} \sin(\varphi - \alpha) - T_{Ar} [1 - \cos(\varphi - \alpha)] \right. \right. \\
& + R_{Br} \sin(\varphi - \alpha_2) - T_{Br} [1 - \cos(\varphi - \alpha_2)] + R_{Cr} \sin(\varphi - \alpha_3) - T_{Cr} [1 - \cos(\varphi - \alpha_3)] \\
& \left. \left. + R_{Dr} \sin(\varphi - \alpha_4) - T_{Cr} [1 - \cos(\varphi - \alpha_4)] \right) [r \sin(\varphi - \alpha_2)] d\varphi \right] = 0 \tag{3.14} \\
\frac{\partial V}{\partial R_C} &= \frac{1}{EI} \left[\int_{\alpha_3}^{\alpha_4} \left(-\frac{q_0 r^2 \varphi^2}{2\varphi_0} \sin \frac{\varphi}{3} + R_{Ar} \sin(\varphi - \alpha) - T_{Ar} [1 - \cos(\varphi - \alpha)] \right. \right. \\
& + R_{Br} \sin(\varphi - \alpha_2) - T_{Br} [1 - \cos(\varphi - \alpha_2)] + R_{Cr} \sin(\varphi - \alpha_3) \\
& \left. \left. - T_{Cr} [1 - \cos(\varphi - \alpha_3)] \right) [r \sin(\varphi - \alpha_3)] d\varphi \right] \\
& + \frac{1}{EI} \left[\int_{\alpha_4}^{\varphi_0} \left(-\frac{q_0 r^2 \varphi^2}{2\varphi_0} \sin \frac{\varphi}{3} + R_{Ar} \sin(\varphi - \alpha) - T_{Ar} [1 - \cos(\varphi - \alpha)] \right. \right. \\
& + R_{Br} \sin(\varphi - \alpha_2) - T_{Br} [1 - \cos(\varphi - \alpha_2)] + R_{Cr} \sin(\varphi - \alpha_3) - T_{Cr} [1 - \cos(\varphi - \alpha_3)] \\
& \left. \left. + R_{Dr} \sin(\varphi - \alpha_4) - T_{Dr} [1 - \cos(\varphi - \alpha_4)] \right) [r \sin(\varphi - \alpha_3)] d\varphi \right] = 0 \\
\frac{\partial V}{\partial R_D} &= \frac{1}{EI} \left[\int_{\alpha_4}^{\varphi_0} \left(-\frac{q_0 r^2 \varphi^2}{2\varphi_0} \sin \frac{\varphi}{3} + R_{Ar} \sin(\varphi - \alpha) - T_{Ar} [1 - \cos(\varphi - \alpha)] \right. \right. \\
& + R_{Br} \sin(\varphi - \alpha_2) - T_{Br} [1 - \cos(\varphi - \alpha_2)] + R_{Cr} \sin(\varphi - \alpha_3) - T_{Cr} [1 - \cos(\varphi - \alpha_3)] \\
& \left. \left. + R_{Dr} \sin(\varphi - \alpha_4) - T_{CDr} [1 - \cos(\varphi - \alpha_4)] \right) [r \sin(\varphi - \alpha_4)] d\varphi \right] = 0
\end{aligned}$$

By solving the Menabrei equations one can determine reactions R_A , R_B , R_C and R_D

$$\begin{aligned}
R_A &= 0.0908 \Delta p b r - 0.4034 T_A - 0.0255 T_B + 0.0073 T_C - 0.0019 T_D = 1548.2 \text{ N} \\
R_B &= 0.2542 \Delta p b r + 0.7128 T_A + 0.3001 T_B - 0.0400 T_C + 0.0104 T_D = 4352.4 \text{ N} \\
R_C &= 0.4593 \Delta p b r + 0.6065 T_A + 0.6777 T_B + 0.3127 T_C - 0.0400 T_D = 7863.2 \text{ N} \\
R_D &= 0.7524 \Delta p b r + 0.6340 T_A + 0.6126 T_B + 0.6750 T_C + 0.3027 T_D = 12880.2 \text{ N}
\end{aligned} \tag{3.15}$$

Finally, using static equilibrium equations (3.13), one can calculate reactions in the beam fixing

$$\begin{aligned}
R_{Ex} &= Q_x - R_{Dx} - R_{Cx} - R_{Bx} - R_{Ax} - T_E - T_{Dx} - T_{Cx} - T_{Bx} - T_{Ax} = 877.0 \text{ N} \\
R_{Ey} &= Q_y - R_{Dy} - R_{Cy} + R_{By} + R_{Ay} + T_{Dy} + T_{Cy} + T_{By} + T_{Ay} = 3747.4 \text{ N} \\
M_E &= Q r \sin \frac{\varphi_0}{3} - R_D r \sin \varphi_1 - R_C r \sin 2\varphi_1 - R_B r \cos \frac{\varphi_1}{2} - R_A r \cos \frac{3\varphi_1}{2} \\
& + T_D (r - r \cos \varphi_1) + T_C (r - r \cos 2\varphi_1) + T_B \left(r + r \sin \frac{\varphi_1}{2} \right) \\
& + T_A \left(r + r \sin \frac{3\varphi_1}{2} \right) = 23.8 \text{ Nm}
\end{aligned} \tag{3.16}$$

4. Calculations of the minimal beam thickness in a fixed cross section

The beam thickness h must satisfy the strength condition for the fixed beam cross section. This cross section is loaded with reaction forces R_C , R_D or R_E for the pump geometric conditions at φ_0 respectively 102° , 132° , 169° and the bending moment M_C , M_D or M_E , respectively. The loads generate a complex state of stress in the fixed cross section. The shearing stress (produced by the tangential component of the reaction denoted generally as R_y) reaches the highest value in central fibres of the cross section while the bending stress reaches the highest value in extreme fibres.

The strength condition concerning the maximum shear stress has the form

$$\tau_{max} = \frac{3}{2} \frac{|R_y|}{bh} \leq k_t \quad (4.1)$$

thus the minimal beam thickness must satisfy the criterion

$$h_{min(\tau)} = \frac{3}{2} \frac{|R_y|}{bk_t} \quad (4.2)$$

The strength condition for the allowable normal stress must take into account the simultaneous action of the tensile (or compressive) stress produced by the reaction component R_x and the bending stress generated by the fixing moment M_u in the extreme fibres

$$\sigma = |\sigma_r| + |\sigma_g| \leq k_r \quad (4.3)$$

By substituting the normal stress values (calculated as for straight bars when beam curvature radius $r > 6h$, the error due to the shift of the neutral beam bending axis does not exceed 0.5%) $\sigma_r = R_x/(bh)$, $\sigma_g = 6M_u/(bh^2)$ into equation (4.3), one gets the following equation for the minimal beam thickness h_{min}

$$bk_r h_{min}^2 - |R_x| h_{min} - 6|M_u| = 0 \quad (4.4)$$

The solution of this equation yields the second value of the minimal beam thickness

$$h_{min(\tau)} = \frac{|R_x| + \sqrt{R_x^2 + 24M_u b k_r}}{2b k_r} \quad (4.5)$$

One should adopt the second value of the two values obtained from formulas (4.2) and (4.5) as the minimal beam width h .

Table 1 shows exemplary minimal beam thickness values calculated for three geometric versions of the pump, assuming the experimental friction forces generated by teeth of the gears $T_i = 7.96$ N, safety factor $n = 1.4$ and permissible stresses: $k_r = 350$ MPa and $k_t = 400$ MPa.

Table 1. Exemplary load values and the minimal thickness h_{min} for the beam with the wrapping angle $\varphi_0 = 102^\circ$

Beam wrapping angle	r	b	p_{1k}	p_2	h_{min}
$\varphi_0 = 102^\circ$	26 mm	26.3 mm	15 MPa	30 MPa	2.98 mm
$\varphi_0 = 132^\circ$	26 mm	26.3 mm	10 MPa	30 MPa	3.26 mm
$\varphi_0 = 169^\circ$	26 mm	26.3 mm	5 MPa	30 MPa	3.99 mm

The results of the static strength calculations show that from among the three versions of the compensating chamber the most advantageous one is the version with the beam with the wrapping angle $\varphi_0 = 102^\circ$ for which the minimal beam thickness amounts to 2.98 mm. In the case of the other versions, the beam thickness needs to be increased:

- for the beam with the wrapping angle $\varphi_0 = 132^\circ$, the minimal thickness amounts to 3.26 mm (an increase by 9.4%),
- for the beam with the wrapping angle $\varphi_0 = 169^\circ$, the minimal thickness amounts to 3.99 mm (an increase by 31%).

Experimental studies are planned to be carried out on prototypes of the pump in order to verify the results of the calculations.

References

1. CHROBOT M., ŁABIK M., SIUDY B., WIECZOREK K., 1997, Hydraulic optimization of axial backlash compensation (in Polish), *Report Series Report*, No. S-019/97
2. DYLAŁ Z., JAKUBOWICZ A., ORŁOŚ Z., 1999, *Strength of Materials* (in Polish), Vol. I/II, WNT, Warsaw
3. JUDIN E.M., 1958, *Gear Pumps* (in Polish), PWT, Warsaw
4. KOLLEK W., 2004, *Fundamental of the Design of Hydraulic Drives and Controls* (in Polish), Wrocław University of Technology Publishing House, Wrocław
5. KOLLEK W., 1996, *Gear Pumps – Design and Operation* (in Polish), Ossolineum, Wrocław
6. KOLLEK W., RADZIWANOWSKA U., 2015, Energetic efficiency of gear micropumps, *Archives of Civil and Mechanical Engineering*, **15**, 1, 109-115
7. NIEZGODZIŃSKI M. E., NIEZGODZIŃSKI T., 1996, *Strength of Materials* (in Polish), PWN, Warsaw
8. OSIŃSKI P., 2012a, An external gear pump (in Polish), Patent application No. P398436, Warsaw
9. OSIŃSKI P., 2012b, An external gear pump (in Polish), Patent application No. P398437, Warsaw
10. OSIŃSKI P., 2013, *High-Pressure and Low-Fluctuation Internal Gear Pumps* (in Polish) Wrocław University of Technology Publishing House, Wrocław
11. OSIŃSKI P., DEPTUŁA A., PARTYKA M.A., 2013, Discrete optimization of a gear pump after tooth root undercutting by means of multi-valued logic trees, *Archives of Civil and Mechanical Engineering*, **13**, 4, 422-431, <http://dx.doi.org/10.1016/j.acme.2013.05.001>
12. OSIŃSKI P., KANIA A., KOLLEK W., WICZKOWSKI E., 2012, An external gear pump (in Polish), Patent application No. P397539, Warsaw
13. OSIŃSKI P., KOLLEK W., 2007, *Modelling and Design of Gear Pumps*, Wrocław University of Technology Publishing House, Wrocław
14. RAGUNATHAN C., MANOHARAN C., 2012, Dynamic analysis of hydrodynamic gear pump performance using design of experiment stand operational parameters, *IOSR Journal of Mechanical and Civil Engineering*, **1**, 6, 17-23
15. SINGAL R.K., SINGAL M., SINGAL R., 2009, *Hydraulic Machines. Fluid Machinery*, I.K. International Publishing House, New Delhi
16. STRYCZEK S., 1995, *Hydrostatic Drives* (in Polish), Vol. I, II. WNT, Warsaw
17. VACCA A., GUIDETTI M., 2011, Modelling and experimental validation of external spur gear machines for fluid power applications, *Simulation Modelling Practice and Theory*, **19**, 2007-2031
18. WANG S., SAKURAI H., KASAREKAR A., 2011, The optimal design in external gear pumps and motors, *ASME Transactions on Mechatronics*, **16**, 5.
19. WICZKOWSKI E., 2012, An external gear pump (in Polish), Patent application No. P397540, Warsaw
20. ZAKRZEWSKI M., ZAWADZKI J., 1983, *Strength of Materials* (in Polish), PWN, Warsaw

ANALYSIS OF PLASTIC DEFORMATION OF SEMI-CRYSTALLINE POLYMERS DURING ECAE PROCESS USING 135° DIE

BENAOUMEUR AOUR, ALI MITSAK

Laboratory of Applied Biomechanics and Biomaterials, Department of Mechanical Engineering, Oran, Algeria
e-mail: ben_aour@yahoo.fr

In this paper, analysis of plastic deformation of high density polyethylene (HDPE) and polypropylene (PP) during an equal channel angular extrusion (ECAE) process is investigated. The effects of ram speed, number of passes, processing route and temperature are tested experimentally using a 135° die. The results show that the pressing force decreases with an increase in the number of passes and reaches a saturation state rapidly for routes *A* and *C* compared to routes *B_A* and *B_C*. Furthermore, it is found that the reduced curvature of the extruded samples is obtained by route *C*, however, the maximum warping is obtained by route *A*. A slight influence of temperature on the reduction of the warping is observed on the extruded samples. In order to predict the plastic strain inside the extruded samples, an elastic viscoplastic model is identified using compressive tests at different strain rates and coupled with the finite element method (FEM). A good correlation is found between the numerical modeling and experimental findings. FEM results show that the PP samples display a higher level of plastic strain compared to HDPE samples. However, almost the same degree of strain heterogeneity is obtained for both polymers. Finally, in order to reduce the warping and improve the strain homogeneity, a controlled back-pressure with small corner angle is expected to be an adequate solution.

Keywords: ECAE, polymers, finite element analysis, plastic strain, back-pressure

1. Introduction

Equal channel angular extrusion (ECAE) is an innovative process to improve physical and mechanical properties of materials by severe plastic deformation (SPD) without alteration of the geometric shape of workpiece. Moreover, since the cross-section of the workpiece is not modified after extrusion, the process can be repeated several times, and by changing the orientation of the workpiece between consecutive extrusions, stylish microstructures can be developed in the extruded materials. Up to now, the majority of research and development on ECAE have been conducted on metallic materials (Segal, 1995; Iwahashi *et al.*, 1996; Valiev and Langdon, 2006). However, for polymeric materials, little work is available to address the mechanical behaviour during ECAE process (Sue and Li, 1998; Campbell and Edward, 1999; Li *et al.*, 2000; Weon *et al.*, 2005; Wang *et al.*, 2006).

According to our knowledge, this process was first applied to polymers by Sue and Li (1998). They showed that the ECAE process is effective in altering the morphology of a linear low density polyethylene (LLDP). Sue *et al.* (1999) reported that for ECAE to be effective, it is necessary that the extrusion be held at temperatures slightly below the glassy transition in the case of polycarbonate (PC). For the same polymer, Li *et al.* (2000) confirmed that the mechanical properties can be tailored by extruding the material via various processing routes and a different number of passes.

The effect of molecular anisotropy on the impact strength of polycarbonate (PC) was examined by Xia *et al.* (2001a). They found that the enhancement of the impact resistance is directly

related to the changes in molecular orientation induced by the ECAE process. According to Xia *et al.* (2001b), the crystallinity and molecular orientation were identified as two important factors affecting the dynamic mechanical properties of the ECAE-oriented semicrystalline polyethylene terephthalate (PET). An improvement of the bending and torsional storage modulus was found. Creasy and Kang (2005) studied fibre fracture during the ECAE process of short fibre-reinforced thermoplastics. They found that the fibre length can be controlled and oriented by setting the process temperature below the melting point of the polymer crystallites. On the other hand, the effect of different ECAE routes on the tensile, fracture toughness, flexural, and ballistic impact properties of polymethylmethacrylate (PMMA) was investigated by Weon *et al.* (2005). A fruitful discussion was reported by Wang *et al.* (2006) on lamellar formation and relaxation in simple sheared polyethylene terephthalate (PET) using the in-situ time resolved synchrotron Small-Angle X-ray Scattering (SAXS) technique. Recently, numerical and experimental investigations were achieved to highlight the effects of the main geometrical and processing parameters on the viscoplastic behaviour of polymers during the ECAE process (Zairi *et al.*, 2008; Aour *et al.*, 2009; Bouaksa *et al.*, 2014).

The findings presented above show that the ECAE process is an effective tool for the improvement of mechanical properties of polymers by inducing molecular orientation in bulk polymers. This feature enables ECAE to have useful applications for the fabrication of many anti-impact components, such as fighter-jet canopies, vehicle structures, windshields, and anti-theft transparencies (Xia *et al.*, 2001a). Furthermore, the ECAE technique can be easily incorporated into the conventional polymer processing setup without much capital investment by attaching, for example, a conventional injection unit to the entrance channel, which can potentially be used for extruding pipes, tubes, rods, sheets, plates and other profiles with significantly improved physical and mechanical properties (Sue *et al.*, 1999).

In this paper, an experimental and numerical investigation of plastic deformation of two semicrystalline polymers (HDPE and PP) during the ECAE process using 135° die is presented. In order to achieve this objective, the paper is organised as follows. The experimental procedure is discussed in Section 2. Section 3 is focused on the presentation of the experimental results obtained for the effects of processing routes, number of passes and temperature. Section 4 is devoted to describe the elastic viscoplastic constitutive law and its identification using compressive tests at different strain rates. Section 5 is reserved for the presentation of the FEM results. A particular attention is made on the effect of the back-pressure on the homogeneity and the level of the plastic strain distribution into the extruded samples. Finally, some concluding remarks are given in Section 6.

2. Experimental procedure

2.1. ECAE device

After an optimization study of various geometrical parameters (Aour *et al.*, 2008), an ECAE device with a channel angle $\Phi = 135^\circ$ and a corner angle $\theta = 34^\circ$ has been designed and manufactured (Fig. 1a). The die consists of two square channels of cross-sectional area $10.1 \text{ mm} \times 10.1 \text{ mm}$, which allows one to apply four routes (A , B_A , B_C and C) as shown in Fig. 1c. The lengths of the entrance and exit channels are respectively 75 mm and 50 mm. An electromechanical Istron 5800 testing machine has been used to extrude the samples through the angular die.

2.2. Processing routes

Figure 1b shows a set of material axes referred to the sample, which is useful in describing the different routes. The X -direction is the zero strain direction (transverse direction: TD), the

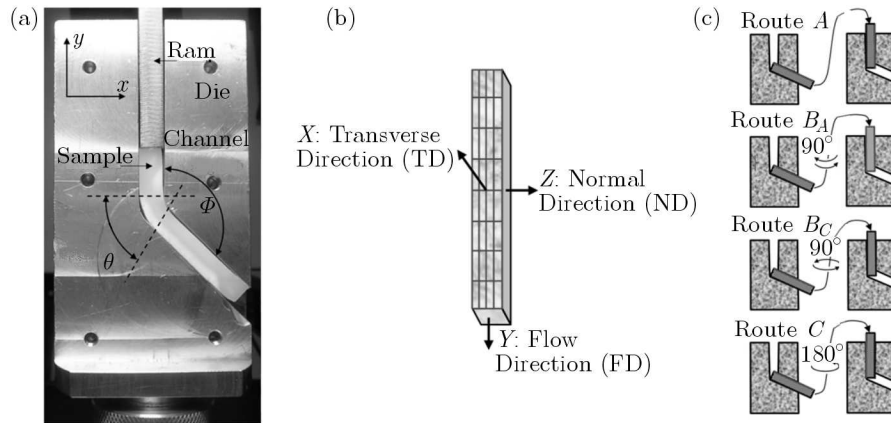


Fig. 1. (a) Photograph of the ECAE device; (b) diagram of the sample showing material axes used to describe different routes; (c) schematic illustration of the processing routes: A , B_A , B_C and C

flow direction (FD) is taken as the Y -direction, and the Z -direction (normal direction: ND) is normal to the plane in which the sample shear occurs. In this study, four different routes are investigated (Fig. 1c):

- Route A : the sample is re-inserted in the same orientation as the previous pass.
- Route B_A : the sample is rotated alternatively by $+90^\circ$ and -90° around the Y -axis between two successive passes.
- Route B_C : the sample is rotated by $+90^\circ$ around the Y -axis after each pass.
- Route C : the sample is rotated around the Y -axis by 180° and then re-extruded.

2.3. Materials and samples preparation

Two semi-crystalline polymers (high density polyethylene HDPE and polypropylene PP) have been selected for this study. These polymers have been supplied by the Goodfellow Company. The crystal content is about 70% for HDPE and 55% for PP. ECAE samples of $10\text{ mm} \times 10\text{ mm}$ cross-section and 70 mm in length have been cut from commercially plates in the same direction, then surfaced simultaneously on the cutting facets and polished. The HDPE and PP samples have been respectively annealed in vacuum at 120°C and 85°C for 2 h.

In this work, four parameters are studied experimentally: the ram speed, number of passes, processing route and temperature effect. The extrusion tests have been performed without lubrication.

3. Experimental results

3.1. Effect of ram speed

Figure 2 illustrates the influence of the ram speed on the evolution of the pressing force using a 135° die in the case of HDPE (Fig. 2a) and PP samples (Fig. 2b). Three different values of ram speeds (0.7, 0.07 and 0.007 mm/s) have been tested without lubrication.

It can be observed that the pressing force required for extrusion increases with an increase in the ram speed for both polymers. Indeed, when the ram speed is increased from 0.7 to 0.007 mm/s, the maximum force required for extrusion of HDPE samples varies from 932 to 1212 N (i.e., a difference of 280 N), however, for PP samples, a difference of 432 N is noticed. Furthermore, at the stage of the steady state of the plastic flow, different trends are revealed for each material. In the case of HDPE, the pressing force remains almost constant, however, in

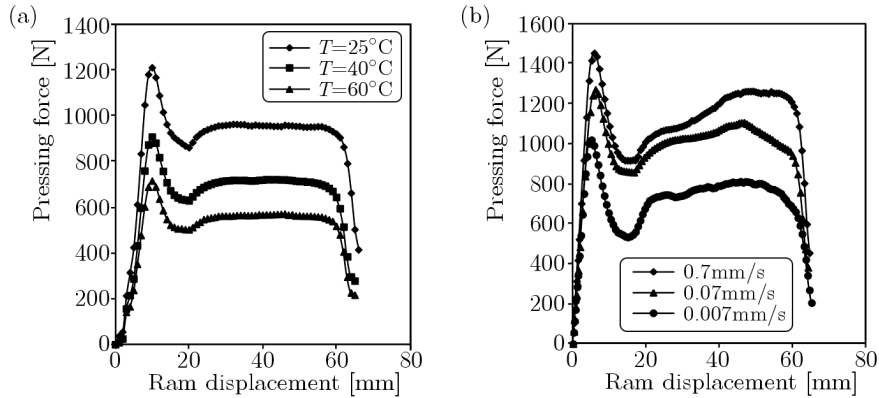


Fig. 2. Variation of the pressing force versus ram displacement in one ECAE pass using 135° die in the case of (a) HDPE and (b) PP samples

the case of PP, a slight increase is observed. This can be attributed to the flexibility of HDPE which is higher than that of PP.

3.2. Effect of the processing route and number of passes

The advantage of the ECAE process, in addition to maintaining constant cross-section of the extruded sample throughout the process, it is possible to generate a number of dissimilar deformation histories and create various forms of molecular orientations if multiple passes with a suitable selection of processing routes are carried out. It was demonstrated by Li *et al.* (2000) that well-controlled morphology can lead to great improvements in physical and mechanical properties of the extruded polymer both along and perpendicular to the extrusion direction. In this subsection, the samples are processed via four ECAE processing routes using a 135° die at room temperature and a ram speed of 0.70 mm/s . In order to make a comparison between the different routes, the evolution of the maximum pressing force versus the number of passes is plotted in Fig. 3. It can be seen that, for routes *A* and *C*, the pressing force decreases with an increase in the number of passes, however in the case of routes *B_A* and *B_C*, a periodic variation is noticed for HDPE samples, and a random variation is highlighted for PP samples. These variations explain that the materials have different strengths in each direction due to anisotropy and mobility of the crystalline lamellae inside the bulk material with respect to ECAE loading. Moreover, it can be observed that the routes *A* and *C* reach their saturation values after almost four passes, while the routes *B_A* and *B_C* require a high number of passes to achieve its saturation state.

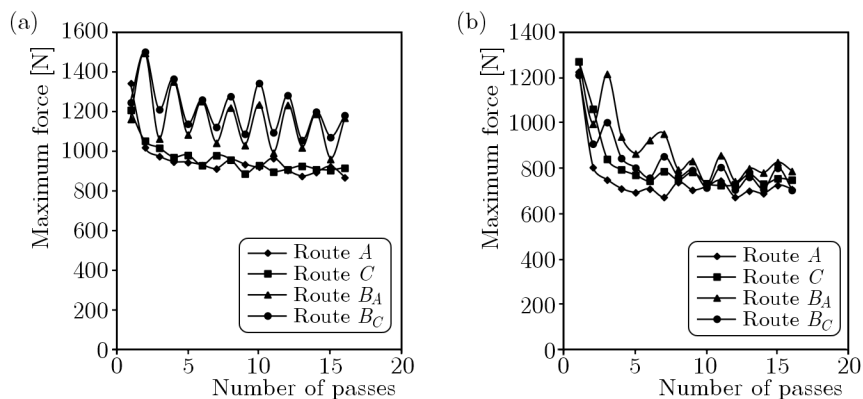


Fig. 3. Variation of the maximum force versus the number of passes during extrusion through a 135° die with different routes for (a) HDPE and (b) PP samples

The warping of the extruded samples due to various processing routes has been also quantified in this experimental part. Figure 4 shows pictures of HDPE samples that have undergone sixteen passes of ECAE by different processing routes. The obtained results for HDPE and PP samples are listed in Table 1. The maximum curvature of the sample (warping) has been quantified by measuring the height of the sample before and after the ECAE process. For both polymers, it has been found that the maximum warping is always obtained by route *A*, however the minimum warping is obtained by route *C*. Furthermore, the warping obtained for PP samples is quite high than that of HDPE samples.

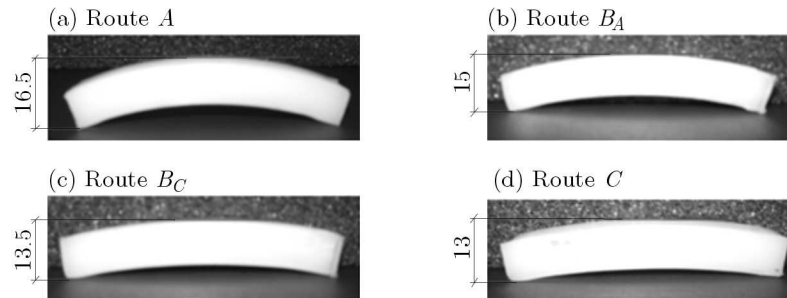


Fig. 4. HDPE samples extruded at room temperature after 16 passes using a 135° die with different processing routes

Table 1. Maximum values of the curvature obtained by different routes using a 135° die and a length of 70 mm after 16 passes on HDPE and PP samples

Route	Extruded material	Height before ECAE H_b [mm]	Height after 16 ECAE passes: H_a [mm]	Curvature $Cu = H_a - H_b$ [mm]
<i>A</i>	HDPE	9.85	16.50	6.65
	PP	9.77	17.20	7.43
<i>B_A</i>	HDPE	10.17	15.00	4.83
	PP	9.29	13.50	4.21
<i>B_C</i>	HDPE	10.13	13.50	3.37
	PP	9.13	13.25	4.12
<i>C</i>	HDPE	9.72	13.00	3.28
	PP	9.65	13.15	3.50

3.3. Effect of temperature

According to Sue *et al.* (1999), the warping is generated due to the existence of residual stress and the concurrent stress relaxation process on the extruded samples. Moreover, it is believed that the stress relaxation process can be greatly accelerated at elevated temperatures. Consequently, in order to highlight the temperature effect on the warping reduction by stress relaxation, the ECAE process has been carried out on HDPE samples at different temperatures $T = \{25^\circ\text{C}, 40^\circ\text{C}, 60^\circ\text{C}\}$ via routes *A* and *C*. The obtained results after sixteen passes are illustrated in Table 2.

It can be seen that a slight reduction of warping is obtained even with several passes and at elevated temperatures. Noting that, in the case of PC samples, a significant reduction of warping was found by Sue *et al.* (1999) via elevation of the extrusion temperature. However, in the case of HDPE and PP, it is advised to test other parameters such as the use of back pressure which will be the subject of the last Section.

Table 2. Maximum values of the curvatures of HDPE samples obtained after 16 passes using a 135° die via routes *A* and *C* at $T = \{25^\circ\text{C}, 40^\circ\text{C}, 60^\circ\text{C}\}$

Route	Temperature [°C]	Height before ECAE H_b [mm]	Height after 16 ECAE passes: H_a [mm]	Curvature $Cu = H_a - H_b$ [mm]
<i>A</i>	25	9.85	16.50	6.65
	40	9.87	16.50	6.63
	60	9.80	15.00	5.20
<i>C</i>	25	9.72	13.00	3.28
	40	9.72	13.00	3.28
	60	9.75	12.50	2.75

4. Elastic-viscoplastic constitutive model

The constitutive equations governing the behaviour of polymers under the ECAE process loadings must take into account complex phenomena such as viscoplasticity, hardening, relaxation and strain memory effect. These phenomena were studied by many authors basing on physical (Arruda *et al.*, 1995; Ahzi *et al.*, 2003; Bouaksa *et al.*, 2014) or purely phenomenological (Chaboche, 1997; Ho and Krempl, 2002; Colak, 2003) considerations. In this paper, a phenomenological constitutive model based upon Chaboche's model is applied (Lemaitre and Chaboche, 1994; Ambroziak and Klosowski, 2006). This model incorporates the initial linear response, the non-linear behavior and the rate-dependent yield stress.

4.1. Constitutive equations

One of the fundamental principles that all constitutive equations have to satisfy is the principle of objectivity. Tensor rates used in the constitutive equations need to be objective. A corotational objective rate of a tensor \mathbf{M} is denoted by

$$\widehat{\mathbf{M}} = \dot{\mathbf{M}} + \mathbf{M}\boldsymbol{\Omega} - \boldsymbol{\Omega}\mathbf{M} \quad (4.1)$$

where $\dot{\mathbf{M}}$ is the material rate with respect to the basis of \mathbf{M} . $\widehat{\mathbf{M}}$ is the objective rate of \mathbf{M} , and $\boldsymbol{\Omega}$ is a skew-symmetric spin tensor. A well-known objective rate is the Jaumann rate. It is obtained by setting $\boldsymbol{\Omega} = \mathbf{W}$ in Eq. (4.1)

$$\widehat{\boldsymbol{\sigma}} = \dot{\boldsymbol{\sigma}} + \boldsymbol{\sigma}\mathbf{W} - \mathbf{W}\boldsymbol{\sigma} \quad (4.2)$$

where $\widehat{\boldsymbol{\sigma}}$ is the objective rate of the Cauchy stress tensor $\boldsymbol{\sigma}$ based upon the spin tensor \mathbf{W} .

The strain rate tensor \mathbf{D} is decomposed into an elastic part \mathbf{D}^e and a viscoplastic part \mathbf{D}^{vp} as follows

$$\mathbf{D} = \mathbf{D}^e + \mathbf{D}^{vp} \quad (4.3)$$

The elastic strain rate tensor \mathbf{D}^e is given by the hypoelastic law

$$\mathbf{D}^e = \mathbf{C}^{-1}\widehat{\boldsymbol{\sigma}} \quad (4.4)$$

where \mathbf{C} is the fourth-order isotropic elastic modulus tensor

$$C_{ijkl} = \frac{E}{2(1+\nu)} \left[(\delta_{ik}\delta_{jl} + \delta_{il}\delta_{jk}) + \frac{2\nu}{1-2\nu} \delta_{ij}\delta_{kl} \right] \quad (4.5)$$

with E , ν and δ are respectively Young's modulus, Poisson's ratio and the Kronecker-delta symbol.

The viscoplastic strain rate tensor \mathbf{D}^{vp} can be written by

$$\mathbf{D}^{vp} = \frac{3}{2} \dot{p} \frac{\boldsymbol{\sigma}' - \mathbf{X}'}{J(\boldsymbol{\sigma} - \mathbf{X})} \quad (4.6)$$

where $J(\boldsymbol{\sigma} - \mathbf{X})$ is a distance in the stress space. For a material meeting the Von Mises criterion, we use

$$J(\boldsymbol{\sigma} - \mathbf{X}) = \sqrt{\frac{3}{2}(\boldsymbol{\sigma}' - \mathbf{X}') : (\boldsymbol{\sigma}' - \mathbf{X}')} \quad (4.7)$$

where $\boldsymbol{\sigma}$ and \mathbf{X} are the stress and back stress tensors, and $\boldsymbol{\sigma}' = \boldsymbol{\sigma} - \text{tr}(\boldsymbol{\sigma})/3\mathbf{I}$ and \mathbf{X}' are the stress and back stress deviatoric tensors in the stress space, respectively. \dot{p} is the equivalent viscoplastic strain rate written as

$$\dot{p} = \left\langle \frac{J(\boldsymbol{\sigma} - \mathbf{X}) - R - k}{K} \right\rangle^n \quad (4.8)$$

The brackets are defined by $\langle w \rangle = wH(w)$, where $H(w)$ is the Heaviside function ($H(w) = 0$ if $w < 0$, $H(w) = 1$ if $w \geq 0$). k is the yield stress at zero plastic strain, K is the viscoplastic resistance, n is the rate sensitivity coefficient and R is the isotropic internal stress or the drag stress.

The strain hardening of the material is described by isotropic and kinematic hardening rules which allow both the expansion and translation of the yield.

The isotropic hardening rule is defined by

$$\dot{R} = b(R_1 - R)\dot{p} \quad \text{with} \quad R(0) = 0 \quad (4.9)$$

where R_1 is the boundary of isotropic hardening and b defines the rate at which the size of the yield surface changes as the plastic straining develops.

Equation (4.9) may be replaced by its integrated form as (Lemaitre and Chaboche, 1994)

$$R = R_1[1 - \exp(-bp)] \quad (4.10)$$

The nonlinear kinematic hardening is defined from the linear-Ziegler rule by adding the recall term as shown in the evolution of the back stress tensor below (MSC.Marc, 2005)

$$\dot{\mathbf{X}} = \frac{C}{R + k}(\boldsymbol{\sigma} - \mathbf{X})\dot{p} - \gamma\mathbf{X}\dot{p} \quad \text{with} \quad \mathbf{X}(0) = 0 \quad (4.11)$$

where C and γ are two material constants. $\gamma = 0$ stands for the linear-kinematic rule.

The evolution law given by (4.11) may be formulated in terms of the objective rate of the back stress \mathbf{X} , say $\hat{\mathbf{X}}$, as follows (Bruhns, 2009)

$$\hat{\mathbf{X}} = \mathbf{K}(\boldsymbol{\tau}, \mathbf{X}, \kappa) : \mathbf{D}^{vp} \quad (4.12)$$

where $\mathbf{K}(\boldsymbol{\tau}, \mathbf{X}, \kappa)$ is a 4th order tensor-valued constitutive function, $\boldsymbol{\tau}$ is the Kirchhoff stress and κ is a scalar internal variable.

4.2. Identification of the material parameters

The material parameters ($E, k, K, n, b, R_1, C, \gamma$) of the elastic-viscoplastic constitutive law have been identified from a least-square regression fitting using the experimental data of compression tests on HDPE and PP specimens at room temperature and under different strain rates (Aour, 2007). The values of the identified parameters for the studied polymers are listed in Table 3. Figure 5 shows a fairly good agreement between the identified constitutive model and experimental stress-strain curves of HDPE and PP. Indeed, the constitutive law is able to reproduce three main features of the behaviour: the linear elastic response, the rollover to yield and the post-yield response.

Table 3. Values of material parameters for HDPE and PP

Parameter	Unit	Values for HDPE	Values for PP
E	MPa	500	1100
ν	–	0.38	0.4
k	MPa	10	10
K	MPa	15.6	30.2
n	–	5.2	6.9
b	–	40	65
R_1	MPa	10	18
C	MPa	50	15
γ	–	–1.1	–3.2

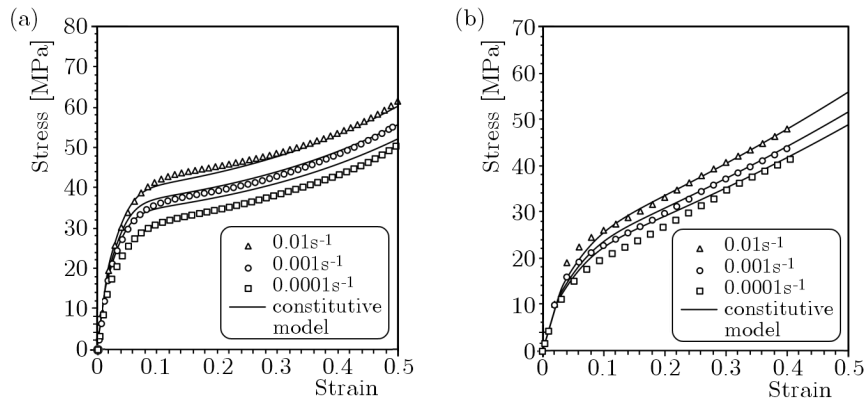


Fig. 5. Stress-strain curves obtained by compression tests and the constitutive model for (a) HDPE and (b) PP at room temperature and different strain rates

5. Finite element results

In order to predict the plastic deformation behaviour of HDPE and PP samples during the ECAE process, finite element simulations have been carried out using the software MSC.Marc© under plane-strain conditions. The die geometry, sample dimensions and processing conditions have been taken similar to those used in the experimental study. The sample has been meshed with 2800 four-node isoparametric elements. The die and the ram have been assumed to be rigid.

5.1. Estimation of the pressing force during ECAE

Figure 6 shows a comparison between the experimental pressing force-ram displacement curves and the finite element results using different friction coefficients for the extrusion of HDPE and PP samples through a 135° die at a ram speed of 0.70 mm/s. The friction conditions between the tooling and the samples are modelled using Coulomb's friction law. As shown in Fig. 6, the FEM results are closer to the experimental data when the friction coefficient is equal to 0.075 for HDPE and 0.025 for PP. It is worth noting that the damage mechanisms, which occur at the elbow of the die (plastic deformation zone), have not been modelled in the present constitutive model. Thus, the comparison is only made for the stage of steady state of the material flow during the ECAE process.

5.2. Estimation of the equivalent plastic strain

Figure 7 shows the equivalent plastic strain contour plots of HDPE and PP samples during the ECAE process with a ram speed of 0.70 mm/s considering the friction coefficients which

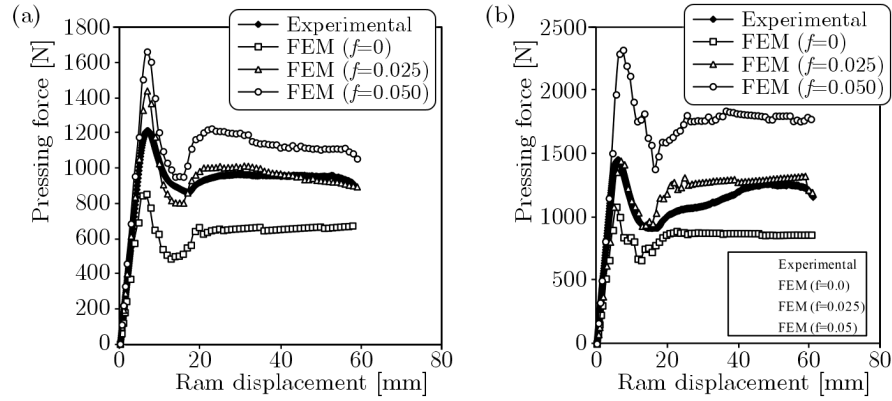


Fig. 6. Comparison between the experimental curve and FEM results using different friction coefficients in the case of (a) HDPE and (b) PP

gave the best agreement with the experimental results, i.e., $f = 0.075$ for HDPE and $f = 0.025$ for PP. It can be observed that the plastic strain is not uniform along width of the samples for both polymers. It should be noted that the effective plastic strain generally decreases from the top surface to the bottom surface of the samples. This can be attributed to the presence of the bending mechanisms since the inner part of the sample flows faster than the outer part. In other words, the deformation mechanism in the bottom region is rather bending than shear. Furthermore, it can be seen that the fronts of the extruded samples have not undergone a high level of plastic deformation. This is mainly due to the filling status of the channel when the sample passed through the elbow.

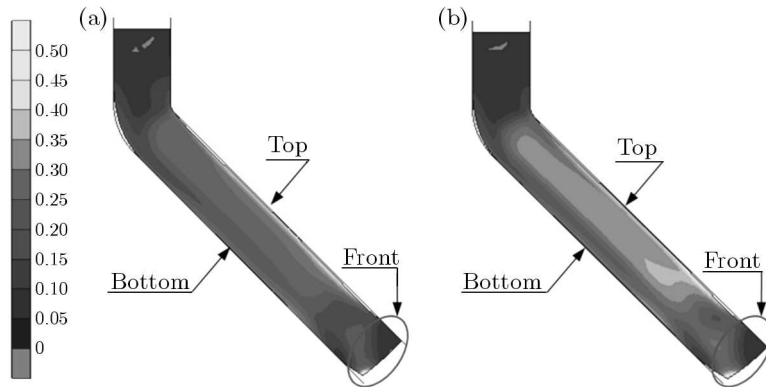


Fig. 7. Equivalent plastic strain contours for ECAE of (a) HDPE and (b) PP samples using a 135° die

In order to quantify the degree of strain homogeneity inside the sample, the distribution of the equivalent plastic strain along the sample width at the steady state region is presented in Fig. 8. It can be seen that the equivalent plastic strain in the PP sample is higher than that of the HDPE sample. However, almost the same degree of strain heterogeneity is obtained for both polymers, since the variation factor is 24% for HDPE and 22% for PP. Noting that the variation factor denoted by V is defined as the ratio of the standard deviation s to the average equivalent plastic strain ε_{ave}^p (Aour *et al.*, 2006)

$$V = \frac{s}{\varepsilon_{ave}^p} = \frac{1}{\varepsilon_{ave}^p} \sqrt{\frac{1}{N} \sum_{i=1}^N (\varepsilon_i^p - \varepsilon_{ave}^p)^2} \cdot 100\% \quad (5.1)$$

where ε_i^p is the equivalent plastic strain value at a given integration point along the sample width, ε_{ave}^p is the arithmetic average of the equivalent plastic strain values computed on N integration points.

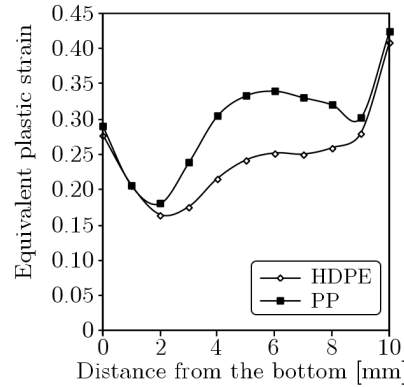


Fig. 8. Distribution of the equivalent plastic strain in HDPE and PP samples extruded by a 135° die

5.3. Equivalent plastic strain rate

It is recognized that the stress-strain behaviour of polymers is strongly dependent on the strain rate due to the viscoplastic nature of polymers (Ward and Hadley, 1995). In order to highlight the spatial variation of the plastic strain and the trends in the degree of homogeneity, the strain rate distribution within the plastic deformation zone (PDZ) is addressed here. Indeed, the more the plastic deformation rate is uniform along the shear plane, the greater is the degree of homogeneity of the plastic deformation into the sample. Figure 9 shows the distribution of the equivalent plastic strain rate $\dot{\epsilon}^p$ at an intermediate stage of the ECAE process using a 135° die for HDPE and PP samples. It can be seen that the distribution of $\dot{\epsilon}^p$ inside the PDZ is neither uniform nor symmetrical with respect to the shear plane, which justifies the heterogeneity of the plastic strain distribution. Furthermore, it can be observed that this later decreases significantly from the inner corner to the outer corner. This aspect can be allotted to the coupled effect of the viscoplastic behaviour and geometrical features of the die.

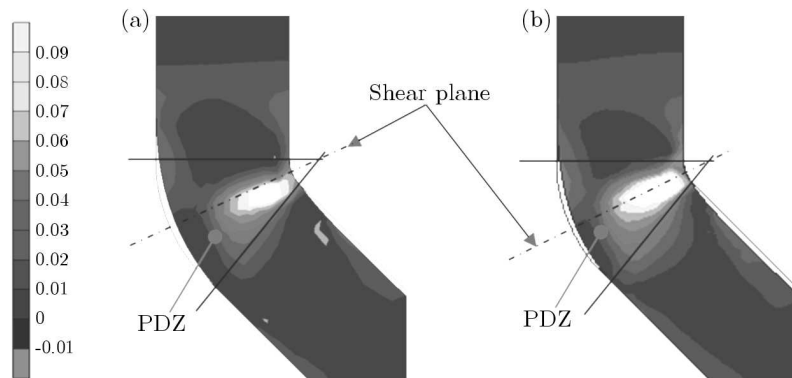


Fig. 9. Distribution of the equivalent plastic strain rate inside (a) HDPE and (b) PP samples during the ECAE process using a 135° die

5.4. Effect of the back-pressure

In order to improve the degree of the plastic strain homogeneity and reduce the warping of the samples, the application of back-pressure seems to be a suitable solution. It consists in applying a constant load to the sample front at the exit channel using a second ram. The obtained results for the equivalent plastic strain distribution along width of the HDPE sample by applying different values of back-pressure are shown in Fig. 10. It can be seen that a significant improvement in plastic strain homogeneity is obtained when the corner angle $\theta = 5^\circ$ and the

back-pressure $P = -500$ N (Fig. 10a), however, when $\theta = 34^\circ$, a slight effect is highlighted (Fig. 10b). Indeed, when $\theta = 5^\circ$, the variation factor is reduced by 11% (from $V_{(P=0\text{N})} = 28\%$ to $V_{(P=-500\text{N})} = 17\%$), however, when $\theta = 34^\circ$, the variation factor is reduced by 4% (from $V_{(P=0\text{N})} = 24\%$ to $V_{(P=-500\text{N})} = 20\%$). Consequently, in order to improve the plastic strain homogeneity, it is advised to use a low outer corner angle with an adequate back-pressure. This allows one to promote shearing deformations and reduction of the bending mechanisms.

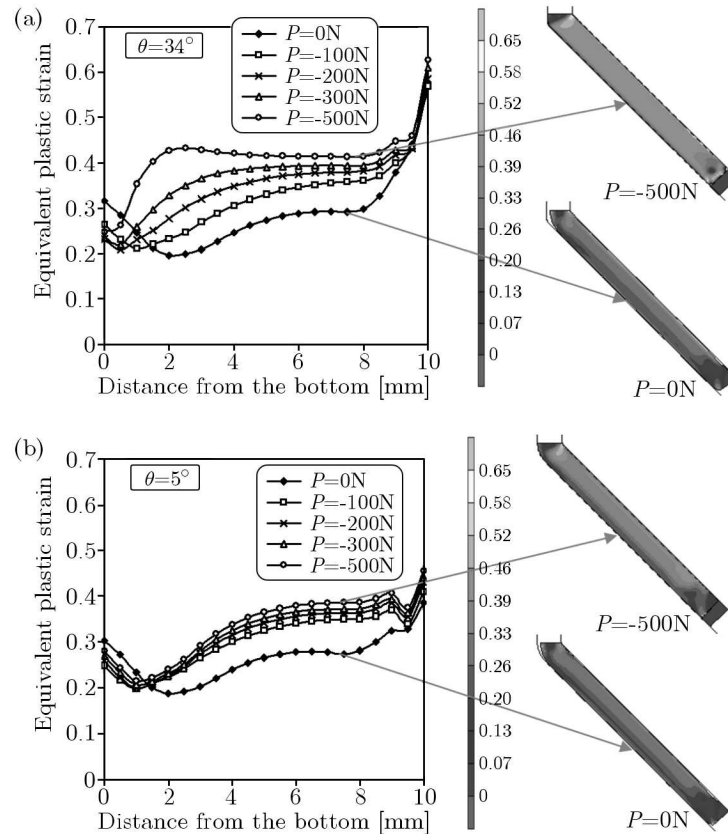


Fig. 10. Effect of back-pressure on the evolution of equivalent plastic strain in the case of a 135° die

6. Conclusion

In this study, the effects of ram speed, processing route, number of passes, temperature and back-pressure on HDPE and PP behaviour during the ECAE process using a 135° die are investigated by experimental testing and finite element modeling. The following conclusions can be drawn:

- It is found that the pressing force required for extrusion increases with an increase in the ram speed, and the pressing force of PP samples is about 200 N higher than that of HDPE.
- For both polymers, the significant reduction of warping is obtained by route C, whereas, the maximum warping is obtained by route A.
- It is found that the pressing force decreases significantly with an increase in temperature, while a slight reduction of warping is observed as the extrusion temperature is increased.
- A good agreement is noticed between the experimental curves and the FEM results when the friction coefficients are equal to 0.075 for HDPE and 0.025 for PP. This allows one to carry out the ECAE process without a lubricant.

- It is found that PP samples display a higher level of plastic strain than HDPE samples. However, almost the same degree of strain heterogeneity is obtained for both polymers.
- The distribution of the equivalent plastic strain rate inside PDZ is found to be neither uniform nor symmetrical about the shear plane.
- It is expected that the use of a low corner angle with an adequate back-pressure can effectively reduce the warping and improve the strain homogeneity as well as the level of shear deformation.

Acknowledgements

The authors thank Profs. Moussa Nait-Abdelaziz, Fahmi Zaïri and Jean-Michel Gloaguen of Polytech'Lille (France) for their assistance in the experimental tests and numerical simulations. The comments from the reviewer are also greatly acknowledged.

References

1. AHZI S., MAKRAZI A., GREGORY R.V., EDIE D.D., 2003, Modelling of deformation behaviour and strain-induced crystallization in poly(ethylene terephthalate) above the glass transition temperature, *Mechanics of Materials*, **35**, 1139-1148
2. AMBROZIAK A., KŁOSOWSKI P., 2006, The elasto-viscoplastic Chaboche model, *Task Quarterly*, **10**, 49-61
3. AOUR B., 2007, Investigation of ECAE process of semicrystalline polymers by a finite element and a coupled boundary element-finite element approach, Doctorate thesis, UST Oran, Algeria
4. AOUR B., ZAÏRI F., GLOAGUEN J.M., NAIT-ABDELAZIZ M., LEFEBVRE J.M., 2006, Numerical investigation on equal channel angular extrusion process of polymers, *Computational Materials Science*, **37**, 491-506
5. AOUR B., ZAÏRI F., NAIT-ABDELAZIZ M., GLOAGUEN J.M., LEFEBVRE J.M., 2009, Finite element analysis of plastic strain distribution in multi-pass ECAE process of high density polyethylene, *Journal of Manufacturing Science and Engineering ASME*, **131**, 031016
6. AOUR B., ZAÏRI F., NAIT-ABDELAZIZ M., GLOAGUEN J.M., RAHMANI O., LEFEBVRE J.M., 2008, A computational study of die geometry and processing conditions effects on equal channel angular extrusion of a polymer, *International Journal of Mechanical Sciences*, **50**, 589-602
7. ARRUDA E.M., BOYCE M.C., JAYACHANDRAN R., 1995, Effects of strain rate, temperature and thermomechanical coupling on the finite strain deformation of glassy polymers, *Mechanics of Materials*, **19**, 193-212
8. BOUAKSA F., OVALLE RODAS C., ZAÏRI F., STOCLET G., NAÏT-ABDELAZIZ M., GLOAGUEN J.M., TAMINE T., LEFEBVRE J.M., 2014, Molecular chain orientation in polycarbonate during equal channel angular extrusion: experiments and simulations, *Computational Materials Science*, **85**, 244-252
9. BRUHNS O.T., 2009, Eulerian elastoplasticity: basic issues and recent results, *Theoretical and Applied Mechanics*, **36**, 167-205
10. CAMPBELL B., EDWARD G., 1999, Equal channel angular extrusion of polyalkenes, *Plastics, Rubber and Composites*, **28**, 467-475
11. CHABOCHE J.L., 1997, Thermodynamic formulation of constitutive equations and application to the visco-plasticity and visco-elasticity of metals and polymers, *International Journal of Solids and Structures*, **34**, 2239-2254
12. COLAK O.U., 2003, Modeling of large simple shear using a viscoplastic overstress model and classical plasticity model with different objective, *Turkish Journal of Engineering and Environmental Sciences*, **27**, 95-106

13. CREASY T.S., KANG Y.S., 2005, Fibre fracture during equal-channel angular extrusion of short fibre-reinforced thermoplastics, *Journal of Materials Processing Technology*, **160**, 90-98
14. HO K., KREMPL E., 2002, Extension of the viscoplasticity theory based on overstress (VBO) to capture non-standard rate dependence in solids, *International Journal of Plasticity*, **18**, 851-872
15. IWAHASHI Y., WANG J., HORITA Z., NEMOTO M., LANGDON T.G., 1996, Principle of ECA pressing for the processing of ultra-fine grained materials, *Scripta Materialia*, **35**, 143-146
16. LEMAITRE J., CHABOCHE J.L., 1994, *Mechanics of Solid Materials*, Cambridge University Press, Cambridge
17. LI C.K.Y., XIA Z.Y., SUE H.J., 2000, Simple shear plastic deformation behaviour of polycarbonate plate. II: Mechanical property characterization, *Polymer*, **41**, 6285-6293
18. SEGAL V.M., 1995, Materials processing by simple shear, *Materials Science and Engineering*, **A197**, 157-164
19. SUE H.J., DILAN HECTOR, LI C.K.Y., 1999, Simple shear plastic deformation behaviour of polycarbonate plate due to the equal channel angular extrusion process. I: Finite element methods modelling, *Polymer Engineering and Science*, **39**, 2505-2515
20. SUE H.J., LI C.K.Y., 1998, Control of orientation of lamellar structure in linear low density polyethylene via a novel equal channel angular extrusion process, *Journal of Materials Science Letters*, **17**, 853-856
21. User handbook, MSC.Marc, Volume A, Version 2005, MSC.Software Corporation
22. VALIEV R.Z., LANGDON T.G., 2006, Principles of equal channel angular pressing as a processing tool for grain refinement, *Progress in Materials Science*, **51**, 881-981
23. WANG Z.G., XIA Z.Y., YU Z.Q., CHEN E.Q., SUE H.J., HAN C.C., HSIAO B.S., 2006, Lamellar formation and relaxation in simple sheared poly(ethylene terephthalate) by small-angle X-ray scattering, *Macromolecules*, **39**, 2930-2939
24. WARD I.M., HADLEY D.W., 1995, *Mechanical Properties of Solid Polymers*, Wiley, New York
25. WEON J.I., CREASY T.S., SUE H.J., HSIEH A.J., 2005, Mechanical behaviour of polymethylmethacrylate with molecules oriented via simple shear, *Polymer Engineering and Science*, **45**, 314-324
26. XIA Z., SUE H.J., HSIEH A.J., 2001a, Impact fracture behaviour of molecularly orientated polycarbonate sheets, *Journal of Applied Polymer Science*, **79**, 2060-2066
27. XIA Z., SUE H.J., HSIEH A.J., HUANG J.W.L., 2001b, Dynamic mechanical behaviour of oriented semi-crystalline polyethylene terephthalate, *Journal of Polymer Science, Part B: Polymer Physics*, **39**, 1394-1403
28. ZAÏRI F., AOUR B., GLOAGUEN J.M., NAÏT-ABDELAZIZ M., LEFEBVRE J.M., 2008, Steady plastic flow of a polymer during ECAE process: experiments and numerical modeling, *Polymer Engineering Sciences*, **18**, 1015-1021

FINITE ELEMENT ANALYSIS OF THE BEHAVIOUR OF A CRACK IN THE ORTHOPEDIC CEMENT

ALI BENOUIS

Djillali Liabes University of Sidi Bel-Abbes, Mechanics and Physics of Materials Laboratory, Larbi Ben Mhidi, Algeria

ABDELKADER BOULENOUAR

Djillali Liabes University of Sidi Bel-Abbes, Mechanical Engineering Department, Laboratory of Materials and Reactive Systems, Larbi Ben Mhidi, Algeria; e-mail: aek_boulenouar@yahoo.fr

BOUALEM SERIER

Djillali Liabes University of Sidi Bel-Abbes, Mechanics and Physics of Materials Laboratory, Larbi Ben Mhidi, Algeria

In this paper, the finite element method is used to analyse the crack behaviour in the orthopedic cement of the total hip replacement by computing the stress intensity factors (SIFs) around the crack tip. In this work, three cases are studied: crack emanating from a cavity, interaction effect of the crack emanating from a cavity with another cavity and the interaction effect of two cracks emanating from two cavities. The stress intensity factors under mixed mode problems at the crack tip are computed for three zones of prosthesis: proximal, median and distal. The obtained results show that the crack initiated from a micro-cavity in the distal zone of cement can be propagated at the same time by opening and shearing of its lips. It is contrary to that initiated in the proximal zone which cannot be propagated. The mechanical behaviour of cracks in the medial zone depends of the crack initiation position.

Keywords: stress intensity factor, crack, cavity, orthopedic cement

1. Introduction

Over estimated 800 000 total hip replacements are being performed worldwide annually (Jasty *et al.* 1991; Leroy 1992). Primary hip arthroplasty is subjected to failure due to the loosening of the implant or the prosthetic cup. 15% of the hip arthroplasty today are revision operations. A successful surgical procedure is developed where a ball-socket structure is used to replace the deceased or damaged hip joint. The replacement cup socket is usually attached to pelvis by acrylic bone cement which consists of a solid component of polymethylmethacrylate (PMMA) powder and a liquid component of monomethylmethacrylate (MMA). After mixing, polymerization takes place and within a few minutes of application to the bone cavity, the mixture becomes solid (Poitout, 1992; Li *et al.*, 2002). The presence of a defect in the cement during mixing can locally lead to a region of stress concentrations producing possible fracture of the cement and consequently the loosening of the prosthetic cup. There are almost three kinds of defects: porosities, inclusions and cracks.

It is known that cracks are the most dangerous defect because of the presence of stress intensity on their front. The majority of cracks identified in the orthopaedic cement are (Hertzler *et al.*, 2002; Bachir Bouiadjra, 2007): cracks initiated at porosities, cracks initiated during cement withdraw and cracks initiated at the junction between the bone and cement or between the cement and cup.

In literature, numerical works have been devoted to study the mechanical behaviour of cracks in the orthopedic cement: Benouis *et al.* (2015) presented numerical modeling of the

crack propagation trajectory in the cement of reconstructed acetabulum. The direction crack was evaluated as a function of the displacement extrapolation technique and the strain energy density theory. Benouis *et al.* (2015) investigated the 3D-FE method to analyse the distribution of equivalent Von Mises stress around a cavity located in the bone cement polymethylmethacrylate (PMMA). The results showed that the micro-porosity located in the proximal and distal zone of the prosthesis was subject to a higher stress field. Sahli *et al.* (2014) studied damage of the orthopedic cement around the micro-cavity and estimated the length of the crack emanating from the microcavity for each position of the human body. The results showed that the damaged area was influenced by the cavity shape. Oshkour *et al.* (2013) investigated the X-FE method to analyze the behaviour of the internal circumferential cracks located in the cement layer of the cement-prosthesis interface during the main phases of the gait cycle. Benbarek *et al.* (2013) presented a numerical analysis of the crack growth path in the cement mantle of the reconstructed acetabulum. The maximal circumferential stresses criterion was used to determine the direction of the crack emanating from a micro-void in the cement layer. Bouziane *et al.* (2013) showed that the stress intensity factor evaluated for a crack emanating from an inclusion was higher than the crack emanating from a cavity. Ouinas *et al.* (2012) used the FEM to analyze the influence of the presence of microvoid and a crack emanating from the microvoid on the fracture behavior of bone cement. Flitti *et al.* (2010) analyzed the propagation criteria of cracks to predict the failure behaviour of cemented hip prostheses under monotonic loading conditions. That analysis was carried out on various zones of the cement along the bone, namely the proximal, the medial and the distal positions. Benbarek *et al.* (2007) investigated the FE method to analyse behaviour of the crack emanating from a microvoid by computing the SIFs at the crack tip. Taylor *et al.* (2003) used analytical and numerical methods to predict damage of the bone.

The use of crack propagation laws based on the stress intensity factor range is the most successful engineering application of fracture mechanics. The stress intensity factors are a very important parameter in fracture analysis. These factors define the stress field close to the crack tip of a crack and provide fundamental information on how the crack is going to propagate. The use of this factor can be an effective tool to analyse the fracture behaviour of cracks in the orthopedic cement.

The aim of this paper is to analyse the behaviour of cracks in the orthopedic cement by computing the SIFs. In this study, three cases are considered: crack emanating from a cavity, crack emanating from a cavity with another cavity and two cracks emanating from two cavities.

1.1. Geometrical model

Figure 1a shows the geometrical model used in this study. A force of 2400 N is applied to the structure as shown in Fig. 1b (Bergmann *et al.*, 1993). The prosthesis is divided into three zones: *proximal*, *median* and *distal* and two parts: *interior* (right part) and *exterior* (left part).

The Finite element standard code ABAQUS V 6.11 (Dassault Systèmes, RI, USA) has been employed for the modeling of the problem. For the mesh generation of our model, the element type 'CPS8R' of ABAQUS code is used. It is a higher order two dimensional, 8-node element having two degrees of freedom at each node (translations in the nodal x and y directions), quadratic displacement behaviour and the capability of forming a triangular-shaped element, which is required at the crack-tip areas (Fig. 2a).

Due to the singular nature of the stress field in the vicinity of the crack, the singular elements, shown in Fig. 2b, are considered at each crack-tip area, which is modeled with a finer mesh.

The model is divided into three regions of different elastic constants with isotropic material properties assumed in each region. The main regions are: implant (Ti-6Al-4V), cement (PMMA)

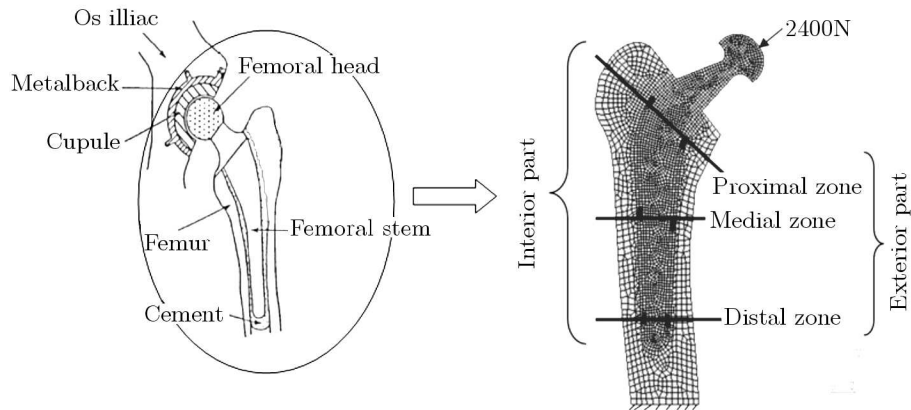


Fig. 1. (a) Geometrical model considered in the study, (b) typical mesh model

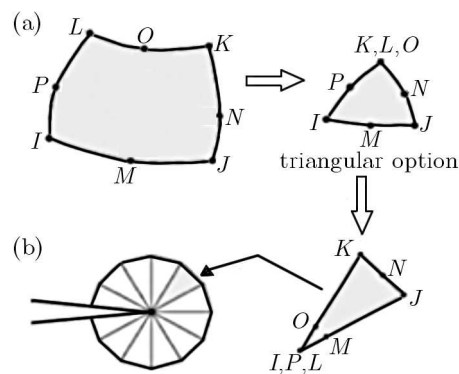


Fig. 2. (a) 'CPS8R' eight-node finite element and (b) singular option

and femoral bone. Table 1 shows the material properties used in this study (Kalapana, 2004; Flitti *et al.*, 2010).

Table 1. Material properties

Material	Young's modulus E [MPa]	Poisson's ratio ν [-]
Implant (Ti-6Al-4 V)	100 000	0.33
Cement (PMMA)	2000	0.25
Femoral bone	20 000	0.25

2. Results and analysis

To analyze the behaviour of cracks in the orthopedic cement, three cases are considered: the crack emanating from a cavity, interaction of the crack emanating from a cavity with another cavity and interaction of two emanating cracks from a cavity (Fig. 3).

2.1. Case I: crack emanating from a cavity

A crack of length a emanating from a circular cavity (with diameter $D = 200 \mu\text{m}$) is supposed to exist in the orthopedic cement for different zones: proximal, medial and distal. Figure 4 shows a typical mesh model of the prosthesis. The stress intensity factors K_I and K_{II} are obtained using the J -integral method. The plane stress state conditions are assumed.

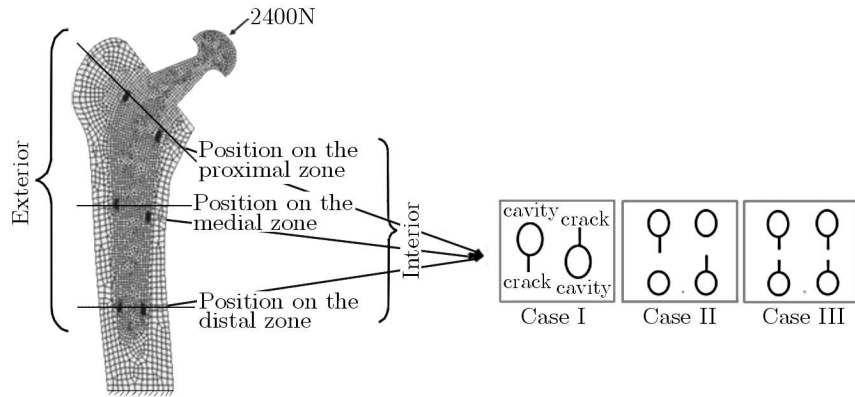


Fig. 3. Schematic representations of various cases: (a) case I: crack emanating from a cavity, (b) case II: crack emanating from a cavity with another cavity, (c) case III: two cracks emanating from two cavities

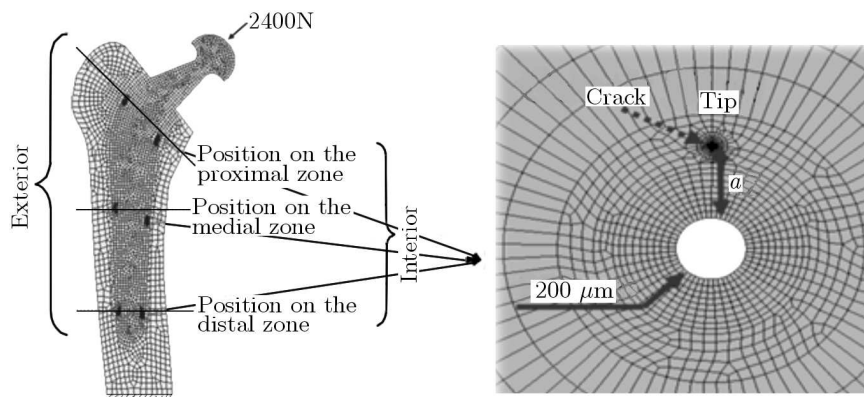


Fig. 4. Crack emanating from a cavity (case I)

Figures 5a and 5b show respectively the variation of mode I and II stress intensity factors (SIF) in function of the crack length for different zones of the prosthesis (proximal, median and distal) and for two parts (interior and exterior).

According to Fig. 5a, it can be seen that the exterior part of the prosthesis is solicited in compression because mode I stress intensity factors are negatives in the different zones (median, distal) except for the zone proximal where mode I SIF is null.

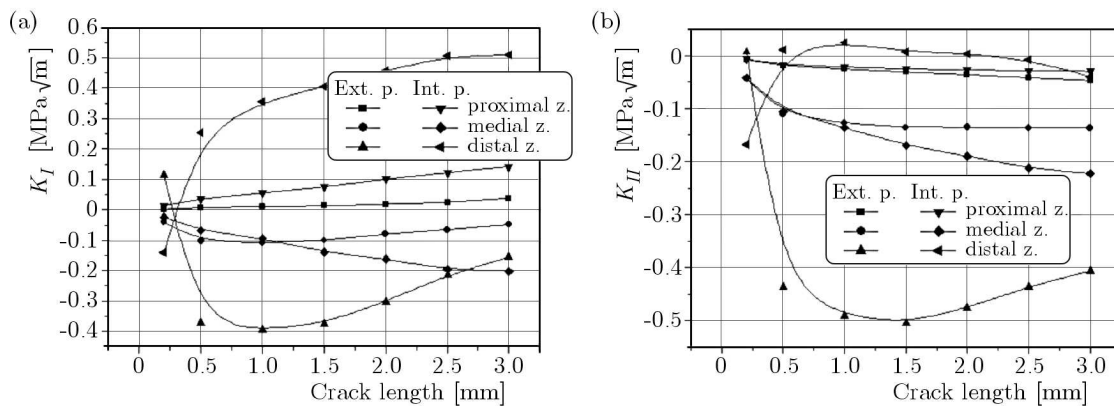


Fig. 5. Variation of SIFs K_I and K_{II} of the crack emanating from a cavity (Case I)

In the interior part, the SIFs K_I increases with the crack length in the distal and medial zones. In fact, the maximal SIFs values are in the distal zone ($0.5 \text{ MPa}\sqrt{\text{m}}$) for a crack length

3 mm. On the other hand, the SIF value in the proximal zone is $0.15 \text{ MPa m}^{1/2}$ for a crack length 3 mm. One notes that the minimal values localized in the medial zone with negative values are $-0.1 \text{ MPa m}^{1/2}$ for a crack size 3 mm. The cement in the distal zone presents the maximal fracture risk of the prosthesis compared to the other zones.

According to Fig. 5b, it can be noted that mode II stress intensity factor (K_{II}) values are null in the distal zone of the interior part for a crack length varied between 0.5 and 2.5 mm. These results indicate that these cracks located in the distal zone can propagate according to the opening mode (mode I) with: $K_I > 0$ and $K_{II} = 0$.

2.2. Case II: interaction effect of the crack emanating from a cavity with another cavity

In this case, a crack of length $a = 0.5 \text{ mm}$ emanating from a circular cavity of diameter $D = 200 \mu\text{m}$ is supposed to exist in the three zones of the prosthesis. Another cavity (of the same diameter D) is located at a distance d from the crack-tip.

The prosthesis is modeled in two dimensions under plane stress conditions using isoparametric quadrilateral CPS8R elements. The crack-tip singularities are modeled using crack-tip elements. The stress intensity factors are calculated using the the J -integral technique. Figure 6 shows a typical mesh model of the prosthesis and the special elements around the crack tip.

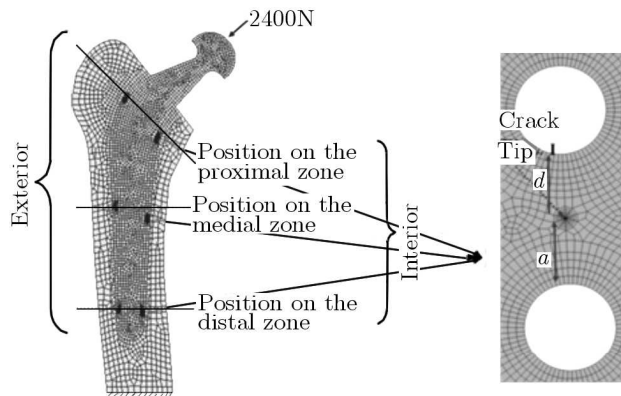


Fig. 6. Crack emanating from a cavity with another cavity (case II)

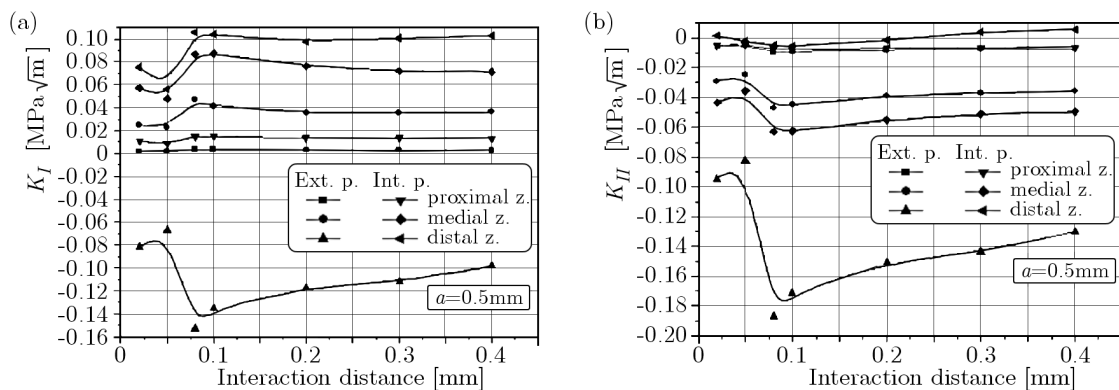


Fig. 7. Variation of SIFs K_I and K_{II} of the crack emanating from a cavity versus the interaction distance d (case II)

The results obtained are illustrated in Figs. 7a and 7b which show the variation of SIFs K_I and K_{II} as a function of the inter-distance d between the tip of the crack emanating from a cavity and the second cavity.

Figure 7a shows that whatever the zone of initiation of the crack (except for the distal zone of the exterior share), SIF K_I is positive. This shows that such a position of the crack leads to the opening of the crack. Indeed, it depends on the intensity of the stress field in which the crack is located. For a distance $d < 0.1$ mm, the SIF increases in a remarkable way. Beyond this distance, the variation of FIC K_I is independent of the distance d . In the distal zone of the exterior part, SIF K_{II} is negative. This shows that when the cavity is distant, the extension risk of the crack per opening is almost null. In Fig. 7b, for $d > 0.1$ mm, the values of SIF K_{II} are independent of the distance d . In the distal zone, this factor increases with an increase in the distance d .

2.3. Case III: interaction effect of two cracks emanating from two cavities

In order to determine the interaction effect of two cracks emanating from a cavity, we choose a crack of length a emanating from a circular cavity of diameter D . Another crack of length a is supposed to emanate from another cavity (of the same diameter D).

In Fig. 8, a and a' are the lengths of two cracks. The inter-distance between the two cracks is given by the parameter d .

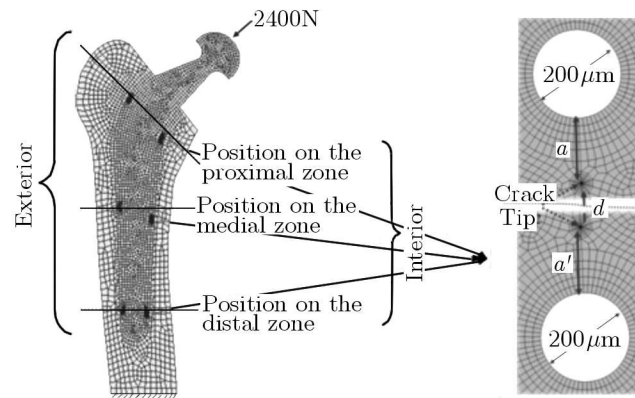


Fig. 8. Two cracks emanating from two cavities (case III)

Figures 9a and 9b show respectively modes I and II stress intensity factors (SIF) of the main crack emanating from a cavity as a function of the distance d between the two cracks tips. The SIFs K_I and K_{II} are evaluated for three zones of prosthesis (proximal, median and distal) and for two parts (interior and exterior).

The results obtained in Fig. 9a show that:

- For distance $d < 0.1$ mm, the SIF K_I increases with reduction in the distance d . This increase is observed in the three zones of the prosthesis, except for the proximal zone of the exterior part (where mode I SIF is null) and in the distal zone of the exterior part (where mode I SIF is negative). The negative values of K_I indicate that the distal zone is solicited in compression.
- The important values of K_I are observed in the distal zone of the interior part, for $d \approx 0.1$ mm. In all the zones, these values are stabilized for $d > 0.2$ mm.

In linear elastic fracture mechanics (LEFM), positive and negative values of K_{II} indicate the direction of crack propagation. This direction is opposite to the sign of K_{II} (Souiyah *et al.*, 2012; Alshoaibi Abdulnaser and Ariffin, 2008). In Fig. 9b, the important values of K_{II} (absolute values) are observed in the distal zone of the interior part, for $d \approx 0.1$. Beyond this distance, the values of K_{II} (absolute values) decrease until the distance $d = 0.2$ mm is reached. For $d > 0.2$ mm, the SIFs K_{II} takes stable values.

The negative values of K_{II} (with $K_I < 0$) indicate that the distal zone of the interior part is solicited in compression.

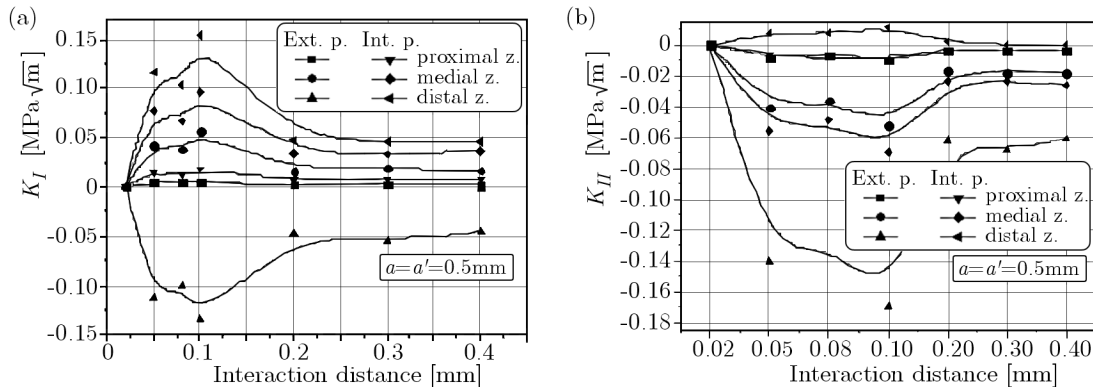


Fig. 9. Variation of SIFs K_I and K_{II} of the main crack emanating from two cavities versus the distance d between two cracks (case III)

3. Conclusion

The predicted values of SIFs for cracks behaviour in the orthopedic cement using the 2D finite element method are presented. In order to obtain a better approximation of the stress field near the crack tip, special quarter point finite elements are used. The analysis of the results obtained shows that a crack initiated from a micro-cavity or from bone debris in the distal zone of the external and interior parts of the cement can be propagated at the same time by opening and shearing of its lips; i.e. under mixed modes. It is contrary to the crack initiated in the proximal zone, which cannot be propagated. The mechanical behaviour of cracks in the medial zone depends on the crack initiation position.

References

1. ABAQUS V 6-11, User Guide, Cornell University, 2004
2. ALSHOAIBI ABDULNASER M., ARIFFIN A.K., 2008, Fatigue life and crack path prediction in 2D structural components using an adaptive finite element strategy, *International Journal of Mechanical and Materials Engineering*, **3**, 1, 97-104
3. BACHIR BOUIADJRA B., BELARBI A., BENBAREK S., ACHOUR T., SERIER B., 2007, FE analysis of the behaviour of microcracks in the cement mantle of reconstructed acetabulum in the total hip prosthesis, *Computational Materials Science*, **40**, 485-491
4. BENBAREK S., BACHIR BOUIADJRA B., ACHOUR T., BELHOUARI M., SERIER B., 2007, Finite element analysis of the behaviour of crack emanating from microvoid in cement of reconstructed acetabulum, *Materials Science and Engineering A*, **457**, 385-391
5. BENBAREK S., BACHIR BOUIADJRA B., BOUZIANE M.M., ACHOUR T., SERIER B., 2013, Numerical analysis of the crack growth path in the cement mantle of the reconstructed acetabulum, *Materials Science and Engineering C*, **33**, 543-549
6. BENOUIS A., BOULENOUAR A., BENSEDDIQ N., SERIER B., 2015, Numerical analysis of crack propagation in cement PMMA: application of SED approach, *Structural Engineering and Mechanics*, **55**, 93-109
7. BENOUIS A., SERIER B., BENBAREK S., 2015, Influence of porosity on the behaviour of cement orthopaedic of total hip prosthesis, *Advances in Biomechanics and Applications*, **2**, 1, 1-10

8. BERGMANN G., GRAICHEN F., ROHLMANN A., 1993, Hip joint loading during walking and running, measured in two patients, *Journal of Biomechanics*, **26**, 969-990
9. BOUZIANE M.M., BACHIR BOUIADJRA B., BENSEDDIQ N., TABETI E.M.H., SERIER B., BENBAREK S., 2013, The effects of cracks emanating from micro-void and bone inclusion in cemented total hip replacement, *Advances in Bio-Mechanical Systems and Materials, Advanced Structured Materials*, Books, Springer
10. FLITTI A., OUINAS D., BACHIR BOUIADJRA B., BENDERDOUCHE N., 2010, Effect of the crack position in the cement mantle on the fracture behaviour of the total hip prosthesis, *Computational Materials Science*, **49**, 598-602
11. HERTZLER J., MILLER M.A., MANN K.A., 2002, Fatigue crack growth rate does not depend on mantle thickness: an idealized cemented stem construct under torsional loading, *Journal of Orthopaedic Research*, **20**, 676-682
12. JASTY M., MALONEY W.J., BRAGDON, C.R. O'CONNOR D.O., HAIRE T., HARRIS W.H., 1991, The initiation of failure in cemented femoral components of hip arthroplasties, *Journal of Bone and Joint Surgery*, **73**, 551-558
13. KALPANA S.K., 2004, Biomaterials in total joint replacement, *Colloids and Surfaces B: Biointerfaces*, **39**, 133-142
14. LEROY R., 1991, Etude et comportement non-uniforme de l'interface entre implant Fémorale et liant polymérique dans le cas de prothèse totale de hanche, Thèse de doctorat, Université Tours
15. LI C., GRANGER C., DEL SCHUTTTE H.R., BIGGERS S.B. JR., KENNEDY J.M., LATOUR R.A., 2002, Progressive failure analysis of laminated composite femoral prostheses for total hip arthroplasty, *Journal of Biomaterials*, **23**, 4249-4262
16. OSHKOUR A.A., DAVOODI M.M., ABU OSMAN N.A., YAU Y.H., TARLOCHAN F., WAN ABAS W.A.B., 2013, Finite element analysis of circumferential crack behavior in cement-femoral prosthesis interface, *Materials and Design*, **49**, 96-102
17. OUINAS D., FLITTI A., SAHNOUN M., BENBAREK S., TAGHEZOUT N., 2012, Fracture behavior of the cement mantle of reconstructed acetabulum in the presence of a microcrack emanating from a microvoid, *International Journal of Materials Engineering*, **2**, 90-104
18. POITOUT D., 1992, *Biomécanique orthopédique*, Editions Masson
19. SAHLI A., BENBAREK S., BACHIR BOUIADJRA B., BOUZIANE M.M., 2014, Effects of interaction between two cavities on the bone cement damage of the total hip prosthesis, *Mechanics and Mechanical Engineering*, **18**, 2, 107-120
20. SOUIYAH M., MUCHTAR A., ARIFFIN A.K., MALEK A., FADHEL M.I., BASEM ABU ZNEID, 2012, Finite element model of crack growth under mixed mode loading, *International Journal of Materials Engineering*, **2**, 67-74
21. TAYLOR D., HAZENBERG J.G., LEE T.C., 2003, The cellular transducer in damage-stimulated bone remodelling: a theoretical investigation using fracture mechanics, *Journal of Theoretical Biology*, **225**, 65-75

GUIDED WAVE PROPAGATION IN THERMAL MEDIA THROUGH THE SEMI ANALYTICAL FINITE ELEMENT METHOD

FAKER BOUCHOUCHA, SONDA CHAABANE

National School of Engineers of Sfax, Unit of Dynamics of the Mechanical Systems, Sfax, Tunisia
e-mail: fakerbouchoucha@yahoo.fr; sonda.chaabene@ec-lyon.fr

MOHAMED NAJIB ICHCHOU

Ecole Centrale de Lyon, Laboratory of Tribology and Dynamics of Systems (LTDS), Lyon, France
e-mail: mohamed.ichchou@ec-lyon.fr

MOHAMED HADDAR

National School of Engineers of Sfax, Unit of Dynamics of the Mechanical Systems, Sfax, Tunisia
e-mail: mohamed.haddar@enis.rnu.tn

In this paper, the issue of the estimation of wave propagation characteristics in thermal media is dealt with. A formulation, named the Thermal Semi Analytical Finite Element, based on the semi analytical finite element approach coupled with the thermal effect is offered. Temperature variations affect the mechanical properties of the waveguide. The question of dispersion curves and group velocities is studied. This study is expected to be of use in the sensitivity analysis of guided waves for wave propagation in thermal environment. Comparisons between numerical and analytical results are given to show the effectiveness of the proposed approach.

Keywords: semi analytical finite element, thermal media, dispersion, velocity

1. Introduction

Guided waves are still a subject of intensive research in several engineering areas. This research focuses on the study of guided wave properties and applications. Structural Health Monitoring (SHM) and Non Destructive Testing (NDT) are among the fields of application of this numerical tool. To study wave propagation in structural waveguides, the semi analytical finite element (SAFE) method has been investigated by many researchers. Hayashi *et al.* (2003) derived the SAFE formulation through virtual work principles and proposed a way to calculate the group velocity using the eigensolution at a given frequency. Damljanovic and Weaver (2004) developed linear triangular elements for the SAFE method using Lagrange's equations to investigate elastic waves in waveguides of arbitrary cross-section. Gavric (1995) calculated the dispersion relationship in a free rail by using triangular and quadrilateral elements obtained from Hamilton's principle. The SAFE method was also adopted to investigate wave propagation characteristics for thin-walled structures by Finnveden (2004), where the polynomial interpolation was used in the propagation axis thus leading to polynomial eigenvalue problems. The method was extended to curved structures by Finnveden and Fraggstead (2008), where isoparametric elements were used.

In the current work, the semi analytical numerical method that may be used for wave propagation and dynamic analysis of waveguide structures is presented. The basic formulations are investigated to illustrate the merits and shortcomings of the method through the virtual work principle.

The effect of temperature on guided wave structural health monitoring has been studied by several authors in the literature, see e.g. Konstantinidis *et al.* (2006). They attempted to correlate modal properties with temperature and also to develop system identification models that could separate the influences of temperature from true indications of damage on dynamic modal parameters (Alashti and Kashiri, 2010). Their research effort extensively examined the causes of the effects of temperature and how they affect dynamic characteristics in a normal real-life of a beam. Some authors have been interested in studying the impact of thermal loading on the guided waves mode shape. A useful research was reported on isotropic beams, plates and shells. Jeyaraj *et al.* (2009) studied the vibration and acoustic response of a composite plate in thermal environment. Kadoli and Ganesan (2006) studied the dynamic behavior of composite and isotropic cylindrical shells with PZT layers under axisymmetric temperature variation.

In this work, the effect of temperature on the wave propagation is studied through the proposed approach, named the thermal semi analytical finite element (TSAFE) method. Indeed, we combine the semi analytical finite element method with thermal treatment to show the effect of temperature on the characteristics of guided wave propagation.

Temperature variations affect various mechanical properties of the structure such as elasticity modulus, density, etc. The modelling of the structure under thermal environment is still a subject of intensive research in several engineering areas. Experimental and theoretical results are offered in many researches to study the material behaviour following thermal variability and evaluate the high-temperature thermal and mechanical properties of the material (Kodur *et al.*, 2012; Li *et al.*, 2013).

The origin of this work is the treatment of wave characteristics (dispersion curves and group velocity) as a function of temperature in order to study the thermal effect on the semi analytical finite element method together with analytical and numerical validations.

2. Description of the Thermal Semi Analytical Finite Element (TSAFE) method

In this Section, we introduce the TSAFE method that may be used for wave propagation and dynamic analysis of waveguide structures in the presence of the thermal effect. Consider a structural waveguide with a uniform cross section. Under thermal environment, the weak form based on the virtual work principle for the dynamic problem may be written as (Hayashi *et al.*, 2003; Gavric 1995)

$$W^e(u^*, u, T) = \int_V \langle \boldsymbol{\varepsilon}_{def}^*(T) \rangle \boldsymbol{\sigma}(T) dv + \int_V \langle \mathbf{u}^* \rangle \rho(T) \ddot{\mathbf{u}} dv = W_{int}(T) - W_{ext}(T) = 0 \quad (2.1)$$

where W^e is the thermal virtual work of the internal forces, T is temperature, $\rho(T)$ is density at temperature T , $*$ denotes virtual quantities, $\boldsymbol{\varepsilon}_{def}(T) = [\varepsilon_{xx}(T), \varepsilon_{yy}(T), \varepsilon_{zz}, 2\varepsilon_{xy}(T), 2\varepsilon_{yz}(T), 2\varepsilon_{xz}(T)]^T$ is the strain vector at temperature T , $\mathbf{u} = [u_x, u_y, u_z]^T$ is the displacement field, $\boldsymbol{\sigma}(T) = [\sigma_{xx}(T), \sigma_{yy}(T), \sigma_{zz}(T), \sigma_{xy}(T), \sigma_{yz}(T), \sigma_{xz}(T)]^T$ is the stress vector at temperature T . $W_{int}(T) = \int_V \langle \boldsymbol{\varepsilon}_{def}^*(T) \rangle \boldsymbol{\sigma}(T) dv$ and $W_{ext}(T) = - \int_V \langle \mathbf{u}^* \rangle \rho(T) \ddot{\mathbf{u}} dv$ are the internal and external virtual work at temperature T , respectively. The harmonic waves in a uniformly cross-sectioned waveguide are described by the orthogonal function $\exp(j\omega t - jkx)$, where k is the wave number in the x direction, ω is the circular frequency. The displacement function can be $u(x, y, z, t) = u(y, z) \exp(j\omega t - jkx)$, where $u(y, z)$ describes the amplitudes of the displacements of the waveguide cross-section. Thus the strain-displacement relationship $\boldsymbol{\varepsilon}_{def}(T) = \mathbf{D}(T)\mathbf{u}$, where $\mathbf{D}(T)$ is a differential operator in the presence of the thermal effect, becomes

$$\boldsymbol{\varepsilon}_{def}(T) = \mathbf{D}_0(T) + k\mathbf{D}_1\mathbf{u} \quad (2.2)$$

Similar to the standard FE method, the natural coordinates can be employed to facilitate the use of the standard Gauss integration formulas. The same shape functions are employed to specify the relation between the global (x, y) and local (ζ, η) coordinate systems. By inserting the interpolation of the displacement functions in the strain-displacement relationship, we obtain

$$\boldsymbol{\varepsilon}_{def}(T) = \mathbf{D}(T)\mathbf{N}\mathbf{u}_i \quad (2.3)$$

where $\mathbf{u}_i = [u_{x_i}, u_{y_i}, u_{z_i}]^T$ is the displacement vector of the finite element, \mathbf{N} is the matrix of the element shape functions.

The relationship between the strain and the stress vectors can be given in the following manner

$$\boldsymbol{\sigma}(T) = \mathbf{C}(T)\boldsymbol{\varepsilon}_{def}(T) \quad (2.4)$$

where $\mathbf{C}(T)$ is the material stiffness matrix at temperature T .

The external virtual work at temperature T can be developed as follows

$$W_{ext}(T) = \langle \mathbf{u}_i^* \rangle \mathbf{M}^e(T) \ddot{\mathbf{u}}_i \quad (2.5)$$

where $\mathbf{M}^e(T)$ is the mass matrix at temperature T , which can be given as

$$\mathbf{M}^e(T) = \int_{\Omega^e} \rho(T) \mathbf{N}^T \mathbf{N} d\Omega^e \quad (2.6)$$

where Ω^e denotes the element domain.

The internal thermal virtual work can be developed as

$$W_{int}(T) = \langle \mathbf{q}_i^* \rangle \mathbf{K}^e(T) \mathbf{q}_i \quad (2.7)$$

where $\mathbf{K}^e(T)$ is the stiffness matrix at temperature T , which can be written as

$$\mathbf{K}^e(T) = \int_{\Omega^e} \mathbf{N}^T [\mathbf{D}(T)]^T \mathbf{C}(T) \mathbf{D}(T) \mathbf{N} d\Omega^e \quad (2.8)$$

Introducing equation (2.2) into equation (2.8) leads to

$$\mathbf{K}^e(T) = \int_{\Omega^e} \mathbf{N}^T [\mathbf{D}_0(T) + k\mathbf{D}_1]^T \mathbf{C}(T) [\mathbf{D}_0(T) + k\mathbf{D}_1] \mathbf{N} d\Omega^e \quad (2.9)$$

Then

$$\mathbf{K}^e(T) = \mathbf{K}_0^e(T) + k\mathbf{K}_1^e(T) + k^2\mathbf{K}_2^e(T) \quad (2.10)$$

where

$$\begin{aligned} \mathbf{K}_0^e(T) &= \int_{\Omega^e} \mathbf{N}^T \mathbf{D}_0^T(T) \mathbf{C}(T) \mathbf{D}_0(T) \mathbf{N} d\Omega^e \\ \mathbf{K}_1^e(T) &= \int_{\Omega^e} \mathbf{N}^T \mathbf{D}_1^T \mathbf{C}(T) \mathbf{D}_0(T) \mathbf{N} d\Omega^e + \int_{\Omega^e} \mathbf{N}^T \mathbf{D}_0^T(T) \mathbf{C}(T) \mathbf{D}_1 \mathbf{N} d\Omega^e \\ \mathbf{K}_2^e(T) &= \int_{\Omega^e} \mathbf{N}^T \mathbf{D}_1^T \mathbf{C}(T) \mathbf{D}_1 \mathbf{N} d\Omega^e \end{aligned} \quad (2.11)$$

The assembly of the element matrices and vectors leads to the governing equation of motion of the waveguide in the presence of the thermal effect

$$[\mathbf{K}_0(T) - \omega^2 \mathbf{M}(T) + k \mathbf{K}_1(T) + k^2 \mathbf{K}_2(T)] \boldsymbol{\varphi} = \mathbf{0} \quad (2.12)$$

where $\boldsymbol{\varphi}$ denotes the nodal displacement vector.

Suppose $\boldsymbol{\varphi}_1$ and $\boldsymbol{\varphi}_2$ denote the eigenvectors associated to k and $-k$, respectively. From the equation of motion, we have

$$\begin{aligned} [\mathbf{K}_0(T) - \omega^2 \mathbf{M}(T) + k \mathbf{K}_1(T) + k^2 \mathbf{K}_2(T)] \boldsymbol{\varphi}_1 &= \mathbf{0} \\ [\mathbf{K}_0(T) - \omega^2 \mathbf{M}(T) - k \mathbf{K}_1(T) + k^2 \mathbf{K}_2(T)] \boldsymbol{\varphi}_2 &= \mathbf{0} \end{aligned} \quad (2.13)$$

The linearization of the equation of motion can be given in the following form

$$\begin{bmatrix} \mathbf{K}_1(T) & \mathbf{K}_0(T) - \omega^2 \mathbf{M}(T) \\ \mathbf{K}_0(T) - \omega^2 \mathbf{M}(T) & 0 \end{bmatrix} \begin{Bmatrix} k \phi_1 \\ \phi_2 \end{Bmatrix} + k^2 \begin{bmatrix} 0 & \mathbf{K}_2(T) \\ \mathbf{K}_2(T) & \mathbf{K}_1(T) \end{bmatrix} \begin{Bmatrix} k \phi_1 \\ \phi_2 \end{Bmatrix} = \mathbf{0} \quad (2.14)$$

where $\phi_1 = \boldsymbol{\varphi}_1 + \boldsymbol{\varphi}_2$ and $\phi_2 = \boldsymbol{\varphi}_1 - \boldsymbol{\varphi}_2$.

The linearized equation of motion presents the eigenvalue problem of the system

$$[\mathbf{A}(T) - \lambda \mathbf{B}(T)] \boldsymbol{\phi} = \mathbf{0} \quad (2.15)$$

where $\boldsymbol{\phi} = [k \phi_1, \phi_2]^T$, $\lambda = k^2$ and

$$\mathbf{A}(T) = \begin{bmatrix} \mathbf{K}_1(T) & \mathbf{K}_0(T) - \omega^2 \mathbf{M}(T) \\ \mathbf{K}_0(T) - \omega^2 \mathbf{M}(T) & 0 \end{bmatrix} \quad \mathbf{B}(T) = - \begin{bmatrix} 0 & \mathbf{K}_2(T) \\ \mathbf{K}_2(T) & \mathbf{K}_1(T) \end{bmatrix}$$

The resolution of this eigenvalue problem leads to calculation of thermal characteristics of the travelling waves.

It can be of interest, in many applicative engineering cases, to consider the wave numbers and velocities and to provide the dispersion curves. Indeed, from the knowledge of the eigenvalue, the wave numbers at temperature T can be extracted as follows

$$k(T) = \pm \sqrt{\lambda(T)} \quad (2.16)$$

And the group velocities can be written as

$$Cg(T) = \frac{\partial \omega}{\partial k(T)} \quad (2.17)$$

3. Numerical results and discussion

In this Section, numerical results are presented and discussed in order to study the efficiency of the proposed method as a tool for guided wave propagation under thermal environment. The numerical simulations are treated using the software MATLAB.

3.1. Validation of the TSAFE method

In this Section, we study the case of a longitudinal wave in order to validate the TSAFE formulation by comparisons with the analytical results. The waveguide is assimilated to the beam element with 2 nodes and 1 dof per node. The used material is steel ($\rho = 7800 \text{ kg/m}^3$, $\nu = 0,3$, $E = 2 \cdot 10^{11} \text{ Pa}$).

The thermal mass and stiffness matrices for the traction compression mode are

$$\mathbf{M}^{tract-comp} = \frac{\rho S d}{6} \begin{bmatrix} 2 & 1 \\ 1 & 2 \end{bmatrix} \quad \mathbf{K}^{tract-comp} = \frac{ES}{d} \begin{bmatrix} 1 & -1 \\ -1 & 1 \end{bmatrix} \quad (3.1)$$

where E is Young's modulus, S is cross section area, ρ is mass density and d is length of the considered element.

Experimental and theoretical results are offered in many researches works on the behaviour of mechanical properties in the presence of thermal environment. The variation of Young's modulus of steel in the temperature range [25^{circ}C - 1000^{circ}C] can be estimated as follows (French Standard, 2007)

$$\frac{E(T)}{E} = 1 + \frac{T}{2000 \log \frac{T}{1100}} \quad (3.2)$$

where $E(T)$ is Young's modulus at temperature T .

The thermal elongation of steel can be governed through the following equation

$$\frac{d(T)}{d} = 1 + \alpha \Delta T \quad (3.3)$$

where α is the linear thermal expansion coefficient ($\alpha_{steel} = 1.27 \cdot 10^{-5} \text{K}^{-1}$), $d(T)$ is length of the structure at temperature T , ΔT is the temperature variation.

The effect of the thermal gradient on density can be given as follows

$$\frac{\rho(T)}{\rho} = \frac{1}{1 + \gamma \Delta T} \quad (3.4)$$

where $\gamma = 3\alpha$ is the volumetric thermal expansion and $\rho(T)$ is the density at temperature T .

In the presence of the thermal effect, the mass and stiffness matrices, for the longitudinal mode, can be given as follows

$$\begin{aligned} \mathbf{M}^{tract-comp}(T) &= \frac{\rho(T) S d(T)}{6} \begin{bmatrix} 2 & 1 \\ 1 & 2 \end{bmatrix} = \frac{(1 + \alpha \Delta T) \rho S d}{(1 + \gamma \Delta T) 6} \begin{bmatrix} 2 & 1 \\ 1 & 2 \end{bmatrix} \\ \mathbf{K}_0^{tract-comp}(T) &= \frac{E(T) S}{d(T)} \begin{bmatrix} 1 & -1 \\ -1 & 1 \end{bmatrix} = \frac{T + 2000 \log \frac{T}{1100}}{2000(1 + \alpha \Delta T) \log \frac{T}{1100}} \frac{ES}{d} \begin{bmatrix} 1 & -1 \\ -1 & 1 \end{bmatrix} \\ \mathbf{K}_1^{tract-comp} &= \left(1 + \frac{T}{2000 \log \frac{T}{1100}}\right) \frac{1}{1 + \alpha \Delta T} \frac{ES}{2d} \begin{bmatrix} 1 & 0 \\ 0 & -1 \end{bmatrix} \\ \mathbf{K}_2^{tract-comp} &= -\left(1 + \frac{T}{2000 \log \frac{T}{1100}}\right) \frac{ES}{3d} \begin{bmatrix} 1 & 1/2 \\ 1/2 & 1 \end{bmatrix} \end{aligned} \quad (3.5)$$

The numerical accuracy and the computational efficiency of the TSAFE method can be demonstrated by comparison with the analytical results given, for the longitudinal mode, in the following form

$$k_{analytical\ tract-comp}(T) = \omega \sqrt{\frac{\rho(T)}{E(T)}} = \omega \sqrt{\frac{\rho}{E}} \sqrt{\frac{2000 \log \frac{T}{1100}}{(1 + \gamma \Delta T) (T + 2000 \log \frac{T}{1100})}} \quad (3.6)$$

Figure 1 illustrates variation of the wave number according to temperature for the longitudinal mode. The thermal effect is treated at different frequencies to study the influence of the coupling phenomenon between the temperature and frequency. The temperature elevation causes a small

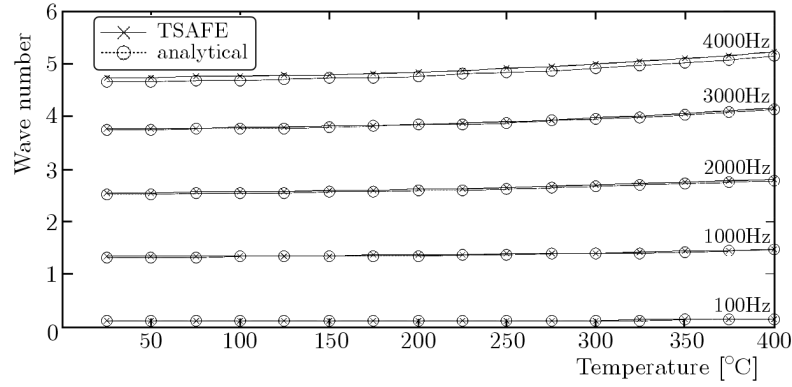


Fig. 1. Thermal dispersion curves for the longitudinal mode

increase in the dispersion curves. This increase is cleared at a high frequency. A good concordance is shown between the TSAFE and analytical results in the domain of the study.

The group velocity is generally used to study the dispersive behavior of the traveling mode. Figure 2 shows the evolution of the group velocity for the traction compression mode according to temperature at $f = 3500$ Hz. The wave velocity decreases with temperature.

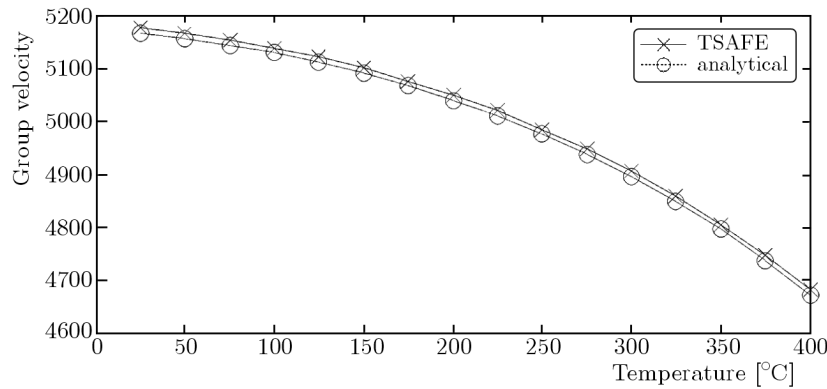


Fig. 2. Thermal group velocity for the longitudinal mode ($f = 3500$ Hz)

3.2. Multimodal propagation through the TSAFE method

In this Section, the TSAFE method is generalized for multimodal propagation to study the temperature effect on the traveling modes such as longitudinal, torsional, flexural and cross sectional modes. The simulation of the dispersion curves and the group velocities of wave propagation in a cylindrical pipe under thermal environment are the objective of this Subsection.

The TSAFE method is applied through the cylindrical pipe (Fig. 3). The used material is steel. We use a surface element with 4 nodes that include 2 dof per node.

The material stiffness matrix at temperature T can be written using the cylindrical coordinate space as

$$\mathbf{C}(T) = \frac{E(T)}{(1+\nu)(1-2\nu)} \begin{bmatrix} 1-\nu & \nu & 0 \\ \nu & 1-\nu & 0 \\ 0 & 0 & (1-2\nu)/2 \end{bmatrix} \quad (3.7)$$

The displacement field through the cylindrical coordinate is

$$u(r, \theta, z, t) = u(r, \theta) \exp[j(\omega t - kz)] \quad (3.8)$$

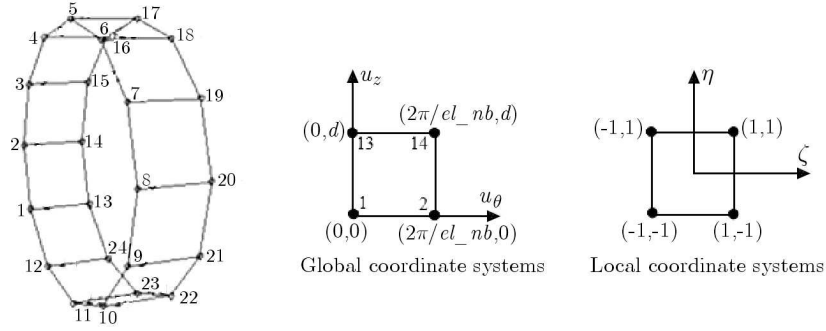


Fig. 3. Substructure of cylindrical pipe

The strain-displacement relationship can be written in the following form

$$\varepsilon_{def} = \mathbf{D}\mathbf{u}(r, \theta, z, t) \quad (3.9)$$

In the presence of thermal environment, the differential operator $\mathbf{D}(T)$ at temperature T is written as

$$\begin{aligned} \mathbf{D}(T) &= \begin{bmatrix} \frac{1}{r(T)} \frac{\partial}{\partial \theta} & 0 \\ 0 & \frac{\partial}{\partial z} \\ \frac{\partial}{\partial z} & \frac{1}{r(T)} \frac{\partial}{\partial \theta} \end{bmatrix} = \frac{1}{1 + \alpha \Delta T} \begin{bmatrix} \frac{1}{r} \frac{\partial}{\partial \theta} & 0 \\ 0 & 0 \\ 0 & \frac{1}{r} \frac{\partial}{\partial \theta} \end{bmatrix} + k \begin{bmatrix} 0 & 0 \\ 0 & -j \\ -j & 0 \end{bmatrix} \\ &= \frac{1}{1 + \alpha \Delta T} \mathbf{D}_0 + k \mathbf{D}_1 \end{aligned} \quad (3.10)$$

The stiffness matrices at temperature T can be given in the following equations

$$\begin{aligned} \mathbf{K}_0^e(T) &= \left(1 + \frac{T}{2000 \log \frac{T}{1100}}\right) \frac{1}{(1 + \alpha \Delta T)^2} \int_{\Omega^e} \mathbf{N}^T \mathbf{D}_0^T \mathbf{C} \mathbf{D}_0 \mathbf{N} \, d\Omega^e \\ \mathbf{K}_1^e(T) &= \left(1 + \frac{T}{2000 \log \frac{T}{1100}}\right) \frac{1}{1 + \alpha \Delta T} \left(\int_{\Omega^e} \mathbf{N}^T \mathbf{D}_1^T \mathbf{C} \mathbf{D}_0 \mathbf{N} \, d\Omega^e + \int_{\Omega^e} \mathbf{N}^T \mathbf{D}_0^T \mathbf{C} \mathbf{D}_1 \mathbf{N} \, d\Omega^e \right) \\ \mathbf{K}_2^e(T) &= \left(1 + \frac{T}{2000 \log \frac{T}{1100}}\right) \int_{\Omega^e} \mathbf{N}^T \mathbf{D}_1^T \mathbf{C} \mathbf{D}_1 \mathbf{N} \, d\Omega^e \end{aligned} \quad (3.11)$$

Using equation (3.4), the mass matrix at temperature T can be given as follows

$$\mathbf{M}^e(T) = \frac{1}{1 + \gamma \Delta T} \int_{\Omega^e} \rho \mathbf{N}^T \mathbf{N} \, d\Omega^e \quad (3.12)$$

In Fig. 4, the dispersion curves for multimodal propagation are presented according to temperature at $f = 4000$ Hz. We can note the thermal effect on the wave number, in particular on the cross sectional mode. Generally, we can confirm that the wave number increases with temperature for the multimodal propagation.

Figure 5 presents the evolution of group velocity for multimodal propagation according to temperature at $f = 4000$ Hz. The wave velocity decreases with temperature. We can say that the dispersive behavior of the traveling modes is affected by temperature elevation in the structure.

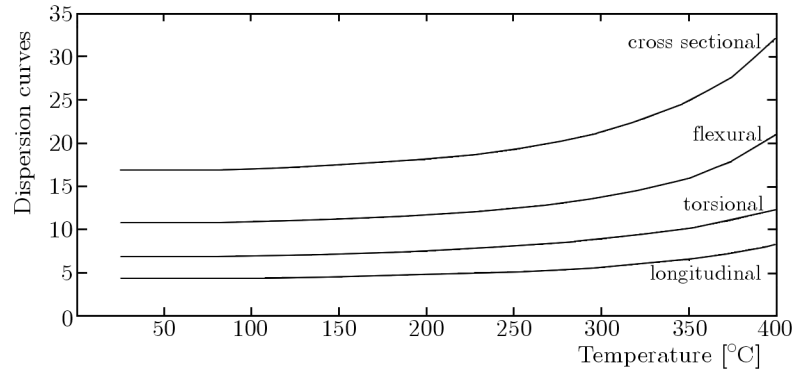


Fig. 4. Thermal dispersion curves for multimodal propagation by the TSAFE method ($f = 4000$ Hz)

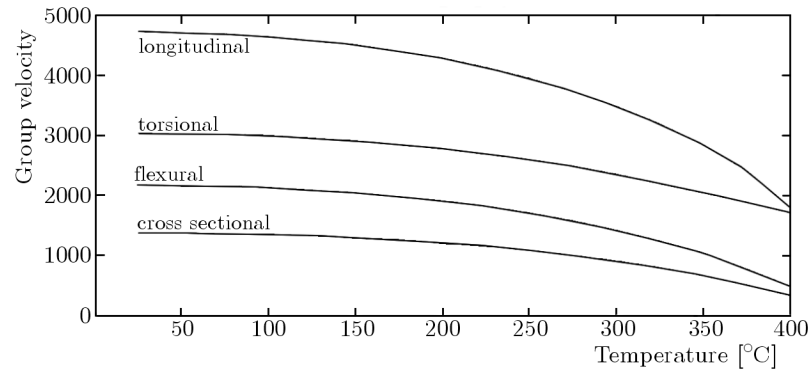


Fig. 5. Thermal group velocity for multimodal propagation by the TSAFE method ($f = 4000$ Hz)

In conclusion, this study shows the temperature effect on the characteristics of the guided waves such as dispersion and velocity. The temperature elevation causes augmentation of the dispersion curves and attenuation of the group velocity. But the guided waves save their efficiency to propagate through the structure at $T \leq 400^\circ\text{C}$ and $f \leq 4000$ Hz.

4. Conclusion

In this paper, the issue of wave propagation parameters estimation in thermal environment through the TSAFE method is dealt with. The proposed approach allows wave characteristics to be defined by dispersion curves and group velocities through thermal media. The thermal effect is introduced into the structural parameters, and by making use of the finite element techniques, the behavior of the wave dispersion is studied. Ultimately, analytical comparisons are given. The main paper findings can be extracted as follows:

- The TSAFE method based on the virtual work principle in the presence of the thermal effect is developed.
- The guided wave propagation characteristics defined by dispersion curves and group velocities are studied under thermal environment.
- The numerical accuracy and the computational efficiency of this method are demonstrated by comparison with the analytical results.

The TSAFE offers some interesting research perspectives. The use of TSAFE for energy issues in a complex wave guide is an important task in our future work. Further investigations are under progress in order to use such numerical methods in the context of smart materials and

structures. In addition of the mentioned axis, the proposed numerical method will be extended soon to the control of wave propagation in two-dimensional structures.

References

1. ALASHTI R.A., KASHIRI N., 2010, The effect of temperature variation of a simply supported curved sandwich beam with a flexible core, *Mechanical Engineering Science*, **225**, 537-547
2. DAMLJANOVIC V., WEAVER R.L., 2004, Propagating and evanescent elastic waves in cylindrical waveguides of arbitrary cross section, *Journal of the Acoustical Society of America*, **115**, 1572-1581
3. FINNVEDEN S., 2004, Evaluation of modal density and group velocity by a finite element method, *Journal of Sound and Vibration*, **273**, 51-75
4. FINNVEDEN S., FRAGGSTEDT M., 2008, Waveguide finite elements for curved structures, *Journal of Sound and Vibration*, **312**, 644-671
5. French Standard, 2007, Document: FA Rules: Prediction method by calculating the fire behavior of steel structures (in French), V2 CD-DTU-150, 92-702
6. GAVRIC L., 1995, Computation of propagative waves in free rail using a finite element technique, *Journal of Sound and Vibration*, **185**, 420-432
7. HAYASHI T., SONG W.J., ROSE J.L., 2003, Guided wave dispersion curves for a bar with an arbitrary cross-section, a rod and rail example, *Ultrasonics*, **41**, 175-183
8. JEYARAJ P., GANESAN N., PADMANABHAN C., 2009, Vibration and acoustic response of composite plate with inherent material damping in a thermal environment, *Journal of Sound and Vibration*, **320**, 322-338
9. KADOLI R., GANESAN N., 2006, Buckling and free vibration analysis of functionally graded cylindrical shells subjected to temperature-specified boundary condition, *Journal of Sound and Vibration*, **289**, 450-480
10. KODUR V., KAND S., KHALIQ W., 2012, Effect of temperature on thermal and mechanical properties of steel bolts, *Journal of Materials in Civil Engineering*, **24**, 6, 765-774
11. KONSTANTINIDIS G., DRINKWATER B.W., WILCOX P.D., 2006, The temperature stability of guided wave structural health monitoring systems, *Smart Materials and Structures*, **15**, 967-976
12. LI H.Y., HU J.D., LI J., CHEN G., 2013, Effect of tempering temperature on microstructure and mechanical properties of AISI 6150 steel, *Journal of Central South University*, **20**, 4, 866-870

Manuscript received November 20, 2014; accepted for print September 4, 2015

APPLICATION OF FRACTIONAL ORDER THEORY OF THERMOELASTICITY TO A 1D PROBLEM FOR A SPHERICAL SHELL

WALEED E. RASLAN

Mansoura University, Department of Mathematics and Engineering Physics, Mansoura, Egypt
e-mail: w_raslan@yahoo.com

In this work, we apply the fractional order theory of thermoelasticity to a one-dimensional problem of distribution of thermal stresses and temperature in a generalized thermoelastic medium in the form of a spherical shell subjected to sudden change in the temperature of its external boundary. Laplace transform techniques are used to solve the problem. Numerical results are computed and represented graphically for the temperature, displacement and stress distributions.

Keywords: fractional calculus, spherical shell, thermoelasticity

1. Introduction

Biot (1956) formulated theory of coupled thermoelasticity to eliminate the paradox inherent in the classical uncoupled theory that elastic changes have no effect on temperature. Lord and Shulman (1967) introduced theory of generalized thermoelasticity with one relaxation time by using the Maxwell-Cattaneo law of heat conduction instead of the conventional Fourier law. The heat equation associated with this theory is hyperbolic and hence eliminates the paradox of infinite speeds of propagation inherent in both the uncoupled and coupled theories of thermoelasticity. Sherief and El-Maghraby (2003, 2005) solved some crack problems for this theory. Sherief and Hamza (1994, 1996) obtained a solution to axisymmetric problems in spherical and cylindrical regions. Sherief and Ezzat (1994) obtained the solution in form of a series. Sherief *et al.* (2005) extended this theory to deal with micropolar materials. That theory was extended to deal with viscoelastic effects by Sherief *et al.* (2011). Lately, Sherief and Hussein (2012) developed theory of generalized poro-thermoelasticity.

Fractional calculus has been successfully used to modify many existing models of physical processes, see Hilfer (2000), Sherief *et al.* (2012), Tenreiro *et al.* (2013). One can state that the whole theory of fractional derivatives and integrals was established in the 2nd half of the 19th century. A good review of the subject can be found in Podlubny (1998), Kaczorek (2011), Kaczorek and Rogowski (2015). Caputo and Mainardi (1971a,b) and Caputo (1974) found a good agreement with experimental results by making use of fractional derivatives for description of viscoelastic materials and established the connection between the fractional derivatives and the theory of linear viscoelasticity. Adolfsson *et al.* (2005) constructed a new fractional order model of viscoelasticity.

Povstenko (2009) made a review of thermoelasticity that uses a fractional heat conduction equation and proposed and investigated new models that incorporate fractional derivatives (Povstenko, 2005, 2011). Recently, the fractional order theory of thermoelasticity was derived by Sherief *et al.* (2010). It was a generalization of both coupled and generalized theories of thermoelasticity. Some contributions to that theory are the works by Raslan (2015), Sherief and Abd El-Latief (2014a,b, 2015).

The aim of the present work is to solve a 1D problem for a spherical shell of a homogeneous, isotropic, thermoelastic medium occupying the region $a \leq r \leq b$ subjected to thermal shock, using the fractional theory of thermoelasticity. The main reason behind the introduction of the fractional theory is that it predicts a retarded response to physical stimuli, as is found in nature and as opposed to the instantaneous response predicted by the generalized theory of thermoelasticity (Raslan, 2015).

2. Formulation of the problem

In this work, we consider a 1D problem for a spherical shell of a homogeneous, isotropic, thermoelastic medium occupying the region $a \leq r \leq b$, using the fractional theory of thermoelasticity. The outer surface of the shell is taken to be traction free and is subjected to thermal shock that is a function of time. The inner surface of the shell is thermally isolated by a rigid material.

From physics of the problem, all functions will depend on the radial distance r and time t only. The displacement vector has only one non-zero component $u(r, t)$ in the radial direction.

The governing equations, in the absence of body forces and heat sources, are given by (Sherief *et al.*, 2010)

$$\begin{aligned} (\lambda + 2\mu) \frac{\partial e}{\partial r} - \gamma \frac{\partial T}{\partial r} &= \rho \frac{\partial^2 u}{\partial t^2} & k \nabla^2 T &= \left(\frac{\partial}{\partial t} + \tau_0 \frac{\partial^{\alpha+1}}{\partial t^{\alpha+1}} \right) (\rho c_E T + \gamma T_0 e) \\ \sigma_{rr} &= \lambda e + 2\mu \frac{\partial u}{\partial r} - \gamma(T - T_0) & q_r + \tau_0 \frac{\partial^\alpha q_r}{\partial t^\alpha} &= -k \frac{\partial T}{\partial r} \end{aligned} \quad (2.1)$$

where T is the absolute temperature, ρ is density, λ and μ are Lamé's constants and $\gamma = \alpha_t(3\lambda + 2\mu)$, where α_t is the coefficient of linear thermal expansion. T_0 is the reference temperature assumed to be such that $|(T - T_0)/T_0| \ll 1$ and α , τ_0 are constants such that $\tau_0 > 0$, $0 \leq \alpha \leq 1$, c_E is the specific heat per unit mass in the absence of deformation and k is the thermal conductivity, σ_{rr} is the normal stress component, q_r is the component of the heat flux vector in the radial direction, and e is the cubical dilatation given by

$$e = \frac{1}{r^2} \frac{\partial}{\partial r} (r^2 u) \quad (2.2)$$

The operator ∇^2 in the above equations is given by

$$\nabla^2 = \frac{\partial^2}{\partial r^2} + \frac{2}{r} \frac{\partial}{\partial r} = \frac{1}{r^2} \frac{\partial}{\partial r} \left(r^2 \frac{\partial}{\partial r} \right)$$

We shall use the following non-dimensional variables

$$\begin{aligned} r^* &= c\eta r & u^* &= c\eta u & t^* &= c^2\eta t & \tau_0^* &= c^{2\alpha}\eta^\alpha\tau_0 \\ \theta^* &= \frac{\gamma(T - T_0)}{\lambda + 2\mu} & \sigma_{rr}^* &= \frac{\sigma_{rr}}{\mu} & q^* &= \frac{\gamma}{k(\lambda + 2\mu)} q \end{aligned}$$

where

$$c = \sqrt{\frac{\lambda + 2\mu}{\rho}} \quad \eta = \frac{\rho c_E}{k}$$

The governing equations, in non-dimensional form, are given by (with the asterisk dropped for convenience)

$$\begin{aligned} \frac{\partial^2 u}{\partial t^2} &= \frac{\partial e}{\partial r} - \frac{\partial \theta}{\partial r} & \nabla^2 \theta &= \left(\frac{\partial}{\partial t} + \tau_0 \frac{\partial^{\alpha+1}}{\partial t^{\alpha+1}} \right) (\theta + \varepsilon e) \\ \sigma_{rr} &= (\beta^2 - 2)e + 2 \frac{\partial u}{\partial r} - \beta^2 \theta & q_r + \tau \frac{\partial^\alpha q_r}{\partial t^\alpha} &= -\frac{\partial \theta}{\partial r} \end{aligned} \quad (2.3)$$

where

$$\varepsilon = \frac{T_0 \gamma^2}{\lambda + 2\mu} k \eta \quad \beta^2 = \frac{\lambda + 2\mu}{\mu}$$

In the above equation, the time fractional derivative of the order α used is taken to be in the sense of the Caputo fractional derivative.

We assume that the boundary conditions have the form

$$\begin{aligned} u(a, t) = 0 & \quad q_r(a, t) = 0 \\ \sigma_{rr}(b, t) = 0 & \quad \theta(b, t) = f(t) \end{aligned} \tag{2.4}$$

The initial conditions are taken to be homogeneous, i.e. we take

$$\begin{aligned} u(r, t) \Big|_{t=0} = \frac{\partial u(r, t)}{\partial t} \Big|_{t=0} = 0 & \quad \theta(r, t) \Big|_{t=0} = \frac{\partial \theta(r, t)}{\partial t} \Big|_{t=0} = 0 \\ \sigma_{rr}(r, t) \Big|_{t=0} = \frac{\partial \sigma_{rr}(r, t)}{\partial t} \Big|_{t=0} = 0 \end{aligned} \tag{2.5}$$

3. Solution in the Laplace transform domain

Applying the Laplace transform with the parameter s (denoted by the overbar) defined by the relation

$$\bar{f}(r, s) = \int_0^\infty e^{-st} f(r, t) dt \tag{3.1}$$

to both sides of equations (2.3), we get the following equations

$$\begin{aligned} s^2 \bar{u} &= \frac{\partial \bar{\varepsilon}}{\partial r} - \frac{\partial \bar{\theta}}{\partial r} & \nabla^2 \bar{\theta} &= (s + \tau_0 s^{\alpha+1})(\bar{\theta} + \varepsilon \bar{\varepsilon}) \\ \bar{\sigma}_{rr} &= \frac{\beta^2 - 2}{r} \bar{u} + \beta^2 \frac{\partial \bar{u}}{\partial r} - \beta^2 \bar{\theta} & \bar{q}_r &= \frac{-1}{1 + \tau_0 s^\alpha} \frac{\partial \bar{\theta}}{\partial r} \end{aligned} \tag{3.2}$$

Applying the operator $\frac{1}{r^2} \frac{\partial}{\partial r}(r^2 \dots)$ to equation (3.2)₁, we obtain

$$(\nabla^2 - s^2) \bar{\varepsilon} = \nabla^2 \bar{\theta} \tag{3.3}$$

Eliminating $\bar{\theta}$ between equations (3.2)₂ and (3.3), we get

$$\left\{ \nabla^4 - \nabla^2 [s^2 + (1 + \varepsilon)(s + \tau_0 s^{\alpha+1})] + s^3(1 + \tau_0 s^\alpha) \right\} \bar{\varepsilon} = 0$$

The above equation can be factorized as

$$(\nabla^2 - k_1^2)(\nabla^2 - k_2^2) \bar{\varepsilon} = 0 \tag{3.4}$$

where k_1^2 and k_2^2 are the roots with positive real parts of the characteristic equation

$$k^4 - k^2 [s^2 + (1 + \varepsilon)(s + \tau_0 s^{\alpha+1})] + s^3(1 + \tau_0 s^\alpha) = 0 \tag{3.5}$$

where k_1^2 and k_2^2 are given by

$$\begin{aligned} k_1^2 &= \frac{s}{2} \left\{ s + (1 + \varepsilon)(1 + \tau_0 s^\alpha) + \sqrt{[s + (1 + \varepsilon)(1 + \tau_0 s^\alpha)]^2 - 4s(1 + \tau_0 s^\alpha)} \right\} \\ k_2^2 &= \frac{s}{2} \left\{ s + (1 + \varepsilon)(1 + \tau_0 s^\alpha) - \sqrt{[s + (1 + \varepsilon)(1 + \tau_0 s^\alpha)]^2 - 4s(1 + \tau_0 s^\alpha)} \right\} \end{aligned} \quad (3.6)$$

Due to linearity, the solution to equation (3.4) has the form

$$\bar{e} = \bar{e}_1 + \bar{e}_2$$

where \bar{e}_i is the solution to the following equation

$$(\nabla^2 - k_i^2)\bar{e}_i = 0 \quad i = 1, 2$$

The above equation can be written as

$$\frac{\partial^2 \bar{e}_i}{\partial r^2} + \frac{2}{r} \frac{\partial \bar{e}_i}{\partial r} - k_i^2 \bar{e}_i = 0 \quad (3.7)$$

Taking the substitution

$$\bar{e}_i = \frac{g_i}{\sqrt{r}}$$

the above equation reduces to

$$r^2 \frac{\partial^2 g_i}{\partial r^2} + r \frac{\partial g_i}{\partial r} - \left(k^2 r^2 + \frac{1}{4}\right) g_i = 0$$

This is the modified Bessel equation whose solution is

$$g_i = A_i k_i^2 I_{1/2}(k_i r) + B_i k_i^2 K_{1/2}(k_i r)$$

Collecting the above results, the solution to (3.7) can be written as

$$e_i = \frac{1}{\sqrt{r}} [A_i k_i^2 I_{1/2}(k_i r) + B_i k_i^2 K_{1/2}(k_i r)] \quad (3.8)$$

where A_i and B_i , $i = 1, 2$ are parameters to be determined from the boundary conditions and $I_\mu(z)$, $K_\mu(z)$ are the modified Bessel functions of the first and second kinds of the order μ , respectively.

Similarly, we can show that

$$\theta_i = \frac{1}{\sqrt{r}} [A_i^* k_i^2 I_{1/2}(k_i r) + B_i^* k_i^2 K_{1/2}(k_i r)] \quad (3.9)$$

Substituting (3.8) and (3.9) into equation (3.3), we get

$$A_i^* = A_i (k_i^2 - s^2) \quad B_i^* = B_i (k_i^2 - s^2) \quad (3.10)$$

Substituting (3.10) into equation (3.9), one obtains

$$\theta_i = \frac{1}{\sqrt{r}} [A_i (k_i^2 - s^2) I_{1/2}(k_i r) + B_i (k_i^2 - s^2) K_{1/2}(k_i r)] \quad (3.11)$$

Thus we obtain

$$\begin{aligned}\bar{e} &= \frac{1}{\sqrt{r}} \sum_{i=1}^2 [A_i k_i^2 I_{1/2}(k_i r) + B_i k_i^2 K_{1/2}(k_i r)] \\ \bar{\theta} &= \frac{1}{\sqrt{r}} \sum_{i=1}^2 [A_i (k_i^2 - s^2) I_{1/2}(k_i r) + B_i (k_i^2 - s^2) K_{1/2}(k_i r)]\end{aligned}\quad (3.12)$$

Differentiating (3.12) with respect to r and substituting into (3.2)₁, gives

$$\bar{u} = \frac{1}{\sqrt{r}} \sum_{i=1}^2 [A_i k_i I_{3/2}(k_i r) - B_i k_i K_{3/2}(k_i r)] \quad (3.13)$$

Differentiating (3.12)₂ and (3.13) with respect to r , gives

$$\begin{aligned}\frac{\partial \bar{\theta}}{\partial r} &= \frac{1}{\sqrt{r}} \sum_{i=1}^2 [A_i k_i (k_i^2 - s^2) I_{3/2}(k_i r) - B_i k_i (k_i^2 - s^2) K_{3/2}(k_i r)] \\ \frac{\partial \bar{u}}{\partial r} &= \frac{1}{\sqrt{r}} \sum_{i=1}^2 \left\{ A_i k_i \left[k_i I_{1/2}(k_i r) - \frac{2}{r} I_{3/2}(k_i r) \right] + B_i k_i \left[k_i K_{1/2}(k_i r) + \frac{2}{r} K_{3/2}(k_i r) \right] \right\}\end{aligned}\quad (3.14)$$

Substituting (3.12) and (3.14)₂ into equation (2.3)₃, gives

$$\sigma_{rr} = \frac{1}{\sqrt{r}} \sum_{i=1}^2 \left\{ A_i \left[\beta^2 s^2 I_{1/2}(k_i r) - \frac{4}{r} k_i I_{3/2}(k_i r) \right] + B_i \left[\beta^2 s^2 K_{1/2}(k_i r) + \frac{4}{r} k_i K_{3/2}(k_i r) \right] \right\} \quad (3.15)$$

Using equation (3.2)₄, boundary conditions (2.4) can be written in the Laplace transform as

$$\begin{aligned}\bar{u}(a, s) &= 0 & \frac{\partial \bar{\theta}(a, s)}{\partial r} &= 0 \\ \bar{\sigma}_{rr}(b, s) &= 0 & \bar{\theta}(b, s) &= \bar{f}(s)\end{aligned}\quad (3.16)$$

Applying boundary conditions (3.16) into equations (3.12)₂, (3.13), (3.14)₁ and (3.15), gives

$$\begin{aligned}\sum_{i=1}^2 [A_i k_i I_{3/2}(k_i a) - B_i k_i K_{3/2}(k_i a)] &= 0 \\ \sum_{i=1}^2 [A_i k_i (k_i^2 - s^2) I_{3/2}(k_i a) - B_i k_i (k_i^2 - s^2) K_{3/2}(k_i a)] &= 0 \\ \sum_{i=1}^2 \left\{ A_i \left[\beta^2 s^2 I_{1/2}(k_i b) - \frac{4}{b} k_i I_{3/2}(k_i b) \right] + B_i \left[\beta^2 s^2 K_{1/2}(k_i b) + \frac{4}{b} k_i K_{3/2}(k_i b) \right] \right\} &= 0 \\ \sum_{i=1}^2 [A_i (k_i^2 - s^2) I_{1/2}(k_i b) + B_i (k_i^2 - s^2) K_{1/2}(k_i b)] &= \sqrt{b} \bar{f}(s)\end{aligned}$$

The above equations can be put in the following form

$$\begin{aligned}a_{11}A_1 + a_{12}B_1 + a_{13}A_2 + a_{14}B_2 &= 0 \\ a_{21}A_1 + a_{22}B_1 + a_{23}A_2 + a_{24}B_2 &= 0 \\ a_{31}A_1 + a_{32}B_1 + a_{33}A_2 + a_{34}B_2 &= 0 \\ a_{41}A_1 + a_{42}B_1 + a_{43}A_2 + a_{44}B_2 &= \sqrt{b} \bar{f}(s)\end{aligned}$$

where

$$\begin{aligned}
 a_{11} &= k_1 I_{3/2}(k_1 a) & a_{12} &= -k_1 K_{3/2}(k_1 a) \\
 a_{13} &= k_2 I_{3/2}(k_2 a) & a_{14} &= -k_2 K_{3/2}(k_2 a) \\
 a_{21} &= k_1(k_1^2 - s^2) I_{3/2}(k_1 a) & a_{12} &= -k_1(k_1^2 - s^2) K_{3/2}(k_1 a) \\
 a_{23} &= k_2(k_2^2 - s^2) I_{3/2}(k_2 a) & a_{24} &= -k_2(k_2^2 - s^2) K_{3/2}(k_2 a) \\
 a_{31} &= \beta^2 s^2 I_{1/2}(k_1 b) - \frac{4}{b} k_1 I_{3/2}(k_1 b) & a_{32} &= \beta^2 s^2 K_{1/2}(k_1 b) + \frac{4}{b} k_1 K_{3/2}(k_1 b) \\
 a_{33} &= \beta^2 s^2 I_{1/2}(k_2 b) - \frac{4}{b} k_2 I_{3/2}(k_2 b) & a_{34} &= \beta^2 s^2 K_{1/2}(k_2 b) + \frac{4}{b} k_2 K_{3/2}(k_2 b) \\
 a_{41} &= (k_1^2 - s^2) I_{1/2}(k_1 b) & a_{42} &= (k_1^2 - s^2) K_{1/2}(k_1 b) \\
 a_{43} &= (k_2^2 - s^2) I_{1/2}(k_2 b) & a_{44} &= (k_2^2 - s^2) K_{1/2}(k_2 b)
 \end{aligned}$$

Solving the above equations, we obtain

$$\begin{aligned}
 A_1 &= -\frac{1}{\Gamma} [a_{12}(a_{23}a_{34} - a_{24}a_{33}) + a_{13}(a_{24}a_{32} - a_{22}a_{34}) + a_{14}(a_{22}a_{33} - a_{23}a_{32})] \sqrt{b} \bar{f}(s) \\
 B_1 &= \frac{1}{\Gamma} [a_{11}(a_{23}a_{34} - a_{24}a_{33}) + a_{13}(a_{24}a_{31} - a_{21}a_{34}) + a_{14}(a_{21}a_{33} - a_{23}a_{31})] \sqrt{b} \bar{f}(s) \\
 A_2 &= -\frac{1}{\Gamma} [a_{11}(a_{22}a_{34} - a_{24}a_{32}) + a_{12}(a_{24}a_{31} - a_{21}a_{34}) + a_{14}(a_{21}a_{32} - a_{22}a_{31})] \sqrt{b} \bar{f}(s) \\
 B_2 &= \frac{1}{\Gamma} [a_{11}(a_{22}a_{33} - a_{23}a_{32}) + a_{12}(a_{23}a_{31} - a_{21}a_{33}) + a_{13}(a_{21}a_{32} - a_{22}a_{31})] \sqrt{b} \bar{f}(s)
 \end{aligned}$$

where

$$\begin{aligned}
 \Gamma &= a_{11}[a_{22}(a_{33}a_{44} - a_{34}a_{43}) + a_{23}(a_{34}a_{42} - a_{32}a_{44}) + a_{24}(a_{32}a_{43} - a_{33}a_{42})] \\
 &\quad - a_{12}[a_{21}(a_{33}a_{44} - a_{34}a_{43}) + a_{23}(a_{34}a_{41} - a_{31}a_{44}) + a_{24}(a_{31}a_{43} - a_{33}a_{41})] \\
 &\quad + a_{13}[a_{21}(a_{32}a_{44} - a_{34}a_{42}) + a_{22}(a_{34}a_{41} - a_{31}a_{44}) + a_{24}(a_{31}a_{42} - a_{32}a_{41})] \\
 &\quad - a_{14}[a_{21}(a_{32}a_{43} - a_{33}a_{42}) + a_{22}(a_{33}a_{41} - a_{31}a_{43}) + a_{23}(a_{31}a_{42} - a_{32}a_{41})]
 \end{aligned}$$

4. Inversion of the Laplace transform

Let $\bar{f}(s)$ be the Laplace transform of $f(t)$. The inversion formula for the Laplace transform has the form (Honig and Hirdes, 1984)

$$f(t) = \frac{e^{dt}}{2\pi} \int_{-\infty}^{\infty} e^{ity} \bar{f}(d + iy) dy$$

where d is a number greater than all the real parts of the singularities of $\bar{f}(s)$.

Using Fourier series over the interval $[0, 2L]$, we get (Honig and Hirdes, 1984)

$$f(t) \approx f_N(t) = \frac{1}{2} c_0 + \sum_{k=1}^N c_k \quad \text{for } 0 \leq t \leq 2L \quad (4.1)$$

where

$$c_k = \frac{e^{dt}}{L} \operatorname{Re} \left[e^{\frac{ik\pi t}{L}} \bar{f} \left(d + \frac{ik\pi}{L} \right) \right] \quad (4.2)$$

The ‘Korrektur’ method has been used to reduce the discretization error while the ε -algorithm has been used to reduce the truncation error (Honig and Hirdes, 1984).

5. Numerical results

Copper has been chosen for purposes of numerical evaluations. The constants of the considered problem are shown in Table 1.

Table 1

$k = 386 \text{ W/(m K)}$	$\alpha_t = 1.78 \cdot 10^{-5} \text{ K}^{-1}$	$c_E = 381 \text{ J/(kg K)}$	$\eta = 8886.73$
$\mu = 3.86 \cdot 10^{10} \text{ kg/(m s}^2\text{)}$	$\lambda = 7.76 \cdot 10^{10} \text{ kg/(m s}^2\text{)}$	$\rho = 8954 \text{ kg/m}^3$	$T_0 = 293 \text{ K}$
$\varepsilon = 0.0168$	$\tau_0 = 0.025 \text{ s}$		

The computations have been carried out for a function $f(t)$ given by

$$f(t) = H(t) \quad \text{for which} \quad \bar{f}(s) = \frac{1}{s}$$

The computations have been carried out for one value of time, namely $t = 0.05$, and two values of α , namely $\alpha = 0.5$ and $\alpha = 1$. The temperature, displacement and stress distributions have been obtained and plotted as shown in Figs. 1, 2 and 3, respectively.

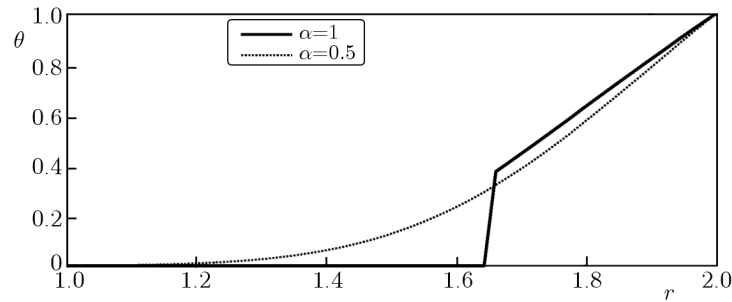


Fig. 1. Temperature distribution for $t = 0.05$

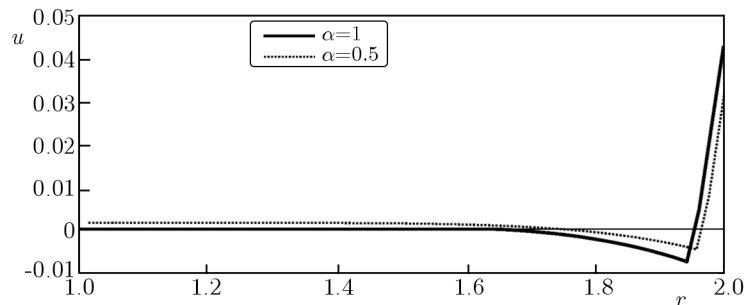


Fig. 2. Displacement distribution for $t = 0.05$

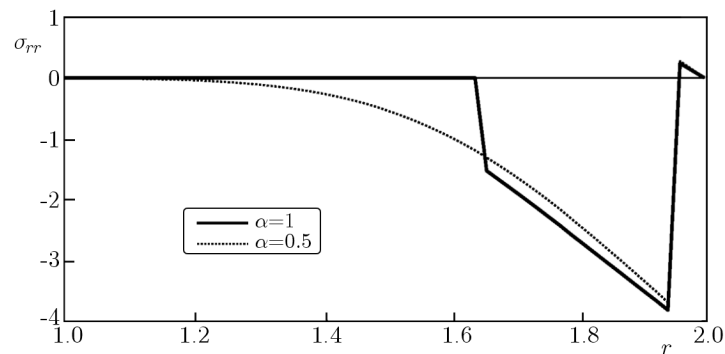


Fig. 3. Stress distribution for $t = 0.05$

Next, the computations have been carried out for one value of α , namely $\alpha = 0.99$, and two values of time, $t = 0.05$ and $t = 0.1$. The temperature, displacement and stress distributions have been obtained and plotted as shown in Figs. 4, 5 and 6, respectively.

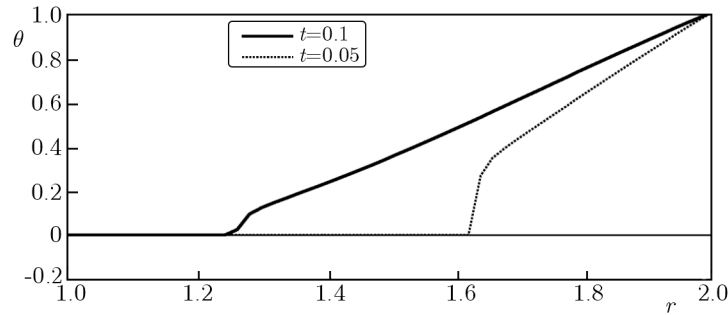


Fig. 4. Temperature distribution for $\alpha = 0.99$

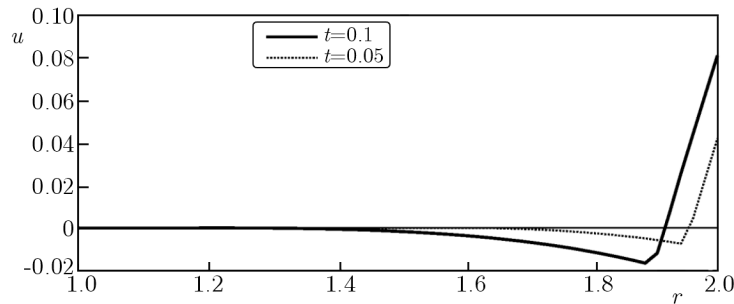


Fig. 5. Displacement distribution for $\alpha = 0.99$

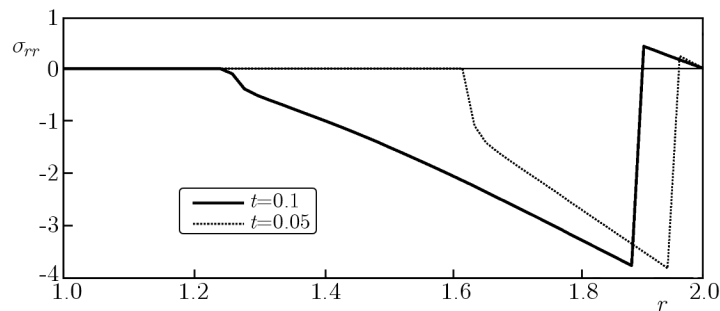


Fig. 6. Stress distribution for $\alpha = 0.99$

For the previous steps, FORTRAN programming language has been used on a personal computer. The maintained accuracy has been 5 digits for the numerical program.

6. Conclusions

The computations show that:

- For $\alpha = 0.5$, the solution behaves like in the coupled theory of thermoelasticity where the velocity of the wave is infinite, but for $\alpha = 1$ the solution becomes that of the generalized theory of thermoelasticity.
- For $\alpha \approx 1$, the solution seems to behave like in the generalized theory of thermoelasticity. This result is very important since the new theory may preserve the advantage of the generalized theory that the velocity of waves is finite. It is difficult to say whether the solution for α approaching 1 has a jump at the wave front or it is continuous with very fast changes (Povstenko, 2011). This aspect invites further investigation.

References

1. ADOLFSSON K., ENELUND M., OLSSON P., 2005, On the fractional order model of viscoelasticity, *Mechanics of Time Dependent Materials*, **9**, 15-34
2. BIOT M., 1956, Thermoelasticity and irreversible thermo-dynamics, *Journal of Applied Physics*, **27**, 240-253
3. CAPUTO M., 1974, Vibrations on an infinite viscoelastic layer with a dissipative memory, *Journal of the Acoustical Society of America*, **56**, 897-904
4. CAPUTO M., MAINARDI F., 1971a, A new dissipation model based on memory mechanism, *Pure and Applied Geophysics*, **91**, 134-147
5. CAPUTO M., MAINARDI F., 1971a, Linear model of dissipation in anelastic solids, *Rivista del Nuovo Cimento*, **1**, 161-198
6. HILFER R., 2000, *Applications of Fractional Calculus in Physics*, World Scientific Publishing, Singapore
7. HONIG G., HIRDES U., 1984, A method for the numerical inversion of the Laplace transform, *Journal of Computational and Applied Mathematics*, **10**, 113-132
8. KACZOREK T., 2011, *Selected Problems of Fractional Systems Theory*, Springer, Berlin
9. KACZOREK T., ROGOWSKI K., 2015, *Fractional Linear Systems and Electrical Circuits*, Springer, Berlin
10. LORD H., SHULMAN Y., 1967, A generalized dynamical theory of thermo-elasticity, *Journal of the Mechanics and Physics of Solids*, **15**, 299-309
11. PODLUBNY I., 1998, *Fractional Differential Equations*, Academic Press, NY
12. POVSTENKO Y.Z., 2005, Fractional heat conduction and associated thermal stress, *Journal of Thermal Stresses*, **28**, 83-102
13. POVSTENKO Y.Z., 2009, Thermoelasticity that uses fractional heat conduction equation, *Journal of Mathematical Sciences*, **162**, 296-305
14. POVSTENKO Y.Z., 2011, Fractional Cattaneo-type equations and generalized thermoelasticity, *Journal of Thermal Stresses*, **34**, 97-114
15. RASLAN W., 2015, Application of fractional order theory of thermoelasticity in a thick plate under axisymmetric temperature distribution, *Journal of Thermal Stresses*, **38**, 733-743
16. SHERIEF H., ABD EL-LATIEF A.M., 2014a, Application of fractional order theory of thermoelasticity to a 1D problem for a half-space, *ZAMM*, **94**, 509-515
17. SHERIEF H., ABD EL-LATIEF A.M., 2014b, Application of fractional order theory of thermoelasticity to a 2D problem for a half-space, *Applied Mathematics and Computation*, **248**, 584-592
18. SHERIEF H., ABD EL-LATIEF A.M., 2015, A one-dimensional fractional order thermoelastic problem for a spherical cavity, *Mathematics and Mechanics of Solids*, **20**, 512-521
19. SHERIEF H., ALLAM M., EL-HAGARY M., 2011, Generalized theory of thermoviscoelasticity and a half-space problem, *International Journal of Thermophysics*, **32**, 1271-1295
20. SHERIEF H., EL-MAGHRABY N., 2003, An internal penny-shaped crack in an infinite thermoelastic solid, *Journal of Thermal Stresses*, **26**, 333-352
21. SHERIEF H., EL-MAGHRABY N., 2005, A mode I crack problem for an infinite space in generalized thermoelasticity, *Journal of Thermal Stresses*, **28**, 465-484
22. SHERIEF H., EL-SAYED A.M.A., ABD EL-LATIEF A.M., 2010, Fractional order theory of thermoelasticity, *International Journal of Solids and Structures*, **47**, 269-275
23. SHERIEF H., EL-SAYED A.M.A., BEHIRY S.H., RASLAN W.E., 2012, Using fractional derivatives to generalize the Hodgkin-Huxley model, *Fractional Dynamics and Control*, Springer, 275-282

24. SHERIEF H., EZZAT M., 1994, Solution of the generalized problem of thermoelasticity in the form of series of functions, *Journal of Thermal Stresses*, **17**, 75-95
25. SHERIEF H., HAMZA F., 1994, Generalized thermoelastic problem of a thick plate under axisymmetric temperature distribution, *Journal of Thermal Stresses*, **17**, 435-452
26. SHERIEF H., HAMZA F., 1996, Generalized two-dimensional thermoelastic problems in spherical regions under axisymmetric distributions, *Journal of Thermal Stresses*, **19**, 55-76
27. SHERIEF H., HAMZA F., EL-SAYED A., 2005, Theory of generalized micropolar thermoelasticity and an axisymmetric half-space problem, *Journal of Thermal Stresses*, **28**, 409-437
28. SHERIEF H., HUSSEIN E., 2012, A mathematical model for short-time filtration in poroelastic media with thermal relaxation and two temperatures, *Transport in Porous Media*, **91**, 199-223
29. TENREIRO J., ALEXANDRA M., TRUJILLO J., 2013, Science metrics on fractional calculus development since 1966, *Fractional Calculus and Applied Analysis*, **16**, 479-500

Manuscript received March 22, 2014; accepted for print September 22, 2015

BINORMAL COOLING ERRORS IN SINGLE HOT-WIRE MEASUREMENTS

RAMIS ÖRLÜ, P. HENRIK ALFREDSSON

Linné FLOW Centre, KTH Mechanics, Stockholm, Sweden

e-mail: ramis@mech.kth.se

In single-wire hot-wire measurements, velocity fluctuations acting normal to the hot-wire and its prongs will cause additional heat transfer known as binormal cooling. With respect to wall turbulence, the influence of this additional cooling is well-studied for crossed wires, while it is commonly ignored in single hot-wire measurements. The latter view is challenged in the recent work by Drózdź and Elsner (2014) that claims significant errors in variance measurements when using single-wire probes in turbulent boundary layers. This short communication revisits these claims and quantifies binormal cooling errors through an expansion of the effective-velocity concept and utilisation of direct numerical simulation data. Results support the common habit that binormal cooling errors can safely be ignored in single hot-wire measurements.

Keywords: hot-wire anemometry, measurement errors, wall turbulence

1. Introduction and motivation

Hot-wire anemometry is still the method that provides the highest degree of accuracy when measuring turbulent fluctuations, in particular, when it comes to temporal and spatial resolution. Recent detailed comparisons between hot-wire measurements and direct numerical simulations (DNS) in turbulent boundary layer (TBL) flows revealed that most of the remaining differences between hot-wire measurements and DNS can be explained by insufficient spatial resolution of the measuring sensor (Örlü and Schlatter, 2013); but is with sufficient care within the scatter of various DNS. On the other hand, there are still open questions when it comes to the scaling of the streamwise velocity variance profile, in particular, with respect to turbulent pipe flows (Örlü and Alfredsson, 2012). Some of the discrepancies, besides spatial resolution (Hutchins *et al.*, 2009), could recently also be related to end-conduction effects (Miller *et al.*, 2014) and frequency response (Hutchins *et al.*, 2015) effects, while the effect of temperature fluctuations were found to be comparably mild (Örlü *et al.*, 2014).

In a recent study by Drózdź and Elsner (2014), the streamwise velocity variance profiles obtained from a single-wire (SW) and crossed-wire, i.e. X-wire (XW), probe in a TBL were compared, and the authors concluded that binormal cooling effects (i.e. velocity fluctuations acting normal to the hot-wire and its prongs that cause additional heat transfer) were not negligible. In particular, they claimed “*that the underestimation of the near-wall peak of streamwise fluctuating component in X-wire measurements results from disregarded wall-normal fluctuations, which is obviously taken [into account] in the case of a single-wire probe*”. This statement implies also that all previous comparisons of streamwise velocity statistics between SW probes and other measurement techniques such as laser Doppler velocimetry (LDV) and Particle Image Velocimetry (PIV), but also numerical simulations such as DNS, have apparently compared different quantities. The authors furthermore concluded that the readings from a SW probe should be compared to the sum of energies of the streamwise (u) and wall-normal (v) component from an

XW probe (assuming the wire is normal to the mean flow direction and parallel to the wall), i.e. $\overline{uu}_{\text{SW}}^+ = \overline{uu}_{\text{XW}}^+ + \overline{vv}_{\text{XW}}^+$, where the superscript + denotes scaling with wall units and the overbar the time-average operator. These results have consequently been used by the authors in follow-up studies (Drózdź and Elsner, 2015) as well as to compare SW results with PIV measurements (Drózdź and Uruba, 2014).

In absence of a quantification of binormal cooling errors in SW measurements in the literature and in light of the consequences, which the aforementioned claims bring for past and future SW measurements, there is a need to address this problem. This short communication will therefore revisit the statements of Drózdź and Elsner (2014), present clarifications for their observations as well as quantify binormal cooling errors based on recent DNS data. It is believed that these will not only be useful to remedy the claims made, but also give confidence in past and future SW measurements, which – none-withstanding the progress in optical measurement techniques – remains *the* measurement technique of choice when single-point streamwise velocity statistics are of interest.

2. Comments and Results

Let us start with the relevant statements by Drózdź and Elsner (2014), which will be reproduced (in *italic*) and commented on:

1) “*Most researchers who do measurements in the turbulent boundary layer believe that the influence of v component is insignificant and can be ignored, ...*”. Indeed, most researchers employing SW probes in wall-bounded flows ignore the effect of the wall-normal and spanwise velocity component as evident from a large number of studies. On the other hand, the effect of the binormal velocity component in turbulence measurements using XW probes has been studied to some extent. It is e.g. well-known that large errors can be obtained in jet flows (Ovink *et al.*, 2001), while the errors in wall-bounded flows are small, but not negligibly (Zhao and Smits, 2006). Hence, this statement by Drózdź and Elsner (2014) is correct, i.e. most researchers who do measurements with SW probes “believe” (or know) that the influence of the binormal component is insignificant, while researchers using XW probes are aware of them.

2) “*... but it is only a simplifying assumption*” and “*... from the physical point of view, the negligible small influence of the v component in a single-wire readings is not so convincing.*” To address this claim, we start out by considering the effective cooling velocity. Accounting for pitch and yaw angles of the effective cooling velocity with respect to a SW aligned normal to the flow and parallel to the wall, the effective cooling velocity (U_e) in a three-dimensional flow is given by (Jørgensen, 1971)

$$U_e^2 = U^2 + h^2 V^2 + k^2 W^2 \quad (2.1)$$

where W denotes the spanwise velocity (i.e. parallel to the hot-wire), k the yaw factor which accounts for the effects of finite wire length and the prong orientation with respect to the flow, and h the pitch factor, which is related to the binormal component. There is a rich literature with regard to the values of these two factors, but they are commonly $k \simeq 0.10$ - 0.20 and $h \simeq 1.02$ - 1.05 for standard wire probes, while they asymptote to 0 and 1 for an infinitely large length-to-diameter ratio (Bruun, 1995). Since $\overline{W} = 0$ and $\overline{V} \approx 0$ (where the overbar indicates the time-average) in the aforementioned canonical wall-bounded flows, $W = w$ and $V \approx v$. Since $h^2 \gg k^2$ and $h \approx 1$, the series expansion of Eq. (2.1) on the assumption that

$$\left| \frac{u}{U} \right|, \left| \frac{v}{U} \right|, \left| \frac{w}{U} \right| \ll 1 \quad (2.2)$$

yields for the mean effective cooling velocity

$$\overline{U}_e = \overline{U} \left(1 + \frac{v'^2}{2\overline{U}^2} + O\left[\frac{u}{\overline{U}}\right]^3 \right) \quad (2.3)$$

while the measured variance becomes

$$u_e'^2 = u'^2 \left(1 + \frac{\overline{uv^2}}{\overline{U}u'^2} - \frac{\overline{u^2v^2}}{\overline{U}^2u'^2} + \frac{\overline{v^4} - v'^4}{4\overline{U}^2u'^2} + O\left[\frac{u}{\overline{U}}\right]^5 \right) \quad (2.4)$$

where the prime denotes the root mean square (rms) value. Similar expressions for the mean and (a truncated form of the) variance can be found in Bruun (1995). As apparent $\overline{U}_e \geq \overline{U}$, since the second term in brackets in Eq. (2.3) is per definition positive, while the situation for $u_e'^2$ is dependent on the sign of the leading order term (i.e. $\sim \overline{uv^2}$). To assess the error between the measured (effective cooling) velocity and the actual horizontal velocity component, the error for the mean

$$\varepsilon_{\overline{U}_e} = \frac{\overline{U}_e - \overline{U}}{\overline{U}} = \frac{v'^2}{2\overline{U}^2} \quad (2.5)$$

and variance

$$\varepsilon_{u_e'^2} = \frac{u_e'^2 - u'^2}{u'^2} = \frac{\overline{uv^2}}{\overline{U}u'^2} - \frac{\overline{u^2v^2}}{\overline{U}^2u'^2} + \frac{\overline{v^4} - v'^4}{4\overline{U}^2u'^2} \quad (2.6)$$

are obtained.

To demonstrate the effect of the binormal velocity component on the readings of a SW probe aligned normal to the mean flow, and not be affected by data that suffers from insufficient spatial and temporal resolution, here DNS data from a TBL (Schlatter and Örlü, 2010) has been utilized. The response of a SW has been imitated by computing the statistics upon utilization of Eq. (2.1) on the time-series data, cf. Segalini *et al.* (2011) and Örlü and Schlatter (2013). Figure 1a depicts the “true” and “measured” (i.e. effective) mean and variance profile. As apparent, the difference between \overline{U}_e and \overline{U} as well as $u_e'^2$ and u'^2 is barely visible and can hence, as commonly done, safely be neglected. The obtained statistics can now be used to compute the aforementioned errors and compare them with the derived simplified expressions given above as depicted in Fig. 1b,c. The mean streamwise velocity is overestimated up to 0.3%, while the variance is underestimated

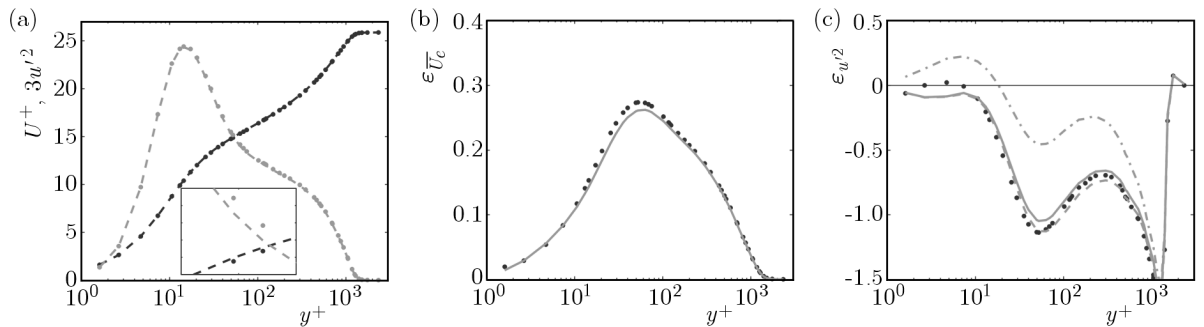


Fig. 1. (a) Inner-scaled mean and variance profile for a TBL at $Re_\tau \approx 1200$ (Schlatter and Örlü, 2010) with the dashed line and dots indicating “measured” (i.e. effective) and real values, respectively. Inset shows the region around $y^+ = 50$, where the error in the mean and variance has its maximum.

Percentile error in the (b) mean velocity and (c) variance, where dots indicate the results computed from the DNS through Eq. (2.1) and the solid line represent the approximation given through Eqs. (2.5) and (2.6). The dashed and dash-dotted line in (c) denote Eq. (2.6) with only the first two and the first term, respectively

up to 1%. This is in contrast to the errors induced in XW measurements when ignoring the binormal velocity, which are approximately fivefold (Zhao and Smits, 2006). Although these errors are obtained for a TBL at a specific Reynolds number, the estimated errors can directly be transferred to pipe and channel flows as well. Furthermore, the errors are representative for a wide range of Reynolds numbers due to the logarithmic dependence of the variance amplitudes (Alfredsson *et al.*, 2011). With regards to the initial statement that “*the negligible small influence of the v component in a single-wire readings is not so convincing*”, it can now clearly be stated that binormal cooling effects on SW probes can safely be neglected in wall-bounded flows, under the premise that assumption (2.2) is not severely violated.¹

3) Drózdź and Elsner (2014) furthermore observed, with respect to a XW, that “*the vector summing these two components (i.e. \overline{uu}_{XW}^+ and \overline{vv}_{XW}^+), obtained from the X-wire probe, gives the shape of fluctuation distribution obtained from the SW (i.e. \overline{uu}_{SW}^+) probe*”. Consequently, the authors compared $(\overline{uu}^+ + \overline{vv}^+)_{XW}$ (Drózdź and Elsner, 2014) or $(\overline{uu}^+ + \overline{vv}^+)_{PIV}$ (Drózdź and Uruba, 2014) and not directly the measured \overline{uu}^+ component with the variance read from a SW probe and found a seemingly better agreement as demonstrated in Fig. 2a, which is a reproduction from Drózdź and Elsner (2014). This proposed workaround is, however, at odds with the aforementioned results, which demonstrated that binormal cooling errors are safely negligible in turbulent boundary layer measurements. Streamwise and wall-normal velocity fluctuations are furthermore strongly anti-correlated and the simple addition of the energies is principally only permissible for fully uncorrelated signals. The reason why the summation of measured variances from an XW probe or PIV measurements lead to a better agreement with SW measurements in the work by Drózdź and Elsner (2014) and Drózdź and Uruba (2014) is simply related to the larger viscous-scaled wire length utilized for the XW measurements (the length of the XW was around three times longer than that of the SW), which causes attenuation of the fluctuation amplitudes (Örlü and Alfredsson, 2010). This can simply be shown by utilising any of the available spatial resolution correction schemes for hot-wire measurements available in the literature (e.g. Segalini *et al.*, 2011; Smits *et al.*, 2011). As demonstrated in Fig. 2b, the streamwise variance profile measured by the SW, \overline{uu}_{SW}^+ , compares well with DNS data and is apparently well-resolved. Matching now the viscous-scaled wire length of the SW with that of the employed XW, by utilization of the scheme by Smits *et al.* (2011), the variance profile attenuates towards the variance read by the XW, \overline{uu}_{XW}^+ . The comparison with the DNS data also reveals that the wall-normal variance profile becomes increasingly overestimated the closer

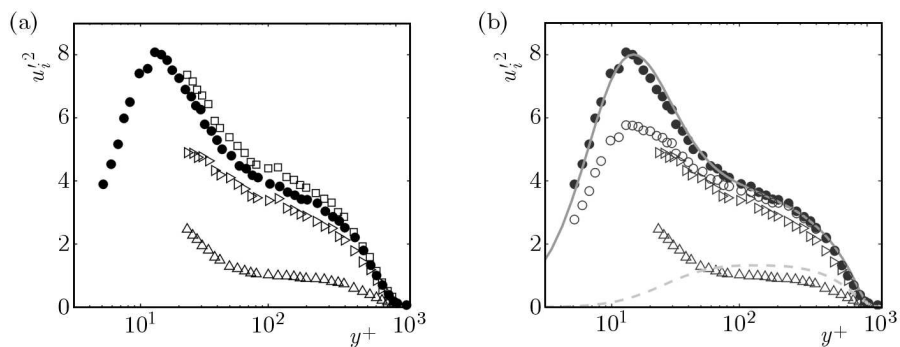


Fig. 2. Inner-scaled variance profile for a TBL at $Re_\tau \approx 1000$ with data taken from Fig. 3 of Drózdź and Elsner (2014). (a) SW, \overline{uu}_{SW}^+ : \bullet , X-wire, \overline{uu}_{XW}^+ : \triangleright , \overline{vv}_{XW}^+ : \triangle , and $\overline{uu}_{XW}^+ + \overline{vv}_{XW}^+$: \square ; (b) reverse application of the spatial resolution correction scheme by Smits *et al.* (2011) on the SW data (\bullet) to match the less resolved of the X-wire (\circ). For reference, also DNS from Schlatter and Örlü (2010) at the same Re for \overline{uu}^+ (—) and \overline{vv}^+ (---) is shown

¹In this respect, it is also worth referring to Kalpakli Vester *et al.* (2015), where the results from a SW and PIV measurements in a rotating pipe flow are compared.

to the wall the probe is. Such an increase is well documented and known to be related to the spatial resolution as well as the spacing between the two inclined wires (Talamelli *et al.*, 2000).

3. Conclusions

The present short communication addresses the claims made by Drózdź and Elsner (2014), viz. that binormal cooling errors in SW measurements are not negligible in wall turbulence. They further claimed that the measured variance by a SW probe needs to be compared to the sum of energies from the streamwise and wall-normal components, e.g. when comparing with results from XW or PIV measurements. These claims have been addressed by means of a simple expansion of the effective velocity, which showed that the effect of binormal cooling in SW measurements can – under the premise that assumption (2.2) is not severely violated – safely be neglected. The results have also been validated by means of DNS data and provide a quantification of binormal cooling errors, which has been missing in the literature, and might have given rise to the claims by Drózdź and Elsner (2014).

References

1. ALFREDSSON P.H., SEGALINI A., ÖRLÜ R., 2011, A new scaling for the streamwise turbulence intensity in wall-bounded turbulent flows and what it tells us about the “outer” peak, *Physics of Fluids*, **23**, 041702
2. BRUUN H.H., 1995, *Hot-Wire Anemometry: Principles and Signal Analysis*, Oxford University Press Inc., New York, USA
3. DRÓZDŹ A., ELSNER W., 2014, Comparison of single and X-wire measurements of streamwise velocity fluctuations in turbulent boundary layer, *Journal of Theoretical and Applied Mechanics*, **52**, 499-505
4. DRÓZDŹ A., ELSNER W., 2015, Analysis of hot-wire measurements accuracy in turbulent boundary, *Open English*, **5**, 307-313
5. DRÓZDŹ A., URUBA V., 2014, Comparison of PIV and hot-wire statistics of turbulent boundary layer, *Journal of Physics: Conference Series*, **530**, 012044
6. HUTCHINS N., MONTY J.P., HULTMARK M., SMITS A.J., 2015, A direct measure of the frequency response of hot-wire anemometers: temporal resolution issues in wall-bounded turbulence, *Experiments in Fluids*, **56**, 18
7. HUTCHINS N., NICKELS T.B., MARUSIC I., CHONG M.S., 2009, Hot-wire spatial resolution issues in wall-bounded turbulence, *Journal of Fluid Mechanics*, **635**, 103-136
8. JØRGENSEN F.E., 1971, Directional sensitivity of wire and fiber-film probes, *DISA Information*, **11**, 31-37
9. KALPAKLI VESTER A., SATTARZADEH S.S., ÖRLÜ R., 2015, Combined hot-wire and PIV measurements of a swirling turbulent flow at the exit of a 90° pipe bend, *Journal of Visualization*, doi:10.1007/s12650-015-0310-1
10. MILLER M.A., ESTEJAB B., BAILEY S.C.C., 2014, Evaluation of hot-wire spatial filtering corrections for wall turbulence and correction for end-conduction effects, *Experiments in Fluids*, **55**, 1735
11. ÖRLÜ R., ALFREDSSON P.H., 2010, On spatial resolution issues related to time-averaged quantities using hot-wire anemometry, *Experiments in Fluids*, **49**, 101-110
12. ÖRLÜ R., ALFREDSSON P.H., 2012, Comment on the scaling of the near-wall streamwise variance peak in turbulent pipe flows, *Experiments in Fluids*, **54**, 1431

13. ÖRLÜ R., MALIZIA F., CIMARELLI A., SCHLATTER P., TALAMELLI A., 2014, The influence of temperature fluctuations on hot-wire measurements in wall-bounded turbulence, *Experiments in Fluids*, **55**, 1781
14. ÖRLÜ R., SCHLATTER P., 2013, Comparison of experiments and simulations for zero pressure gradient turbulent boundary layers at moderate Reynolds numbers, *Experiments in Fluids*, **54**, 1547
15. OVINK R., LAMERS A.P.G.G., VAN STEENHOVEN A.A., HOEIJMAKERS H.W.M., 2001, A method of correction for the binormal velocity fluctuation using the look-up inversion method for hot-wire anemometry, *Measurement Science and Technology*, **12**, 1208
16. SCHLATTER P., ÖRLÜ R., 2010, Assessment of direct numerical simulation data of turbulent boundary layers, *Journal of Fluid Mechanics*, **659**, 116-126
17. SEGALINI A., ÖRLÜ R., SCHLATTER P., ALFREDSSON P.H., RÜEDI J.D., TALAMELLI A., 2011, A method to estimate turbulence intensity and transverse Taylor microscale in turbulent flows from spatially averaged hot-wire data, *Experiments in Fluids*, **51**, 693-700
18. SMITS A.J., MONTY J.P., HULTMARK M., BAILEY S.C.C., HUTCHINS N., MARUSIC I., 2011, Spatial resolution correction for wall-bounded turbulence measurements, *Journal of Fluid Mechanics*, **676**, 41-53
19. TALAMELLI A., WESTIN K.J.A., ALFREDSSON P.H., 2000, An experimental investigation of the response of hot-wire X-probes in shear flows, *Experiments in Fluids*, **28**, 425-435
20. ZHAO R., SMITS A.J., 2006, Binormal cooling errors in crossed hot-wire measurements, *Experiments in Fluids*, **40**, 212-217

Manuscript received August 19, 2015; accepted for print November 13, 2015

SEMI-ACTIVE LINEAR VACUUM PACKED PARTICLES DAMPER

ROBERT ZALEWSKI, PAWEŁ CHODKIEWICZ

Warsaw University of Technology, Institute of Machine Design Fundamentals, Warsaw, Poland
e-mail: robertzalewski@wp.pl; pawel@chodkiewicz.com.pl

In this paper, the authors focus on the proposition of an innovative semi-active linear damper prototype working on the basis of granular materials. Vacuum Packed Particles (VPP) belong to the class of materials whose mechanical (rheological, dissipative) properties may be quickly changed by applying a partial vacuum inside the system. The concept of an innovative linear damper based on VPP is presented in the paper. Typical experimental results are presented to reveal changeable damping characteristics of the device. Additionally, the mathematical model is proposed to capture extraordinary features of the investigated damper.

Keywords: Vacuum Packed Particles, modeling, underpressure, experiments

1. Introduction

Vacuum Packed Particles (VPP) are a class of “smart structures” whose physical properties may be rapidly changed by pulling out the pressure from the system and generating the so called underpressure. This change is in proportion to the magnitude of the internal partial vacuum generated and is quickly reversible. VPP, from the macroscopic point of view, are viscoplastic solid bodies and can be modeled by various constitutive models (Zalewski and Pyrz, 2013). The VPP structure can be also compared to magnetorheological materials and, consequently, modeled by typical rheological models developed for MR fluids. Typical, well commercialized engineering applications of VPP are universal robot grippers (Brown *et al.*, 2010), flexible endoscopes (Loeve *et al.*, 2010), “smart layers” in sandwich beam structures (Bajkowski *et al.*, 2015) or vacuum mattresses (Luscombe and Williams, 2003).

The discussed granular structures are conglomerates that consist of loose granular materials placed in a soft and hermetic envelope. When exposed to a partial vacuum, the so called “jamming mechanism” occurs and loose particles interact to form a solid-like structure that resists various types of deformations or flow (Cates *et al.*, 1998). This change in the structure appears as a dramatic increase in apparent viscosity, and the “plastic” structure develops characteristics of a semisolid state (Majmudar *et al.*, 2007). The magnitude of this transformation is controlled by the value of the partial vacuum and is immediately reversed upon removing the underpressure.

Noting the apparent similarities of the considered VPP and magnetorheological (MR) fluids (Makowski and Knap, 2014), the authors propose an “innovative” semi-active linear VPP damper prototype. Taking advantage of the previous, fundamental research on VPP, in this paper the authors propose an original engineering application of the previously mentioned granular conglomerates. In the modeling Section, a mathematical model including damage functions is proposed. Typical laboratory tests results are presented in the experimental Section. The impact of underpressure on recorded dissipative characteristics is introduced and discussed. The model has been calibrated using an Evolutionary Algorithm.

2. Model of the system

In our experiment we consider a system that consists of a spring that is attached to a rigid support at the top and has a mass attached to it at the bottom end (Fig. 1). The spring encloses a flexible and hermetically sealed sleeve that is full with a granular material, which acts as the damper.

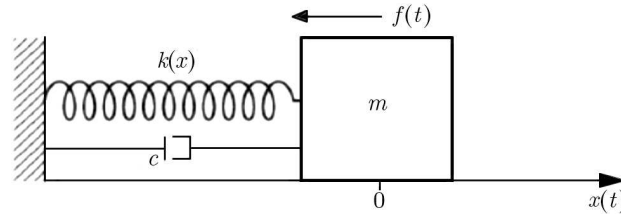


Fig. 1. Model of the nonlinear mass-spring-damper system

To capture real behavior of the proposed VPP damper prototype, the following mathematical model is proposed

$$\begin{aligned} \dot{v} + c\zeta v + kx + \mu g \operatorname{sgn}(v) &= f \\ D(t) &= d_s \int_0^t |v(s)| ds \\ \dot{\zeta} &= -d_f(|x| - \lambda_f)_+ - D \\ x(0) &= x_0 \quad v(0) = v_0 \quad \zeta(0) = \zeta_0 \end{aligned} \quad (2.1)$$

where m , k , c are positive material coefficients, μ is the coefficient of friction and g is the gravitational acceleration. The introduced D function with the rate d_s is related to gradual wear of single grains caused by the “intergranular” friction phenomenon. The global damage function ζ also consists of the part related to rearrangement of the grains along the total path traveled. The damping damage coefficients d_f and d_s are based on experiments, and we assume that they depend on the underpressure. λ_f is the critical amplitude below which the granular material does not change its internal arrangement.

The problem is rewritten as a system of three first order differential equations with appropriate initial conditions. A forward-type Euler algorithm (2.2) has been used to solve the system (2.1)

$$\begin{aligned} v_{n+1} &= v_n - \frac{cv_n - kx_n + \mu g \operatorname{sgn}(v_n) + f_{n+1}}{m} h \\ x_{n+1} &= x_n + v_{n+1} h \\ D_{n+1} &= D_n + d_s |v_{n+1}| h \\ \zeta_{n+1} &= \zeta_n - [d_f(|x_{n+1}| - \lambda_f)_+ - D_{n+1}] h \end{aligned} \quad (2.2)$$

3. Experiments

The structural scheme of the device is depicted in Fig. 2. It consists of two rigid discs (3, 5), coupled by the main spring (2). The heart of the device is a granular core (4). It is formed of a cylindrical envelope filled by loose plastomer grains (also small cylinders). Thanks to the special valve mounted in a handle (1), it is possible to connect the system to a vacuum pump and generate the appropriate value of a partial vacuum inside the system.

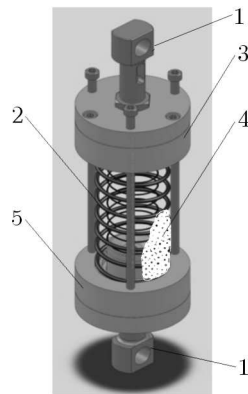


Fig. 2. Scheme of the investigated damper; 1 – handles, 2 – spring, 3 – upper disc, 4 – granular core, 5 – lower disc

The VPP damper prototype has been investigated on a specially designed laboratory stand (Fig. 3). A kinematical sine excitation rule with various frequencies was considered in the laboratory tests. Different underpressure values from the range 0.01 to 0.09 MPa were taken into considerations. Typical experimental results are depicted in Fig. 4.



Fig. 3. Laboratory stand for investigations of VPP dampers

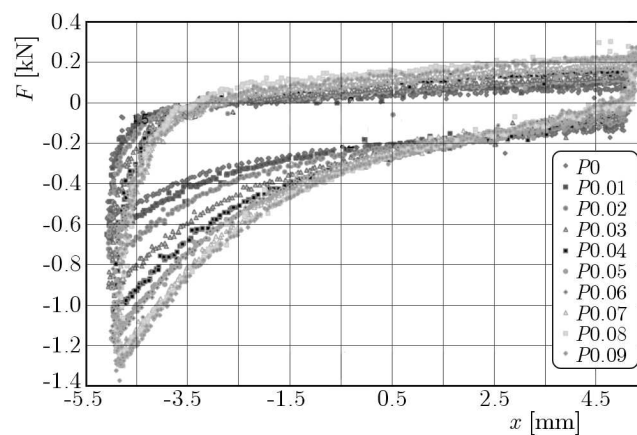


Fig. 4. Damping characteristics of the VPP damper for various values of underpressure and the excitation frequency $f = 1.4$ Hz

Analyzing the experimental results presented in Fig. 4, it can be observed that the underpressure parameter has a great impact on the recorded energy dissipation loops. A higher

underpressure value results in increased damping properties of the VPP damper prototype. This phenomenon shows that changing the value of partial vacuum inside the system enables one to control the global properties of the discussed devices. In the authors opinion, it confirms that investigated devices can be placed among the family of “smart dampers” next to MR or ER devices.

The recorded data also reveal a nonsymmetrical response of the damper, which complicates the mathematical description of the damper. The results of laboratory tests, in the next stage of research, are the base for the mathematical model calibration process.

4. Model calibration

The model has been calibrated for two various values of the underpressure. We used the Evolutionary Algorithm (EA) optimization method to find 6 parameters of the model presented in Section 2. The EA developed in the *Mathematica* software applies a population of 40 individuals and simulated the evolution process for 200 generations. Each iterative step includes three stages: selection, mutation and crossover. Crossover and mutation operators are applied randomly with 50% probability. The following fitness function is taken into consideration

$$E_r = \frac{1}{n} \sum_{i=1}^n \frac{|F_{exp}^i - F^i|}{|F_{exp}^i|} \rightarrow \min \quad (4.1)$$

where F_{exp} is a temporary experimental force value, F – numerical force value, n – total number of discrete points.

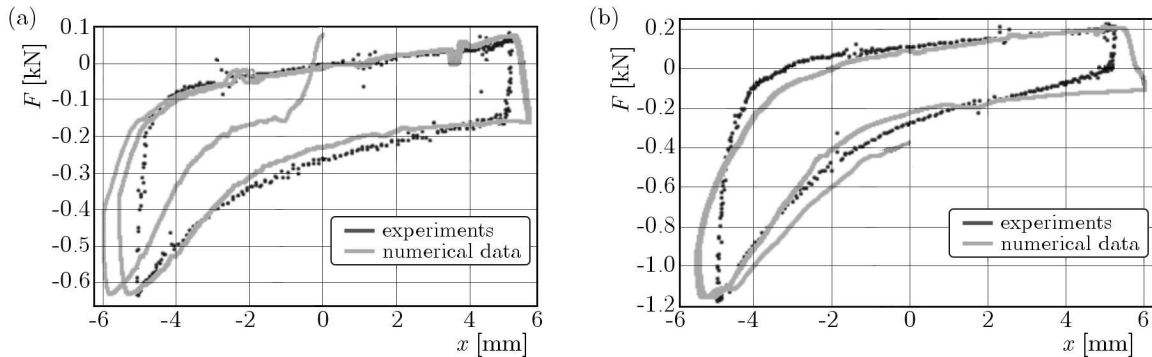


Fig. 5. Verification of the model calibration processes for (a) $P = 0.01$ MPa; (b) $P = 0.07$ MPa

The old population is replaced by new individuals for which new fitness values are calculated. The best results obtained after 200 iterations are presented in Table 1. The numerical simulation results carried out for the identified model parameters have been verified with direct experimental data (Fig. 5). In the initial step of numerical investigations, damage functions $(2.1)_{2,3}$ were turned off during the calibration process. As the properties of the VPP damper are influenced by the underpressure value and the direction of velocity (Fig. 4), we assumed that all investigated parameters can be described as

$$c(P, \text{sgn}(v)) = \begin{cases} c_0 & \text{for } v \geq 0 \\ c_1 & \text{for } v < 0 \end{cases} \quad k(P, \text{sgn}(v)) = \begin{cases} k_0 & \text{for } v \geq 0 \\ k_1 & \text{for } v < 0 \end{cases}$$

$$n(P, \text{sgn}(v)) = \begin{cases} n_0 & \text{for } v \geq 0 \\ -n_1 & \text{for } v < 0 \end{cases}$$

Finally, the estimated values of the model parameters for two selected underpressures (0.01 and 0.07 MPa) are presented in Table 1. For the simplicity of calculations it has been assumed that $n = \mu g$.

Table 1. Model parameters for various underpressure values

P [MPa]	c_0 [kg/s]	k_0 [kN/mm]	c_1 [kg/s]	k_1 [kN/mm]	n_0 [kN]	n_1 [kN]
0.01	34.14	42.22	50.57	145.51	0.40	0.44
0.07	72.53	117.96	51.10	297.13	0.82	0.69

5. Conclusions

In the paper, an innovative semi-active damper prototype, based on Vacuum Packed Particles is proposed and investigated. The experimental results confirmed the possibility of controlling the dissipative properties of the device by changing the value of partial vacuum. Higher underpressure provides intensification of grains compaction and results in increasing the damping properties of the device.

The proposed mathematical model assumes two types of damage functions. Most important damage mechanisms, encountered during experimental research, are related to the ongoing wear of single grains material and large, exceeding the assumed range, rearrangements of the granular system.

The model has been calibrated basing on the obtained experimental results using the EA strategy. Verification of the numerical and laboratory tests results revealed quite a good correctness of the proposed model (global error less than 7%).

The previous experimental research did not include destructive tests of the investigated VPP prototype. To identify the damage functions, a multi-cycle loading of the testing device has to be applied. Moreover, the nonlinear underpressure functions have to be identified and introduced to the proposed model.

Future design works should be focused on developing semi-active granular devices with optional, not necessarily nonsymmetrical damping characteristics.

In the authors' opinion, semi-active linear VPP dampers may in a near future replace much more expensive and complex magnetorheological or electrorheological devices. More than 500 times cheaper and uncomplicated VPP dampers seem to be competitive to already well commercialized and popular "intelligent" dampers.

References

1. BAJKOWSKI J.M., DYNIEWICZ B., BAJER C.I., 2015, Damping properties of a beam with vacuum-packed granular damper, *Journal of Sound and Vibration*, **341**, 74-85
2. BROWN E., RODENBERG N., AMEND J., ET AL., 2010, Universal robotic gripper based on the jamming of granular material, *Proceedings of the National Academy of Sciences of the United States of America*, **107**, 44, 18809-18814
3. CATES M.E., WITTMER J.P., BOUCHAUD J.P., CLAUDIN P., 1998, Jamming, force chains and fragile matter, *Physical Review Letters*, **81**, 1841-1844
4. LOEVE A.J., VAN DE VEN O.S., VOGEL J.G., BREEDVELD P., DANKELMANN J., 2010, Vacuum packed particles as flexible endoscope guides with controllable rigidity, *Granul Matter*, **12**, 6, 543-54
5. LUSCOMBE M.D., WILLIAMS J.L., 2003, Comparison of a long spinal board and vacuum mattress for spinal immobilization, *Emergency Medicine Journal*, **20**, 1, 476-478

6. MAJMUDAR T.S., SPERL M., LUNDIG S., BEHRINGER R.P., 2007, Jamming transition in granular systems, *Physical Reviews Letters*, **98**, 058001
7. MAKOWSKI M., KNAP L., 2014, Reduction of wheel force variations with magnetorheological devices, *Journal of Vibration and Control*, **20**, 10, 1552-1564
8. ZALEWSKI R., PYRZ M., 2013, Experimental study and modeling of polymer granular structures submitted to internal underpressure, *Mechanics of Materials*, **57**, 75-85

Manuscript received June 10, 2014; accepted for print November 29, 2015

INFORMATION FOR AUTHORS

Journal of Theoretical and Applied Mechanics (JTAM) is devoted to all aspects of solid mechanics, fluid mechanics, thermodynamics and applied problems of structural mechanics, mechatronics, biomechanics and robotics. Both theoretical and experimental papers as well as survey papers can be proposed.

We accept articles in English only. The text of a *JTAM* paper should not exceed **12 pages of standard format A4** (11-point type size, including abstract, figures, tables and references).

- The material for publication should be sent to the Editorial Office via electronic journal system: <http://www.ptmts.org.pl/jtam/index.php/jtam>

Papers are accepted for publication after the review process. Blind review model is applied, which means that the reviewers' names are kept confidential to the authors. The final decision on paper acceptance belongs to the Editorial Board.

- After qualifying your paper for publication we will require the following:
 - L^AT_EX or T_EX or Word document file
 - graphical files in grey scale, 300 dpi, in print quality (e.g.: *.png, *.bmp, *.jpg, *.eps).

Requirements for paper preparation

Contents of the manuscripts should appear in the following order:

- Title of the paper
- Authors' full name, affiliation and e-mail
- Short abstract (maximum 100 words) and 3-5 key words (1 line)
- Article text (equations should be numbered separately in each section; each reference should be cited in the text by the last name(s) of the author(s) and the publication year)
- References in alphabetical order. See the following:
 1. Achen S.C., 1989, A new boundary integral equation formulation, *Journal of Applied Mechanics*, **56**, 2, 297-303
 2. Boley B.A., Weiner J.H., 1960, *Theory of Thermal Stresses*, Wiley, New York
 3. Canon W., 1955, Vibrations of heated beams, Ph.D. Thesis, Columbia University, New York
 4. Deresiewicz H., 1958, Solution of the equations of thermoelasticity, *Proceedings of Third U.S. National Congress of Applied Mechanics*, 287-305
- Titles of references originally published not in English, should be translated into English and formulated as follows:
 5. Huber M.T., 1904, Specific work of strain as a measure of material effort (in Polish), *Czasopismo Techniczne*, **XXII**, 3, 80-81

All the data should be reported in SI units.

New *JTAM* offer for short communication!

Since July 2013, short research communications have been accepted for publication in *JTAM* with all the requirements concerning standard publications, except for their volume that is limited to 4 pages.
